



International Committee for Future Accelerators

Sponsored by the Particles and Fields Commission of IUPAP

Beam Dynamics Newsletter

No. 69

**Issue Editor:
E. Métral**

**Editor in Chief:
Y. H. Chin**

December 2016

Contents

1 FOREWORD	5
1.1 FROM THE CHAIR	5
1.2 FROM THE EDITOR	6
2 THEME SECTION: COLLECTIVE EFFECTS IN PARTICLE ACCELERATORS	8
2.1 INTRODUCTION TO COLLECTIVE EFFECTS IN PARTICLE ACCELERATORS	8
2.1.1 Introduction	8
2.1.2 Space Charge	9
2.1.3 Wake Fields and Impedances, Classical instabilities	9
2.1.4 Coherent Synchrotron Radiation	10
2.1.5 Beam-Beam Interaction	11
2.1.6 Touschek and Intrabeam Scattering	12
2.1.7 Ion Effects	12
2.1.8 Electron Cloud	13
2.1.9 Dust Particles	13
2.1.10 Compound Effects	13
2.1.11 Acknowledgements	13
2.1.12 References	13
2.2 SPACE CHARGE EFFECTS IN LOW ENERGY BEAM TRANSPORT AND LINACS	18
2.2.1 Introduction	18
2.2.2 Space Charge Control in Low Energy Beam Transport, Neutralisation	18
2.2.3 Space Charge in the First Stage of Acceleration (Radio Frequency Quadrupoles)	20
2.2.4 Space Charge in LINACS	21
2.2.5 Space Charge Independent Matching	21
2.2.6 Emittance Reconstruction in Presence of Space Charge	29
2.2.7 References	30
2.3 EFFECT OF SPACE CHARGE AND NONLINEARITIES IN CIRCULAR MACHINES	31
2.3.1 The Issue of Space Charge Limit	31
2.3.2 Space Charge Induced Resonance Crossing	31
2.3.3 Third Order Coupling Resonance	31
2.3.4 Third Order Resonance Mitigation	33
2.3.5 Effect of High Intensity on Bunch Dynamics	35
2.3.6 Issues 36	
2.3.7 Acknowledgment	37
2.3.8 References	37
2.4 INTRABEAM SCATTERING	38
2.4.1 Introduction	38
2.4.2 Piwinski Model	38

2.4.2.1	<i>Collisional Momentum Kinematic and Emittance Variations</i>	38
2.4.2.2	<i>Averaging over the Scattering Angles and All Particles</i>	40
2.4.2.3	<i>Calculation of Rise Times Neglecting α_x, z and Dx, z'</i>	42
2.4.2.4	<i>Invariant</i>	44
2.4.3	Bjorken-Mtingwa Model	45
2.4.3.1	<i>Beam Phase Space Density and Invariants</i>	45
2.4.3.2	<i>Two-Body Scattering: Rate of Change of Emittances and Momentum</i>	46
2.4.3.3	<i>Intrabeam Scattering Growth Rates</i>	47
2.4.4	Zenkevich Model	48
2.4.4.1	<i>Fokker-Planck Formalism</i>	48
2.4.4.2	<i>Single Pair-Collision Event</i>	50
2.4.4.3	<i>Monte Carlo Binary Collision Model</i>	52
2.4.5	Benchmarking of the IBS Theoretical Models with Monte-Carlo Codes	55
2.4.6	Summary	58
2.4.7	Acknowledgements	58
2.4.8	References	58
2.5	THE BIRTH AND CHILDHOOD OF THE COUPLING IMPEDANCE AND STABILITY MAPS	60
2.5.1	The First Breakthrough Innovation: the Phase Stability	60
2.5.2	The Second Breakthrough Innovation: the Alternating Gradient	60
2.5.3	The Collider Age. Looking Far	60
2.5.3.1	<i>Hamburger Intermezzo</i>	61
2.5.3.2	<i>Collider Contest: Frascati vs. Princeton</i>	61
2.5.4	The Analysis of Instabilities. A Step Forward	62
2.5.5	An Impedance is in the Air. The Banality of Invention	62
2.5.6	The Universal Stability Charts	63
2.5.7	References	65
2.6	WAKEFIELDS AND IMPEDANCES	67
2.6.1	Introduction	67
2.6.2	Definition of Wakes	67
2.6.3	The “Catch-Up” Distance	69
2.6.4	Transverse Wakes in Axisymmetric Systems	70
2.6.5	Wakefield of a Bunch of Particles	70
2.6.6	Wake at Origin for a Periodic Structure	71
2.6.7	Impedances	72
2.6.8	Resonator Wakefield and Impedance	73
2.6.9	Resistive Wall Impedance	74
2.6.10	References	76
2.7	WAKE FIELD AND BEAM COUPLING IMPEDANCE SIMULATIONS	78
2.7.1	Introduction	78
2.7.2	Definitions and Assumptions for the Computation of Wakefields and Impedances	78
2.7.3	Time Domain Simulation Tools and Methods	80
2.7.4	Flexible RF-Finger Structures	80
2.7.5	Frequency Domain Solver Example	84
2.7.6	Acknowledgements	86

2.7.7	References	86
2.8	BEAM-COUPLING IMPEDANCE AND WAKE FIELD – BENCH MEASUREMENTS.....	88
2.8.1	Introduction	88
2.8.2	The Coaxial Wire Method	88
2.8.2.1	<i>Motivation and Validation</i>	89
2.8.2.2	<i>Longitudinal Coupling Impedance</i>	90
2.8.2.3	<i>Transverse Coupling Impedance</i>	93
2.8.3	Resonant Structures	94
2.8.4	Conclusions	95
2.8.5	References	95
2.9	BUILDING THE IMPEDANCE MODEL OF A REAL MACHINE	97
2.9.1	Introduction	97
2.9.2	Assess Impedance of Individual Elements	98
2.9.2.1	<i>Calculation of the Beam Couplings Impedance</i>	98
2.9.2.2	<i>Bench Measurements of the Beam Coupling Impedance: the Wire Method</i>	100
2.9.2.3	<i>Summing the Different Impedance Sources to Build the Impedance Model of a Real Machine</i>	101
2.9.3	Compute Beam Observables and Compare with Measurements.....	101
2.9.3.1	<i>Single Bunch Tune Shift / Growth Rate versus Intensity</i>	101
2.9.3.2	<i>Impedance Localization Techniques</i>	103
2.9.3.3	<i>Single Bunch Octupole Threshold</i>	104
2.9.4	References	105
2.10	WAKE FIELD DRIVEN BEAM INSTABILITIES AND DAMPING MECHANISMS IN LINEAR MACHINES	110
2.10.1	Introduction	110
2.10.2	Wake Fields Effects in Linear Accelerators.....	110
2.10.2.1	<i>Single Bunch Beam Break-Up: Two-Particle Model</i>	110
2.10.2.2	<i>BNS Damping</i>	111
2.10.2.3	<i>Single Bunch Beam Break-Up: General Distribution</i>	112
2.10.2.4	<i>Multi-Bunch Beam Break-Up</i>	114
2.10.3	References	118
2.11	LOSS OF LANDAU DAMPING FOR BUNCH LONGITUDINAL OSCILLATIONS	119
2.11.1	Introduction	119
2.11.2	Main Equations.....	119
2.11.3	Steady State solution	121
2.11.4	Van Kampen Modes	123
2.11.5	Resistive Wall Impedance	124
2.11.6	Inductive Impedance	128
2.11.7	Conclusions	130
2.11.8	References	130
2.12	IMPEDANCE-INDUCED BEAM INSTABILITIES AND DAMPING MECHANISMS IN CIRCULAR MACHINES – LONGITUDINAL - SIMULATIONS	132
2.12.1	Introduction	132

2.12.2	Common Approach in Wakefield Simulations.....	133
2.12.3	Simulations With Short-Range Wakefields.....	135
2.12.4	Simulations With Long-Range Wakefields.....	136
2.12.5	Damping Mechanisms	138
2.12.6	Vlasov-Fokker-Planck Solvers and Other Methods.....	139
2.12.7	References	139
2.13	HEAD-TAIL AND TRANSVERSE MODE-COUPLING INSTABILITIES (TMCI).....	142
2.13.1	Introduction	142
2.13.2	Head-Tail Instability.....	142
2.13.3	Sacherer's Head-Tail Instability Theory	144
2.13.4	TMCI Theory.....	147
2.13.5	Historical Record.....	148
2.13.6	Acknowledgements	149
2.13.7	References	149
2.14	DAMPING OF TRANSVERSE INSTABILITIES OF BUNCHED BEAMS.....	151
2.14.1	Introduction	151
2.14.2	Broadband impedance	152
2.14.3	LHC at Top Energy	158
2.14.4	Feedbacks and Landau Damping.....	162
2.14.5	Conclusions	164
2.14.6	References	164
2.15	TRANSVERSE INSTABILITIES OF BUNCHED BEAMS AT STRONG SPACE CHARGE - THEORY	165
2.15.1	Introduction	165
2.15.2	Main Equation	165
2.15.3	Solution.....	168
2.15.4	Damper Details	169
2.15.5	Instability Thresholds	169
2.15.6	References	170
2.16	EFFECTS OF SPACE-CHARGE ON TRANSVERSE IMPEDANCE-INDUCED BEAM INSTABILITIES - SIMULATIONS.....	171
2.16.1	Introduction	171
2.16.2	Space-Charge Tune Shifts	171
2.16.3	Coasting Beams	172
2.16.4	Head-Tail Instability.....	173
2.16.5	Transverse Mode Coupling Instability	175
2.16.6	References	175
2.17	IMPEDANCE-INDUCED BEAM INSTABILITIES AND DAMPING MECHANISMS IN CIRCULAR MACHINES – TRANSVERSE – SIMULATIONS	177
2.17.1	Introduction	177
2.17.2	A Brief Overview over Contemporary Simulation Tools	177
2.17.2.1	<i>Frequency Domain Vlasov Solvers</i>	177
2.17.2.2	<i>Circulant Matrix Models</i>	178
2.17.2.3	<i>Macroparticle Tracking Codes</i>	179

2.17.3	Benchmarking for Transverse Mode Coupling Instability in the SPS..	179
2.17.4	Examples of Simulations and Use Cases	180
2.17.4.1	<i>Stabilization from Incoherent Betatron Tune Spread</i>	180
2.17.4.2	<i>Impact of Multi-Harmonic Rf Systems and Transverse Damper on TMCI</i>	182
2.17.5	References	184
2.18	BEAM-BASED LONGITUDINAL AND TRANSVERSE IMPEDANCE/INSTABILITY MEASUREMENTS	186
2.18.1	Introduction	186
2.18.2	Transverse Impedance Measurements with Beam	187
2.18.2.1	<i>Tune Shifts with Intensity and Instability Growth Rates with Chromaticity</i>	187
2.18.2.2	<i>Transverse Impedance Measurements with Beam: Transverse Mode Coupling Instability (TMCI) Thresholds</i>	192
2.18.3	Longitudinal Impedance Measurements with Beam	196
2.18.3.1	<i>Incoherent Synchrotron Frequency Shift</i>	196
2.18.3.2	<i>Coherent Synchrotron Frequency Shift</i>	197
2.18.3.3	<i>Synchronous Phase Shift</i>	199
2.18.4	Acknowledgements	201
2.18.5	References	201
2.19	SCHOTTKY NOISE AND BEAM TRANSFER FUNCTIONS.....	203
2.19.1	Introduction	203
2.19.2	Beam Transfer Functions	203
2.19.3	Schottky Signals	205
2.19.4	Conclusions	206
2.19.5	References	207
2.20	ELECTRON CLOUD EFFECTS.....	208
2.20.1	Introduction	208
2.20.2	Secondary Electron Emission.....	208
2.20.3	The EC Buildup Mechanism	210
2.20.4	Effects of Externally Applied Magnetic Fields	215
2.20.5	Impact of EC Effects on the Accelerator's Performances.....	216
2.20.5.1	<i>Impact on Beam Dynamics: Coherent and Incoherent Effects</i>	216
2.20.5.2	<i>Other effects</i>	219
2.20.6	Mitigation Strategies	220
2.20.7	References	223
2.21	FAST BEAM-ION INSTABILITY	227
2.21.1	Introduction	227
2.21.2	Theoretical and Numerical Studies	227
2.21.2.1	<i>Early Studies Made by Raubenheimer and Zimmermann</i>	227
2.21.2.2	<i>Nonlinear Tune Spreads</i>	230
2.21.2.3	<i>Effective Wake Induced by Ions</i>	230
2.21.3	Experimental Studies.....	231
2.21.3.1	<i>Demonstration of FBII in Some Rings by Artificially Injecting Gas into the Vacuum Chamber</i>	231

2.21.3.2	<i>Characterizations in SPEAR-III</i>	232
2.21.3.3	<i>FBII Arising from Local Outgassing due to Impedance</i>	232
2.21.4	Mitigations of FBII	233
2.21.5	Conclusion	234
2.21.6	References	234
2.22	BEAM-BEAM EFFECTS IN LINEAR COLLIDERS	237
2.22.1	Overview	237
2.22.2	Introduction	237
2.22.3	Beam-Beam Physics	238
2.22.3.1	<i>Beam Parameters and Luminosity Drivers</i>	238
2.22.3.2	<i>Beam-Beam Dynamics and Disruption</i>	239
2.22.3.3	<i>Beamstrahlung</i>	239
2.22.3.4	<i>Vertical Beam Size and Waist Shift</i>	240
2.22.3.5	<i>Beam Offsets</i>	241
2.22.3.6	<i>The Banana Effect</i>	242
2.22.3.7	<i>Beam-beam Background and its Impact on the Detector Design</i>	242
2.22.4	Choice of Horizontal Beam Size	242
2.22.5	Conclusion	244
2.22.6	References	244
2.23	BEAM-BEAM EFFECTS IN CIRCULAR HADRON COLLIDERS	246
2.23.1	Introduction	246
2.23.2	Beam-Beam Force	246
2.23.3	Head-On Beam-Beam Interactions	247
2.23.3.1	<i>Beam-Beam Parameter</i>	247
2.23.3.2	<i>Non-Linear Effects</i>	248
2.23.3.3	<i>Dynamic β</i>	248
2.23.3.4	<i>Landau Damping due to the Beam-Beam Interaction</i>	248
2.23.4	Long-Range Beam-Beam Interactions	249
2.23.4.1	<i>Beam-Beam Induced Orbit Effects</i>	249
2.23.4.2	<i>PACMAN Effects</i>	250
2.23.5	Coherent Beam-Beam Effects	252
2.23.6	Coherent Beam-Beam Modes	252
2.23.7	Compensation of Beam-Beam Effects	253
2.23.7.1	<i>Electron Lenses</i>	254
2.23.7.2	<i>Electrostatic Wire</i>	254
2.23.7.3	<i>Passive Compensation with Alternating Crossing Schemes</i>	254
2.23.8	References	254
2.24	COLLISION SCHEMES OF CIRCULAR ELECTRON-POSITRON FACTORIES	256
2.24.1	Present Generation Electron-Positron Factories	256
2.24.2	Novel Concepts	257
2.24.3	Crab Waist Collision Scheme	259
2.24.4	References	261
2.25	THREE-BEAM INSTABILITY IN THE LHC	264
2.25.1	Introduction	264
2.25.2	Facts and Hypotheses	264

2.25.3	E-Cloud as Nonlinear Lens	267
2.25.4	Impedance and E-Cloud	269
2.25.5	Summary	273
2.25.6	Acknowledgment.....	274
2.25.7	Appendix: Long-Range Beam-Beam Tune Shift	274
2.25.8	References	274
2.26	MITIGATION OF COLLECTIVE EFFECTS BY OPTICS OPTIMIZATION	276
2.26.1	Introduction	276
2.26.2	Impact of Optics Parameters on Collective Effects.....	276
2.26.3	High-Power Synchrotrons	278
2.26.4	Low Emittance Rings	278
2.26.5	High-Brightness Synchrotrons	280
2.26.6	Summary	283
2.26.7	References	283
3	WORKSHOP AND CONFERENCE REPORTS	285
3.1	THE 7 TH INTERNATIONAL PARTICLE ACCELERATOR CONFERENCE, IPAC'16.....	285
3.2	THE 57 TH ICFA ABDW ON HIGH-INTENSITY AND HIGH-BRIGHTNESS HADRON BEAMS, HB2016	286
3.3	THE 28 TH INTERNATIONAL LINEAR ACCELERATOR CONFERENCE, LINAC 2016.....	288
3.4	3 RD ICFA MINI WORKSHOP ON HIGH ORDER MODES IN SUPERCONDUCTING CAVITIES 2016, HOMSC16.....	290
3.5	WORKSHOP ON THE FRONTIERS OF INTENSE BEAM PHYSICS MODELING	292
4	RECENT DOCTORIAL THESES	294
4.1	SPACE CHARGE EFFECTS AND ADVANCED MODELLING FOR CERN LOW ENERGY MACHINES	294
4.2	DEVELOPMENT OF A HIGH-PRECISION LOW-LATENCY POSITION FEEDBACK SYSTEM FOR SINGLE-PASS BEAMLINES USING STRIPLINE AND CAVITY BEAM POSITION MONITORS	295
4.3	BEAM MEASUREMENTS OF THE LONGITUDINAL IMPEDANCE OF THE CERN SUPER PROTON SYNCHROTRON	295
4.4	STUDIES OF LONGITUDINAL COUPLED-BUNCH INSTABILITIES IN THE LHC INJECTORS CHAIN	296
4.5	FAST LUMINOSITY MONITORING USING DIAMOND SENSORS FOR SUPERKEKB ...	297
4.6	DEVELOPMENT OF DIAMOND SENSORS FOR BEAM HALO AND COMPTON SPECTRUM DIAGNOSTICS AFTER THE INTERACTION POINT OF ATF2	298
5	FORTHCOMING BEAM DYNAMICS EVENTS	300
5.1	59 TH ICFA ADVANCED BEAM DYNAMICS WORKSHOP ON ENERGY RECOVERY LINACS (ERL17).....	300
5.2	INTERNATIONAL CONFERENCE ON RF SUPERCONDUCTIVITY (SRF2017)	300

5.3	ADVANCED AND NOVEL ACCELERATORS FOR HIGH ENERGY PHYSICS ROADMAP WORKSHOP 2017 (ANARW2017).....	301
5.4	INTERNATIONAL CONFERENCE ON ACCELERATORS AND LARGE EXPERIMENTAL PHYSICS CONTROL SYSTEMS (ICALEPCS2017)	302
5.5	WORKSHOP ON THE “STATUS OF ACCELERATOR DRIVEN SYSTEMS RESEARCH AND TECHNOLOGY DEVELOPMENT”	302
5.6	ICFA MINI-WORKSHOP ON IMPEDANCES AND BEAM INSTABILITIES IN PARTICLE ACCELERATORS	303
5.7	INTERNATIONAL BEAM INSTRUMENTATION CONFERENCE (IBIC 17)	304
5.8	ICFA MINI-WORKSHOP ON "BEAM DYNAMICS MEETS VACUUM, COLLIMATIONS, AND SURFACES"	304
5.9	8 TH INTERNATIONAL PARTICLE ACCELERATOR CONFERENCE, IPAC’17, COPENHAGEN, DENMARK, 14-19 MAY 2017.....	305
5.10	FUTURE CIRCULAR COLLIDER WEEK 2017	305
5.11	CLIC WORKSHOP 2017.....	305
6	ANNOUNCEMENTS OF THE BEAM DYNAMICS PANEL	308
6.1	ICFA BEAM DYNAMICS NEWSLETTER	308
6.1.1	Aim of the Newsletter	308
6.1.2	Categories of Articles	308
6.1.3	How to Prepare a Manuscript	308
6.1.4	Distribution	309
6.1.5	Regular Correspondents.....	309
6.2	ICFA BEAM DYNAMICS PANEL MEMBERS	310

1 Foreword

1.1 From the Chair

Yong Ho Chin, KEK
Mail to: yongho.chin@kek.jp

This September, Weiren Chou, has stepped down from the chair of ICFA Beam Dynamics Panel, leaving his longstanding achievements with strong and successful leadership which cemented the very foundation of this panel as the central platform for international collaborations on beam dynamics studies for now and future. I was appointed by ICFA as the new panel chair to succeed his legacy and lead this international panel to play an even more active role in the accelerator community. It is my greatest honor and pleasure to serve on the very important panel with wonderful panel members and to serve to the accelerator community in terms of the beam dynamics collaboration.

The mission of this panel is, as stated in the website, to encourage and promote international collaboration on beam dynamics studies for present and future accelerators. For this end, we have organized ICFA Advanced Beam Dynamics Workshops and sponsored ICFA Mini-Workshops. These activities have been stimulating discussions and collaborations among participants with great success. I believe that we can expand our activities further, for example, to serve as a forum to exchange useful and valuable information, in particular on small workshops or events, among the accelerator community with great ease. I will try to implement this idea, though my immediate task is to reorganize and reboot some of the panel activities that have been inactive for some time.

As the first task, I have already moved the ICFA Beam Dynamics Panel website from FNAL to KEK. The new website URL is

<http://icfa-bd.kek.jp>

Please update your address book to this new URL. When you access to the old FNAL site, you will be automatically redirected to this new site. Most of contents of the site were updated and I am planning to update the web design in future for a better look.

Good news of 2016 are successful commissioning and lasing at PAL-XFEL in Pohang, Korea and a partial but milestone commissioning of long-awaited European XFEL at DESY, Germany. The Phase-I commissioning of SuperKEKB has been also successfully carried out at KEK, Japan. We expect that the year 2017 will be even more prosperous.

The editor of this issue is Dr. Elias Métral, a panel member and a senior scientist at CERN, Geneva. The theme is “Collective Effects in Particle Accelerators.” He collected 26 well-written articles, which cover almost entire subjects under the collective effects, including space-charge, wakefields, impedance, beam instabilities, beam-beam interaction, ion and electron clouds effects and so on. They provide very good and comprehensive reviews of this important field in beam dynamics.

In this issue there are also five workshop/conference reports (IPAC16, HB2016, LINAC16, HOMSC16, Workshop on the Frontiers of Intense Beam Physics Modeling), six recent doctoral thesis abstracts (Adrian Oeftiger (CERN), Neven Blaskovic Kraljevic (Oxford), Alexandre Lasheen (CERN), Letizia Ventura (CERN), Dima El Khechen (LAL), and Shan Liu (DESY)) and eleven conference/workshop announcements (ERL17, SRF2017, ANARW2017, ICALEPS2017, Workshop on the “Status of Accelerator Driven Systems Research and Technology Development”, ICFA Mini-Workshop on Impedances and Beam Instabilities in Particle Accelerators, IBIC17, ICFA Mini-Workshop on “Beam Dynamics meets Vacuum, Collimations, and Surfaces”, IPAC17, Future Circular Collider Week 2017, and CLIC Workshop 2017). I want to thank Elias for editing a valuable newsletter of high quality for the accelerator community after one year break of Newsletter.

1.2 From the Editor

Elias Métral
CERN, 1211 Geneva 23, Switzerland
Mail to: Elias.Metral@cern.ch

This newsletter is devoted to collective effects in particle accelerators. The subject is discussed in 26 articles, structured as follows. In the first article, Frank Zimmermann (CERN) introduces the field of collective effects in particle accelerators, discussing the main mechanisms, which have been studied over the last decades. The article 2 is devoted to space charge effects in sources and linacs (by Alessandra Lombardi et al., CERN), while article 3 focuses on space charge effects in circular machines (by Giuliano Franchetti et al., GSI). Intra-Beam Scattering is discussed in detail in the article 4 (by Michel Martini et al., CERN) before moving to the concept of impedance, introduced in particle accelerators exactly 50 years ago, in the articles 5 to 9, reviewing the early history (article 5 by Vittorio Vaccaro, Naples), the theoretical definitions of impedances and related wake fields (article 6 by Gennady Stupakov et al., SLAC), the simulation aspects (article 7 by Uwe Niedermayer et al., TU Darmstadt) and finally the measurements on a bench (article 8 by Andrea Mostacci et al., La Sapienza) before putting together all the pieces to build a realistic impedance model (article 9 by Benoit Salvant et al., CERN). The coherent instabilities induced by these impedances (and the mitigations) are then discussed in the following articles: first in linear machines (article 10 by Massimo Ferrario et al., INFN-LNF) and then in circular machines. In the latter, the longitudinal plane is discussed first theoretically (article 11 by Alexey Burov, FNAL) and then from the simulation side (article 12 by Mauro Migliorati et al., La Sapienza). The theory of transverse instabilities is reviewed in the article 13 (by Yong Ho Chin, KEK), while the theoretical aspects of the different damping mechanisms are analyzed in the article 14 (by Alexey Burov, FNAL). The particular effect of space charge of transverse instabilities is examined in detail from the theoretical side in the article 15 (by Alexey Burov, FNAL) while the simulations are considered in the article 16 (by Vladimir Kornilov, GSI). Simulations of transverse instabilities are discussed in the article 17 (by Kevin Li et al., CERN) while the main beam-based measurements, both in the longitudinal and transverse planes, are reviewed in the article 18 (by Giovanni Rumolo et al., CERN). With the article 19 we move to two other important areas of research, Schottky noise and Beam Transfer Function (article 20 by Mike Blaskiewicz, BNL) and with the article 20 we enter into the field of the two-beam effects: electron cloud in article 20 (by

Giovanni Iadarola et al., CERN), fast beam-ion in article 21 (by Ryutaro Nagaoka, SOLEIL) and beam-beam in the following articles. For the latter mechanism, linear colliders are discussed first (article 22 by Daniel Schulte, CERN), while circular hadron colliders are reviewed in the article 23 (by Werner Herr, CERN) and finally the different collision schemes of circular electron-positron factories are studied in the article 24 (by Mikhail Zobov, INFN-LNF). The concept of three-beam instability, introduced few years ago to try and explain some instabilities observed in the CERN LHC, is examined in the article 25 (by Alexey Burov, FNAL). Finally, the last article is devoted to the possible mitigations of collective effects by optics optimization (by Yannis Papaphilippou et al., CERN).

As usual, there are also sections on workshop and conference reports, recent doctoral theses abstracts, forthcoming beam dynamics events and announcements of the beam dynamics panel.

I really would like to warmly thank all the contributors for their excellent contributions and co-operation. It was a great pleasure for me to edit this ICFA Beam Dynamics NewsLetter no.69 and I do hope that you will find this issue informative and useful.

2 Theme Section: Collective Effects in Particle Accelerators

2.1 Introduction to Collective Effects in Particle Accelerators

Frank Zimmermann
CERN, 1211 Geneva 23, Switzerland
Mail to: frank.zimmermann@cern.ch

2.1.1 Introduction

The beam intensity and the beam brightness of particle accelerators or colliders operated for high-energy physics were, and are, often severely limited by “collective effects” (e.g. [1]). By contrast, new light sources, such as linac-based free electron lasers, may even rely on collective instabilities to accomplish their mission!

The term “collective effects” refers to the interaction of beam particles with each other through a variety of processes, e.g. (1) non-delayed self-fields and image fields present even for constant perfectly conducting and magnetic boundaries (direct and indirect “space-charge effects”), (2) longer-lived electro-magnetic “wake fields” due to a finite chamber resistivity or geometric variation in the beam-pipe cross section, which typically affect later parts of the beam, (3) coherent synchrotron radiation, which on a curved trajectory may even influence earlier parts of the beam, giving rise to “non-causal” wake fields, otherwise not normally encountered for ultra-relativistic beams, (4) beam-beam collisions, (5) particle-particle scattering inside the beam (single scattering called “Touschek effect” and multiple scattering known as “intrabeam scattering”), (6) gas ionization (“trapped-ion” or “fast-ion” instability), and (7) ionization electrons, photoelectrons and secondary electrons (“electron cloud effects”). Arguably also the appearance of (8) micron-size “dust” particles near the beam (“UFO effect”) could be considered a collective effect, as it is not observed, or does rarely happen, at low beam current.

Half a century ago, collective effects were often overlooked or could not be well computed. The design of the storage ring collider SPEAR, for example, seems to have considered beam currents of up to 40 A [2], but it only achieved 30 mA [3]. By contrast, the Intersection Storage Rings (ISR) at CERN were constructed with a careful assessment and minimization of the “impedance” for all their components, and, as a result, the ISR reached maximum (coasting) beam currents around 50 A. Indeed the first solid theories of wake-field induced beam instabilities, by Neil and Sessler [4], and even the term “impedance,” introduced in the accelerator field by Vaccaro [5], date from about this era. Nowadays, the impedance or wake fields of most accelerator components can be calculated fairly reliably, using modern simulation codes run on powerful computers. Probably the first such code was developed by Weiland [6]. The impedance of special elements or for particular situations (e.g. two-beam impedance) still require care, however. Our understanding is rapidly evolving for other types of collective effects such as those driven by electron cloud or ions. The formation of beam tails and the required beam collimation also are important subject of active research. And so is the interplay between the optical lattice and collective effects. Micro-bunching instability, free-electron lasing or other types of coherent photon-beam interactions, e.g. beam interactions with FEL “seed laser” beams passing through undulators,

as well as the harmful hose instability and the desired self-modulation instability in plasma acceleration (relevant for the AWAKE experiment at CERN), are further tantalizing manifestations of collective effects in modern and future particle accelerators.

2.1.2 Space Charge

Formulae to estimate coherent and incoherent space charge effects were already derived by Laslett [7]. These have been refined and extended over the years. For example, a recent study calculated the corrections for combined function magnets, as in the CERN PS ring, and for beam screens of almost arbitrary multi-polygon shape [8].

Space-charge effects in proton injectors limit the achievable brightness of hadron colliders, which is the primary motivation for the LHC injector upgrade (LIU), presently underway at CERN.

Space charge also restrains the brightness of electron RF guns and photo-injectors as needed for injection into electron linacs and linac-based FELs. For these injectors an efficient compensation scheme based on solenoid focusing was first proposed by Carlsten [9,10]

Interestingly, space charge effects can be important up to highest energy, including the final-focus systems of future linear lepton colliders with beam energies of 100s of GeV [11].

2.1.3 Wake Fields and Impedances, Classical instabilities

A formalism to describe and model single- and multi-bunch instabilities driven by impedances and to compute instability growth rates has been established by Sacherer [12]. Several excellent textbooks, monographs and review articles describe wake fields, wake functions and their Fourier transforms – the impedances – plus the resulting instabilities, e.g. [13,14,15,16,17,18]. Various powerful computer codes – CST Microwave Studio [19], ABCI, Gdfidl, ECHO3D, Omega3P, etc. exist to model vacuum chamber and to compute, in particular, geometric wake fields with any desired precision. The resistive wall wake field and impedance for various common beam pipe shapes of constant cross section have been derived analytically, including higher-order nonlinear components, e.g. by Piwinski [20,21] and Yokoya [22]. The resistive wall impedance for a superconducting beam pipe has also been calculated [23].

Particularly difficult components are those which combine elements of geometric wake fields and resistive elements, like tapered collimators, or dielectric structures.

Also the impedances of surface roughness and of the small random pumping slots on LHC beam screens are more difficult to model, as are the wake fields and instabilities in situations with more than one beam, and for two or more beams, possibly moving in different directions, e.g. as in the interaction region of a collider and in the arcs or the acceleration section of an energy recovery linac.

Different sets of computer codes are available to simulate instabilities by macroparticle tracking or to calculate instability thresholds by solving the Vlasov or Sacherer equations. From the pertinent analytical dispersion relations also the conditions for Landau damping may be derived.

Sometimes one hears the argument that wake field effects are less important for higher-energy accelerators, e.g. for the ILC as compared with the ATF-2 (KEK). Yet, the SLC at almost 50 times the beam energy of the ATF-2 suffered significantly from wake fields in its final focus system. The SLC final-focus behaviour agreed with expectations only for

intensities 5-10 lower than design, just as it seems to be the case at the ATF-2. A similar situation is seen for hadron beams - resistive-wall instabilities for the FCC-hh, at 3.3 TeV appear at least as severe as in the LHC at 0.45 TeV, and more dangerous than in the SPS at 0.026 TeV/c.

This can be tentatively understood from scaling laws. For example, the relative deflection from a single transition of smaller radius b is approximately [24]

$$\frac{\Delta y'}{\sigma_y'} \approx \beta \frac{2r_e N_b}{\gamma} \frac{1}{b^2}. \quad (1)$$

Now assume there is an aperture transition every cell with cell length scaling as β , β scaling as square root of energy, the normalized transverse emittance ε_N to be independent of energy, the length of the system to grow in proportion to energy, and b to scale with the rms beam size. This would yield a total wake field effect scaling as

$$\left. \frac{\Delta y'}{\sigma_y'} \right|_{\text{tot}} \propto \beta \frac{1}{\gamma} \frac{1}{\beta/\gamma} \sim 1, \quad (2)$$

actually suggesting a constant importance of wake fields for systems at higher beam energy. A similar or even stronger dependence on energy is found for the resistive wall wake fields [25]. Kubo compared scaling laws for cavity BPM wake fields with those for the resistive wall, and found that, under certain assumptions, the effects of the cavity BPM wake fields become less important at higher beam energy [25].

Mitigation measures for wake-field induced instabilities include octupole magnets which generate an amplitude-dependent tune spread providing ‘‘Landau damping’’ (e.g. at the LHC [26]), non-zero chromaticity (e.g. at the LHC [26], or earlier at the Tevatron [27]), controlled blow up of the longitudinal emittance during acceleration (e.g. in the CERN proton accelerator chain), and wide-band bunch-by-bunch feedback systems. Even intra-bunch feedbacks have been, and are being, developed [28]. Also, lower temperature reduces the wall resistivity, e.g. for the LHC beam screen. For the Future Circular Collider, coating of the chamber wall with a high-temperature superconductor is being considered, a technological approach first proposed by Rossi [29].

In linear accelerators an energy-position correlation can be introduced to counteract single-bunch beam break up driven by the strong wake field of the accelerating structures. This scheme is called ‘‘BNS damping’’, after Balakin, Novokhatski, and Smirnov [30].

2.1.4 Coherent Synchrotron Radiation

Following classical earlier work [31,32,33,34], coherent synchrotron radiation (CSR) has recently gained more and more prominence. It is an active field of research. CSR is a concern for future colliders with intense fairly short bunches such as SuperKEKB, and an important effects for linac-based FELs. Pioneering simulations, including the impact on the beam, were developed by Li at JLAB [35], by Kabel, Dohlus, and Limberg at DESY [36], and Borland at ANL [37]. The shielding by the vertical and horizontal chamber boundaries and the transients at the transition between curved and straight trajectories are among the interesting topics. Over the last decade several further numerical codes have been developed to compute the CSR wake field and the effect on the beam. All of the recent codes are based on a parabolic equation. They are using a mode expansion or mesh methods to compute the

field and consider different field and vacuum-chamber configurations. Noteworthy are the codes of Agoh and Yokoya [38], Stupakov and Kotelnikov [39], Oide [40], Zhou [41], Stupakov and Zhou [42] plus Warnock and Bizzozero [43]. For the case of a single bend followed by an infinite drift in a rectangular chamber, Zhou’s code (CSRZ) was benchmarked against Stupakov’s and Oide’s. In general the results are consistent.

2.1.5 Beam-Beam Interaction

The beam-beam collisions can reduce the beam lifetime, cause emittance growth or generate unacceptable beam tails. Empirically a maximum value for the beam-beam tune shift can be reached [44]. This maximum tends to be an order of magnitude lower for hadron colliders than for lepton colliders, which is attributed to the strong damping due to synchrotron radiation in the case of lepton colliders. Simulations do, however, suggest that, in the absence of any “errors” and imperfections, hadron colliders should be able to reach even higher beam-beam tune shifts than lepton collisions [45]. The head-on beam-beam collisions also introduce an important betatron tune spread and thereby provide Landau damping. At the LHC this Landau damping can be reduced by a transverse separation at the main collision points, e.g. when the beams are brought into collision [46].

The “errors” contributing to the beam-beam limit can come from the optical lattice, but strong perturbations and resonance-driving terms may also be introduced by the collision scheme, e.g. by the crossing angle. Crab cavities are one possibility to avoid the beam-dynamics consequences of a crossing angle, and they indeed helped raising the beam-beam limit at KEKB (though less than expected, due to other residual aberrations). A newer scheme is the “crab waist” scheme, realized by special sextupoles [47]. This scheme eliminates the excitation of transverse betatron resonances (e.g. low order resonances coupling the x and y motion) by the collision. It has been successfully implemented at DAFNE. The crab waist collision scheme also is an important ingredient for future high-luminosity high-energy lepton colliders like the FCC-ee.

Table 1 compares some relevant beam-beam parameters for DAFNE, SuperKEKB, CEPC, and FCC-ee.

Table 1: IP parameters for several present and future circular e^+e^- colliders with and without crab waist scheme. The CEPC values are taken from the CEPC pre-CDR.

collider	DAFNE	SuperKEK B	CEPC	FCC-ee Z	FCC-ee top
beam energy [GeV]	0.51	4 (e^+), 7 (e^-)	120	45.6	175
crossing angle [mrad]	50	83	0	30	30
rms hor. beam size [μm]	265	10	70	10	36
rms vert. beam size [nm]	4200	50	150	45	70
bunch population [10^{10}]	2.05	9(e^+), 6.5(e^-)	38	3.3	17
IP beta $\beta_{x,y}^*$ [mm]	250, 8.4	30, 0.3	800, 1.2	1000, 2	1000, 2
beam-beam parameter $\xi_{x,y}$	0.011(x), 0.04 (y)	0.002 (x), 0.09 (y)	0.12, 0.08	0.05, 0.13	0.08, 0.12
rms bunch length [mm] (incl. beamstrahlung)	16	6, 5	2.65	3.8	2.5
Piwinski angle	1.5	25	0	5.7	1.0
crab waist	YES	NO	NO	YES	YES

For future colliders an important beam-beam effect is beamstrahlung [48], i.e., synchrotron radiation emitted in the field of the opposing beam. For linear colliders this effect is very strong and greatly degrades the purity of the differential luminosity spectrum (luminosity per energy interval). Limiting the number of beamstrahlung photons per particle per collision to about 1 is an important design constraint for linear colliders. A non-negligible part of the beamstrahlung is spin-flip radiation and along with spin precession in the strong magnetic field of the opposing beam, this lowers the effective polarization of the collision.

For circular colliders at highest energy presently considered (around 350 GeV c.m.), e.g. for t-tbar operation, the beamstrahlung can lead to so large an energy loss of the emitting electron that the latter falls out of the energy acceptance of the storage ring [49]. This effect limits the beam lifetime. As for linear colliders, an easy mitigation is to collide flat(ter) bunches, and, if necessary, to increase the bunch length or to reduce the bunch charge. In addition, the collider-ring optics should provide a reasonably large momentum acceptance of 1.5-2.0%. At lower energy, e.g. at the Z pole, the beamstrahlung implies emission of low energy photons over many turns, which together with the weak radiation damping here increases the bunch length and the energy spread [50,51]. This effect must be included in the overall parameter optimization. In monochromatization schemes, operating with nonzero dispersion at the collision point (of interest, e.g. for direct Higgs production), also the transverse emittance is blown up due to the beamstrahlung [52].

The beam-beam effect has been compensated with electron lenses [53] at FNAL (long-range collision) and RHIC (head on collision) [54], significantly increasing the luminosity performance. In addition, current-fed wire compensators can mitigate the effect of parasitic collisions with a large transverse offset. Also the further correction of nonlinear optics aberrations, the use of crab cavities, a crab-waist collision scheme [47], or additional beam cooling may allow reaching higher values of the beam-beam tune shift.

2.1.6 Touschek and Intrabeam Scattering

Touschek and intrabeam scattering can be fairly accurately calculated by analytical expressions, which need to be integrated over the ring circumference [55,56,57,58,59,60]. These calculations are programmed in standard design programmes like MAD-X and SAD. Lattices of existing storage rings can be modified to reduce the effect of intrabeam scattering [61]. Uncertainties may arise from the presence of betatron and synchro-betatron coupling, in particular close to betatron or synchro-betatron resonances

2.1.7 Ion Effects

Ionized molecules and atoms of the residual gas can be trapped and accumulate over successive turns or at least over the length of a bunch train giving rise to a nonlinear tune shift and potentially to trapped-ion [62] or fast beam-ion instabilities [63,64], respectively. The fast beam-ion instability had first been predicted from analytical theory and simulations, before it was unambiguously demonstrated in dedicated beam experiments [65]. Mitigation measures include establishing a low vacuum pressure in the presence of beam, antechambers, additional gaps in the bunch train or high chromaticity [67], bunch-by-bunch feedback systems, as well as the intentional creation of dispersion waves or beta beating across the arcs [66].

2.1.8 Electron Cloud

Electron cloud can be created by gas ionization, photoelectrons, and secondary emission or, often, by a combination thereof. Modern simulation code, e.g. PyELOUD [68], can give results in good agreement with observation if the beam-pipe surface parameters are known. Conversely critical surface parameters, and their evolution time (“scrubbing” of the secondary emission yield) can be deduced by benchmarking simulations against experimental data, e.g. measured heat load per unit length or synchronous phase shift. Electron clouds can drive coupled-bunch [69] and single-bunch instabilities [70].

The wake-field and impedance concepts, including their Fourier transforms, have been extended to higher dimensions in order to describe single-bunch electron-cloud effects [71,72,73].

2.1.9 Dust Particles

Dust particles or “UFOs” have been seen at high beam current in many electron or antiproton storage rings [74], including light sources. Due to its extreme sensitivity to local beam loss, the LHC appears to be the first proton ring (operating with a positively charged beam) where such dust particles are observed, albeit they are expelled from the beam vicinity after a short moment of time [75,76].

2.1.10 Compound Effects

In real life various collective effects, like the wake fields, beam-beam collisions, and electron cloud can conspire to render the beam more easily unstable than it would be from one of the single phenomena alone. Despite some pioneering work [77,0], the study and reliable prediction of such combined effects still is in its infancy.

2.1.11 Acknowledgements

I am grateful to Elias Metral from CERN for inviting me to write this introduction to collective effects. I would also like to thank Katsunobu Oide and Demin Zhou, both from KEK, for some helpful information and comments.

2.1.12 References

1. M. Zisman, Influence of Collective Effects on the Performance of High-Luminosity Colliders, LBNL-28820 (1990).
2. M. Sands, The Physics of Electron Storage Rings, SLAC-121 (1979), Fig. 51.
3. R.M. Barnett et al., Particle Data Group, Review of Particle Properties, Phys. Rev. D 54, 1 (1996).
4. V.K. Neil and A.M. Sessler, Longitudinal Resistive Instabilities of Intense Coasting Beams in Particle Accelerator, Rev. Sci. Instr. 36, 429 (1965).
5. V.G. Vaccaro, Longitudinal Instability of a Coasting Beam Above Transition, due to the Action of Lumped Discontinuities, CERN ISR-RF/66-35 (1966).
6. T. Weiland, On the Numerical Solution of Maxwell’s Equations and Applications in the Field of Accelerator Physics, Part. Acc. 15 (1984) 245-2092; CERN / ISR-TH / 80-46 (1980).

7. L. J. Laslett, BNL Report No. 7535 (1963) p. 154,
<http://lss.fnal.gov/conf/C630610/p324.pdf>
8. S. Hirländer, Analytic Solutions of Transverse Field Effects in Circular Accelerators with Application to CERN LHC and PS, PhD thesis, TU Wien, 2016.
9. B.E. Carlsten, "New Photoelectric Injector Design for the Los Alamos National Laboratory XUV FEL Accelerator," NIM A Vol. 285 (1989) p. 313.
10. B.E. Carlsten, "Space charge induced emittance compensation in high brightness photoinjectors," Part. Acc. 49:27-65 (1995) p.27.
11. F. Zimmermann, T. Raubenheimer, Longitudinal Space Charge in Final-Focus Systems for Linear Colliders, NIM A Vol. 390, Issue 3, 11 (1997) 279-285.
12. F.J. Sacherer. Transverse space-charge effects in circular accelerators Berkeley, CA PhD thesis, Univ. of California at Berkeley, UCRL-18454 (1968).
13. S.A. Heifets and S.A. Kheifets, Coupling Impedance in Modern Accelerators, Rev. Mod. Phys. 63, 631 (1991).
14. A.W. Chao, Physics of Collective Beam Instabilities in High Energy Accelerators, John Wiley & Sons (1993).
15. F. Ruggiero, "Single-Beam Collective Effects in the LHC," Part. Accel. 50 (1995), pp. 83-104.
16. B.W. Zotter and S.A. Kheifets, Impedances and Wakes in High Energy Particle Accelerators, World Scientific (1998).
17. K.Y. Ng, Physics of Intensity Dependent Beam Instabilities, World Scientific (2005).
18. A.W. Chao, K.H. Mess, M. Tigner, F. Zimmermann, Handbook of Accelerator Physics and Engineering, 2nd Edition, World Scientific (2013).
19. CST Computer Simulation Technology AG, <https://www.cst.com>
20. A. Piwinski, "Bunch Lengthening and Power Losses due to the Vacuum chamber walls," DESY 72/72 (1972).
21. A. Piwinski, "Impedances in Lossy Elliptical Vacuum Chambers," DESY-94-068 (1994).
22. K. Yokoya, "Resistive Wall Impedance of Beam Pipes of General Cross-Section," Part. Accel. 41 (1993).
23. F. Zimmermann, "Impedance and Wake Field in a Superconducting Beam Pipe," Phys. Rev. E 57, 7146 (1998).
24. F. Zimmermann, K. Bane, C. Ng, "Collimator Wake Fields in the SLC Final Focus," Proc. EPAC'96 Sitges, Barcelona (1996), p. 504.
25. K. Kubo, "Cavity BPM Wakefield effect in FF line, comparison with ILC," 15th ATF2 Project Meeting, KEK, 23-25 January 2013.
26. E. Métral et al., "Measurement and Interpretation of Transverse Beam Instabilities in the CERN Large Hadron Collider (LHC) and Extrapolations to HL-LHC," Proc. HB2016 Malmö, Sweden and CERN-ACC-2016-0098 (2016).
27. F. Zimmermann et al., "Tevatron Study Report: Proton Beam Lifetime at 150 GeV, Chromaticity and Tune Scans, Aperture, scraping 12/03-04/02," CERN AB-Note-2003-012-MD (2003).
28. J. Dusatko et al., "Recent Upgrades to the CERN SPS Wideband Intra-bunch Transverse Feedback Processor," Proc. IPAC'16 Busan (2016) p. 2687.
29. O. Bruning et al., "High Energy LHC - Document Prepared for the European HEP Strategy Update," CERN-ATS-2012-237 (2012), and W. Barletta et al., "Future hadron colliders from physics perspectives to technology R&D," Nucl. Instr. and Meth A 764 (2014) 352-368.

30. V. Balakin, A. Novokhatsky and V. Smirnov, VLEPP: Transverse Beam Dynamics, Proc. of the 12th International Conference on High-Energy Accelerators, Batavia, Illinois, p. 119 (1983).
31. J.S. Nodvick and D.S. Saxon, "Suppression of Coherent Radiation by Electrons in a Synchrotron", Phys. Rev. 96 (1954).
32. J.B. Murphy, S. Krinsky, and R.L. Gluckstern, "Longitudinal Wakefield for an Electron Moving on a Circular Orbit", Part. Accel. 57, 9 (1997).
33. E.L. Saldin, E.A. Schneidmiller, M.V. Yurkov, "On the coherent radiation of an electron bunch moving in an arc of a circle," NIM A 398 (1997) 373-394.
34. Y. Derbenev, V. Shiltsev, "Transverse Effects of Microbunch Radiative Interaction," SLAC-PUB0-7181 (1996).
35. R. Li, "Self-consistent simulation of the CSR effect on beam emittance," Nucl. Instrum. Meth. Phys. Res. A 429, 310 (1998).
36. A. Kabel, M. Dohlus, T. Limberg, "Numerical Calculation of CSR Effects Using TraFiC4," NIM A 455 (2000) 185-189.
37. M. Borland, "Simple method for particle tracking with coherent synchrotron radiation," PRST-AB 4, 070701 (2001)
38. T. Agoh and K. Yokoya, "Calculation of Coherent Synchrotron Radiation Using Mesh," Phys. Rev. ST Accel. Beams 7, 054403 (2004).
39. G. V. Stupakov and I. A. Kotelnikov, "Calculation of Coherent Synchrotron Radiation Impedance using the Mode Expansion Method," Phys. Rev. ST Accel. Beams, 12(10):104401 (2009).
40. K. Oide et al., "A few issues on the upgrade of KEKB B-factory," in Proceedings of PAC09, Vancouver, BC, Canada (2009) p. 23
41. D. Zhou et al., Calculation of Coherent Synchrotron Radiation Impedance for a Beam Moving in a Curved Trajectory, Jpn. J. Appl. Phys. 51: 016401 (2012).
42. G. Stupakov and D. Zhou, "Analytical theory of coherent synchrotron radiation wakefield of short bunches shielded by conducting parallel plates," Phys. Rev. Accel. Beams 19, 044402 (2016).
43. Robert L. Warnock and David A. Bizzozero, "Efficient Computation of Coherent Synchrotron Radiation in a Rectangular Chamber," Phys. Rev. Accel. Beams 19, 090705 (2016).
44. J. Seeman, "Observations of the Beam-Beam Interaction," Nonlinear Dynamics Aspects of Particle Accelerators, Proceedings, Sardinia 1985, ed. J. Jowett, M. Month, S. Turner (1985) 126-137.
45. K. Ohmi and F. Zimmermann, "Fundamental Beam-Beam Limit from Head-On Interaction in the Large Hadron Collider," Phys. Rev. ST Accel. Beams 18, 121003 (2015).
46. X. Buffat et al., "Head-On and Long Range Beam-Beam Interactions in the LHC: Effective Tune Spread and Beam Stability Due to Landau Damping," Proc. IPAC'13, Shanghai (2013), pp.1421.
47. P. Raimondi, M. Zobov, D. Shatilov, "Suppression of Beam-Beam Resonances in Crab-Waist Collisions," Proc. EPAC08 Genoa (2008) 2620.
48. K. Yokoya and P. Chen, "Beam-Beam Phenomena in Linear Colliders," Proc. 4th US-CERN School on Particle Accelerators, Springer Lect. Notes Phys. 400 (1992) 415-445.
49. V.I. Telnov, "Restriction on the Energy and Luminosity of e^+e^- Storage Rings due to Beamstrahlung," Phys. Rev. Lett. 110, 114801 (2013).

50. K. Ohmi, F. Zimmermann, "FCC-ee/CepC Beam-beam Simulations with Beamstrahlung," Proc. IPAC14 Dresden (2014) p. 3766
51. M.A. Valdivia García, F. Zimmermann, "Effect of Beamstrahlung on Bunch Length and Emittance in Future Circular e^+e^- Colliders," Proc. IPAC16 Busan (2016) p. 2438.
52. M.A. Valdivia García, F. Zimmermann, A. Faus-Golfe, "Towards a Mono-chromatization Scheme for Direct Higgs Production at FCC-ee," Proc. IPAC2016 Busan (2016) p. 2434.
53. V.D. Shiltsev, "Electron Lenses for Super-Colliders," Springer ISBN: 978-1-4939-3315-0 (2016).
54. W. Fischer et al., "Operational Head-on Beam-Beam Compensation with Electron Lenses in the Relativistic Heavy Ion Collider," Phys. Rev. Lett. 115, 264801 (2015).
55. J. Le Duff, "Single and Multiple Touschek Effects," Proc. CERN Accelerator School: Accelerator Physics, Berlin, Germany, 14-25 Sep 1987, CERN-1989-001, pp.114-130 (1989).
56. A. Piwinski, "Intrabeam Scattering," Proc. 9th Int. Conf. on High Energy Accelerators SLAC, USA, 405 410 (1974).
57. A. Piwinski, "The Touschek Effect in Strong Focusing Storage Rings," DESY 98-179 (1998).
58. J.D. Bjorken, S.K. Mtingwa, "Intrabeam Scattering," Part. Acc. Vol. 13 (1983) 115-143.
59. K. Kubo and K. Oide, "Intrabeam Scattering in Electron Storage Rings," Phys. Rev. ST Accel. Beams 4, 124401 (2001).
60. F. Antoniou and F. Zimmermann, "Revision of Intrabeam Scattering with Non-Ultrarelativistic Corrections," CERN-ATS-2012-066 (2012).
61. A.V. Fedotov et al., "IBS Suppression Lattice in RHIC: Theory and Experimental Verification," Proc. HB2008, Nashville (2008), p. 148.
62. Y. Baconnier, G. Brianti, "The Stability of Ions in Bunched Beam Machines," CERN-SPS-80-2-DI (1980).
63. T. O. Raubenheimer and F. Zimmermann, "Fast Beam-Ion Instability. I. Linear theory and Simulations," Phys. Rev. E 52, 5487 (1995).
64. G. V. Stupakov, T. O. Raubenheimer, and F. Zimmermann, "Fast Beam-Ion Instability. II. Effect of Ion Decoherence," Phys. Rev. E 52, 5499 (1995)
65. J. Byrd et al., "First Observations of a "Fast Beam-Ion Instability," Phys. Rev. Lett. 79, 79 (1997).
66. J. Seeman, private communication (1997).
67. F. Zimmermann et al., "Recent Experiments on the Fast Beam Ion Instability and a Study of Potential Cures at ALS and PEP-II," Frascati Phys.Ser. 10 (1998) pp. 399-404.
68. G. Iadarola and G. Rumolo, "PyECLLOUD and Build-Up Simulations at CERN," Proc. ECLLOUD12, La Biodola, CERN-2013-002 (2013) pp.189-194.
69. K. Ohmi, "Beam-Photoelectron Interactions in Positron Storage Rings," Phys. Rev. Lett. 75, 1526 (1995).
70. K. Ohmi and F. Zimmermann, "Head-Tail Instability Caused by Electron Clouds in Positron Storage Rings," Phys. Rev. Lett. 85, 3821 (2000).
71. E. Perevedentsev, "Head-Tail Instability Caused by an Electron Cloud," Proc. ECLLOUD'02 Workshop, CERN, 15-18 April 2002, CERN Yellow Report CERN-2002-001 (2002) p. 171

72. G. Rumolo, F. Zimmermann, "Electron Cloud Simulations: Beam Instabilities and Wakefields," PRST-AB 5, 121002 (2002).
73. G. Rumolo, presentation at Mini-Workshop on SPS Scrubbing Results and Implications for the LHC, 28 June 2002 (2002).
74. F. Zimmermann, J.T. Seeman, M. Zolotarev, W. Stoeffl, "Trapped Macroparticles in Electron Storage Rings," Proc. IEEE PAC Dallas (1995) pp. 517-519.
75. T. Baer et al., "UFOs in the LHC," Proc. IPAC2011, San Sebastián, Spain (2011), p. 1347
76. S. Rowan et al., "Interactions Between Macroparticles and High-Energy Proton Beams," Proc. IPAC2015 Richmond (2015) p. 2112
77. K. Ohmi, E. Perevedentsev, A. Valishev, A. Chao, "Combined Phenomenon of the Beam-Beam and the Beam-Electron-Cloud Effects," presentation at ECLOUD'02, CERN, 15-19 April 2002.
78. A. Burov, "Three-Beam Instability in the LHC," arxiv.org/pdf/1301.0443 (2013).

2.2 Space Charge Effects in Low Energy Beam Transport and Linacs

Veliko Dimov, Jean-Baptiste Lallement, Jacques Lettry, Alessandra Lombardi, Richard Scrivens, Cristhian Valerio*

CERN, 1211 Geneva 23, Switzerland

* Universidad Autonoma de Sinaloa Facultad De Ciencias Físico-Matemáticas

Mail to: Alessandra.Lombardi@cern.ch

2.2.1 Introduction

Particle sources, Low Energy Beam Transports (LEBT) and Linacs are single-pass devices that generate and increase the energy of a charged particle beam by means of a (radio frequency) electric field. They are equipped with magnetic elements (quadrupoles, solenoids) to keep the charged particles confined in controlled volumes. The beam quality at the end of the linac (and therefore the brilliance available in the downstream circular machines) is determined by the control of the non-linear forces during the extraction and acceleration process, of which space charge is one of the most important.

The velocity of the beam varies from basically zero in the source plasma to something between 30 and 50% of the speed of light at the end of the linac, consequently the effects of space charge are very different in the various sections. In this chapter we will report on few characteristics issues related to space charge, very specific for each part. The illustrative examples are taken from LINAC4 [1,2,3], the new 160 MeV H⁻ linac under commissioning at CERN, as the authors are more familiar with the setup.

There are two critical moments during the beam generation in preparation for RF acceleration, one is the definition of the transverse emittance in the extraction and low energy beam transport, the other is the formation of the longitudinal emittance in the Radio Frequency Quadrupole. In particular a widely used technique to control the emittance growth is to inject gas in the section between the source and the RFQ. A description of this technique is presented in the next chapter.

2.2.2 Space Charge Control in Low Energy Beam Transport, Neutralisation

Beam space charge compensation (SCC) is crucial to overcome the beam transport limitations of high intensity ion beams in LEBT region, where high space charge forces due to the beam low energy lead to fast beam size and emittance growth. SCC is a technique that reduces the space charge forces by adding opposite charge particles into the beam region. The SCC studied here occurs when particles of the negative beam ionize residual gas molecules through impact ionization and create ions through the process shown in Eq. (1)



In the case of negative beams once the secondary ions are created the electrons are expelled to the beam pipe walls and the positive ions are trapped by the beam potential leading to a decrease of the local charge density and therefore the electric field inside the beam [4]. The critical parameters for the SCC are the secondary particles, the stripping of the primary beam and the time it takes. Secondary particles are those that are created by the interaction of the beam particles with the system (positive ions and electrons). It takes to a primary beam ion to create one secondary ion, in the case of a particle beam only a small fraction of particles interact with the neutral gas, this time is of extreme interest because it

also says how long it takes to have an equal number of secondary ions to beam ions (assuming none are lost), this time is also known as the compensation time.

When the neutral gas is a gas mixture the compensation time is determined by the sum of all gases present, as given in Eq. (2), where n_{H_2} and n_x are the residual gas densities of H₂ and other gas, $\sigma_{H_2}(E)$ and $\sigma_x(E)$ are the respective cross sections for ionization of this atom or molecule by the beam [5]

$$\tau = \frac{1}{(n_{H_2} \cdot \sigma_{H_2}(E) + n_x \cdot \sigma_x(E)) \cdot v_b} \quad (2)$$

Once the beam is compensated the system enters in a steady state, during the SCC build-up the beam parameters are time dependent, and mismatch to the accelerator is expected. Often this problem is compensated by chopping away part of the beam after the first phase of acceleration but this is a difficult operation and not all linacs are equipped with a dedicated chopper at medium energy.

For Linac4, the compensation time has been evaluated for different gas pressures and an the theoretical compensation time from Eq. (2) is shown in Fig. 1.

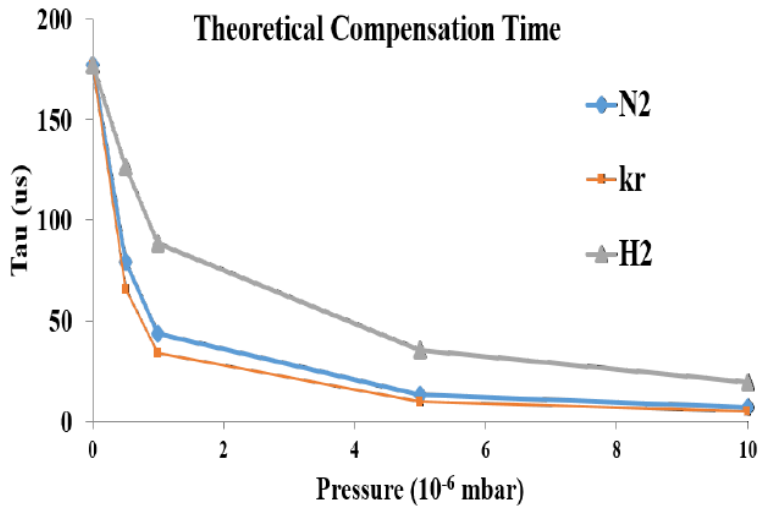


Figure 1: Theoretical compensation time from Eq. (2). The baseline pressure consists of $(1 \cdot 10^{-6} \text{ mbar}) \text{ H}_2$.

By increasing the residual gas density inside the beam pipe is possible to reduce the compensation time, however a balance with the increase in stripping losses should be found. In the following Fig. 2 we report the variation of the beam parameters along the pulse measured at the LINAC4 test stand. The space charge reaches steady state and the emittance becomes stable after 360 μs at low pressure, after 300 μs at medium pressure, and after 200 μs at high pressure.

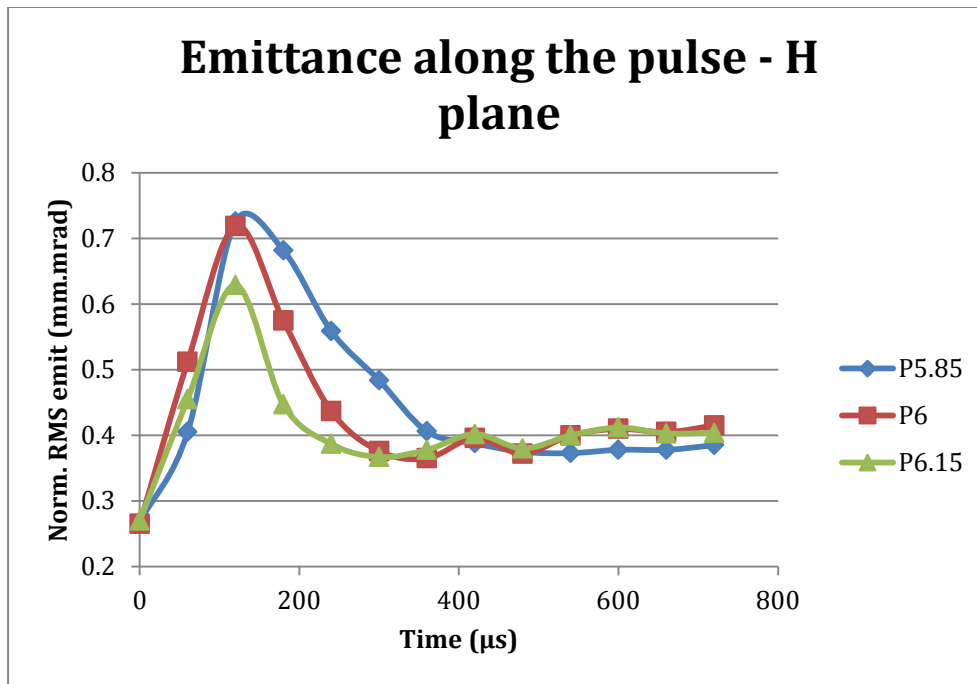


Figure 2: Emittance evolution along the pulse for 3 different residual gas pressures.

2.2.3 Space Charge in the First Stage of Acceleration (Radio Frequency Quadrupoles)

In hadron linacs the first stage of acceleration is generally performed by a Radio Frequency Quadrupole [6]. The Radio Frequency Quadrupole is a linear accelerator, which focuses, bunches and accelerates a continuous beam of charged particles with high efficiency and preserving the emittance. The focusing as well as the bunching and acceleration are performed by a Radio Frequency (RF) electric field. In the RFQ, it is where the crucial transition between a continuous beam, undergoing only 2D space charge effects, is transformed in a bunched beam, undergoing 3D space charge effects. The process of bunching is necessary for any further acceleration in a RF field. Mastering the transition of space charge forces from 2D to 3D is a key in the design of high intensity RFQ and the way it is done has a crucial input on the final longitudinal emittance. Going into more details, the bunching is done adiabatically over several cells in order to maximize the capture and minimize the emittance. When the beam is fully bunched, the phase is gradually tapered up to bring the beam to the final energy. All the time the transverse parameters are set as to keep a constant transverse phase advance per cell, by compensating the variation of the rf defocusing term and the space charge term during the process of bunching and acceleration. Schematically the RFQ is designed in 3 distinct parts: the shaper, to give the beam a longitudinal structure; the gentle buncher, to bunch and begin acceleration; and the accelerator to bring the beam to the final energy. The relative variation of the characteristics RFQ geometrical parameters (aperture modulation and phase) is controlled to fulfil these tasks sequentially.

The main difference when designing RFQs comes from the space charge effects. For high intensity beam, when the space charge term dominates the emittance term in the equation of motion, it is important to start acceleration almost at the same time of shaping and bunching in order to compensate for the increased space charge defocusing during longitudinal compression. A RFQ designed for a high intensity beam will result in a longer

structure than one designed for the corresponding low intensity beam and, generally, will produce a higher output longitudinal emittance. Table 1 contains the main difference in the design strategy for high and low intensity beam.

Table 1: Difference between a high intensity and a low intensity RFQ.

Parameter	Space charge dominated	Emittance dominated
RMS	...	10.5
SHAPER	Shaping and acceleration	Over many cells w/o acceleration
PRE-BUNCHER	Not used	Fast bunching
GENTLE BUNCHER	Bunching and acceleration	Complete the bunching (almost no energy increase up to here)
BOOSTER	Not used	Fast transition to accelerating phase
ACCELERATOR	Beam bunched around $\varphi = -35, -30$	Beam strongly bunched ($\varphi = -20, -15$)

2.2.4 Space Charge in LINACS

After extraction and the first phase of acceleration and bunching in an RFQ a hadron beam is accelerated by an efficient linear accelerator, like a Drift Tube Linac. The beam enters the second phase of acceleration with energy between 3 and 5 MeV generally, at this point space charge effects are important but less severe than in the LEBT. Recipes have been proven useful of maintain a given ratio between transverse and longitudinal phase advance to avoid resonances [7]. A smooth transition between sections is also important to control space charge. As the linac is a synchronous machine with the phases (and consequently the longitudinal phase advance) determined by the geometrical length of each cell, the control of the relation transverse /longitudinal phase advance in presence of space charge are performed by varying the intensity of the quadrupoles.

More and more in modern linacs the choice is made to adopt a permanent magnet focusing channel, as it is very economical, simplifies the drift tube geometry and allows the use of high frequency at low velocity.

The choice of Permanent Magnet Quadrupoles called for a new development in the design of linear accelerators which goes under the name of space charge independent matching. This scheme, which was tried at LINAC4 amongst others, foresee the design of a fixed focusing channel for different space charge intensity, with all the flexibility built into the matching line between the RFQ and the next stage of acceleration. Details of this design are given in the following chapters.

2.2.5 Space Charge Independent Matching

As a practical case of space charge independent matching we would like to illustrate the case of linac4 [1,2,3]. The pre-injector includes a source followed by a Low Energy Beam Transport at 45 keV, a Radio Frequency Quadrupole, which accelerates the beam to 3 MeV

and a Medium Energy Beam Transport line (MEBT). The MEBT, 3.6 m in length, houses a fast chopper with the purpose of removing selected micro-bunches in the 352 MHz sequence and therefore avoid losses at capture in the CERN PSB (1 MHz). The beam is then further accelerated to 50 MeV by a conventional Drift Tube Linac (DTL) equipped with Permanent Magnet Quadrupoles (PMQ), to 100 MeV by a Cell-Coupled Drift Tube Linac (CCDTL) and to 160 MeV by a π -mode structure (PIMS). The focusing after 100 MeV is provided by Electromagnetic Quadrupoles (EMQ) whereas between 50 and 100 MeV by a combination of PMQs and EMQs.

The quadrupole settings of the chopper-line were arranged in order to insure a good chopping efficiency and a perfect matching to the DTL for beams of varying current. The main beam parameters at the MEBT output are listed in the Table 2.

Table 2: Chopper output beam parameters.

	Transmission (%) - mA	X RMS Emittance (π .mm.mrad)	Y RMS Emittance (π .mm.mrad)	Z RMS Emittance (π .deg.MeV)
20mA	99.1% - 19.5mA	0.282	0.283	0.116
40mA	98.7% - 38.5mA	0.275	0.275	0.120
60mA	95.6% - 54.7mA	0.270	0.286	0.140
70mA-Nominal	95.7% - 62.5mA	0.290	0.297	0.155
80mA	95.2% - 68.5mA	0.296	0.329	0.165
100mA	95.3% - 75.1mA	0.332	0.348	0.185

The transmission is better for the low current cases. Note that the difference of transmission between the 60 and 100 mA cases is negligible (less than 1%), but not the emittance increases. If we refer to Table 2, transverse emittance increases in the MEBT are equal to 4.3%, 22% and 43% respectively for the 20, 70 and 100 mA cases. For the longitudinal plane, the emittance behaves the same (4.3%, 17% and 27%).

The eleven quadrupoles gradients have been changed to match the beam to the DTL and the chopping efficiency has been recovered for all the cases. In Table 3, the remaining proportions of the beam are listed for 2 different voltages seen by the beam. It shows that for the 100 mA cases, we would need more than 450 V effective voltage between the chopper plates in order to completely chop the beam. In fact, the dump aperture is fixed but the beam size increases with the current. The higher the current, the higher the chopping voltage should be.

Table 3: Remaining beam after chopping.

Remaining Beam	450V	400V
20mA	0%	0.14%
40mA	0%	0.25%
60mA	0%	0.32%
70mA-Nominal	0%	0.31%
80mA	0%	0.26%
100mA	0.2%	0.25%

We kept fixed the focusing in the DTL and in the CCDTL considering that the focusing schemes are established by PMQs (Permanent Magnet Quadrupoles). We cannot, as we did in the chopper-line, adjust the line to current. We have to adjust the initial beam parameters to the line by using the 4 last quadrupoles of the MEBT. The regular focusing layout of the DTL can be adapted to many currents and emittances as far as we are able to adjust the beam parameters (Twiss parameters) at the input. The third buncher of the MEBT and its four last quads insure a proper matching to the regular DTL lattice. The transition CCDTL-PIMS needed some re-matching adjustments performed with the 4 first electromagnets of PIMS. Figure 3 shows the beam profiles at the DTL input for the 20 and 100 mA cases. As expected, the beam size is bigger and the halo much more developed in the 100 mA case. Figure 4 shows the transverse envelope of the beam along DTL CCDT and PIMS for the different current cases, 20, 40, 60, 70, 80 and 100 mA. For all these cases, the matching has been done to the same DTL-CCDTL channel thanks to the last part of the chopper-line. It means that only the 4 first quadrupole gradients of the PIMS were slightly adjusted. All the other parameters (quad gradients, gap phases and fields...) of the 65 meters line are the same for all the cases. We give in the following Table 4 the DTL input beam parameters for several currents.

Table 4: Matched DTL input Twiss Parameters from 0 to 80 mA.

Current (mA)	AlphaX	BetaX (mm/mrad)	AlphaY	BetaY (mm/mrad)	AlphaZ	BetaZ (mm/mrad)
0	0.901	0.112	-1.701	0.410	-0.0104	0.225
20	0.993	0.138	-1.952	0.475	-0.0122	0.299
40	1.082	0.158	-2.148	0.532	-0.0143	0.346
60	1.165	0.177	-2.309	0.577	-0.0161	0.378
80	1.192	0.181	-2.396	0.601	-0.0160	0.384

The values in Table 4 bring us to the same conclusions as Table 1 (RFQ case). The evolution of the input Twiss parameters is smooth, and we managed to reach them by using the matching section of the chopper-line. Figure 4 shows that the beam is matched for all the 6 currents. Except for the 4 first quadrupoles of PIMS, all the settings are exactly the same, and, as done for the input beam. We can notice that the beam size is smaller at low currents. The main beam parameters at the outputs of the 3 structures are listed in the Tables 5, 6 and 7.

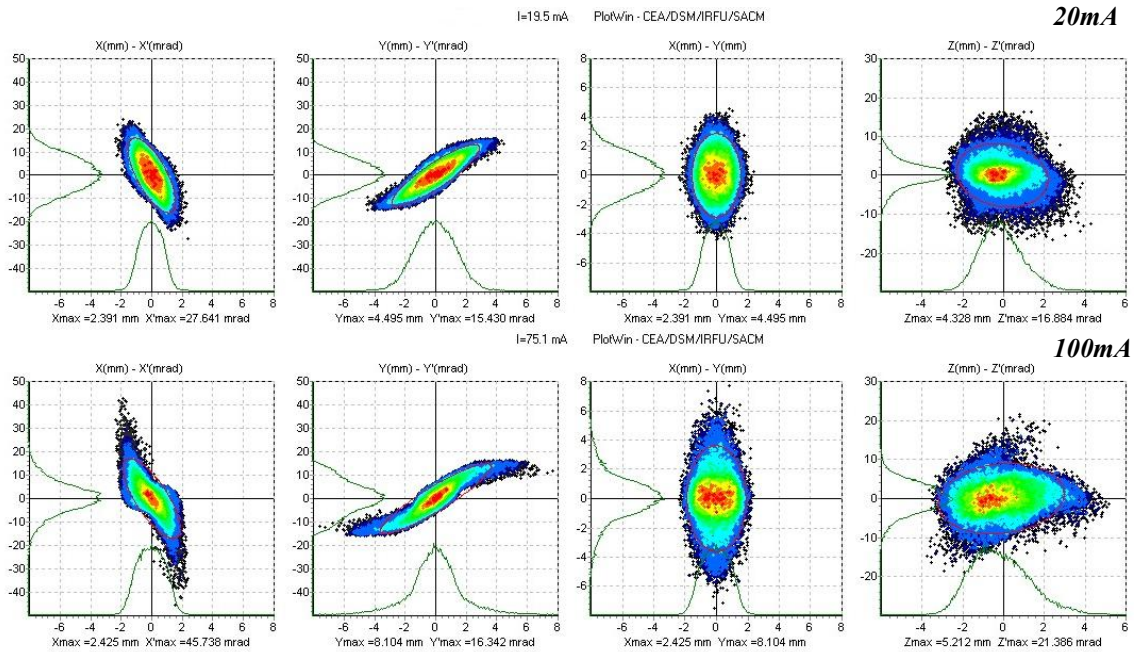


Figure 3: DTL input beam profile for 20 and 100mA cases.

Excepted few losses ($< 0.5\%$) in the DTL for the 100 mA case, the transmission is 100 % for all the cases in all the 3 accelerating parts. In the 3 structures, the conclusions on emittance increases are the same. The emittances increase more for the high current cases. The beam parameters evolutions are summarized in Table 8 for the “RFQ to PIMS” simulations.

Even if we noticed a bigger emittance increase in the RFQ for the low current case, the balance is reversed in chopper-line, DTL, CCDTL and PIMS. At the end of Linac4 we can conclude that transmission and emittance increases are correlated with the input beam current. Above 70 mA input beam current, we can expect more than 10 % of losses and emittance increases higher than 30 % in transverse and 50 % in longitudinal plane unless we increase the RFQ voltage. The emittance evolutions from chopper-line to PIMS are shown in Figs. 5,6 and 7.

The evolution of the emittances is very similar for all the cases and higher the current, higher the emittance increase. Concerning the low current cases, there is almost no emittance increase in transverse planes and it is very low in longitudinal. Figure 8 compiles the results for all the input currents all over the Linac4 structures. The ratio of the output current of each structure over the transverse emittance gives us an idea of the beam quality. This ratio cannot increase along the Linac or take a value above the reference. A decrease of this ratio can be explained by losses and/or emittance increase. From this figure, we can find a summary of the results discussed previously. The evolution of the quality factor for the RFQ is linear and really close to the reference for the currents below 70-80 mA. This tells us that for this range of current, the losses in RFQ are compensated by a decrease of the emittance. Above 80 mA, it's not the case anymore. The losses become so important, that they cannot be balanced by an adjustment in emittance value. The chopper signature is really similar to the RFQ one. The factor is proportional until 70-80 mA and starts to be degraded above 80 mA. From 20 to 70 mA, the difference between the RFQ beam quality factor and the chopper one is mainly due to the losses in the

MEBT. Above 70 mA, the emittance increase in the chopper-line is becoming quite high and adds to the losses to saturate the beam quality factor.

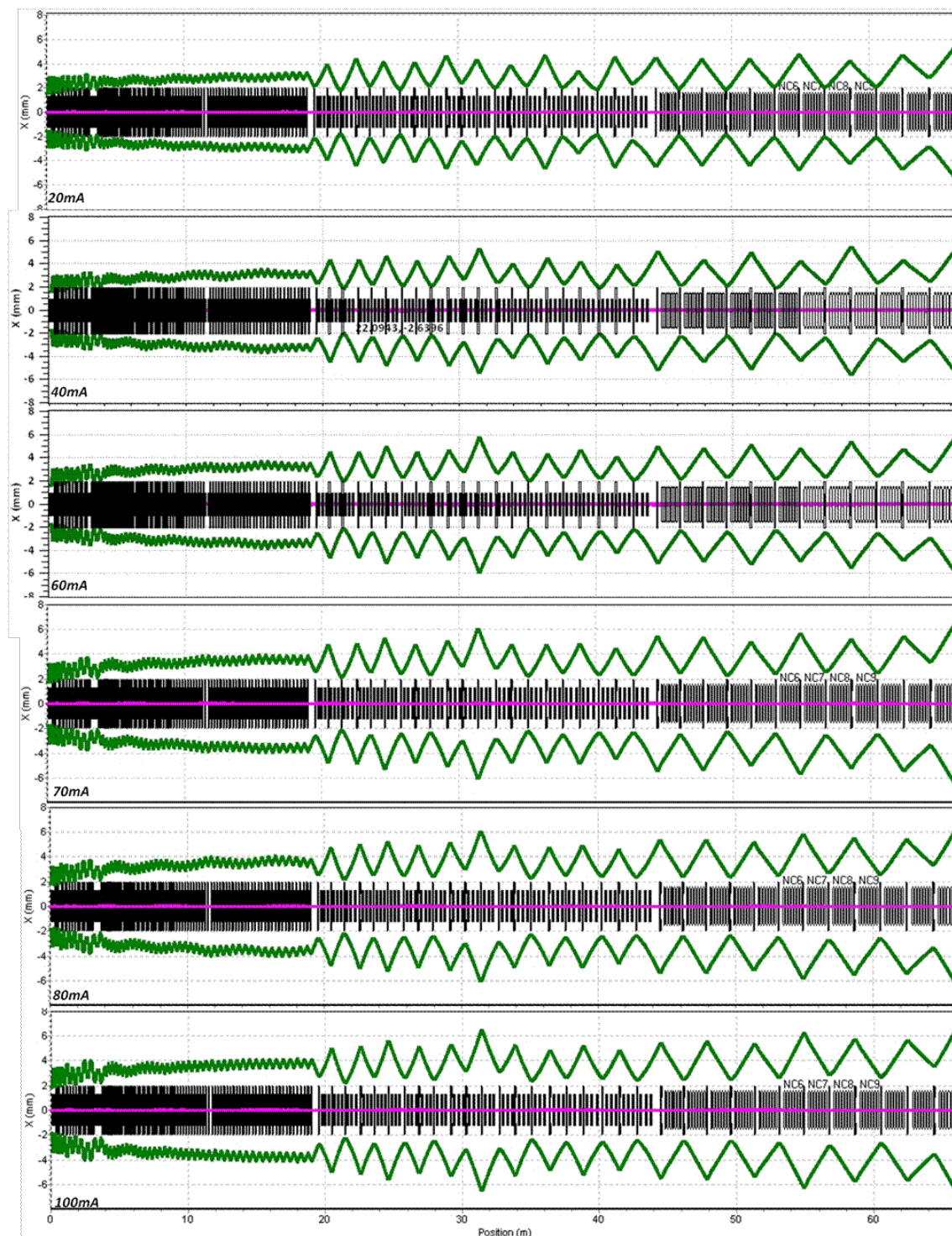


Figure 4: Transverse beam envelope along DTL and CCDTL.

Table 5: DTL output beam parameters.

	Transmission (%) - mA	X RMS Emittance (π .mm.mrad)	Y RMS Emittance (π .mm.mrad)	Z RMS Emittance (π .deg.MeV)
20mA	100% - 19.5mA	0.279	0.281	0.126
40mA	100% - 38.5mA	0.286	0.278	0.128
60mA	100% - 54.7mA	0.289	0.287	0.16
70mA-Nominal	100% - 62.5mA	0.31	0.309	0.186
80mA	100% - 68.5mA	0.335	0.334	0.202
100mA	99.97% - 75.1mA	0.372	0.360	0.222

Table 6: CCDTL output beam parameters.

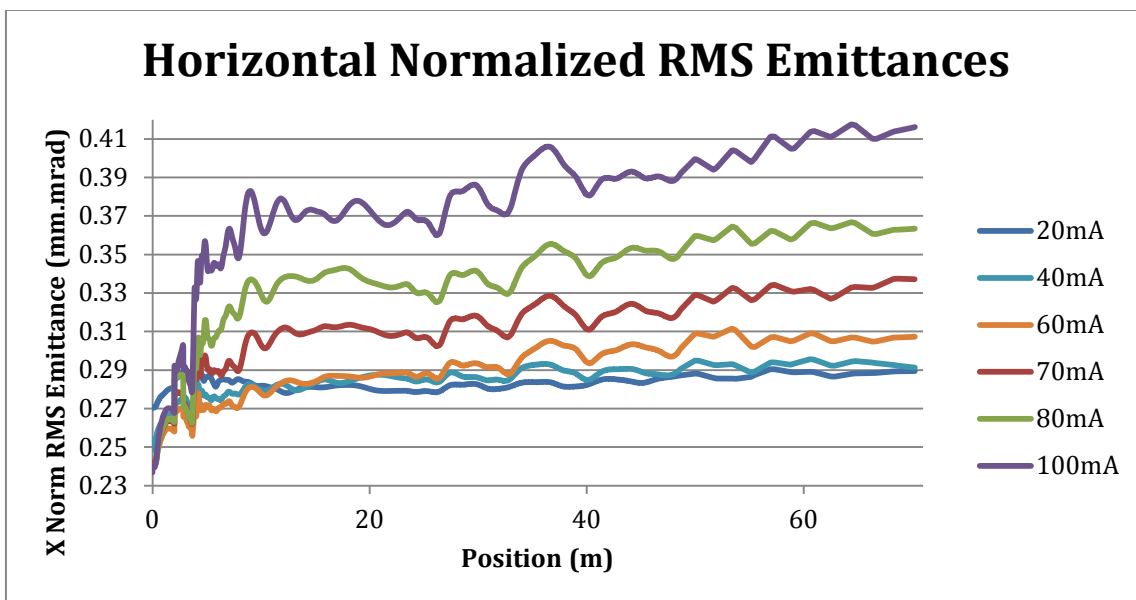
	Transmission (%) - mA	X RMS Emittance (π .mm.mrad)	Y RMS Emittance (π .mm.mrad)	Z RMS Emittance (π .deg.MeV)
20mA	100% - 19.5mA	0.287	0.283	0.129
40mA	100% - 38.5mA	0.289	0.288	0.136
60mA	100% - 54.7mA	0.299	0.299	0.167
70mA-Nominal	100% - 62.5mA	0.319	0.324	0.199
80mA	100% - 68.5mA	0.349	0.347	0.215
100mA	100% - 75.1mA	0.389	0.378	0.236

Table 7: PIMS output beam parameters.

	Transmission (%) - mA	X RMS Emittance (π .mm.mrad)	Y RMS Emittance (π .mm.mrad)	Z RMS Emittance (π .deg.MeV)
20mA	100% - 19.5mA	0.289	0.283	0.129
40mA	100% - 38.5mA	0.291	0.293	0.143
60mA	100% - 54.7mA	0.307	0.306	0.17
70mA-Nominal	100% - 62.5mA	0.337	0.327	0.199
80mA	100% - 68.5mA	0.363	0.352	0.212
100mA	100% - 75.1mA	0.416	0.382	0.232

Table 8: Beam parameters evolution along Linac4.

	Transmission (%) - mA	X RMS Emittance Increase	Y RMS Emittance Increase	Z RMS Emittance increase (from RFQ)
20mA	97.5% - 19.5mA	15.6%	13.2%	16.2%
40mA	96.2% - 38.5mA	16.4%	17.2%	31.2%
60mA	91.2% - 54.7mA	22.8%	22.4%	34.9%
70mA-Nominal	87.6% - 61.3mA	34.8%	30.8%	51.1%
80mA	85.6% - 68.5mA	45.2%	40.8%	54.6%
100mA	75.1% - 75.1mA	66.4%	52.8%	59.5%

**Figure 5:** Horizontal emittance evolution from MEBT to PIMS.

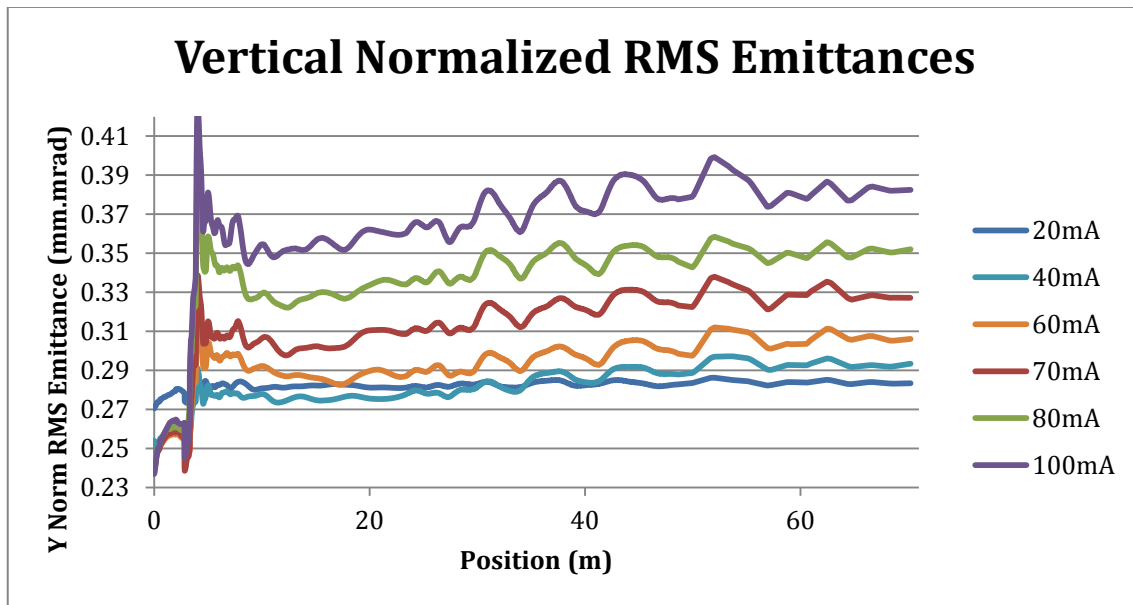


Figure 6: Vertical emittance evolution from MEBT to PIMS.

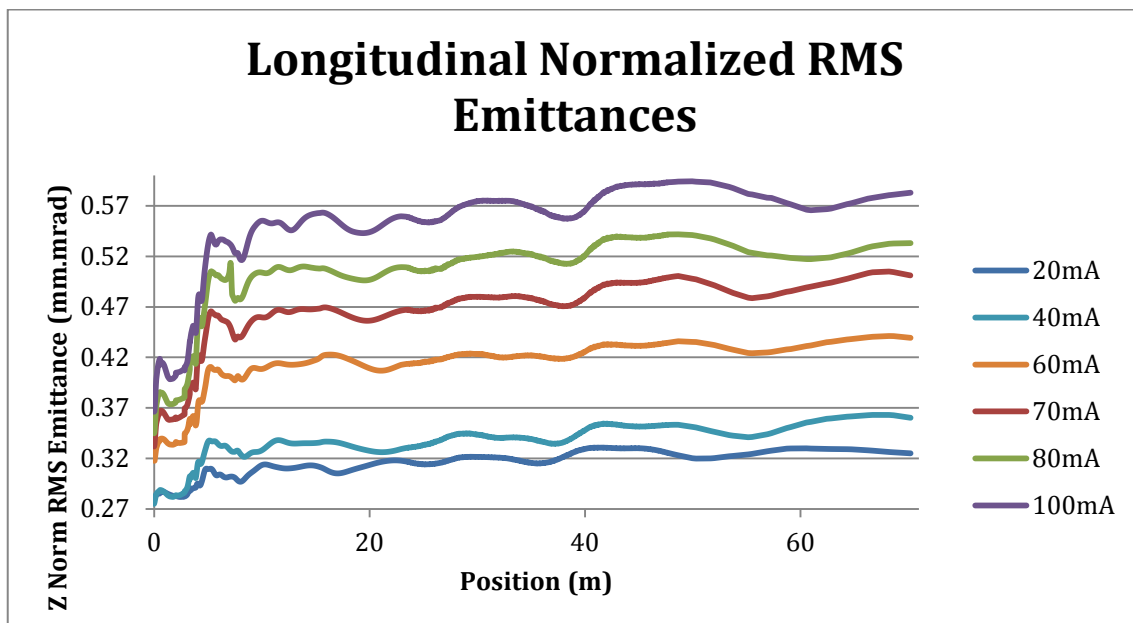


Figure 7: Longitudinal emittance evolution from MEBT to PIMS.

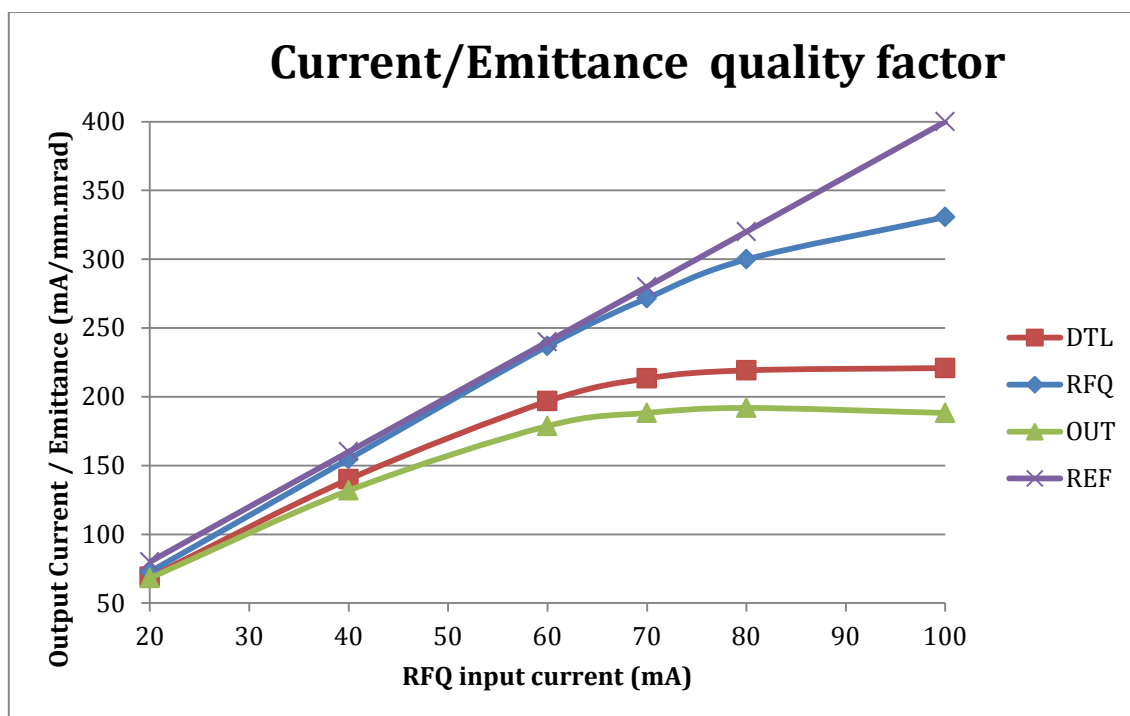


Figure 8: Linac4 structures beam quality factor.

By looking at the evolution of beam quality factor at the Chopper and PIMS outputs, we can notice that the beam quality is almost not degraded along the path between the two structures. As there is no loss in the 70 meters of DTL, CCTL and PIMS, the slight beam degradation is only due the emittance increase. We can then conclude that the Linac4 delivers a constant beam quality until 70-80 mA (considering as acceptable a transmission of 90 % from RFQ to PIMS). Above 80 mA, we observe a saturation effect that over rides the advantages of increasing the source current.

2.2.6 Emittance Reconstruction in Presence of Space Charge

The space charge has an effect not only in the design of a linac but also in the measurements techniques that can be used during the commissioning and operation of a linac. The measurement of the transverse beam emittance at each energy milestone is an essential step during the commissioning of a Linac. At low energy, as the beam penetration depth and activation are low, a direct method based on a slit and grid system is preferred [8]. In this case the effect of space charge happens between the slit and the grid and accurate calculations should be done to evaluate the effect of space charge on the final emittance measurement accuracy. When the beam reaches energies of few tens of MeV the technical realisation of the slit becomes more challenging and therefore indirect methods to measure the emittance are preferred especially for a temporary measurement line. The classical emittance reconstruction techniques, based on measuring the beam profile at three different location, is reliable only if the emittance is conserved and there aren't any self-forces acting on the beam in between the 3 monitors. This latter condition is not fulfilled in the energy range 10-100 MeV for a beam, which carries about 80 mA of peak current. To compensate for this drawback the classical method has been extended by combining it with an iterative process of multi-particle tracking which starts from upstream the suite of monitors and

propagate the beam “forwards” taking into account space charge effects. This very efficient technique - which we call “forward method”- has been applied to the LINAC4 beam at 30, 50, 100 and 160 MeV energy in preparation for the respective beam commissioning stages [3].

An example of the effectiveness of this method is shown in Fig. 9, where the emittance measured by direct method is compared to the emittance obtained from profiles and corrected for space charge effects with the “forward method”.

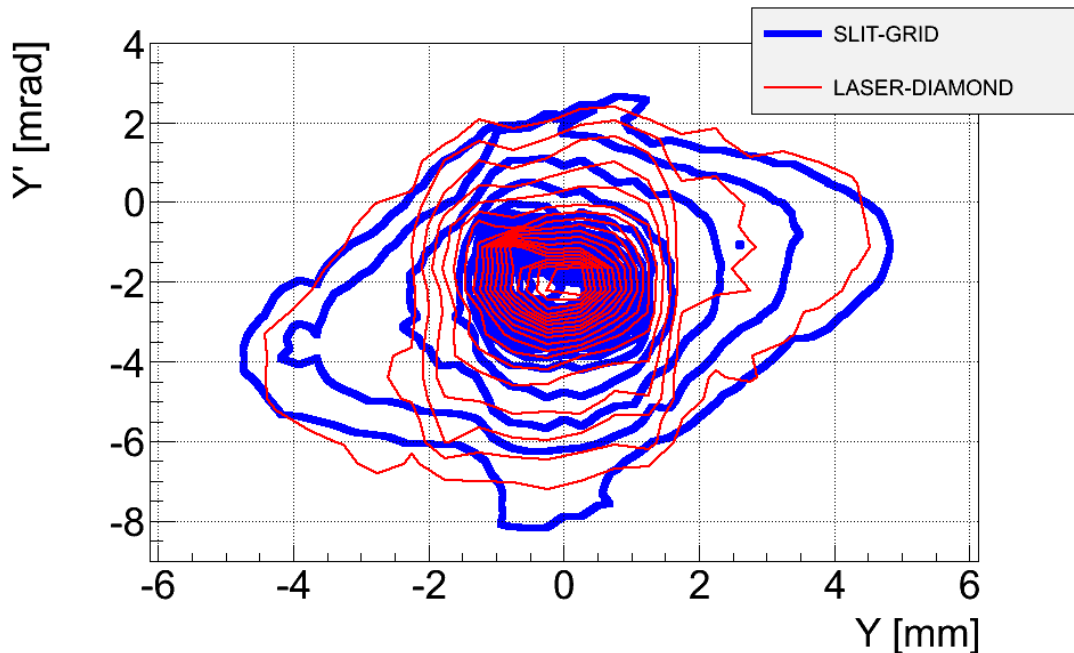


Figure 9: Transverse emittance measured at the linac4 with a 12 MeV. Comparison between measurement with a direct method and indirect method corrected for the effects of space charge.

2.2.7 References

1. M. Vretenar ed., LINAC4 technical Design Report, CERN-AB-2006-084 ABP/RF (2006).
2. A.M. Lombardi, et al., “Beam Dynamics in Linac4 at CERN”, HB’08, Nashville, Tennessee 2008; <http://www.JACoW.org>
3. A.M. lombardi., “Commissioning Of The Low-Energy Part Of Linac4”, in *Proc. Linac’14*, Geneva, Switzerland.CA. Valerio-Lizarraga et al., Space charge compensation in the Linac4 Low Energy Beam Transport line with negative hydrogen ions, *Rev. Sci. Instrum.* 85 , 02A505 (2014).
4. A. J. T. Holmes, *Phys. Rev. A*, Vol. 19, No 1 January (1979).
5. M.E. Rudd, et al., *Phys. Rev. A*. 28, 3244 (1983).
6. M.WEISS, “Radio Frequency Quadrupole”, CERN-PS/87-51 (CAS Aarhus,1986)
7. I. Hofmann et al., “Review of beam dynamics and space charge resonances in high intensity linacs”, EPAC’02 proceedings, Paris, France (2002).
8. J.B. Lallement, et al, “Linac4 Transverse and Longitudinal Emittance Reconstruction in the Presence of Space Charge”, THPP033, these proceedings, LINAC14, Geneva, Switzerland (2014).

2.3 Effect of Space Charge and Nonlinearities in Circular Machines

G. Franchetti, S. Aumon, F. Kesting, H. Liebermann, C. Omet, D. Ondreka, R. Singh
 GSI, Planckstrasse 1
 64291 Darmstadt, Germany
 Mail to: G.Franchetti@gsi.de

2.3.1 The Issue of Space Charge Limit

The beam dynamics of high intensity beams in a circular machine has undergone a change of focus in the past 15 years. The effects of pure space charge studied in the previous decades have become more mixed with the details of the machine, in particular the nonlinear dynamics deriving from the magnet nonlinear components. Accelerator wisdom suggests to limit intensity according to a space charge limit defined as

$$N_{tot} = B_f \frac{4(2\pi)^2 \epsilon_0 m A \gamma^3 v^2}{e^2 Z^2} \frac{|\Delta Q_{xl}|}{f'} \tilde{\epsilon}_x \left(1 + \sqrt{\frac{\langle \beta_y \rangle_s \tilde{\epsilon}_y}{\langle \beta_x \rangle_s \tilde{\epsilon}_x}} \right) \quad (1)$$

where B_f is the bunching factor, m the mass of a nucleon, A the mass number, e the elementary charge, Z the charge state of the ion, $\tilde{\epsilon}_x$ the rms horizontal emittance and $\tilde{\epsilon}_y$ the rms vertical emittance, $|\Delta Q_{xl}|$ the incoherent tune-shift allowed, the “space charge limit”. In addition, $\langle \beta_x \rangle_s$ and $\langle \beta_y \rangle_s$ are the average horizontal and vertical beta functions along the machine. The coefficient f' depends on the type of beam distribution: $f' = 1$ for a transverse KV beam distribution, $f' = 4/3$ for a Waterbag and $f' = 2$ for a Gaussian. The conservative approach to the space charge limit was to assume a limit for $|\Delta Q_{xl}|$ of ~ 0.25 . This number stems from practice where it is assumed that the most dangerous machine resonances are accounted up to the fourth order.

2.3.2 Space Charge Induced Resonance Crossing

The results of the space charge tune-spread overlapping some resonance is the creation of emittance increase or beam loss. Long term beam loss is due to several factors, but lattice nonlinearities and high intensity certainly rank among the main cause. In fact, numerical and experimental studies at the CERN PS have shown that periodic resonance crossing induced by space charge in a bunched beam is a deleterious effect for beam survival (See Ref. [1]). The focus in that study was on the one-dimensional resonance $4Q_x = 25$, which was artificially excited by octupoles. A later study in GSI Ref. [2] has considered the natural resonance $3Q_x = 13$. The underlying mechanism leading to beam loss and emittance growth is explained, for 1D resonances, in terms of instantaneous stable islands in the two-dimensional phase space and their crossing of particles orbits [3].

2.3.3 Third Order Coupling Resonance

Detailed studies for SIS100 have shown that in the injection scenario of the Uranium ions,

random components of magnet nonlinearities excite a significant web of resonances including 2D resonances [4], the simpler of which is third order $Q_x + 2Q_y = N$. The details of the periodic resonance crossing induced by space charge for coupled resonances have never been studied due to the high complexity. In fact, while for 1D resonances the mechanism is relatively well understood, for 2D resonances it is not, as the dynamics is now fully 4-dimensional in phase space. Indication of this complexity, have been observed in the experimental campaign at the CERN-PS in 2012, where space charge studies near the resonance $Q_x + 2Q_y = 19$ have shown that beam profiles for some machine tunes acquired an anomalous asymmetry. In this scenario, new nonlinear dynamics objects called fix-lines play a similar role as the fixed points for the crossing of the 1D resonances. A full study of the fix-lines is reported in Ref. [5]. The code requirements for simulation of long term storage in presence of space charge are discussed in [6].

In SIS100 operational requirements do not allow beam loss to exceed $\sim 5\%$, and the issue of whether a resonance compensation may be carried out for a long-term storage of a high intensity bunched beam or not is of high relevance. Recent numerical studies have shown that resonance compensation in simulations using a frozen space charge model has a beneficial effect on long-term beam loss [4, 7]. However, it remains to be established if this procedure is effective in a real high intensity bunched beam. In fact, resonance compensation is obtained by creating an artificial driving term that counteracts the driving term of the machine nonlinearities [8]. This procedure relies on the assumption that a resonance is excited mainly by a single harmonic. While this assumption works well in standard operational regimes for low intensity beams, it is not obvious what the consequences for multiple periodic resonances crossing induced by space charge are. Below (Fig. 1) is shown an example of single crossing of a 3rd order resonance.

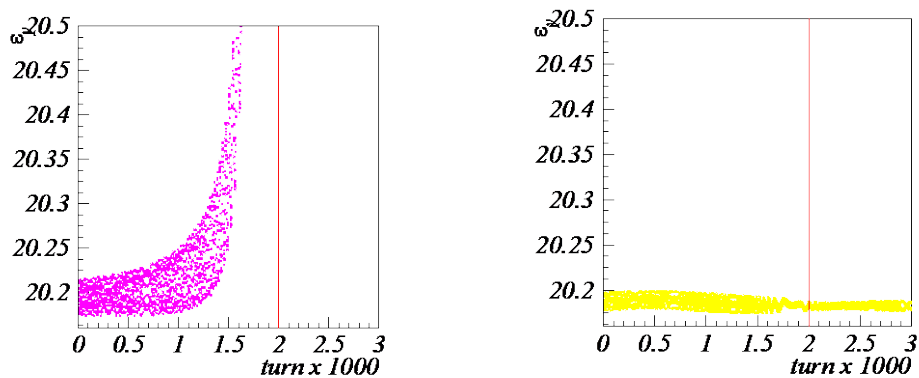


Figure 1: Beam emittance blow up when crossing a third order resonance (left), and for the case with the compensated driving term (right).

In the left picture of Fig. 1 we show the vertical emittance growth for an artificially induced crossing of a third order resonance in a computer simulation. In this example the third order resonance is excited in a computer model creating the driving term $\Lambda_c = 0.45E-01$, $\Lambda_s = 0$. The effect of the resonance is to make the vertical emittance growth entirely caused by the nonlinear dynamics as the space charge is here not included. On the right

picture of Fig. 1, the driving term of the resonance is compensated by using two sextupoles and the yellow curve shows that no emittance growth takes place (as expected). However, in Fig. 2, when the high intensity is activated, the compensation of the driving term is affected by space charge, and a small emittance growth is detected (black curve). The consequences of this residual driving term in a regime of periodic resonance crossing are not easy to estimate, and due to the complexity of the topic, at GSI a campaign for testing the effectiveness of a resonance compensation in presence of space charge has been undertaken.

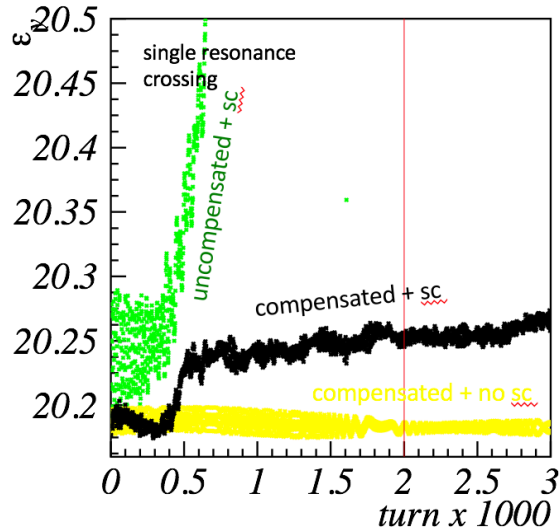


Figure 2: Emittance growth for a single resonance crossing. The black curve shows that the presence of space charge disturbs the compensation of the original resonance driving term.

2.3.4 Third Order Resonance Mitigation

Figure 3 shows the resonance chart of SIS18 after the recent realignment of the accelerator magnets. The apparent mismatch of some of the resonance lines with the theoretical solid lines is due to small systematic tune-shifts present in the machine model used by the control system. The third order resonance $Q_x + 2Q_y = 11$, visibly excited, is of particular interest because a similar resonance will affect the SIS100 for the preliminary working point for ions (example for the Uranium beam scenario at the working point $Q_x = 18.84$, $Q_y = 18.73$) and fast extraction [9]. This resonance strength was estimated by measuring beam loss with Trafo [10] while the resonance is crossed with linear ramp from $Q_y = 3.45$ to $Q_y = 3.35$ in 1 second keeping $Q_x = 4.2$. The beam was coasting with an intensity low enough to prevent space charge effects; in fact, for 2×10^8 ions of U73+, the tune-shift is $\Delta Q_x \approx -2.5 \times 10^{-3}$, $\Delta Q_y \approx -5 \times 10^{-3}$. This is obtained via beam profile measurements [11], and also with the methods in Ref. [12]. In addition, the beam was injected so to fill the transverse acceptances of SIS18, thus emphasizing the beam loss due to resonances. Figure 4 left shows the beam survival during the crossing of the uncompensated machine: only $\sim 35\%$ of the beam survives. The beam loss stop-band is found in $450 \div 750$ ms, which corresponds to $Q_y = 3.375 \div 3.405$.

In order to compensate the resonance $Q_x + 2Q_y = 11$ we created a controlled resonance

driving term by using the normal sextupoles of SIS18. We used two sextupoles (GS05KS3C, GS07KS3C) of strength $K_{2,1}$, $K_{2,2}$, which generate a driving characterized by the strength Λ and by an angle α . As the problem is completely invertible, by setting Λ , α , we obtain $K_{2,1}$, $K_{2,2}$.

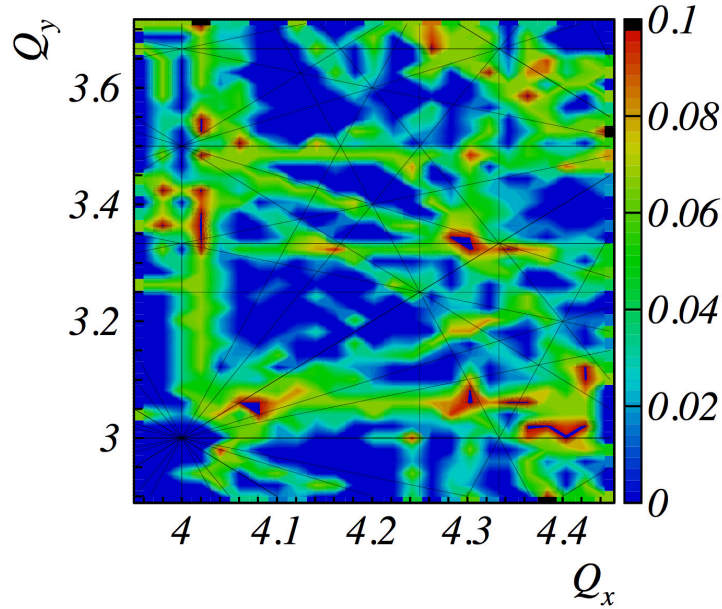


Figure 3: Resonances of SIS18 measured on the 16/7/2014 after the magnets realignment. This picture has been obtained by using SISMODI control system.

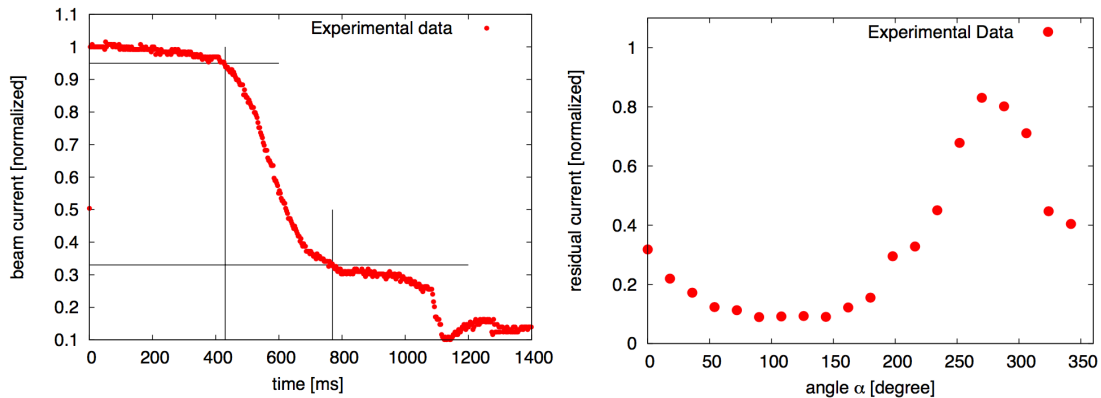


Figure 4: Left: beam survival by crossing the resonance $Q_x + 2Q_y = 11$ in 1 second. The survival is $\sim 35\%$. Right: best compensation for $\Lambda = 0.025$ at $\alpha = 270$ degrees.

Attempts of compensating this resonance at injection energy were obstructed by the resolution of the power supply of the correcting sextupoles. For this reason, the resonance compensation was performed at higher energy 300 MeV/u, so that the overall increase of rigidity would also increase the driving term of the resonance allowing the compensation. We proceed first varying α keeping Λ fixed, in this way we found that the angle $\alpha \sim 270$ degrees is 180 degrees from the phase of the natural driving term. Afterwards we kept fixed

$\alpha = 270$ degrees and vary Λ to find the optimal value that minimized the beam loss for the crossing the resonance. We find that $\Lambda = 0.025$ (the units of Λ are of integrated sextupole strength, as used in the LSA setting generation system). With this procedure, we improved the beam survival from $\sim 35\%$ to $\sim 85\%$, see Fig. 4 right. The reasons of why a better compensation could not be reached could not be found in the beam time available.

2.3.5 Effect of High Intensity on Bunch Dynamics

The result of the trade-off with energy plateau for compensating the resonance is the creation of bunches of moderated high intensity. With these bunches the robustness of the best compensation achieved was tested. For this measurement, the beam was injected, bunched, accelerated, and stored for 1 second keeping the machine tunes fixed (standard operation mode). We explored the bunched beam survival for several working points along the vertical line in the vertical tune, while keeping $Q_x = 4.2$. The beam intensity allowed for a moderate space charge tunes-shift of $\Delta Q_y \sim 0.05$ corresponding to 6.5×10^8 ions of U^{73+} present in the machine before bunching. This tune-spread is not significantly affected by the chromaticity because the momentum spread of the beam at injection is $(\delta p/p)_{\text{rms}} \sim 7.5 \times 10^{-4}$, which for the natural chromaticity yields a maximum tune spread of $(\delta Q_y)_{\text{max}} \sim \pm 7.2 \times 10^{-3}$. Hence the space charge is the dominant perturbation on the linear dynamics. The same argument shows that the effect of the dispersion enlarges/reduces particles amplitudes of ~ 6 mm, which compared with full machine acceptance, becomes of minor relevance.

The results of the scan are shown in Fig. 5. The red markers show the beam survival without resonance correction. We identify three “valleys” corresponding to the effect of three resonances: the half integer $2Q_y = 7$, the third order 2D resonance $Q_x + 2Q_y = 11$, and the third order 1D resonance $3Q_y = 10$. If we set the tune at the edge of the 2D resonance stop-band at $Q_x = 3.405$ of the scan line, the impact on beam survival is dramatic: in 1 second only $\sim 10\%$ of the beam survives, whereas in absence of periodic resonance crossing due to space charge, the beam survival on this working point is nearly 100%.

The blue markers in Fig. 5 show the very same measurements with the two correcting sextupoles activated for the best correction of $Q_x + 2Q_y = 11$, i.e. for creating $\Lambda = 0.025$, $\alpha = 270$ degrees (Fig. 4 left). We find that the partial resonance compensation achieved still yields an advantage to mitigate beam loss induced by the periodic resonance crossing over 1 second storage. In particular, the blue markers show an increased beam survival to $\sim 70\%$ in the range $3.435 < Q_y < 3.46$. For $Q_y = 3.42$ the advantage is evident as beam survival goes from $\sim 30\%$ for the machine uncompensated to $\sim 75\%$ with compensation active.

At tune $Q_y \sim 3.43$ the red curve exhibits a localized change of slope indicating the presence of a weaker resonance possibly of higher order. The effect of this weak resonance is evident when the resonance $Q_x + 2Q_y = 11$ is compensated by the appearing of a new valley in the beam survival. We have no information on the nature of this resonance, except of its weak strength suggested by small beam loss.

We also observe that the resonance compensation here implemented does not affect the other two neighbour resonances, one of which is shown in Fig. 5 (yellow band). In fact, in

the region $3.35 < Q_y < 3.37$ and $3.45 < Q_y < 3.48$, blue and red markers fully overlap showing that the compensating method really affects only this resonance (green band in Fig. 5). Other resonances far away from the investigated area might be excited by this compensation scheme, but the discussion of their effect is not part of this study.

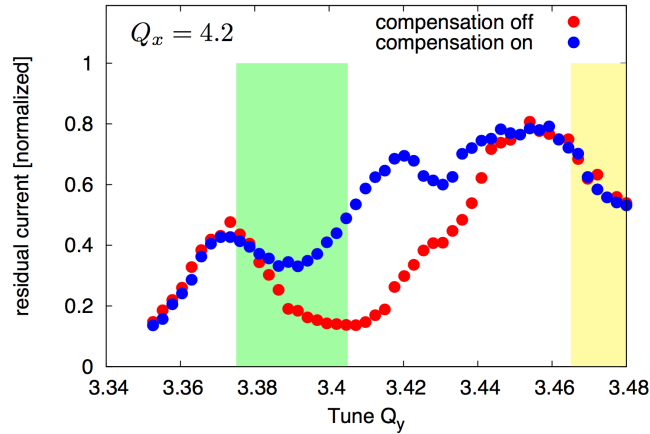


Figure 5: Beam survival for a bunched beam stored for 1 second as function of Q_y . The blue curve is obtained for the partially compensated third order resonance, whereas the red curve is measured for the naked machine.

2.3.6 Issues

The measurements and the results obtained in this campaign allow to conclude the following: 1) The technique used to compensate the resonance seems a promising tool for a first order compensation. The implementation of this “fast” technique completely relies on the feature of the new settings generation system (LSA) for automatizing the data acquisition process. 2) The experimental evidence shows that the resonance compensation for a third order resonance allows mitigating the beam loss due to the effect of moderate space charge in bunched beams stored for 1 second. The physics case, and further details on these measurements will appear in dedicated studies.

The following issues remain to be investigated: 1) We have no clear evidences of why we cannot compensate completely the resonance. This may lay in the imperfect knowledge of the optics at the location of the sextupole correctors, or due to other unknown details of the machine. In fact, there are experimental evidences that different pairs of sextupoles excited to create the same driving term do not produce the same beam survival. All these discrepancies require further investigations to consolidate the method and/or to improve it. 2) The verification with the bunched beams was made with a relatively low intensity $\Delta Q_y \sim 0.05$. The space charge tune-shift here obtained do not compare with that foreseen in the SIS100 scenario, which is expected to be a factor 4 larger. Further measurements on a single third order resonance with more intense beam have to be foreseen to consolidate these first findings.

2.3.7 Acknowledgment

The research leading to these results has received funding from the European Commission under the FP7 Research Infrastructures project EuCARD-2, grant agreement no. 312453.

2.3.8 References

1. G. Franchetti, I. Hofmann, M. Giovannozzi, M. Martini, E. Métral, Phys. Rev. ST Accel. Beams 6, 124201 (2003); E. Métral, G. Franchetti, M. Giovannozzi, I. Hofmann, M. Martini, R. Steerenberg, Nucl. Instr. and Meth. A 561, (2006).
2. G. Franchetti, O. Chorniy, I. Hofmann, W. Bayer, F. Becker, P. Forck, T. Giacomini, M. Kirk, T. Mohite, C. Omet, A. Parfenova, P. Schuett, Phys. Rev. ST Accel. Beams 13, 114203 (2010).
3. G. Franchetti and I. Hofmann, Nucl. Instr. and Meth. A 561, (2006), 195-202; A.W. Chao and M. Month, Nucl. Instrum. Methods 121, 129 (1974).
4. G. Franchetti, S. Sorge, Proc. of IPAC2011, S. Sebastian, Spain. MOPS002. p. 589.
5. G. Franchetti, F. Schmidt, <http://arxiv.org/abs/1504.04389>.
6. F. Schmidt, et al. Proc. of HB 2014, East Lansing, MI, USA 2014.
7. G. Franchetti, S. Sorge, Proc. of IPAC2013, Shanghai, China. TUME001. pag. 1556; G. Franchetti, Proc. of HB2012, Beijing, China, 2012. WEO1C01. pag. 429.
8. A. Schoch, CERN Report No. CERN 57-23, 1958; G. Guignard, "A general treatment of resonances in accelerators", CERN Report No. CERN 78-11, 1978.
9. G. Franchetti, O. Boine-Frankenheim, I. Hofmann, V. Kornilov, P. Spiller, J. Stadlmann, Proc. of 10th European Particle Accelerator Conference, Edinburgh, 2006, ed. C. Biscari, p. 2793.
10. H. Reeg et al., "Current Transformers for GSI's KeV/u to GeV/u Ion Beams - An Overview", Proc. of DIPAC 2001, Grenoble, France, 2001.
11. T. Giacomini et al., "Development of Residual Gas Profile Monitors at GSI", Proc. of BIW'04, Knoxville, U.S.A, 2004.
12. R. Singh et al., "HIGH INTENSITY EFFECTS ON BETATRON TUNE AT GSI SIS-18", Proc. BIW'12, Newport News, U.S.A, 2012.

2.4 Intrabeam Scattering

Michel Martini, Fanouria Antoniou, Yannis Papaphilippou
 CERN, 1211 Geneva 23, Switzerland
 Mail to: Michel.Martini@cern.ch

2.4.1 Introduction

Intrabeam scattering (IBS) consists in the diffusion effects caused by multiple Coulomb scattering on charged particle beams in a storage ring, in both the transverse and the longitudinal beam dimensions. This phenomenon induces the growth in beam emittances and, in some situations, leads to the redistribution of partial beam emittances and energy spread. Thereby, it can cause undesirable beam dilution in phase space or could heat the beam as a whole, i.e. increase the partial beam emittances and energy spread simultaneously. Different compartment results from scattering depending on whether the ring operates below or above transition.

Below transition, small-angle scattering between particles is analogous to particle collisions in a gas, where collisions lead to an equilibrium beam distribution. Above transition, the longitudinal behaviour differs from the one below transition; namely, an energy rise entails a longitudinal velocity decrease as the revolution frequency decreases. The analogy with particles in a gas is no longer valid. Instead, above transition, both the transverse emittances and (longitudinal) energy spread can all grow indefinitely, the energy for the growing oscillation amplitudes being supplied by the radio frequency system.

In the following, we review the conventional IBS Piwinski and Bjorken-Mtingwa formalisms for bunched beams covered in Refs. [1-2], with adaptation of the original Piwinski theory [1] to include the variations of the optical parameters [2], [3]. The Zenkevich Monte Carlo IBS simulation formalism Refs. [11-12] based on binary collision models are also discussed in Refs. [14-15]. Finally, the benchmarking of the IBS theoretical models with Monte-Carlo codes is being presented before the conclusion.

2.4.2 Piwinski Model

2.4.2.1 Collisional Momentum Kinematic and Emittance Variations

According to Piwinski [1], for two particles, labelled 1 and 2, colliding with each other, the momentum changes in longitudinal and transverse directions for particle 1 can be written as follows, with $\delta\vec{p}_1 = \delta p_{s_1}\hat{s} + \delta p_{x_1}\hat{x} + \delta p_{z_1}\hat{z}$:

$$\frac{\delta\vec{p}_1}{p} = \frac{\vec{p}'_1 - \vec{p}_1}{p} = \begin{cases} \frac{1}{2} [2\gamma\alpha \cos\bar{\phi} \sin\bar{\psi} + \gamma\xi(\cos\bar{\psi} - 1)] \\ \frac{1}{2} \left[\left(\zeta \sqrt{1 + \frac{\xi^2}{4\alpha^2}} \sin\bar{\phi} - \frac{\xi\theta}{2\alpha} \cos\bar{\phi} \right) \sin\bar{\psi} + \theta(\cos\bar{\psi} - 1) \right], \\ \frac{1}{2} \left[\left(\theta \sqrt{1 + \frac{\xi^2}{4\alpha^2}} \sin\bar{\phi} - \frac{\xi\zeta}{2\alpha} \cos\bar{\phi} \right) \sin\bar{\psi} + \zeta(\cos\bar{\psi} - 1) \right] \end{cases} \quad (1)$$

where $p = |\vec{p}|$ is the mean particle momentum, $\bar{\psi}, \bar{\phi}$ are the scattering and azimuthal angles in the centre of mass (CM) of a two particles collisional event and γ is the Lorenz factor.

The variable ξ, θ, ζ will be used as integration variables for the averaging process of the particle density distribution inside a bunch, γ is the Lorenz factor:

$$\xi = \frac{p_1 - p_2}{\gamma p}, \quad \theta = \frac{p_{x1} - p_{x2}}{p} \equiv x'_1 - x'_2, \quad \zeta = \frac{p_{z1} - p_{z2}}{p} \equiv z'_1 - z'_2, \quad (2)$$

$$2\alpha = \alpha_1 + \alpha_2 = \sqrt{(x'_1 - x'_2)^2 + (z'_1 - z'_2)^2} = \sqrt{\theta^2 + \zeta^2}. \quad (3)$$

A particle velocity in the CM frame is assumed non-relativistic i.e. $\bar{\beta} = \sqrt{1 - \bar{\gamma}^{-2}} \ll 1$ and the particle angles made with the longitudinal axis are small, $\xi, \theta, \zeta \ll 1$.

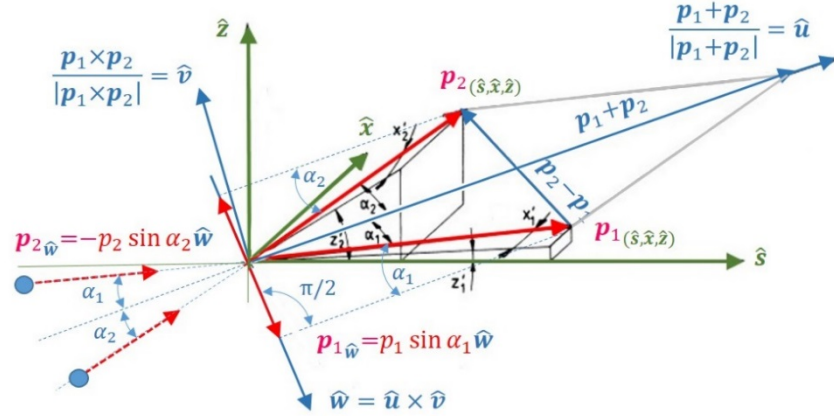


Figure 1: Connexion between the LAB coordinate system $(\hat{s}, \hat{x}, \hat{z})$ and the overlaid $(\hat{u}, \hat{v}, \hat{w})$ coordinate system aligned on the CM motion (cf. Piwinski [1]).

The invariants of the motion are the transverse emittances $\varepsilon_{x,z}$ (Courant–Snyder invariant) and the quantity H for the longitudinal plane assuming a bunched beam.

$$\varepsilon_x = \gamma_x x_\beta^2 + 2\alpha_x x_\beta x'_\beta + \beta_x x_\beta'^2, \quad H = \left(\frac{\Delta p}{p}\right)^2 + \frac{1}{\Omega_s^2} \left[\frac{d}{dt} \left(\frac{\Delta p}{p}\right) \right]^2, \quad (4)$$

where $\alpha_x, \beta_x, \gamma_x$ are the Twiss parameters, with $\beta_x \gamma_x - \alpha_x^2 = 1$, $2\alpha_x = -\beta'_x$ and Ω_s is the synchrotron frequency.

The alteration in the particle momenta after collision leads to a corresponding change in the particle invariants. Supposing the transverse particle locations stay fixed over the collision time allows calculating the invariant change. The change $\delta\varepsilon_{x,z}$ and δH in the invariant after a single scattering event can be written as:

$$\begin{aligned} \delta H &= 2 \frac{\Delta p}{p} \frac{\delta p}{p} + \left(\frac{\delta p}{p}\right)^2, \\ \frac{\delta\varepsilon_x}{\beta_x} &= -\frac{2}{\beta_x} [x_\beta (\gamma_x D_x + \alpha_x D'_x) + x'_\beta \tilde{D}'_x] \frac{\delta p}{p} + \frac{D_x^2 + \tilde{D}_x^2}{\beta_x^2} \left(\frac{\delta p}{p}\right)^2, \\ &+ 2 \left(x'_\beta + \frac{\alpha_x}{\beta_x} x_\beta\right) \frac{\delta p_x}{p} + \left(\frac{\delta p_x}{p}\right)^2 - \frac{2\tilde{D}_x}{\beta_x} \frac{\delta p}{p} \frac{\delta p_x}{p}, \end{aligned} \quad (5)$$

where $D_{x,z}$ are the horizontal and vertical dispersions, $\tilde{D}_{x,z} = \alpha_{x,z} D_{x,z} + \beta_{x,z} D'_{x,z}$ with $\delta(\Delta p/p) = \delta p/p$ as the reference momentum stays constant when the beam is not accelerated. We have neglected the time variation of the synchrotron frequency during the collision. From now on the short notation $\eta \stackrel{\text{def}}{=} \Delta p/p$ will be used.

To calculate the mean value of the emittance and momentum deviation change for one particle, we have to average with respect to the second particle betatron angles and momentum deviations. Therefore, to get the overall mean value of the emittance and momentum deviation changes for all particles, we have to average further with respect to all betatron angles, momentum deviations and positions of the first particle. This means that we have to integrate over all phase space volume V of betatron coordinates, momentum deviations and azimuthal positions of two interacting particles, using a probability density function P for the betatron amplitudes and angles, momentum deviations and azimuthal positions of the interacting particles:

$$\left\langle \frac{d}{d\bar{t}} \frac{\langle \varepsilon_{x_1} \rangle}{\beta_x} \right\rangle = \int_{\bar{V}} 2c\bar{\beta} \bar{P} d\bar{V} \int_{\bar{\psi}_{min}}^{\pi} d\bar{\psi} \int_0^{2\pi} d\bar{\phi} \bar{\sigma}(\bar{\psi}) \sin \bar{\psi} \frac{\delta \varepsilon_{x_1}}{\beta_x}, \quad (6)$$

where the outer and inner brackets denote the average value over the ring optical parameters and the average over the particle beam. An overhead bar symbol refers to the CM frame. Here, $\bar{\sigma}(\bar{\psi})d\bar{\Omega}$ is the Coulomb scattering cross-section in the CM frame for a scattering event into a solid angle $d\bar{\Omega}(\bar{\psi}, \bar{\phi}) = \sin \bar{\psi} d\bar{\psi} d\bar{\phi}$. The time intervals in CM and LAB frames are $d\bar{t}$ and dt ($dt = \gamma d\bar{t}$), c is the speed of light, $2c\bar{\beta}$ is the relative velocity of two interacting particles in the CM frame and P is a probability density function of 12 phase space variables for the particle pair in the LAB frame (and $\bar{P} = P/\gamma$ in CM). P reduces to 9 variables as $s_1 = s_2$ and $x_{\beta_1} + D_x \eta_1 = x_{\beta_2} + D_x \eta_2$ (idem for $z_{\beta_{1,2}}$) since the positions the particles are supposed to remain constant during the collision, i.e.

$$P \stackrel{12\text{var}}{\iff} P_{\eta_s}(\eta_1, s_1) P_{\eta_s}(\eta_2, s_2) P_{x_{\beta} x'_{\beta}}(x_{\beta_1} x'_{\beta_1}) P_{x_{\beta} x'_{\beta}}(x_{\beta_2} x'_{\beta_2}) P_{z_{\beta} z'_{\beta}}(z_{\beta_1} z'_{\beta_1}) P_{z_{\beta} z'_{\beta}}(z_{\beta_2} z'_{\beta_2}), \quad (7)$$

$$P \stackrel{9\text{var}}{\iff} P_{\eta}(\eta_1) P_{\eta}(\eta_2) P_s(s_1) P_{x_{\beta}}(x_{\beta_1}) P_{x'_{\beta}}(x'_{\beta_1}) P_{x'_{\beta}}(x'_{\beta_2}) P_{z_{\beta}}(z_{\beta_1}) P_{z'_{\beta}}(z'_{\beta_1}) P_{x'_{\beta}}(z'_{\beta_2}).$$

2.4.2.2 Averaging over the Scattering Angles and All Particles

Using the ‘‘classical’’ Rutherford differential cross-section $\sigma(\bar{\psi})$ the likelihood of a collision per unit time and solid angle element $d\bar{\phi}$ in CM frame, denoted P_{scat} , is determined by the particle density distribution in phase space P (LAB frame). Since $2\bar{\beta}c$ is the relative velocity between two colliding particles we can write

$$P_{\text{scat}}(\bar{\psi}, \bar{\phi}, P) = \frac{2\bar{\beta}cP\sigma(\bar{\psi})d\bar{\Omega}}{\gamma^2}, \quad \bar{\sigma}(\bar{\psi})d\bar{\Omega} = \frac{r_i^2}{16\bar{\beta}^4 \sin^4[\frac{\bar{\psi}}{2}]} \sin \bar{\psi} d\bar{\psi} d\bar{\phi}, \quad r_i = \frac{e^2 Z^2}{4\pi\epsilon_0 m c^2 A}, \quad (8)$$

r_i is the classical ion radius in SI units, with the ion mass and charge A, Z , relative to proton or the electron mass m and electron charge e (the second γ^2 comes from an ‘‘underlying’’ time interval $d\bar{t} = dt/\gamma$). Let us mention that for non-relativistic collisions the maximum impact parameter \bar{b}_{max} gives a cut-off value $\bar{\psi}_{\text{min}}$ for the scattering angle, \bar{C}_{log} is the ‘‘Coulomb logarithm’’:

$$\tan \frac{\bar{\psi}_{\text{min}}}{2} \approx \frac{r_i}{2\bar{\beta}^2 \bar{b}_{\text{max}}}, \quad \text{if } \bar{\psi}_{\text{min}} \ll 1: \quad \bar{C}_{\text{log}} \stackrel{\text{def}}{=} \log \frac{\bar{b}_{\text{max}}}{\bar{b}_{\text{min}}} \approx \log \frac{2}{\bar{\psi}_{\text{min}}} \approx \log \frac{2\bar{\beta}^2 \bar{b}_{\text{max}}}{r_i}. \quad (9)$$

In the LAB frame $b_{\text{max}} = \bar{b}_{\text{max}}$ and the Coulomb logarithm is defined alike $C_{\text{log}} \approx \log \frac{2\beta^2 b_{\text{max}}}{r_i}$. For example, integrating $\langle \delta H_1 \rangle / \gamma^2$ over $\bar{\phi}$ and $\bar{\psi}$ gives with Eq. (9)

$$\int_{\bar{\psi}_{min}}^{\pi} d\bar{\psi} \int_0^{2\pi} d\bar{\phi} \bar{\sigma}(\bar{\psi}) \sin \bar{\psi} \left\{ \frac{\delta H_1}{\gamma^2} \right\} = \frac{\pi r_i^2}{4\bar{\beta}^4} \log \left[\frac{2\bar{\beta}^2 \bar{b}_{max}}{r_i} \right] \left\{ -\frac{4\eta_1}{\gamma} \xi + \theta^2 + \zeta^2 \right\}. \quad (10)$$

At this stage we make the following ad-hoc change of phase space variables, in conformity with Eq. (2), to compute the mean change of the invariants $\varepsilon_{x,z}$ and H . Here, the density distribution P transforms into \mathcal{P} , using new variables including the angles ξ, θ, ζ :

$$P(\eta_1, \eta_2, s_1, x_{\beta_1}, x'_{\beta_1}, x_{\beta_2}, x'_{\beta_2}, z_{\beta_1}, z'_{\beta_1}, z_{\beta_2}, z'_{\beta_2}) \mapsto \mathcal{P}(\eta, \xi, s, x_{\beta}, x'_{\beta}, \theta, z_{\beta}, z'_{\beta}, \zeta), \quad (11)$$

$$\begin{aligned} x_{\beta_{1,2}} &= x_{\beta} \mp \frac{D_x \gamma \xi}{2}, & x'_{\beta_{1,2}} &= x'_{\beta} \pm \frac{\theta - D'_x \gamma \xi}{2}, & \eta_{1,2} &= \eta \pm \frac{\gamma \xi}{2}, \\ z_{\beta_{1,2}} &= z_{\beta} \mp \frac{D_z \gamma \xi}{2}, & z'_{\beta_{1,2}} &= z'_{\beta} \pm \frac{\zeta - D'_z \gamma \xi}{2}, & \eta_{1,2} &= \eta \pm \frac{\gamma \xi}{2}. \end{aligned} \quad (12)$$

Obviously, \mathcal{P} is symmetric with respect to ξ, θ, ζ and thus the integrals vanish for the linear terms in ξ, θ, ζ of the integrands. Then, keeping only the factors ξ^2, θ^2, ζ^2 and using the variables $\eta, \xi, s, x_{\beta}, x'_{\beta}, \theta, z_{\beta}, z'_{\beta}, \zeta$ defined in Eqs. (11-12) to integrate the three invariants (see Eq. (6)) yields Eq. (12), where the phase space volume element expressed in the new variables is $d\mathcal{V} = d\eta d\xi ds dx_{\beta} dx'_{\beta} d\theta dz_{\beta} dz'_{\beta} d\zeta$:

$$\left\langle \frac{d}{dt} \begin{bmatrix} \langle H \rangle / \gamma^2 \\ \langle \varepsilon_x \rangle / \beta_x \\ \langle \varepsilon_z \rangle / \beta_z \end{bmatrix} \right\rangle = \frac{\pi c r_i^2}{2} \int_{\mathcal{V}} \frac{d\mathcal{V}}{\beta^3 \gamma} \mathcal{P}(\eta, s, \xi, x_{\beta}, x'_{\beta}, \theta, z_{\beta}, z'_{\beta}) \log \left[\frac{2\bar{\beta}^2 \bar{b}_{max}}{r_i} \right] \left\{ \begin{aligned} &\theta^2 + \zeta^2 - 2\xi^2 \\ &\xi^2 + \zeta^2 - 2\theta^2 + \frac{D_x^2 + \bar{D}_x^2}{\beta_x^2} \gamma^2 (\theta^2 + \zeta^2) - \frac{2\gamma_x D_x^2}{\beta_x} \gamma^2 \xi^2 - \frac{2D'_x}{\beta_x} (\alpha_x D_x + \bar{D}_x) \gamma^2 \xi^2 \\ &\xi^2 + \theta^2 - 2\zeta^2 + \frac{D_z^2 + \bar{D}_z^2}{\beta_z^2} \gamma^2 (\theta^2 + \zeta^2) - \frac{2\gamma_z D_z^2}{\beta_z} \gamma^2 \xi^2 - \frac{2D'_z}{\beta_z} (\alpha_z D_z + \bar{D}_z) \gamma^2 \xi^2 \end{aligned} \right\}. \quad (13)$$

This formula for the mean change of the invariants makes no supposition about the distribution \mathcal{P} of particles in the bunch. Therefore, the integral can be in principle computed for arbitrary probability laws. However, since ‘‘Gaussian integration’’ is easily performed, many analytical IBS models are based on Gaussian distributions.

So, we use here bi-Gaussian density distributions for the betatron amplitudes and angles $P_{x_{\beta} x'_{\beta}}(x_{\beta_{1,2}}, x'_{\beta_{1,2}})$, $P_{z_{\beta} z'_{\beta}}(z_{\beta_{1,2}}, z'_{\beta_{1,2}})$ and the momentum and bunch length $P_{\eta s}(\eta_{1,2}, s_{1,2})$. Also, to shorten the formalism and obtain manageable formulae we will neglect the derivatives of the dispersion and transverse betatron functions:

$$D'_{x,z} = 0, \quad \beta'_{x,z} = -2\alpha_{x,z} = 0, \quad \bar{D}_{x,z} = \alpha_{x,z} D_{x,z} + \beta_{x,z} D'_{x,z} = 0, \quad \gamma_{x,z} = \frac{1}{\beta_{x,z}}. \quad (14)$$

Then, with the change of variables (Eq. (12)), we rewrite the Gaussian distributions in terms of the nine new variables, $\eta, s, \xi, x_{\beta}, x'_{\beta}, \theta, z_{\beta}, z'_{\beta}, \zeta$:

$$\begin{aligned} \mathcal{P}_{x_{\beta} x'_{\beta}} \left(x_{\beta} \mp \frac{D_x \gamma \xi}{2}, x'_{\beta} \pm \frac{\theta}{2} \right), & \quad \mathcal{P}_{z_{\beta} z'_{\beta}} \left(z_{\beta} \mp \frac{D_z \gamma \xi}{2}, z'_{\beta} \pm \frac{\zeta}{2} \right), \\ \mathcal{P}_{\eta} \left(\eta \pm \frac{\gamma \xi}{2} \right), & \quad \mathcal{P}_s(s). \end{aligned} \quad (15)$$

After integration of the distribution \mathcal{P} over the 6 variables $x_\beta, x'_\beta, z_\beta, z'_\beta, \eta, s$, we get:

$$\begin{aligned} \mathcal{P}(\xi, \theta, \zeta) &\equiv N_b \prod_{u=x_\beta, x'_\beta}^{\eta, s} \int_{-\infty}^{\infty} \mathcal{P}_u du \\ &= \frac{\mathcal{A} \beta^3 \gamma^4}{c r_1^2 \pi} \exp \left[-\frac{\gamma^2 \xi^2}{4} \left(\frac{1}{\sigma_\eta^2} + \frac{D_x^2}{\sigma_{x_\beta}^2} + \frac{D_z^2}{\sigma_{z_\beta}^2} \right) - \frac{\theta^2}{4 \sigma_{x'_\beta}^2} - \frac{\zeta^2}{4 \sigma_{z'_\beta}^2} \right], \\ \mathcal{A} &= \frac{c r_1^2 N_b}{64 \pi^2 \beta^3 \gamma^4 \sigma_{x_\beta} \sigma_{x'_\beta} \sigma_{z_\beta} \sigma_{z'_\beta} \sigma_\eta \sigma_s} = \frac{c r_1^2 N_b}{64 \pi^2 \beta^3 \gamma^4 \varepsilon_x \varepsilon_z \varepsilon_s}, \end{aligned} \quad (16)$$

where N_b is the number of particles in the bunch, $\varepsilon_s = \sigma_\eta \sigma_s$ and $\varepsilon_{x,z} = \sigma_{x_\beta, z_\beta}^2 / \beta_{x,z} \equiv \sigma_{x'_\beta, z'_\beta}^2 \beta_{x,z}$ are the longitudinal and transverse rms emittances. Assuming non-relativistic particle velocities in the CM frame, we express β in LAB frame by means of a momentum-energy Lorentz transformation from CM to LAB. We obtain (Ref. [1]):

$$\bar{\beta} \approx \frac{\beta \gamma}{2} \sqrt{\left(\frac{\eta_1 - \eta_2}{\gamma} \right)^2 + (x'_1 - x'_2)^2 + (z'_1 - z'_2)^2} = \frac{\beta \gamma}{2} \sqrt{\xi^2 + \theta^2 + \zeta^2}. \quad (17)$$

Finally, it remains to transform the change of momenta and energy for the two colliding particles back to the LAB frame, replacing $\bar{\beta}$ by its approximation Eq. (17). Let us define the parameter $q = \gamma \sqrt{2 \beta^2 b_{\max} / r_1}$. Since $D'_{x,z} = \alpha_{x,z} = 0$ we can rework Eq. (13) this way:

$$\begin{aligned} \left\langle \frac{d}{dt} \left[\frac{\langle H \rangle / \gamma^2}{\langle \varepsilon_x \rangle / \beta_x} \right] \right\rangle &= 4 \mathcal{A} \iiint_{-\infty}^{\infty} \exp \left[-\frac{\gamma^2 \xi^2}{4} \left(\frac{1}{\sigma_\eta^2} + \frac{D_x^2}{\sigma_{x_\beta}^2} + \frac{D_z^2}{\sigma_{z_\beta}^2} \right) - \frac{\theta^2}{4 \sigma_{x'_\beta}^2} - \frac{\zeta^2}{4 \sigma_{z'_\beta}^2} \right] \\ &\left\{ \begin{array}{l} \theta^2 + \zeta^2 - 2\xi^2 \\ \xi^2 + \zeta^2 - 2\theta^2 + \frac{D_x^2}{\beta_x^2} \gamma^2 (\theta^2 + \zeta^2 - 2\xi^2) \\ \xi^2 + \theta^2 - 2\zeta^2 + \frac{D_z^2}{\beta_z^2} \gamma^2 (\theta^2 + \zeta^2 - 2\xi^2) \end{array} \right\} \log \left[\frac{q^2}{4} (\xi^2 + \theta^2 + \zeta^2) \right] \frac{d\xi d\theta d\zeta}{\xi^2 + \theta^2 + \zeta^2} \end{aligned} \quad (18)$$

The remaining three integrals still need to be computed to get the mean change of the invariants. To this end, let us do a first change of variables $\xi, \theta, \zeta \rightarrow 2(u, v, w)/q$ to transform Eq. (18) to the coordinates (u, v, w) , followed, by a second spherical-like change of variables $(u, v, w) \rightarrow \sqrt{r}(\sin \mu \cos \nu, \sin \mu \sin \nu, \cos \mu)$. This trick will allow us to derive the IBS growth rates in a synchrotron after some more approximations.

2.4.2.3 Calculation of Rise Times Neglecting $\alpha_{x,z}$ and $D'_{x,z}$

The IBS growth rates can be expressed in the form

$$\frac{1}{T_\eta} = \frac{1}{\sigma_\eta} \frac{d\sigma_\eta}{dt} \equiv \frac{1}{2\langle H \rangle} \frac{d\langle H \rangle}{dt}, \quad \frac{1}{T_{x,z}} = \frac{1}{\sigma_{x_\beta z_\beta}} \frac{d\sigma_{x_\beta z_\beta}}{dt} \equiv \frac{1}{2\langle \varepsilon_{x,z} \rangle} \frac{d\langle \varepsilon_{x,z} \rangle}{dt}, \quad (19)$$

where T_η, T_x and T_z are the longitudinal, horizontal, and vertical IBS rise times, and $H = \eta^2$, supposing negligible synchrotron frequency values (i.e. $\Omega_s \approx 0$) for the duration of a particle-pair collision. Evidently, the time derivatives of $\langle H \rangle / \gamma^2$ and $\langle \varepsilon_{x,z} \rangle / \beta_{x,z}$ in Eq. (18) have to

be revisited to match the growth rate definition. For this, let us define the following parameters and functions [6]

$$\frac{1}{\sigma_h^2} = \frac{1}{\sigma_\eta^2} + \frac{D_x^2}{\sigma_{x\beta}^2} + \frac{D_z^2}{\sigma_{z\beta}^2}, \quad \sigma_h^2 = \frac{\sigma_\eta^2 \sigma_{x\beta}^2}{D_x^2 \sigma_\eta^2 + \sigma_{x\beta}^2 \left[1 + \left(\frac{D_z \sigma_\eta}{\sigma_{z\beta}} \right)^2 \right]} \xrightarrow{D_z=0} \sigma_h = \frac{\sigma_\eta \sigma_{x\beta}}{\sigma_x},$$

$$a = \frac{\sigma_h}{\gamma \sigma_{x\beta}'} \equiv \frac{\sigma_h}{\gamma} \sqrt{\frac{\varepsilon_x}{\beta_x}} \xrightarrow{D_z=\alpha_{x,z}=0} a = \frac{\beta_x \sigma_\eta}{\gamma \sigma_x}, \quad b = \frac{\sigma_h}{\gamma \sigma_{z\beta}'} \equiv \frac{\sigma_h}{\gamma} \sqrt{\frac{\varepsilon_z}{\beta_z}} \xrightarrow{D_z=\alpha_{x,z}=0} b = \frac{\beta_z \sigma_\eta}{\gamma \sigma_z}, \quad (20)$$

$$c = q \sigma_h = \left(\gamma \sqrt{\frac{2\beta^2 b_{\max}}{r_i}} \right) \sigma_h \stackrel{\text{Eq.9}}{\iff} \gamma \exp\left[\frac{C_{\log}}{2}\right] \sigma_h,$$

$$D(\mu, \nu) = \frac{1}{c^2} (b^2 \cos^2 \mu + \sin^2 \mu (\cos^2 \nu + a^2 \sin^2 \nu)),$$

$$g_1(\mu, \nu) = 1 - 3 \sin^2 \mu \cos^2 \mu \quad g_2(\mu, \nu) = 1 - 3 \sin^2 \mu \sin^2 \nu, \quad (21)$$

$$g_3(\mu, \nu) = 1 - 3 \cos^2 \mu,$$

where C_{\log} is the Coulomb logarithm (cf. Eq. (9)). Thus Eq. (19) can be written

$$\begin{aligned} \begin{bmatrix} 1/T_\eta \\ 1/T_x \\ 1/T_z \end{bmatrix} &= \left\langle \frac{q^2}{2c^2} \begin{bmatrix} \sigma_h^2 / \sigma_\eta^2 \\ a^2 \\ b^2 \end{bmatrix} \frac{d}{dt} \begin{bmatrix} \langle H \rangle / \gamma^2 \\ \langle \varepsilon_x \rangle / \beta_x \\ \langle \varepsilon_z \rangle / \beta_z \end{bmatrix} \right\rangle = \frac{\mathcal{A}}{c^2} \int_0^\infty dr \int_0^\pi d\mu \int_0^{2\pi} d\nu \\ &\times \sin \mu \exp[-rD(\mu, \nu)] \log[r] \begin{Bmatrix} \frac{\sigma_h^2}{\sigma_\eta^2} g_1(\mu, \nu) \\ a^2 g_2(\mu, \nu) + \frac{D_x^2 \sigma_h^2}{\beta_x \varepsilon_x} g_1(\mu, \nu) \\ b^2 g_3(\mu, \nu) + \frac{D_z^2 \sigma_h^2}{\beta_z \varepsilon_z} g_1(\mu, \nu) \end{Bmatrix} \end{aligned} \quad (22)$$

We can rewrite a more compact form of Eq. (22), replacing the 3 functions g_i by the ‘‘scattering function’’ $f(a, b, c)$, where $\rho=r/c^2$ replaces r and adding the function D_0 :

$$D_0(\mu, \nu) = \sin^2 \mu (a^2 \cos^2 \nu + b^2 \sin^2 \nu) + \cos^2 \mu, \quad (23)$$

$$f(a, b, c) = 2 \int_0^\pi d\mu \int_0^{2\pi} d\nu \sin \mu (1 - 3 \cos^2 \mu) \\ \times \int_0^\infty d\rho \log[c^2 \rho] \exp[-\rho D_0(\mu, \nu)]. \quad (24)$$

The integral over ρ can be solved analytically:

$$\int_0^\infty d\rho \log[c^2 \rho] \exp[-\rho D_0(\mu, \nu)] = \frac{-C_{\text{Euler}} + 2 \log c - \log[D_0(\mu, \nu)]}{D_0(\mu, \nu)}, \quad (25)$$

were $C_{\text{Euler}} \approx 0.5772$ is Euler’s constant. From Eq. (20), we get $\log c^2 = C_{\log} + \log[\gamma^2 \sigma_h^2] \approx C_{\log}$ assuming that $C_{\log} \gg \log[\gamma^2 \sigma_h^2]$. This sounds fine as in most cases $10 \lesssim C_{\log} \lesssim 20$ (e.g. for the LHC: $\gamma=7000$, $\sigma_\eta \approx 10^{-4}$, $C_{\log} \approx 20$, and with $\sigma_h \approx \sigma_\eta$ we get $\log[c^2] \approx C_{\log} \gg \log[\gamma^2 \sigma_\eta^2] = -0.7$). The remaining variables μ, ν are then transformed into $x = \cos \mu$, $z = 2\nu$ using symmetry properties of trigonometric functions. Hence, using Eq.

(25), f can be reduced to a single integral (see Ref. [7]) and cast into the form (with $\tilde{C}=2 \log c - C_{\text{Euler}}$):

$$f(a, b, c) = 8\pi \int_0^1 dx \left(2 \log \left[\frac{\tilde{c}}{2} \left\{ \frac{1}{\sqrt{P(x)}} + \frac{1}{\sqrt{Q(x)}} \right\} \right] - C_{\text{Euler}} \right) \frac{1-3y^2}{\sqrt{P(y)Q(y)}}, \quad (26)$$

$$P(y) = a^2 + (1-a^2)y^2 \quad Q(y) = b^2 + (1-b^2)y^2.$$

After some work, the IBS growth rates for bunched beams (Eq. 22) are written as in [6]-[9]:

$$\begin{pmatrix} \frac{1}{T_\eta} \\ \frac{1}{T_x} \\ \frac{1}{T_z} \end{pmatrix} = \mathcal{A} \begin{pmatrix} \left\langle \frac{\sigma_h^2}{\sigma_\eta^2} f(a, b, c) \right\rangle \\ \left\langle f\left(\frac{1}{a}, \frac{b}{a}, \frac{c}{a}\right) + \frac{D_x^2 \sigma_h^2}{\beta_x \varepsilon_x} f(a, b, c) \right\rangle \\ \left\langle f\left(\frac{1}{b}, \frac{a}{b}, \frac{c}{b}\right) + \frac{D_z^2 \sigma_h^2}{\beta_z \varepsilon_z} f(a, b, c) \right\rangle \end{pmatrix}. \quad (27)$$

The first term in each transverse growth rate of Eq. (27) corresponds to a straight excitation of their own emittance. Each of the second term relates to the longitudinal growth rate T_η^{-1} and to the dispersion $D_{x,z}^2$ that possibly makes a coupling of the longitudinal growth into their respective transverse planes.

Many storage rings are planar (with reference orbit in the median plane (s, x) i.e. zero vertical dispersion $D_z=0$). So, Eq. (26) shortens to (with $1 - D_x^2 \sigma_\eta^2 / \sigma_x^2 = \sigma_h^2 / \sigma_\eta^2$):

$$\begin{pmatrix} \frac{1}{T_\eta} \\ \frac{1}{T_x} \\ \frac{1}{T_z} \end{pmatrix} = \mathcal{A} \begin{pmatrix} \left\langle \left[1 - \frac{D_x^2 \sigma_\eta^2}{\sigma_x^2} \right] f(a, b, c) \right\rangle \\ \left\langle f\left(\frac{1}{a}, \frac{b}{a}, \frac{c}{a}\right) + \frac{D_x^2 \sigma_\eta^2}{\sigma_x^2} f(a, b, c) \right\rangle \\ \left\langle f\left(\frac{1}{b}, \frac{a}{b}, \frac{c}{b}\right) \right\rangle \end{pmatrix}, \quad (28)$$

which is the original IBS Piwinski's formula [1]. As the growth times change with the momentum spread (square) η^2 and the emittances $\varepsilon_{x,z}$, an iterative procedure is needed to compute the evolution of growth time, and so update η^2 and $\varepsilon_{x,z}$ (cf. last chapter).

2.4.2.4 *Invariant*

In the presence of IBS, bunched beams may experience phase space dilution leading to continuous growth of the momentum spread and/or growth of one or both transverse emittances. The performance of the beam can be described via an invariant that is arranged in a form close to the sum of the mean value of the change in emittance and that in momentum deviation due to the particle collisions (supposing $H=\eta^2$).

$$\left(\frac{1}{\gamma^2} - \left\langle \frac{D_x^2}{\beta_x^2} \right\rangle - \left\langle \frac{D_z^2}{\beta_z^2} \right\rangle \right) \eta^2 + \left\langle \frac{1}{\beta_x} \right\rangle \varepsilon_x + \left\langle \frac{1}{\beta_z} \right\rangle \varepsilon_z = \text{constant}. \quad (29)$$

Each term on the left hand side of Eq. (29) is positive in case the coefficient of η^2 is positive. So, the sum of the three positive invariants, and thus of the three oscillation energies, is limited and the beam can attain an equilibrium (i.e. the IBS emittance growth is bounded). In case the coefficient of η^2 is negative the total oscillation energy can increase

as long as it does not exceed further limitations. Then, no beam equilibrium can exist. Noting that, unlike planar rings, the conditions for beam equilibrium do not depend whether the storage rings are below or above the transition.

For planar rings with $D_z = 0$ the latter formula can be rewritten, assuming the “smooth focusing approximation” holds, as:

$$\left(\frac{1}{\gamma^2} - \frac{1}{\gamma_t^2}\right)\eta^2 + \left\langle\frac{1}{\beta_x}\right\rangle\epsilon_x + \left\langle\frac{1}{\beta_z}\right\rangle\epsilon_z = \text{constant}, \quad (30)$$

$$\langle D_x \rangle \equiv \frac{R}{Q_x^2}, \quad \alpha_p = \left\langle\frac{D_x(s)}{\rho(s)}\right\rangle \equiv \frac{1}{\gamma_t^2}, \quad \eta_t = \frac{1}{\gamma_t^2} - \frac{1}{\gamma^2},$$

where γ_t is the transition energy, α_p the momentum compaction factor, η_t the slip factor and Q_x the machine tune. As a result, below the transition ($\eta_t < 0$) the coefficient of η^2 is positive and the beam can reach an equilibrium. Above transition ($\eta_t \geq 0$) the coefficient of η^2 is negative and the beam cannot reach an equilibrium.

Figure 2 shows an application of the Piwinski’s IBS model to the “Extra low energy antiproton” synchrotron (ELENA ≈ 30 m circumference). ELENA is a below transition ring with $\eta_t \approx -0.72$ (for $\gamma \approx 1$ at 100 keV), designed to decelerate antiprotons at 5.31 MeV kinetic energy (100 MeV/c) sent by the Antiproton Decelerator (AD), to yield dense beams at 100 keV (13.7 MeV/c). ELENA cycle with electron-cooling plateaus and deceleration ramps is overlaid to the plot.

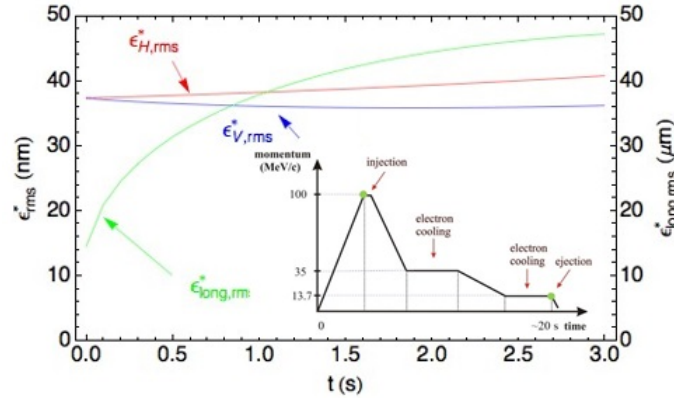


Figure 2: Antiproton deceleration down the 3s ELENA second ramp, from 0.65 MeV (35 MeV/c) to 100 keV, after the second cooling plateau. Initial rms emittances are $\epsilon_{x,z}^* = 37.3$ nm (physical emittances $\epsilon_{x,z} = 1 \mu\text{m}$), $\epsilon_s^* = 14.4$ nm (or $\epsilon_s^* = 0.56$ meVs). The emittance evolution is calculated with IBS, by iteratively re-evaluating the growth rates, as they are determined by the emittance values, and since the energy decreases versus time. With regard to the plot, there is no strong argument to discard slow deceleration ramps between plateaus with electron cooling. (*Mathematica* code written by C. Carli, with linear coupling).

2.4.3 Bjorken-Mtingwa Model

2.4.3.1 Beam Phase Space Density and Invariants

The IBS model formulated as in [2], in line with the work of Piwinski [1], considers Gaussian laws for the beam density distributions in phase space:

$$P(\vec{r}, \vec{p}) = \frac{N_b}{\Gamma} \exp[S(\vec{r}, \vec{p})], \quad \Gamma = \int \exp[S(\vec{r}, \vec{p})] d^3\vec{r} d^3\vec{p},$$

$$S(\vec{r}, \vec{p}) = \frac{1}{2} \sum_{i,j=1}^3 (A_{ij} \delta p_i \delta p_j + B_{ij} \delta p_i \delta r_j + C_{ij} \delta r_i \delta r_j) = S^{(x)} + S^{(z)} + S^{(s)}, \quad (31)$$

where $P(\vec{r}, \vec{p})$ is the phase space density of a beam holding N_b particles, Γ is the phase beam space volume and $S(\vec{r}, \vec{p})$ is the Gaussian particle beam density distribution, $\delta\vec{r}$ and $\delta\vec{p}$ are the position and momentum from the reference values \vec{r} and \vec{p} . Working out the coefficients A_{ij} , B_{ij} and C_{ij} , the particle beam density distribution can be written

$$S^{(x)} = \frac{\beta_x}{2\sigma_{x\beta}^2} (\gamma_x x_\beta^2 + 2\alpha_x x_\beta x'_\beta + \beta_x x'^2_\beta),$$

$$S^{(z)} = \frac{\beta_z}{2\sigma_{z\beta}^2} (\gamma_z z_\beta^2 + 2\alpha_z z_\beta z'_\beta + \beta_z z'^2_\beta), \quad S^{(s)} = \frac{\eta^2}{2\sigma_\eta^2} + \frac{\eta(s-s_0)^2}{2\sigma_\eta^2}. \quad (32)$$

Like in Eq. (16) $\varepsilon_s = \sigma_\eta \sigma_s$ and $\varepsilon_{x,z} = \sigma_{x\beta, z\beta}^2 / \beta_{x,z} \equiv \sigma_{x'_\beta, z'_\beta}^2 \beta_{x,z}$ are the longitudinal and transverse emittances and $\sigma_\eta, \sigma_s, \sigma_{x,z}, \sigma'_{x,z}$ the rms momentum spread, length, width and height of a bunch beam.

2.4.3.2 Two-Body Scattering: Rate of Change of Emittances and Momentum

Unlike Piwinski, the approach to IBS of Bjorken and Mtingwa is based on the time-evolution operator « S-matrix » that relates transitions from an initial quantum state $|i\rangle$ to a final state $|f\rangle$ of a physical system experiencing a scattering process. The matrix elements of S are inner products symbolized $\langle f|S|i\rangle$. The S-matrix is proportional to the amplitude \mathcal{M} that represents the physics of the interaction process.

Following [2] (see also [4], where they proceed through a slightly different way) the “transition rate” for a two-particle scattering process, namely the number of scattering events per unit time, is given by Ref. [10]:

$$\frac{d\varphi}{dt} = \frac{1}{2} \int d^3\vec{r} \frac{d^3\vec{p}_1}{\gamma_1} \frac{d^3\vec{p}_2}{\gamma_2} P(\vec{r}, \vec{p}_1) P(\vec{r}, \vec{p}_2) |\mathcal{M}|^2 \frac{d^3\vec{p}'_1}{\gamma'_1} \frac{d^3\vec{p}'_2}{\gamma'_2} \frac{\delta^4(\vec{p}_1 + \vec{p}_2 - \vec{p}'_1 - \vec{p}'_2)}{(2\pi)^2}, \quad (33)$$

where a prime ' refers to the particle parameters after collision, $\gamma_{1,2} = E_{1,2}/m$, $E_{1,2}$ are the two colliding particle' energy (in Heaviside Lorentz units in which $\epsilon_0 = \hbar = c = 1$), m their mass and \mathcal{M} is the Coulomb “scattering amplitude” of a particle-pair collision. Then, using the beam density distribution $S(\vec{r}, \vec{p})$ allows to compute the rate of change of the emittances ε_u ($u=x, z, s$); we obtain:

$$\frac{d\varepsilon_u}{dt} = \frac{1}{2\Gamma^2} \int d^3\vec{r} \frac{d^3\vec{p}_1}{\gamma_1} \frac{d^3\vec{p}_2}{\gamma_2} \exp[-S(\vec{r}, \vec{p}_1)] P(\vec{r}, \vec{p}_1) P(\vec{r}, \vec{p}_2)$$

$$\times |\mathcal{M}|^2 (\varepsilon_u(\vec{p}_1) - \varepsilon_u(\vec{p}'_1) + \varepsilon_u(\vec{p}'_2) - \varepsilon_u(\vec{p}_2)) \frac{d^3\vec{p}'_1}{\gamma'_1} \frac{d^3\vec{p}'_2}{\gamma'_2} \frac{\delta^4(\vec{p}_1 + \vec{p}_2 - \vec{p}'_1 - \vec{p}'_2)}{(2\pi)^2}. \quad (34)$$

The aim is to compute the scattering amplitude \mathcal{M} . This will be done by means of the “Feynman rules”, using the “Feynman diagram” representation of a scattering process stemming from quantum electrodynamic theory (Ref. [10]):

$$|\mathcal{M}|^2 = \frac{e^4}{\vec{p}^4 \sin^4[\psi/2]}. \quad (35)$$

At this point the calculations are still far from finished, and also they are not easy to perform. After some difficult manipulations the rate of change of the emittances $d\varepsilon_u/dt$, can be recast in the form given by Eq. (36) below. See [2] for details of the rather lengthy calculations required to derive the following Bjorken–Mtingwa growth rates.

2.4.3.3 *Intrabeam Scattering Growth Rates*

The formula for the IBS growth rates derived by the Bjorken-Mtingwa formalism are:

$$\frac{1}{T_u} = \frac{d \log \varepsilon_u}{dt} = \frac{\pi^2 N_b c r_i^2 C_{\log}}{\gamma \Gamma} \left\langle \int_0^\infty d\lambda \sqrt{\frac{\lambda}{\det[L+\lambda I]}} \left\{ \text{Tr}[L_u] \text{Tr} \left[\frac{1}{L+\lambda I} \right] - 3 \text{Tr} \left[\frac{1}{L_u+\lambda I} \right] \right\} \right\rangle, \quad (36)$$

with

$$\Gamma = (2\pi)^2 (\beta\gamma)^3 \varepsilon_x \varepsilon_z \sigma_\eta \sigma_s = (2\pi)^2 (\beta\gamma)^3 \varepsilon_x \varepsilon_z \varepsilon_s, \quad (37)$$

$$L_x = \frac{\beta_x \gamma^2}{\varepsilon_x} \begin{bmatrix} \frac{1}{\gamma^2} & -\frac{\phi_x}{\gamma} & 0 \\ -\frac{\phi_x}{\gamma} & \frac{H_x}{\beta_x} & 0 \\ 0 & 0 & 0 \end{bmatrix}, \quad L_z = \frac{\beta_z \gamma^2}{\varepsilon_z} \begin{bmatrix} 0 & 0 & 0 \\ 0 & \frac{H_z}{\beta_z} & -\frac{\phi_z}{\gamma} \\ 0 & -\frac{\phi_z}{\gamma} & \frac{1}{\gamma^2} \end{bmatrix}, \quad L_s = \frac{\gamma^2}{\sigma_\eta^2} \begin{bmatrix} 0 & 0 & 0 \\ 0 & 1 & 0 \\ 0 & 0 & 0 \end{bmatrix}, \quad (38)$$

$$\phi_{x,z} = \frac{D_{x,z} \alpha_{x,z} + D'_{x,z} \beta_{x,z}}{\beta_{x,z}}, \quad H_{x,z} = \frac{D_{x,z} \alpha_{x,z} + \beta_{x,z}^2 \phi_{x,z}^2}{\beta_{x,z}}. \quad (39)$$

In Eq. (36) the Coulomb logarithm C_{\log} is defined in Refs. [2,5,8] in terms of the maximum and minimum impact parameters and minimum scattering angle. Diverse definitions for C_{\log} exist. Luckily, its logarithmic dependence means that it varies slowly over a large range of the parameters involved in its definition (e.g. Eq. (9)). Ref. [2] takes the fixed Coulomb logarithm $C_{\log}=20$. Also, c is the speed of light, r_i is the classical ion radius, \vec{p} and E_0 the particle momentum rest energy, and $\gamma = \sqrt{E_0^2 + p^2}/E_0$. The matrices inside the brackets depend on the emittances, momentum spread and bunch length (with $\varepsilon_s = \sigma_\eta \sigma_s$ in m). For matched beams the longitudinal emittance is defined as $\varepsilon_s = \pi p \sigma_\eta \sigma_s \beta^{-1} c^{-1}$ in eVs. After expansion of the integrand in the brackets of Eq. (36) and some lengthy computations, the growth rates are finally stated in the form given in Ref. [3], with $u=x, z, s$:

$$\frac{1}{T_u} = \frac{\pi^2 N_b c r_i^2 C_{\log}}{\gamma \Gamma} \Delta_u \left\langle \int_0^\infty d\lambda \frac{\sqrt{\lambda}(a_u \lambda + b_u)}{(\lambda^3 + a\lambda^2 + b\lambda + c)^{3/2}} \right\rangle, \quad (40)$$

$$\Delta_x = \frac{\gamma^2 H_x}{\varepsilon_x}, \quad \Delta_z = \frac{\gamma^2 H_z}{\varepsilon_z}, \quad \Delta_s = \frac{\gamma^2}{\sigma_\eta}.$$

The nine coefficients $a, b, c, a_x, b_x, a_z, b_z, a_s, b_s$ depend on the optics parameters. They are not reproduced here (cf. Ref. [3] for the full list). The Bjorken-Mtingwa IBS growth rates seem somewhat dissimilar from the ones in the Piwinski formulae. However, the two groups of formulae match fairly well with certain approximations. In Ref. [4], Kubo, Mtingwa and Wolski develop the high-energy approximation ‘‘Completely integrated modified Piwinski’’ (CIMP) which shows an asymptotic equivalence with the Bjorken-Mtingwa growth rates formulae.

2.4.4 Zenkevich Model

Other IBS models based on non-Gaussian distributions have been formulated using the kinetic analysis for the modelling of small angle multiple Coulomb scattering. The method exposed here is based on the solution of the Fokker–Planck equation (FPE) for the particle density distribution, expressed in the position-momentum phase space. The FPE is an integro-differential equation with friction and diffusion coefficients with account of the multiple IBS.

Here, we summarize the approach developed by Zenkevich, to solve the FPE using Monte Carlo tool for IBS simulations in three degrees of freedom by means of a macro-particle algorithm called “binary collision map” (BCM) and realized in the macro-particle code “Monte-Carlo code” (MOCAC) for numerical modelling of IBS effects in accelerators and storage rings. Afterwards, another macro-particle code called “Software for Intrabeam Scattering and Radiation Effects” (SIRE) was developed to simulate the evolution of beam particle distributions in storage rings, taking into account IBS, radiation damping and quantum excitation. MOCAC and SIRE are both tracking codes where the beam is represented by a large number of macro-particles occupying points in the six-dimensional position-momentum phase space.

2.4.4.1 Fokker–Planck Formalism

The evolution of the particle distribution in a non-equilibrium beam facing to multiple micro Coulomb scattering can be expressed by the Fokker–Planck approach, where the collision term considers the many interactions between the charged particles as a series of small-angle scatterings. Assume that we know how to find a function $P(\vec{u}, \Delta\vec{u})$ such that it represents the conditional transition probability of a change in momentum \vec{u} to $\vec{u} \rightarrow \vec{u} - \Delta\vec{u}$ in time Δt of a particle in an individual collision. Hence, the time evolution of the position-momentum distribution $f(\vec{r}, \vec{u}, t)$ of particles in phase space is (Eq. (41) shows in what manner $f(\vec{r}, \vec{u}, t)$ happens to be just how it is at time t as a result of how it was at an earlier time $t - \Delta t$):

$$f(\vec{r}, \vec{u}, t) = \int f(\vec{r}, \vec{u} - \Delta\vec{u}, t - \Delta t) P(\vec{u} - \Delta\vec{u}, \Delta\vec{u}) d\Delta\vec{u}, \quad \int P(\vec{u}, \Delta\vec{u}) d\Delta\vec{u} = 1, \quad (41)$$

$$\iint_{|\vec{r}|^3 |\vec{u}|^3} f(\vec{r}, \vec{u}, t) d\vec{r} d\vec{u} = N.$$

N is the number of particles in the whole or a part of the beam, $d\vec{w} \stackrel{\text{def}}{=} d|\vec{w}|^3$ and $d\vec{r} \stackrel{\text{def}}{=} d|\vec{r}|^3$ are the momentum and space volume elements and $|\vec{r}|^3 |\vec{u}|^3$ indicates the phase space volume to integrate; \vec{u} and \vec{r} will be well-defined later (Eq. (46)). Truly f could just be thought as a momentum distribution of \vec{u} and t , but keeping \vec{r} offers flexibilities.

Multiple small-angle scattering is dominant in IBS process where $\Delta\vec{u}$ is small for small Δt . This allows expanding in Taylor’ series, to first order in Δt and second order in $\Delta\vec{u}$ the product fP inside the integral:

$$f(\vec{r}, \vec{u} - \Delta\vec{u}, t - \Delta t) P(\vec{u} - \Delta\vec{u}, \Delta\vec{u}) \approx f(\vec{r}, \vec{u}, t) P(\vec{u}, \Delta\vec{u})$$

$$- \Delta t \frac{\partial}{\partial t} [f(\vec{r}, \vec{u}, t) P(\vec{u}, \Delta\vec{u})] - \Delta\vec{u} \cdot \frac{\partial}{\partial \vec{u}} [f(\vec{r}, \vec{u}, t) P(\vec{u}, \Delta\vec{u})] \quad (42)$$

$$+ \frac{1}{2} \sum_{i,j} \Delta u_i \Delta u_j \frac{\partial^2}{\partial u_i \partial u_j} [f(\vec{r}, \vec{u}, t) P(\vec{u}, \Delta\vec{u})]$$

Inserting this result in $f(\vec{r}, \vec{u}, t)$ (Eq. (41)) yields (integrations over momentum volumes):

$$\begin{aligned} f(\vec{r}, \vec{u}, t) &= f(\vec{r}, \vec{u}, t) \int P(\vec{u}, \Delta\vec{u}) d\Delta\vec{u} - \Delta t \frac{\partial f(\vec{r}, \vec{u}, t)}{\partial t} \int P(\vec{u}, \Delta\vec{u}) d\Delta\vec{u} \\ &\quad - \int \Delta\vec{u} \cdot \frac{\partial}{\partial \vec{u}} [f(\vec{r}, \vec{u}, t) P(\vec{u}, \Delta\vec{u})] d\Delta\vec{u} \\ &\quad + \frac{1}{2} \int \sum_{i,j} \frac{\partial^2}{\partial u_i \partial u_j} [f(\vec{r}, \vec{u}, t) \Delta u_i \Delta u_j P(\vec{u}, \Delta\vec{u})] d\Delta\vec{u} \end{aligned} \quad (43)$$

Then, P is normalized to one and f does not depend on $\Delta\vec{u}$, Eq.(43) transforms into the rate of change of the density distribution $f(\vec{r}, \vec{u}, t)$ for any momentum $\vec{u}=(u_x, u_y, u_z)$ (subscripts x, y, z refer to the momentum directions, i, j stand for x, y, z):

$$\frac{\partial f(\vec{r}, \vec{u}, t)}{\partial t} = - \frac{\partial}{\partial \vec{u}} \cdot \left[f(\vec{r}, \vec{u}, t) \frac{\langle \Delta\vec{u} \rangle}{\Delta t} \right] + \frac{1}{2} \sum_{i,j} \Delta u_i \Delta u_j \frac{\partial^2}{\partial u_i \partial u_j} \left[f(\vec{r}, \vec{u}, t) \frac{\langle \Delta u_i \Delta u_j \rangle}{\Delta t} \right]. \quad (44)$$

The quantities $\langle \Delta\vec{u} \rangle \stackrel{i=x,y,z}{\iff} \langle \Delta u_i \rangle$ and $\langle \Delta u_i \Delta u_j \rangle$ are the mean changes in $\Delta\vec{u}$ and $\Delta u_i \Delta u_j$ in time Δt as a result of scattering events, that is the first and mixed moments of the transition probability function $P(\vec{u}, \Delta\vec{u})$, referred to as \vec{F} and D_{ij} :

$$\vec{F} \stackrel{\text{def}}{=} \left\langle \frac{\Delta\vec{u}}{\Delta t} \right\rangle = \int \frac{\Delta\vec{u}}{\Delta t} P(\vec{u}, \Delta\vec{u}) d\Delta\vec{u}, \quad D_{ij} \stackrel{\text{def}}{=} \frac{1}{2} \left\langle \frac{\Delta u_i \Delta u_j}{\Delta t} \right\rangle = \frac{1}{2} \int \frac{\Delta u_i \Delta u_j}{\Delta t} P(\vec{u}, \Delta\vec{u}) d\Delta\vec{u}. \quad (45)$$

The two collision terms $\langle \Delta\vec{u} \rangle / \Delta t$ and $\langle \Delta u_i \Delta u_j \rangle / \Delta t$ characterize a ‘‘frictional dynamic’’ and a ‘‘diffusion in momentum space’’, with opposite sign in Eq. (44), which may be in balance for an equilibrium. Inserting \vec{F} and D_{ij} in Eq. (44) results in the compact formulation:

$$\frac{\partial f}{\partial t} = - \frac{\partial}{\partial \vec{u}} \cdot (\vec{F} f) + \sum_{i,j} \frac{\partial^2}{\partial u_i \partial u_j} (D_{ij} f). \quad (46)$$

The transport process Eqs. (44-46) is the Fokker-Planck equation (Refs. [16]-[17]). To solve it one must specify $P(\vec{u}, \Delta\vec{u})$ to get $\langle \Delta\vec{u} \rangle$. Yet, there is an indirect way to do it. Suppose that multiple collisions are handled as series of particle-pair collisions, then, the mean momentum changes $\langle \Delta\vec{u} \rangle$ and $\langle \Delta u_i \Delta u_j \rangle$ are computable via the Coulomb scattering cross-section (since $\langle \Delta\vec{u} \rangle$ contains the physics of the scattering process via Eq. (48) below).

Let us work out the friction \vec{F} and diffusion D_{ij} terms. For this purpose, we explore the different ways collisions are able to change the momentum of a ‘‘test’’ particle in a time Δt , and average all the occurrences of $\Delta\vec{u}$ and $\Delta u_i \Delta u_j$. For ease, this will first be resolved in the CM frame and then converted back to the LAB frame (if wanted). The incidence of collisions in time Δt on a test particle is evaluated for a certain ‘‘field’’ particle momentum by averaging $\Delta\vec{u}$ on all possible factors that affect $\Delta\vec{u}$ (i.e. azimuthal and scattering angles in IBS events). Next, averaging is computed for all field particle momenta \vec{w} via the density distribution $f(\vec{r}, \vec{w}, t)$. Just after collisional time interval Δt , each field particle momentum is replaced by $\vec{w} \rightarrow \vec{w} + \Delta\vec{w} \equiv \vec{w}^*$ (the sign $*$ refer to post collision momenta).

2.4.4.2 Single Pair-Collision Event

In the framework of particle-pair collision events, let us define the position \vec{r} and dimensionless momentum \vec{P} vectors for a test particle \vec{u} and a field particle \vec{w} as:

$$\vec{r} = (z - z_s, x, y), \quad \vec{P} = \left(\frac{\eta}{\gamma} \stackrel{\text{def}}{=} \frac{1}{\gamma} \frac{\Delta p}{p}, x' \stackrel{\text{def}}{=} \frac{p_x}{p}, y' \stackrel{\text{def}}{=} \frac{p_y}{p} \right) = \begin{cases} \vec{u} & \text{test particle} \\ \vec{w} & \text{field particle} \end{cases} \quad (47)$$

The vectors (\vec{r}, \vec{u}) are the phase space coordinates, where z is the longitudinal deviation of a moving particle about the design orbit, with respect to the bunch centre z_c and x, y are the horizontal and vertical deviations of that particle in a plane perpendicular to the design orbit. In addition, η, x', y' are the relative longitudinal and transverse momenta, assuming a constant reference particle momentum p . The kinematics of the relative momentum changes after a pair collision between particles \vec{u} and \vec{w} in transverse and longitudinal directions are taken from the Piwinski model Eq. (1), with $\Delta\vec{u} = \Delta u_x \hat{x} + \Delta u_y \hat{y} + \Delta u_z \hat{z}$:

$$\Delta\vec{u} = \vec{u}^* - \vec{u} = \begin{cases} \frac{1}{2} \left[\frac{U_y U \sin \bar{\phi} - U_z U_x \cos \bar{\phi}}{U_\perp} \sin \bar{\psi} + U_x (\cos \bar{\psi} - 1) \right] \\ \frac{1}{2} \left[\frac{U_x U \sin \bar{\phi} - U_z U_y \cos \bar{\phi}}{U_\perp} \sin \bar{\psi} + U_y (\cos \bar{\psi} - 1) \right], \\ \frac{1}{2} [U_\perp \cos \bar{\phi} \sin \bar{\psi} + U_z (\cos \bar{\psi} - 1)] \end{cases} \quad (48)$$

where

$$\vec{U} = \vec{u} - \vec{w} = (U_z, U_x, U_y), \quad U_\perp = \sqrt{U_x^2 + U_y^2}, \quad U = |\vec{U}| = \sqrt{U_z^2 + U_x^2 + U_y^2} = |\vec{u} - \vec{w}| = \sqrt{\frac{(\eta_u - \eta_w)^2}{\gamma^2} + (x'_u - x'_w)^2 + (y'_u - y'_w)^2}, \quad (49)$$

in which $\bar{\psi}$ and $\bar{\phi}$ are the scattering and azimuthal angles in the centre of mass frame (CM). For elastic collisions we have $\Delta\vec{w} = -\Delta\vec{u}$, namely $\vec{u}^* - \vec{u} = \vec{w}^* - \vec{w}$ or $\vec{u}^* - \vec{w}^* = \vec{u} - \vec{w}$. Figure 3 pictorially displays the kinematic of a collision between a pair of particles with momenta \vec{u} and \vec{w} in the centre of mass of the particles, using the notation in Eqs. (47-49).

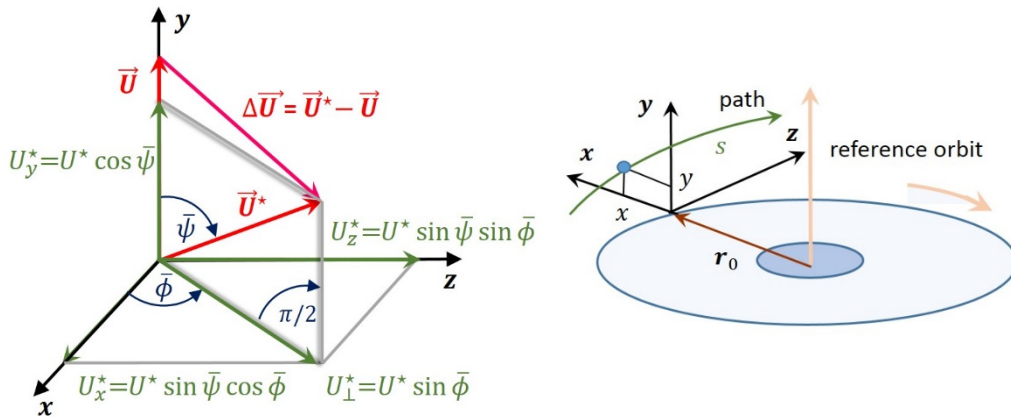


Figure 3: Left figure: Binary collision in the CM frame. Before collision, the two particles, with momenta \vec{u} and \vec{w} , move non-relativistically in opposite direction parallel to the vertical y -axis.

Relative particle momenta $\vec{U}=\vec{u}-\vec{w}$ before and after collision are outlined. The reference trihedral is such that before collision \vec{U} lays on the y-axis i.e. $\vec{U}=\|\vec{u}-\vec{w}\|\hat{y}$, and is perpendicular to the longitudinal z-axis of the reference orbit (the hat means unit vector). After collision $\vec{U}^*=\vec{u}^*-\vec{w}^*=U_x^*\hat{x}+U_y^*\hat{y}+U_z^*\hat{z}$; likewise $\Delta\vec{U}=\vec{U}^*-\vec{U}=\Delta\vec{u}-\Delta\vec{w}$. So with the momenta shown in the sketch we get the result $\Delta\vec{U}/U=\sin\bar{\psi}\cos\bar{\phi}\hat{x}+(\cos\bar{\phi}-1)\hat{y}+\sin\bar{\psi}\sin\bar{\phi}\hat{z}$, since $\vec{U}\parallel\hat{y}$. Right figure: Frenet-Serret curved coordinate system in a storage ring, with the reference orbit and an individual particle trajectory. The particle location is: $r(s)=r_0(s)+x(s)\hat{x}+y(s)\hat{y}$.

As a primary step to evaluate the change in particle momentum change let us average $\Delta\vec{u}(\bar{\psi}, \bar{\phi})$ over the angle $\bar{\phi}$ only by way of Eq. (48), that is not including the scattering angle $\bar{\psi}$. We then obtain:

$$\langle\Delta\vec{u}\rangle_{\phi}=\frac{1}{2\pi}\int_0^{2\pi}\Delta\vec{u}\sin\bar{\psi}d\bar{\phi}=-\sin^2\frac{\bar{\psi}}{2}(\vec{u}-\vec{w}), \quad (50)$$

in which integrating $\Delta\vec{u}$ gives the vector $-\sin^2\psi/2\{U_z, U_x, U_y\}$, from which the above average follows since $\vec{U}=\vec{u}-\vec{w}$. We will use this result later. Now, to find the momentum mean changes during particle-pair collisions because of IBS we use the expression P_{scat} to quantify the chance of collisions per unit time (in CM frame, with the a solid angle element $d\bar{\Omega}=\sin\bar{\psi}d\bar{\psi}d\bar{\phi}$):

$$P_{\text{scat}}(\vec{r}, \vec{u}, \bar{\psi}, \bar{\phi}, t)=\frac{2\bar{\beta}cf(\vec{r}, \vec{u}, t)\bar{\sigma}(\bar{\psi})d\bar{\Omega}}{\gamma^2}, \quad \bar{\sigma}(\bar{\psi})=\left(\frac{r_i}{4\bar{\beta}^2\sin^2\left[\frac{\bar{\psi}}{2}\right]}\right)^2. \quad (51)$$

The density distribution $f(\vec{r}, \vec{u}, t)$ is defined in LAB frame and $\bar{\sigma}(\bar{\psi})$ is the Rutherford cross-section (Eq. (8)). In analogy with Eq. (46), the FPE in phase space relevant to study the beam evolution in storage rings attributable to IBS effects is

$$\frac{\partial}{\partial t}f(\vec{r}, \vec{u}, t)=-\frac{\partial}{\partial\vec{u}}\cdot[\vec{F}f(\vec{r}, \vec{u}, t)]+\sum_{i,j}\frac{\partial^2}{\partial u_i\partial u_j}[D_{ij}f(\vec{r}, \vec{u}, t)], \quad (52)$$

in which the summation is made over repeating indices. The frictional and diffusion coefficients are definite in terms of averaged scattering events, noting that $P_{\text{scat}}(\vec{r}, \vec{u}, \bar{\psi}, t)$ acts for the transition probability $P(\vec{u}, \Delta\vec{u})$ used in Eq. (45):

$$\begin{aligned} \vec{F} &\equiv \left\langle\frac{\Delta\vec{u}}{\Delta t}\right\rangle_{\vec{w}}=\int\frac{\Delta\vec{u}}{\Delta t}P_{\text{scat}}(\vec{r}, \vec{u}, \bar{\psi}, t)d\vec{u}, \\ D_i &\equiv \frac{1}{2}\left\langle\frac{\Delta u_i\Delta u_j}{\Delta t}\right\rangle_{\vec{w}}=\frac{1}{2}\int\frac{\Delta u_i\Delta u_j}{\Delta t}P_{\text{scat}}(\vec{r}, \vec{u}, \bar{\psi}, t)d\vec{u}. \end{aligned} \quad (53)$$

Then, using $\Delta\vec{u}\stackrel{\text{def}}{=} \Delta u_i=(\Delta u_x, \Delta u_y, \Delta u_z)$ (cf. Eq. (48)), the average $\langle\Delta\vec{u}\rangle_{\vec{w}}$ of $\Delta\vec{u}$ for a test particle (in CM frame) is computed in two steps: the first average, named $\langle\Delta\vec{u}\rangle_{\phi\psi}$, integrate $\Delta\vec{u}$ on all possible azimuthal and scattering angles $\bar{\phi}, \bar{\psi}$; the second average, named $\langle\langle\Delta\vec{u}\rangle_{\phi\psi}\rangle_{\vec{w}}$, integrate $\langle\Delta\vec{u}\rangle_{\phi\psi}$ over all field particles \vec{w} with phase space distribution $f(\vec{r}, \vec{u}, t)$ (for shortness $\langle\langle\Delta\vec{u}\rangle_{\phi\psi}\rangle_{\vec{w}}$ is renamed $\langle\Delta\vec{u}\rangle_{\vec{w}}$ hereinafter). The result of double integration is:

$$\begin{aligned}
\langle \Delta \vec{u} \rangle_{\phi\psi} &= \int_{\bar{\psi}_{\min}}^{\pi} \int_0^{2\pi} \Delta \vec{u} P_{\text{scat}} d\bar{\phi} d\bar{\psi} = -\frac{\pi c r_i^2}{\bar{\beta}^3 \gamma^2} \log \left[\frac{2\bar{\beta}^2 \bar{b}_{\max}}{r_i} \right] (\vec{u} - \vec{w}), \\
\langle \Delta \vec{u} \rangle_{\vec{w}} &\stackrel{\text{def}}{=} \int_{|\vec{w}|^3} \langle \Delta \vec{u} \rangle_{\phi\psi} f(\vec{r}, \vec{w}, t) d\vec{w} = \rho_r(\vec{r}, t) \int_{|\vec{w}|^3} \langle \Delta \vec{u} \rangle_{\phi\psi} \tilde{f}(\vec{r}, \vec{w}, t) d\vec{w} \\
&= -\left\langle \frac{\pi c r_i^2 \rho(\vec{r}, t)}{\bar{\beta}^3 \gamma^2} \log \left[\frac{2\bar{\beta}^2 \bar{b}_{\max}}{r_i} \right] (\vec{u} - \vec{w}) \right\rangle_{\vec{w}}, \\
\rho_r(\vec{r}, t) &\stackrel{\text{def}}{=} \int_{|\vec{w}|^3} f(\vec{r}, \vec{w}, t) d\vec{w}, \quad \tilde{f}(\vec{r}, \vec{w}, t) = f(\vec{r}, \vec{w}, t) / \rho_r(\vec{r}, t),
\end{aligned} \tag{54}$$

where $\langle \cdot \rangle_{\vec{w}}$ means averaging over the field particles \vec{w} , $\rho_r(\vec{r}, t)$ is the distribution in position coordinates after integration of $f(\vec{r}, \vec{w}, t)$ over $d\vec{w}$, and $\tilde{f}(\vec{r}, \vec{w}, t)$ is the local distribution in momentum coordinates for a given \vec{r} . Therefore, integrating $\rho_r(\vec{r}, t)$ over $d\vec{r}$ yields the number N of particles in the bunch, like integrating $f(\vec{r}, \vec{w}, t)$ over $d\vec{r}d\vec{w}$ (Eq. (41)). Differently the integral of $\tilde{f}(\vec{r}, \vec{w}, t)$ over $d\vec{r}d\vec{w}$ is unity. By way of Eq. (17) the Lorentz factor $\bar{\beta}$ in CM converts to $\bar{\beta} \approx \beta \gamma |\vec{u} - \vec{w}|/2$ in LAB; so, the first moments are:

$$\langle \Delta \vec{u} \rangle_{\vec{w}} = -\left\langle \frac{\pi c r_i^2 \rho_r(\vec{r}, t)}{\bar{\beta}^3 \gamma^2} \bar{C}_{\log} \right\rangle_{\vec{w}}, \quad \langle \Delta \vec{u} \rangle_{\vec{w}} = -\left\langle \frac{8\pi c r_i^2 \rho_r(\vec{r}, t)}{\beta^3 \gamma^5} C_{\log}(\vec{u}, \vec{w}) \frac{\vec{u} - \vec{w}}{|\vec{u} - \vec{w}|^3} \right\rangle_{\vec{w}}, \tag{55}$$

in which \bar{C}_{\log} is the CM frame Coulomb logarithm and $C_{\log}(\vec{u}, \vec{w})$ is the ‘‘extended’’ Coulomb logarithm defined in LAB frame:

$$\bar{C}_{\log} = \log \left[\frac{2\bar{\beta}^2 \bar{b}_{\max}}{r_i} \right], \quad C_{\log}(\vec{u}, \vec{w}) = \log \left[\frac{\beta^2 \gamma^2 \bar{b}_{\max}}{2r_i} (\vec{u} - \vec{w})^2 \right]. \tag{56}$$

We proceed similarly to compute the second moments in LAB frame by computing the averages of $\Delta \vec{u} \Delta \vec{u} \stackrel{\text{def}}{=} \Delta u_i \Delta u_j = (\Delta u_x \Delta u_x, \Delta u_x \Delta u_y, \dots, \Delta u_z \Delta u_z)$. The result is:

$$\langle \Delta u_i \Delta u_j \rangle_{\vec{w}} \approx \left\langle \frac{4\pi c r_i^2 \rho_r(\vec{r}, t)}{\beta^3 \gamma^5} C_{\log}(\vec{u}, \vec{w}) \frac{\delta_{ij} |\vec{u} - \vec{w}|^2 - (u_i - w_i)(u_j - w_j)}{|\vec{u} - \vec{w}|^3} \right\rangle_{\vec{w}}, \tag{57}$$

where $\delta_{ij} = 1$ if $i=j$, $\delta_{ij} = 0$ if $i \neq j$ is the Kronecker symbol.

The study of the beam evolution in phase space of the distribution $f(\vec{r}, \vec{u}, t)$ demands in theory to solve a kinetic equation such as FPE (Eq. (52)) including the computation of \vec{F} and D_{ij} by integration of $f(\vec{r}, \vec{u}, t)$ as shown in the above three formulae. If one might solve the FPE, the knowledge of particle positions and momenta resulting from the phase space density $f(\vec{r}, \vec{u}, t)$ would give the progression of longitudinal and transverse beam emittances caused by multiple particle-pair collisions inside the beam. Yet in practice the FPE is complicated to solve in both the six and three-dimensional forms. Instead, we consider a different technique using macro-particles for IBS simulation, founded on the Zenkevich ‘‘binary collision map’’ (BCM).

2.4.4.3 Monte Carlo Binary Collision Model

The BCM is an algorithm that allows to ‘‘reduce’’ the effects of the continuous time dynamical IBS system to a discrete time ‘‘map’’ in momentum space. Indeed, BCM, replaces a multiple scattering process acting in a time gap Δt by a discrete set of binary collision events. This method operates on each pair of macro-particles and calculates the change of momenta during a collision event (shown through the angles ψ and ϕ). The BCM algorithm

first proceeds by sampling at random macro-particle pairs (\vec{u}^i, \vec{w}^j) for approximate the continuous densities $\tilde{f}(\vec{r}, \vec{u}, t)$ and $\rho_r(\vec{r}, t)$ in Eq. (54), that are now changed to the discrete distributions $\tilde{f}_N(\vec{r}, \vec{u}, t)$ and $\rho_N(\vec{r}, t)$, formally written as:

$$\begin{aligned} \tilde{f}_N(\vec{r}, \vec{u}, t) &= \frac{1}{N} \sum_{i=1}^N \delta(\vec{r} - \vec{r}^i) \delta(\vec{u} - \vec{u}^i), \quad \rho_N(\vec{r}, t) = \int_{|\vec{u}|^3} f_N(\vec{r}, \vec{u}, t) d\vec{u}, \\ \iint_{|\vec{r}|^3 |\vec{u}|^3} \tilde{f}_N(\vec{r}, \vec{u}, t) d\vec{r} d\vec{u} &= 1, \quad \int_{|\vec{r}|^3} \rho_N(\vec{r}, t) d\vec{r} = N, \end{aligned} \quad (58)$$

where δ is the Dirac delta function, and the superscripts i, j stand for a macro-particle numbers. N is either the number of macro-particles populating a 6-D phase space or a 3-D spatial volume. By means of the discretization procedure the macro-particles \vec{r}^i, \vec{u}^i can be grouped into an input “list” and identified by their 6-D position-momentum vectors. We assume the functions \tilde{f}_N and ρ_N remain stable during the interaction time Δt and that a given macro-particle in the list collides only once. So $\tilde{f}_N = \tilde{f}_N(\vec{r}, \vec{u})$ and $\rho_N = \rho_N(\vec{r})$ are time-independent. Observing the mean momentum changes $\langle \Delta \vec{u} \rangle_\phi$ in Eq. (50) and $\langle \Delta \vec{u} \rangle_{\phi\psi}$ in Eq. (54) show that they are similar providing the scattering angle $\bar{\psi}^{ij}$ or ψ^{ij} (CM/LAB frames) is defined as follows and the azimuthal angle $\bar{\phi}^{ij}$ or ϕ^{ij} is randomly chosen in the interval $[0, 2\pi]$ (see Refs. [11-13]). For shortness, we add the coefficients:

$$\bar{A}_0 = \frac{\pi c r_1^2}{\beta^3 \gamma^2}, \quad A_0 = \frac{8\pi c r_1^2}{\beta^3 \gamma^5}.$$

Hence:

$$\begin{aligned} \sin \left[\frac{\bar{\psi}^{ij}}{2} \right] &= \sqrt{\bar{A}_0 \rho_N(\vec{r}) \log \left[\frac{2\bar{\beta}^2 b_{\max}}{r_i} \right] \Delta t}, \quad \sin \left[\frac{\bar{\psi}^{ij}}{2} \right] = \sqrt{\bar{A}_0 \rho_N(\vec{r}) \bar{C}_{\log} \Delta t}, \\ \sin \left[\frac{\psi^{ij}}{2} \right] &= \sqrt{A_0 \frac{\rho_N(\vec{r}) \log \left[\frac{\beta^2 \gamma^2 b_{\max} |\vec{u}^i - \vec{w}^j|^2}{2r_i} \right] \Delta t}{|\vec{u}^i - \vec{w}^j|^3}}, \quad \sin \left[\frac{\psi^{ij}}{2} \right] = \sqrt{A_0 \frac{\rho_N(\vec{r}) C_{\log} [\vec{u}^i, \vec{w}^j] \Delta t}{|\vec{u}^i - \vec{w}^j|^3}}. \end{aligned} \quad (59)$$

The time interval Δt in the formula acts to fit the units as $\langle \Delta \vec{u} \rangle_{\vec{w}}$ is in 1/s while $\langle \Delta \vec{u} \rangle_\phi$ has no unit. In addition, Δt is the time step of a collisional cycle, supposed short enough for noticeable variation of beam momenta and $\Delta t \ll T_{z,x,y}$ the IBS rise times. The maximum impact parameter b_{\max} is taken as the beam height or half the beam diameter, $\rho_N(\vec{r})$ is the discrete particle density.

The BCM algorithm first divides the N macro-particle domain representing the beam into “cells” with equal volume; then, it groups at random all the macro-particles into $N/2$ pairs and distributes the pairs in the cells to form a discrete macro-particle density distribution as illustrated in Fig. 4.

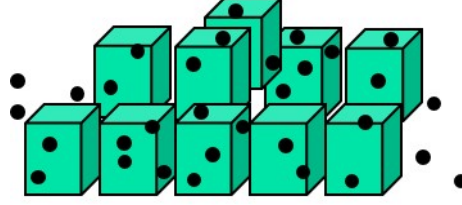


Figure 4: Pictorial representation of the macro-particle domain split into cells with macro-particles grouped at random within the cells. Each pair of macro-particles picked undertakes a single collision within the duration Δt of an interaction cycle.

Clearly the 3-D macro-particle distribution $\rho_N(\vec{r}, t)$ for the total or a fraction of the beam also applies to macro-particle distributions in little cell volumes. Let us assume that the density inside each cell is uniform and that two colliding macro-particles in the same cell have an equal spatial location. Note that the macro-particle positions, namely longitudinal and transverse displacements about the design orbit remain unchanged through the collision mapping. To simulate real IBS effects we must adjust the cell density $\rho_N(\vec{r}, t)$ to the number of real particles (i.e. macro-particles \times particle number per macro-particle). For suitability, the “scattering angle” $\bar{\psi}^{ij}$ in every pair of macro-particles in each cell is chosen to refer to the CM frame (Eq. (59) upper formula).

The collisional simulation is realized by a recurrent mapping procedure, that is we insert \bar{u}^i , \bar{w}^i and $\sin \bar{\phi}^{ij}$, $\cos \bar{\psi}^{ij}$ onto the Piwinski’s formula (Eq. (48)), which returns $\Delta \bar{u}^i$ and $\Delta \bar{w}^i$ for each pair $\{\bar{u}^i, \bar{w}^j\}$ within the cycle time Δt . So the post collisional momenta are $\bar{u}^{i*} = \bar{u}^i + \Delta \bar{u}^i$ and $\bar{w}^{i*} = \bar{w}^i + \Delta \bar{w}^i$. After each cycle, in every cell the momentum distribution is updated for all macro-particle pair as $\{\eta^{i*}, x^{i*}, y^{i*}\} = \{\eta^i + \Delta \eta^i, x^i + \Delta x^i, y^i + \Delta y^i\}$, where $\{\Delta \eta^i, \Delta x^i, \Delta y^i\}$ stands for both \bar{u}^i and \bar{w}^i . A new cycle of length Δt is next started until the end of the simulation time. Once a cycle is over the post collision macro-particle invariants ε_z^i (for bunched beams), ε_x^i and ε_y^i are upgraded. They are derived from the following expressions:

$$\varepsilon_z^i = \gamma_z (\Delta z^i)^2, \quad \gamma_z \stackrel{\text{def}}{=} \frac{v_s^2}{\eta_t^2 R^2},$$

$$\varepsilon_x^i = \gamma_x (x^i - D_x \eta^i)^2 + 2\alpha_x (x^i - D_x \eta^i)(x'^i - D'_x \eta^i) + \beta_x (x'^i - D'_x \eta^i)^2, \quad (60)$$

$$\varepsilon_y^i = \gamma_y (y^i - D_y \eta^i)^2 + 2\alpha_y (y^i - D_y \eta^i)(y'^i - D'_y \eta^i) + \beta_y (y'^i - D'_y \eta^i)^2,$$

where $v_s = |\Omega_s|/\omega_0$ is the synchrotron tune, Ω_s the synchrotron frequency, ω_0 the revolution frequency, η_t the slip factor and R the mean storage ring radius; $\alpha_{x,y}, \beta_{x,y}, \gamma_{x,y}$ are the Twiss parameters and $D_{x,y}, D'_{x,y}$ the dispersion functions and their derivatives varying, along the reference orbit. Inversely related, the particle phase space positions and momentum coordinates $\Delta z^i, x^i, y^i$, and η^i, x'^i, y'^i are stated by means of the invariants and phases $\phi_{z,y,x}$:

$$\begin{aligned}
\frac{\Delta p^i}{p} &= \eta^i = -\sqrt{\frac{\varepsilon_z^i}{\beta_z}} (\alpha_z \cos \phi_z + \sin \phi_z) = -\sqrt{\frac{\varepsilon_z^i}{\beta_z}} \sin \phi_z, & z^i - z_s^i &= \Delta z^i = \sqrt{\beta_z \varepsilon_z^i} \cos \phi_z, \\
\frac{p_x^i}{p} &= x'^i = -\sqrt{\frac{\varepsilon_x^i}{\beta_x}} (\alpha_x \cos \phi_x + \sin \phi_x) + D'_x \eta^i, & x^i &= (\beta_x \varepsilon_x^i)^{1/2} \cos \phi_x + D_x \eta^i, \\
\frac{p_y^i}{p} &= y'^i = -\sqrt{\frac{\varepsilon_y^i}{\beta_y}} (\alpha_y \cos \phi_y + \sin \phi_y) + D'_y \eta^i, & y^i &= (\beta_y \varepsilon_y^i)^{1/2} \cos \phi_y + D_y \eta^i,
\end{aligned} \tag{61}$$

where $\beta_z \stackrel{\text{def}}{=} \frac{|\eta t| R}{v_s} = \text{constant}$, which implies that $\alpha_z \stackrel{\text{def}}{=} \frac{\beta_z'}{2} \equiv 0$ (Ref. [5]).

- In the binary collision method implemented in MOCAC and SIRE tracking codes, the macro-particle beam is a set of 6-D position-momentum vectors. An initial macro-particle density distribution is generated by sampling a Gaussian probability law. Extra selective laws with non-Gaussian tails can be added if needed. Anyhow, at the beginning of the simulation the initial distribution must reflect the Courant-Snyder and longitudinal invariants of the beam.
- Non-uniform synchrotron lattices are modelled as series of sets attached to the optical parameters located at separate azimuthal “points” around a lattice period; and, then averaged over the period. The mapping is reiterated all the way in each cell, through every time step Δt , in different points of the lattice period.

Now combining all macro-particles within a bunch, we can compute the average values of the individual invariants $\varepsilon_{z,x,y}^i$ around the ring by means of Eq. (60) and considering the variations of the Twiss parameters and dispersion functions with their derivatives. Lastly, the longitudinal, horizontal and vertical IBS growth rates write:

$$\varepsilon_{z,x,y} = \langle \varepsilon_{z,x,y}^i \rangle, \quad \frac{1}{T_{z,x,y}} = \frac{1}{\sqrt{\varepsilon_{z,x,y}}} \frac{d\sqrt{\varepsilon_{z,x,y}}}{dt} = \frac{1}{2\varepsilon_{z,x,y}} \frac{d\varepsilon_{z,x,y}}{dt}. \tag{62}$$

2.4.5 Benchmarking of the IBS Theoretical Models with Monte-Carlo Codes

The IBS theoretical models have been studied in detail and benchmarked with experimental data for hadron beams over the years [18, 19]. In hadron machines, the IBS effect causes emittance dilution with time, limiting their performance. Lepton machines on the other hand, were operating until today in regimes where the IBS effect was negligible. Future linear collider Damping Rings, new generation light sources and B-factories, however, enter in regimes where the IBS effect can be predominant. It is thus important to study the IBS theories in the presence of synchrotron radiation damping (SRD) and quantum excitation (QE), benchmark the existing theoretical models and tracking codes with experimental data and identify their limitations. Even though e^+/e^- rings run normally above transition, where IBS leads to continuous emittance growth and equilibrium does not exist, synchrotron radiation damping counteracts the IBS growth, leading to new steady-state emittances. The beam transverse emittance and relative energy spread evolution due to the effects of IBS and SRD can be obtained by solving numerically the three coupled differential equations:

$$\begin{aligned}\frac{d\varepsilon_i}{dt} &= -\frac{2}{\tau_i}(\varepsilon_i - \varepsilon_{i0}) + \frac{2\varepsilon_i}{T_i(\varepsilon_x, \varepsilon_y, \sigma_p)}, \quad i = x, y, \\ \frac{d\sigma_p}{dt} &= -\frac{1}{\tau_p}(\sigma_p - \sigma_{p0}) + \frac{\sigma_p}{T_p(\varepsilon_x, \varepsilon_y, \sigma_p)},\end{aligned}\tag{63}$$

using small time iteration steps δt which are much smaller than the damping time and for which the emittances change adiabatically. The symbols ε_{x0} , ε_{y0} , σ_{p0} denote the zero-current (without the effect of IBS) equilibrium horizontal and vertical emittances and rms energy spread. τ_x , τ_y , τ_p are the synchrotron radiation damping times. From the IBS growth times T_x , T_y , T_p , one can obtain the steady state properties, for which: $\frac{d\varepsilon_x}{dt} = \frac{d\varepsilon_y}{dt} = \frac{d\sigma_p^2}{dt} = 0$.

The CLIC DR is a wiggler-dominated lattice, targeting ultra-low emittances in all three planes and small damping times. The output emittances are strongly dominated by the IBS effect; thus, it is an interesting testbed for the comparison between different theoretical models and the multi-particle tracking code SIRE, in the presence of synchrotron radiation and quantum excitation. Table 1 summarizes some basic lattice and beam properties of the CLIC DRs lattice design [20].

Table 1: Basic equilibrium lattice parameters for the CLIC DR lattice.

Parameter	Value
Energy [GeV]	2.86
Circumference [m]	427.5
Bunch population [10^{11}]	4.1
Hor. emittance [nm rad] w/wo IBS	0.056
Vert. emittance [pm rad] w/wo IBS	0.56
Bunch length [mm] w/wo IBS	1.6
Energy spread w/wo IBS	1e-3
Damping times [$\tau_x/\tau_y/\tau_l$] [ms]	2/2/1

For the IBS growth rate calculations, the IBS kicks are distributed over an adequate amount of points across the ring, such that the variation of the optics is taken into account and the areas where IBS is predominant are well represented. Table 2 summarizes the steady state horizontal geometrical emittance as estimated by the theoretical models of Bjorken-Mtingwa (BM) and Piwinski (Piw.) and the high energy approximations of Bane [21] and CIMP [4]. BM, Bane and CIMP are in good agreement, while Piwinski underestimates the effect with respect to the other three. The same study was performed for other low emittance lattices as well, coming to the same conclusion: In regimes where the IBS effect acts as a perturbation, all theoretical models are in very good agreement while in regimes where the steady state emittances are dominated by the IBS effect, the theoretical models diverge [22].

Table 2: Steady state hor. emittance calculated by BM, P, Bane and CIMP for the CLIC DR.

Parameter (model)	ε_x (BM)	ε_x (Piw.)	ε_x (Bane)	ε_x (CIMP)
Steady state emittance [pm-rad]	95.4	85.8	98.1	97.2

Figure 5 shows a comparison between the theoretical models of Bjorken-Mtingwa and Piwinski with the multi-particle tracking code SIRE for one turn of the CLIC DR lattice. As SIRE is a Monte-Carlo code, the tracking simulations were performed several times and the

one standard deviation error-bars are also shown in the plots. The results from SIRE simulations are shown in green, from Bjorken-Mtingwa in black, from Piwinski in red and from Bane in magenta. The classical formalism of Piwinski is in perfect agreement with the SIRE results, in all planes. This is not a surprise, as both Piwinski formalism and the tracking codes use the Rutherford cross-section, to calculate the scattering probability in a solid angle. All theories and simulations predict the same trend for the emittance evolution along the ring and are in fairly good agreement within 3σ in all planes.

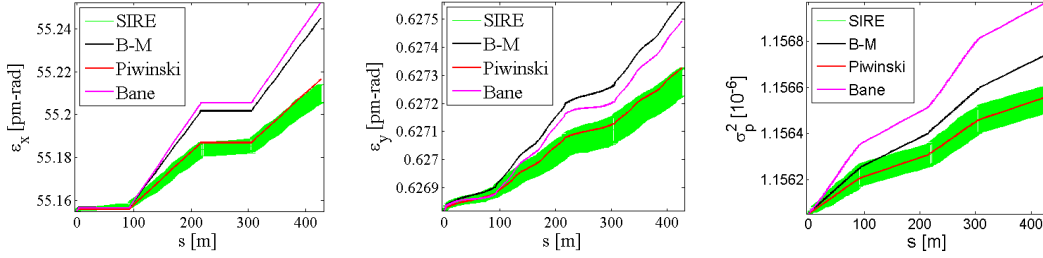


Figure 5: One turn comparison for the horizontal (left) and vertical (middle) emittance and energy spread (right) between the tracking code SIRE (green) and the theoretical models BM (black), Piwinski (red) and Bane (magenta) for the CLIC DR lattice.

For the LHC/HL-LHC proton beams at collision energy, synchrotron radiation turns into a perceptible effect as well. It continuously shrinks the emittances with damping times of 12.9 h in the longitudinal plane and of 26.0 h in the two transverse planes. The effects of IBS and SRD on the expected evolution of the LHC and SLHC beam emittances during physics coasts at 7 TeV were examined in [23] and SIRE was benchmarked against the Bjorken-Mtingwa formalism for different cases.

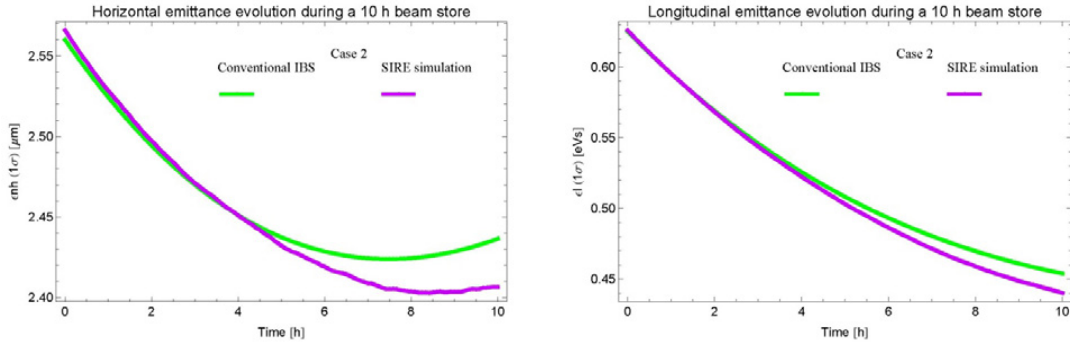


Figure 6: Comparison of ε_H^N (left) and ε_L (right) between SIRE (magenta) and analytical IBS (B-M) (green) computations (case 2, Table 1): difference $\delta_{\max}(\Delta\varepsilon_H/\varepsilon_H) \sim 1\%$ and $\delta_{\max}(\Delta\varepsilon_L/\varepsilon_L) \sim 2\%$.

Figure 6 compares the evolution of the emittances for the first IR upgrade with reduced emittances [23] between SIRE simulation and the straight IBS computation, taking into account the joint effects of IBS and radiation damping. Including quantum excitation effect in Bjorken-Mtingwa calculations would yield negligible change of the LHC proton beam equilibrium emittances (assuming 1% coupling between the horizontal and vertical planes). Examination of the joint intrabeam and synchrotron radiation damping phenomena during a 10 hours physics beam store at 7 TeV in the first IR upgrade of LHC shows that over the

full physics fill duration the evolution of emittances is kept inside the design values, as the IBS growth is largely balanced by the synchrotron radiation damping.

Even though SIRE simulation algorithm and Bjorken-Mtingwa analytical formalism make use of distinct approaches to tackle the IBS issue, both techniques agree rather well.

2.4.6 Summary

The conventional IBS Piwinski and Bjorken-Mtingwa formalisms for bunched beams and the Zenkevich Monte Carlo IBS simulation formalism based on binary collision models have been reviewed.

The Piwinski formalism is using the “classical” Rutherford differential cross-section for the Coulomb scattering. Unlike Piwinski, the approach to IBS of Bjorken and Mtingwa is based on the time-evolution operator « S-matrix » that relates transitions from an initial quantum state $|i\rangle$ to a final state $|f\rangle$ of a physical system experiencing a scattering process. Both models consider Gaussian laws for the beam density distributions in phase space in order to derive analytical formulas for the IBS rise times.

Other IBS models based on non-Gaussian distributions have been formulated using the kinetic analysis for the modelling of small angle multiple Coulomb scattering. Zenkevich’s approach was to develop a Monte Carlo based macro-particle algorithm called “binary collision map” (BCM), realized in the macro-particle code “Monte-Carlo code” (MOCAC) for numerical modelling of IBS effects in accelerators and storage rings. An extension of it called “Software for Intrabeam Scattering and Radiation effects” (SIRE) was developed to simulate the evolution of beam particle distributions in storage rings, taking into account IBS, radiation damping and quantum excitation.

A benchmarking of the IBS theoretical models with the Monte Carlo SIRE code for the case of the CLIC Damping Rings, which is an intrabeam scattering dominated ring in the presence of strong synchrotron radiation and for the LHS/HL-LHC proton beams at collision energy, where synchrotron radiation turns into a noticeable effect as well, shows very good agreement of the simulation tools and the conventional models.

2.4.7 Acknowledgements

We warmly acknowledge the major contribution of P. Zenkevich to the ideas leading to the development of an IBS Monte-Carlo code and to A. Vivoli for the development of SIRE and many fruitful discussions. We would like also to thank C. Carli for his contribution in the production of the plot in Fig. 2.

2.4.8 References

1. A. Piwinski, “Intra-beam scattering”, Proc. 9th Int. Conference on High Energy Accelerators, Stanford, CA, 1974 (SLAC, Stanford, CA, 1974), p. 405.
2. J. Bjorken, S. Mtingwa, “Intrabeam scattering”, Part. Accel. 13 (1983) 115.
3. F. Antoniou, F. Zimmermann, “Revision of intrabeam scattering with non-ultrarelativistic corrections and vertical dispersion for MAD-X”, CERN-ATS-2012-066 (2012).
4. K. Kubo, S. Mtingwa, A. Wolski, “Intrabeam scattering formulas for high energy beams” (2005) 081001. <http://dx.doi.org/10.1103/PhysRevSTAB.8.081001>.
5. A. Wolski, “Beam dynamics in high energy particle accelerators”, Imperial College

Press, March 2014.

6. A. Woslki, "Space Charge, Intrabeam scattering and Touschek effects", Fourth International Accelerator School for Linear Colliders, Beijing, September 2009. <http://uspas.fnal.gov/materials/12MSU/DampingRings-Lecture6>.
7. L. Evans and B. Zotter, "Intrabeam scattering in the SPS", CERN/SPS/80-15-DI (1980).
8. M. Martini, "Intrabeam scattering in the ACOL-AA machines", CERN PS/84 9 (1984).
9. M. Martini, "Intrabeam scattering: Anatomy of the theory", Proc. CAS-CERN Accelerator School "Intensity Limitations in Particle Beams", Geneva, November 2015.
10. J. Bjorken, S. Drell, "Relativistic quantum mechanics", McGraw-Hill, New York, (1964).
11. P. Zenkevich, "Last advances in analysis of intra-beam scattering in the hadron storage rings", Nuclear Instruments and Methods in Physics Research (2007), <http://dx.doi.org/10.1016/j.nima.2007.02.04>.
12. P. Zenkevich, A. Bolshakov, O. Boine-Frankenheim, "Kinetic effects in multiple intra-beam scattering", ICFA HB204, Bensheim, 2005 [AIP Conf. Proc. 773 (2005) 425].
13. N. Alekseev, A. Bolshakov, E. Mustafin, P. Zenkevich, "Numerical code for Monte-Carlo simulation of ion storage", [AIP Conf. Proc. 480 (1999) 31], <http://scitation.aip.org/content/aip/proceeding/aipcp/480?ver=pdfcov>.
14. M. Martini, A. Vivoli, "Effect of intrabeam scattering and synchrotron radiation damping when reducing transverse emittances to augment the LHC luminosity", CERN-sLHC-PROJECT-Report-0032 (2010).
15. T Akizuka, H. Abe, "A binary collision model for plasma simulation with a particle code", Journal of computational physics 25 (1977).
16. J. Bittencourt, "Fundamentals of plasma physics" (Springer, New York, 2004).
17. P. Bellan, "Fundamentals of plasma physics" (Cambridge University Press, 2012).

2.5 The Birth and Childhood of the Coupling Impedance and Stability Maps

Vittorio Giorgio Vaccaro
 Istituto Nazionale di Fisica Nucleare. Sezione di Napoli
 Mail to: vaccaro@na.infn.it

At beginning of sixties important breakthrough innovations were already accomplished in accelerator science, which produced leaps forward in the performances of particle accelerators.

2.5.1 The First Breakthrough Innovation: the Phase Stability

The basic principles of synchrotron design (phase stability) were proposed independently by Vladimir Veksler in the Soviet Union (1944) and Edwin McMillan in the United States (1945). According to this principle, it is possible to accelerate bunches of charged particles of finite dimensions.

Based on the principles stated by Vladimir Veksler and Edwin McMillan a proton synchrotron was built at Brookhaven National Laboratory, named **Cosmotron**. Its construction started in 1948 and it reached its full energy in 1953. It was the first particle accelerator to exceed the GeV wall, accelerating protons to 3.3 GeV. Since when Brookhaven's Cosmotron went into operation in the early 1950's, scientists knew that achieving the higher energies was going to be a difficult problem. Calculations showed that, using existing technology, building a proton accelerator 10 times more powerful than the 3.3GeV Cosmotron would require 100 times as much steel.

2.5.2 The Second Breakthrough Innovation: the Alternating Gradient

While the first strictly used the toroid shape, the strong focusing principle independently discovered by Nicholas Christofilos (1949) and Ernest Courant (1952) allowed the complete separation of the accelerator into the guiding magnets and focusing magnets, shaping the path into a round-cornered polygon. Without strong focusing, a machine as powerful as the Alternating Gradient Synchrotron (AGS) would have needed apertures (the gaps between the magnet poles) between 0.5 m and 1.5 m instead of apertures of less than 0.1 m. The construction of AGS was accomplished in 1960.

2.5.3 The Collider Age. Looking Far

Even before the successful achievements of PS and AGS, the scientific community was aware that another step forward was needed. Indeed, the impact of particles against fixed targets is very inefficient from the point of view of the energy actually available for new experiments: much more efficient could be the **head on collisions** between high-energy particles. With increasing energy, the energy available in the Inertial Frame with fixed targets is incomparably smaller than in the head-on collision (HC), as Wideroe thought some decades before. If we want the same energy in IF, using fixed targets one should build gigantic accelerators. The challenge was to produce intense and high-collimated beams.

2.5.3.1 *Hamburger Intermezzo*

Touschek was born and attended school in Vienna. Because of racial reasons, he was not allowed to finish high school. However, he could continue his studies in a precarious way. After Anschluss, he moved to Hamburg, where nobody knew of his origins. There he met Rolf Wideroe with whom he started cooperating in building a betatron and discussing on Wideroe's visionary thoughts. However, Touschek was discovered and arrested by the Gestapo in 1945, Wideroe visited him in prison, bringing cigarettes, food and, during these meetings they continued to talk about the betatron. Incidentally, in that context Touschek conceived the idea of radiation damping for electrons. When the Allied army reached Hamburg Wideroe, suspected of collaboration, was arrested. Sometime after, he was found not guilty and released. After the war, Touschek roamed about Europe. Finally, in 1952 he decided to stay in Rome permanently, receiving the position of researcher at the National laboratories of the Istituto Nazionale di Fisica Nucleare in Frascati, near Rome.

2.5.3.2 *Collider Contest: Frascati vs. Princeton*

A contest between Princeton and the Frascati Laboratories started: both labs were developing collider programs accelerating electrons and positrons. Princeton chose an eight-shaped structure: two circular rings in which electrons and positron were circulating with the same orientation, meeting at the collision point. Frascati team, which took the field later, was even more audacious: they used a single ring with "counter-rotating" beams of electrons and positrons.

The enterprise began on March 7, 1960, when Bruno Touschek held a seminar at Frascati Laboratories. He was proposing to build an electron-positron storage ring, according to Wideroe's visionary ideas concerning storage rings and colliders. On March 14, a preliminary study demonstrated the feasibility of the proposal. The storage ring was named ADA (Anello Di Accumulazione = Storage Ring). Touschek pointed out the extreme scientific interest of high-energy collisions between particles and antiparticles, and the simplicity of realization of such an accelerator. The machine was conceived as a feasibility experiment to provide a sound basis for the realization of electron-positron colliders of larger center of mass energy and luminosity. The total cost of the project (converted to the present purchasing power) was around 800.000 €.

A first stored beam of few electrons was obtained at the end of May 1961, using the Frascati Electron Synchrotron as an injector. The first electron-positron interactions were observed at the beginning of 1964. The impact of the ADA Collider has been immense in enabling a new chapter of accelerator physics to be established with the machine being the first particle-antiparticle collider and the first electron-positron storage ring. In addition to this grand accomplishment, the machine was also able to prove the idea that one could accelerate and collide a beam of particles and antiparticles in the same machine.

Many laboratories started programs of to accelerate and store particles in order to prove the feasibility to intense beams. Surprisingly enough, a longitudinal instability below transition energy was discovered in 1963 in the *MURA 40 MeV* electron accelerator. At the same time vertical instabilities in the *MURA 50 MeV* were observed [1]. At that time, it was a common place that above transition energy, a beam could be unstable since it was postulated that the prevalent electromagnetic interaction with the vacuum pipe was capacitive. Furthermore, it was not known that there could exist some stabilizing mechanism.

2.5.4 The Analysis of Instabilities. A Step Forward

Two companion papers [2,3] appeared in 1965 on the Review of Scientific Instruments, one concerning longitudinal coherent instability and a second one transverse coherent instability. The approach to the problem was the usual one adopted for modulational instability, which arises from the coupling between the equation of the particle dynamics and the electromagnetic interaction a coasting particle beam with the surrounding pipe of a circular accelerator.

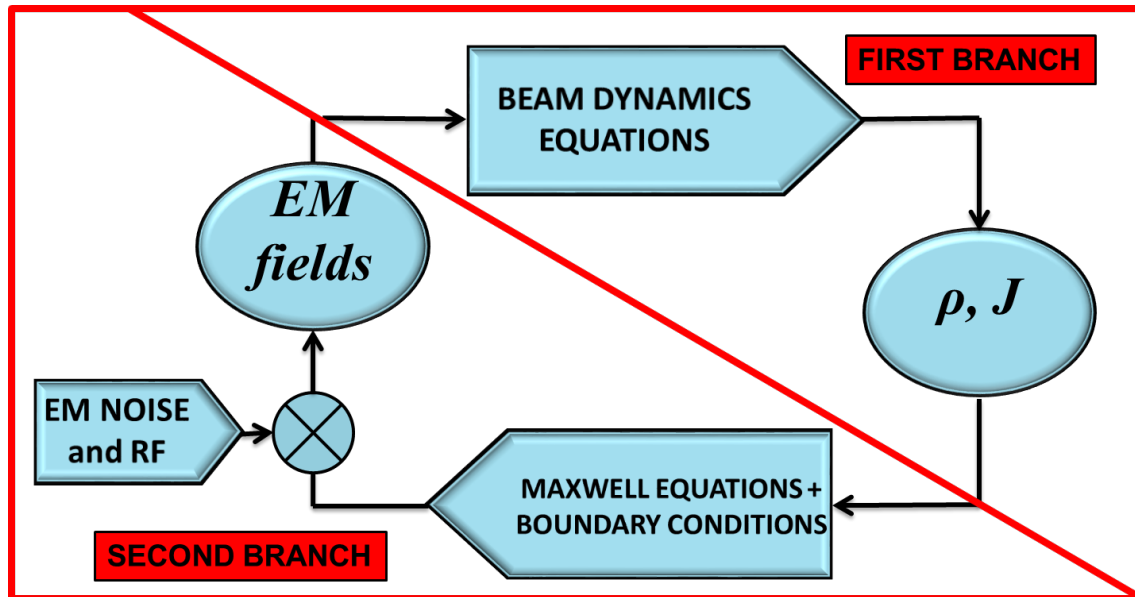


Figure 1: Block diagram of the coupling between e-magnetic equation and dynamics equation.

The novelty was the use of Vlasov equation where it is assumed that the beam particles have an energy distribution function. The problem is solved by means of perturbative techniques that lead to a dispersion relation. The role of Landau damping of the instability coming from the energy spread was emphasized. The pipe is supposed circular, smooth, and lossy and with circular or rectangular cross-section.

In both paper the case in the absence of frequency spread was examined and it was found that the rise time depends on the conductivity of the pipe. However, allowing for a finite spread, the stability criteria obtained from the dispersion relation do not involve the pipe losses. It is worth noting that the stability criteria were derived assuming Gaussian or Lorentzian distribution functions. Four years later, in a CERN internal report [4], a more accurate analysis showed that, taking in account a more realistic distribution function, the stability criteria do involve the pipe losses. This aspect tells the amplitude and the generality of the concepts presented in the two papers. The stream of research born in 1965 and still lasting gave and gives results that have of fundamental importance for particle accelerator.

2.5.5 An Impedance is in the Air. The Banality of Invention

When I was hired by CERN on June 1966, I joined the RF group of the Intersecting Storage Ring (ISR) Department. ISR was under construction and was destined to be the world's first hadron collider. It ran from 1971 to 1984, with a maximum center of mass

energy of 62 GeV. At that time at CERN, there was big concern about stability of the beams because of large number and various kind of lumped equipment (300 pairs of clearing electrodes, pick-ups, cavities, etc.), which could be “seen” by the beam. Unfortunately, the stability criteria did not apply to the situation of ISR. I was committed to work on this problem. The task to introduce in the dispersion relation the contribution of a lumped element, e.g. cavity of impedance Z_c (eventually clearing electrodes)

$$I_i = \text{const} \langle 2\pi R E_\theta \rangle \int \frac{d\psi_0}{dW} \frac{dW}{[\omega - n\omega_0(W)]}, \quad (1)$$

where I_i is the incipient perturbed current in the beam and ω the frequency of the instability. The procedure is described in Ref. [5]. The impressed voltage at the cavity gaps V_i is calculated assuming that the image current, that loads the cavity is equal to the perturbed beam current I_i . The field distribution in the accelerator is expanded in travelling waves inside the pipe. Then, only the n th harmonic is retained which is riding with the perturbation. Therefore, the mean integral in the above equation may be written as:

$$\langle 2\pi R E_\theta \rangle = -Z_c I_i. \quad (2)$$

The concept of coupling impedance was then extended to pipe with uniform properties. Of course, the above procedure consisted in a brute force approach. Its validity is restricted to wavelengths much larger than the cavity gap and of the pipe radius; however, this limitation does not affect the principle. Fifty years have passed. In the meantime, exact approaches were performed resorting to numerical codes or to analytical-numerical techniques such as the mode matching. Few months after my arrival, Andy Sessler, on leave of absence from LBL, joined the ISR-RF group. I was committed to him and I showed him the manuscript of my results. He reviewed it, making corrections, suggesting integrations and then he stated that the report had to appear with my name only. However, the paper was issued in closed distribution restricted to AR and ISR Scientific Staff. At the same time, he proposed a general treatment of impedance of arbitrary electrical properties [6]. There is another important aspect which should be taken into account: the concept of coupling impedance is a handy concept. This is very well illustrated by Sessler in one of his papers [7]: “It was emphasized - and, it was the main point of [6] - that Z described the impedance of the wall elements and as, thus, amenable to computation - or measurement - by means of all the standard techniques employed in electrical engineering. This engineering technique was applied to a number of problems, such as helical conducting walls [8], and allowed complicated structures to be readily analyzed. Maybe this feature has been one of the factors that determined the success of the coupling impedance concept.

2.5.6 The Universal Stability Charts

The introduction of coupling impedance concept is tightly linked to the analysis of the dispersion relation. The first step was done. The success of the first one influenced the advancement of the second one. Then, when the picture of the longitudinal instability phenomenon was clear, the problem of transverse instability was tackled.

Except in particular cases, Eq. (2) cannot be solved analytically; namely, given the impedance, the distribution function, the harmonic number n and the function $\omega_0(W)$ it is not in general possible to find analytically the frequency ω of the instability, if any. A

collaboration with Sandro Ruggiero was set up, which tackled the problem with another point of view: find the coupling impedance for a given value of the complex frequency ω , assuming a linear dependence of ω_0 on W ; repeat the procedure for various distribution functions [4]. Therefore, we had to perform analytically the integral for several reasonable distributions:

$$Z(\omega) = -\frac{1}{\text{const} \int \frac{d\psi_0}{dW} \frac{dW}{[\omega - n\omega_0(W)]}}. \quad (3)$$

This is nothing but a conformal mapping of the complex variable ω into the complex variable Z . The interest is to explore the region where the imaginary part of ω is negative, namely where the oscillation is exponentially increasing. A particular interest was devoted to the mapping of the lines where the frequency is real with a vanishing imaginary part, namely

$$\omega = \omega_r + j0_-. \quad (3)$$

This procedure gave quite surprising results:

- The mapping of the lower half-plane covers almost entirely the Z plane.
- The mapping of the upper half plane covers the same region of the Z plane.
- There is a “neutral region”, which is not covered by none of the two mapping and is defined as the stable region.
- The stable region is finite if the tails of the distribution function are finite.
- The stable region of a monoenergetic distribution (infinitesimal tails) is the positive imaginary axis.

In Fig. 2 the result of the mapping for a Lorentzian distribution function is reported (similarly to Refs. [2,3]). The impedance is normalized in such a way to get a universal stability diagram. The dashed domain is the stability region, contour of which is a parabola. It is apparent that the stable domain is infinite. The coupling impedance of smooth pipe has small real part due to the pipe resistivity and a large positive imaginary (normalized) part and one could infer that the beam should be stable, which was the same conclusion inferred by the authors. Other distribution functions were considered, such as the Gaussian one (which produces also an infinite stability region), a 2nd, 3rd and 4th order parabola and a truncated cosine. According to the available data, the working point of MURA accelerator was very close to the imaginary axis and had a very large imaginary component. This means that, the detected instability is compatible with the results obtained from the Vlasov equation, provided, that one takes a realistic distribution function. That was an excellent result confirming that correctness of the Vlasov equation approach.

The successful aftermaths stimulated the extension of the research on transverse instabilities. An example is reported in Fig. 3. In this case it is taken into account not only the frequency spread but also the distribution function of the betatron amplitude oscillation. Coupling impedance is fifty this year, but it does not show...

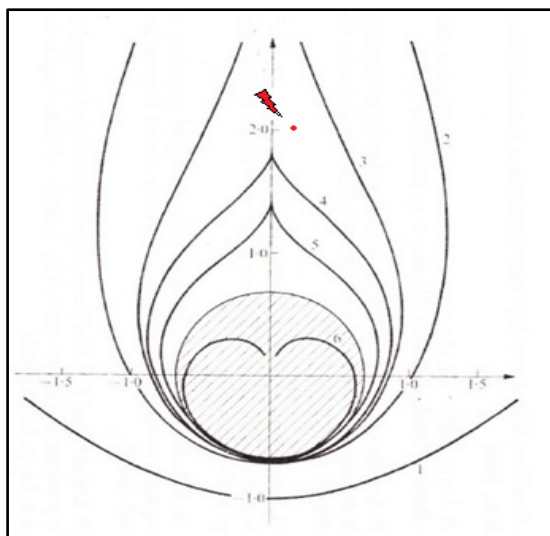


Figure 2: Stability boundaries for various distribution functions.

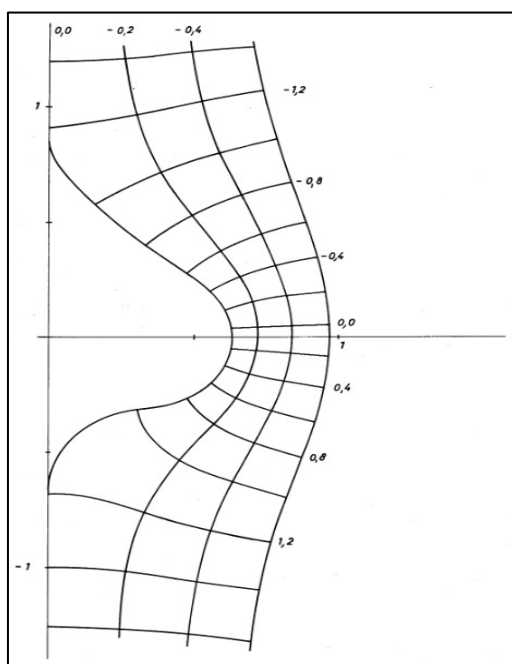


Figure 3: Transverse stability chart with curves at constant rise time.

2.5.7 References

1. C.P. Curtis et al., Proc. of the International Conference on High Energy Accelerators (Atomizdat, Moscow, 1963).
2. V.K. Neil and A.M. Sessler, Rev. Sci. Instr. 36,429 (1964).
3. L.J. Laslett, V.K. Neil, and A.M. Sessler, Rev. Sci. Instr. 36,436 (1964).
4. A.G. Ruggiero, V.G. Vaccaro, Solution of the Dispersion Relation for Longitudinal Stability of an Intense Coasting Beam in a Circular Accelerator. CERN-Report ISR-TH 68-33 (1968).
5. V.G. Vaccaro, Longitudinal Stability of an Intense Coasting Beam in a Circular

Accelerator CERN, ISR-RF/66-35, 1966.

6. A.M. Sessler, V.G. Vaccaro, Longitudinal Instabilities of Azimuthally Uniform Beams in Circular Vacuum Chambers with Walls of Arbitrary Electrical Properties, CERN-Report ISR-RF 67-2 (1967).
7. A.M. Sessler, Beam-Surrounding Interaction and the Stability of Relativistic Particle Beam, PAC1971-1039.
8. A.M. Sessler, Passive Compensation of Longitudinal Space Charge Effects in Circular Accelerators: the Helical Insert, CERN-Report ISR-RF 68-1 (1968).

2.6 Wakefields and Impedances

K. Bane and G. Stupakov
 SLAC National Accelerator Laboratory, Menlo Park, CA 94025, USA
 Mail to: stupakov@slac.stanford.edu

2.6.1 Introduction

The problem of beam stability is fundamental for modern accelerators where acceleration and storage of intense relativistic beams with small emittances are crucial for machine operation. This complex problem interconnects the properties of the beam environment with the beam dynamics through electromagnetic fields excited by the beam in the vacuum chamber. To simplify the analysis of the beam stability, it is customary to split the study of the fields excited by the beam into a separated topic through introduction of the notion of the wakefield. Wakefields can usually be calculated using a simplified assumption about the beam trajectory - in many cases considering the trajectory as a straight line passing through an element of the vacuum chamber that excites the wake. Moreover, due to the linearity of Maxwell's equations, the wakefield can be first calculated for a point charge, and then convoluted with the beam distribution to obtain the field inside the beam.

In this text we will introduce main concepts associated with wakefields. In our consideration we use an assumption of relativistic particles for which the Lorentz factor $\gamma \gg 1$.

2.6.2 Definition of Wakes

The interaction between particles of a beam and the electromagnetic field generated by an inhomogeneity in the beam pipe in many cases is localized in a region that is small when compared to the length of the beam orbit. It also occurs on a time scale much smaller than the characteristic oscillation times of the beam in the accelerator (such as the betatron and synchrotron periods). This allows us to consider the interaction of the beam in the impulse approximation and characterize it by the amount of integrated momentum transferred from the electromagnetic field to the particle.

The concept of the *wakefield* or *wake* is introduced in the following way. Consider a leading particle 1 of charge q moving along the axis z with a velocity close to the speed of light, $v \approx c$, so that $z = ct$ (see Fig. 1). A trailing particle 2 of unit charge moves parallel to the leading one, with the same velocity, at a distance s with offset $\boldsymbol{\rho}$ relative to the z -axis. The vector $\boldsymbol{\rho}$ is a two-dimensional vector perpendicular to the z -axis, $\boldsymbol{\rho} = (x, y)$. Although the two particles move in vacuum, there are material boundaries in the problem that scatter the electromagnetic field and lead to an interaction between the particles through this electromagnetic field.

Let us assume that we have solved Maxwell's equations and found the electromagnetic field generated by the first particle. We calculate the change of momentum $\Delta\boldsymbol{p}$ of the second particle caused by this field as a function of the offset $\boldsymbol{\rho}$ and distance s ,

$$\Delta\boldsymbol{p}(\boldsymbol{\rho}, s) = \int_{-\infty}^{\infty} dt [\boldsymbol{E}(\boldsymbol{\rho}, z, t) + c\hat{\boldsymbol{z}} \times \boldsymbol{B}(\boldsymbol{\rho}, z, t)]_{z=ct-s}. \quad (1)$$

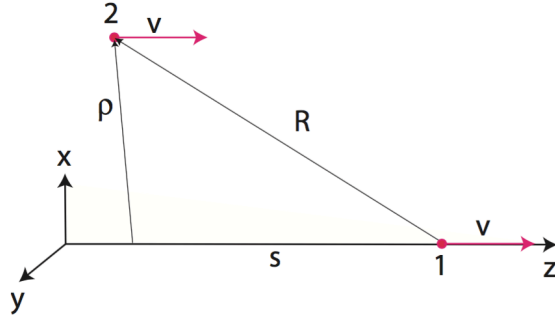


Figure 1: A leading particle 1 and a trailing particle 2 move parallel to each other in a vacuum chamber.

Note that here we integrate along a straight line - the unperturbed orbit of the second particle. The integration limits in Eq. (1) are extended from minus to plus infinity, assuming that the integral rapidly converges outside of the element that generates the fields.

Since the beam dynamics is different in the longitudinal and transverse directions, it is useful to separate the longitudinal momentum Δp_z from the transverse component $\Delta \mathbf{p}_\perp$. With the proper sign and the normalization factor c / q , these two components are called the *longitudinal* and *transverse wake functions*,

$$\begin{aligned} w_l(\boldsymbol{\rho}, s) &= -\frac{c}{q} \Delta p_z = -\frac{c}{q} \int dt E_z|_{z=ct-s}, \\ w_t(\boldsymbol{\rho}, s) &= \frac{c}{q} \Delta \mathbf{p}_\perp = \frac{c}{q} \int dt [\mathbf{E}_\perp + c\hat{\mathbf{z}} \times \mathbf{B}]_{z=ct-s}. \end{aligned} \quad (2)$$

Note the minus sign in the definition of the longitudinal wake function - it is introduced so that the positive longitudinal wake corresponds to the energy loss of the trailing particle (if both the leading and trailing particles have the same sign of charge). The so defined wakes have dimension V/C in SI units and cm^{-1} in CGS units (a useful relation between the units is: $1 \text{ V/pC} = 1.11 \text{ cm}^{-1}$).

There is an important relation that connects the longitudinal and transverse wakes defined by Eq. (2)

$$\frac{\partial w_t}{\partial s} = \nabla_\rho w_l. \quad (3)$$

This relation is usually referred to as the Panofsky-Wenzel theorem.

Because we have assumed that the leading particle is moving with the speed of light, the field that it generates in a vacuum chamber cannot propagate ahead of it. This is the causality principle, which means that the wake is zero for negative values of s ,

$$w_l(\boldsymbol{\rho}, s) \equiv 0, \quad w_t(\boldsymbol{\rho}, s) \equiv 0, \quad \text{for } s < 0. \quad (4)$$

It was assumed above that the electromagnetic field is localized in space and time and the integral in Eq. (1) converges. There are cases, however, such as the resistive wall wake of a long pipe, when this is not true and the source of the wake is uniformly distributed along an extended path. In this case, it is more convenient to introduce the wake per unit length of the path by dropping the integration in Eq. (1)

$$\begin{aligned} w_l(\boldsymbol{\rho}, s) &= -\frac{1}{q} E_z|_{z=ct-s}, \\ \mathbf{w}_t(\boldsymbol{\rho}, s) &= \frac{1}{q} [\mathbf{E}_\perp + \hat{\mathbf{z}} \times \mathbf{B}]_{z=ct-s}. \end{aligned} \quad (5)$$

In this definition, the wakes acquire an additional dimension of inverse length, and have the dimension cm^{-2} in CGS and V/C/m in SI.

Another example where the wakes per unit length are more appropriate than the integrated wakes is the case of periodic structures. For such structures, the fields and the wakes in Eq. (5) are understood as averaged over one structure period with the total wake given by multiplying the wake per unit length by the length of the structure.

2.6.3 The “Catch-Up” Distance

As mentioned earlier, for a beam particle moving along a straight line with the speed of light, due to causality, the electromagnetic field scattered off discontinuities on the wall of the pipe does not affect the charges that travel ahead of it. This field can only interact with the charges in the beam that are behind of the particle that generates the field. For short bunches, the time needed for the fields scattered off the wall of the vacuum chamber to reach the beam on the axis may not be negligible, and the interaction with this field may occur well downstream of the point where the field was generated. Let us find where the electromagnetic field produced by a leading charge reaches a trailing particle traveling at a distance s behind the leading one. Assume that a discontinuity located on the surface of a pipe of radius b at coordinate $z = 0$ is passed by the leading particle at time $t = 0$ (see Fig. 2).

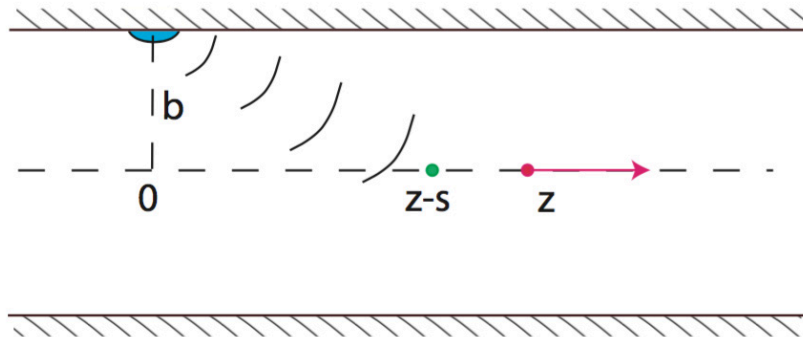


Figure 2: A wall discontinuity located at $z = 0$ scatters the electromagnetic field of a relativistic particle. When the particle moves to location z , the scattered field arrives to point $z - s$.

If the scattered field reaches point $z - s$ at time t , then $(ct)^2 = (z - s)^2 + b^2$, where z is the coordinate of the leading particle at time t , $z = ct$. Assuming that $s \ll b$, from these two equations we find

$$z \approx \frac{b^2}{2s}. \quad (6)$$

The distance z given by this equation is often called the catch-up distance. Only after the leading charge has traveled that far away from the discontinuity, a particle at point s behind it starts to feel the wake field generated by the discontinuity.

2.6.4 Transverse Wakes in Axisymmetric Systems

In the general case of a vacuum chamber which does not have symmetries, the transverse wake defined by the second equation in (5) can be directed at arbitrary angle to the offset of the leading particle. Of special interest for applications is the case of an axisymmetric vacuum chamber. From the axisymmetry, we first conclude that $\boldsymbol{w}_t = 0$ if the leading particle travels on axis of the vacuum chamber. Moreover, in view of the symmetry, for a nonzero offset of the leading particle, the wake \boldsymbol{w}_t is directed along the offset. In this case, instead of the vectorial wake \boldsymbol{w}_t a scalar wake w_t is used which is defined as the projection of \boldsymbol{w}_t onto the direction of the offset.

Since w_t is zero for zero offset, it is small for small offsets. In the lowest order, it can be approximated as a linear function of the offset of the leading particle r

$$w_t = rW(s). \quad (7)$$

Note that in this approximation the wake does not depend on the offset of the trailing particle. The quantity $W(s)$ is the wake per unit offset. It has dimension of V/(pC m) in SI units and cm^{-2} in CGS units. It is normally called the dipole wake.

2.6.5 Wakefield of a Bunch of Particles

Given the interaction of two point charges we can calculate the wakefield inside a bunch that contains N particles assuming $N \gg 1$. Let the longitudinal distribution function of the bunch be $\lambda(s)$ (the distribution function is defined so that $\lambda(s)ds$ gives the probability of finding a particle near point s). The coordinate s here is measured along the direction of the bunch motion; the head of the bunch corresponds to positive s , and the tail - to negative s . This meaning of s should not be confused with s shown in Fig. 1: there, it is the distance from the leading and trailing particles and is measured in the direction opposite to the direction of motion. To find the change of the longitudinal momentum of a particle located at point s inside the bunch we sum the wakes generated by all other particles at s ,

$$\Delta p_z(s) = -\frac{Ne^2}{c} \int_s^\infty ds' \lambda(s') w_t(s' - s). \quad (8)$$

Here we have used the causality principle and integrated only over the part of the bunch in front of point s . In the relativistic limit, the energy loss $\Delta E(s)$ caused by the wake field is equal to $-c\Delta p_z$, so Eq. (8) can also be rewritten as

$$\Delta E(s) = Ne^2 \int_s^\infty ds' \lambda(s') w_l(s' - s). \quad (9)$$

Two important integral characteristics of the strength of the wake are given by the average value of the energy loss ΔE_{av} , and the rms spread in energy, ΔE_{rms} , generated by the wake. These two quantities are defined by the following equations

$$\Delta E_{av} = \int_{-\infty}^\infty ds \Delta E(s) \lambda(s) = Ne^2 \int_{-\infty}^\infty ds \lambda(s) \int_s^\infty ds' \lambda(s') w_l(s' - s) \quad (10)$$

and

$$\Delta E_{rms} = \left[\int_{-\infty}^\infty ds (\Delta E(s) - \Delta E_{av})^2 \lambda(s) \right]^{1/2}. \quad (11)$$

The average energy loss normalized by the product eQ , where $Q = Ne$ is the bunch charge, is called the loss factor. Denoting the loss factor by κ we have a relation $\kappa = \Delta E_{av} / eQ$.

2.6.6 Wake at Origin for a Periodic Structure

When a short bunch passes through a single structure, such as a single-cell cavity, connected to infinitely long beam pipes, it can lose a large amount of energy to the wakefields. In fact, the diffraction model of wakes says that the bunch energy loss for this situation depends on bunch length, σ_z , as $\sigma_z^{-1/2}$, and the corresponding point charge wake depends on s as $w_l \sim s^{-1/2}$.

For periodic structures (which includes the case of structures with translational symmetry) this changes, and $w_l(0^+)$ appears to equal a constant that depends on the aperture of the structure. In an axisymmetric structure that constant is given by

$$w_l(0^+) = \frac{Z_0 c}{\pi a^2}, \quad (12)$$

where a is the radius of the aperture. The parameter Z_0 is the impedance of free space, equal to $(4\pi/c)$ in the cgs system, and 377Ω in the MKS system. This relation has been found to hold for a smooth resistive pipe [1], a metallic pipe with a thin dielectric layer [2], a disk-loaded accelerator structure [3], and a metallic pipe with small corrugations [2]. It seems to be a general property of axisymmetric, periodic structures. (Ref. [4] claims to have a general proof that it is.) For the transverse wake, in an axisymmetric structure, the slope of the dipole wake at the origin depends only on the pipe radius,

$$\frac{dW}{ds}(0^+) = \frac{2Z_0c}{\pi a^4}. \quad (13)$$

In flat geometry - e.g. the beam passes on the symmetry plane between two, infinitely wide, resistive plates - $w_l(0^+)$ is given by the result of Eq. (12) multiplied by the factor $(\pi^2/16)$, with a now half the distance between the plates.

These properties give one the upper limit of how quickly energy can be removed from the beam by the wakefield and how strong the transverse force can be. Note that these relations concerning the wakes at the origin do not depend on the material properties of the structure, provided that the region within the aperture contains, as usual, only vacuum.

2.6.7 Impedances

Knowledge of the longitudinal and transverse wake functions gives us a fairly complete understanding of the electromagnetic interaction of the beam with its environment. However, in many cases, especially in the study of beam instabilities, it is more convenient to use the Fourier transform of the wake functions, which gives us the impedances. Also, it is often easier to calculate the impedance for a given geometry of the beam pipe, rather than the wake function.

For historical reasons the longitudinal Z_l and transverse $Z_{t,q}$ impedances are defined as Fourier transforms of wakes with different factors

$$\begin{aligned} Z_l(\omega) &= \frac{1}{c} \int_0^\infty ds w_l(s) e^{i\omega s/c}, \\ Z_{t,q}(\omega) &= -\frac{i}{c} \int_0^\infty ds w_{t,q}(s) e^{i\omega s/c}, \end{aligned} \quad (14)$$

where index q denotes a transverse component, $q = x, y$. Note that the integration in Eqs. (14) can actually be extended into the region of negative values of s , because w_l and $w_{t,q}$ are equal to zero there.

Impedance can also be defined for complex values of ω such that $\text{Im } \omega > 0$ and the integrals of Eq. (14), converge. So defined, the impedance is an analytic function in the upper half-plane of the complex variable ω .

Note that other authors use definitions of the impedance that differ from Eq. (14). In Refs. [5, 6] the longitudinal impedance is defined as a complex conjugate to the one given by Eqs. (14). Here we follow the definitions of Refs. [7, 8].

From the definitions in Eqs. (14) it follows that the impedance satisfies the following symmetry relations

$$\begin{aligned} \text{Re } Z_l(\omega) &= \text{Re } Z_l(-\omega), & \text{Im } Z_l(\omega) &= -\text{Im } Z_l(-\omega), \\ \text{Re } Z_{t,q}(\omega) &= -\text{Re } Z_{t,q}(-\omega), & \text{Im } Z_{t,q}(\omega) &= \text{Im } Z_{t,q}(-\omega). \end{aligned} \quad (15)$$

The inverse Fourier transform expresses the wakes in terms of the impedances

$$\begin{aligned}
w_l(s) &= \frac{1}{2\pi} \int_{-\infty}^{\infty} d\omega Z_l(\omega) e^{-i\omega s/c}, \\
w_{t,q}(s) &= \frac{i}{2\pi} \int_{\infty}^{\infty} d\omega Z_{t,q}(\omega) e^{-i\omega s/c}.
\end{aligned}
\tag{16}$$

2.6.8 Resonator Wakefield and Impedance

The resonator model of wakes and impedances is quite useful in accelerator physics. For example, the impedance of the individual (trapped) modes of an RF cavity can be described with this model. The parameters are shunt resistance R_s , resonant frequency ω_r , and quality factor Q . This model is also used at times to describe the impedance of a storage ring, typically with Q taken to be 1, and the other parameters deduced from machine physics studies. In the Large Electron Positron Collider (LEP) at CERN, for example, this approach was taken to model both the longitudinal and transverse impedances of the ring [9]. Note that, unlike in the previous section, where the impedance and wake were per unit length for periodic structures, for the resonator model they are normally per object. The longitudinal impedance of the resonator model is given by

$$Z_l(\omega) = \frac{R_s}{1 + iQ\left(\frac{\omega_r}{\omega} - \frac{\omega}{\omega_r}\right)}.
\tag{17}$$

The corresponding wake becomes

$$w_l(s) = 2H(s)\kappa \exp\left(-\frac{\omega_r s}{2Qc}\right) \cdot \left[\cos \frac{\bar{\omega}_r s}{c} - \frac{1}{\sqrt{4Q^2 - 1}} \sin \frac{\bar{\omega}_r s}{c} \right],
\tag{18}$$

with the unit step function $H(s) = 0$ (1) for $s < 0$ ($s > 0$), the mode loss factor $\kappa = \omega_r R_s / (2Q)$, and $\bar{\omega}_r = \omega_r \sqrt{1 - 1/(4Q^2)}$. If R_s is in units of ohms, then so is the impedance, and the loss factor (and wake) have units of V/C. For $Q \gg 1$, we can approximate

$$w_l(s) \approx 2H(s)\kappa \exp\left(-\frac{\omega_r s}{2Qc}\right) \cos \frac{\omega_r s}{c}.
\tag{19}$$

For $Q = 1$, the resonator impedance is plotted in Fig. 3, and the corresponding wake in Fig. 4.

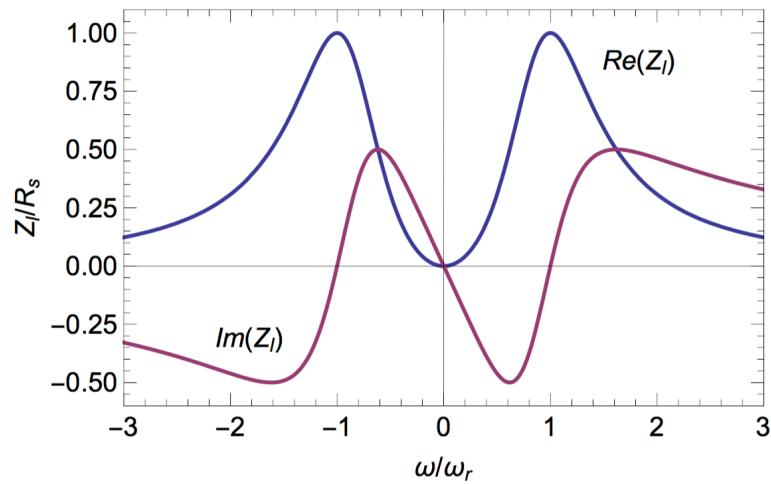


Figure 3: The real (blue) and imaginary (red) parts of the resonator impedance, assuming $Q = 1$.

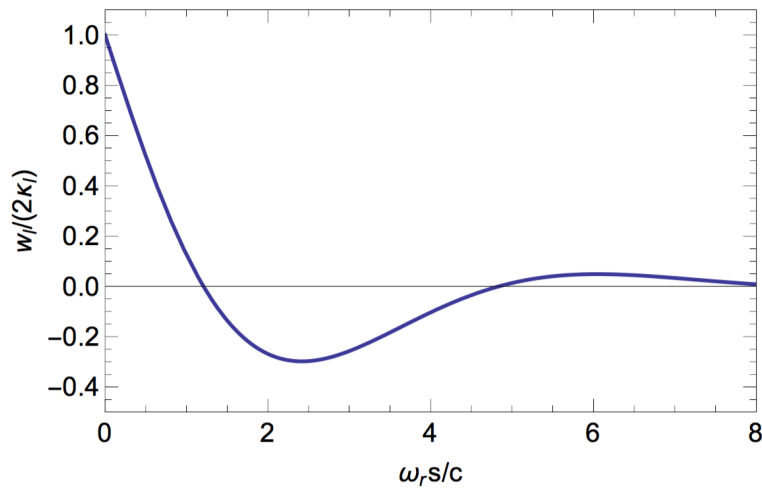


Figure 4: The longitudinal wake for the resonator impedance, assuming $Q = 1$.

The resonator impedance can also be used to model the transverse impedance and wake of a cavity or a storage ring. For example, assuming cylindrical symmetry, with the beam near the axis, the dipole impedance and wake will dominate the transverse wake force. In this case the transverse impedance is of the same form as Eq. 17, but with R_s replaced by cR_{sd} / ω , where R_{sd} has units of Ohm/m^2 in the MKS system.

2.6.9 Resistive Wall Impedance

One of the first impedances studied in accelerator physics was the resistive wall (rw) impedance, in particular, the low-frequency, transverse rw impedance. This impedance is often a limiting factor in the average current that can be stored in a storage ring. (Note that the equations presented here, with slightly different notation, can be found in [7].)

The low-frequency longitudinal rw impedance (the interaction per unit length) is given by

$$Z_l(\omega) = \frac{(1-i)}{2\pi a} \sqrt{\frac{Z_0 \omega}{2c\sigma_c}}, \quad (20)$$

where a is beam pipe radius, σ_c is wall conductivity. A more general expression for Z_l , valid also for high frequencies, is given by

$$Z_l(\Lambda) = \left(\frac{Z_0 s_0}{2\pi a^2} \right) \left(\frac{2}{1-i} \frac{1}{\sqrt{\Lambda}} - i \frac{\Lambda}{2} \right)^{-1}, \quad (21)$$

where $\Lambda = \omega s_0 / c$ and the length scale s_0 is

$$s_0 = \left(\frac{2a^2}{Z_0 \sigma_c} \right)^{1/3}. \quad (22)$$

This general form of the longitudinal rw wall impedance is needed when considering bunches of length $\sigma_z \lesssim s_0$. Normally, s_0 is a very short distance. For example, for a Cu ($\sigma_c = 5.9 \times 10^7 \Omega^{-1} \text{m}^{-1}$) pipe of radius $a = 1$ cm, $s_0 = 21 \mu\text{m}$.

The longitudinal rw wake (again given per unit length) corresponding to the impedance of Eq. (21) is a universal function of $x = s / s_0$

$$w_l(x) = H(x) \frac{4Z_0 c}{\pi a^2} \left(\frac{1}{3} e^{-x} \cos \sqrt{3}x - \frac{\sqrt{2}}{\pi} \int_0^\infty dy \frac{y^2 e^{-xy^2}}{y^6 + 8} \right). \quad (23)$$

The longitudinal rw impedance is plotted in Fig. 5, and the corresponding wake in Fig. 6.

These calculations have assumed that the conductivity of the pipe wall is a constant. A more involved calculation, including the so-called ‘‘ac conductivity’’ of the metal wall has also been performed. In fact, a calculation also including the anomalous skin effect - an effect that tends to be a low temperature effect - has also been done. Finally, the corresponding calculations have been carried out for the transverse rw impedance and wake in a round structure. Equations (20) and (23) imply that the long-range longitudinal rw wake asymptotically varies as $s^{-3/2}$, whereas the long-range dipole rw wake varies as $s^{-1/2}$, which is why the transverse rw wake can limit the average current stored stably in a ring, whereas the corresponding longitudinal wake tends not to.

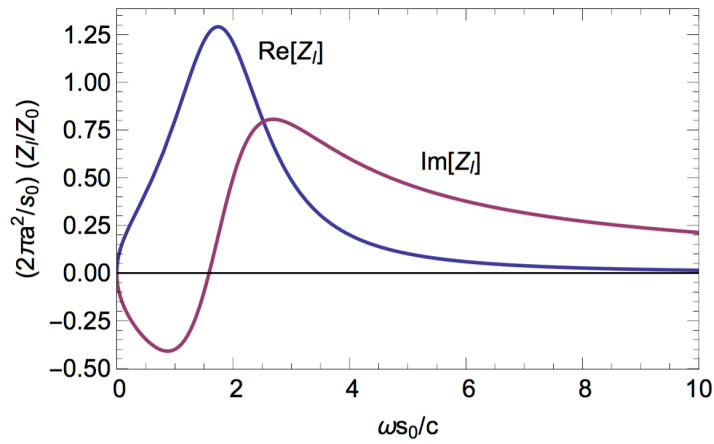


Figure 5: The real (blue) and imaginary (red) parts of the longitudinal resistive wall impedance.

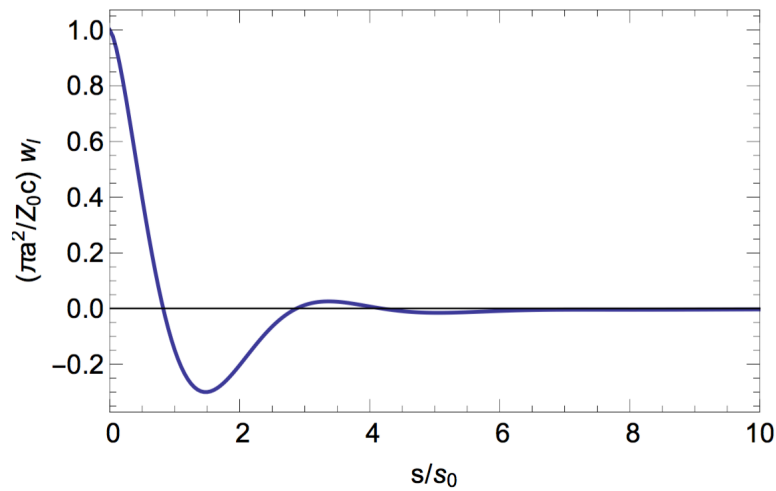


Figure 6: The longitudinal resistive wall wake.

2.6.10 References

1. K.L.F. Bane and M. Sands, in Micro Bunches Workshop, AIP Conference Proceedings No. 367, edited by E. B. Blum, M. Dienes, and J. B. Murphy (AIP, New York, 1996) p. 131.
2. A. Novokhatski and A. Mosnier, in Proceedings of the 1997 Particle Accelerator Conference (IEEE, Piscataway, NJ, 1997) pp. 1661–1663.
3. K.L.F. Bane, A. Mosnier, A. Novokhatskii, and K. Yokoya, Calculations of the Short-Range Longitudinal Wakefields in the NLC Linac, Report SLAC-PUB-7862 (Revised) (SLAC, 1998).
4. S.S. Baturin and A.D. Kanareykin, Phys. Rev. Lett. 113, 214801 (2014).
5. B.W. Zotter and S.A. Kheifets, Impedances and Wakes in High-Energy Particle Accelerators (World Scientific, Singapore, 1998).
6. P.B. Wilson, in Proc. US Particle Accelerator School: Physics of Particle Accelerators, Batavia, 1987, AIP Conference Proceedings No. 184, edited by M. Month and M. Dienes (American Institute of Physics, New York, 1989) pp. 525–564.
7. A.W. Chao, Physics of Collective Beam Instabilities in High Energy Accelerators

(Wiley, New York, 1993).

8. S.A. Heifets and S.A. Kheifets, *Review of Modern Physics* 63, 631 (1991).
9. D. Brandt et al., in *Proceedings of the 2nd European Particle Accelerator Conference, (EPAC 90) (Nice, France, 1990)* pp. 240–242.

2.7 Wake Field and Beam Coupling Impedance Simulations

Uwe Niedermayer and Erion Gjonaj
Institut für Theorie elektromagnetischer Felder,
Technische Universität Darmstadt
Schlossgartenstr. 8, 64289 Darmstadt, Germany
Mail to: niedermayer@temf.tu-darmstadt.de

2.7.1 Introduction

Wake potentials and beam coupling impedances can be calculated analytically only if the structures are fairly simple and an appropriate coordinate system can be attached. In practice this is often not the case and one has to rely on numerical techniques. Although the term beam coupling impedance was introduced first in the Frequency Domain (FD) by Vaccaro [1] in 1966, first numerical wake field computations were performed in the Time Domain (TD) by Balakin et al. [2] in 1978, and Weiland [3] in 1980. Nowadays, TD methods on structured meshes are the most common way to determine beam coupling impedances; they are available in many commercial and non-commercial codes.

Explicit TD methods require only matrix-vector multiplications for time stepping, which makes them computationally efficient. Usually they are based on Finite Differences Time Domain (FDTD [4]) or Finite Integration Technique (FIT [5]), which result in a coinciding space discretization on a Cartesian mesh. However, in general, mesh and method are independent. For example FIT or the Finite Element Method (FEM) can be applied on tetrahedral, hexahedral, or even mixed meshes.

In explicit TD simulations stability requires fulfilling the Courant Friedrichs Lewy (CFL) condition [6]. This makes them well suited for wave-propagation dominated problems but not well suited for structure-dominated problems, particularly at Low Frequency (LF). The small time step, which is tied to the space step by the CFL condition leads to a massive oversampling of an LF wave. Moreover, sub-relativistic beams and dispersive materials are difficult to treat in TD.

In these rather exotic cases, it makes sense to compute the beam coupling impedance directly in FD. Such computations are somewhat oriented on analytical methods [7], but generalized to arbitrary geometries by discretization methods as FIT or FEM. The current status of FD methods, however, is not as advanced as for TD methods. In particular, there is no high performance tool to compute beam coupling impedance in FD for three-dimensional structures.

In this paper, we will first discuss relevant assumptions and requirements for the computation of wake potentials and impedances in TD and FD. Then we give an overview of methods and codes. In the end, we give two examples; one is a three-dimensional RF-finger bellow structure planned to be used in the LHC which we address in TD and the other is a scenario for FCC-hh beam pipe addressed by a two-dimensional FD approach.

2.7.2 Definitions and Assumptions for the Computation of Wakefields and Impedances

The definition of wake potentials decouples the electromagnetical and the mechanical problems in beam dynamics by making the two assumptions:

- Rigid beam approximation: all particles move through the structure with constant velocity,
- Kick approximation: the force continuously acting on the trailing charge is lumped to a single kick (instantaneous change of momentum) after the passage through the structure.

The three-dimensional wake function is generally defined as (see e.g. [8])

$$\vec{W}(\vec{r}_1, \vec{r}_2, s) = \frac{1}{q} \int_{-\infty}^{\infty} [\vec{E} + \vec{v} \times \vec{B}](\vec{r}_2, z_2, t = (s+z)/v) dz_2, \quad (1)$$

where \vec{r}_1, \vec{r}_2 are the transverse coordinates of the leading and trailing charge, respectively. Equation 1 fulfills the Panofsky-Wenzel (PW) theorem [9] as $\nabla \times \vec{W}(\vec{r}_1, \vec{r}_2, s) = 0$, where the relative gradient is $\nabla' = (\partial_{x_2}, \partial_{y_2}, -\partial_s)^T$. A supplement to the PW theorem is the fact that the longitudinal wake function is a harmonic function of the transverse coordinates in the ultra-relativistic limit. This is the basis of several methods to modify the wake integration contour [10,11]. Among the most famous ones are the indirect test beam method [12] and the indirect interfaces [13] method. An approach to avoid lengthy wake integration for evanescent waveguide modes in the beam pipe after a cavity is presented in [14]. Finally, generalized methods for arbitrary structures are discussed in an abstract mathematical framework in [15].

The improper integral (1) exists only if the assumed infinite beam pipe connections do not cause any wakefields, i.e. the following conditions have to be fulfilled:

- smooth pipe (no geometric wake fields),
- perfectly conducting pipe (no resistive wake fields),
- ultra-relativistic beam (no space-charge wake fields).

Note that the last two requirements can be relaxed by taking into account a pipe stub impedance per unit length. However inserting a nonrelativistic beam into a 3D structure is involved and requires a numerical Lorentz transformation [16].

The wake potential is connected to the wake function by convolution with the bunch profile (line density $\lambda(s)$),

$$W_{pot}(s) = \int_{-\infty}^{\infty} W(s') \lambda(s-s') ds'. \quad (2)$$

Due to the minimal duration–bandwidth product, a Gaussian bunch

$$\lambda(z, t) = \frac{q}{\sqrt{2\pi}\sigma_s} \exp(0.5(z-vt)^2 / \sigma_s^2) \quad (3)$$

is usually employed for the excitation. Fourier transform over $s = vt-z$ leads to

$$|\lambda(\omega)| = \frac{q}{v} \exp(0.5\omega^2 / \sigma_\omega^2), \quad \sigma_\omega = v / \sigma_s. \quad (4)$$

Note that the excitation bunch length σ_s in a TD simulation does not necessarily correspond to the true bunch length in the operated accelerator, but rather to the frequency of interest. The point charge impedance is recovered by applying the convolution theorem as

$$Z(\omega) = \frac{1}{\lambda(\omega)} \int_{-\infty}^{\infty} W_{pot}(s) \exp(-i\omega s/v) ds. \quad (5)$$

For ultra-relativistic beams the dipolar and quadrupolar transverse impedances can be obtained by displacing the source bunch or the wake integration line, respectively. If the displacement is small, the impedance scales linearly with it and thus one defines a transverse dipolar or quadrupolar impedance in units of Ohms/m, which is obtained from the wake potential in the same way as the longitudinal impedance.

The beam coupling impedance can also be defined directly in FD by the power loss integral of a beam with finite transverse size as

$$Z(\omega) = -\frac{1}{q^2} \int_{beam} \vec{E} \cdot \vec{J}^* dV, \quad (6)$$

where \vec{J}, \vec{E} are the beam current density and the electric field spectral densities, respectively. The dipolar transverse impedance can be obtained accordingly by using a dipolar excitation current density and the PW theorem. Note that the representation of the impedance by a volume integral over the longitudinal electric field and the current density is particularly convenient for the computation on a mesh since discretization noise is averaged out. Moreover, it allows for consistent computation of the space charge impedance in the case of $v < c$ [17].

2.7.3 Time Domain Simulation Tools and Methods

Computational loads in wake field computation can be heavy, thus parallel codes lead to a significant progress. Nowadays, more than $1e9$ mesh cells are easily handled in parallel codes on cluster computers, while on a single machine the limit is at about $1e7$ to $1e8$. Moreover, an important recent improvement was the introduction of boundary conformal meshing, increasing the convergence order and avoiding extremely fine meshes to approximate the geometry accurately.

For the computation of short range wakes, it is advantageous to use a moving window, i.e. a mesh which moves along with the bunch and re-discretizes the geometry in every time step. The moving mesh approach was first introduced by Bane and Weiland [18] and is nowadays implemented in many codes such as PBCI [19] or GdfidL [20]. For long-range wakes, however, where the desired wake length is much longer than the structure, the moving mesh is rather inappropriate, since the entire wake length needs to be meshed.

Another important property for short-range wake computation in TD is the suppression of numerical dispersion in direction of beam propagation. This can be achieved by e.g. longitudinal-transversal-splitting [19] or TE-TM-splitting [21]. An overview of different TD codes can be found in [22], where these properties are discussed in more detail.

2.7.4 Flexible RF-Finger Structures

We investigate the structure shown in Fig. 1, which is designed to serve as a shielding for the LHC triplet bellows in point 1 and point 5. The fingers are made from a single copper beryllium sheet of 0.1 mm thickness. In total, it is considered to have 32 such structures in the LHC [23]. The beam coupling impedance is computed using the commercial CST Particle Studio (PS) [24] wake field solver and the PBCI code. The latter is a dedicated

dispersion free, moving window, parallel wake field solver developed at TEMF, TU Darmstadt. Recently, also conformal meshing was added to PBCI.

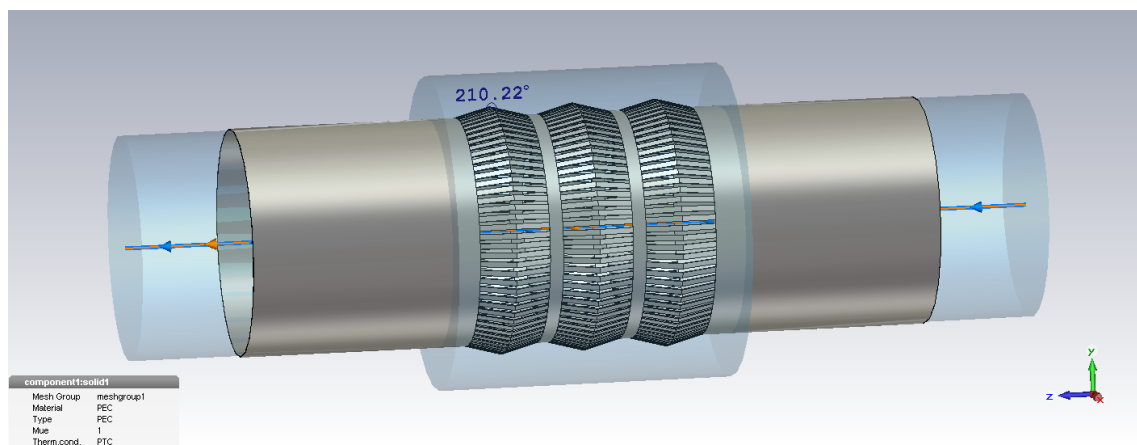


Figure 1: RF-Finger and bellow structure.

Since the structure is symmetric with respect to both the x-z and y-z planes, only one quarter of the geometry needs to be modeled when the beam is on axis (see Fig. 2) and only half needs to be modeled for dipolar excitation. When wakefield integration by means of indirect interfaces (see also [13]) is applied, the beam pipe stubs can be chosen to be very short, which reduces the number of cells in the structured mesh significantly. Wave guide port boundaries taking into account at least 50 modes guarantee that the reflections at the beam entry and exit are small. The excitation is applied as a Gaussian bunch with $\sigma_s = 12$ mm.

The simulated wake potential is displayed in Fig. 3, where the different parameters for the PBCI runs are given in Table 1. Figure 4 shows the real and imaginary parts of the impedance obtained by CST PS, where long wake lengths can be easily realized. Finally, Fig. 5 shows a comparison of CST and PBCI impedance magnitude, also for the structure fingers closed, such that only a bellow structure remains. This can be simulated much easier, and the results show good agreement with the simulation of the original structure. From this, one can conclude that the structure works as it should, i.e. shielding the beam from the outside in the frequency range of the beam spectrum. The expected cutoff at which significant field transmission occurs is at $f=c/2d=60\text{GHz}$, where $d=2.5\text{mm}$ is the gap between two fingers. Finally, Fig. 6 shows the transverse impedance that also behaves almost identically in both the finger and closed cases.

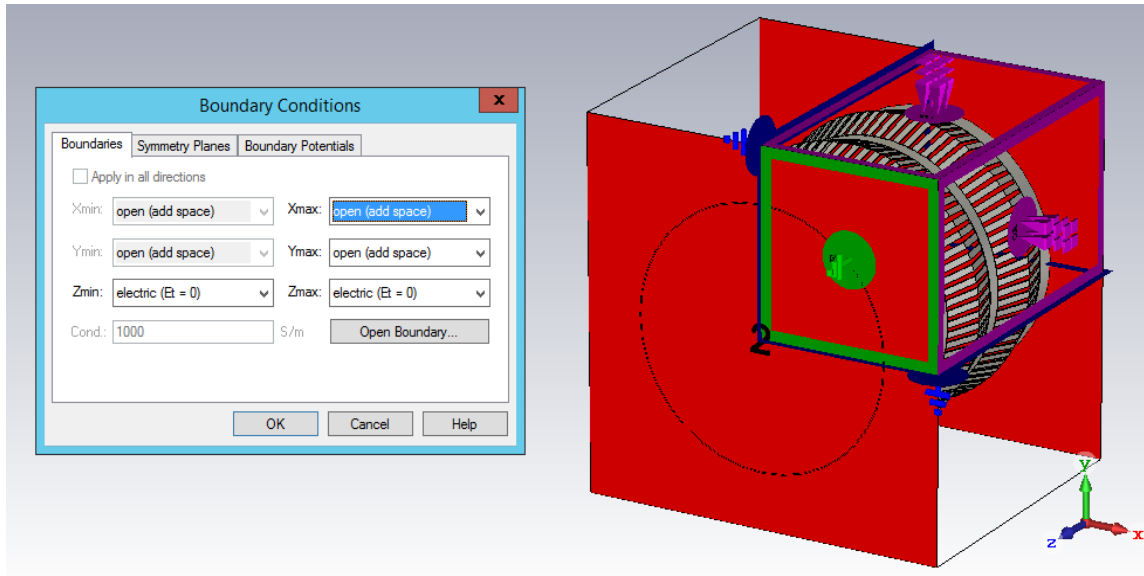


Figure 2: Boundary and symmetry conditions.

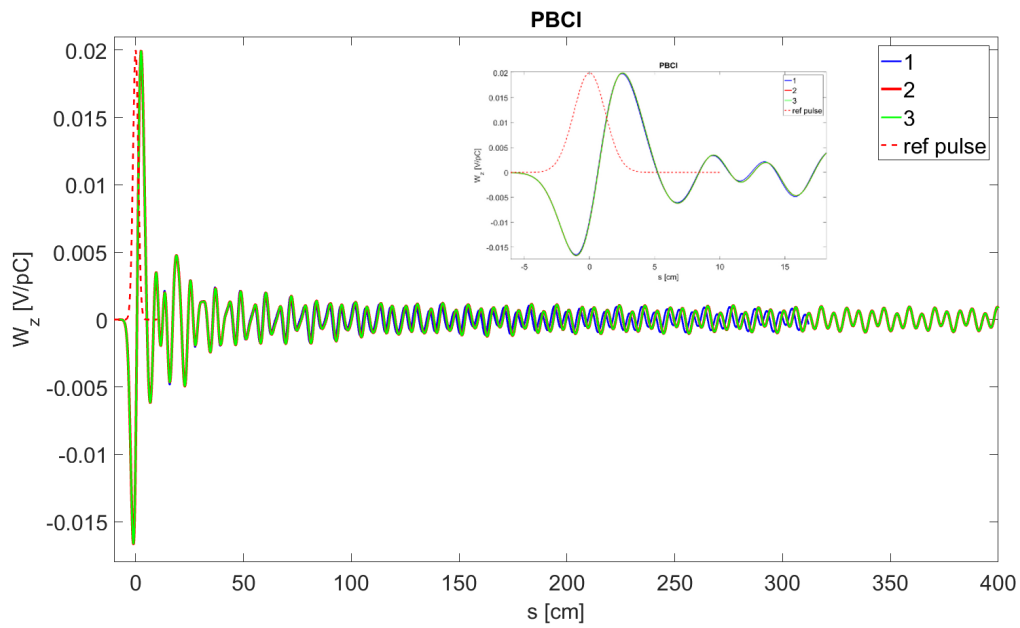


Figure 3: Longitudinal wake potential.

Table 1: Parameters of PBCI simulation runs.

	#cells	Wake length	Processes
PBCI1	8.6e7	3.2m	83
PBCI2	5e8	6.4m	332
PBCI3	1e9	12.8m	162

We interpret the impedance curves in Figs. 5 and 6 as follows: the first resonance at 5.1 GHz (3.6 GHz for the dipolar impedance) corresponds to a cavity mode. In the absence of losses its quality factor tends to infinity. In the simulations the height of the peak is

limited by the finite wake length and thus increases with increasing wake length. The second peak at 7.8 GHz (6.3 GHz for the dipolar impedance) is independent of the wake length. This is a broadband resonance caused by leaky cavity modes, i.e. cavity modes, which decay due to losses through the pipe. The small peak at 2.28 GHz (1.73 GHz for the dipolar impedance) corresponds to the cutoff of the first TM (TE) waveguide mode.

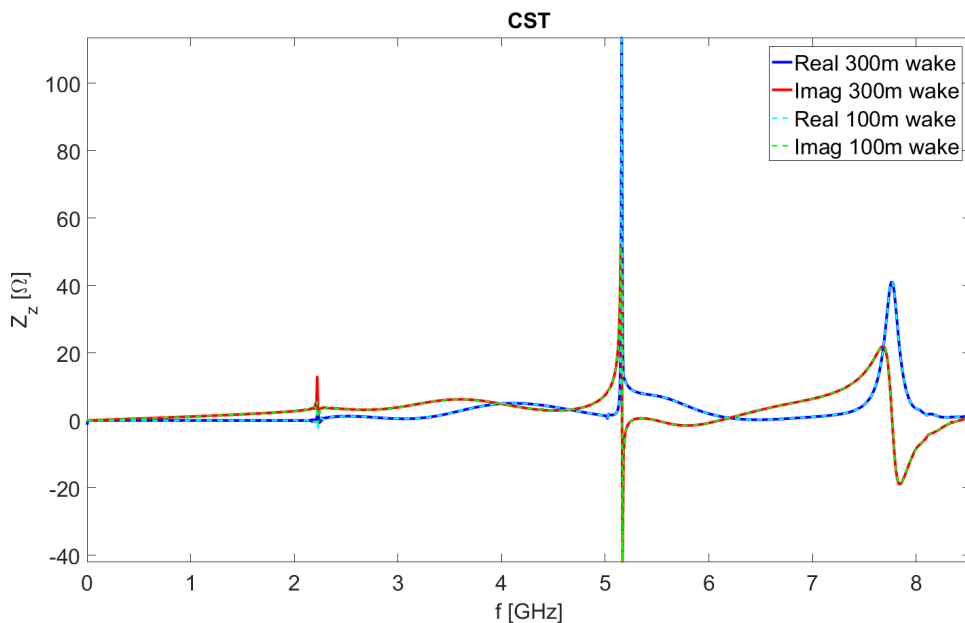


Figure 4: Real and imaginary part for different wake lengths.

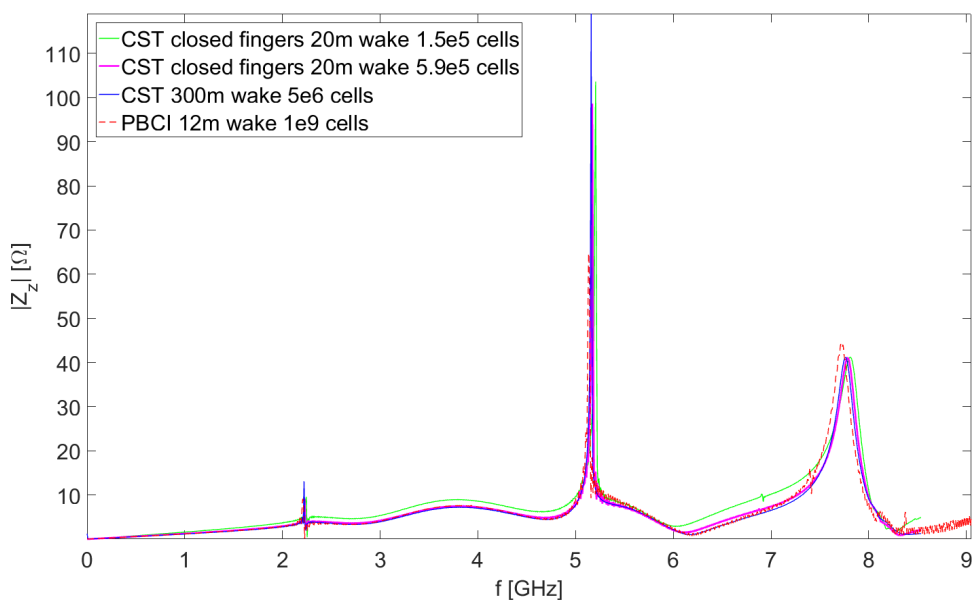


Figure 5: Comparison of PBCI and CST, also for the closed structure.

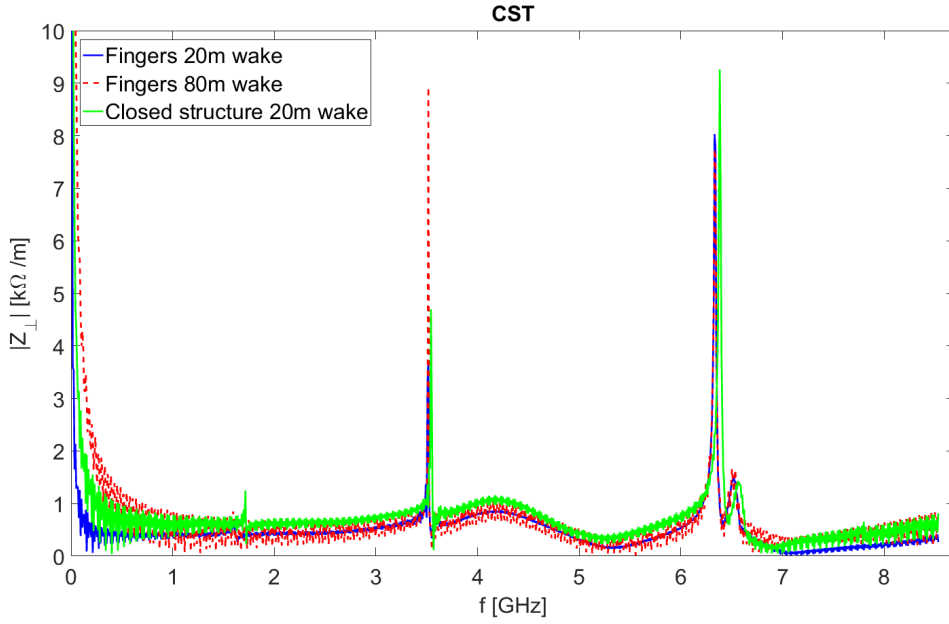


Figure 6: Dipolar transverse impedance magnitude.

2.7.5 Frequency Domain Solver Example

In FD, there is no direct advantage from the FIT diagonal material matrices, which favors the FEM on an unstructured mesh. However, in practice FIT is also used, since the structured mesh makes the implementation of Floquet boundary conditions simple [25]. Particularly in the absence of bulk materials, the Boundary Element Method (BEM) is also an attractive option in FD [26, 27]. The beam velocity and dispersive material data are just parameters in FD that can in principle be chosen arbitrarily. However, such parameters influence the condition number of the system matrix, which becomes an issue when a large System of Linear Equations (SLE) has to be solved for each frequency point.

We address an example for the FCC-hh [28] design study, i.e. a beam pipe design proposal (see Fig. 7), with the FEM code BeamImpedance2D [17]. The code solves the curl-curl equation

$$\nabla \times \underline{\mu}^{-1} \nabla \times \underline{\vec{E}} - \omega^2 \underline{\epsilon} \underline{\vec{E}} = -i\omega \underline{\vec{J}}$$

for the electric field $\underline{\vec{E}}: R^2 \rightarrow C^3$, subject to the beam current density $\underline{\vec{J}}$ as the excitation.

Note that $\underline{\vec{E}}$ and $\underline{\vec{J}}$ are not free of divergence due to the beam's charge. The permeability and permittivity are allowed to be complex, i.e. conductive, polarization and magnetization losses are taken care of. For the solution of the system Nedelec finite elements are used.

Since those are (at lowest order) not capable of modelling the divergence of $\underline{\vec{E}}$, a Helmholtz split needs to be performed to calculate the (quasi) static fields from a complex potential separately (see [17]). Furthermore, the code allows using a Surface Impedance Boundary Condition (SIBC) to avoid meshing the extremely small skin depth at high frequency.

Figure 7: Proposed FCC beam pipe design (R. Kersevan) and GMSH mesh (T. Egenolf).

Figure 7 shows the proposed FCC-hh beam pipe design, where the green color indicates vacuum domains. The inner surface of the beam screen is covered by a copper layer of thickness $80 \mu\text{m}$. In order to avoid meshing the material behind the copper, a two-layer surface impedance is used [29]. Figure 8 shows the transverse impedance of the structure, together with analytical results by ReWall [30] for circular pipes with the

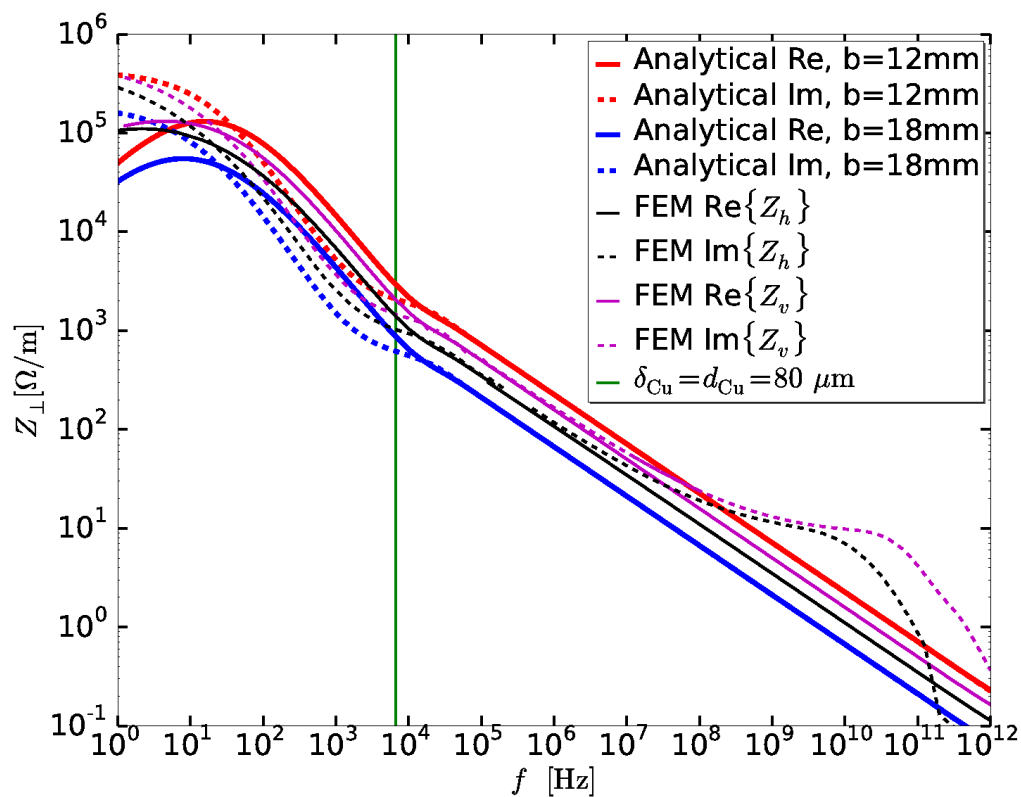


Figure 8: Transverse impedance of the FCC pipe.

the smaller and larger semi-axis radii 12mm and 18mm. As expected, the impedance curves for the real structure are between the two analytical curves and the horizontal is smaller than the vertical impedance due to the larger distance to the wall. The bump of the imaginary part at high frequency is a numerical artifact, due to improper cancelation of the electric and magnetic parts of the space charge impedance at the extremely high $\gamma=50000$. At low frequency the discrepancies between the analytical and numerical results are due to different modelling of the structure. In ReWall the titanium behind the copper is considered with its thickness of 2mm and vacuum behind. The SIBC for BeamImpedance2D assumes infinite thickness of the titanium. However, this modeling discrepancy matters only for extremely low frequencies below 100Hz.

2.7.6 Acknowledgements

The authors wish to thank Benoit Salvant (CERN) for providing the CST model of the finger structure and Thilo Egenolf (TEMF) for modelling the FCC pipe.

2.7.7 References

1. V. G. Vaccaro, "Longitudinal Instability of a Coasting Beam above Transition, due to the action of Lumped Discontinuities," CERN report ISR-RF/66-35, Tech. Rep., 1966.
2. V. Balakin, I. Koop, A. Novokhatsky, A. Skrinsky, and V. Smirnov, "Beam Dynamics of a Colliding Linear Electron-Positron Beam (VLEPP)," Tech. Rep. SLAC Trans 188, 1978.
3. T. Weiland, "Transient Electromagnetic Fields Excited by Bunches of Charged Particles in Cavities of Arbitrary Shape," CERN ISR-TH/80-24, Tech. Rep., 1980.
4. K. Yee, IEEE Trans. Antennas Propag. 14 (1966) 302.
5. T. Weiland, Electronics and Communication 31 (1977) 116.
6. R. Courant, K. Friedrichs and H. Lewy, Über die partiellen Differenzgleichungen der mathematischen Physik, Math. Ann. 100 (1928) 32.
7. R. Gluckstern, Analytic methods for calculating coupling impedances, Cern Accelerator School, 2000.
8. A. Chao, Lecture Notes on Topics in Accelerator Physics, 2002
9. W.K.H. Panofsky and W.A. Wenzel, Rev. Sci. Instrum. 27 967, 1956.
10. O. Napoly, "The Wake Potentials from the Fields on the Cavity Boundary," Particle Accelerators, vol. 36, pp. 15–23, 1991.
11. O. Napoly, Y. H. Chin, and B. Zotter, "A generalized method for calculating wake potentials," Nucl. Instrum. Meth. Section A, vol. 334, no. 2-3, pp. 255–265, Oct. 1993.
12. T. Weiland, "Comment on Wake Field Computation in the Time Domain," NIM, vol. 216, pp. 31–34, 1983
13. H. Henke and W. Bruns, "Calculation of Wake Potentials in general 3D structures," in Proc. of EPAC, no. 8, 2006, pp. 2170–2172
14. X. Dong, E. Gjonaj, W. F. O. Mueller and T. Weiland, "Eignemode Expansion Method in the indirect calculation of wake potential in 3D structures" proc. of ICAP 2006 Chamonix, TUPPP31, 2006
15. I. Zagorodnov, "Indirect methods for wake potential integration," Phys. Rev. ST Accel. Beams, 9, 102002 (2006).

16. M. Balk, R. Schuhmann and T. Weiland, Nucl. Instrum. Methods Phys. Res. A 558, 54, 2006.
17. U. Niedermayer, O. Boine-Frankenheim and H. De Gersem, “Space charge and resistive wall impedance computation in the frequency domain using the finite element method“ Phys. Rev. ST Accel. Beams 18, 032001 (2015)
18. K. Bane and T. Weiland, “Wake force computation in the Time Domain for Long Structures”, SLAC-PUB-3173, 1983
19. E. Gjonaj et al., ICFA Beam Dynamics Newsletter 45 (2008)
20. www.gdfidl.de
21. I. Zagorodnov and T. Weiland, Phys. Rev. ST Accel. Beams 8 (2005) 042001.
22. E.Gjonaj and T. Weiland, “Impedance Calculation. Time Domain”, Handbook of Accelerator physics and Technology, 2nd edition edited by A.W. Chao, K.H. Mess, M. Tigner, F. Zimmermann, World Scientific (2013)
23. B. Salvant, private communication
24. www.cst.com
25. U. Niedermayer and O. Boine-Frankenheim, “Numerical Calculation of Beam Coupling Impedances in the Frequency Domain using FIT,” in Proc. of ICAP 2012, Rostock, 2012.
26. K. Yokoya, Resistive Wall Impedance of Beam Pipes of General Cross Section, KEK Preprint 92-196 (1993).
27. A. Macridin, P. Spentzouris and J. Amundson, Phys. Rev. ST Accel. Beams 16 121001 (2013).
28. www.fcc.web.cern.ch
29. U. Niedermayer, O. Boine-Frankenheim and H. De Gersem, proc. of ICAP Shanghai, 2015
30. N. Mounet and E. Metral, Electromagnetic field created by a macroparticle in an infinitely long and axisymmetric multilayer beam pipe, CERN-BE-2009-039 (2009).

2.8 Beam-Coupling Impedance and Wake Field – Bench Measurements

A. Mostacci

University of Rome La Sapienza - Italy, INFN-Roma1

F. Caspers

CERN, 1211 Geneva 23, Switzerland

Mail to: Andrea.Mostacci@uniroma1.it

2.8.1 Introduction

Bench measurements nowadays represent an important tool to estimate the coupling impedance [1] of any resonant and not resonant device present in modern particle accelerators. A complete review of the most common methods, including as well practical suggestions, is reported in Ref. [2].

For the non resonant components, the most well-known technique based on the coaxial wire method allows to excite in the device under test a field similar to the one generated by an ultra-relativistic point charge. We discuss the basics of the coaxial wire method and review the formulae widely used to convert measured scattering parameters to longitudinal and transverse impedance data.

For resonant devices (such as accelerating and deflecting cavities) the way to estimate the impedance is the well-known bead-pull technique used, as well, in the design, construction and tuning the structures themselves.

Nowadays, numerical simulations are useful tools also in the measurement stage to compare results and to guide the measurements in order to avoid measurement artifacts. The tools have been described in the previous section; here we will briefly comment on the (typical) reliability of such comparisons against bench measurements.

2.8.2 The Coaxial Wire Method

After the introduction of the beam coupling impedance concept by V. Vaccaro it was realized soon that for highly relativistic beams a very close similarity exists between the Transvers Electric Magnetic (TEM) like field of the charged particles and the field of a wire in a coaxial structure. This is the main basis and motivation of the coaxial wire method.

We review the early concepts of this method in order to show the motivation; we show some issues (and advantages) concerning the practical implementation of those concepts with modern instruments; we show some practical cases to compare the different approaches.

Longitudinal impedance measurements are straightforward, but also transverse impedance measurements using two wires carrying currents with opposite polarity were already done on the late 70s. The concept was extended to the evaluation of dipole and quadrupolar transverse impedances [3] by applying a single displaced wire and pair of wires. We discuss the basis of those methods and present some examples relevant for modern accelerator components.

The coaxial wire set-up can also be used to study the properties of the structure when excited by a beam passing through; trapped modes or beam transfer impedance can, for example, be measured in this way [4].

2.8.2.1 *Motivation and Validation*

The field of a relativistic point charge q in the free space (or in a perfectly conducting beam pipe) is a TEM wave, namely it has only components transverse to the propagation direction (z -axis). The amplitude scales inversely with the distance r from the propagation axis and the propagation constant is ω/c . The fundamental mode of a coaxial wave guide is a TEM wave as well, with the same amplitude dependence on $1/r$ and the same propagation constant.

Therefore the excitation due to a relativistic beam in a given Device Under Test (DUT) can be “simulated” by exciting a TEM field by means of a conductor placed along the axis of the structure. The impedance source on the DUT will scatter some field, i.e. exciting some higher order modes; such modes must not propagate otherwise the propagating field will not be anymore similar to the TEM beam field. In principle, then, simulating the beam field with the TEM mode of a coaxial waveguide is possible only at frequencies below the first higher mode cut-off, namely below the TM_{01} cut-off frequency for circular waveguides. One can also demonstrate that the modes of the coaxial waveguide converges for vanishing wire radius to the analogous mode of the cylindrical waveguide, at least at the beam pipe boundary, where the impedance source is usually located.

To compare the excitation of a given DUT by a coaxial wire and with the beam itself, we review some measurements done in the framework of the investigations of the shielding properties of coated ceramic vacuum chambers [5]. The 500 MeV CERN EPA electron beam was sent through two identical ceramic vacuum chamber sections; the first one was internally coated with a layer of 1.5 μm depth. Magnetic field probes were placed to measure the beam field just outside the two ceramic chambers (the coated and the reference one). In a first experiment, shielding properties of the resistive coating (thinner than the skin depth) were demonstrated, confirming previous indirect measurements and simulations [6]. In a following experiment, among other results, it was proved that the screening properties of the coating can be spoiled by the addition of a second conducting layer placed outside the field probes and electrically connected to the metallic vacuum chamber sections. In this case, in fact, the magnetic field probe was measuring clearly the field of the 1 ns (r.m.s.) bunched beam (see Fig. 1).

The same chamber in the same configuration (i.e. with this additional external conductor) was then measured in the bench set-up: a 0.8 mm diameter wire was stretched on the axis of the structure. One end of the wire was connected to a 50 Ω load while the other end was connected to one port of a Vector Network Analyzer (VNA); matching resistors were used. The other port of the VNA was connected to the field probe. The network analyzer was set to send through the wire a synthetic pulse (using the so called “time domain option”) with 300 MHz bandwidth and measured the transmission between the ports, i.e. the signal through the probe.

This particular kind of set-up is not very often used, but it is very similar to the “time domain” measurement originally proposed by Sands and Rees in the 70s [7]; nowadays time domain measurements are often performed with synthetic pulse techniques in many microwaves applications. The measurement with the beam and with the wire should give virtually the same result, apart from a scaling factor due to the difference of the power carried by the beam and by the VNA signal. The results are shown in Fig. 1 where the beam and the bench data have been normalized and time shifted so that the traces coincides in their minimum point.

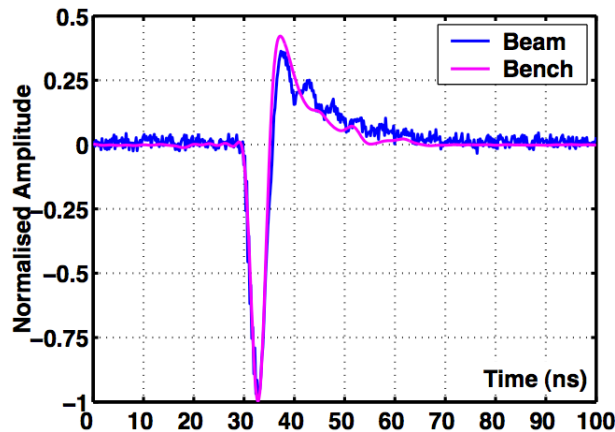


Figure 1: Signal from the field probe after normalization and time shifting in the EPA experiment on coated chamber shielding properties. The field probe is inserted between the coated ceramic and an external conductor connected to the beam pipe.

The external shield, having a DC resistance much smaller than the coating, carries the image currents, the field penetrates the ceramic and the field probe can measure a clear signal. This is only one of the configurations measured both with the beam and in the bench set-up; the agreement with other measurements is similar to the one of Fig. 1.

The results of that comparison confirm the validity of the coaxial wire approach to simulate the beam field effect on a given DUT. Coaxial wire measurements are widely used to estimate impedances of many accelerator devices.

2.8.2.2 *Longitudinal Coupling Impedance*

The wire stretched in the DUT of length L can be modeled, as mentioned before, as a TEM coaxial line of length L . In general, such a line is considered to have distributed parameters but in case of L much smaller than the wavelength λ , the lumped elements approximation is applicable. The DUT beam coupling impedance is then modeled as a series impedance of an ideal reference line (REF). Therefore coupling impedance can be obtained from the REF and DUT characteristic impedances and propagation constants of the lines (see for example Ref. [8]). It is well known that any transmission line can be characterized by measuring its scattering S-parameters, for example with VNA. In principle both reflection (i.e. S_{11}) and transmission measurement (i.e. S_{12}) are possible, but usually transmission measurements are preferred for practical reasons.

In the framework of this transmission line model, the DUT coupling impedance can be exactly computed from measured S-parameters but the procedure is cumbersome and not practically convenient. Therefore a number of approximated formulae are derived in literature and we will report the most used ones, highlighting their approximations.

All the following formulae do not consider the effect of the mismatch at the beginning and at the end of the perturbed transmission line. Therefore matching networks (resistive networks or cones) are normally used in the actual bench set-ups. Cones are mechanically difficult and act as a frequency dependent distributed transformer, which doesn't work at low frequency; on the contrary resistive networks are affected by parasitic inductances and capacitances affecting their performance at high frequency (depending on the components actually used). Approximated formulas and the "exact" transmission line solution are numerically compared in Ref. [9].

Being Z_c the characteristic impedance of the wire inside the DUT, the beam coupling impedance Z_{\parallel} can be estimated with the “improved log-formula” [8]

$$Z_{LOG} = -Z_c \ln \left(\frac{S_{21}^{DUT}}{S_{21}^{REF}} \right) \left[1 + \frac{\ln(S_{21}^{DUT})}{\ln(S_{21}^{REF})} \right] \quad (1)$$

Expressing the S_{21}^{REF} in terms of the DUT electrical length L , one can get another equation analogous to Eq. (1) [10]:

$$Z_{LOG} = -Z_c \ln \left(\frac{S_{21}^{DUT}}{S_{21}^{REF}} \right) \left[1 + \frac{jc}{2\omega L} \ln \left(\frac{S_{21}^{DUT}}{S_{21}^{REF}} \right) \right] \quad (2)$$

which can be useful in practice. The improved impedance expression requires the knowledge of the electrical length of the DUT and its accuracy decreases for shorter devices [11]. Reference [9] suggests the use of improved log-formula for DUT longer than the wavelength λ .

For small ratios Z_{\parallel}/Z_c , the so-called “standard log-formula” has been proposed for the distributed impedances [12]:

$$Z_{log} = -2Z_c \ln \left(\frac{S_{21}^{DUT}}{S_{21}^{REF}} \right) \quad (3)$$

The log-formula Eq. (3) is generally applicable including lumped components, provided that no strong resonance is present and the perturbation treatment is justified.

For lumped elements, i.e. when the DUT electric length is much smaller than the wavelength, the previous expressions converge to the so called “lumped element formula” [13]:

$$Z_{HP} = -2Z_c \frac{S_{21}^{DUT} - S_{21}^{REF}}{S_{21}^{DUT}} \quad (4)$$

The lumped impedance formula is applicable to single resonances and has the advantage that the scattering coefficient ratio is directly converted into an impedance by the network analyzer [14].

The quantities Z_{LOG} , Z_{log} , Z_{HP} are estimations of the beam coupling impedance Z_{\parallel} ; the smaller the ratio Z_{\parallel}/Z_c , the more accurate the approximated formulae. As an example, a wire in a perfectly conducting cylindrical beam pipe with circular cross section has a characteristic impedance equal to

$$Z_c = \frac{Z_0}{2\pi} \ln \left(\frac{b}{a} \right) \quad (5)$$

where a is the wire radius, b is the (inner) pipe radius and Z_0 is the vacuum impedance. Therefore a smaller wire has an higher Z_c , resulting in a more accurate measurement of the

coupling impedance. A detailed discussion of the systematic error done in estimating the beam coupling impedance $Z_{||}$ with Z_{LOG} , Z_{log} or Z_{HP} is reported in Ref. [11].

The difference between the improved log formula of Eqs. (2, 3) and the standard one of Eq. (4) can be shown in measurements performed on the 7 cells module of the MKE kicker [15]. The coupling impedance is much bigger than the characteristic impedance of the wire in the DUT ($\approx 300\Omega$) and therefore the improved log formula must be used:

$$Z_{LOG} = Z_{log} \left[1 + \frac{jc}{2\omega L_f} \ln \left(\frac{S_{21}^{DUT}}{S_{21}^{REF}} \right) \right] \quad (6)$$

Equation (6) differs from Eq. (2) because the length of the ferrite ($L_f = 1.66\text{m}$) is used instead of the length of the whole kicker tank ($L = 2.31\text{m}$), as discussed in Ref. [15]. Figure 2 shows the wire measurement results interpreted with the improved formula Eq. (6) (green line) and the standard one Eq. (3) (blue line). The comparison with theory (black line) shows that, at least for the real part of the impedance, the improved log formula gives a result closer to theoretical expectations for frequencies higher than few hundreds of MHz. At lower frequencies, i.e. where the DUT length is comparable to the wave-length and the impedance is much closer to the characteristic impedance of the wire in the DUT, the standard log formula is a better estimation of the coupling impedance.

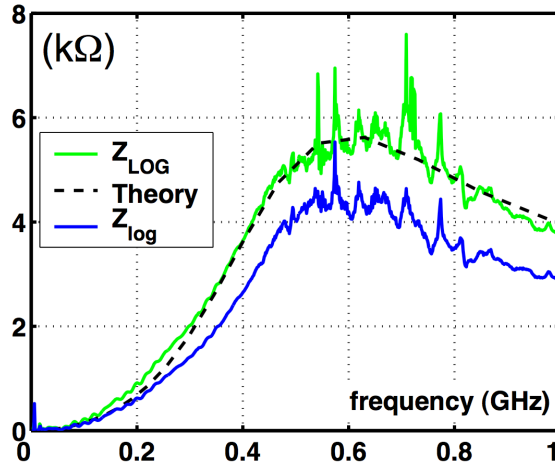


Figure 2: Real part of the longitudinal coupling impedance for the 7 cells MKE kicker module [15]. The measured data are interpreted via the improved log formula (green line) or the standard log formula (blue line) and compared to theoretical expectations (dashed line).

In conclusion, longitudinal coupling impedance bench measurements are reasonably well understood and the technique is well established. Moreover, with modern simulation codes, one can derive directly the coupling impedance or simulate the bench set-up with wire, virtually for any structure. Evaluation of coupling impedance from measured or simulated wire method results require the same cautions; but simulations and RF measurements usually agree well. Moreover comparisons with numerical results are very useful to drive and to interpret the measurements. One should pay attention that simulation may require a simplified DUT model, which will only reproduce the main DUT electromagnetic features.

2.8.2.3 *Transverse Coupling Impedance*

The transverse impedance is proportional at a given frequency to the change in longitudinal impedance due to the lateral displacement of the beam in the plane under consideration (vertical or horizontal). Therefore the transverse impedance is proportional to the transverse gradient of the longitudinal impedance (Panowsky-Wenzel theorem [1]). Based on this theorem, the most common method to bench measure transverse impedance uses two parallel wires stretched along the DUT [2]. Opposite currents are sent through the wires (odd mode excitation); instead of the wires, a loop can be used to increase the signal to noise ratio [16]. The bench transverse impedance $Z_{\perp,bench}$ is given by [17]

$$Z_{\perp,bench} = \frac{Z_{\parallel,bench}c}{\omega\Delta^2} \quad (7)$$

where Δ is the wire spacing (usually about 10% of the DUT radius). $Z_{\parallel,bench}$ is the longitudinal coupling impedance measured from the S-parameters as discussed above, e.g. using the improved log-formula

$$Z_{\perp,LOG} = -\frac{Z_c c}{\omega\Delta^2} \ln\left(\frac{S_{21}^{DUT}}{S_{21}^{REF}}\right) \left[1 + \frac{\ln(S_{21}^{DUT})}{\ln(S_{21}^{REF})}\right] \quad (8)$$

where now Z_c is the characteristic impedance of the odd mode of a two wires transmission line. Concerning LHC (and other modern machines as well), low frequency transverse impedance is interesting and therefore the lumped element Eq. (4) must be used in Eq. (8). A practical example of low frequency transverse impedance is reported in Ref. [16] for a simple case; results are compared to theoretical expectations to define a reliable measurement procedure.

In the two wires bench set-up only dipole field components are excited because of the symmetry of the wires/coil; therefore there is no electric field component on the axis. In numerical simulations, this is analogous to putting a metallic image plane between the wires. Nevertheless some accelerator devices may exhibit a strong asymmetry in the image current distribution due to azimuthal variation of conductivity (e.g. ferrite in kickers) or to cross section shape. Two wire techniques can be used with some cautions in these cases because the field in the structure is not TEM-like; in order to get a more complete view of the transverse kick on the beam, it may be useful to characterize the device with a single wire [18].

The transverse impedance itself can be measured with a single wire displaced in various positions, which is measuring the longitudinal coupling impedance as a function of the displacement x_0 of a single wire. From the Panowsky- Wenzel theorem we get

$$Z_{\perp,bench} \simeq \frac{c}{\omega} \frac{Z_{\parallel,bench}(x_0) - Z_{\parallel,bench}(x_0 = 0)}{x_0^2} \quad (9)$$

provided that x_0 is small with respect to the typical variation length of the bench measured coupling impedance $Z_{\parallel,bench}$.

From the practical point of view, transverse impedance measurement techniques are more delicate and require particular attention for asymmetric devices (e.g. traveling wave

kickers like). Novel techniques optimized for particular DUTs, are also being proposed, e.g. SNS kicker measurements reported in Ref. [19]. Numerical simulations are necessary to control and validate the measurement procedure. One should pay attention that DUT models feasible for simulations do not introduce non-physical symmetries or approximations; in principle, dealing with transverse problem may require more complex simulations than the longitudinal case.

2.8.3 Resonant Structures

An important class of accelerator devices includes cavities, which are now used both for accelerating and deflecting the particle beam. Each cavity is characterized by its resonant frequency f_0 , the quality factor of the resonance Q and its shunt impedance R . One can think of measuring all these quantities with the coaxial wire set-up, i.e. measuring strong notches in the transmission scattering coefficient between the ends of the wire. But the wire perturbs longitudinal cavity modes, e.g. lowers the Q and detunes the frequency. Therefore the coaxial wire set-up is not usually recommended for cavity measurements and it is advisable only for special cases, mainly transverse modes [2].

The most used technique to characterize cavities is the “bead pull” measurement [20]. The field in the cavity can be sampled by introducing a perturbing object and measuring the change in resonant frequency: where the field is maximum (minimum) the resonance frequency will be more (less) perturbed. Since it is a perturbation method, the perturbing object must be so small that the field does not vary significantly over its largest linear dimension. Shaped beads are used to enhance perturbation and give directional selectivity among different field components.

Quantitatively, the change of the resonant frequency is related to the perturbed cavity field by the Slater theorem. For the typical case of longitudinal electric field on the axis of accelerating cavities, the variation of the resonance frequency Δf from the unperturbed one is [21]

$$\frac{\Delta f}{f_0} = -\Delta V \varepsilon_0 k_E \frac{E_z^2}{4U} \quad (10)$$

for a conducting bead of volume ΔV ; E_z is the field at the perturbing object position and U is the electromagnetic energy stored in the cavity. The form factor k_E of the perturbing object can be exactly calculated for ellipsoids or can be calibrated in a known field (e.g. TM_{0n0} of a pillbox cavity).

The frequency variation can be measured by the variation of the phase ϕ at the unperturbed resonant frequency, according to [22]

$$\frac{\Delta f}{f_0} = \frac{\tan \phi(f_0)}{2Q_L} \simeq \frac{\phi(f_0)}{2Q_L} \quad (11)$$

where Q_L is the (loaded) quality factor of the resonance. Even if a very precise initial tuning is needed, this method allows easily measuring the field of many points (as many as the points of the instrument trace). The field shape can also be directly visualized on the

instrument screen, greatly facilitating the structure tuning procedure, which is typically a very cumbersome procedure in multicell cavities.

An important cavity design parameter is the R/Q, which can be obtained from electric field data using

$$\frac{R/Q}{L_c} = \frac{1}{U\omega L_c} \left| \int_0^{L_c} E_z(z) \exp\left(j\frac{\omega}{c}z\right) dz \right|^2 \quad (12)$$

where L_c is the length of the structure.

In general measurement on resonant structures are accurate and in very good agreement with simulations. Bead pull measurements are often used to check if the DUT fits the design specifications and they are still required for tuning the multiple cell cavities. R/Q measurements agree always with simulations within the few %.

2.8.4 Conclusions

Bench measurements are used for estimating the coupling impedance of accelerator devices, exploiting the very accurate instrumentation used in microwave measurement in the frequency domain (namely vector network analyzer). We have reviewed the standard methods used for non resonant and resonant devices; coaxial wire set-up are used for the first class of devices while the second class of devices are bench measured with bead-pull techniques. The main idea of the coaxial wire technique is the analogy between the field of an ultra-relativistic charged beam and the one of a coaxial waveguide; thus the beam is simulated by an electric pulse travelling on the inner wire. Bead pull techniques allow measuring the resonant field in cavities through perturbation of the cavity space, according to Slater theorem; from the measured field on the beam path, one can compute the resonance parameters (e.g. R/Q). In this paper we have reviewed the most common concepts used in bench measurement, focusing on the motivation, their limit of validity and trying to compare their different results.

2.8.5 References

1. L. Palumbo, V.G. Vaccaro and M. Zobov, in Fifth Advanced Accelerator Physics Course, CAS Cern Accelerator School, CERN 95-06 (1995), p.331. See also INFN LNF-94/041 (1994).
2. F. Caspers in Handbook of Accelerator Physics and Engineering, A. Chao and M. Tinger (editors), World Scientific, Singapore (1998), p.570.
3. S. Heifets, A. Wagner, B. Zotter, SLAC AP110 (1998).
4. A. Mostacci et al, NIM A517 (2004), p. 19.
5. L. Vos, F. Caspers, A. Mostacci et al., CERN AB-Note- 2003-02 MD EPA (2003).
6. F. Caspers, E. Jensen, F. Ruggiero et al., "RF Screening by Thin Resistive Layers", PAC'99, New York (1999).
7. M. Sands, J. Rees, SLAC report PEP-95 (1974).
8. V.G. Vaccaro, INFN/TC-94/023 (1994).
9. E. Jensen, CERN PS/RF/Note2000-001 (2000).
10. F. Caspers, C. Gonzalez, M. Dyachkov, E. Shaposhnikova, H. Tsutsui, CERN PS/RF/Note 2000-004 (2000).

11. H. Hahn, Phys. Rev. ST Accel. Beams **3**, 122001 (2000).
12. L. Walling et al, NIM A281 (1989), p.433.
13. H. Hahn, F. Pedersen, BNL 50870 (1978).
14. H. Hahn, Phys. Rev. ST Accel. Beams **7**, 012001 (2004).
15. F. Caspers, A. Mostacci, H. Tsutsui, CERN SL-2000-071 AP (2000).
16. F. Caspers, A. Mostacci, U. Iriso, CERNAB-2003-051 (RF) and PAC'03, Portland (2003).
17. G. Nassibian, F. Sacherer, CERN ISR-TH/77-61 (1977).
18. H. Tsutsui, CERN SL-Note-2002-034 (2002).
19. H. Hahn, Phys. Rev. ST Accel. Beams **7**, 103501 (2004).
20. R. Rimmer, M. Tinger in *Handbook of Accelerator Physics and Engineering*, A. Chao and M. Tinger (editors), World Scientific, Singapore (1998), p.403.
21. T.P. Wangler, *Principles of RF Linear Accelerator*, JohnWiley and Sons Inc., Canada (1998).
22. F. Caspers, G. Dome, CERNSPS/85-46ARF (1984).

2.9 Building the Impedance Model of a Real Machine

Nicolò Biancacci, Benoît Salvant, Carlo Zannini
CERN, 1211 Geneva 23, Switzerland
Mail to: Benoit.salvant@cern.ch

2.9.1 Introduction

While equipment heating due to beam coupling impedance is usually localized to that piece of accelerator equipment, the impedance contributions to beam instabilities add up for the whole machine. Therefore impedance models have been built for many existing machines, upgrades and projects in order to assess their stability limit.

Impedance models in various levels of complexity were developed over the years depending on the needs and knowledge at the time of implementation: for example for the CERN ISR [1], PS [2,3,4], PSB [5], SPS [6,7,8,9], LEP [10], LEP2 [11] LHC [11,12], RHIC [13] at Brookhaven National Lab, TeVatron [14] at Fermi National Lab, HERA [15] at DESY, KEKB [16], as well as many light sources: NSLS-II [17], PETRA [18] SOLEIL [19], ALBA [20], to name only a few.

Since impedance related instabilities can be a significant limitation and can drive fundamental parameters of the accelerator, impedance models are nowadays developed at the very early stage of machine design: for instance transverse instabilities required increasing the aperture of the beam screen for the Future Circular Collider project [21].

The complexity of an impedance model can range from a single number to an elaborated tool, which is able to recompute wake functions and complex impedance contributions as a function of frequency and their related thresholds with slight changes of machine configuration (e.g. energy, number of devices, beta function at the location of the devices, gaps of moving devices).

A complete impedance model should in fact compute the longitudinal, transverse driving and transverse detuning contributions (also referred to as dipolar and quadrupolar) [22] for obtaining all resistive wall, broadband and narrow band contributions over a frequency range that would span from the first potentially unstable frequency to the maximum frequency that can be excited by the various single bunch and multibunch modes. It is in particular crucial to disentangle the driving and detuning contributions as their respective impact on beam dynamics is very different: the driving impedance contributes to the growth of Headtail modes (see for instance [8]), while the detuning impedance is not expected to.

In practice, it is important to assess how the impedance model will be used in order to tailor the parameters of the computations/simulations or measurements: instability thresholds can be computed using macroparticle tracking codes or Vlasov solvers, that take impedance or wake functions as input, for single bunch or multi-bunch estimates. Several tools require fitting the impedance by one single resonator or several resonators, while other beam dynamics tools can use any type of impedance or wake as input.

Since impedance computations can be heavily time and resource consuming, it is important to identify what drives the accuracy of the impedance in the range of interest. For 3D simulations, the antagonistic requirements for (1) very short excitation source size to assess the high frequency components correctly and (2) very long wakes to take into account low frequency components and multi bunch effects accurately tend to always increase CPU needs and simulation times. For instance, single-bunch single-turn simulations with the macroparticle code HEADTAIL [23] require a wake function, which

can be computed with a very short source excitation over the length of the tracked bunch. Taking into account the multibunch/multi-turn effect requires much longer wakes, which makes it usually very difficult to keep a very short exciting source due to the very large number of mesh cells it needs. The long-range wake can therefore be assessed in a second simulation with a longer exciting source bunch, or by using a simpler model such as external circuits [24]. These two short-range and long-range wakes from these two computations can later be combined, with great care for the overlapping region and with convergence studies.

2.9.2 Assess Impedance of Individual Elements

Electromagnetic simulations are necessary to calculate the contribution to the total impedance of single accelerator components. Time domain simulations are of special interest, because the wake fields they provide can be fed directly into macroparticle simulation codes in order to predict their effects on the beam in realistic conditions.

2.9.2.1 *Calculation of the Beam Couplings Impedance*

The impedance can be calculated analytically or numerically. Analytical models could be used for simple geometries (resistive wall, simplified structures, pillbox). Numerical simulations are fundamental to account for all features of complex structures (e.g. kickers, collimators, cavities, beam diagnostic devices, etc.). CST Particle Studio 3D electromagnetic simulations [25] can be used to calculate wakes and/or impedances of simple accelerator structures. The software has been benchmarked with the known analytical solutions for several structures [24] (resistive wall, pillbox cavities, simplified models of kicker magnets, asymmetric chambers). Moreover the results of CST beam coupling impedance simulations were used to build the PSB, PS and SPS impedance models, which were found in very good agreement with experimental observations (beam induced heating, coherent tune shift and instability growth rate [4, 5, 8, 24]).

CST Studio Suite is a commercial 3-D electromagnetic Computer Aided Design (CAD) software. In particular, the Wakefield solver of Particle Studio solves Maxwell's equations in Time Domain (TD), using a particle bunch as excitation of the structure under study. Standard outputs of the code are the wake potentials produced by the exciting Gaussian bunch (called "source") as a function of the time delay τ with respect to the passage of the source (i.e. the integrated electromagnetic force felt by a witness charge that goes through the structure a time τ behind the source) and its equivalent in Frequency Domain (FD), the Fourier transform normalized to the bunch spectrum, i.e. the beam coupling impedance. Besides, since the code allows defining separately the transverse position of the exciting bunch and that of the computation point, we can also separately simulate the driving and the detuning terms of the transverse wake potentials.

The main interest of simulating accelerator structures in time domain lies in the fact that the output of the simulation in terms of wake function may be directly used in particle tracking simulations to study the impact of these elements on the beam stability. In particular, wake functions in form of tables can be fed as an input into the HEADTAIL code, which is typically used for studying collective effects in beam dynamics. Since the wake functions are needed, the source bunch used in CST simulations should be short enough to be consistent with the length of the bunch slices simulated in HEADTAIL. This obviously limits the analysis to a maximum frequency defined by the bunch slicing, but it can be

applied when no higher frequency mechanisms are expected in the given beam dynamics problem.

Resistive wall, Indirect Space Charge (ISC), magnetic kickers, collimators, stripline kickers, RF cavities, beam pipe transitions and beam diagnostics elements like wire scanner and Beam Position Monitors (BPMs), constitute a non-exhaustive list of classical impedance sources. Some of these elements could be not relevant for the overall impedance budget but could suffer of beam induced heating and then limit the beam intensity at which these elements can be used (e.g. wire scanners).

Resistive wall: in general, the resistive wall impedance describes the coupling between the beam and an external chamber with finite conductivity. Analytical derivations are possible when dealing with chambers with simple geometries. Many of the existing theories are based on the field matching technique [12, 26, 27, 28, 29]. Alternative models for resistive wall calculations are based on the Transmission Line (TL) theory [24, 30, 31, 32]. For more complicated geometries (asymmetries, small beam pipe ceramic breaks or thin inserts [33, 34], holes [35], etc.), a theoretical estimation without involving numerical electromagnetic simulations becomes more involved. An example of interest in this sense is the LHC beam-screen where CST 3D simulations were used for the impedance estimation [24].

Indirect space charge: usually it is computed analytically. For complex vacuum chambers it can be computed numerically using form factors which could be obtained performing non-relativistic CST simulations [25] or using the BeamImpedance2D code [36].

Kicker magnets: they are the most important impedance source in the CERN SPS. In a very simple approximation a SPS ferrite loaded kicker can be modelled as two parallel plates of ferrite. For this simple geometrical model all the impedance terms (longitudinal, driving and detuning horizontal and vertical impedances) can be calculated analytically [37, 38, 39]. CST 3D simulations were found to be in very good agreement with the analytical results [24]. The excellent agreement between analytical model and numerical simulations can be read as an important benchmark for the simulation code in the correct solution of electromagnetic problems involving dispersive materials such a ferrite. In the framework of an improvement of the SPS kicker impedance model a step by step simulation study has been performed starting from the simplest model and introducing one by one the new features that make the model gradually closer to reality. This approach allows for a good understanding of the different contributions brought to the kicker impedance by the different aspects. First, the ferrite is assumed to be C-shaped and the whole finite length device is inserted in the vacuum tank and equipped with an inner conductor [40]. In order to further approach a more realistic model other aspects have to be included: the cell longitudinal structure, also called segmentation, which determines a significant increase of the beam coupling impedance for the SPS injection kickers (due to the short cell length) and the serigraphy for the SPS extraction kickers. More details about the SPS kicker impedance model can be found in Ref. [24].

Collimators: in the case of the LHC [12], the collimation system represents the largest source of impedance in the machine due to the collimator jaws proximity to the beam. Detailed calculations could proceed with CAD models and codes like CST [25], HFSS [41], GdfidL [42] or ACE3P [43]. A first approximation is considering the jaws of the collimator as two parallel plates for which codes like [12] can provide accurate impedance calculation. One should note that, for very small collimator gaps, the nonlinear wakefield introduced by the beam distribution may play an

important role [44].

Stripline kickers: analytical models could be used for a first estimation [45, 46, 47]. For the final calculation a 3D EM simulation should be performed in order to include all the relevant features of the kicker.

RF cavities: a model could be developed based on the RF parameters of the cavity. However, a good estimation of the beam coupling impedance of the RF cavities would require measuring the actual cavities or simulate the 3D geometry of the tuned cavity.

Transitions between different vacuum chambers: the beam coupling impedance of these elements can be accurately calculated by using CST Particle Studio. Analytical models are available for simple geometries of the vacuum chambers [24, 48, 49].

Beam diagnostic elements: for complex devices a simplified calculation is strongly advised in order to have a good understanding of the beam coupling impedance contribution.

2.9.2.2 *Bench Measurements of the Beam Coupling Impedance: the Wire Method*

Ideally measurements of beam coupling impedances of a device should be done by exciting the device with the beam itself [50]. However, in most cases this solution is not possible and one must resort to bench measurement techniques in which the beam is simulated by a current pulse flowing through a wire stretched along the beam axis. For beam coupling impedance evaluations, the Wire Method (WM) is a common and appreciated choice.

This technique was proposed in the first half of the 70's, based on intuitive considerations. By means of WM, Faltens et al. [51] measured the wall contributions to the beam coupling impedance. M. Sands and J. Rees (1974) [52] measured the energy loss of a stored beam to a cavity due to the higher mode excitation. Moreover, at BNL and at CERN, the method was employed to measure the longitudinal and transverse beam coupling impedance [53, 54] of a kicker in the frequency domain. The method of Sands and Rees requires a complex numerical manipulation to obtain the beam coupling impedance from the measured quantities, because of the presence of multiple reflections in the measuring devices [52]. An improved method of measurement that does not need this manipulation was proposed by V.G. Vaccaro [55].

Since many years it has become customary to use the coaxial wire method [52, 55] to measure the beam coupling impedance of accelerator devices (e.g. [56, 57, 58, 59, 60, 61, 62, 63]). Nevertheless, the results obtained from wire measurements might not entirely represent the solution of our initial problem, because the presence of the stretched wire perturbs the electromagnetic boundary conditions. The most evident consequence of the presence of another conductive medium in the center of the device under study is the fact that it artificially allows TEM propagation through the device, with zero cut-off frequency. The presence of a TEM mode among the solutions of the electromagnetic problem will have the undesired effect to cause additional losses during the measurement. Theoretical studies about the validity limits of the Sands and Rees method in relation to the presence of the central wire that simulates the beam can be found in Ref. [64], where, by means of a general theoretical approach, the effect of the central conductor with small but finite radius has been studied. As results for an example of application (pill-box cavity with a radius of 15 cm using a wire with a diameter of 1.12 mm) the longitudinal beam coupling impedance of the DUT, calculated with this approach, is very similar to the impedance obtained with the Sands and Rees formula (Fig. 2 of Ref. [64]). Details about the measurement setup used in [64] can be found in [65]. However, the mode analyzed in this study is above the cut off

frequency of the beam chamber. For modes below this frequency, due to the TEM propagation introduced by the wire, the WM is found to provide inaccurate results, as investigated in Ref. [66] comparing the impedance with and without a wire for a Copper pillbox, by means of the Mode Matching Technique.

2.9.2.3 *Summing the Different Impedance Sources to Build the Impedance Model of a Real Machine*

The impedance model of the machine can be obtained summing the contributions of all the impedance sources analysed. In the transverse plane the sum has to be weighted by the respective beta functions as expressed in the following formula (see e.g. [12]):

$$Z_{\perp}(f) = \sum_{i=1}^N \frac{\beta_{\perp}^i}{\langle \beta_{\perp} \rangle} Z_{\perp}^i(f) \quad (1)$$

where β_{\perp}^i is the beta function of the i^{th} element (since the element extends over a certain length the beta function should be averaged over the element length), $\langle \beta_{\perp} \rangle$ is the average beta function of the ring and $Z_{\perp}^i(f)$ is the transverse impedance of the i^{th} element.

As an example, Fig. 1 shows the full SPS impedance model, which includes kicker magnets, wall, BPMs, RF cavities and broadband impedance from step transitions for the horizontal and vertical driving and detuning impedances [8].

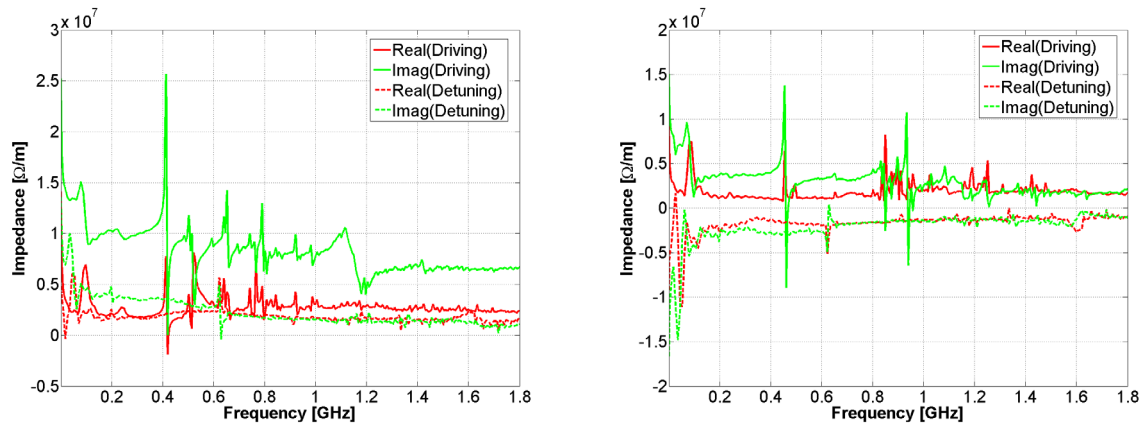


Figure 9: Horizontal (left) and vertical (right) SPS impedance model.

2.9.3 Compute Beam Observables and Compare with Measurements

When an impedance model is produced for an accelerator machine, it allows to perform beam stability predictions and to calculate the impact of upgraded (or removed) equipment in the machine. A series of benchmark can be performed in order to ensure the good agreement between impedance model and beam observables. In the following we will introduce some of the most common procedures used to validate an impedance model.

2.9.3.1 *Single Bunch Tune Shift / Growth Rate versus Intensity*

Measuring the complex betatron coherent frequency shift with intensity gives information on the total transverse impedance according to Sacherer's theory [67]. Given a

beam with Gaussian longitudinal distribution we can calculate the total machine tune shift with intensity as

$$\Delta Q_{\perp} = -\frac{qZ\bar{I}T_0}{8\pi^{\frac{3}{2}}A\beta E_0\sigma_t} \sum_k \beta_{\perp k} Z_{\perp k}^{eff}, \quad (2)$$

where ΔQ_{\perp} is the complex machine transverse betatron tune, q the elementary charge, $\bar{I} = qZN_b f_0$ the beam current (with N_b number of particles, Z the charge number, and $f_0 = 1/T_0$ the revolution frequency), β relativistic beta factor, $E_0 = \gamma A m_u c^2$ is the energy of a traveling ion with m_u nucleon rest mass, A number of mass, γ the relativistic gamma and c speed of light, σ_t is the rms bunch length, $Z_{\perp k}^{eff}$ the effective transverse impedance of the k^{th} element weighted by the corresponding betatron function $\beta_{\perp k}$. The effective impedance is defined as

$$Z^{eff} = \frac{\int_{-\infty}^{\infty} Z(\omega) \|S(\omega)\|^2 d\omega}{\int_{-\infty}^{\infty} \|S(\omega)\|^2 d\omega}, \quad (3)$$

where ω is the angular frequency, $\|S(\omega)\|^2$ the beam power spectrum. For a Gaussian beam distribution we have

$$\|S(\omega)\|^2 = e^{-\omega^2 \sigma_t^2}. \quad (4)$$

From Eq. (2), we infer that a measurement of the tune frequency shift versus intensity can give information on the imaginary part of the total transverse effective impedance of the machine, while the measurement of the corresponding growth rate would give information on the real part. In practice, this is usually done injecting in the machine few bunches of different intensity and measuring their tune frequency shift versus intensity. If the machine duty cycle is high, the measurement could be done injecting one bunch per cycle with different intensity. The growth rate can be measured moving the machine to negative (positive) chromaticity if operating above (below) the transition energy. The agreement or disagreement with the impedance model predicted tune shift can point to a lack of knowledge of the machine impedance in which case one would have to refine it including those elements not yet included in the model or performing impedance localization measurements. In Fig. 2 we show the progressive refinement of the SPS impedance model accounting for kickers and, progressively, wall, BPMs, RF cavities and flanges impedance [24].

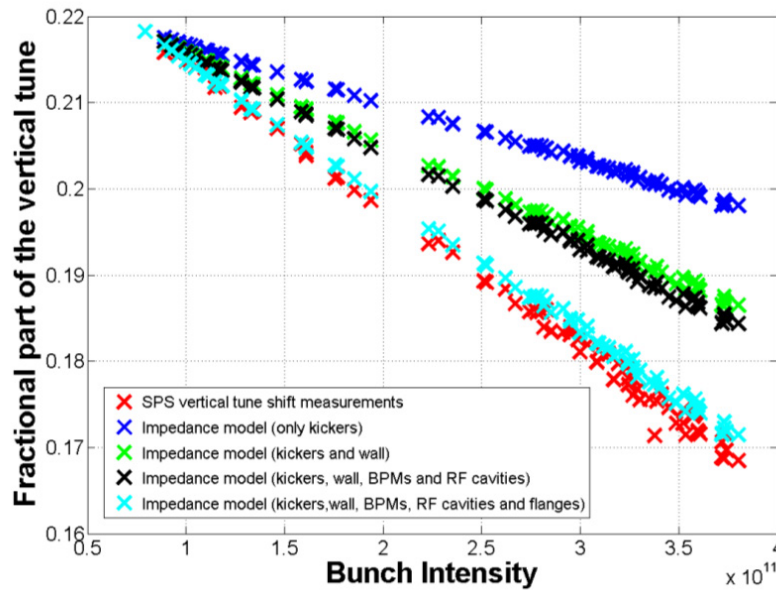


Figure 2: Measured tune shift in the CERN SPS compared with impedance model simulations accounting for kickers and, progressively, wall, BPMs, RF cavities and flanges impedance.

For particular equipment, where the impedance presents Higher Order Modes (HOMs) with considerably high shunt impedance, the tune shift estimation may not be enough to get the full picture of the equipment impact on the machine performance. In this case the full Sacherer's theory should be applied, especially studying the effect of the HOMs on the most unstable couple bunch growth rate. As an example, the HL-LHC crab cavities are planned to be installed close to the LHC interaction points IP1 and IP5 [68] where large β functions are expected. The HOMs introduced by the cavities are therefore magnified by the β function according to Eq. (1) and the impact on the corresponding coupled bunch most unstable mode has been addressed [69].

2.9.3.2 *Impedance Localization Techniques*

An extension of the tune shift method for measuring the reactive part of transverse localized impedances was proposed the first time in 1995 at CERN [70]: measuring the impedance-induced betatron phase advance shift with intensity, the LEP RF sections were found to be important impedance contributors. A similar method, based on the impedance-induced orbit shift with intensity, was proposed in 1999 in the Novosibirsk VEPP-4M electron-positron storage ring [71] and in 2001 in the Argonne APS synchrotron accelerator [72]. Later in 2002, the same method was tried in the Grenoble ESRF [73]. The CERN research on the impedance localization method using phase advance shift with intensity was continued in 2004 in the SPS [74, 75] and in BNL RHIC [76]. The method has been recently successfully employed in the CERN PS [77] as shown in Fig. 3 and in Alba [78] and extended to the use of AC dipoles in order to achieve a higher signal to noise ratio and sufficient measurement resolution to detect impedance sources [79].

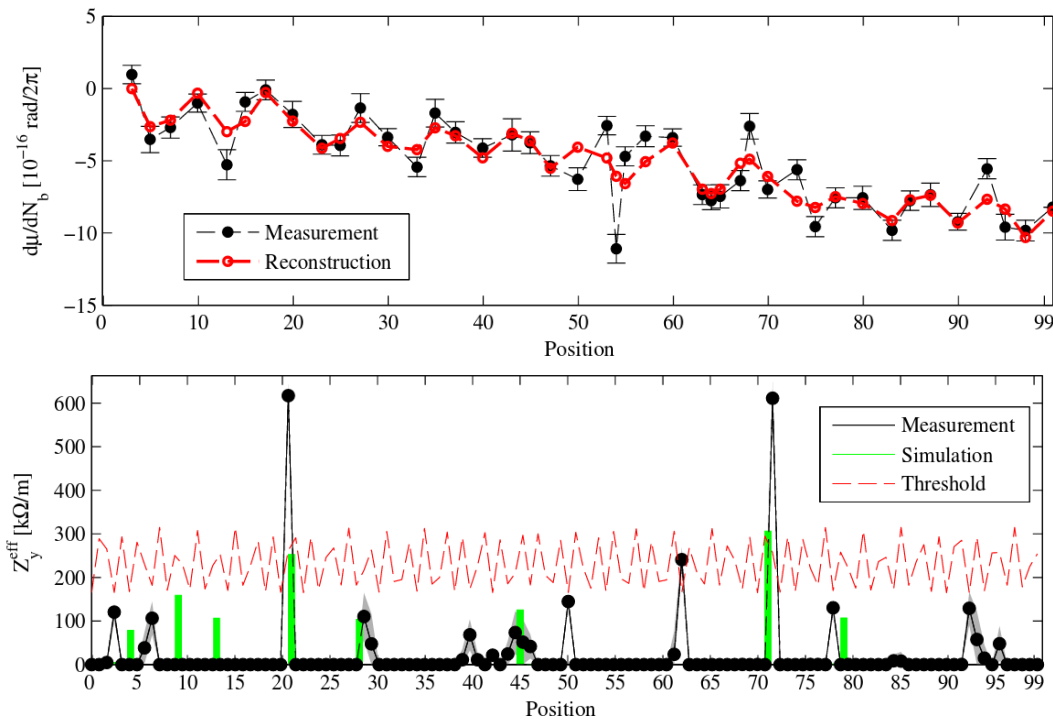


Figure 3: Impedance-induced phase advance beating (top) and corresponding reconstruction with detected impedance sources along the PS ring (bottom).

2.9.3.3 *Single Bunch Octupole Threshold*

In machines like the LHC, the beam stability at high energy is ensured by the combined stabilizing effect of transverse damper and Landau octupoles [80]. The threshold for stability as a function of the damper gain and/or octupole current can give information of the accuracy of the impedance model. This approach assumes the impedance to be the only source of instability, which is not always the case, especially when operating with train of bunches where electron cloud effects are not negligible, or two beams, where beam-beam effects play a role. As long as single bunches are accelerated, the octupole threshold can be measured and correlated with the machine impedance. Figure 4 shows the overall picture of the LHC octupole threshold as a function of chromaticity [81] measured and simulated with DELPHI [82]: a good agreement is obtained for positive chromaticities while discrepancies are present for negative and close to zero chromaticities where, probably, a refined damper model is required and currently being investigated.

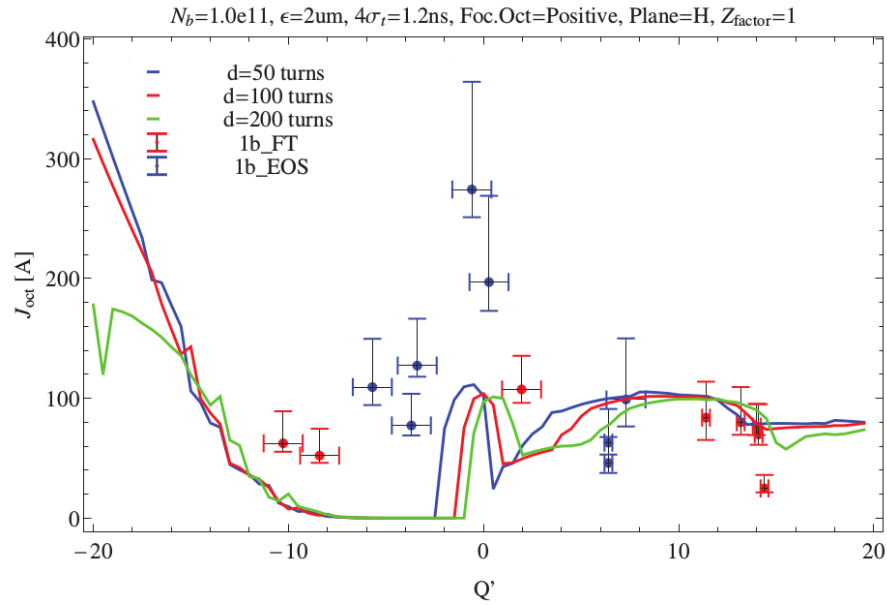


Figure 3: LHC octupole current threshold J_{oct} as a function of Q' for different damper gains d measured at flat top (FT) and end of the squeeze (EOS).

2.9.4 References

1. A. Hofmann et al. (1985, October). The ISR Impedance between 40 kHz and 40 GHz. IEEE Transactions on Nuclear Science, Vol. A&32. No. 5. October 1985.
2. D. Möhl (1974), Equipment Responsible for Transverse Beam Instability in the PS, CERN MPS/DL/Note 74-6.
3. R. Capii (1995), Observations of High-Order Head-Tail Instabilities at the CERN-PS, CERN/PS 95-02 (PA).
4. S. Persichelli (2015, February), The beam coupling impedance model of CERN Proton Synchrotron, PhD thesis, University of Rome la Sapienza, Dipartimento di Scienze di Base e Applicate per l'Ingegneria.
5. C. Zannini et al (2015, May), Transverse Impedance Model of the CERN PSB, Presented at the 6th International Particle Accelerator Conference, Richmond, VA, USA.
6. P. Collier et al (1997, March), The SPS as injector for LHC: a conceptual design, CERN report, CERN-SL-97-07-DI.
7. B. Salvant (2010, March), Impedance Model of the CERN SPS and aspects of LHC Single Bunch Stability, EPFL PhD thesis 4585.
8. C. Zannini et al (2015, May), Benchmarking the CERN-SPS Transverse Impedance Model with Measured Headtail Growth Rates, Presented at the 6th International Particle Accelerator Conference, Richmond, VA, USA.
9. J.E. Varela et al (2015, May), An Extended SPS Longitudinal Impedance Model, Presented at the 6th International Particle Accelerator Conference, Richmond, VA, USA.
10. D. Brandt et al (May 1993) Presented at 15th IEEE Particle Accelerator Conference, Washington, DC, USA, pp.3429-3431.
11. O. Brüning (1997, May), An Impedance Database program for LEP2 and the LHC, Presented at 19th IEEE Particle Accelerator Conference, Vancouver, BC, Canada.

12. N. Mounet (2012, January), The LHC Transverse Coupled Bunch Instability, EPFL PhD thesis 5305.
13. S. Peggs et al (June 1994), An Impedance Model of the Relativistic Heavy Ion Collider, RHIC, Presented at the 4th European Particle Accelerator Conference, London, UK, pp.1102.
14. Fermilab report (1998), “Run II Handbook”, p. 6.58, http://www-bd.fnal.gov/lug/runII_handbook/.
15. F. Gallucio (1994, December), The impedance budget of HERA-p: a preliminary selection of contributing elements, Internal Report DESY M-94-10.
16. Y. H. Chin and K. Satoh, Impedance Budget for the KEK B-Factory (1995, May), Presented at the 18th IEEE Particle Accelerator Conference, Dallas, TX, USA.
17. A. Blednykh, and S. Krinsky (2007, June), Preliminary Impedance Budget for NSLS-II Storage Ring, BNL report BNL-79153-2007-CP.
18. R. Wanzenberg et al (2005, May), The Impedance of Selected Components of the Synchrotron Light Source Petra III, Presented at the 21st IEEE Particle Accelerator Conference, Knoxville, TN, USA.
19. R. Nagaoka (2004, July), Numerical Evaluation of Geometric impedance for SOLEIL, Presented at the European Particle Accelerator Conference, Lucerne, Switzerland.
20. T. Gunzel et al (2008), Impedance and Instabilities for the ALBA Storage Ring, Presented at the European Particle Accelerator Conference, Genova, Italy.
21. D. Schulte (2016, April), FCC-hh Machine Layout and Optics, FCC week 2016. <https://indico.cern.ch/event/438866>.
22. E. Métral and G. Rumolo (2009, June), USPAS course, Albuquerque, USA.
23. G. Rumolo and F. Zimmermann (2002, November), Practical user guide for HEADTAIL. Technical Report SL-Note-2002-036-AP, CERN, Geneva, Switzerland.
24. C. Zannini (2013), Electromagnetic simulation of CERN Accelerator Components and Experimental Applications, EPFL PhD Thesis 5737.
25. CST, www.cst.com
26. N. Mounet and E. Métral (2010 June), “Impedances of an Infinitely Long and Axisymmetric Multilayer Beam Pipe: Matrix Formalism and Multimode Analysis”, CERN-ATS-2010-065.
27. A. Burov and V. Lebedev (2002), “Transverse Resistive Wall Impedance for Multi-layer Round Chambers”, *FERMILAB-CONF-2002-100-T*.
28. A. Burov and V. Lebedev (2002), “Transverse Resistive Wall Impedance for Multi-Layer Flat Chambers”, *FERMILAB-CONF-2002-101-T*.
29. E. Métral, B. Salvant, and B. Zotter (2007), “Resistive-Wall Impedance of an Infinitely long Multi-Layer Cylindrical Beam Pipe”, *CERN-LHC-PROJECT-Report-1014*.
30. L. Vos (2003, October) “The Impedance of Multi-layer Vacuum Chambers,” *CERN-AB-2003-093-ABP*.
31. L. Vos (2003 February), “The Transverse impedance of a cylindrical pipe with arbitrary surface impedance”, *CERN-AB-2003-005-ABP*.
32. A. Koschik, F. Caspers, E. Métral, L. Vos, and B. W. Zotter (2004, August), “Transverse Resistive Wall Impedance and Wake Function with Inductive Bypass”, *CERN-AB-2004-065*.
33. N. Biancacci, V. G. Vaccaro, E. Métral, B. Salvant, M. Migliorati, and L. Palumbo (2014), Phys. Rev. ST Accel. Beams 17, 02100.

34. Y. Shobuda, Y. H. Chin, and K. Takata (2014), *Phys. Rev. ST Accel. Beams* 17, 091001
35. A. Mostacci, L. Palumbo, and F. Ruggiero (1999), *Phys. Rev. ST Accel. Beams* 2, 124401
36. U. Niedermayer, O. Boine-Frankenheim, and H. De Gersem (2015, March), “Space charge and resistive wall impedance computation in the frequency domain using the finite element method”, *Phys. Rev. ST Accel. Beams*, 18:032001.
37. H. Tsutsui (2000, June), “Longitudinal impedances of some simplified ferrite kicker magnet models”, *CERN-SL-2000-050-AP*.
38. H. Tsutsui and L. Vos (2000, September), “Transverse Coupling Impedance of a Simplified Ferrite Kicker Magnet Model”, *LHC-PROJECT-NOTE-234*.
39. B. Salvant, N. Mounet, C. Zannini, E. Métral, and G. Rumolo (2010, June), “Quadrupolar Transverse Impedance of Simple Models of Kickers”, *CERN-ATS-2010-076*.
40. C. Zannini et al. (2012), *Effect of the TEM mode on the kicker impedance*. IPAC12, New Orleans, USA.
41. HFSS <http://www.ansys.com>
42. W. Bruns <http://www.gdfidl.de>
43. Massively parallel electromagnetic ACE3P Simulation Suite. https://portal.slac.stanford.edu/sites/ard_public/acd.
44. F. Zimmermann, et al (2006, August), “Tune shift induced by nonlinear resistive wall wake field of flat collimator.” CERN-AB-2006-070.
45. J. Laslett (1966, September), “Proceedings of the international symposium on electron and positron storage rings”, vol. IV, pp. 5.1–5.9.
46. D. Goldberg, G. Lambertson (1992), “Dynamic Devices: A primer on Pickups and Kickers”, AIP Conf. Proc. No. 249.
47. A. Chao and M. Tigner (1998), “Handbook of Accelerator Physics and Engineering”, World Scientific Publishing Co. Pte. Ltd.
48. L. Palumbo, V. G. Vaccaro and M. Zobov (1994, September), “Wake fields and impedance”, *LNF-94-041-P*.
49. D. Davino, G. Dome, G. Miano, G. Panariello, V. Vaccaro, and L. Verolino (1999), “Longitudinal Coupling Impedance of an abrupt junction”, *Nuovo Cimento 112A(12)*.
50. L. Palumbo and V. G. Vaccaro (1989, May), “Wake fields measurements” Frascati Report *LNF-89-035-P*.
51. A. Faltens, et al (1971), “An analog method for measuring the longitudinal coupling impedance of a relativistic particle beam with its environment”, *8th International Conference on High Energy Accelerator*, CERN, Geneva, Switzerland.
52. M. Sands and J. Rees (1974, August), “A Bench Measurement of the Energy Loss of a Stored Beam to a Cavity”, *LBL-PEP-NOTE-95*.
53. G. Nassibian and F. J. Sacherer (1979), “Methods for measuring transverse coupling impedances in circular accelerators”, *Nucl. Instrum. Methods*, vol. 159, no. 1, pp. 21–27.
54. L. Hahn and F. Pedersen (1978 April), “On a coaxial wire measurements of the Longitudinal Beam Coupling Impedance”, *BNL-50870*.
55. V.G. Vaccaro (1994, November), “Coupling impedance measurements: an improved wire method”, *INFN-94-023*.
56. E. Métral, F. Caspers, M. Giovannozzi, A. Grudiev, T. Kroyer, and L. Sermeus,

- (2006, July), “Kicker impedance measurements for the future multiturn extraction of the CERN Proton Synchrotron”, *CERN-AB-2006-051*.
57. M. J. Barnes, F. Caspers, T. Kroyer, E. Métral, F. Roncarolo, and B. Salvant (2009, July), “Measurement of the longitudinal and transverse impedance of kicker magnets using the coaxial wire method”, *CERN-ATS-2009-018*.
 58. T. Kroyer, F. Caspers, and E. Gaxiola (2007, July), “Longitudinal and Transverse Wire Measurements for the Evaluation of Impedance Reduction Measures on the MKE Extraction Kickers”, *CERN-AB-Note-2007-028*.
 59. F. Caspers, C. González, M. Dyachkov, E. Shaposhnikova, and H. Tsutsui (2000, February), “Impedance measurement of the SPSMKE kicker by means of the coaxial wire method”, *CERN-PSRF-NOTE-2000-04*.
 60. E. Jensen (2000, January), “An improved log-formula for homogeneously distributed impedance”, *CERN-PS-RF-NOTE-2000-001*.
 61. J. N. Weaver, J. B. Styles, and P. B. Wilson (1979), “Bench Measurements of the Loss Impedance for PEP Beam Line Components”, *IEEE Trans. Nucl. Sci.* 26.
 62. G. Di Massa and M. R. Masullo (1990), “Beam Impedance Measurement Using a Synthetic Pulse Technique”, *2nd European Particle Accelerator Conference*, Berlin, Germany.
 63. H. Day, M. Barnes, F. Caspers, E. Métral, B. Salvant, C. Zannini, and R. Jones, (2011, October), “Coaxial wire measurements of ferrite kicker magnets”, *CERN-ATS-2011-275*.
 64. A. Argan, L. Palumbo, M. R. Masullo, and V. G. Vaccaro (1999), “On the Sands and Rees Measurement Method of the Longitudinal Coupling Impedance”, *IEEE Particle Accelerator Conference PAC 99*, New York City, USA.
 65. M. Migliorati, L. Palumbo, A. Argan, F. Console, and S. De Santis, (2000), “Measurements of the Longitudinal Impedance of a Coaxial Cavity coupled with a Circular Pipe through Slots”, *7th European Particle Accelerator Conference*, Chicago, IL, USA.
 66. R. Masullo, M. G. Vaccaro, V. and Paniello (2010), “The stretched wire method: a comparative analysis performed by means of the mode matching technique”, *LINAC10*, Tsukuba, Japan.
 67. F. J. Sacherer (1974, April). Transverse bunched beam instabilities: theory. (CERN- MPS-INT-BR-74-8). Ninth international conference on high energy accelerators, Stanford, 2-7 May 1974. Proceedings, Springfield, Nat. Tech. Inf. Serv., CONF 740522, p. 347-351.
 68. G. Apollinari, I. Bjar Alonso, O. Brüning, M. Lamont, and L. Rossi (2015). *High-Luminosity Large Hadron Collider (HL-LHC): Preliminary Design Report*. CERN, Geneva.
 69. N. Biancacci, K. Li, E. Métral, and B. Salvant (2016), “The HL-LHC Impedance Model and Aspects of Beam Stability”, in proc. of IPAC16, Busan, Korea.
 70. D. Brandt et al (1995, June) “Measurements of impedance distributions and instability thresholds in LEP”, *CERN-SL-95-34 AP*.
 71. V. Kiselev and V. Smaluk (2000) “A method for measurement of transverse impedance distribution along storage ring”, *Proceedings of 4th European Workshop on Beam Diagnostics and Instrumentation for Particle Accelerators (DIPAC 99)*.
 72. L. Emery, G. Decker, and J. Galayda (2001), “Local Bump Method for

- Measurement of Transverse Impedance of Narrow-Gap ID Chambers in Storage Rings”, in Proceedings of the Particle Accelerator Conference, Chicago, IL, USA.
73. E. Plouviez and L. Farvacque (2002), Probing the Transverse Impedance of the Ring”, in Proceedings of the European Particle Accelerator Conference (EPAC), edited by J. L. Laclare (CERN, Geneva, Switzerland).
 74. G. Arduini, C. Carli, and F. Zimmermann (2004, August), “Localizing Impedance Sources from Betatron phase Beating in the CERN SPS”, CERN-AB-2004-083.
 75. G. Arduini E. Métral G. Papotti D. Quattraro G. Rumolo B. Salvant R. Calaga and R. Tomás (2009). “Transverse impedance localization using intensity dependent optics”, Proceedings of the 23rd Particle Accelerator Conference, Vancouver, Canada.
 76. R. Calaga (2010), “Transverse impedance measurements in RHIC”, in APEX Workshop, Stony Brook University, NY, USA, (Stony Brook University, NY, 2010).
 77. N. Biancacci (2014, July) “Improved techniques of impedance calculation and localization in particle accelerators”, PhD thesis, CERN.
 78. M. Carlà et al (2016) “Local Impedance Measurements at ALBA from Turn-by-Turn Acquisition”, In Proceedings, 7th International Particle Accelerator Conference (IPAC 2016), Busan, Korea.
 79. N. Biancacci and R. Tomás (2016, May), “Using ac dipoles to localize sources of beam coupling impedance”, *Phys. Rev. Accel. Beams*, 19:054001.
 80. O. Brüning, P. Collier, P. Lebrun, S. Myers, R. Ostojic, J. Poole, and P. Proudlock (2004), *LHC Design Report*. CERN, Geneva, Switzerland.
 81. L. R. Carver et al. (2016) “Current Status of Instability Threshold Measurements in the LHC at 6.5 TeV”, in Proc. of International Particle Accelerator Conference (IPAC’16), Busan, Korea.
 82. N. Mounet (2014, April), “DELPHI: an analytic Vlasov solver for impedance-driven modes”, HSC meeting, CERN, Geneva, Switzerland.

2.10 Wake Field Driven Beam Instabilities and Damping Mechanisms in Linear Machines

M. Ferrario, M. Migliorati and L. Palumbo
 INFN-LNF, Via E. Fermi 40, 00044 Frascati (Roma)
 and Università di Roma “La Sapienza”, Piazzale Aldo Moro 5, 00185 Roma
 Mail to: Massimo.Ferrario@lnf.infn.it

2.10.1 Introduction

Self induced electromagnetic (e.m.) forces in an accelerator, are generated by a charged particle beam which interacts with all the components of the vacuum chamber. These components may have a complex geometry: kickers, bellows, r.f. cavities, diagnostics components, special devices, etc. The study of the fields generally requires of solving the Maxwell’s equations in a given structure taking the beam current as source of fields. This could result a quite complicated task, and therefore several dedicated computer codes, used to study and design accelerator devices, which solve the e.m. problem in the frequency or in the time domain, have been developed. These include, for example, CST Studio Suite [1], GDFIDL [2], ACE3P [3], ABCI [4], and others. In this paper we study the effects of the wake fields, based on the analytical models introduced in the previous contributions, on the dynamics of a beam in a LINAC, such as single and multi-bunch Beam Break-Up (BBU) instability [5,6,7], and the way to cure it [8].

2.10.2 Wake Fields Effects in Linear Accelerators

A beam injected off-center in a LINAC, because for example of focusing quadrupoles misalignment, executes betatron oscillations. The bunch displacement produces a transverse wake field in all the devices crossed during the flight, which deflects the trailing charges (single bunch beam break-up), or other bunches following the first one in a multi-bunch regime (multi-bunch beam break-up). The first observation of the BBU was made at SLAC back in 1966 [9].

2.10.2.1 Single Bunch Beam Break-Up: Two-Particle Model

In order to understand this effect, we consider a simple model with only two charges $q_1=q_0/2$ (leading = half bunch) and $q_2=q$ (trailing = single charge) travelling with $\beta=1$.

The leading charge executes free betatron oscillations of the kind:

$$y_1(s) = \hat{y}_1 \cos\left(\frac{\omega_y}{c}s\right) \quad (1)$$

The trailing charge, at a distance z behind, over a length L_w experiences an average deflecting force proportional to the displacement y_1 , and dependent on the distance z , which, from the definition of the transverse dipole wake field is:

$$\langle F_y(z, y_1) \rangle = \frac{qq_0}{2L_w} w_{\perp}(z) y_1(s) \quad (2)$$

Notice that L_w is the length of the device for which the transverse wake has been computed. For example, in the case of a cavity cell L_w is the length of the cell. This force drives the motion of the trailing charge:

$$y_2^* + \left(\frac{\omega_y}{c}\right)^2 y_2 = \frac{qq_0 w_{\perp}(z)}{2E_o L_w} \hat{y}_1 \cos\left(\frac{\omega_y}{c} s\right) \quad (3)$$

This is the typical equation of a resonator driven at the resonant frequency. The solution is given by the superposition of the “free” oscillations and “forced” ones, which, being driven at the resonant frequency, grow linearly with s , as shown in Fig. 1:

$$y_2(s) = \hat{y}_2 \cos\left(\frac{\omega_y}{c} s\right) + y_2^{forced} \quad (4)$$

$$y_2^{forced} = \frac{cqq_0 w_{\perp}(z)s}{4\omega_y E_o L_w} \hat{y}_1 \sin\left(\frac{\omega_y}{c} s\right) \quad (5)$$

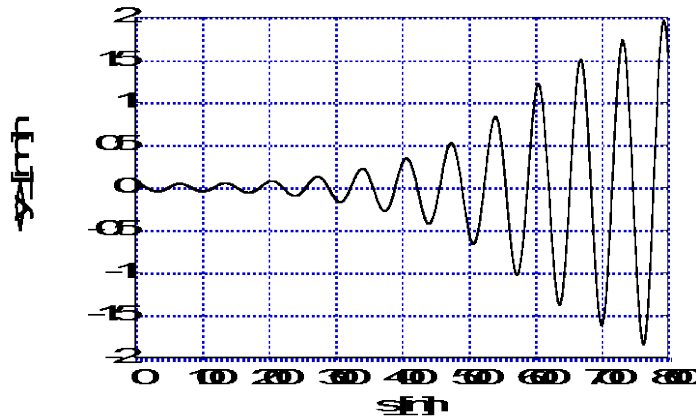


Figure 1: HOMDYN [10] simulation of a typical BBU instability, 50 μm initial bunch offset, no energy spread.

At the end of the LINAC of length L_L , the oscillation amplitude is grown by ($\hat{y}_1 = \hat{y}_2$):

$$\left(\frac{\Delta\hat{y}_2}{\hat{y}_2}\right)_{\max} = \frac{cNw_{\perp}(z)L_L}{4\omega_y(E_o/e)L_w} \quad (6)$$

If the transverse wake is given per cell, the relative displacement of the tail with respect to the head of the bunch depends on the number of cells. It depends, of course, also on the focusing strength through the betatron frequency ω_y .

2.10.2.2 BNS Damping

The BBU instability is quite harmful and hard to take under control even at high energy with a strong focusing, and after a careful injection and steering. A simple method to cure it has been proposed observing that the strong oscillation amplitude of the bunch tail is mainly due to the “resonant” driving head. If the tail and the head move with a different frequency, this effect can be significantly removed [8].

Let us assume that the tail oscillates with a frequency $\omega_y + \Delta\omega_y$, so that Eq. (3) becomes:

$$y_2'' + \left(\frac{\omega_y + \Delta\omega_y}{c}\right)^2 y_2 = \frac{Ne^2 w_\perp(z)}{2E_o L_w} \hat{y}_1 \cos\left(\frac{\omega_y s}{c}\right) \quad (7)$$

the solution of which is:

$$y_2(s) = \hat{y}_2 \cos\left(\frac{\omega_y + \Delta\omega_y}{c} s\right) - \frac{c^2 Ne^2 w_\perp(z)}{4\omega_y \Delta\omega_y E_o L_w} \hat{y}_1 \left[\cos\left(\frac{\omega_y + \Delta\omega_y}{c} s\right) - \cos\left(\frac{\omega_y}{c} s\right) \right] \quad (8)$$

In this case we observe that the amplitude of the oscillation is limited and does not grow up linearly with s any more. Furthermore, by a suitable choice of $\Delta\omega_y$, it is possible to fully depress the oscillations of the tail. Indeed, by setting:

$$\Delta\omega_y = \frac{c^2 Ne^2 w_\perp(z)}{4\omega_y E_o L_w} \quad (9)$$

if $\hat{y}_2 = \hat{y}_1$, from Eq. (8) we get:

$$y_2(s) = \hat{y}_1 \cos\left(\frac{\omega_y}{c} s\right) \quad (10)$$

that is the tail oscillates with the same amplitude of the head and with the same betatron frequency. This method of curing the single bunch BBU instability is called BNS damping by the names of the authors Balakin, Novokhatsky, and Smirnov who proposed it [8]. In order to have the BNS damping, Eq. (9) imposes an extra focusing at the tail, which must have a higher betatron frequency than the head. This extra focusing can be obtained by: 1) using a RFQ, where head and tail see a different focusing strength, 2) create a correlated energy spread across the bunch which, because of the chromaticity, induces a spread in the betatron frequency. An energy spread correlated with the position is attainable with the external accelerating voltage or with the wake fields. In Fig. 2 we show the betatron oscillation corresponding to Fig. 1 but with a 2% of energy spread.

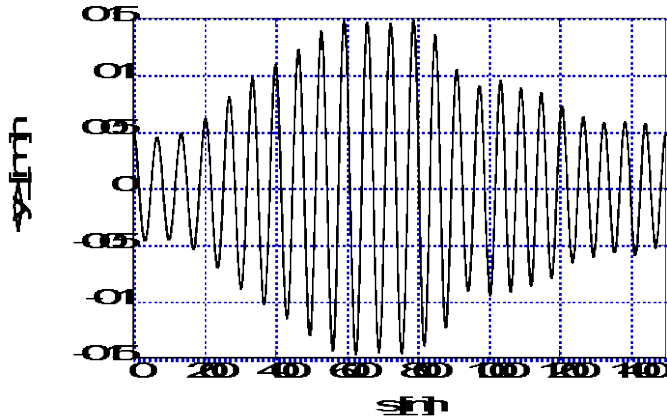


Figure 2: HOMDYN simulation of a typical BNS damping, 50 μm bunch initial offset, 2% energy spread.

2.10.2.3 Single Bunch Beam Break-Up: General Distribution

To extend the analysis we did in the previous section to a particle distribution, we write the transverse equation of motion of a single charge q with the inclusion of the transverse wake field effects as [7]:

$$\frac{\partial}{\partial s} \left[\gamma(s) \frac{\partial y(z, s)}{\partial s} \right] + k_y^2(s) \gamma(s) y(z, s) = \frac{q}{m_0 c^2 L_w} \int_z^{\infty} y(s, z') w_{\perp}(z' - z) \lambda(z') dz' \quad (11)$$

where $\gamma(s)$ is the relativistic parameter, which varies along the LINAC, and $1/k_y(s)$ the betatron function. Notice that the integral of the longitudinal distribution function $\lambda(z)$ is the total charge of the bunch q_0 . We solve the above equation by applying a perturbation method to obtain the solution at any order in the wake field intensity. Indeed we write:

$$y(z, s) = \sum_n y^{(n)}(z, s) \quad (12)$$

with n representing the n^{th} order solution. The first order solution is found without the wake field effect from the equation

$$\frac{\partial}{\partial s} \left[\gamma(s) \frac{\partial y^{(0)}(z, s)}{\partial s} \right] + k_y^2(s) \gamma(s) y^{(0)}(z, s) = 0 \quad (13)$$

It is important to notice that the above equation does not depend on z any more. This means that the bunch distribution remains constant along the structure. If the s -dependence of $\gamma(s)$ and $k_y^2(s)\gamma(s)$ is moderate, we can use the WKB approximation [5], and the solution of the above equation with the starting conditions $y(0) = \hat{y}$, $y'(0) = 0$ is:

$$y^{(0)}(s) = \sqrt{\frac{\gamma_0 k_{y0}}{\gamma(s) k_y(s)}} \hat{y} \cos[\psi(s)] \quad (14)$$

where

$$\psi(s) = \int_0^s k_y(s') ds' \quad (15)$$

Equation (14) represents the unperturbed transverse motion of the bunch in a LINAC. The differential equation of the second order solution is obtained by substituting the first order solution (14) in the right side of Eq. (11) thus giving

$$\frac{\partial}{\partial s} \left[\gamma(s) \frac{\partial y^{(1)}(z, s)}{\partial s} \right] + k_y^2(s) \gamma(s) y^{(1)}(z, s) = \frac{q}{m_0 c^2 L_w} y^{(0)}(s) \int_z^{\infty} w_{\perp}(z' - z) \lambda(z') dz' \quad (16)$$

We are interested in the forced solution of the above equation that can be written in the form

$$y^{(1)}(z, s) = \hat{y} \frac{q}{m_0 c^2 L_w} \sqrt{\frac{\gamma_0 k_{y0}}{\gamma(s) k_y(s)}} G(s) \int_z^{\infty} w_{\perp}(z' - z) \lambda(z') dz' \quad (17)$$

where

$$\begin{aligned}
G(s) &= \int_0^s \frac{1}{\gamma(s')k_y(s')} \sin[\psi(s) - \psi(s')] \cos[\psi(s')] ds' = \\
&= \frac{1}{2} \int_0^s \frac{\sin[\psi(s) - 2\psi(s')]}{\gamma(s')k_y(s')} ds' + \frac{1}{2} \sin[\psi(s)] \int_0^s \frac{1}{\gamma(s')k_y(s')} ds'
\end{aligned} \tag{18}$$

The first integral undergoes several oscillations with s and, if $\gamma(s)$ and $k_y(s)$ do not vary much, it is negligible, so that we can finally write

$$y^{(1)}(z, s) = \hat{y} \frac{q}{2m_0 c^2 L_w} \sqrt{\frac{\gamma_0 k_{y0}}{\gamma(s) k_y(s)}} \sin[\psi(s)] \int_0^s \frac{ds'}{\gamma(s') k_y(s')} \int_z^{\infty} w_{\perp}(z' - z) \lambda(z') dz' \tag{19}$$

Note that the last integral in the above equation is proportional to the transverse wake potential produced by the whole bunch. This solution can then be substituted again in the right side of Eq. (11) to obtain a third order solution and so on. If we consider constant $\gamma(s)$ and $k_y(s)$, Eq. (19) gives the same result of the two-particle model of Eq. (5) when we substitute $\lambda(z)$ with $q_0/2$ representing the leading half bunch affecting a trailing charge q . If the BBU effect is strong, it is necessary to include higher order terms in the perturbation expansion. Under the assumption of:

- rectangular bunch distribution $\lambda(z) = q_0/l_0, -l_0/2 < z < l_0/2, l_0$ bunch length;
- monoenergetic beam;
- constant acceleration gradient $dE_0/ds = \text{const}$;
- constant beta function;
- linear wake function inside the bunch $w_{\perp}(z) = w_{10}z/l_0$;

the sum of Eq. (12) can be written in terms of powers of the adimensional parameter η also called BBU strength

$$\eta = \frac{qq_0}{k_y(dE_0/ds)} \frac{w_{10}}{L_w} \ln\left(\frac{\gamma_f}{\gamma_i}\right) \tag{20}$$

with γ_i and γ_f respectively the initial and final relativistic parameter. By using the method of the steeping descents [6], it is possible to obtain the asymptotic expression of $y(z, s)$ thus finding, at the end of the LINAC,

$$y(L_L) = y_m \sqrt{\frac{\gamma_i}{6\pi\gamma_f}} \eta^{-1/6} \exp\left[\frac{3\sqrt{3}}{4} \eta^{1/3}\right] \cos\left[k_y L_L - \frac{3}{4} \eta^{1/3} + \frac{\pi}{12}\right] \tag{21}$$

that, differently from the two-particle model and from the first order solution, gives a tail displacement growing exponential with η .

2.10.2.4 Multi-Bunch Beam Break-Up

We have seen in the previous sections that when a bunch passes off-axis (due, for example, to betatron oscillations) in an axis-symmetric accelerating structure, it excites transverse wake fields which may cause the tail of the bunch to oscillate with increasing amplitude as the bunch goes along the LINAC. In the same way, the whole bunch may excite deflecting trapped modes in the RF cavities of the LINAC that may cause trailing bunches to be deflected, whether they are on axis or not. These angular deflections are

transformed into transverse displacements through the transfer matrices of the focusing system and the displaced bunches will themselves create similar wake fields in the downstream accelerating structures of a LINAC. The subsequent bunches will be further deflected leading to a beam blow-up. Due to the long range wake fields, there is a coupling in the motion of the bunches that are more and more deflected as they proceed along the LINAC in a process that is called multi-bunch BBU. Even if the bunches are not lost, the transverse beam emittance can be greatly increased, leading to a significant luminosity reduction.

We summarize here the analytical study of multi-bunch BBU performed with the formalism used in [7]. All the bunches are considered to be rigid macro-particles, like delta-functions, separated by period T , and we assume all bunches injected with the same initial offset x_0 . We consider the transverse equation of motion of a bunch as a whole, ignoring internal structures; the beam is therefore made of a train of bunches with same charge (Q_b) evenly spaced by period T , which is an integer number of the RF period of the accelerating mode. We also consider all the cells of the LINAC accelerating structure identical and with the same dipole trapped mode in each cell of length L_w . Rigorously the analytical approach requires that many betatron oscillations are performed in the LINAC and the BBU remains moderate within a betatron oscillation. Moreover, the theory is valid if the beam energy does not change too much in a betatron wavelength. This last hypothesis is also called adiabatic acceleration. The transverse wake field force experienced by the k^{th} bunch, spaced kT from the first bunch, depends on the transverse wake field generated by the preceding bunches (and thus by their transverse displacement). The dipole long range wake field is produced by a high order deflecting mode, identical in all the cavities of the structure, and it is described in terms of its resonant frequency ω_r , the quality factor Q and the dipole shunt resistance R_{\perp} (expressed in ohm/meter). The equations of motion are then written in terms of the Z -transform [11] since the displacement $x(kT, s)$ of the k^{th} bunch at the position s is a discrete function of time. The solution can be retrieved with a perturbation method, which considers its expansion into a series of the driving wake field force. The 0^{th} order solution is given for a vanishing driving force, i.e. a pure betatron oscillation (unperturbed motion). It represents the motion of the first bunch, which is not affected by any wake field because of the causality principle (the wake field cannot travel ahead of the bunch itself). The n^{th} order solution is driven by the wake field excited by the solution of the order $n-1$. Thus the 1^{st} order solution is computed from the motion of the first bunch and it affects all the bunches, except the first one; it means that the n^{th} order solution affects only bunches of index larger than n . Therefore the summation of the series can be stopped at the M^{th} order of a train of M bunches. The n^{th} order solution in the Z -domain can be written as [7]

$$x_n(z, s) = \sqrt{\frac{\gamma_0 k_{y0}}{\gamma(s) k_y(s)}} x_0 e^{i\psi(s)} \frac{a^n(s)}{i^n n!} G_n(z) \quad (22)$$

where $a(s)$ is the so called dimensionless BBU strength given, in case of constant $k_y(s)$, by

$$a(s) = \frac{Q_b}{2k_{y0}G} \omega_r \frac{R_{\perp}}{L_w Q} \ln \left[\frac{\gamma(s)}{\gamma_0} \right] \quad (23)$$

with G is the accelerating gradient (in V/m), and

$$G_n(z) = \frac{z}{z-1} \tilde{w}_{\perp}^n(z) \quad (24)$$

with

$$\tilde{w}_\perp(z) = \frac{1}{2i} \left(\frac{z}{z-z_1} - \frac{z}{z-z_2} \right) \quad (25)$$

and

$$z_{1,2} = e^{\frac{T\omega_r}{2Q}} e^{\pm i\omega_r T} \quad (26)$$

The inverse Z-transform of $x_n(z,s)$, that is $x_n(kT,s)$, can then be summed to get the transverse displacement of the k^{th} bunch as

$$x(kT,s) = \sum_{n=0}^{\infty} x_n(kT,s) \quad (27)$$

We remember that the sum can be stopped at the M^{th} term for a beam containing M bunches.

For $a(s) \ll 1$ the series expansion can be stopped at the first order term, while, if the BBU strength parameter a is moderate, it is sufficient to keep only few terms of the summation.

In the z -domain the n^{th} order solution, given by Eq. (22) has been determined analytically, and the same is possible with its infinite sum, but its inverse z -transform (27) is, in general, not possible to write in a closed analytical form. It is however possible to compute the exact solution for the n^{th} bunch as a sum of n terms if the BBU instability is moderate in a betatron period. Moreover, it is possible to use an asymptotic technique, valid when the blow-up is strong, to have an expression of the transverse displacement that puts in evidence the main parameters playing an important role in the instability. The asymptotic transverse displacement of the k^{th} bunch, expressed in terms of the oscillation amplitude only, is [7]

$$x(kT,s) = x_\infty(s) + \sqrt{\frac{\gamma_0 k_{y0}}{\gamma(s) k_y(s)}} \frac{x_0 e^{-k \frac{T\omega_r}{2Q}}}{\sqrt{2\pi} \left(2e^{\frac{T\omega_r}{2Q}} \right)^{1/2} \left[\cosh\left(\frac{T\omega_r}{2Q}\right) - \cos(\omega_r T) \right]^{1/2}} \frac{[2a(s)k]^{1/4}}{2k} e^{[2a(s)k]^{1/2}} \quad (28)$$

where $x_\infty(s)$ is the steady state solution that is reached when long (rigorously infinite) train of bunches are accelerated. In Fig. 3 we show a comparison between the analytical solution obtained by numerically solving Eq. (27) and a simple tracking code that considers the bunches in the train as rigid macro-particles, but which can also take into account the contribution of several resonant modes, and different initial offsets and displacements of the bunches. The parameters used for the calculations are given in Table 1. They refer to a C-band LINAC with the BBU effect produced by a HOM. In the vertical axis the normalized transverse position, evaluated at the exit of the LINAC, is defined as:

$$\frac{x(kT,s)}{x_0} \sqrt{\frac{\gamma(s) k_y(s)}{\gamma_0 k_{y0}}} \quad (29)$$

From Eq. (22) we see that one possible way to reduce the BBU instability is to act on the dimensionless BBU strength given by Eq. (23). For example we can reduce the bunch

charge Q_b or the betatron function, i.e. increase the focusing strength. A better approach is to remove the source of the instability by damping the transverse dipole mode, for example with an improved electromagnetic design of the accelerating cells.

The other main approach to the BBU instability suppression is to detune the cell frequencies in order to introduce a spread in the resonance frequency of the dangerous mode so that it will no longer be excited coherently by the beam. Indeed by properly detuning each cell, a damping of the BBU instability is produced by a de-coherence of the various cell wake fields. It has been demonstrated [12] that a Gaussian distribution of the cell frequencies, which provides a rapid drop in the wake field for a given total frequency spread, would be optimal. The analytical approach to determine the effectiveness of this detuning technique for the BBU multi-bunch instability can be found in Ref. [7], where it is also shown that the damping increases with the amplitude of the frequency spread.

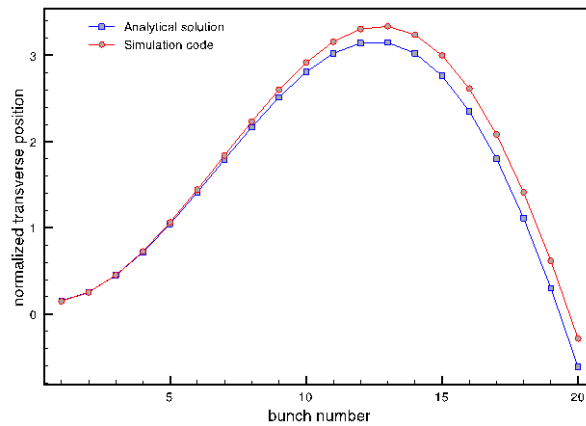


Figure 3: Normalized transverse position as a function of the bunch number: comparison between the analytical solution and a tracking code.

Table 1: Beam parameters used for comparing the analytical solution of multi-bunch BBU with the results of a tracking code.

Linac length	30 m
Initial energy	80 MeV
Energy gradient	30 MeV/m
Betatron function $1/k_y$	1 m
Bunch spacing T	15 ns
Bunch charge	1 nC
HOM resonant frequency f_r	8.4 GHz
HOM transverse impedance R_{\perp}	50 M Ω /m
HOM quality factor	11000
Cell length	17.5 cm

2.10.3 References

1. CST AG, Darmstadt, Germany, www.cst.com.
2. W. Bruns, "GdfidL: A Finite Difference Program with Reduced Memory and CPU Usage", 1997 Particle Accelerator Conference, Vancouver, B.C., Canada, (1997), pp. 2651-2653.
3. C. Ng, et al., "State of the Art in EM Field Computation", Proceedings of EPAC 2006, Edinburgh, Scotland, pp. 2763-2767.
4. Y. H. Chin, KEK Report No. 2005-06, KEK, Tsukuba, Japan, 2005.
5. K. Yokoya, DESY 86-084, 1986.
6. A. Chao, "Physics of Collective Beam Instabilities in High Energy Accelerators", John Wiley and Sons Inc., (1993).
7. A. Mosnier, "Instabilities in linacs", CAS Accelerator School, CERN 95-06 (1995), Vol. I, pp. 459-514.
8. V. E. Balakin, A.V. Novokhatsky, V. P. Smirnov, Proc. 12th Int. Conf. on High Energy Accelerators, Batavia, 1983.
9. H. Altenmueller, et al., "Beam Break-Up experiments at SLAC", 1966 Linear Accelerator Conference, Los Alamos, October 1966, also SLAC-PUB-224 October 1966.
10. M. Ferrario, V. Fusco, B. Spataro, M. Migliorati, L. Palumbo, "Wake Fields Effects In The Sparc Photoinjector", Proc of EPAC 2004, Lucerne, Switzerland.
11. See, e.g., E. I. Jury, "Theory and application of the Z-transform method", John Wiley & Sons, New York (1964).
12. K. L. F. Bane, R. L. Gluckstern, SLAC-PUB-5783 (1992).

2.11 Loss of Landau Damping for Bunch Longitudinal Oscillations

A. Burov
FNAL, Batavia, IL 60510, U.S.A
Mail to: burov@fnal.gov

2.11.1 Introduction

Conditions for the existence, uniqueness and stability of self-consistent bunch steady states are considered. For the existence and uniqueness problems, simple algebraic criteria are derived for both the action and Hamiltonian domain distributions. For the stability problem, van Kampen theory is used [1-3]. The onset of a discrete van Kampen mode means the emergence of a coherent mode without any Landau damping; thus, even a tiny couple-bunch or multi-turn wake is sufficient to drive the instability. The method presented here assumes an arbitrary impedance, RF shape, and beam distribution function. Available areas on the intensity-emittance plane are shown for resistive wall wake and single harmonic, bunch shortening and bunch lengthening RF configurations. Thresholds calculated for the Tevatron parameters and impedance model are in agreement with the observations. These thresholds are found to be extremely sensitive to the small-argument behaviour of the bunch distribution function. Accordingly, a method to increase the LLD threshold is suggested. This article summarizes and extends recent author's publications [4, 5].

2.11.2 Main Equations

Let $H(z,p)$ be a Hamiltonian for longitudinal motion inside an RF bucket distorted by the wake field

$$\begin{aligned} H(z, p) &= \frac{p^2}{2} + U(z) + V(z, t); \\ U(z) &= U_{\text{rf}}(z) - \int \lambda(z') \mathcal{W}(z - z') dz'; \\ V(z, t) &= - \int \rho(z', t) \mathcal{W}(z - z') dz'. \end{aligned} \tag{1}$$

Here z and p are the offset and the momentum of a particle, $U(z)$ is the steady state potential with $U_{\text{rf}}(z)$ as its RF part, $\lambda(z)$ is steady state linear density, $\mathcal{W}(z)$ is the wake function, $V(z, t)$ and $\rho(z, t)$ are small perturbations of the potential and linear density. For the potential well $U(z)$, action I and phase φ variables can be found:

$$\begin{aligned} I(H) &= \frac{1}{\pi} \int_{z_{\min}}^{z_{\max}} \sqrt{2(H - U(z))} dz; \\ \Omega(I) &= \frac{dH}{dI}; \quad \frac{dz}{d\varphi} = \frac{\sqrt{2(H - U(z))}}{\Omega(I)}. \end{aligned} \tag{2}$$

The linear density λ and its perturbation ρ can be related to steady state phase space density $F(I)$ and its perturbation $f(I, \varphi, t)$

$$\begin{aligned}\lambda(z) &= \int F(I) dp ; \\ \rho(z, t) &= \int f(I, \varphi, t) dp .\end{aligned}\quad (3)$$

Below, the steady state distribution $F(I)$ is treated as an input function, determined either by cooling-diffusion kinetics, or by injection. The perturbation $f(I, \varphi, t)$ satisfies the Boltzmann-Jeans-Vlasov (BJV) equation [6]

$$\frac{\partial f}{\partial t} + \Omega(I) \frac{\partial f}{\partial \varphi} - \frac{\partial V}{\partial \varphi} F'(I) = 0 .\quad (4)$$

Equations (1-4) assume given input functions $U_{rf}(z)$, $W(z)$ and $F(I)$, with $F'(I) \equiv dF/dI$, while the steady state solution $U(z)$, $I(H)$, $\lambda(z)$ and all the eigenfunctions of the BJV Eq. (4) are to be found.

To obtain the steady state solution, the following set of three equations must be solved:

$$\begin{aligned}U(z) &= U_{rf}(z) - \int \lambda(z') W(z - z') dz' \equiv U_{RHS}[\lambda]; \\ I(H) &= \frac{1}{\pi} \int_{z_{\min}}^{z_{\max}} \sqrt{2(H - U(z))} dz \equiv I_{RHS}[U]; \\ \lambda(z) &= 2 \int_{U(z)}^{H_{\max}} \frac{F(I(H))}{\sqrt{2(H - U(z))}} dH \equiv \lambda_{RHS}[I, U].\end{aligned}\quad (5)$$

For any given input functions $U_{rf}(z)$, $W(z)$ and $F(I)$, the solution can be obtained numerically by means of the relaxation method. Indeed, let it be assumed that initially there is no wake, so that the entire potential well is equal to the RF potential $U(z) = U_0(z) = U_{rf}(z)$. With that assumption, initial action and linear density functions $I_0(H)$ and $\lambda_0(z)$ can be found from the 2nd and 3rd equations of the set (5). Then the following iteration procedure can be applied

$$\begin{aligned}U_n(z) &= U_{n-1}(z) - \varepsilon (U_{n-1}(z) - U_{RHS}[\lambda_{n-1}]); \\ I_n(H) &= I_{RHS}[U_n]; \\ \lambda_n(z) &= \lambda_{RHS}[I_n, U_n] \quad ; \quad n = 1, 2, \dots\end{aligned}\quad (6)$$

If the solution exists and the convergence parameter $\varepsilon > 0$ is sufficiently small, the process is very likely to converge. Stability of the steady state solution can be determined by analysis of the BJV Eq. (4). Following Oide and Yokoya [7], the eigenfunctions may be expanded in Fourier series over the synchrotron phase φ

$$f(I, \varphi, t) = e^{-i\omega t} \sum_{m=1}^{\infty} [f_m(I) \cos m\varphi + g_m(I) \sin m\varphi]\quad (7)$$

With the zero-phase at the left stopping point,

$$\begin{aligned}z(I, \varphi = 0) &= z_{\min}(I); \quad z(I, \varphi = \pi) = z_{\max}(I); \\ z(I, -\varphi) &= z(I, \varphi); \quad p(I, -\varphi) = -p(I, \varphi),\end{aligned}\quad (8)$$

yield an equation for the amplitudes $f_m(I)$

$$\begin{aligned}
& \left[\omega^2 - m^2 \Omega^2(I) \right] f_m(I) = \\
& -2m^2 \Omega(I) F'(I) \sum_{n=1}^{\infty} \int dI' V_{mn}(I, I') f_n(I'); \\
V_{mn}(I, I') = & \\
& -\frac{2}{\pi} \int_0^{\pi} d\varphi \int_0^{\pi} d\varphi' \cos(m\varphi) \cos(n\varphi') W(z(I, \varphi) - z(I', \varphi')).
\end{aligned} \tag{9}$$

The matrix elements $V_{mn}(I, I')$ can be also expressed in terms of the impedance $Z(q)$. After [8, Sec. 2.3, Eq. (2.69)]

$$W(z) = -i \int_{-\infty}^{\infty} \frac{dq}{2\pi} \frac{Z(q)}{q} \exp(iqz) \tag{10}$$

$V_{mn}(I, I')$ is then given by

$$\begin{aligned}
V_{mn}(I, I') = & -2 \operatorname{Im} \int_0^{\infty} dq \frac{Z(q)}{q} G_m(q, I) G_n^*(q, I'); \\
G_m(q, I) \equiv & \int_0^{\pi} \frac{d\varphi}{\pi} \cos(m\varphi) \exp[iqz(I, \varphi)].
\end{aligned} \tag{11}$$

Note that there is no bunch-to-bunch interaction in the formulas above - long-range wakes are omitted for the sake of simplicity. Equations (9-11) reduce the integro-differential BJV Eq. (4) to a standard eigen-system problem of linear algebra after the action integral in Eq. (9) is expressed as a proper sum.

2.11.3 Steady State solution

The algorithm of Eq. (6) allows the determination of a numerical solution of the steady state problem. In this section, the problem of the existence and uniqueness of that solution is considered.

It is well known that the steady-state solution does not necessarily exist. For example, below a certain temperature threshold, there is no thermodynamic equilibrium (no solution of the Haissinski equation [9]) for the space charge wake above transition, $W(z) \sim \delta(z)$ [8,10]. For this case though, the distribution function is given in the Hamiltonian domain, $F = C \exp(-H/T)$, not in the action domain, as in the previous section. As a consequence, the normalization constant C for the Haissinski equation is yet to be found from the normalization condition

$$2\pi C \int_0^{\infty} \exp(-H(I)/T) dI = 1$$

which is to be added to the entire set of Eqs. (5) and must be solved jointly with them. If the temperature T is low enough, the normalization condition leads to an algebraic equation having no solutions. This situation is not specific to thermodynamic equilibrium only. A similar phenomenon appears for any distribution function in the Hamiltonian domain. For instance, the same problem emerges for the Hofmann-Pedersen distribution $F = C \sqrt{H_{\max} - H}$, as is shown in Ref. [8, Chapter 6.2]. For space charge above transition,

and some other wakes, the bunch momentum spread and average Hamiltonian turn out to be limited from below: for a given RF and bunch population, they cannot be smaller than a certain value for any longitudinal emittance. That is why it may be wrong to assume an arbitrary distribution function in terms of the Hamiltonian. On the contrary, Eqs. (5) assume distribution density as a function of action. Therefore it is a priori explicitly defined and normalized; thus, the specific limitations for Hamiltonian-domain distribution functions do not apply.

The following estimation shows when Eqs. (5) do have a solution. Let \bar{I} be the rms bunch emittance, and l be the rms bunch length. The rms momentum spread is then estimated to be $\bar{p} \cong \bar{I}/l$, and the average synchrotron frequency is $\Omega \cong \bar{p}/l \cong \bar{I}/l^2$. It is also known that $\Omega^2 - \Omega_0^2 \propto \text{Im}(Z(l^{-1}))/l^2$, where Ω_0 is the bare RF synchrotron frequency (note that RF nonlinearity is neglected at this point). Combination of these two expressions yields (compare with Ref. [8], p. 285)

$$\bar{I}^2 q^4 = 1 + q^2 \text{Im} Z(q);$$

where $q=1/l$ is the inverse bunch length to be found from this equation; q is measured in inverse radians of RF phase. The emittance \bar{I} is dimensionless, and its value in conventional eVs units can be found after multiplication by a factor of $E_0 \Omega_0 / (\eta \omega_{\text{rf}}^2)$, where $E_0 = \gamma m c^2$ is the beam energy. The dimensionless impedance $Z(q)$ of this paper, Eq. (10), relates to the conventional $Z_{\parallel}(q)$ as $Z(q) = D Z_{\parallel}(q)$ with the intensity factor $D = N r_0 \eta c \omega_{\text{rf}}^2 / (\Omega_0^2 \gamma C)$, where N is the bunch population, r_0 - the classical radius, $\eta = \gamma_t^{-2} - \gamma^{-2}$ - the slippage factor, ω_{rf} - RF angular frequency, γ - relativistic factor, and C - the machine circumference. Note that this equation does not give an exact solution for the bunch length. Instead, it is an estimate showing the existence of the solution and its dependence on the parameters. It follows that the solution exists if the wake is not too singular: at high frequencies the impedance may not grow too fast, providing $\lim_{q \rightarrow \infty} \text{Im} Z(q) / q^2 = 0$, which is true for all realistic cases. For non-monotonic impedances there may, in general, be several solutions. For the space charge and the resistive wall impedances there is always a unique steady state.

However, since the RF potential is never an infinite parabola, Eqs. (5) may still have no solution. Indeed, the bucket has a limited acceptance; thus, it cannot hold a bunch with an emittance that is greater than that acceptance. Moreover, in many cases, wake fields reduce bucket capacity. This could lead to some beam loss to DC, even if the bunch fits within the bare RF bucket.

In a case where the distribution function is given as a function of Hamiltonian, with \bar{H} as its average value, the steady state estimation for the parabolic RF is written as

$$\bar{H} q^2 = 1 + q^2 \text{Im} Z(q)$$

In this case, the existence of a solution is not intensity-limited for slow-growing or bunch-lengthening impedances only, when $D \lim_{q \rightarrow \infty} \text{Im} Z_{\parallel}(q) \leq 0$. The last condition is not satisfied for the space charge above transition and the resistive wall below transition. Thus, for these impedances and sufficiently high intensity, there are either no solutions, or there are two of

them. In the case of two solutions, they have identical Hamiltonian distributions, but different phase space densities.

2.11.4 Van Kampen Modes

More than half a century ago, N.G. van Kampen found an eigensystem of the BJV equation for infinite plasma [1-3]. In general, this spectrum consists of continuous and discrete parts. The continuous spectrum essentially describes single-particle motion, accompanied with a proper plasma response. The frequency band of the continuous spectrum is one of the incoherent frequencies. For any velocity v within the distribution function, there is a continuous van Kampen mode with a frequency kv , where k is the wave number. Continuous modes are described by singular functions in the velocity space, underlying their primary relation to single-particle motion. In these terms, Landau damping results from phase mixing of van Kampen modes of the continuous spectrum. Unlike the continuous spectrum, discrete one not necessarily exists. If it does, the discrete modes are described by regular functions, and some of them do not decay with time. Indeed, since the original equations (analogue of Eq. (9)) possess real coefficients, the mode frequencies are either real or form complex-conjugate pairs. The first case corresponds to a pure Loss of Landau damping (loss of LD, or LLD), while the second describes an instability. Plasma with a monotonic density distribution has been shown to be always stable [11]. The discrete modes of pure LLD type may only appear if the distribution function is of a finite width.

Most of the plasma results are applicable to circulating bunches in accelerators. However, two issues distinguish bunches and plasma. First, for beams, particle interaction may be described by various wake functions, being more diverse than pure Coulomb forces of the classical plasma. Second, the frequency spectrum for bunch particles is always limited, while in plasma the velocity spectrum may be considered infinite in extent, at least formally.

The eigenvalue problem of the BJV equation for bunch longitudinal motion was first considered by A.N. Lebedev [12]. Although the suggested formalism was not numerically tractable, an important result was analytically obtained. It was proved that for the space charge impedance above transition, a bunch steady state is always stable (which does not exclude LLD). The numerically tractable algorithm was suggested more than twenty years later by Oide and Yokoya [7].

For a parabolic RF potential, van Kampen modes were analyzed for power wakes [7], capacitive [13], broad-band wakes [7,13], and modified inductive wakes [14]. For that RF potential, rigid bunch oscillations at the unperturbed synchrotron frequency are always a solution of equation of motion [13]. Indeed, the single-particle equations of motion can be written as

$$\ddot{z}_i + \Omega_0^2 z_i = \sum_j W'(z_i - z_j); \quad i, j = 1, \dots, N$$

The solution can be presented as a sum of a steady-state-related part \hat{z}_i and a small perturbation \tilde{z}_i . It is clear that rigid-bunch mode, $\tilde{z}_i = \text{const} \cdot \cos(\Omega_0 t)$ satisfies this equation. While the rigid-bunch frequency is intensity-independent, all of the incoherent frequencies are typically either suppressed or elevated by the potential well distortion. Thus, this mode normally stays outside the incoherent band, and so is a discrete LLD-type mode. This conclusion may not apply when the core and the tail particles have opposite signs of their

incoherent tune shifts. As was shown in Ref [13], for a broad band impedance model, core and tail incoherent frequencies may correlate with intensity in the opposite direction, so that the rigid-bunch mode may be covered by incoherent frequencies. Thus, the rigid-bunch mode should be Landau-damped in that case. In Ref. [15], loss of Landau damping was analyzed for the space charge impedance and various RF shapes, arbitrarily assuming the coherent motion as the rigid-bunch one. It is shown in the next section that such an assumption is not correct when the RF frequency spread is taken into account. The action dependence of the emerging discrete mode is normally very different from that of the rigid-bunch case. Because of that, rigid bunch approximation overestimates the threshold intensity.

Without interaction, there are no discrete modes for Eqs. (9). All modes belong to a continuous spectrum, $\omega=m\Omega(I)$. If the bunch intensity is low enough, the weak head-tail approximation may be applied, allowing the omission of terms with different azimuthal numbers. In this case, it is straightforward to show that for monotonic distributions, $dF/dI<0$, and for symmetric potential wells, $U(-z)=U(z)$, Eq. (9) reduces to one with a symmetric matrix. In that case all of its eigenvalues are real. Since there are no unstable modes, all of the discrete modes, if any, belong to the pure LLD type. In practice there are always some energy losses, and so the distorted potential well $U(z)$ is always somewhat asymmetric. However, my attempts to find the weak head-tail instability in numerical solutions for monotonic distributions over frequencies, some realistic wakes and purposely asymmetric RF potentials have not yet succeeded. If the frequency distribution is not monotonic, a mode coupling instability is possible. To save CPU time, the stability analysis was limited by the weak head-tail approximation and considering only the dipole azimuthal mode. In other words, for the following analysis only the $m=n=1$ matrix elements are left in Eq. (9).

This paper takes into account two possible reasons for bunch intensity limitations: reduction of the bucket acceptance by wake fields and the emergence of a discrete mode (LLD).

2.11.5 Resistive Wall Impedance

In this section, the intensity limitations for resistive wall impedance are summarized. The beam energy is assumed to be above transition. The RF potential is written as

$$U_{\text{rf}}(z) = (1 - \cos z) + \alpha_2(1 - \cos 2z) / 4 \quad (12)$$

Three options for the second RF harmonic are considered: single harmonic (SH) with $\alpha_2=0$, bunch shortening (BS) with $\alpha_2=1$, and bunch lengthening (BL) with $\alpha_2=-1$. Equation (12) assumes the synchrotron frequencies are given in units of zero-amplitude synchrotron frequency provided by the first RF harmonic only, Ω_0 . For the SH case, the RF bucket acceptance (maximal action) in these dimensionless units is $8/\pi \approx 2.54$. The energy offset is related to the dimensionless momentum by $\delta E / E_0 = -p\Omega_0 / (\eta\omega_{\text{rf}})$. The time offset is z/ω_{rf} . The dimensionless wake function and impedance of a round chamber with radius b are written as

$$W(s) = -k / \sqrt{-s} ;$$

$$Z(q) = k(1 - i \operatorname{sgn} q) \sqrt{\pi |q| / 2} ;$$

$$k = \frac{Nr_0 \eta \omega_{rf}^2}{\pi \gamma b \Omega_0^2} \sqrt{\frac{\omega_{rf}}{\sigma}} ,$$

where the wall conductivity σ stays in the CGS units of 1/s.

An example with the parabolic RF potential suggests that wake fields act more on incoherent frequencies than on the coherent ones. For the parabolic potential, the first discrete mode does not depend on the impedance at all. Thus, at a certain threshold, a first discrete mode comes off the continuous spectrum, since its frequency is not suppressed or increased as much as the incoherent frequencies are. For the SH and BS RF, above transition, mostly lowest-amplitude particles are excited for this mode, since their frequencies are closer to the coherent frequency.

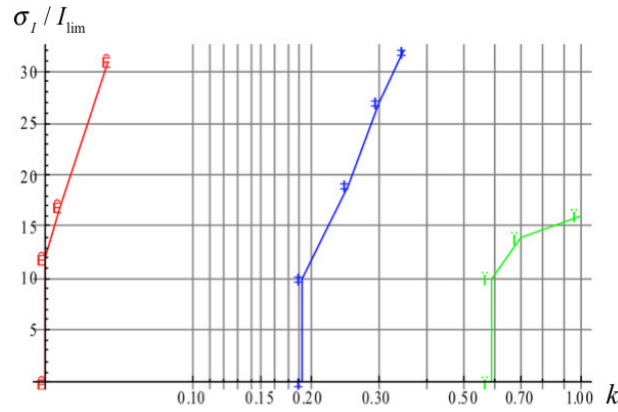


Figure 1: Relative width of the discrete mode $\sigma_l / I_{\text{lim}}$ (%) versus the intensity parameter k for the distribution $F(I) \sim (I_{\text{lim}} - I)^{1/2}$ and emittances $I_{\text{lim}} = 0.5$, 1.0 and 1.5 (red, blue and green), SH case.

An assumption of rigid-bunch discrete mode normally is far from being correct. In Fig.1, the relative width of that discrete mode $\sigma_l / I_{\text{lim}}$ is shown as a function of the intensity parameter k for 3 emittances and the Hoffman-Pedersen distribution $F(I) \sim (I_{\text{lim}} - I)^{1/2}$. The relative width is defined as

$$\sigma_l = \sqrt{\frac{\int dI f^2(I) (I - \bar{I})^2}{\int dI f^2(I)}} , \quad \bar{I} \equiv \frac{\int dI f^2(I) I}{\int dI f^2(I)}$$

The mode widens rather fast above threshold as a consequence of being singular at the threshold. All of the modes are primarily located at small amplitudes, $\bar{I} \approx \sigma_l$.

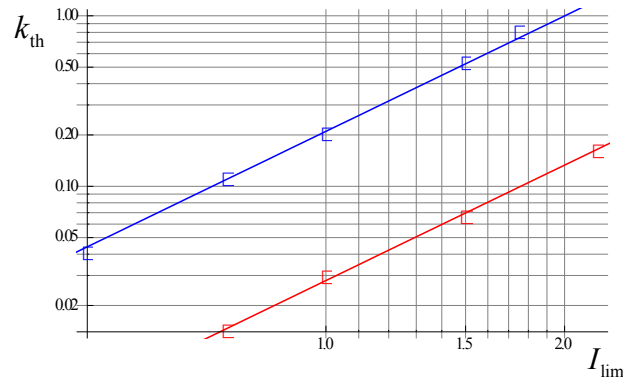


Figure 2: LLD threshold of the resistive wall intensity parameter k_{th} for SH RF, versus the bunch emittance for $F(I) \propto (I_{\text{lim}} - I)^P$. Blue dots : $P=1/2$, red dots: $P=2$, lines are fits with $k_{\text{th}} \propto I_{\text{lim}}^{9/4}$. Note the strong dependence on the distribution parameter P .

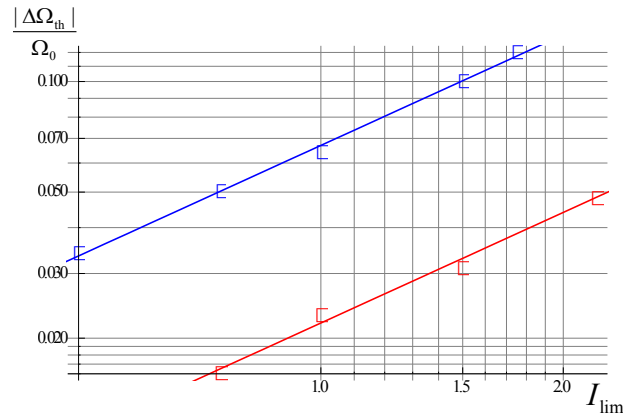


Figure 3: Same thresholds as in Fig. 2, in terms of the relative shift of zero-amplitude synchrotron frequencies $\Delta\Omega = \Omega(0) - \Omega_0$. Lines are linear fits $\Delta\Omega_{\text{th}} \propto I_{\text{lim}}$. Note that the threshold frequency shifts are fairly low, even for the blue line.

LLD thresholds for the intensity parameter k versus emittance I_{lim} for two different distributions are presented in Fig.2. The power law $k_{\text{th}} \propto I_{\text{lim}}^{9/4}$ agrees with a dependence obtained by method of Ref. [16], i. e. by means of comparison of the zero-amplitude synchrotron tune shift $\Delta\Omega = \Omega(0) - \Omega_0 \propto \text{Im} Z(l^{-1})/l^2$, with the synchrotron tune spread in the nonlinear SH RF, $\delta\Omega \propto l^2$. Equating these two values with the bunch length $l \propto \sqrt{I_{\text{lim}}}$, and $\text{Im} Z(l^{-1}) \propto l^{-1/2}$ one gets the thresholds $k_{\text{th}} \propto I_{\text{lim}}^{9/4}$ for the resistive wall impedance. For inductive impedance, it gives $k_{\text{th}} \propto I_{\text{lim}}^{5/2}$. For any impedance, at the LLD threshold $\Delta\Omega \cong \delta\Omega \propto I_{\text{lim}}$. Although this scaling is based on the small bunch frequency spread formula, $\delta\Omega \propto l^2$, it appears to be valid up to full bucket case, see Figs. (2, 3). A reason for that is that the discrete mode in this case appears above all the incoherent spectrum, so it is mostly associated with the low-amplitude particles. That is why the mode is mostly sensitive to the frequency spread of those particles, for which the small-bunch approximation $\delta\Omega \propto l^2$ is always valid.

Contrary to the SH and BS RF cases, for the BL case incoherent frequency is not a monotonic function of action, it has a maximum at $I=I_m \approx 1.5$. That is why, for the considered case of an effectively repulsive wake, the discrete mode emerges from the tail particle frequencies if the bunch limiting emittance is small, ($I_{lim} < I_m$). For BL RF, the emergence of the discrete mode is sensitive to the tails of the distribution: even a tiny tail covering the coherent frequency yields Landau damping, killing that discrete mode. If the bunch emittance is not that small ($I > I_m$), the discrete mode emerges above the incoherent maximum. Since this mode emerges outside the entire bucket area of the incoherent frequencies, Landau damping cannot be restored by tiny perturbations of the distribution function. That is why this kind of LLD, which cannot be cured by tiny corrections of the distribution function, is called hereinafter “radical LLD.” To avoid that tail ambiguity, only radical LLD is taken as a real stability limit here.

Figure 4 shows radical LLD limitations for BL RF, for two different distributions. Note that LLD restricts the available acceptance by $I_m \approx 1.5$, while the entire BL bucket area is about twice higher. Stability limitation associated with the maximum of incoherent synchrotron frequencies was pointed out in Ref. [17, 18]; it was studied at CERN SPS (see Ref. [19] and references therein). To overcome this limitation of the BS mode, a phase shift of the two RF harmonics can be applied; the bunch flatness would be lost in this case [20].

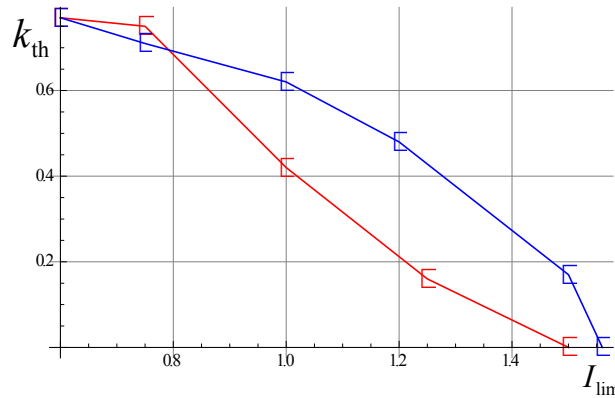


Figure 4: Threshold intensity k_{th} versus emittance I_{lim} for BL RF and two distribution functions: $F(I) \sim (I_{lim}-I)^{1/2}$ (red) and $F(I) \sim (I_{lim}-I)^2$ (blue).

On the k - I_{lim} area, the availability is limited by LLD and the bucket acceptance. For the three RF configurations, SH, BS and BL, their areas of availability are shown in Fig. 5 with $F(I) \sim (I_{lim}-I)^{1/2}$. Clearly, every RF configuration has its own beneficial area: hot and low-intensity beams better fit into SH, cold high-intensity ones are more suitable for BL, and the intermediate case is for BS RF.

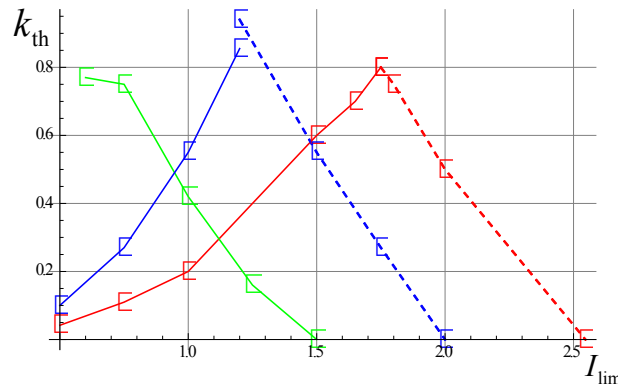


Figure 5: Intensity-emittance k - I_{lim} areas of availability for $F(I) \sim (I_{\text{lim}} - I)^{1/2}$. Red lines are for SH, blue – for BS, green – for BL. Solid lines show radical LLD, dashed – limiting bucket capacity.

2.11.6 Inductive Impedance

Hadron machines are normally dominated by resistive wall and inductive (or space charge) impedances (see e. g. Ref. [19]). In the dimensionless units, the inductive wake function and impedance are written as

$$\begin{aligned}
 W(s) &= -k\delta(s); \\
 Z(q) &= -ikq; \\
 k &= -\frac{2Nr_0\eta\omega_{\text{rf}}^3}{\gamma c\Omega_0^2} \frac{\text{Im} Z_{\parallel}}{nZ_0},
 \end{aligned}$$

where $Z_0 = 4\pi/c = 377$ Ohm, and n is the revolution harmonic number. LLD threshold lines, k_{th} versus I_{lim} , are presented in Fig (6) for SH RF, $k > 0$ and three distribution functions: $F(I) \sim (I_{\text{lim}} - I)^{1/2}$ (most stable), $F(I) \sim (I_{\text{lim}} - I)^2$ (medium stable) and $F(I) \propto (I_{\text{lim}} - I)^2 (1 + \cos(8\pi I / I_{\text{lim}}))$ (least stable). The last distribution mimics a coalesced proton bunch in the Tevatron [21]. It takes about an hour for memory of the constituent 7 bunches be smeared in the coalesced proton bunch in the Tevatron.

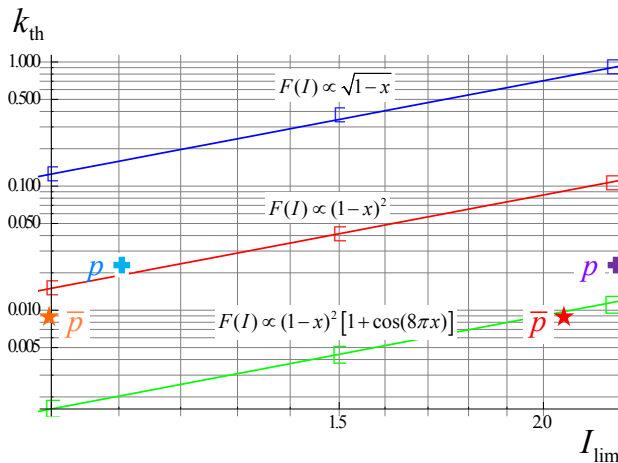


Figure 6: Threshold LLD intensity parameter k_{th} for SH RF versus the bunch emittance for 3 denoted distributions $F(I)$, where $x = I / I_{\text{lim}}$. Lines are fits with $k_{\text{th}} \propto I_{\text{lim}}^{5/2}$. Crosses and stars show

protons and antiprotons at Tevatron at injection (violet and red, on the right part) and top energy (blue and orange, on the left).

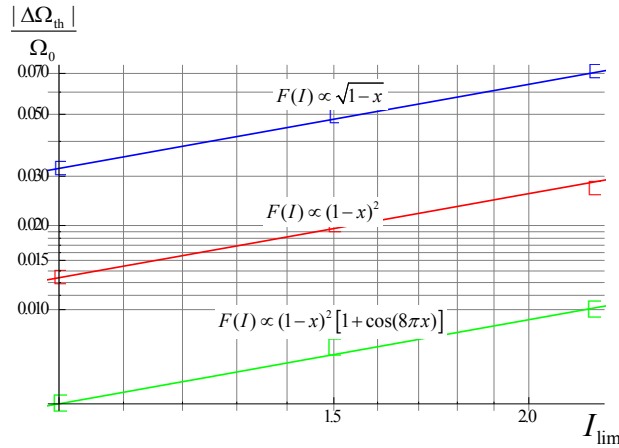


Figure 7: Same thresholds as above, in terms of the zero-amplitude relative incoherent frequency shifts. Lines are linear fits.

Threshold dependences $k_{th} \propto I_{lim}^{5/2}$, $\Delta\Omega_{th} \propto I_{lim}$ are in agreement with scaling law of Ref. [16]. The plots in Figs. (2,3,6,7) show the strong dependence of the threshold intensity on details of the distribution function. Qualitatively, this can be interpreted as a high sensitivity to steepness of the bunch distribution at small arguments. That high sensitivity should not be too surprising. Indeed, for both resistive wall and inductive impedances, the threshold phase space density k_{th} / I_{lim} goes down with the bunch length. It may sound counter-intuitive, but it is what is shown above: at a given phase space density, the least stable are the less populated bunches! A reason for that follows from a fact that, at fixed phase space density, the less populated bunch is shorter. The wake effect is stronger for shorter bunches, and the stabilizing frequency spread is weaker for them. That is why a small central portion of a bunch is less stable than the entire bunch. The ability of that small portion to be effectively disconnected from the entire bunch depends on the distribution function: the steeper the distribution at small amplitudes, the stronger this ability is.

According to the Tevatron impedance model [22], its proton bunches at injection are 2 times above the green line LLD threshold of Fig. (6). At the top energy, they are ~ 20 times above that threshold. This agrees with the observations: in the reality, the protons were always “dancing” in the Tevatron, unless the damper was on [21]. According to these calculations, the antiprotons stay slightly below the green line threshold at injection, and they are ~ 10 times above it at the top energy. In reality, they are stable at injection, and unstable at collisions. To conclude, both proton and antiproton stability observations are in agreement with the model described.

Since the LLD threshold strongly depends on the small-argument steepness of the distribution function, its local flattening there should increase the LLD threshold. That local flattening can be realized by means of RF phase modulation at a narrow frequency band around the zero-amplitude synchrotron frequency, smearing the distribution for the resonant particles. Dedicated experiments with this bunch shaking were performed at the Tevatron; it was realized that this bucket shaking indeed stops bunch dancing, see Ref. [23].

It may be supposed that LLD was a reason for the persistent bunch oscillations observed at RHIC [24, 25] and CERN SPS [19] as well. To the author's point of view, the LLD explanation is rather a supplement than a competitor to the soliton theory of Refs. [24, 25]. Indeed, being linear, LLD describes a mode growth from whatever small initial perturbation due to multi-turn or couple-bunch wakes. This growth can be saturated at nonlinear stage of the coherent motion, where the soliton theory takes over.

2.11.7 Conclusions

This paper includes a general treatment of a bunch self-consistent steady state in a distorted potential well, and van Kampen mode analysis for the steady state case. Criteria of existence and uniqueness for the steady state problem in action and Hamiltonian domains are formulated. A relaxation method for numerical solution of the steady state problem is described and used.

The language of van Kampen modes is a powerful tool for studying beam stability. This method leads to an eigensystem problem, so it is straightforward to implement numerically. Sum of the growth rates of the emergent discrete modes is zero; thus, some of them do not decay; there is loss of Landau damping for them. By definition, the discrete modes lie outside the continuous incoherent spectrum, but they may still stay within the bucket. In the last case, the discrete mode would disappear after a tiny portion of resonant particles being added. However, if the discrete mode lies outside the bucket, Landau damping cannot be restored by a tiny perturbation of the particle distribution; this sort of LLD is characterised as radical.

For a given bunch emittance and RF voltage, the intensity is limited either by reduction of the bucket acceptance or by (radical) LLD. In this paper, results are presented for longitudinal bunch stability in the weak head-tail approximation for resistive wall and inductive impedances. For the resistive wall impedance, three RF configurations are studied: single harmonic (SH), bunch shortening (BS) and bunch lengthening (BL). It is shown that every one of these RF configurations may be most preferable, depending on the bunch emittance and intensity.

The LLD threshold intensities are typically very low. For the cases under study, the threshold low-amplitude incoherent frequency shifts vary from 10% to 1% at full bucket. Although LLD itself means in many cases the emergence of a mode with zero growth rate, even a tiny multi-turn or couple-bunch wake can drive the instability for the discrete mode. In that sense, LLD is similar to the loss of the immune system of a living cell, when any microbe becomes fatal for it.

Specific results of this paper agree with the power laws for LLD suggested by Ref. [16]. However, the numerical factors obtained here for these laws strongly depend on the bunch distribution function. Particularly, for SH RF and inductive impedance above transition, for the three examined distributions, the highest LLD threshold intensity exceeds the lowest one by almost two orders of magnitude. Based on that observation, a method of beam stabilization was suggested and implemented [23].

The author is thankful to V. Lebedev and E. Shaposhnikova for useful discussions.

2.11.8 References

1. N. G. van Kampen, *Physica (Utrecht)* 21 (1955) 949.
2. N. G. van Kampen, *Physica (Utrecht)* 23 (1957) 647.

3. G. Ecker, "Theory of Fully Ionized Plasmas", Academic Press, 1972.
4. A. Burov, "Van Kampen modes for bunch longitudinal motion", Proc. HB 2010, Switzerland.
5. A. Burov, "Dancing bunches as van Kampen modes", Proc. PAC'11, New York.
6. M. Heñon, Astron. Astrophys., 114, 211-212 (1982).
7. K. Oide and K. Yokoya "Longitudinal Single-Bunch Instability in Electron Storage Rings", KEK Preprint 90-10 (1990).
8. A. Chao, "Physics of Collective Beam Instabilities", Wiley Interscience, 1993.
9. J. Haissinski, Nuovo Cimento 18B, No. 1, 72 (1973).
10. A. Burov, "Bunch lengthening, self-focusing and splitting", Thesis (in Russian) (1991).
11. O. Penrose, Phys. Fluids, **3**, 258 (1960).
12. A. N. Lebedev, Atomnaya Energiya 25 (2), p. 100 (1968).
13. M. D'yachkov and R. Baartman, Part. Acc. 50, p.105 (1995); also TRIUMF preprint TRI-PP-94-45 (1994).
14. Y. Shobuda and K. Hirata, Phys. Rev. E, v. 60 (2), p. 2414 (1999).
15. O. Boine-Frankenheim and T. Shukla, Phys. Rev. ST-AB, 8, 034201 (2005).
16. A. Hofmann and F. Pedersen, IEEE Trans. Nucl. Sci. **26**, 3526 (1979).
17. V. I. Balbekov and S. V. Ivanov, "Longitudinal beam instabilities in proton synchrotrons", Proc. 13th Int. Conf. On High-Energy Acc., Novosibirsk, 1987, v. 2, p.127 (in Russian).
18. E. Shaposhnikova, CERN SL/94-19 (RF), 1994.
19. E. Shaposhnikova, "Cures for beam instabilities in CERN SPS", Proc. HB 2006 Conf., Tsukuba, 2006.
20. T. Argyropoulos, E. Shaposhnikova, and A. Burov, "Loss of Landau Damping for Inductive Impedance in a Double RF System", Proc. IPAC 2013, Shanghai, China.
21. R. Moore et al., "Longitudinal bunch dynamics in the Tevatron", Proc. PAC 2003, p. 1751 (2003).
22. Fermilab report, "Run II Handbook" http://www-bd.fnal.gov/lug/runII_handbook/RunII_index.html, p. 6.58 (1998).
23. C-Y Tan and A. Burov, Phys. Rev. Accel. Beams **15**, 044401 (2012).
24. M. Blaskiewicz et al., "Longitudinal solitons in RHIC", Proc. PAC 2003, p. 3029.
25. M. Blaskiewicz et al., Phys. Rev. ST Accel. Beams **7**, 044402 (2004).

2.12 Impedance-Induced Beam Instabilities and Damping Mechanisms in Circular Machines – Longitudinal - Simulations

M. Migliorati^(1,2), D. Quartullo^(1,3)

¹⁾University of Rome La Sapienza - Italy, ²⁾INFN-Roma1 - Italy,

³⁾CERN, 1211 Geneva 23, Switzerland

Mail to: mauro.migliorati@uniroma1.it

2.12.1 Introduction

When studying the dynamics of high intensity beams, in addition to the external guiding fields, it is necessary to take into account, in a self-consistent way, the effects of the self-induced electromagnetic fields, for which in time domain we use the word wakefields, and in frequency domain coupling impedances [1]. In this article we discuss the principal issues and solutions which emerge from simulation codes dealing with longitudinal beam instabilities induced by coupling impedances in circular machines.

To simplify the beam dynamics study, it is generally convenient to distinguish between short-range wakefields, which influence the single turn beam dynamics (often also called single bunch beam dynamics), and long-range wakefields, which last for many turns, are generated by resonant electromagnetic modes with high quality factors, are excited by one or a train of bunches, and produce, under some conditions, coupled-bunch instabilities (multi-turn or multi-bunch beam dynamics). In both cases a linear perturbation theory is generally used to study analytically these instabilities.

However, in order to analyze the behavior of the beam under the influence of wakefields also in the non-linear regime, and for more reliable results, very often simulation codes are used. In these codes, which take into account collective effects related to impedance-induced instabilities, the used equations of motion of a single charge in a bunch are quite simple. However, the inclusion of the effects of wakefield, which is also called beam induced voltage, and which couples the motion of different particles, can be very tricky due to the possible introduction of numerical noise and non-physical phenomena.

The basic idea behind the numerical calculation of the beam induced voltage in longitudinal beam dynamics codes has not changed since the 1980s [2]. The first official release in 1984 of the well-known FermiLab code ESME [3] has been an important reference for many years to calculate the beam induced voltage and its effect on the beam dynamics. Over a period of more than thirty years, several codes using short-range wakefields for longitudinal [4,5,6] and transverse [7,8] beam dynamics, long-range wakefields [9,10], and both short- and long-range wakefields [11,12,13] in circular accelerators have been developed and have been proved to be reliable tools in the comprehension of the collective effects. Many laboratories prefer to rely on their own codes, such as, for example, Fermilab (United States) [14], CERN (Switzerland) [7,15], J-PARC (Japan) [16], CSNS (China) [17]. All these codes use the same techniques or close variants. Certainly the code evolution cannot be compared with the exponential increase in computational power during the past forty years [18].

In order to include the wakefields in a simulation, a convolution sum, which takes into account the electromagnetic fields acting on a charge and produced by all the others, is needed. This issue is discussed in the following section. The evaluation of the effects of short- and long-range wakefields generally requires different approaches which are reviewed in sections 2.12.3 and 2.12.4 respectively, while in section 2.12.5 we briefly

mention some damping mechanisms, both natural and induced, that can be included in simulations, and, finally, other methods of simulation for impedance-induced instabilities, different from tracking codes, are presented in section 2.12.6.

2.12.2 Common Approach in Wakefield Simulations

In order to write the longitudinal equations of motion of a single particle in a circular accelerator to be used in a simulation code, we assume, for simplicity, that the energy exchange between a charge and the surrounding accelerator environment is localized in a single place of the machine. In addition, we suppose that the minimum time interval to be integrated is the revolution period T_0 , and the variation of the charge longitudinal position and energy with respect to the synchronous particle is evaluated every T_0 . These assumptions are generally satisfied in many circular machines. However, in some particular cases, they are not valid. For example, the FCC accelerator [19] has a design circumference of about 100 km, and the previous approximations are too rough. In such cases it is possible to divide the circumference in several sectors and apply the procedure here described to each sector. Also the inclusion of the space charge generally requires to split the circumference, since the local effect of this force varies over one turn because of different environment conditions along the ring, such as beam pipe cross section shapes and dimensions.

If we call ε the energy difference of a charge q with respect to the synchronous particle divided by the nominal energy, which we consider equal to the synchronous particle energy E_s , its variation in one turn, $\Delta\varepsilon$, depends on the energy gain due to the RF system, on the beam induced voltage, and on other sources of energy exchange, such as the synchrotron radiation, possible higher order RF cavities for bunch length control, electron cooler, betatron acceleration due to changing magnetic field in synchrotrons [20], etc.

Without loss of generality, let us consider here only the energy exchange due to the main RF system, the wakefield and the synchrotron radiation, so that $\Delta\varepsilon$ can be written as:

$$\Delta\varepsilon = \frac{qV_{RF}(\sin\phi - \sin\phi_s) - qV_{WF}(\phi) + R(T_0)}{E_s} - 2\frac{T_0}{\tau_s}\varepsilon \quad (1)$$

where V_{RF} is the RF peak voltage, $V_{WF}(\phi)$ the induced wakefield voltage, $R(T_0)$ a stochastic variable changing each turn and taking into account the fact that the electromagnetic radiation occurs in quanta of discrete energy, and τ_s the longitudinal damping time, these last two terms related to synchrotron radiation effects and important, in particular, in electron machines [21]. In the above equation, ϕ and ϕ_s are the phases, with respect to the RF voltage, of the charge q and of the synchronous particle, respectively. The value of ϕ_s depends on the acceleration in synchrotrons and on the energy loss per turn due to synchrotron radiation. In the above equation, if necessary, it is possible to add terms due to other sources of energy exchange.

The second quantity necessary to describe 1-D motion in simulations is related to the longitudinal position of the charge with respect to the synchronous particle. Its variation in one turn is given by the relation

$$\Delta(\phi - \phi_s) = -\frac{2\pi h\eta}{\beta^2}\varepsilon \quad (2)$$

with h the RF harmonic number, η the slippage factor equal to $1/\gamma^2 - \alpha_c$ with γ the relativistic factor and α_c the momentum compaction, and β the ratio between the particle velocity and the speed of light. In the above equation we have assumed $\phi - \phi_s > 0$ for a particle behind the synchronous one, that is with positive time delay.

The common approach used in longitudinal simulation codes models each bunch as an ensemble of particles, each one governed by the above two coupled equations, and tracks these particles turn after turn. Since in a bunch the number of charges is in the range $10^8 - 10^{12}$ and, sometimes, even more, it would be necessary a very high computing power, with the help of parallel clusters, to track all the particles. For this reason, generally, macro-particles, which gather together the behavior of a given number of charges, are used. The maximum possible number of simulated macro-particles depends on the available computing power, but, nowadays, codes with 10^7 charges can be run on a personal PC.

Without the presence of wakefield, the two equations can be easily solved turn by turn, and they are independent from one macro-particle to another. The term which couples the equations of different particles, making the tracking more complicated, is the induced wakefield voltage $V_{WF}(\phi)$. This is the voltage acting on a charge in a position ϕ , and induced by all the others. This voltage depends on the normalized longitudinal bunch distribution $\lambda(\phi)$ according to the relation

$$V_{WF}(\phi) = Q_{tot} \int_{bunch} d\phi' w_{||}(\phi - \phi') \lambda(\phi') \quad (3)$$

where the integration is performed over the bunch length, Q_{tot} is the total charge of a bunch, and $w_{||}$ is the wake function of a point charge or Green function. The convolution integral is also called wake potential. It represents the energy gained or lost by a unity charge due to the entire bunch. If a charge is travelling with the speed of light, due to the causality property, the upper bound of the integral can be stopped at ϕ because $w_{||}(x) = 0$ for $x < 0$. The opposite happens for simulations having coherent synchrotron radiation effect, for which the wake function is different from zero only ahead of the charge that created it. The above equation is valid only if we take into account the short-range wakefields. In order to include also the long-range wakefields for coupled bunch simulations, we have to add a sum over previous bunches and turns in the above convolution integral, as we will discuss in section 2.12.4.

In writing Eq. (3) we have described the behavior of the particle ensemble, representing a bunch, with a continuous distribution function, as it is generally done with theoretical methods, even if the real structure of a bunch is discrete. With a simulation code we have the opposite approach, which uses a number of macro-particles reduced with respect to the real number of charges in a bunch. In this case Eq. (3), or the expanded version with the long-range wakefields, can be transformed into

$$V_{WF}(\phi_i) = \frac{Q_{tot}}{N_m} \sum_{j=1}^{N_m} w_{||}(\phi_i - \phi_j) \quad (4)$$

with ϕ_i the longitudinal position of the i^{th} macro-particle and N_m the total number of macro-particles. If the bunch is travelling with the speed of light, due to the fundamental theorem of beam loading [22], in the above summation we have to use $w_{||}(0)/2$ instead of $w_{||}(0)$ when $\phi_i = \phi_j$. Equation (4) has to be evaluated at each turn and for each macro-

particle. This means that, at each turn, the calculation of wakefields in simulations requires in general N_m^2 operations, and $(N_m - 1)N_m/2$ for the ultra-relativistic case. In order to track $10^6 - 10^7$ macro-particles, at each turn more than 10^{11} operations are needed, and this task can be accomplished, at least for the moment, only on parallel computing clusters. In order to reduce the computing time and only in the evaluation of the wakefield effects, the bunch is generally divided into N_s slices, or bins, of width Δ and center $\phi_{i\Delta}$, each one containing $n_i(\Delta)$ macro-particles. By supposing that slices act as point charges, the induced voltage at the center of each slice is then evaluated by using the relation

$$V_{WF}(\phi_{i\Delta}) = \frac{Q_{tot}}{N_m} \sum_{j=1}^{N_s} n_j(\Delta) w_{||}(\phi_{i\Delta} - \phi_{j\Delta}) \quad (5)$$

Once the induced voltage is known in the positions $\phi_{i\Delta}$, a linear interpolation (or higher order ones) permits to evaluate the wake potential acting on any macro-particle of the bunch. Since in general the number of slices is between few hundreds to some thousands, this greatly reduces the number of operations.

This kind of approach has been widely used in simulations, and in the years it has demonstrated to give reliable results. However, a particular care has to be taken when deciding the size and the number of the slices (and, of course, of macro-particles). A low number of slices reduces the computing time, but it could suppress some physical microstructures in the bunch leading to instabilities. On the other side, slices can introduce numerical noise additional to that of macro-particles, making necessary, in some cases, a parametric study to investigate any possible dependence of the results on the number of slices and of macro-particles inside the slices.

One possible approach to determine the slice size is to plot the absolute value of the product of the bunch spectrum and the impedance. This allows to identify a certain f_{max} above which the product can be considered negligible. This frequency defines the length of the slices since $\Delta t_{slice} = 1/(2f_{max})$. Once the slices are fixed, the number of macro-particles is increased by steps until a convergence is reached.

2.12.3 Simulations With Short-Range Wakefields

Single-bunch simulations can be performed according to the previous equations once the short-range wake function $w_{||}$ of a circular accelerator, or the corresponding coupling impedance, is known.

The coupling impedance model of a machine is generally obtained with the help of dedicated electromagnetic computer codes, such as CST Particle Studio[®] [23], GdfidL [24], or ACE3P [25]. From the impedance, with the inverse Discrete Fourier Transform (DFT), the wakefield $w_{||}$ in Eq. (5) can be obtained. Another method to calculate directly the induced voltage in circular machines without the use of Eq. (5) is to multiply the impedance by the spectrum of the longitudinal distribution and take the inverse DFT of the result. Often these two methods in time and frequency domain give the same result, even if different numbers of slices and macro-particles have to be chosen to obtain the same accuracy. Of course particular attention has to be paid to the inverse DFT in order to avoid non-physical results.

One important problem that sometimes arises in simulations is the necessity to use a too high number of slices such that the code becomes too cumbersome and other solutions have

to be found. As an example, let us take the wake field of a broad-band resonator, which sometimes is used as a simplified impedance model of an accelerator. Depending on its resonant frequency and on the bunch length, it may happen that a high number of slices is necessary to properly reconstruct the correct induced voltage.

In Fig. 1 we show, for example, the induced voltage for a broad-band resonator with unit quality factor, produced by a Gaussian bunch with RMS bunch length 2.4 times higher than the resonant wavelength in the relativistic case. If we consider that, generally, for single bunch simulations, a longitudinal interval of $\pm 5\sigma$, with σ the RMS bunch length, is used, in order to have about 20 slices for wavelength, about 480 slices are needed. Indeed, from the figure, we can see that, with 500 slices, Eq. (5) for the Gaussian bunch gives a slightly different result (green line) with respect to the theoretical wake potential, and only with $1e3$ slices (red curve) the induced voltage is very close to the theoretical one, represented with the black curve.

With such a high number of slices, also a very high number of macro-particles has to be used, because there is the need to have a reasonable number of particles in each slice for proper beam simulations. If the number is not sufficiently high, the strong fluctuations of macro-particles from one slice to another could produce non-physical effects.

There is however the possibility to bypass this problem by using, in Eq. (5), instead of the Green function, the wake potential (induced voltage) of a very short Gaussian bunch. Indeed, in the same figure, with the cyan dashed line, we have also represented the induced voltage as given directly by a simulation with only 100 slices, for which we have used in Eq. (5) in place of $w_{||}$, the wake potential of a Gaussian bunch 10 times shorter than the simulated one. As can be seen from the figure, with 100 slices we obtain a result similar to that obtained with 1000 slices and the Green function. Also with the method in frequency domain described at the beginning of this section, it is possible to obtain the correct induced voltage with only about 150 slices.

2.12.4 Simulations With Long-Range Wakefields

For the multi-bunch simulations, in addition to the slice problem, the main issue is the necessity to know the wakefield as a function of time until it becomes zero. Since the long range wakefields are generated by resonant modes with a high quality factor, depending on its value and on the resonant frequency, these modes can last for several hundreds of nanoseconds up to microseconds, influencing many bunches for many turns, and then requiring the calculation of a very long interaction of the wakefield with the beam.

Different simulation codes have different approaches to tackle this problem.

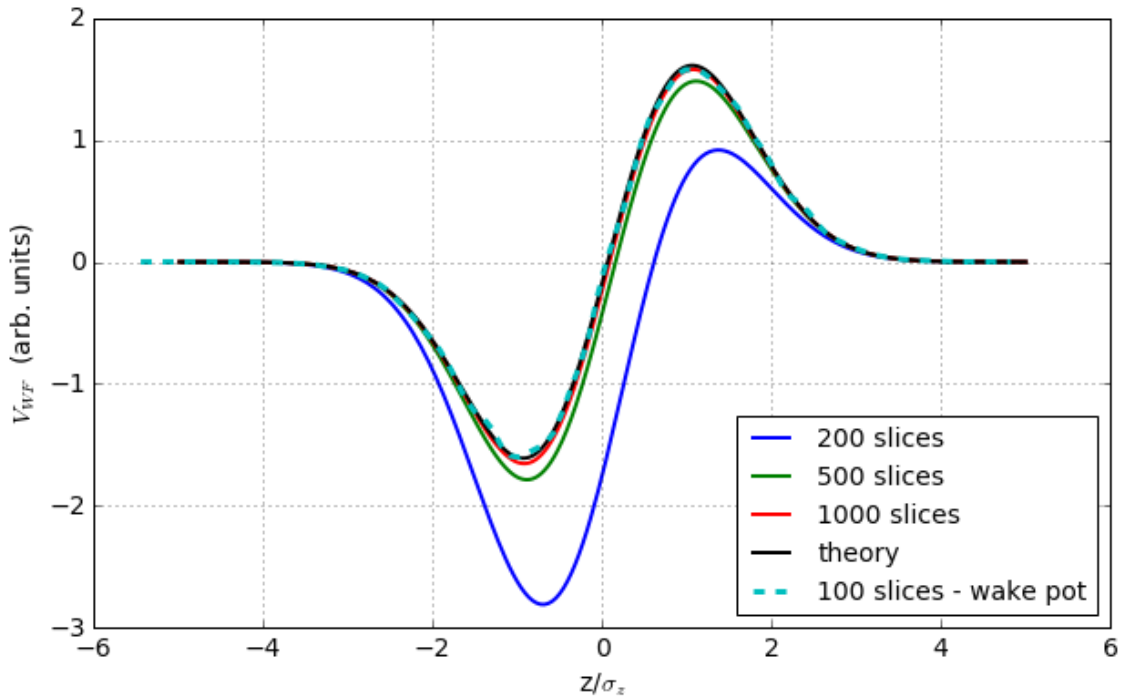


Figure 1: Induced beam voltage for a broad-band resonator produced by a Gaussian bunch with RMS length a factor 2.4 higher than the resonant wavelength. The voltage has been obtained by using 200 slices (blue), 500 slices (green), 1000 slices (red). The cyan dashed line represents the induced voltage obtained with only 100 slices by using, as Green function, the wake potential of a Gaussian bunch 10 times shorter. The black line is the theoretical induced voltage.

For example, in the BLoND code [13], different routines can be selected depending on the length of the wakefield. In particular, two different approaches are used to memorize the long range wakefields. The first one stores into memory, at each turn, the sum of the present induced voltage extended to the future and the induced voltage derived from the past after appropriate time shift of one revolution period. A complication arises in presence of acceleration: the time frame, which length is the revolution period, shrinks turn after turn and, as a consequence, an interpolation is needed each turn when the present voltage is summed to the voltage from the past.

To avoid potentially expensive interpolations in computing time, another approach, operating in frequency domain, has been introduced considering that a multiplication of a Fourier-transformed function by a complex exponential in frequency domain is equivalent to a shift of the same function in time domain. The algorithm uses a $M \times N$ matrix with M the number of turns to be stored, and N the number of slices (this time of the whole accelerator and not of the single bunch) times M . At each turn the beam spectrum is multiplied by the impedance and the result saved into a matrix row. All the remaining rows are multiplied by a complex exponential to shift the past induced voltage by one turn, all the rows are summed element by element, and the result, after an inverse DFT, gives the induced voltage in the present time frame. After the last row of the matrix is filled in, at the turn $M + 1$, the first row of the matrix is overwritten, since the known wakefield has a length corresponding to M turns. The downside of this second approach is that the size of M influences heavily the computation time and the user has to choose wisely which method to use depending on the simulation parameters.

Another method, used in the tracking parallel code SPACE [11], expands the long range wake force in Taylor series and stores the moments of the longitudinal distribution of all the bunches in previous turns. This method requires a slowly varying wake function and, in addition, the number of terms N_{TL} for the Taylor expansion has to be wisely chosen together with the order of the method to calculate the N_{TL} derivatives of the wake. However, the strength of the algorithm derives from the fact that the induced voltage acting on a certain bunch can be calculated in parallel via master-to-slave processor communications. This means that at each turn, after having applied the single particle equations of motion, the various moments of the present longitudinal bunch profiles are calculated independently by different processors. These independent computations are then communicated to the master processor which can sum them to the other calculated moments from previous turns which have been stored into memory.

In some cases, mostly when the distance between the source and the test charges is big, it is reasonable supposing that the wake function doesn't change significantly. This idea has been implemented in [10]. Whenever the wake amplitude does not change more than 0.1% in a certain longitudinal frame, then all the slices contained in that window are replaced by a single slice characterised by a wake that is just an average of the wake values of all the concerned slices. The frame length can be even of the order of the bunch length or the revolution period. Using this approximation, the convolution sum to calculate the long range wakefields can be significantly simplified.

An alternative approach, which has been developed and used in the simulation code MuSiC [12], exploits a matrix formalism to transport the wakefield of resonators, both broadband and narrow band, from one macro-particle to the following one, removing the necessity to resort to the convolution sum, avoiding problems related to bunch slices, and eliminating the necessity to store long range wakefields. The code allows to simulate, simultaneously, the effects of short and long range wakefields without the necessity to distinguish between the single and multi-bunch beam dynamics and including intra-bunch motion. It also contains a frequency domain feedback system to damp coupled bunch instabilities. The drawback of the MuSiC approach is that it requires to fit the machine coupling impedance with a sum of resonators, which are used as input parameters in place of the wakefield.

2.12.5 Damping Mechanisms

Intrinsic damping mechanisms, such as Landau damping, are naturally included in simulation codes if the number of macro-particles is high enough. Cases of Landau damping effects in simulations can be found in Refs. [12, 15, 26]. Also the radiation damping is simulated by means of the last term in Eq. (1). A particular mention regards feedback systems. For example, a coupled bunch feedback can be simulated in a given point of the machine exchanging energy with the macro-particles. The correct amount of energy to be exchanged has to be evaluated according to the kind of feedback. In case of time domain, for example, each bunch is treated separately by the others, while in frequency domain the motion of all the bunches has to be first decomposed as sum of eigenmodes, turn after turn, and then the feedback energy kick acting on each eigenmode has to be proportional to its oscillation amplitude.

Examples of coupled bunch feedback systems included in simulation codes can be found in Refs. [15, 27] for the time domain, and in Ref. [12] for the frequency domain.

2.12.6 Vlasov-Fokker-Planck Solvers and Other Methods

In addition to simulation codes, which track macro-particles turn after turn, a different approach can be used, and it consists in solving numerically the time domain Vlasov-Fokker-Planck equation with the inclusion of wakefields.

By considering the same effects discussed for Eq. (1), that is damping and fluctuations produced by the synchrotron radiation, the Vlasov's nonlinear integro-differential equation, with the inclusion of the Fokker-Planck terms, can be written as [28]

$$\frac{\partial f}{\partial t} + \frac{\partial f}{\partial q} \frac{\partial H}{\partial p} - \frac{\partial f}{\partial p} \frac{\partial H}{\partial q} = 2 \frac{T_0}{\tau_s} \frac{\partial}{\partial p} (pf) + D \frac{\partial^2}{\partial p^2} f \quad (6)$$

where f is the phase space longitudinal distribution, (q, p) are the canonical coordinates related to the position ϕ and relative energy ε respectively, H the Hamiltonian accounting for both the external fields and the collective force produced by the wakefields, and D a diffusion constant of the random process related to $R(T_0)$. If the right hand side of Eq. (6) is zero, hypothesis valid, for example, with a good approximation for proton beams, we have the so-called Vlasov equation. In writing the above equation, we made a sort of smooth approximation in which the dissipation and fluctuations are distributed homogeneously in the independent variable t . The nonlinearity in Eq. (6) derives from the collective force contained in the Hamiltonian, which is proportional to the convolution integral between the wakefield and the longitudinal distribution, according to Eq. (3).

As first approach, it would seem that the above equation could be treated by the usual methods for partial differential equations, as the finite differences, to approximate the phase space longitudinal distribution function f on nodes of a finite grid.

However, such a technique fails completely with or without implicit time stepping, and not because of any effect of the nonlinear terms, but because it does not preserve the symplectic form. Different and more appropriate methods must therefore be applied to preserve the symplectic structure of the equation, as, for example, the one of Ref. [29], where the integration of the equation is based on discretization of the local Perron Frobenius operator. In Ref. [30] instead, an algebraic technique of solution, that is suited for general evolution-type equations and that can also be applied to the Vlasov equation, extended to the non-linear case, has been developed, and it is based on the evolution operator technique, widely exploited in the solution of quantum mechanical problems.

Codes solving Vlasov-Fokker-Planck equations have been developed to study single bunch effects [31, 32] as alternative to multi-particle tracking codes, and they generally guarantee a very smooth evolution of the beam distribution function in time that allows to reduce, and in some cases to completely eliminate, the effect of numerical noise. Usually, the computing time for a simulation solving the Vlasov-Fokker-Planck equation is comparable to that of the multi-particle tracking codes because the problem due to the slices previously discussed is avoided, but, in any case, in order to calculate the collective force in the Hamiltonian term, the convolution integral of Eq. (3) has to be performed over a finite phase space grid.

2.12.7 References

1. L. Palumbo, V. G. Vaccaro, M. Zobov, CERN 95-06, pp. 331-390, CERN, Geneva, Switzerland (1995).

2. R. H. Siemann, CLNS 84/626 (1984).
3. J. A. MacLachlan, J. F. Ostiguy, Proceedings of 17th Particle Accelerator Conference, Vancouver, Canada, 12 - 16 May 1997, pp. 2556.
4. G. Dattoli, et al., NIMA 471, pp. 403-411 (2001).
5. R. Boni, et al., NIMA 418, pp. 241-248 (1998).
6. D. Alesini, et al., Phys. Rev. ST Accel. Beams, 6 (074401) (2003).
7. G. Rumolo and F. Zimmermann, Phys. Rev. ST Accel. Beams, 5 (121002), (2002).
8. M. Blaskiewicz, Phys. Rev. ST Accel. Beams, 1 (044201), (1998).
9. D. Briggs, et al., IEEE Particle Accelerator Conference, San Francisco, May 6-9, (1991).
10. N. Mounet, PhD Thesis, EPFL, Lausanne, Switzerland, (2012).
11. G. Bassi, A. Blednykh, and V. Smaluk, Phys. Rev. Accel. Beams, 19 (024401), (2016).
12. M. Migliorati, L. Palumbo, Phys. Rev. ST Accel. Beams, 18 (031001), (2015).
13. D. Quartullo, S. C. P. Albright, E. N. Shaposhnikova, H. Timko, Proceedings of HB2016, Malmö, Sweden, July 2016, pp. 140-145.
14. V. A. Lebedev, J. F. Ostiguy, C.M. Bhat, "Modeling Longitudinal Dynamics in the FERMILAB Booster Synchrotron", Proceedings of IPAC2016, Busan, Korea.
15. H. Timko, J. Esteban Müller, A. Lasheen, and D. Quartullo, "Benchmarking the Beam Longitudinal Dynamics Code BLonD", Proceedings of IPAC2016, Busan, Korea.
16. M. Yamamoto, Proceedings of HB2016, Malmö, Sweden, July 2016, pp. 110-114.
17. Y. Yuan, N. Wang, S. Xu, S. Wang, "A Code for the Optimization of RF Voltage Waveform and Longitudinal Beam Dynamics Simulation in an RCS", Nuclear Instruments and Methods in Physics Research A729 (2013) 864-869.
18. R. D. Ryne, "Advanced Computing Tools And Models For Accelerator Physics", Proceedings of EPAC08, Genoa, Italy.
19. <https://fcc.web.cern.ch/Pages/default.aspx>.
20. J. A. MacLachlan, "Difference Equations for Longitudinal Motion in a Synchrotron", FN-529, Fermilab (USA), (1989).
21. M. Sands, "The Physics Of Electron Storage Rings - An Introduction", SLAC- 121 UC-28 (ACC), Univ. of California, Santa Cruz, USA, (1970).
22. P. B. Wilson, AIP Proc. 87, Phys. High Energy Accel., Fermilab, 1981, p. 450.
23. CST AG, Darmstadt, Germany, <http://www.cst.com>.
24. W. Bruns, IEEE Particle Accelerator Conference, Vancouver, B.C., Canada, p. 2651, (1997).
25. See, e.g., L. Ge et al, Proceedings of IPAC2015, Richmond, VA, USA, May 2015, pp. 720-704.
26. T. Sen, C. M. Bhat, H. J. Kim, J-F Ostiguy, "Dynamics of Flat Bunches with Second Harmonic RF", Proceedings of IPAC2010, Kyoto, Japan.
27. S. Bartalucci, et al., Particle Accelerators , 1995, Vol. 48, pp. 213-237.
28. See, e. g., K. Y. Ng, "Physics of Intensity Dependent Beam Instabilities", Fermilab-FN-0713, January 2002.
29. R. L. Warnock, J. A. Ellison, SLAC PUB-8404, March, 2000.
30. M. Migliorati, A. Schiavi, G. Dattoli, Proceedings of ICAP 2006, Chamonix, France, pp. 110-113.
31. R. L. Warnock, Nucl. Instrum. Methods Phys. Res., Sect. A 561, (2006) 186-194.
32. G. Dattoli, M. Migliorati, A. Schiavi, Nucl. Instrum. Methods Phys. Res., Sect. A

574 (2007) 244–250.

2.13 Head-Tail and Transverse Mode-Coupling Instabilities (TMCI)

Yong Ho Chin

KEK, 1-1 Oho, Tsukuba-shi, Ibaraki-ken, 305-0803, Japan

Mail to: yongho.chin@kek.jp

2.13.1 Introduction

In this article, we first describe the head-tail instability, as much as visually, so that readers can get fresh and vivid ideas about this classical phenomenon. We then review Sacherer's head-tail instability theory and Transverse Mode-Coupling Instability (TMCI) theory to get more quantitative understanding. The article is concluded with some historical records on how the concept of "mode-coupling" was developed, not only in transverse instabilities (TMCI), but also in longitudinal ones (the bunch lengthening) in early 1980s.

2.13.2 Head-Tail Instability

In a long proton bunch, every parts along the longitudinal direction do not have to oscillate together transversely. For example, it is possible that the head and the tail of the bunch oscillate 180 degrees out of phase, as illustrated in Fig. 1 (right).

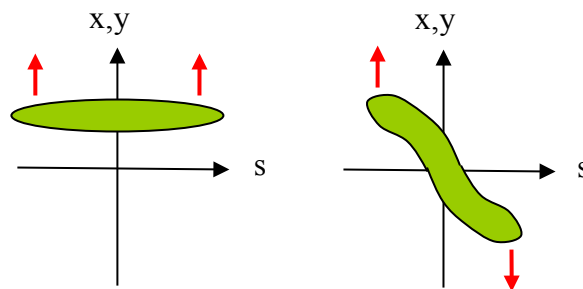


Figure 1: Snapshots of beam oscillations when the head and the tail of a bunch oscillate in phase (left) and out of phase (right).

In order for the head and the tail of the bunch to oscillate 180 degrees out of phase, we need a fast oscillating wake field which changes the phase by 180 degrees during the passage of the bunch. Such rapid phase oscillation is possible only by high frequency impedance. For synchronizing with the high frequency impedance, the intra-bunch motion needs to be more complex than a simple dipole oscillation. That introduces the synchrotron motion.

Let us explain the head-tail effect using the two-particle model (see Fig. 2). Only the particle behind can feel the wake fields created by the particle ahead. Since the degree of freedom is two (two particles), we have two modes in which the head and the tail of the bunch oscillate either in phase or out of phase, as illustrated in Fig. 3. Their motion can be unstable depending on the strength of the bunch intensity.

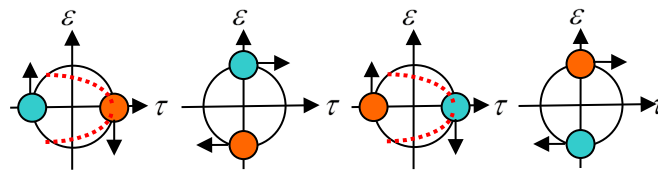


Figure 2: Position of the two particles in the synchrotron phase space and wake fields at every quarter of the synchrotron oscillation. The wake fields are denoted by the red dashed lines.

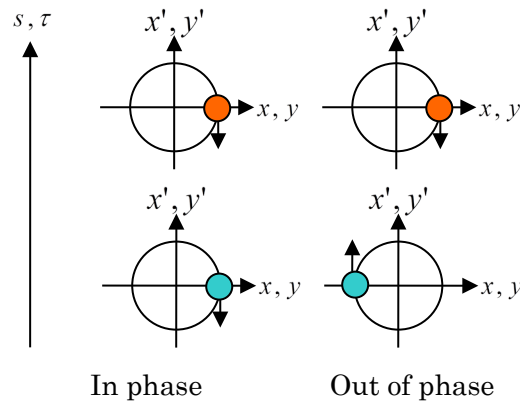


Figure 3: Two modes in which the head and the tail of the bunch oscillate in phase (left) and out of phase (right).

Unstable coherent oscillations with different betatron phase advances inside a bunch have been observed in many machines such as CERN PS. This phenomenon was called the head-tail instability [1-3]. Figure 4 shows the measured signals of the dipole moment at CERN PS Booster [2].

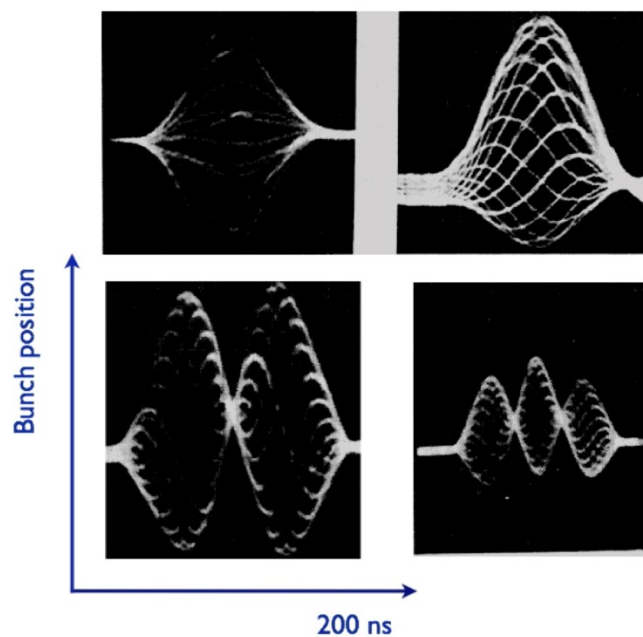


Figure 4: The measured signals of the dipole moment at CERN PS Booster [2].

2.13.3 Sacherer's Head-Tail Instability Theory

The important element of Sacherer's head-tail instability theory is the chromaticity. It is defined by

$$\xi = \frac{d\omega_\beta}{\omega_\beta} / \delta \quad (1)$$

where ω_β is the angular betatron frequency and $\delta = \Delta p/p$ is the relative momentum deviation. In other words, the betatron frequency depends on the momentum deviation as

$$\omega_\beta(\delta) = \omega_{\beta 0}(1 + \xi\delta). \quad (2)$$

When a particle moves along the ring, the accumulated betatron phase advance is developed as

$$\begin{aligned} \phi_\beta(s) &= \int \omega_\beta(\delta) \frac{ds}{\beta c} = \omega_{\beta 0} \left(\frac{s}{\beta c} + \xi \int \delta \frac{ds}{\beta c} \right) \\ &= \omega_{\beta 0} \left(\frac{s}{\beta c} - \frac{\xi}{\eta} \tau \right) \equiv \omega_{\beta 0} \frac{s}{\beta c} - \omega_\xi \tau \end{aligned} \quad (3)$$

where τ is the arrival time difference of the particle at the position s (positive toward the head of bunch), βc is the velocity of the particle, and η is the slippage factor. Thus, the betatron phase advance varies linearly along the bunch and attains its minimum (maximum) at the head (tail) of the bunch as illustrated in Fig. 5.

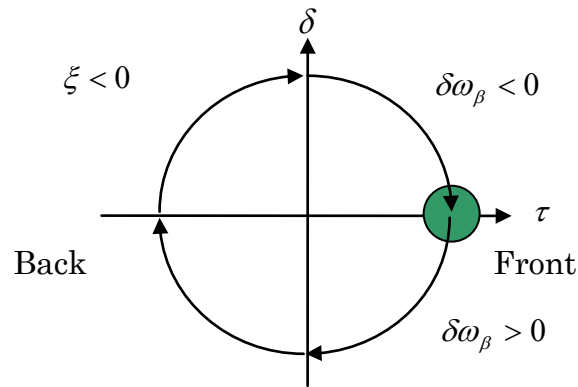


Figure 5: Change of the betatron oscillation below transition energy ($\eta < 0$).

To investigate how the difference of phase advance between the head and the tail of the bunch varies over one synchrotron oscillation period, let us look at the four-particle model in the synchrotron phase space, as illustrated in Fig. 6 [4]. We assume that the arrival time is oscillating as

$$\tau = \hat{\tau} \cos(2\pi\nu_s k), \quad (4)$$

where ν_s is the synchrotron oscillation tune and k is the revolution turn. We also assume that the chromaticity is negative and the ring is operated below the transition energy ($\eta < 0$). Thus particles move clockwise in synchrotron phase space.

In principle, the betatron phase advance slows down (quickens up) by $\omega_\xi \hat{\tau}$ for every quarter period of synchrotron oscillation as the particle moves forward (backward) along the synchrotron orbit, respectively. As can be seen in Fig. 6, the initial phase relationship along the bunch is preserved after the quarter period of synchrotron oscillation. One can quickly check that the phase pattern remains stationary over the full period of the synchrotron oscillation. In other words, the difference of the phase advance between the head and the tail of the bunch is constant, and we denote this constant as χ :

$$\chi = \phi_{\beta Tail} - \phi_{\beta Head} = 2\omega_\xi \hat{\tau} = \text{constant} \quad (5)$$

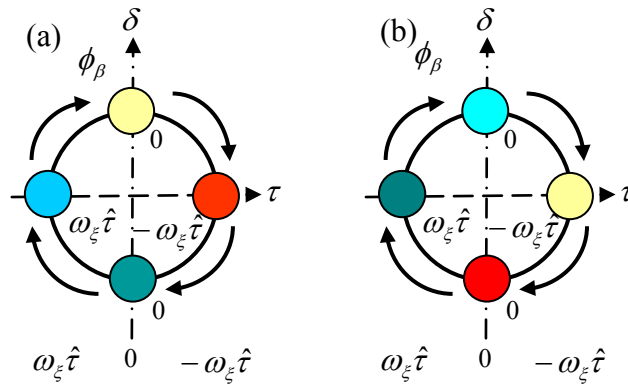


Figure 6: (a) The initial phase advance setting of the four particles. (b) The phase advance after a quarter period of the full synchrotron oscillation. The phase difference between the head and the tail of the bunch remains the same: $\chi = \phi_{\beta Tail} - \phi_{\beta Head} = 2\omega_\xi \hat{\tau}$ after a quarter period of the full synchrotron oscillation.

Let us assume that the dipole moment observed at a single point in the ring has the following standing wave pattern [1]:

$$p_m(t) = \begin{cases} \cos(m+1)\pi \frac{t}{\tau_L} \propto \frac{1}{2} \left(\exp(i(m+1)\pi \frac{t}{\tau_L}) + \exp(-i(m+1)\pi \frac{t}{\tau_L}) \right) & m = 0, 2, 4, \dots \\ \sin(m+1)\pi \frac{t}{\tau_L} \propto \frac{1}{2i} \left(\exp(i(m+1)\pi \frac{t}{\tau_L}) - \exp(-i(m+1)\pi \frac{t}{\tau_L}) \right) & m = 1, 3, 5, \dots \end{cases} \quad (6)$$

where τ_L is the total bunch length. The transverse pick-up signal observed at that point on the k -th revolution turn is given by

$$I_m(t) \propto p_m(t) \exp(i\phi_\beta(s)) = p_m(t) \exp(i\omega_\xi t + i2\pi k \nu_{\beta 0}), \quad (7)$$

where $\nu_{\beta 0}$ is the betatron tune. Typical time evolutions of the transverse oscillation signals are shown in Fig. 7.

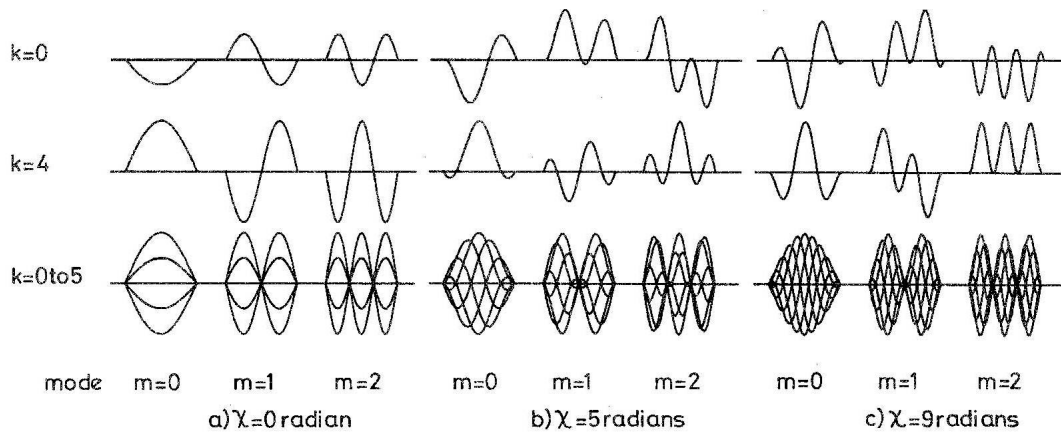


Figure 7: Typical time evolutions of the transverse oscillation signals for different χ [2].

The effect of the travelling-wave component $\exp(i\omega_\xi t + i2\pi k v_{\beta 0})$ over the standing-wave dipole moment $p_m(t)$ is to shift the bunch spectrum by ω_ξ . Figure 8 shows an example where the transverse resistive-wall impedance and the narrow-band kicker impedance are shown as impedance examples. The spectra are drawn for the head-tail modes 0 and 1 with positive phase difference χ . In this example, the mode 0 is stabilized, while the mode 1 becomes unstable by the transverse resistive-wall impedance at low frequency.

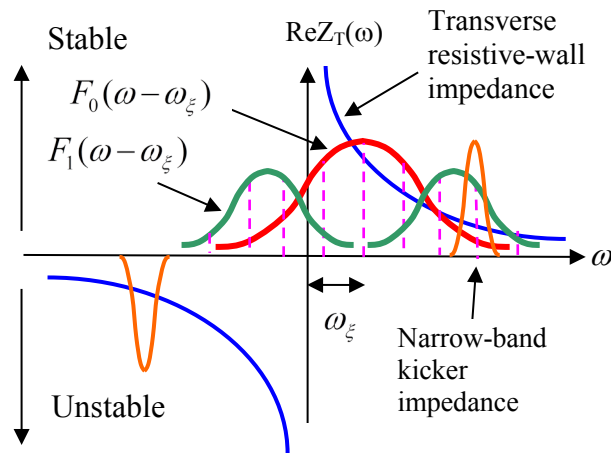


Figure 8: An example of the bunch spectrum shift by non-zero chromaticity.

The physical reason for the spectrum shift is as follows. When χ is large, the head and the tail of the bunch oscillate with large betatron phase difference. In order to excite such an intra-bunch oscillation, the wake field has to change its phase rapidly during the passage of the bunch. In other words, the impedance around the frequency ω_ξ can now best synchronize with the fast intra-bunch motion.

The shift of the left peak of the bunch spectrum of the mode 1 means that a part of the mode now oscillates slowly. The head and the tail of the bunch will move almost in phase,

not out of phase, to synchronize with the low frequency impedance. On the other hand, the shift of the right peak of the mode 1 bunch spectrum implies that this part of the mode now oscillates faster. In summary, the mode $m=1$ is degenerated at zero chromaticity, but are now split to slower and faster oscillating parts by non-zero chromaticity. These split modes are equally excited due to the standing-wave condition of head-tail modes, and thus they always have a node at the center just like the $m=1$ mode at zero chromaticity.

The coherent tune shift of head-tail mode can be calculated by solving the Vlasov equation. Here, we only show the analytical result with the airbag model [3]:

$$\begin{aligned} \nu - \nu_{\beta 0} - m \nu_{s0} &\cong -i \frac{I_b R}{4\pi \nu_{\beta 0} E_0 / e} \sum_{p=-\infty}^{\infty} Z_T(\omega'_p) \\ &\times J_m^2((\omega'_p - \omega_\xi) \hat{\tau}) \end{aligned} \quad (8)$$

Here $Z_T(\omega)$ is the transverse impedance and

$$\omega'_p = (p + \nu_{\beta 0} + m \nu_{s0}) \omega_0. \quad (9)$$

The other parameters are: I_b is the bunch current, R is the ring radius, E_0 is the beam energy and $J_m(x)$ is the Bessel function.

2.13.4 TMCI Theory

When the beam intensity is increased, the interaction between different head-tail modes becomes non-negligible. We now have to solve the entire matrix including the interaction between various head-tail modes [5,6]. The eigen-solution ν , the coherent tune, can be obtained by solving the following equation (for the airbag model [3]):

$$\det((\nu - \nu_{\beta 0}) \mathbf{I} - \mathbf{A}) = 0. \quad (10)$$

Here \mathbf{I} is the unit matrix and the matrix element of \mathbf{A} is given by

$$A_{mn} = m \nu_{s0} \delta_{mn} + M_{mn}, \quad (11)$$

where

$$M_{mn} = -i \frac{I_b R}{4\pi_0 \nu_{\beta 0} E_0 / e} i^{m-n} \sum_p Z_T(\omega'_p) \cdot J_m((\omega'_p - \omega_\xi) \hat{\tau}) \cdot J_n((\omega'_p - \omega_\xi) \hat{\tau}) \quad (12)$$

Let us examine how the interaction between head-tail modes changes the behavior of the instability. The real part of the coherent tune (the coherent tune shift from the unperturbed tune $\nu_{\beta 0} + \nu_{s0}$) is determined by the sum of the imaginary part (multiplied by the bunch spectrum) of the transverse impedance over frequency. Therefore, broadband impedance, rather than narrow one, tends to excite a larger tune shift. In conventional head-tail instability, the broadband impedance has a little effect on its excitation. But, when the beam intensity is increased and exceeds a certain threshold value, the tunes of two modes can merge and then suddenly, a strong instability occurs, as illustrated in Fig. 9. The growth

time of the instability can be as fast as the synchrotron oscillation period. This instability is called the Transverse Mode-Coupling Instability (TMCI) or the strong head-tail instability. TMCI has been observed mostly in electron machines such as PETRA, PEP [5] and LEP [7] where a bunch is short, but it has been observed also in proton machines such as SPS [8] where a bunch is relatively short compared to most of other proton machines.

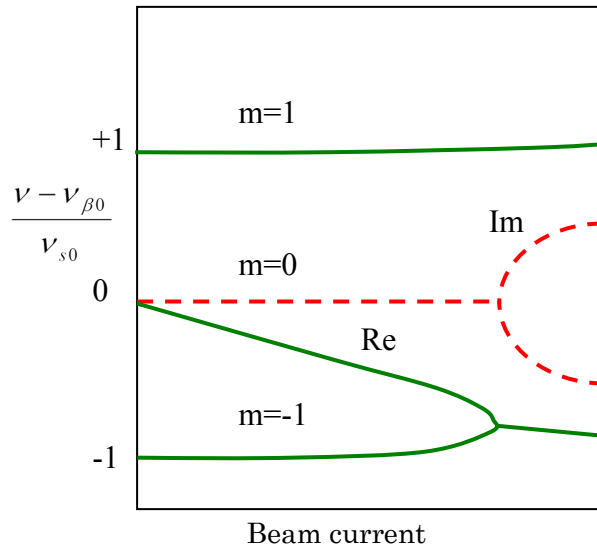


Figure 9: Typical behavior of coherent tune shifts as a function of the beam current. The real and the imaginary parts of the tune shifts are denoted by the solid and dashed lines. When the two tune shifts merge, the imaginary part of the tune shift (the growth rate) starts to increase rapidly.

2.13.5 Historical Record

By 1983, accelerator theorists faced two challenging instability problems to solve. One was the bunch lengthening phenomenon (longitudinal) and other was a transverse one, which is now called TMCI. The both phenomena have clear thresholds in the bunch current, and thus they are distinct from conventional Robinson-type instabilities.

By that time, there was common understanding among the accelerator theorists that the both phenomena are caused by mode-couplings. At the first glance, the bunch lengthening seemed to be easier to solve, since it involves only the longitudinal motion and the construction of the theory was simpler. However, such attempt encountered a big problem: the calculated threshold is much higher than the measured one. It is because the bunch lengthening is accompanied with the potential-well distortion, and thus the non-linear effect should have a significant role in the theory, which a simple linear theory cannot cope with. The breakthrough of this dilemma came out when Oide and Yokoya introduced the action-angle variable technique to solve the linearized Vlasov equation with an arbitrary potential well [9].

The TMCI theory was more complicated, but straightforward, since it involves no non-linearity. It is interesting to point out that the period of time when the TMCI theory was developed coincided with time when the independent variable in the instability theory was changed from “time t ” to “position s or θ ” in a ring, in order to be more precise and straightforward. Up to then, instability theories were written with time as the independent variable, as seen in Sacherer’s model Eqs. (6) and (8). This introduces annoying correction terms to be consistent with measurements, and there was strong demand to straighten the

theoretical foundation. Nowadays, it sounds too natural to describe beam instabilities developing as a beam moves along a ring, but the snapshot type understanding used to be dominant those days.

The picture like Fig. 9, now familiar with TMCI, first appeared in Chin and Satoh's theoretical paper [5]. As seen from Fig. 9, the first mode-coupling happens usually between $m=0$ and $m=-1$ modes. There is a clear asymmetrical behavior between positive and negative m modes. However, in Sacherer's head-tail model (Eqs. (6) and (8)), positive and negative m modes are supposed to be symmetrical. The only difference between them is that they rotate in the opposite direction in the synchrotron phase space. In this way, they together create a standing wave pattern and Sacherer's head-tail modes are described only by positive m numbers. Notice that the bunch spectrums in Fig. 8 are only for positive (no negative) m . Measured dipole signals such as shown in Fig. 4 have clear nodes, which demonstrates the validity of the standing wave model. On the other hands, measured tune shifts show the behavior, as illustrated in Fig. 9, and positive and negative m modes are clearly distinct, especially close to the TMCI threshold. This thinking exercise reveals that Sacherer's standing wave model and the bunch spectrum shift by non-zero chromaticity, as illustrated in Fig. 8, are valid only at low beam intensity. It may be interesting to investigate how the degeneracy of positive and negative m modes starts to break down as a function of the beam intensity and how head-tail modes look like in that regime, in particular, close to the TMCI threshold, to bridge Sacherer's model and the TMCI theory.

2.13.6 Acknowledgements

At first and foremost, *I would like to express my sincere gratitude and appreciation to Bruno Zotter for his lasting support, encouragement, and hospitality during my stay at CERN. He was one of my best competitors and collaborators, and most of all, the best friend. He built the foundation of the instability and impedance theories with his strong mathematical skill. We should be aware that the present instability theory was not completed at once, but has been slowly developed by efforts of many theorists like Bruno. He was also one of pioneers of the TMCI theory.*

2.13.7 References

1. F. Sacherer, "Theoretical Aspects of the Behavior of Beams in Accelerators and Storage Rings", CERN 77-13 (1977), p.198.
2. J. Gareyte and F. Sacherer, in Proc. of 9th Int. Conf. on High Energy Accelerators (Stanford, 1974), p. 341.
3. A. W. Chao, "Physics of Collective Beam Instabilities in High Energy Accelerators" (John Wiley & Sons, Inc., New York, 1993).
4. Y. H. Chin, "Analysis of Transverse Instabilities Observed at J-PARC MR and their Suppression using Feedback Systems", in Proc of the 2013 North American Particle Accelerator Conference (Pasadena, California, USA, 29 September – 4 October, 2013), MOYBB1, p.27.
5. Y. H. Chin, and K. Satoh, "Transverse Mode-Coupling in a Bunched Beam", IEEE Trans. Nucl. Sci. NS-30, No. 4, 2566 (1983), and Nucl. Instrum. Methods, 207, 309 (1983).
6. B. Zotter, "Transverse Mode Coupling and Head-Tail Turbulence", CERN/ISR-TH/82-10.

7. A. Wagner and B. Zotter, "A 3-Dimensional Simulations of Collective Effects in Particle Accelerators", in Proc. of the 1996 European Particle Accelerator Conference (EPAC96) (Sitges, Spain, 10-14 June, 1996), p.1256.
8. B. Salvant et. al, "Transverse Mode-Coupling Instability in the CERN SPS: Comparing MOSES Analytical Calculations and HEADTAIL Simulations with Experiments in the SPS", in Proc of the 2008 European Particle Accelerator Conference (EPAC08) (Genova, Italy, 23-27 June, 2008), TUPP067, p.1694.
9. K. Oide and K. Yokoya, "Longitudinal Single-Bunch Instability in Electron Storage Rings," KEK Tech. Rep Preprint 90-10 (April, 1990).

2.14 Damping of Transverse Instabilities of Bunched Beams

A. Burov

FNAL, Batavia, IL 60510, U.S.A

Mail to: burov@fnal.gov

Which gain and phase have to be set for a bunch-by-bunch transverse damper, and at which chromaticity it is better to stay? These questions are considered by means of the author's Nested Head-Tail Vlasov Solver (NHT) for the broadband impedance, and for the LHC impedance model. 3D plots for the growth rate at the chromaticity-intensity and chromaticity-gain planes and possibilities to use them are shown and discussed. It is demonstrated that feedbacks may generate asymmetry of the tune shift distribution, which requires positively-shifted stability diagrams.

2.14.1 Introduction

How one has to use the bunch-by-bunch damper for the most efficient suppression of the transverse instabilities of bunched beams? This problem has so many parameters and input functions, associated with the beam, impedance and damper, that its full treatment seems hardly possible. In this situation, studies of especially interesting cases by means of available models suggest a reasonable way to get a better understanding. This paper is an example of that sort of research; its more extended version is suggested by Ref. [1].

One-particle model is the simplest one; still it is useful for the Robinson and coupled-bunch instabilities [2,3]. Without limitation of the accuracy, the coupled-bunch instability can be separated in two stages: at the first one the bunches are treated as macroparticles, while at the second stage a distribution of the obtained coupled-bunch growth rates over the head-tail degrees of freedom can be found [3].

The two-particle model [2, 4-6] is the next after the simplest one. It certainly sheds light on the head-tail factors, but its practical use is too limited: it can both underestimate and overestimate possible instabilities, and it is hard to tell in advance by how much. After the two-particle model, the next in complexity is the hollow-beam or air-bag one [2], which represents the bunch by a homogeneously populated circle in the longitudinal phase space.

In this paper, I am using my own method of analysis, the Nested Head-Tail Vlasov Solver (NHT), which represents the bunch by a reasonable number of concentric air-bags and takes into account intra- and inter-bunch wake fields, as well as the damper [7]. One may consider NHT as an extension of the air-bag model with its reduction of the Vlasov equation to the standard eigensystem problem of linear algebra. Although NHT allows computing Landau damping as well, and hence the instability thresholds, that sort of problems is predominantly left beyond the scope of this paper.

With the NHT, two impedance models were analyzed: the broadband impedance and the LHC model [8]. For both of them, it is shown that with the resistive damper there is an area of stability in the gain-chromaticity plane, centered at slightly negative chromaticity, where the multi-bunch beam is stable even without radiation or Landau damping. It is shown that the shapes of these areas of stability, as well as their limitations by the beam intensity, vary a lot. While for the broadband impedance this area allows to increase the TMCI threshold by up to a factor of four, for the LHC model it disappears almost exactly at the same intensity as the no-gain, zero-chromaticity TMCI onset (addressed below just as the TMCI threshold), so one cannot use it close to or above this threshold. That is why at sufficiently

high intensity of separated LHC beams, the optimal strategy is to work at high chromaticity and sufficient gain area, or in the *valley of slow instabilities*.

2.14.2 Broadband impedance

In this section, we discuss the main features of single-bunch instabilities for broadband impedance, taking the ring and bunch parameters of the Advanced Photon Source (APS) of Argonne National Laboratory, a storage ring of 1.1km circumference and electron beam energy of 7GeV [9]. We will assume the synchrotron tune $Q_s = \omega_s / \omega_0 = 0.008$, rms bunch length $\sigma_z = 1.5 \text{ cm}$, and rms momentum spread $\delta p / p = 0.001$. The computations are done for a broadband impedance model

$$Z_{\perp}(\omega) = \frac{\omega_r}{\omega} \frac{R_r}{1 + iQ_r \left(\frac{\omega_r}{\omega} - \frac{\omega}{\omega_r} \right)}, \quad (1)$$

with $Q_r = 1$, $\omega_r / (2\pi) = 3 \text{ GHz}$, and the weighted shunt impedance $R_r \beta = 10 \text{ M}\Omega$, where β is the average beta-function. The vacuum chamber is assumed to be round.

For the given beam and impedance, NHT computes the entire beam spectrum; the total number of modes is limited by two modelling factors: first, by a number of radial rings representing the bunch longitudinal distribution, and second, by the truncating azimuthal harmonic. For these calculations, the former was taken to be 5, and the latter was limited by ± 10 ; thus, the total number of intra-bunch modes is $(10 + 10 + 1) \cdot 5 = 105$.

Growth rate of the fastest growing mode is presented in Figs. 1 and 2 as a function of beam intensity and reactive damper gain; the chromaticity is zero. The intensity parameter $\text{Imp}F = N / N_0$ (impedance factor) is defined as a ratio of the bunch population N to its value $N_0 = 4 \cdot 10^{10}$ taken as the nominal. Terms *resistive* and *reactive* for the dampers are conventional: the former assumes 90° phase advance between the pickup and the kicker signals, while for the latter this phase is zero. The absolute value of the feedback gain $|g|$ is defined as the rate at which the bunch dipole moment decays if the damper is resistive; it is conventionally measured in the units of the synchrotron frequency ω_s . In the same units are measured the eigenvalues q , the coherent frequency shifts; the symbol $\text{Im} q_*$ stands for the maximal growth rate at the given machine and beam parameters, i.e., for the growth rate of the most unstable mode. It is worth noting that the growth rate is not a monotonic function of the gain, neither in its focusing nor defocusing direction. At a small gain, $|g| \leq 1$, the positive (focusing) sign allows to double the instability threshold, while the defocusing one may reduce the threshold up to a factor of three. However, a further increase of the gain value makes the situation worse in both directions, up to $g \approx -2.5$ when the instability threshold jumps more than 4 times compared to its zero-gain value of 1.6, saturating there for higher defocusing gain values, as one can see in Fig. 2. To reach the same threshold for the focusing damper, gain three times higher is needed, while the saturation threshold for the focusing sign is only $\sim 20\%$ higher than for the defocusing one.

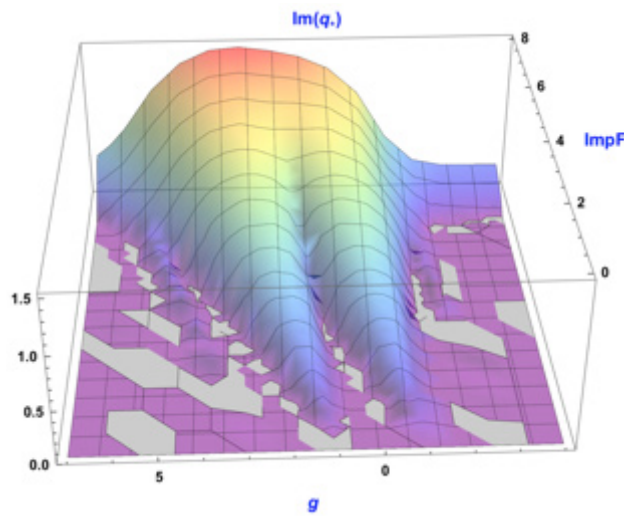


Figure 1: Maximal growth rate $\text{Im} q_s = (\omega_s \tau)^{-1}$ versus gain g and intensity parameter $\text{Imp}F = N / N_0$ for reactive damper and zero chromaticity. Gain is in units of ω_s ; its positive sign corresponds to focusing.

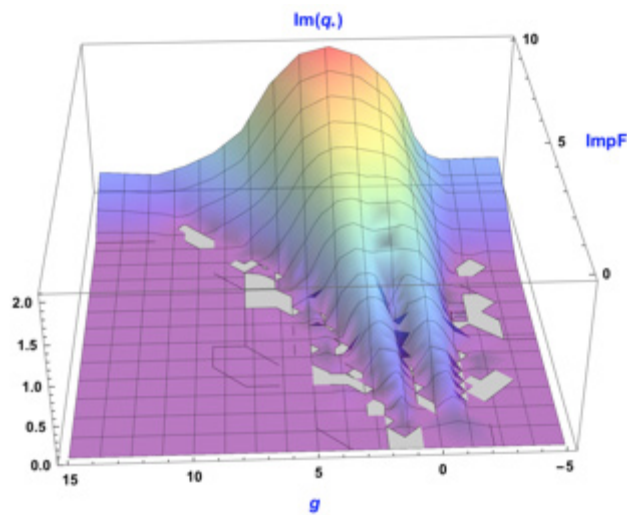


Figure 2: Same as Fig. 1 but for a larger range of the variables.

As one may conclude from Figs. 3 and 4, the reactive damper is not very effective for non-zero chromaticity: outside of a very narrow range of chromaticity, the ravine around zero, the reactive damper is insignificant.

Before going into details of the resistive damper, it is instructive to see the growth rate versus intensity and chromaticity for the no-damper case as it is shown in Fig. 5. Similar plots for the resistive case with $g=1$ and $g=10$ are presented in Figs. 6 and 7. Figure 8 shows how the growth rate depends on the chromaticity for various resistive gains, to compare with the similar results for the reactive damper presented in Fig. 4. Figure 9 demonstrates that at a high resistive gain and proper chromaticity, the threshold saturates approximately at a four times higher value than the TMCI threshold.

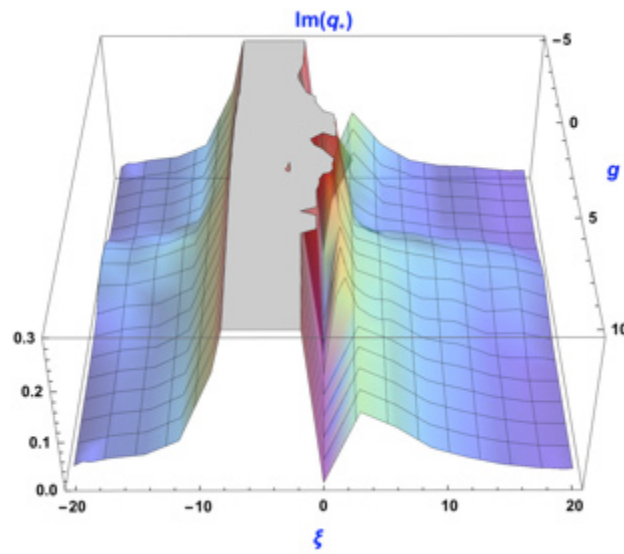


Figure 3: The growth rate versus chromaticity and reactive gain for intensity twice exceeding zero-gain zero-chromaticity TMCI threshold, i.e. for $\text{Imp}F = 3.2$.

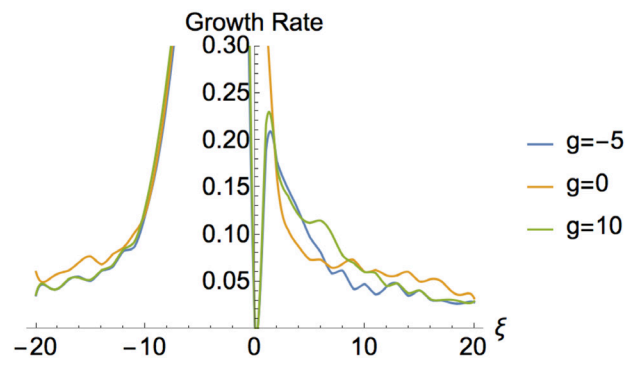


Figure 4: Same as Fig. 3 but for three selected gains.

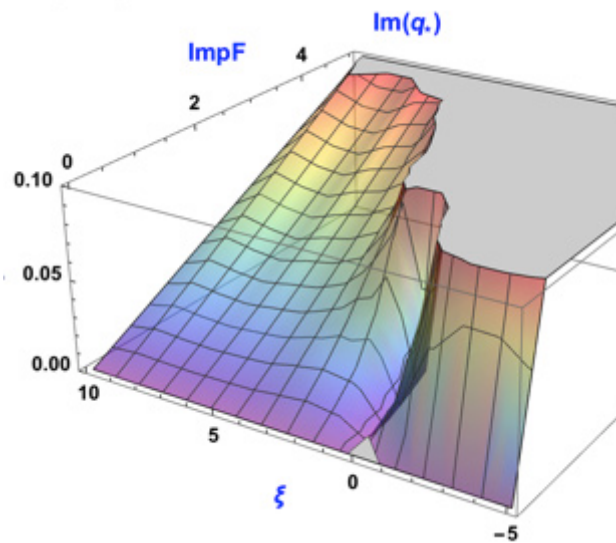


Figure 5: Growth rate versus intensity and chromaticity; the damper is off.

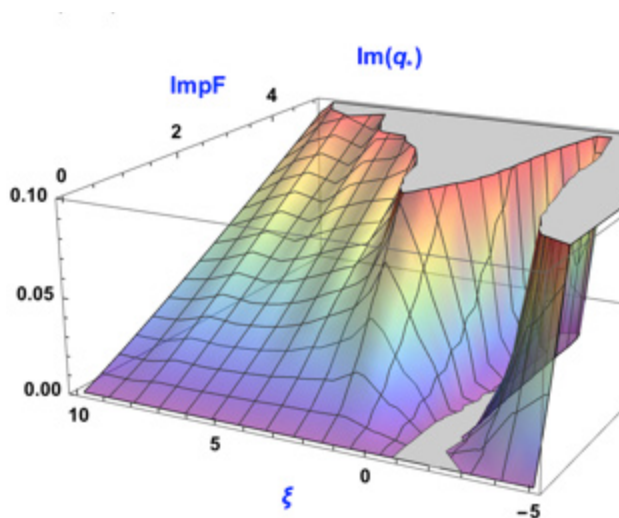


Figure 6: Same as Fig. 5 for resistive $g = 1$.

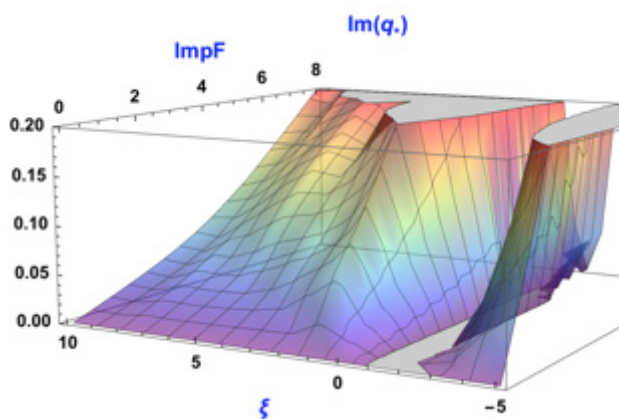


Figure 7: Same as Fig. 5 for resistive $g = 10$.

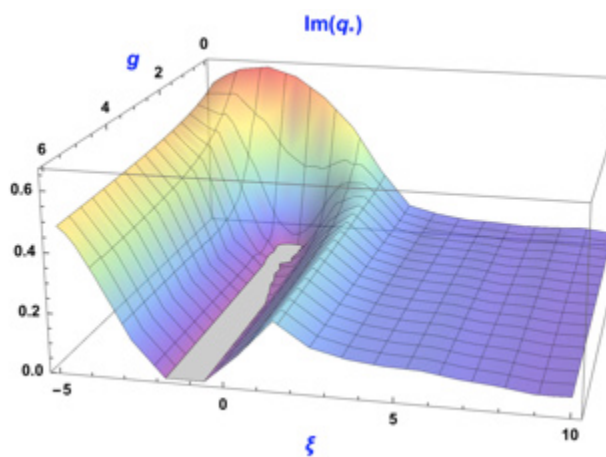


Figure 8: Same as Fig.3 but for the resistive damper. Note the fjord of stability.

For the reactive damper with any gain, the growth rate can be zero only at zero chromaticity. Contrary to that, for the resistive damper there is a fjord of stability, as one can see in Figs. 6-8. Above the transition energy, this area typically corresponds to small negative values of the rms head-tail phase, centered at

$$\chi_{\text{rms}} = \frac{\xi(\delta p / p)_{\text{rms}}}{Q_s} \simeq -(0.1 \div 0.2) \quad (2)$$

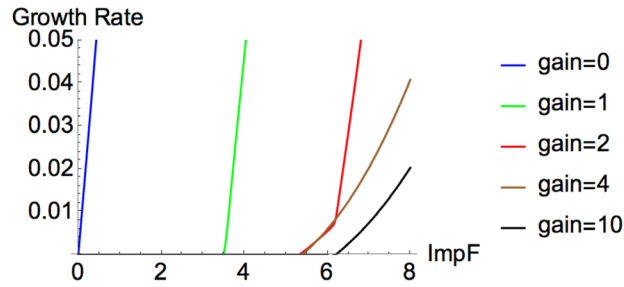


Figure 9: The growth rate for $\xi = -1$ vs. intensity for selected resistive gains. At high gains, the threshold saturates approximately at four times higher value than its damper-off zero-chromaticity value (6.4:1.6).

The reason for this was in fact explained in Ref. [10]. At slightly negative head-tail phase and below TMCI threshold, impedance makes all the modes stable except the zeroth one, corresponding to an almost rigid bunch motion. Since the zeroth mode is perfectly seen by the damper, the feedback's damping rate goes almost entirely to the zeroth mode. All other modes are poorly seen by the damper at small chromaticity, but there is no need in that since they decay due to impedance (see e.g. Ref.[2] p.351). Thus, at low and negative head-tail phase and below the TMCI threshold, the resistive damper stabilizes the only unstable mode and almost does not influence stability of other modes, which are already stable. How far above the TMCI threshold this area of stability may exist is one of the questions of this paper.

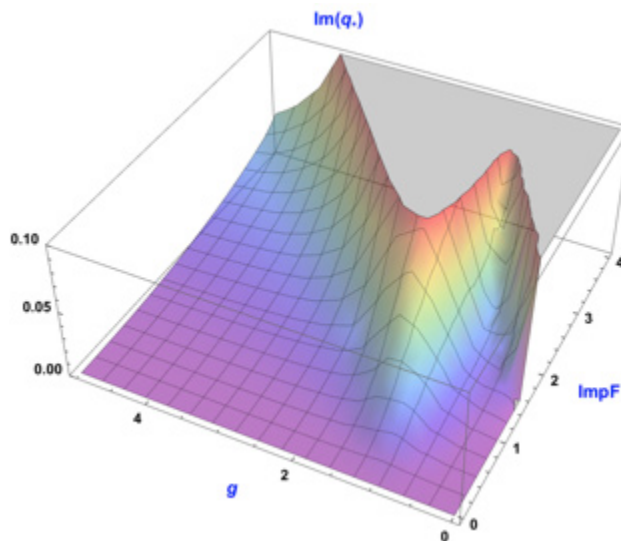


Figure 10: Growth rate for zero chromaticity and almost reactive damper, which phase declines towards resistive by 18° .

Figures 10 and 11 demonstrate sensitivity of effectiveness of the reactive damper to its small phase variation. These figures show the growth rate versus intensity and gain for zero chromaticity and an almost reactive damper, when its phase declines to the resistive direction by 18° .

Let's imagine, for example, that common action of radiation and Landau damping provides damping rate 0.02, and that available gain cannot be higher than 3.0. Then, as we can see from Fig. 11, this feedback allows increasing the intensity threshold at best by 25%, from 1.6 to 2.0. If the gain deviates from its optimal value in one or another direction, the benefit from the feedback would be even smaller. In this respect, the resistive damper is much more robust also, as one can see from Figs. 12 and 13, where 50% phase deviation towards the reactive one creates almost no effect.

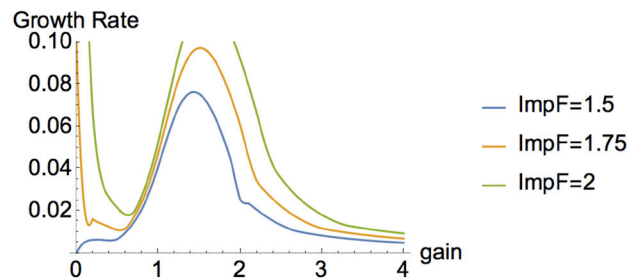


Figure 11: Same as the previous figure, for selected intensities.

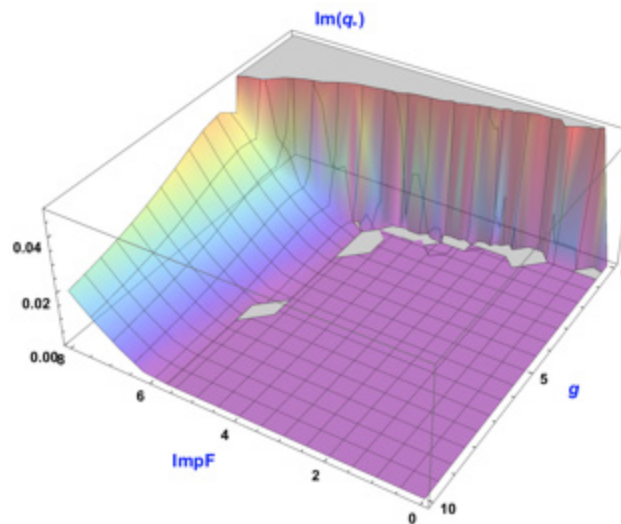


Figure 12: Growth rate for the resistive feedback and chromaticity $\xi = -1$.

Thus, for the single bunch and the broadband impedance we may conclude about definite advantage of the resistive damper over reactive one. While in both cases the instability threshold, in principle, could be increased up to 4-5 times, tolerance to the offsets of chromaticity and the feedback phase is much better for the former than for the latter.

In the following section we will see how different are the results for the LHC impedance model and how significant can the coupled-bunch contribution be.

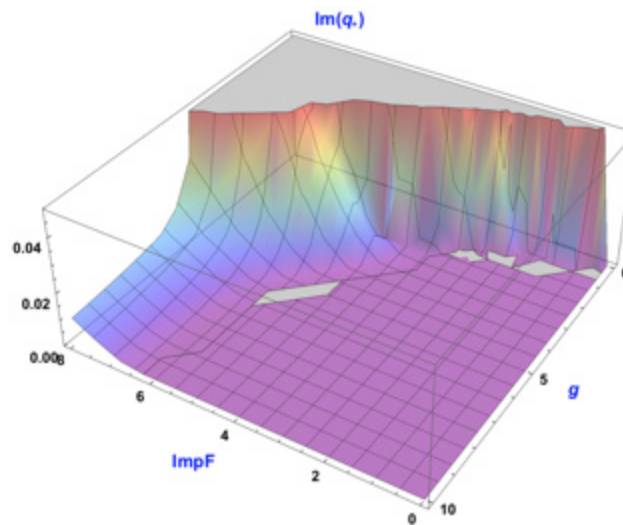


Figure 13: Same for the feedback phase $\pi/4$, i.e. 50% resistive and 50% reactive. Comparison with the previous figure shows how robust the resistive damper is against the phase variations at the proper chromaticity.

2.14.3 LHC at Top Energy

Transverse instabilities of the LHC beams have been studied with the NHT code in Ref. [7] for the Run I parameters. In this section that is reworked with new details for the Run II beam with the energy of 6.5TeV, the bunch separation of 25ns, the synchrotron tune $Q_s = 2.1 \cdot 10^{-3}$, the rms length of a Gaussian bunch $\sigma_z = 7.5 \text{ cm}$, the nominal bunch population $N_0 = 2.2 \cdot 10^{11}$, and with the same resistive-wall-like impedances [8].

Figure 14 shows the highest growth rate for a single bunch and no feedback. The TMCI threshold is at $\text{Imp}F = 2.4$. Figure 15 demonstrates a decent lake of stability for the resistive damper and the full 25ns beam, with the impedance factor $\text{Imp}F = 1.5$, or 62.5% of the TMCI threshold. Note a difference with Fig.7: while for the LHC impedance its area of stability is a lake, for the broadband one it is a fjord. Figure 16 demonstrates one more specific feature of the LHC: the lake of stability disappears almost at the TMCI threshold, $\text{Imp}F = 2.4$. Thus, by itself the resistive damper cannot increase the instability threshold for the LHC impedance, even for the single bunch. Variation of the damper phase does not help much: for intermediate resistive-reactive phases the lake disappearance threshold could be increased only by $\sim 15\%$.

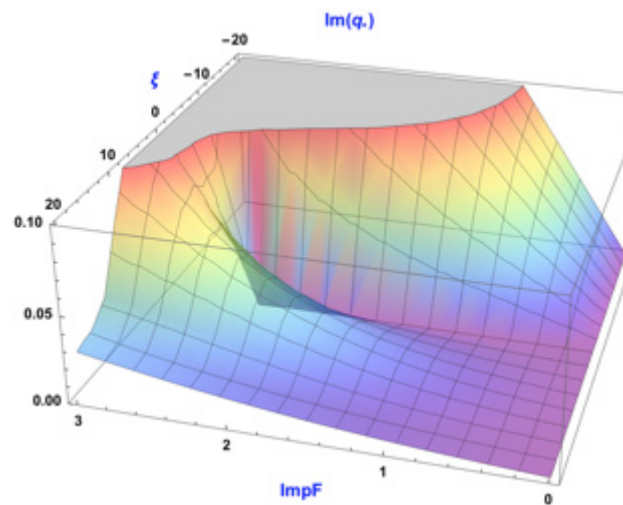


Figure 14: Growth rate for a single bunch LHC beam and no feedback. The TMCI threshold is at $\text{Imp}F = 2.4$.

Sufficiently below the TMCI threshold, when the lake is wide enough, the resistive damper tuned to the lake presents an attractive option. Near and above this threshold the only reasonable option for the LHC is to work at the high chromaticity valley of slow instabilities, relying on Landau damping for the suppression of these relatively slow instabilities that remain there when the damper effect is saturated, see Fig. 16-18.

Figure 19 makes clear that the reactive damper is almost as effective for the LHC as it is for the broadband case: operated at its proper zero chromaticity, for the single bunch it allows to increase the instability threshold more than three times. However, the reactive damper helps very little for the suppression of coupled-bunch instabilities, which all are maximally powerful at zero chromaticity, see Fig. 20. Thus, for the LHC, with its huge number of bunches, the reactive feedback would not be reasonable.

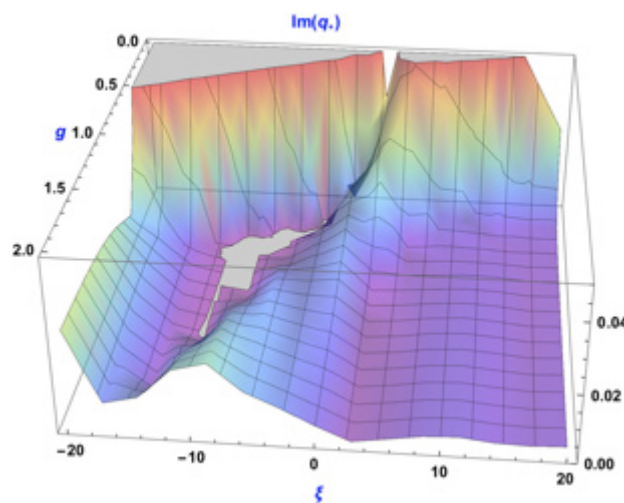


Figure 15: Growth rate for 25ns LHC beam with the resistive feedback and $ImpF = 1.5$. Coupled bunch interaction is included. Note the lake of stability; for the multi-bunch regime, the lake is limited by $ImpF = 1.7$.

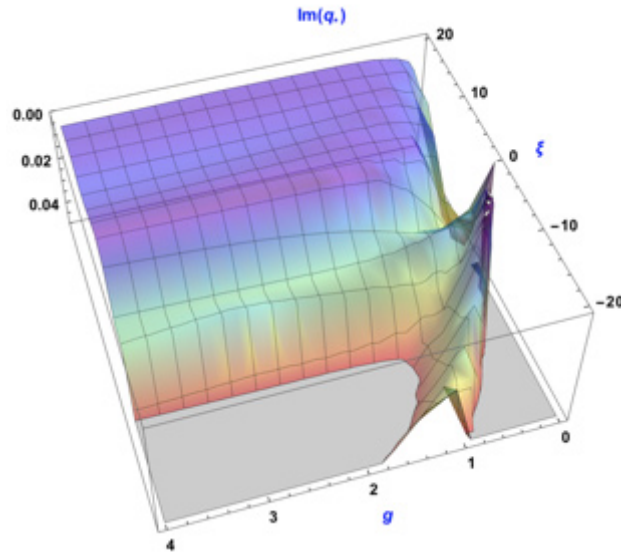


Figure 16: Single bunch growth rate for the resistive damper and TMCI threshold intensity $ImpF = 2.4$. Note that the lake of stability (shown upside down) almost vanished.

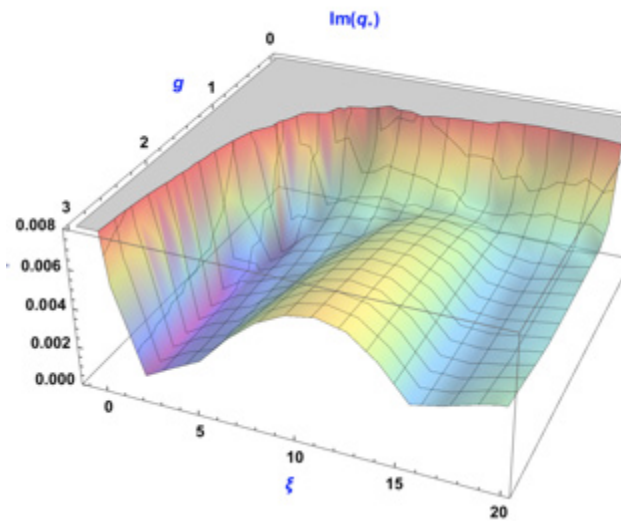


Figure 17: The same damper phase and bunch intensity for the full 25ns beam.

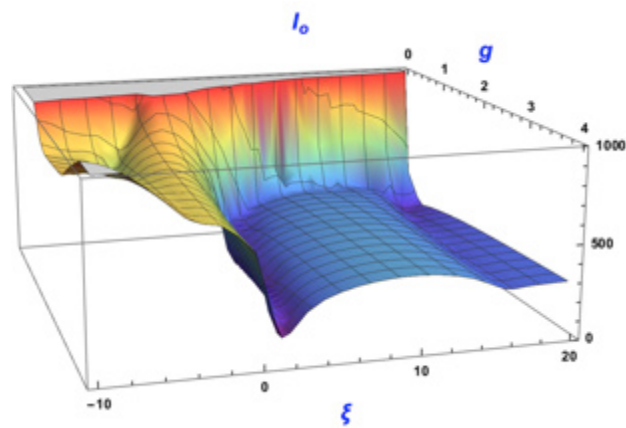


Figure 18: Threshold current of the Landau octupoles, in Amperes, for the same case as Fig. 17, computed according to Ref. [7].

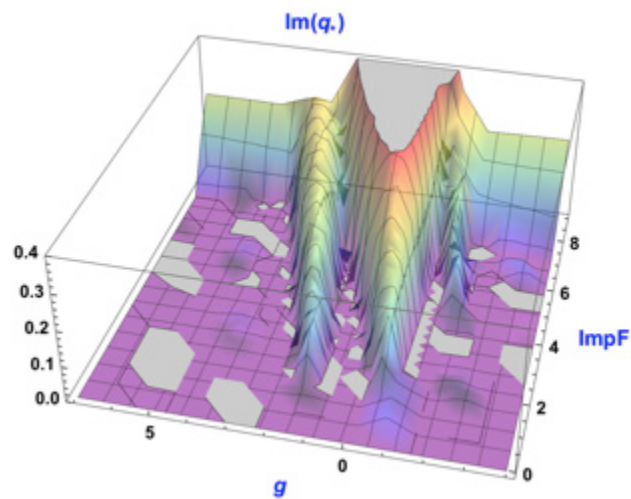


Figure 19: Growth rate for the single LHC bunch, reactive damper and zero chromaticity. Compare with Fig. 1 for the broadband impedance.

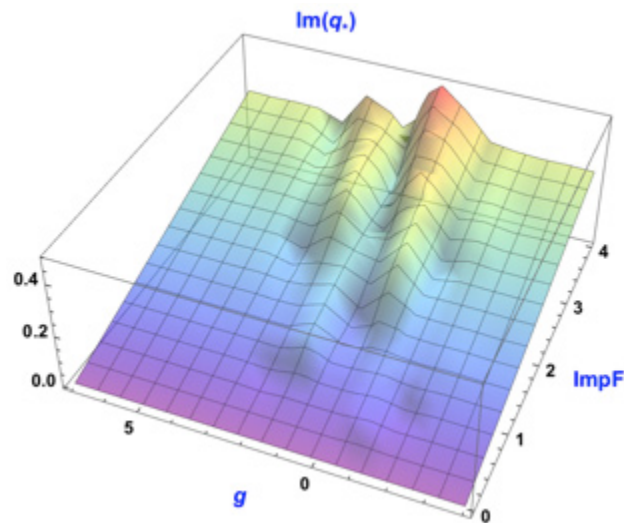


Figure 20: Same as above, but for the full 25ns beam. The average linear slope towards higher intensity reflects contribution of the coupled-bunch motion. It can be approximated as $\text{Im } q_* \approx 0.075 \text{ Imp}F$.

2.14.4 Feedbacks and Landau Damping

Generally speaking, there are three factors, which may contribute to beam stability: radiation, Landau damping, and feedbacks. The first of them is efficient only for electron beams; it is determined by the beam orbit, focusing, and by sizes of a vacuum chamber shielding coherent synchrotron radiation. This damping is independent of feedbacks, and can be added separately to the total sum of the stabilizing factors. Landau damping is a mechanism of dissipation of a collective mode due to a transfer of its energy to incoherent degrees of freedom of individual particles that happened to be in resonance with this mode. Landau damping is determined by the phase space density of the resonance particles, i.e. both by the separation between the coherent tune and the centre of the incoherent spectrum, as well as by the tails of the incoherent spectrum. If the beam is sufficiently relativistic, the space charge effects can be neglected. In such a case, which is the only one considered in this paper, the collective spectrum is determined by the wakes and feedbacks, while the incoherent one is a function of the optics' nonlinearity. Thus, since feedbacks play a role in shaping of beam collective modes, they modify Landau damping also.

With the exception of extremely long bunches or very broadband feedbacks, typical bunch-by-bunch dampers react only on the bunch centroid, mostly kicking the bunch as a whole. As a result, for sufficiently high resistive gain, the bunch center of mass is blocked, while all other possibilities of the bunch motion are not affected by the damper. For round vacuum chambers, as well as for the vertical direction in flat chambers, tunes of modes with significant motion of the center of mass are shifted down for typical wakes [2]. Since these center-of-mass dominated modes are normally most unstable, one should expect a certain asymmetry of the modes on the complex tune shift plane. First, with the damper off, this chart of unstable modes should be dominated by the left-hand-sided, or by the negative tune-shifted. When a significant gain is applied, the left-hand-sided modes should be significantly suppressed, while the right-hand-sided, if there are such, most likely should not

improve, and might even become worse. That sort of behavior of the chart of unstable modes can be seen in Figs. 21 and 22, for the LHC and broadband impedance respectively.

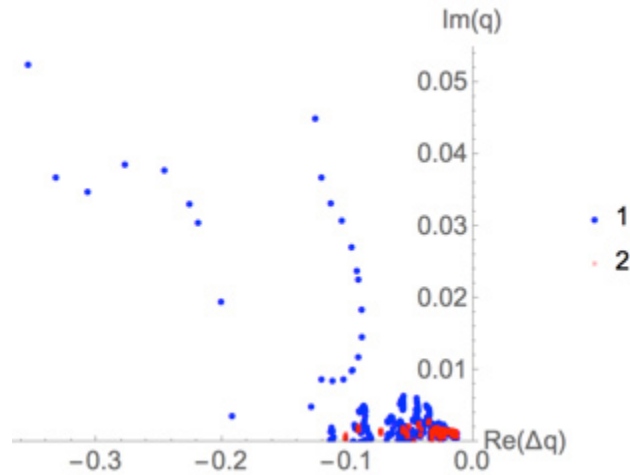


Figure 21: Tune shifts of unstable modes for the full 25ns LHC beam at chromaticity $\xi = 18$, $ImpF = 2$, damper off (blue, 1), and with resistive gain $g = 1.4$ (red, 2). Both with and without damper, there are no unstable modes with positive tune shifts. Seventeen representative coupled-bunch mode numbers are depicted.

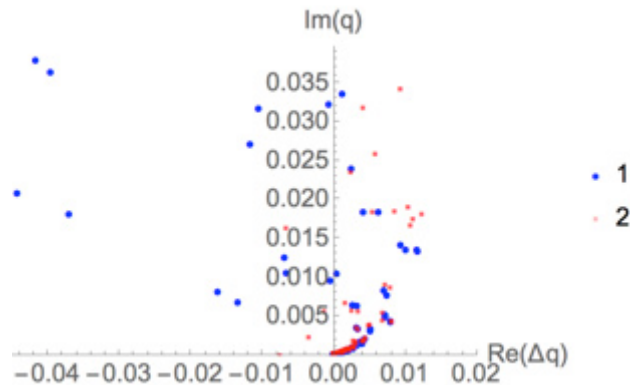


Figure 22: Tune shifts of unstable modes for the APS single bunch broadband impedance model at chromaticity $\xi = 10$, $ImpF = 2$, damper off (blue, 1), and with resistive gain $g = 1.4$ (red, 2).

We see here a pronounced dependence of the asymmetry on a sort of impedance. With the damper off, both Fig. 21 and Fig. 22 dominate by the left-hand-side modes. However, when it is on, one of them remains to be left-hand sided, while another becomes right-hand-sided. This asymmetry is especially important for electron machines where one of the emittances, the horizontal one, is much higher than another, the vertical. Due to that, transverse nonlinearity makes the stability diagram one-sided too, scaled by the horizontal emittance only, since the vertical emittance is too small to play a role. That is why, for the electron rings, one has to choose whether the diagram has to be designed as right- or left-hand-sided. The correct answer depends, as we just saw, on the type of impedance. Another approach to this problem of the one-sidedness of the stability diagram of electron beams is

to provide electrons with the missing sign of the tune shift by means of the second order chromaticity which sign is made opposite to the one of the horizontal nonlinearity.

2.14.5 Conclusions

Possible strategies of beam stabilization by means of a feedback were considered for the broadband and the LHC impedance models by means of the Nested Head-Tail Vlasov Solver (NHT). Advantages, challenges and limitations for reactive and resistive dampers are formulated. Existence and details of the 2D area of stability in the gain-chromaticity and intensity-chromaticity planes is shown to depend on the type of impedance. One-sidedness of the mode tune shifts, as well as stability diagrams is pointed out as a source of instability. Possible solutions for this problem are outlined.

The author is thankful to Elias Metral (CERN), Alexander Zholents (ANL) and Vadim Sajaev (ANL) for multiple discussions, both encouraging and clarifying.

This work was performed at Fermilab, operated by Fermi Research Alliance, LLC under Contract No. DE-AC02-07CH11359 with the U.S. Department of Energy.

2.14.6 References

1. A. Burov, Phys. Rev. Accel. Beams **19**, 084402 (2016).
2. A. Chao, "Physics of Collective Beam Instabilities in High Energy Accelerators", John Wiley & Sons, Inc (1993)
3. A. Burov, "Coupled-Beam and Coupled-Bunch Instabilities", <http://arxiv.org/abs/1606.07430> (2016), submitted to Phys. Rev. Accel. Beams.
4. R.D. Kohaupt, "Simplified Presentation of Head - Tail Turbulence" DESY M-80/19 (1980).
5. R. Talman, "The Influence Of Finite Synchrotron Oscillation Frequency On The Transverse Head-Tail Effect", CERN ISR-TH/81-17 (1981); Nucl. Instr. Meth. **193**, 423 (1982).
6. R. Ruth, "Reactive Feedback In The Two Particle Model", CERN LEP-TH/83-22 (1983)
7. A. Burov, "Nested head-tail Vlasov solver", Phys. Rev. Accel. Beams **17**, 021007 (2014).
8. N. Mounet, "The LHC Transverse Coupled-Bunch Instability" CERN-THESIS-2012-055 (2012).
9. M. Borland, G. Decker, L. Emery, W. Guo, K. Harkay, V. Sajaev, C.-Y. Yao, "[APS Storage Ring Parameters](#)", 2010.
10. L. Arnaudon, S. Myers, R. Olsen and E. Peschardt "Transverse Feedback and LEP Performance", Proc. EPAC'92, p.66.

2.15 Transverse Instabilities of Bunched Beams at Strong Space Charge - Theory

A. Burov
FNAL, Batavia, IL 60510, U.S.A
Mail to: burov@fnal.gov

2.15.1 Introduction

This paper collects main general formulas related to stability of bunched beams at strong space charge, i.e. when the maximal space charge tune shift is much bigger than the synchrotron tune.

2.15.2 Main Equation

Space charge is known to be able to change dramatically collective modes [1-3]. For transverse oscillations of bunched beams, a parameter of the space charge strength is a ratio of the maximal space charge tune shift to the synchrotron tune. When this parameter is large, the transverse oscillations are described by a one-dimensional integral-differential equation derived in Ref. [2] and reproduced here for the sake of convenience

$$\begin{aligned}
 \nu y + \frac{1}{Q_{\text{eff}}} \frac{d}{d\tau} \left(u^2 \frac{dy}{d\tau} \right) &= \kappa N (\hat{W}y + Dy) \\
 \hat{W}y &= \int_{-\infty}^{\infty} W(\tau-s) \exp[i\zeta(\tau-s)] \rho(s) y(s) ds \\
 Dy &= y(\tau) \int_{-\infty}^{\infty} D(\tau-s) \rho(s) ds \\
 \left. \frac{dy}{d\tau} \right|_{\tau \rightarrow \pm\infty} &= 0
 \end{aligned} \tag{1}$$

Here $y = y(\tau)$ and ν are the eigenfunction and the eigenvalue to be found for the bunch transverse oscillations, τ and s are longitudinal positions within the bunch, W and D are the dipole and quadrupole (or the driving and detuning) wakes, ρ is the normalized line density

$$\int \rho ds = 1 \tag{2}$$

N is the number of particles per bunch,

$$\kappa = \frac{r_0 R}{4\pi\beta^2\gamma Q_b} \tag{3}$$

with r_0 as the classical radius, R as the average machine radius, β and γ as the relativistic factors and Q_b as the bare betatron tune. The parameter ζ staying in the exponents of the

wake integral is a negated ratio of the chromaticity $\xi = pdQ_b / dp$ and the slippage factor $\eta = \gamma_i^{-2} - \gamma^{-2}$, i.e. $\zeta = -\xi / \eta$. The symbol $Q_{\text{eff}} = Q_{\text{eff}}(\tau)$ stays for the space charge tune shift at the given position along the bunch τ , averaged over the both transverse action, see Ref. [2]. Thus, the effective space charge tune shift is proportional to the local line density

$$Q_{\text{eff}}(\tau) = Q_{\text{eff}}(0)\rho(\tau) / \rho(0) \quad (4)$$

For the transversely Gaussian bunch,

$$Q_{\text{eff}}(\tau) = 0.52Q_{\text{max}}(\tau) \quad (5)$$

where $Q_{\text{max}}(\tau)$ is the space charge tune shift at the bunch axis. The symbol $u^2 = u^2(\tau)$ stays for the average square of the particle longitudinal velocity $v_i = d\tau_i / d\theta$, with time measured as the angle θ along the machine circumference, at the given position τ

$$u^2 = \langle v^2 \rangle = \frac{\int f(v, \tau)v^2 dv}{\int f(v, \tau)dv} \quad (6)$$

where $f(v, \tau)$ is the longitudinal distribution function. For the longitudinally Gaussian distribution with the rms bunch length σ_τ , the temperature function u^2 is constant along the bunch

$$u^2 = Q_s^2 \sigma_\tau^2 \quad (7)$$

where Q_s is the synchrotron tune.

In general, the wake term $\hat{W}\mathbf{y}$ is a sum of single-bunch (SB), coupled-bunch (CB) wakes and the damper (G) terms

$$\hat{W}\mathbf{y} = \hat{W}_{\text{SB}}\mathbf{y} + \hat{W}_{\text{CB}}\mathbf{y} + \hat{G}\mathbf{y} \quad (8)$$

The single-bunch term $\hat{W}_{\text{SB}}\mathbf{y}$ is described exactly as in Eq. (1), where only $s > \tau$ contributes due to the causality, and the integral is taken along the single-bunch interval only

$$\hat{W}_{\text{SB}}\mathbf{y} = \int_{\text{SB}} W(\tau - s) \exp[i\zeta(\tau - s)] \rho(s) \mathbf{y}(s) ds \quad (9)$$

The coupled-bunch term results from summations of the fields left by preceding passages of the bunches through the given position of the ring. This summation is especially simple when the bunches are equidistant. In this case, due to the symmetry, the offsets of the neighbor bunches, being taken at the same time, differ only by the phase factors $\exp(i\psi_\mu)$

$$\mathbf{y}(s + s_0) = \exp(i\psi_\mu) \mathbf{y}(s) \quad (10)$$

For M bunches in the ring,

$$\psi_\mu = \frac{2\pi\mu}{M}; \quad \mu = 0, 1, \dots, M-1 \quad (11)$$

where integer μ is a counter of the coupled-bunch modes. After that, we have to take into account that the given reference bunch sees the fields left behind by other bunches not at the same time, but certain time ago, proportional to the distance between the bunches. This leads to an additional time-related factor to be taken into account together with the space-related phase factor:

$$y(s + s_0, \theta - s_0) = \exp(i\phi_\mu) y(s, \theta);$$

$$\phi_\mu = \psi_\mu + \frac{2\pi Q_b}{M}. \quad (12)$$

Remember that both time and space are measured as the angles of revolution, and the leading particles have higher coordinate than the following ones. From here, the coupled-bunch contribution in Eq. (8) follows as a single-bunch integral

$$\hat{W}_{\text{CB}} y = \int_{\text{SB}} \tilde{W}_\mu(\tau, s) \exp[i\zeta(\tau - s)] \rho(s) y(s) ds;$$

$$\tilde{W}_\mu(\tau, s) = \sum_{k=1}^{\infty} W(\tau - s - ks_0) \exp(ik\phi_\mu). \quad (13)$$

For those cases when the wake function of the neighbour bunch does not change much along the reference bunch, i.e. the coupled-bunch wake is flat [4],

$$W(\tau - s - ks_0) \approx W(-ks_0) \quad (14)$$

the result of summation in the right hand side of Eq. (13) does not depend on the specific positions s , τ within the bunches; thus, the effective coupled bunch wake \tilde{W}_μ is a constant which can be taken out of the integral

$$\hat{W}_{\text{CB}} y = \tilde{W}_\mu e^{i\zeta\tau} \int_{\text{SB}} e^{-i\zeta s} \rho(s) y(s) ds. \quad (15)$$

In principle, the damper term $\hat{G}y$ in Eq. (8) is similar to the coupled-bunch one. If the feedback bandwidth is much smaller than the inverse bunch length, the damper takes just one parameter per bunch. This parameter can be chosen as an offset of the centre of mass, and the kick can be designed to be flat along the bunch. Then the damper term is represented similar to Eq. (15)

$$\hat{G}y = \tilde{G}_\mu e^{i\zeta\tau} \int_{\text{SB}} e^{-i\zeta s} \rho(s) y(s) ds \quad (16)$$

If the damper is bunch-by-bunch, there is no coupled-bunch mode dependence in the feedback factor \tilde{G}_μ , i.e. $\tilde{G}_\mu = \tilde{G}$.

Similarly to the driving wake factor, Eq. (8), there is a certain coupled-bunch contribution in the detuning wake as well

$$\begin{aligned}
Dy &= D_{\text{SB}}y + D_{\text{CB}}y; \\
D_{\text{SB}} &= \int_{\text{SB}} \rho(s)D(\tau-s)ds; \\
D_{\text{CB}} &= \int_{\text{SB}} \rho(s)\tilde{D}(\tau,s)ds; \\
\tilde{D}(\tau,s) &= \sum_{k=1}^{\infty} D(\tau-s-ks_0).
\end{aligned} \tag{17}$$

If the detuning wake is flat in the same sense as in Eq. (14), its coupled-bunch contribution is identical for all the particles, so it works as a constant quadrupole without any influence to the beam dynamics unless it leads to a dangerous resonance crossing.

To be precise, the strong space charge approximation requires the effective space charge tune shift $Q_{\text{eff}}(\mathbf{0})$ to be much bigger than all other tune shifts: the synchrotron tune times the mode number, as well as the wake-related tune shifts, the rms chromatic tune shift and the rms octupolar tune shift.

2.15.3 Solution

To find the spectrum of Eq. (1), its eigenfunctions can be expanded over its zero-wake solutions $y_k^0(\tau)$ satisfying the following equation

$$\begin{aligned}
\nu^0 y^0 + \frac{1}{Q_{\text{eff}}} \frac{d}{d\tau} \left(u^2 \frac{dy^0}{d\tau} \right) &= 0; \\
\left. \frac{dy^0}{d\tau} \right|_{\tau \rightarrow \pm\infty} &= 0
\end{aligned} \tag{18}$$

All the eigenfunctions $y_k^0(\tau)$ are orthogonal and can be normalized, so that

$$\int_{\text{SB}} ds \rho(s) y_k^0(s) y_m^0(s) = \delta_{km} \tag{19}$$

For the Gaussian distribution, the spectrum of this equation has been described in Refs. [2,3]; similarly, it can be found for any potential well and distribution function.

Expansion of the eigenfunction $y(\tau)$ over the no-wake set $y^0(\tau)$,

$$y(\tau) = \sum_{k=0}^{\infty} B_k y_k^0(\tau) \tag{20}$$

with the amplitudes B to be found, with the following multiplication of Eq. (1) on $y_l^0(\tau)\rho(\tau)$ and its integration over the bunch length, leads to

$$\left[\kappa N \hat{\mathbf{W}} + \kappa N \hat{\mathbf{D}} + \text{Diag}(\nu^0) \right] \mathbf{B} = \nu \mathbf{B} \tag{21}$$

Here $\text{Diag}(\nu^0)$ is a diagonal matrix with the no-wake eigenvalues of Eq. (18) as the diagonal elements, $\hat{\mathbf{W}}$ and $\hat{\mathbf{D}}$ are the matrices of the driving and detuning wakes in the basis of the no-wake modes of Eqs. (18) and (19)

$$\begin{aligned}\hat{\mathbf{W}} &= \hat{\mathbf{W}}_{\text{SB}} + \hat{\mathbf{W}}_{\text{CB}} + \hat{\mathbf{G}}; \\ \hat{\mathbf{D}} &= \hat{\mathbf{D}}_{\text{SB}} + \hat{\mathbf{D}}_{\text{CB}};\end{aligned}\quad (22)$$

$$\begin{aligned}(\hat{\mathbf{W}}_{\text{SB}})_{lk} &= \iint_{\text{SB}} W(\tau-s)\rho(\tau)\rho(s)e^{i\zeta(\tau-s)}y_l^0(\tau)y_k^0(s)d\tau ds; \\ (\hat{\mathbf{W}}_{\text{CB}})_{lk} &= \iint_{\text{SB}} \tilde{W}_\mu(\tau,s)\rho(\tau)\rho(s)e^{i\zeta(\tau-s)}y_l^0(\tau)y_k^0(s)d\tau ds;\end{aligned}\quad (23)$$

$$\begin{aligned}\hat{\mathbf{G}}_{lk} &= \tilde{G}_\mu I_l(\zeta)I_k^*(\zeta); \\ I_l(\zeta) &= \int_{\text{SB}} \rho(\tau)e^{i\zeta\tau}y_l^0(\tau)d\tau;\end{aligned}\quad (24)$$

$$\begin{aligned}(\hat{\mathbf{D}}_{\text{SB}})_{lk} &= \int_{\text{SB}} F_{\text{SB}}(\tau)\rho(\tau)y_l^0(\tau)y_k^0(\tau)d\tau; \\ F_{\text{SB}}(\tau) &= \int_{\text{SB}} D(\tau-s)\rho(s)ds;\end{aligned}\quad (25)$$

$$\begin{aligned}(\hat{\mathbf{D}}_{\text{CB}})_{lk} &= \int_{\text{SB}} F_{\text{CB}}(\tau)\rho(\tau)y_l^0(\tau)y_k^0(\tau)d\tau; \\ F_{\text{CB}}(\tau) &= \int_{\text{SB}} \tilde{D}(\tau,s)\rho(s)ds.\end{aligned}\quad (26)$$

2.15.4 Damper Details

In case when the feedback takes something different from the centre of mass and its kick is not flat over the bunch, the damper matrix has to be modified with provided pickup and kicker functions $P(s), K(\tau)$

$$\begin{aligned}\hat{\mathbf{G}}_{lk} &= \tilde{G}_\mu K_l(\zeta)P_k^*(\zeta); \\ K_l(\zeta) &= \int_{\text{SB}} K(\tau)\rho(\tau)e^{i\zeta\tau}y_l^0(\tau)d\tau; \\ P_k^*(\zeta) &= \int_{\text{SB}} P(s)\rho(s)e^{-i\zeta s}y_k^0(s)ds.\end{aligned}\quad (27)$$

Equation (21) is a standard linear algebra eigensystem problem which solution is straightforward as soon as the wake functions, the feedback properties, the potential well, and the beam distribution functions, longitudinal and transverse, are given. This equation allows computing the instability growth rates for fairly general situations when the Landau damping can be neglected. However, without Landau damping nothing can be said about the instability threshold, so the theory is significantly incomplete in this case.

2.15.5 Instability Thresholds

For the strong space charge, Landau damping rates were estimated in Ref. [2]. Numerical simulations give a possibility for more accurate knowledge of the damping rates, with the numerical factors to be found with a good precision. This work has been started by V. Kornilov and O. Boine-Frankenheim several years ago with their PATRIC code [5,6] and has been joined recently by A. Macridin et al. with the Synergia program [7]. A good agreement with the analytical estimations of the intrinsic damping rates of Ref. [2] for no-wake case gives a hope that the same general formulas will work well with wake fields too. Checking this, as well as the octupole-driven damping rates, with the Synergia simulations is planned at the Fermilab. Potential importance of the image charges and currents for Landau damping was shown in Refs. [5,6]. As soon as Landau damping rates are included in Eq. (21), theory of transverse stability of bunched beams at strong space charge would be complete.

FNAL is operated by Fermi Research Alliance, LLC under Contract No. De-AC02-07CH11359 with the United States Department of Energy.

2.15.6 References

1. M. Blaskiewicz, Phys. Rev. ST Accel. Beams 1, 044201 (1998); Phys. Rev. ST Accel. Beams 6, 014203 (2003).
2. A. Burov, Phys. Rev. ST Accel. Beams 12, 044202 (2009).
3. V. Balbekov, Phys. Rev. ST Accel. Beams 12, 124402 (2009).
4. A. Burov, Phys. Rev. ST Accel. Beams 17, 021007 (2014).
5. V. Kornilov and O. Boine-Frankenheim, Phys. Rev. ST Accel. Beams 13, 114201 (2010).
6. V. Kornilov, O. Boine-Frankenheim, D.J. Adams, B. Jones, B.G. Pine, C.M. Warsop, R.E. Williamson, “Thresholds of the Head-Tail Instability in Bunches with Space Charge”, HB’2014 workshop, East Lansing, MI, USA.
7. A. Macridin, A. Burov, E. Stern, J. Amundson, and P. Spentzouris, Phys. Rev. ST Accel. Beams **18**, 074401 (2015).

2.16 Effects of Space-Charge on Transverse Impedance-Induced Beam Instabilities - Simulations

Vladimir Kornilov

GSI Helmholtzzentrum für Schwerionenforschung, Planckstr.1, 64291 Darmstadt, Germany

Mail to: v.kornilov@gsi.de

2.16.1 Introduction

There is a number of different transverse instabilities which have always been a limiting factor for the accelerator performance. Broad reviews and physical explanations can be found in the books of Ng [1], Chao [2], the Handbook of Accelerator Physics and Engineering [3], etc. The main effects of space-charge on the collective transverse instabilities can be best illustrated using a few basic phenomena in the transverse beam dynamics. These can be the eigenmodes of the coasting beam, the head-tail modes in the bunches, the coupling of the bunch head-tail modes which results in the transverse mode coupling instability. The implications for the coupled-bunch instabilities, e-cloud driven transverse instabilities, beam breakup, etc., follow from the basic principles. In this paper we try to focus on the limited aspects of the space-charge effect on the basic transverse eigenmodes. Another essential aspect of the space-charge effect is related to Landau damping which is discussed in the dedicated paper of this Newsletter.

2.16.2 Space-Charge Tune Shifts

Transverse space-charge effects can be described by the characteristic tune shift ΔQ_{sc} ,

$$\Delta Q_{sc} = \frac{\lambda_0 r_p R}{4\gamma^2 \beta \epsilon_{tr}}, \quad (1)$$

which is the tune shift in the rms-equivalent K-V beam, defined as the absolute value of a negative tune shift. This means that, for example, the maximum space-charge tune shift for a Gaussian transverse profile is ($-2\times$) of this value. For bunches, the relevant line density λ_0 is the peak density, normally in the bunch middle $z=0$. The ring equivalent radius is $R=C/2\pi$, r_p is the classical particle radius, γ and β are the relativistic parameters, $\epsilon_{tr} = 0.5(\epsilon_x + [\epsilon_x \epsilon_y Q_x / Q_y]^{1/2})$ is the effective transverse emittance, ϵ_x , ϵ_y are the normalized horizontal, vertical rms emittances. This is the expression for the horizontal plane, for the vertical plane it is in the analogous way.

The parameter for the effect of space-charge in a bunch is defined as a ratio of the characteristic space-charge tune shift to the synchrotron tune,

$$q = \frac{\Delta Q_{sc}}{Q_s}. \quad (2)$$

The beam parameters with $q \ll 1$ imply weak space-charge, while $q \gg 1$ means the strong space-charge regime. The space-charge parameter can strongly change during the synchrotron magnetic cycle due to changes in the beam energy, the transverse radius and the bunch length, and due to the evolving synchrotron tune. Figure 1 demonstrates on the

example of the SIS100 synchrotron how the space-charge parameter range can change during the ramp [4]. The tune shift ΔQ_{sc} decreases from the strong space-charge regime to a rather weak space-charge, while the bunch dynamics related parameter q stays in a narrow range, due to decrease of Q_s .

It is intuitive to assume that a higher intensity always means stronger space-charge. However, this also can be different. An example of measurements in CERN PS Booster in Fig. 2 shows [5] that a nearly linear dependence of the transverse emittance on the beam intensity can result in an almost constant space-charge tune shift.

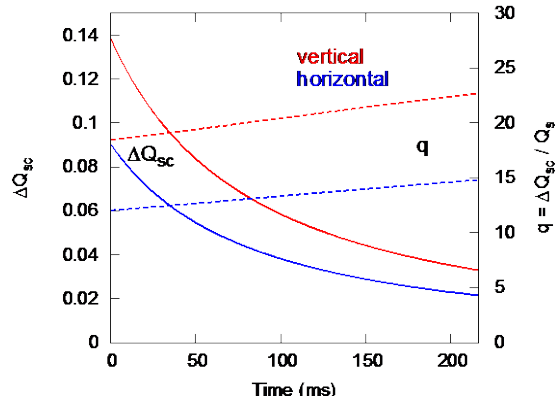


Figure 1: Space-charge tune shift Eq. (1) (the full lines, left axis) and the bunch space-charge parameter Eq. (2) (the dashed lines, right axis) for the nominal SIS100 heavy ion bunches along the ramp, from [4].

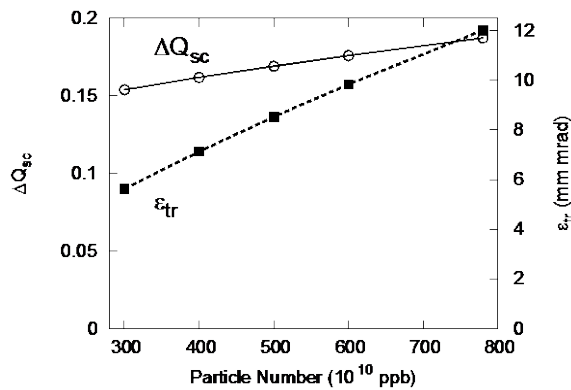


Figure 2: Space-charge tune shift Eq. (1) (the full line, left axis) and the horizontal effective emittance (the dashed line, right axis) in PS Booster in a dependence on the intensity, from [5].

2.16.3 Coasting Beams

A transverse collective instability in one of the transverse planes can be regarded as a decoupled wave with the eigenmode $x(z) = x_0 \exp(inz/R)$, with the mode index n , which gives the number of waves in the “snake” of the instability along the ring in the snapshot observation. The eigenfrequency is directly related to the mode index, $\Omega = (n - Q_0)\omega_0$, where ω_0 is the revolution frequency. This is the slow wave, which is driven by a positive real impedance, while the fast wave is damped. Space-charge does not change the space- and the

time structure of the coasting beam instability. It was also confirmed in numerous numerical and experimental observations.

A small shift can be caused by the inductive impedance of the image charges, which is sometimes considered as a part of space-charge [3]. In this case the coherent frequency is shifted to $\Omega = (n - Q_0 - \Delta Q_{coh})\omega_0$, and the real impedance is probed at this frequency.

The most important effect of space-charge on the coasting beam instability is the loss of Landau damping. Many good reviews for this can be found in the CAS proceedings, for example [6]. There is a dedicated paper about Landau damping in this Newsletter, thus we only mention that space-charge shifts the incoherent spectrum away from the coherent line Ω , and Landau damping (due to momentum spread, nonlinearities, etc.) can become inefficient.

Space-charge tune shift is different for every individual particle because of the transverse profile nonlinearity. This produces an additional tune spread, which changes Landau damping in the beam [7-12], even if there is no Landau damping due to nonlinear space-charge alone in a coasting beam.

2.16.4 Head-Tail Instability

The head-tail modes [13] represent the eigenmodes of the transverse oscillations in bunches. Although these instabilities are often observed in many different ring machines, it is still not straightforward to explain the time- and space structure of the most unstable modes [5, 21, 22] in observations. The effects of space-charge may sometimes play a role.

It has been repeatedly assumed in experiments that space-charge does not cause visible modifications of the head-tail instability space structure. The usual reason for the distortions in comparison to the classical symmetrical standing-wave pattern is the strong driving impedance, which deforms the eigenmodes. For example, observations in the CERN PS Booster [5] show two instabilities at different times during the ramp, see Fig. 3 and Fig. 4. Both seem to be the $k=3$ head-tail mode. Both instabilities evolved in a similarly strong space-charge condition, $q \approx 100$. But, while a slower instability in Fig. 3 ($\text{Im}(\Delta Q)/Q_s = 0.025$) has well-pronounced nodes of the standing-wave structure, the faster instability in Fig. 4 ($\text{Im}(\Delta Q)/Q_s = 0.13$) is much strongly distorted.

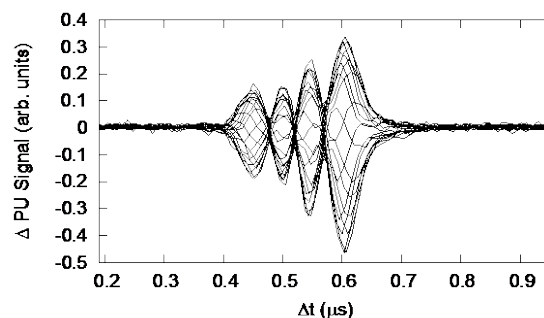


Figure 3: Transverse head-tail instability observed in CERN PS Booster in single-rf operation, $N_p = 400 \times 10^{10}$ ppb, the growth rate is $\text{Im}(\Delta Q) = 0.036 \times 10^{-3}$, from [5].

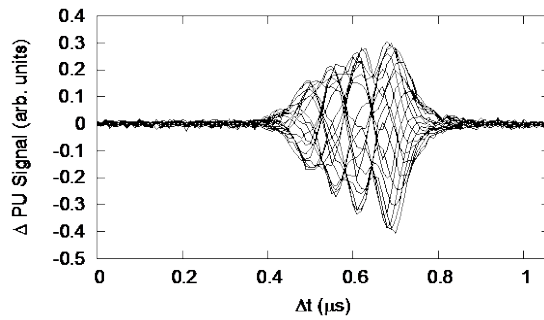


Figure 4: Transverse head-tail instability observed in CERN PS Booster in single-rf operation, $N_p=370 \times 10^{10}$ ppb, the growth rate is $\text{Im}(\Delta Q)=0.23 \times 10^{-3}$, from [5].

The conclusion, that space-charge only weakly changes the space structure of the head-tail eigenmodes, has also been confirmed in theoretical studies [14-16] and observed in particle simulations [18].

The effect of space-charge on head-tail modes is rather important and strong in the time domain. A good description for this effect is given by the "airbag" model [14], $\text{Re}(\Delta Q)/Q_s = -0.5q \pm (0.25q^2 + k^2)^{1/2}$. These space-charge tune shifts are illustrated in Fig. 5. Despite the simplicity of the model, it appeared as a useful tool of the bunch transverse dynamics. The model has been perfectly confirmed by particle tracking simulations for airbag bunches. Analytical studies and particle simulations indicated that this model gives reasonable predictions for the realistic (e.g. Gaussian) bunches [15-18]. The validity of this description for the space-charge effect has been also confirmed in experimental observations [19, 20].

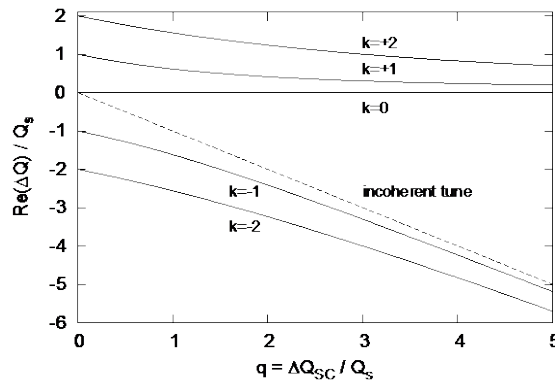


Figure 5: Effect of space-charge on eigenfrequencies of the head-tail modes from the airbag theory [14].

The increment of an instability can be calculated in the frequency domain, as a convolution of the bunch spectrum with the frequency function of the complex impedance [13]. This can also be done in the space domain, as a convolution of the mode eigenfunctions with the wake functions of the facility [2, 15]. For both methods, it is clear that the mode frequencies and eigenfunctions determine the resulting instability growth rate. The effect of space-charge on the eigenmodes saturates for strong space-charge, thus the instability growth rates saturate for strong space-charge as well [14, 15, 18]. Since the frequency shifts within the sidebands are relatively small, and the eigenmode modifications

due to space-charge are weak, the effect on the instability growth rates is rather weak, especially for strong space-charge.

Similarly to the coasting beam case, an important effect of space-charge on instabilities is Landau damping [15-19]. This is a decisive factor of the transverse stability for beams with space-charge, and is considered in a dedicated chapter of the Newsletter.

2.16.5 Transverse Mode Coupling Instability

As soon as two head-tail modes cross in frequency under the effect of an impedance, a Transverse Mode Coupling Instability is excited [1, 2, 24]. Since space-charge has a strong effect on the frequencies of the head-tail modes, it can change the thresholds of the coupling and the instability. The effect of TMCI suppression has been found in theoretical and numerical studies [25, 15]. It is especially clear for the coupling of the $k=0$ mode with the $k=-1$ mode, because there is a strong difference in the space-charge effect on these two modes. Space-charge drives these two modes apart and a stronger wake (and thus, a higher beam intensity) is needed to make the coupling possible. This results in higher instability thresholds, or instability suppression.

Some observations, for example in the CERN SPS [26], have suggested that there was only a weak effect of space charge on TMCI. A possible explanation is related to the finding that the TMCI in SPS was due to the coupling of the $k=-2$ mode with the $k=-3$ mode. Analytical modes and the airbag model (see also Fig. 5) indicate a nearly parallel dependence of eigenfrequencies of these modes on the space-charge strength. Thus, there can be a different effect of space-charge on specific mode coupling, under conditions of the driving impedance and beam- and machine settings.

2.16.6 References

1. K.Y. Ng, *Physics of Intensity Dependent Beam Instabilities*, World Scientific, 2006
2. A. Chao, *Physics of Collective Beam Instabilities in High Energy Accelerators* (John Wiley Sons, Inc., New York, 1993).
3. *Handbook of Accelerator Physics and Engineering*, 2nd Edition, edited by A. Chao, et. al., World Scientific, 2013
4. V. Kornilov, O. Boine-Frankenheim, Proc. IPAC2012, p. 2934, 2012
5. V. Kornilov, et. al., CERN-ACC-NOTE-2014-0025, 2013
6. A. Hofmann, Landau Damping, CERN Accelerator School, Rhodes, Greece, 1993 (CERN 95-06 v.1, p. 275).
7. D. Möhl and H. Schönauer, Proc. IX International Conf on High Energy Acc, Stanford, 1974, p.380
8. J.S. Berg, F. Ruggiero, CERN SL-AP-96-71, 1996
9. E. Metral, F. Ruggiero, Proc. EPAC2004, p. 1897
10. V. Kornilov, O. Boine-Frankenheim, and I. Hofmann, Phys. Rev. ST Accel. Beams 11, 014201 (2008).
11. A. Burov and V. Lebedev, Phys. Rev. ST Accel. Beams 12, 034201 (2009).
12. D.V. Pestrikov, Nucl. Instrum. Methods Phys. Res., Sect. A 562, 65, 2006
13. F. Sacherer, Proc. First Int. School of Particle Accelerators, Erice, p. 198, 1976
14. M. Blaskiewicz, Phys. Rev. ST Accel. Beams 1, 044201 (1998)
15. A. Burov, Phys. Rev. ST Accel. Beams 12, 044202 (2009); A. Burov, Phys. Rev. ST Accel. Beams 12, 109901(E) (2009)

16. V. Balbekov, Phys. Rev. ST Accel. Beams 12, 124402 (2009)
17. D. Möhl, CERN/PS 95-08 (DI), 1995
18. V.Kornilov and O. Boine-Frankenheim, Phys. Rev. ST Accel. Beams 13, 114201 (2010)
19. V.Kornilov and O. Boine-Frankenheim, Phys. Rev. ST Accel. Beams 15, 114201 (2012)
20. R. Singh, et. al., Phys. Rev. ST Accel. Beams 16, 034201 (2013)
21. V. Kornilov, et. al., Proc. of HB2014, East Lansing, USA, November 10-14 (2014)
22. G.H. Rees, Particle Accelerators 39, pp.159-167 (1992)
23. V. Kornilov, O. Boine-Frankenheim, HB2016, Malmö, Sweden, July 3-8, 2016
24. J. Gareyte, CERN report CERN-SL-2000-075, 2000
25. M. Blaskiewicz, Phys. Rev. ST Accel. Beams 1, 044201 (1998)
26. B. Salvant, et. al, Proc. EPAC2008, p. 1694

2.17 Impedance-Induced Beam Instabilities and Damping Mechanisms in Circular Machines – Transverse – Simulations

Kevin Li, Michael Schenk
 CERN, 1211 Geneva 23, Switzerland
 Mail to: kevin.shing.bruce.li@cern.ch

2.17.1 Introduction

The effects of impedance on beam dynamics can be studied with a variety of methods. For example, they can be analyzed (semi-)analytically by means of two-particle models or by using approximate solutions emerging from the Vlasov equation or circulant matrix models. The latter allow also to more accurately obtain the beam eigenmodes and eigenfrequencies in the presence of impedances when solved with numerical methods. And then, there are the macroparticle models which provide the greatest flexibility in the types of physical processes that can be modeled. These include non-linearities in both the transverse and longitudinal motion, complex feedback systems and other highly non-linear and dynamic processes.

We will briefly describe some of the methods available and used today and show how they compare to each other. We will then show a few selected examples of beam dynamics studies in the presence of impedances and how modern simulation tools can be used to improve our understanding.

2.17.2 A Brief Overview over Contemporary Simulation Tools

2.17.2.1 Frequency Domain Vlasov Solvers

Frequency domain Vlasov solvers are used to numerically solve the beam mode eigensystem in order to directly obtain the eigenmodes and the eigenvalues. In the Vlasov formalism, impedance induced wake fields are treated as a perturbation which in turn lead to a perturbation on top of an equilibrium distribution. To construct the eigensystem to be solved, the Vlasov equation is written down up to first order in all perturbations. Assuming purely dipolar wake fields, all transverse degrees of freedom can be eliminated. An expansion of the remaining perturbation term in the longitudinal degrees of freedom then leads to the eigenvalue problem:

$$(\Omega - \omega_\beta - l \omega_s) a_l b_{kl} = \sum_{k', l'} a_{l'} b_{k' l'} M_{kk', ll'}. \quad (1)$$

Here, Ω is the complex tune giving the coherent tune shift and the rise time of the respective eigenmodes (k, l) , thus characterizing the beam stability, and ω_β and ω_s are the betatron and synchrotron frequencies, respectively. $M_{kk', ll'}$ is the interaction matrix described in detail in [1]. This equation resembles an eigenvalue problem that can be diagonalized to obtain the eigenmodes and the eigenfrequencies of the perturbation. There are several codes available to solve it [2, 3, 4]. The modern ones also include feedback systems in the special form of an impedance. The code DELPHI [4] uses an expansion in Laguerre polynomials which provides certain advantages in the convergence of the solutions and for the implementation of automated convergence checks.

Roughly speaking, when neglecting mode coupling, the interaction matrix corresponds to the effective impedance, such that [1]:

$$M \propto (Z_1^\perp)_{eff} = \frac{\sum_p Z(\omega') h_l(\omega' - \omega_\xi)}{\sum_p h_l(\omega' - \omega_\xi)}, \quad \omega' = p\omega_0 + \omega_\beta + l\omega_s, \quad \omega_\xi = \xi \frac{\omega_\beta}{\eta}. \quad (2)$$

Here, Z is the impedance, ω_0 the revolution frequency, ξ the chromaticity and η the slippage factor. For analytical estimations, where the system is not strictly diagonalized, one often makes an educated guess on the eigenmodes $h_l(\omega')$ assuming that they diagonalize the problem reasonably well, and uses these to compute the effective impedance and thus the complex tune shifts [1, 5].

2.17.2.2 Circulant Matrix Models

Impedances are typically computed only up to leading order, generating dipolar and quadrupolar wake fields. Then, all the involved forces are linear which makes matrix formalisms a natural choice to study beam stability. To describe the beam interaction with wake fields in the presence of betatron and synchrotron motion, correctly taking into account the synchro-betatron coupling generated via the wake fields, circulant matrix models have proven to be extremely powerful [6, 7]. They rely on a similar discretization of the longitudinal phase space as is done for Vlasov solvers, i.e. using polar coordinates. The full transverse dynamics is then described via a linear one-turn-map expressed by the matrix:

$$M = S_0 \otimes B \otimes C_w, \quad (3)$$

with

$$S_0 = \mathbb{I}_{N_r} \otimes (P_{N_s})^{N_s Q_s}, \quad P_{N_s} = \begin{pmatrix} 0 & 1 & & 0 \\ & 0 & 1 & \\ & & \ddots & \ddots \\ 1 & & & 0 & 1 \end{pmatrix},$$

$$B = w(z, \delta) B_0(z, \delta),$$

$$[C_w]_{ij} = \begin{cases} \begin{pmatrix} 1 & 0 \\ \sum_k W_{quad}(s_i - s_k) & 1 \end{pmatrix}, & \text{if } i = j \\ \begin{pmatrix} 0 & 0 \\ \sum_k W_{dip}(s_i - s_k) & 0 \end{pmatrix}, & \text{if } i \neq j \end{cases}.$$

The one-turn-map is constructed via tensor products, the final dimensionality being given as $\dim(M) = N_{dof} \times N_r \times N_s$, with N_{dof} the number of degrees of freedom in the transverse plane (typically 4), and N_r and N_s as the number of rings and slices used for the discretization, respectively. S_0 is a permutation matrix describing the synchrotron motion, $w(z, \delta) B_0(z, \delta)$ is the distribution weighted betatron motion over one turn for a given cell element and can contain chromatic effects via the dependency on the longitudinal coordinates. And, finally, C_w contains the coupling of the cells via the dipole and quadrupole wake fields W_{dip} and W_{quad} , respectively.

The eigenmodes and eigenfrequencies can be computed easily, again, by diagonalizing the obtained one-turn-matrix. With a systematic expansion in dimensions, multi-bunch effects can be added in a straightforward manner. The formalism allows additional inclusion of further linearized forces such as the ones introduced by long-range and head-on beam-

beam effects. In that sense it provides a highly efficient way of computing multi-bunch or even multi-beam effects as long as all forces are linear. At the same time, however, this is also one of the main limitations as any non-linear forces are excluded. This means that for example Landau damping cannot be modeled.

2.17.2.3 *Macroparticle Tracking Codes*

Macroparticle models provide the most flexible way of implementing physical effects in computer simulations. Very little abstraction is needed as the particle system along with the external and internal forces are directly mapped to the computer system via the complete and explicit implementation of the equations of motion. The basic idea is that a cluster of neighboring physical particles can be numerically represented by its center of mass dynamics as a single macroparticle. If the physical particles are close enough to each other and collision effects are neglected this is a valid approximation. This dramatically reduces the number of degrees of freedom and makes the modelling of realistic particle systems computationally accessible.

The equations of motion are integrated numerically in that each macroparticle is propagated in small time steps according to the equations of motion. Here, in principle any effect that can be described in terms of equations of motion can be included. They can be external electromagnetic fields as well as collective forces from either the same or from another macroparticle system. Highly non-linear and time-dependent fields, such as the ones encountered when modeling electron cloud interaction, as well as complex feedback or feedforward systems can be integrated. The price to pay for the enhanced flexibility is the increase in the requirements for computational power as little approximations are made and the full set of equations of motion needs to be solved for a macroparticle system that can contain several millions of macroparticles. Moreover, solving the equations of motion takes place in time domain and the complex tune shift can only be accessed indirectly in a post-processing step. The real part is extracted from a frequency analysis, while the imaginary part is obtained by fitting rise times. Hence, to access slow rise times, tracking may need to be performed over millions of turns.

By varying the time step interval and the macroparticle number one can check the convergence and thus the potential validity of the solution. To obtain full confidence in the obtained solutions, typically different codes using different approaches, such as the ones described here, are used to benchmark results against each other. This is used complementary to the ultimate benchmarks which come from machine observations.

2.17.3 **Benchmarking for Transverse Mode Coupling Instability in the SPS**

Using the three beam dynamics models introduced in section 2.16.2 above, the coherent mode spectra are evaluated and compared to one another. The codes used are the Vlasov solver DELPHI [4], the circulant matrix model BimBim [6] and the macroparticle tracking code PyHEADTAIL, all of which are developed at CERN.

The Transverse Mode Coupling Instability (TMCI) in the Super Proton Synchrotron (SPS) at CERN serves as an excellent use case to study different accelerator beam dynamics models. To obtain clear results, the SPS impedance model is approximated by only a broadband resonator. It is worth mentioning that even with such a simple model, one manages to reproduce the main observations made in the machine [8]. The results from simulations are given in Fig. 1 and show the intensity-dependent mode spectra and the tune shifts induced by the presence of the impedance. The overlay of the mode spectra obtained with DELPHI, BimBim and PyHEADTAIL shows a very good agreement between the three approaches. The tune shifts are reproduced with all the models and the mode couplings occur at the same intensities. Some small differences are currently under investigations.

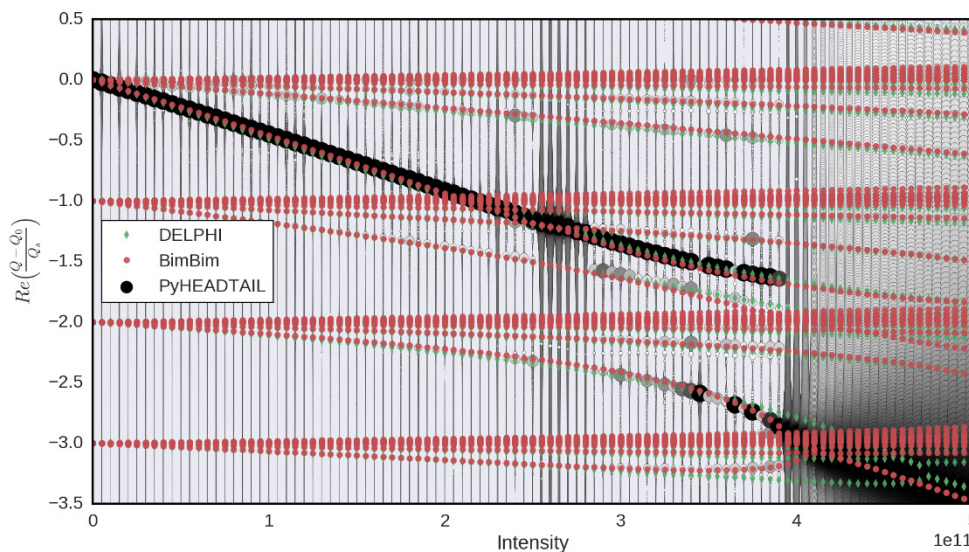


Figure 1: Mode spectra for the SPS obtained for a broadband resonator impedance with DELPHI (green), BimBim (red) and PyHEADTAIL (grey).

2.17.4 Examples of Simulations and Use Cases

We will show two examples of use cases for studying impedance induced instabilities and damping mechanisms which involve modern simulation techniques. Both rely on an accurate modeling also of the synchrotron motion. The first example shows Landau damping in the LHC achieved in two different fashions. Using the LHC impedance model, instabilities observed at 3.5 TeV can be reproduced in simulations. These instabilities are then shown to be mitigated using the installed Landau octupoles. The same instabilities can also be mitigated by means of an rf quadrupole which introduces a betatron tune spread via the longitudinal action. The second example shows the impact of a multi-harmonic rf system on the transverse mode coupling instability in the HL-LHC. Finally, the interplay with a bunch-by-bunch damper on the same type of instability is briefly discussed.

2.17.4.1 *Stabilization from Incoherent Betatron Tune Spread*

One successful stabilizing mechanism for the so-called slow head-tail instabilities [1] is the effect of Landau damping [9]. It is present when there is a spread in the betatron

frequency, or tune, of the particles in a bunch. A necessary, though not sufficient, condition for Landau damping is that the real part of the complex coherent tune shift $\Delta\Omega$, induced by the impedance, lies within the incoherent tune spread of the beam. The details of the stabilizing mechanism are e.g. discussed in [1] and references therein.

The incoherent betatron tune spread results from non-linearities in the machine, e.g. space-charge forces, beam-beam interactions at collision, etc. In addition, they are often introduced by design through dedicated elements. The tune spread is produced through detuning with amplitude, i.e. a dependence of the betatron tunes (Q_x^i, Q_y^i) on the action (J_x^i, J_y^i, J_z^i) of a particle i . In practice, dedicated magnetic octupoles, so-called Landau octupoles, have been successfully used for that purpose. They change the betatron tunes of a particle i depending on its transverse actions (J_x^i, J_y^i), which is also known as detuning with *transverse* amplitude. A typical tune footprint generated by magnetic octupoles is shown in Fig. 2, left. The stabilizing effect from Landau octupoles has been studied extensively in experiments, simulations and using stability diagram theory [10, 11]. An example of a PyHEADTAIL simulation proving the stabilizing effect from magnetic octupoles is shown in Fig. 3, left.

Alternatively to betatron detuning with *transverse* amplitude, one can introduce a detuning with *longitudinal* amplitude, i.e. $\langle \Delta Q_{x,y}^i \rangle_{T_s} = f(J_z^i)$, where $\langle \dots \rangle_{T_s}$ denotes the average detuning over one synchrotron period T_s . Such a detuning can be achieved for instance by means of a non-zero second-order chromaticity $Q''_{x,y}$, where

$$\Delta Q_{x,y}^i(t) = \frac{Q''_{x,y}}{2} \delta_i^2, \quad \text{and hence} \quad \langle \Delta Q_{x,y}^i \rangle_{T_s} = \frac{Q''_{x,y}}{2} \sigma_\delta J_z^i. \quad (4)$$

δ_i denotes the momentum error of particle i , and σ_δ is the momentum spread. The averaging is done assuming linear synchrotron motion. Alternatively, a so-called rf quadrupole structure can be used, which is a dedicated rf cavity operating in a quadrupolar mode, therewith introducing a harmonic dependence of the betatron tunes along the longitudinal coordinate of the bunch:

$$\Delta Q_{x,y}^i(t) \propto \cos\left(\frac{\omega}{\beta c} z_i(t)\right) \approx 1 - \frac{1}{2} \left(\frac{\omega}{\beta c}\right)^2 z_i^2(t), \quad \text{hence} \quad \langle \Delta Q_{x,y}^i \rangle_{T_s} \propto 1 - \frac{1}{2} \left(\frac{\omega \sigma_z}{\beta c}\right)^2 J_z^i, \quad (5)$$

where ω is the rf frequency, βc the particle speed, z_i the longitudinal position, and σ_z the rms bunch length. The equations are valid under the assumptions of linear synchrotron motion and given that $\sigma_z \ll \beta c / \omega$. The two methods are discussed in more detail in [12].

Up until now, betatron detuning with longitudinal amplitude has not been deliberately employed as a means of stabilization in real machines. However, with the planned upgrade from LHC to High Luminosity LHC (HL-LHC), or the Future Circular Collider (FCC), it has gained more interest and is under extensive study, both theoretically and experimentally. The reason is that compared to detuning with transverse amplitude, detuning with longitudinal amplitude can be much more efficient, since in machines of this type, the longitudinal action spread is by orders of magnitude larger than the transverse ones [13]. Moreover, for reasons of stability in the longitudinal plane, the longitudinal emittance and thus the longitudinal action spread is held constant along the energy ramp, while the transverse action spread suffers from adiabatic damping. Consequently, the incoherent tune spread can be generated more easily by means of a dependence on J_z . A typical tune distribution introduced by $Q''_{x,y}$ is shown on the right hand side of Fig. 2 for comparison to that obtained from magnetic octupoles. There are two major differences. First, the tune

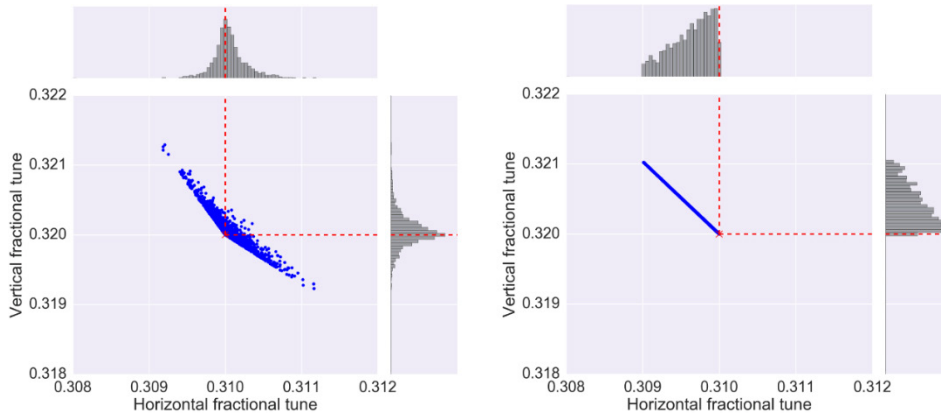


Figure 2: Simulated tune footprints caused by detuning with transverse (magnetic octupoles, left) and longitudinal (second-order chromaticity, right) amplitude.

footprint from $Q''_{x,y}$ shows a full correlation between Q_x and Q_y , since there is only one independent variable J_z causing the detuning. Second, the projection histograms reveal an asymmetry for the incoherent tune distributions for detuning with longitudinal amplitude. The latter may have consequences on the stabilizing effect and is currently under study. Nevertheless, the numerical proof-of-principle for Landau damping from detuning with longitudinal amplitude has been achieved with the PyHEADTAIL macroparticle tracking code and was presented in [12, 14].

The main result is summarized in Fig. 3, where an LHC weak head-tail instability in the horizontal plane observed at 3.5 TeV is suppressed by means of Landau damping once with magnetic octupoles (left) and once with an rf quadrupole (right). The required current in the LHC Landau octupoles is in good agreement with experiment and stability diagram theory [10].

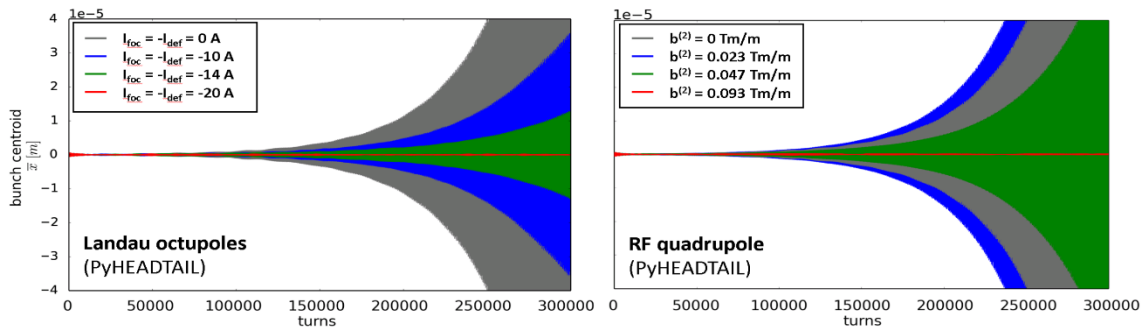


Figure 3: LHC at 3.5 TeV. Horizontal weak head-tail instability suppressed thanks to Landau damping. Left: Using LHC magnetic octupoles. Right: With an rf quadrupole. $\mathbf{b}^{(2)}$ denotes the quadrupolar strength of the cavity in magnetic units.

2.17.4.2 *Impact of Multi-Harmonic Rf Systems and Transverse Damper on TMCI*

The HL-LHC impedance leads to a transverse mode coupling instability at sufficiently high intensities. Although the instability threshold is well beyond the design value, it is worth studying this threshold in order to assess the available margin. The particular features of the HL-LHC impedance results in a coupling of modes 0 and -1 and a rough scaling law

for the TMCI intensity threshold described as $I_{threshold} \propto \sigma_z Q_s$ [15], where σ_z is the rms bunch length and Q_s is the synchrotron tune.

A multi-harmonic rf system is studied as a possible option for HL-LHC to enhance Landau damping in the longitudinal plane. This will change the bunch lengths as well as the synchrotron tune spectrum and will therefore have an impact also on the transverse stability. To model the beam dynamics consistently in all three planes, macroparticle models again provide the most straightforward and flexible way. Figure 4 shows the synchrotron tune spectrum obtained with a PyHEADTAIL simulation running with a single 200 MHz rf system and compares it to a combined 200 and 400 MHz system operated in bunch shortening and bunch lengthening mode, respectively.

Figure 5 shows the impact of the different operating modes on the TMCI threshold. It becomes clear that from the TMCI point of view, bunch shortening mode is the most favourable due to the strongly enhance synchrotron tune.

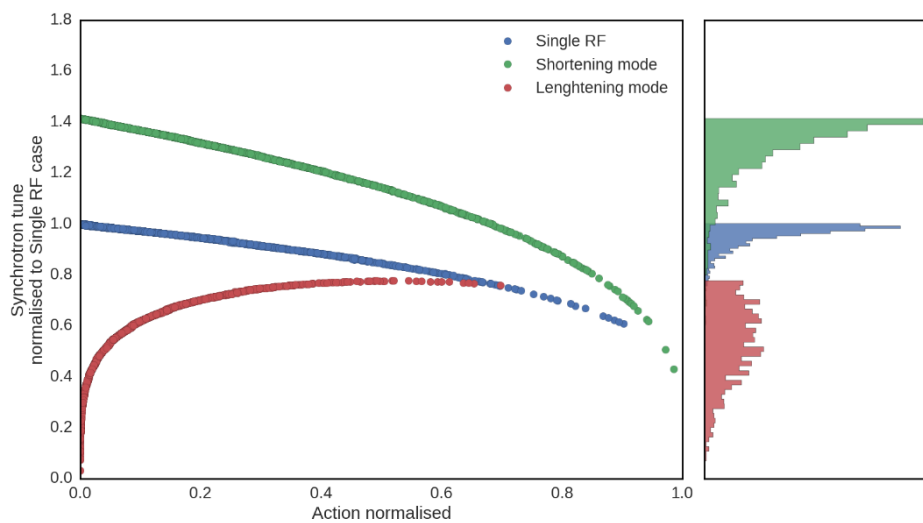


Figure 4: The synchrotron tune distribution evaluated from macroparticle simulations for different configurations of a double harmonic rf system.

In a final example, a bunch-by-bunch damper is added to the simulation in an attempt to entirely mitigate the TMCI. As illustrated in Fig. 6, the bunch-by-bunch damper successfully mitigates the dipole component of the motion and moves the TMCI threshold. However, it also modifies the impedance and, with its limited bandwidth, excites a mode 1 type head-tail motion even below the TMCI threshold. It is likely linked to the limited bandwidth and a feedback system with a larger bandwidth could potentially overcome this limitation. Feedback systems of this type are currently being investigated in simulations [16].

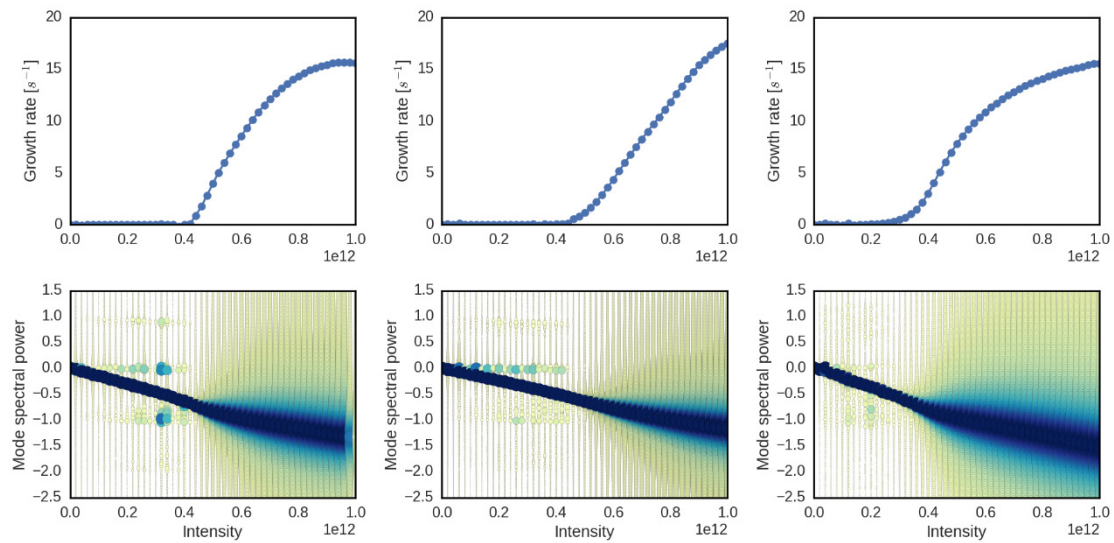


Figure 5: Transverse mode coupling instability compared for different configurations of a double harmonic rf system, with just a single rf (left), a double rf in bunch shortening mode (center) and a double rf in bunch lengthening mode (right).

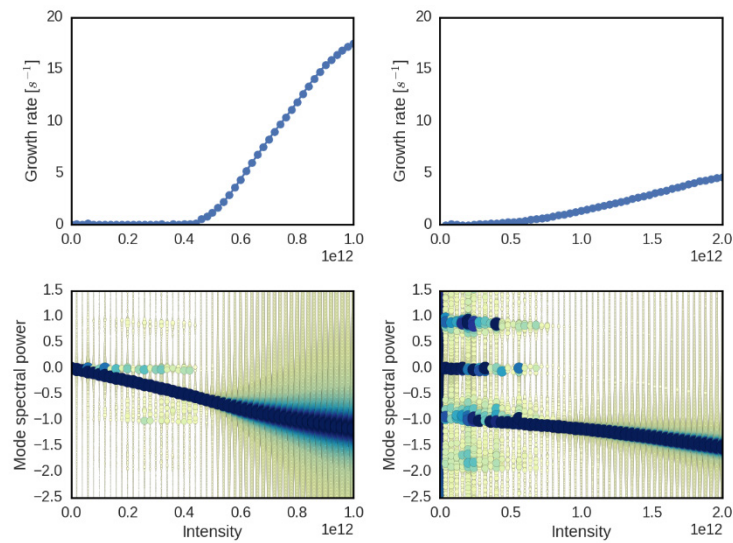


Figure 6: TMCI (left) and its mitigation using a transverse damper (right). In addition, it is clearly visible how, instead, a head-tail mode -1 is excited.

2.17.5 References

1. A. W. Chao, “Physics of Collective Beam Instabilities in High Energy Accelerators”, New York: Wiley, 1993.
2. Y. Chin, “MOSES users guide: MOde-coupling Single bunch instability in an Electron Storage ring”, CERN/SPS/85-2 & CERN/LEP-TH/88-05.
3. A. Burov, “Nested head-tail Vlasov solver”, Phys. Rev. ST AB 17, 021007 (2014).
4. N. Mounet, “DEHLPI: an analytic Vlasov solver for impedance-driven modes”, 12th

HSC Meeting, CERN, 2014.

5. F. Sacherer, "Bunched Beams", 1st International School of Particle Accelerators "Ettore Majorana", Erice, Italy, 10 - 22 Nov 1976.
6. X. Buffat, "Transverse beams stability studies at the Large Hadron Collider", PhD thesis, EPFL, 2015.
7. E. A. Perevedentsev and A. A. Valishev, "Simulation of the head-tail instability of colliding bunches", Phys. Rev. ST AB 4, 024403 (2001).
8. B. Salvant, "Impedance model of the CERN SPS and aspects of LHC single-bunch stability", CERN-THESIS-2010-087, 2010.
9. L. Landau, "On the vibration of the electronic plasma", J. Phys. USSR 10, 1946.
10. E. Métral et al., "Stabilization of the LHC single bunch transverse instability at high energy by Landau octupoles", Tech. Rep. CERN-ATS-2011-102, 2011.
11. S. Berg and F. Ruggiero, "Stability diagrams for Landau damping", LHC-Project-Report-121, 1997.
12. M. Schenk et al., "Use of rf quadrupole structures to enhance stability in accelerator rings", Proceedings of HB2016, Malmö (Sweden), 2016.
13. A. Grudiev, "Radio frequency quadrupole for Landau damping in accelerators", Phys. Rev. ST Accel. Beams 17, 011001, 2014.
14. A. Grudiev et al., "Radio frequency quadrupole for Landau damping in accelerators: Analytical and numerical studies", Proceedings of HB2014, East-Lansing (USA), 2014.
15. E. Métral, "Collimation-driven Impedance", Conceptual Design Review LHC Phase II Collimation, CERN, 02-03/04/2009.
16. K. Li et al., "Instabilities simulations with wideband feedback systems: CMAD, HEADTAIL, WARP", Proceedings of the 2012 ELOUD Workshop, La Biodola, Isola d'Elba, Italy, 2012.

2.18 Beam-Based Longitudinal and Transverse Impedance/Instability Measurements

G. Rumolo, E. Shaposhnikova
 CERN, 1211 Geneva 23, Switzerland
 Mail to: Giovanni.Rumolo@cern.ch

2.18.1 Introduction

The wake function of an accelerator device is defined as the integral along the full electromagnetic length of the device of the electromagnetic force generated by a point charge going through the device at the speed of light and acting on a witness point charge placed at a distance z from the source. For the longitudinal plane, both source and witness are assumed to be traveling on axis – usually defined by the symmetry axis of the device, or by the closed orbit trajectory when the device is placed in an accelerator. For the transverse plane (horizontal and vertical), one has to consider offsetting either the source particle (dipolar wake) or the witness particle (quadrupolar wake) by an arbitrarily small amount, and redefine the wake as the electromagnetic force normalised to the given offset. The beam coupling impedance is the Fourier transform of the wake function (additionally multiplied by the imaginary unit i in the case of the transverse impedance) and therefore describes the same type of interaction in the frequency domain. Note that, due to the normalisation to the offset in the definitions, transverse wakes/impedances have an additional m^{-1} in the dimensions with respect to their longitudinal counterparts. Due to the validity of superposition and if one assumes that adjacent devices can be considered electromagnetically decoupled, the beam coupling impedance of a sequence of devices turns out to be a simple weighted sum of the beam coupling impedances of the single devices. The weights are given by the optical beta functions at the locations of the devices for the horizontal and vertical impedances, while they are just unitary for the longitudinal impedances. A full accelerator ring can be described through a global beam coupling impedance, which represents the beta function weighted sum of the beam coupling impedances of its individual components in the transverse plane and their simple sum in the longitudinal plane (see Section 2.9). While wake functions are widely used in macroparticle simulations to express the driving terms representing the electromagnetic interaction of the beam in the equations of motion of the single macroparticles, beam coupling impedances are commonly used to describe electromagnetically single devices and make comparative studies. Furthermore, since analytical models usually solve the beam equations in frequency domain, global or individual beam coupling impedances can also be fed in handy formulae to estimate quantities like power loss, synchronous phase shift, betatron and synchrotron tune shifts and instability/damping rates in controlled operating conditions. Beam coupling impedances of single devices can be measured either in a laboratory prior to their installation in a machine (see Section 2.8) or with beam directly in the accelerator in which they are installed, using specific local techniques, some of which will be shortly addressed in one of the next subsections. The global beam coupling impedance of an accelerator can be estimated using techniques based on direct global beam observables, like the quantities listed above, for which simplified analytical expressions exist. Different techniques have to be used to estimate separately the real and the imaginary parts of the impedance, while different frequency ranges can be probed according to the beam parameters used in the measurement, as will be explained in this chapter at a later stage.

In the following subsections, we will solely focus on the review of a subset of the most common existing techniques to measure the beam coupling impedance of a full accelerator ring based on global beam measurements. However, it is worth mentioning briefly at this stage that there exist also techniques to estimate the impedance of single components with beam. Here are some examples:

- Differential global measurements can be used for elements that can be moved in and out, like collimators, scrapers, experimental insertions, movable diagnostics, or in-vacuum undulators. The contribution to the impedance given by these elements in their ‘in’ position can be evaluated by difference measuring the global impedance of the ring when they are retracted and when they are inserted.
- Global impedance measurements can also be made in the same beam conditions before and after the installation of a certain element into an accelerator ring. This provides a direct estimation of the impedance of the element installed. For both this case and the case above, this type of measurement is possible only if the relative contribution of the device under test to the global impedance of the ring is high enough to be detectable within the accuracy of the measurement.
- Another technique that has been attempted in many accelerators is the transverse impedance localisation through the measurement of the shift of the phase advance between successive beam position monitors with intensity. This method is expected to provide information about the detailed breakdown of the total impedance of a machine over its elements and identify at least the most significant contributors.
- The longitudinal impedance of a certain element can be directly estimated if the beam induced heating of this element can be measured. This is usually the case for devices like ferrite kickers, whose temperature is monitored to prevent them from overheating and reaching the Curie temperature, or cold vacuum chambers or pieces of equipment, e.g. in superconducting magnets (like the LHC beam screen) or superconducting RF cavities.

It should be noted that in many cases the impedance model of a device or a machine is also built independently via electromagnetic simulations and/or bench measurements (ideally, already in the design phase of the accelerator to predict its performance), and then simply validated through beam based measurements. For completeness, in the next sections we will always illustrate selected applications of the various methods to running accelerators.

2.18.2 Transverse Impedance Measurements with Beam

2.18.2.1 *Tune Shifts with Intensity and Instability Growth Rates with Chromaticity*

The kinetic theory based on the solution of the Vlasov equation can be applied to a single bunch under the effect of a dipolar transverse wake/impedance and the evolution of the bunch distribution function in phase space can be resolved resorting to mode decomposition. In particular, it can be demonstrated that, for sufficiently low intensity values, any coherent transverse oscillation of a single Gaussian bunch circulating in a given machine can be decomposed into an infinity of modes, whose frequencies are given by the following formula [1]:

$$\Omega^{(l)} - \omega_\beta - l\omega_s \approx -\frac{i}{4\pi} \frac{\Gamma(l + \frac{1}{2})}{2^l l!} \frac{N e^2 \bar{\beta}_{x,y}}{m_0 \gamma C \sigma_z} \frac{\sum_{p=-\infty}^{\infty} Z_1^\perp(\omega') h_l(\omega' - \omega_\xi)}{\sum_{p=-\infty}^{\infty} h_l(\omega' - \omega_\xi)} \quad (1)$$

where l is the mode number, C is the circumference of the accelerator, ω_β is the betatron frequency (i.e. the machine tune $Q_{x,y}$ multiplied by the revolution frequency $\omega_0 = 2\pi c/C$), ω_s is the synchrotron frequency (i.e. the synchrotron tune Q_s multiplied by the revolution frequency $\omega_0 = 2\pi c/C$), N is the number of particles in the bunch, $\bar{\beta}_{x,y}$ is the average beta function of the accelerator, γ is the relativistic factor, σ_z is the rms bunch length, $Z_1^\perp(\omega)$ is the global transverse impedance of the machine, $h_l(\omega)$ are the spectra of the different modes of the Gaussian bunch, given by the following equation:

$$h_l(\omega) = \left(\frac{\omega \sigma_z}{c}\right)^{2l} \exp\left(-\frac{\omega^2 \sigma_z^2}{c^2}\right) \quad (2)$$

ω' is defined by

$$\omega' = p\omega_0 + \omega_{\beta x,y} + l\omega_s \quad (3)$$

ω_ξ is the chromatic frequency defined by:

$$\omega_\xi = \frac{\xi_{x,y} \omega_{\beta x,y}}{\eta} \quad (4)$$

η is the slippage factor of the accelerator, which depends on the momentum compaction factor α and the relativistic factor γ according to

$$\eta = \alpha - \frac{1}{\gamma^2} \quad (5)$$

With this convention, η is positive if the accelerator ring is operated below transition ($\gamma < 1/\sqrt{\alpha}$) and it is negative above transition. The modes given by Eq. (1) are called ‘azimuthal modes’. In reality, for each azimuthal mode there exists also an infinity of ‘radial modes’, but this can be neglected in the regime we are considering. To be noted that the last fraction present at the RHS of Eq. (1), featuring at the numerator the weighted summation of the sampled transverse impedance multiplied by the bunch modal spectrum (shifted by the chromatic frequency), is usually defined as effective impedance Z_{eff} and does not depend on frequency.

From Eq. (1) we can derive two possible classes of observables:

- 1) If the chromaticity is zero, the $l=0$ mode represents a pure centroid (rigid bunch) oscillation. Its frequency is purely real and depends solely on the imaginary part of the

impedance. The LHS of Eq. (1), divided by the revolution frequency, reduces to the coherent betatron tune shift of the bunch. It can be measured in practice by exciting the bunch (by means of a kick or continuous excitation) and determining the deviation of its tune, as obtained by Foutier analysing the turn-by-turn data acquired with a position pick up, from the nominal tune of the machine (zero intensity tune). This measurement can be repeated for different intensities and the measured slope $\text{Re}(\Delta\Omega)/(N\omega_0)$ would provide direct information about the effective transverse impedance. It is important to point out here that the slope of the coherent tune shift with intensity is always negative because the summation at the numerator of the LHS of Eq. (1) reduces to i times a positive quantity (this can be demonstrated from the properties of the impedances). Physically, this means that the effect of an impedance on a bunch is always globally defocusing. Modes with $l \neq 0$ represent components of the bunch oscillation accounting for the relative dephasing between head and tail. These modes exist also in absence of chromaticity, as they are introduced by the synchro-betatron coupling due to the beam coupling impedance itself – and the formula above would provide their shift with intensity similarly to mode $l=0$. However, since they are usually very weak and difficult to detect, the shift with intensity of high order headtail modes is not a handy observable to make impedance estimations. In practice, these modes tend to become visible only for higher intensities, when Eq. (1) breaks down and adjacent modes tend to couple, giving rise to strong headtail instabilities. This will be covered to some extent in the next subsection. It is important to highlight at this stage that, although Eq. (1) was obtained by assuming in the model only the presence of a dipolar type of impedance, in reality the transverse impedance that can be inferred through the measurement of the coherent tune shift with intensity is what accelerator physicists usually refer to as ‘generalised impedance’, i.e. the sum of the dipolar and quadrupolar components of the transverse impedance [2]. This has to be kept in mind when applying this method, as in most accelerators the quadrupolar component of the impedance is of the same order of magnitude as the dipolar component and its contribution to the tune shift is not negligible. This may result in either a significantly larger value of impedance with respect to what could be expected from a model based on dipolar impedances alone or in an almost zero impedance measured, as the quadrupolar component can have opposite sign with respect to the dipolar component and the two contributions to the coherent tune shift would therefore tend to cancel out.

2) If chromaticity is nonzero, the pattern of the $l=0$ mode is associated with a headtail dephasing and the oscillation frequency of this mode is complex. One can see that the imaginary part of this complex number, which only depends on the real part of the transverse impedance, is positive (growth rate, which is the inverse of the rise time) if chromaticity is negative above transition energy. In a similar fashion, this mode will be also unstable for positive chromaticity if the accelerator ring is operating below transition. The rise time of this instability can be measured for different chromaticity values providing not only an estimation of the resistive part of the impedance but also providing information on its frequency spectrum, roughly scanned via the change of the chromatic frequency. Usually, this mode is quite strong and its rise time is a clearly measurable quantity. Modes with $l \neq 0$ are headtail oscillations that tend to become unstable in a complementary fashion with respect to the $l=0$ mode (i.e. with positive chromaticity above transition and with negative chromaticity below transition). This is certainly true with impedances of resistive wall type, while the situation is

more complicated with broad-band types of impedances and depends on the bunch length and resonance frequency of the broad band resonator. Measurements of the growth rates of these high order headtail modes, usually possible in presence of a strong resistive wall impedance, are quite difficult in other cases, because they have long rise times for low intensities and can be easily stabilised by other mechanisms (e.g. Landau damping).

In the case of the growth rates of the headtail modes (of whatever order l), the mechanism that drives the instability is only linked to the dipolar impedance. As a consequence, the measurement can only reveal the real part of the dipolar component of the impedance, while no information on the quadrupolar component can be inferred using this method.

It is worth noting also that using short bunches (as low σ_z as possible) for the evaluation of Eq. (1) has the twofold benefit to i) produce potentially larger tune shifts with intensity and make the tune shift more easily detectable and freer from resolution errors; and ii) result in wider bunch spectra $h_l(\omega)$, sampling the impedance over a larger frequency span. An important implication of this simple fact is that measurements with different bunch lengths can be conducted to potentially assess the high frequency content of the impedance spectrum. If increasing the bunch length results in a tune shift with intensity scaling like the inverse of the bunch length, one could deduce that the transverse impedance spectrum does not extend significantly beyond the bandwidth of the longest bunch used in the measurements; if, conversely, the relation is more complicated, information on the integrated impedance spectrum in the ranges of frequency progressively covered by the different bunch spectra can be found.

Measurements of coherent tune shift with intensity for about constant bunch length carried out at the CERN Super Proton Synchrotron (SPS) in 2012 are displayed in Fig. 1 [3].

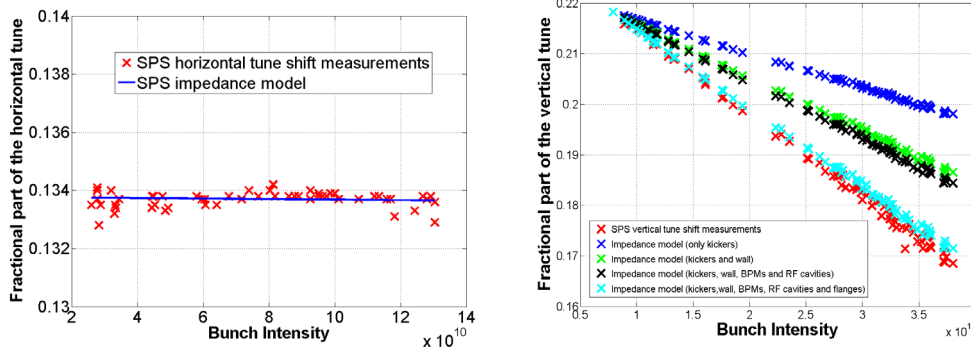


Figure 1: Fractional part of the horizontal (left) and vertical (right) tune as a function of the bunch intensity in the CERN SPS. The red crosses correspond to the measured points.

In both plots shown in Fig. 1, we can see the measured tunes at the different intensities (red crosses) as well as the calculations using the existing SPS impedance model, built from summing up the contributions of the individual elements (at least those deemed to be most significant in the global impedance assessment). In the case of the vertical plane, in addition, the breakdown of the different contributions to the global impedance model of the machine has been explicitly included. Looking at the different lines, one can easily deduce that the magnetic kickers are responsible for about 40% of the total vertical impedance for the SPS (blue crosses), the vacuum chamber wall for 20% (blue to green crosses), other components

– e.g. Beam Position Monitors and RF cavities – for about 5% (green to black crosses), and the vacuum flanges and chamber discontinuities for 25% (black to cyan crosses). In total, the imaginary part of the vertical impedance of the SPS is known up to 90% and this is proven also by complementary measurements shown in the following.

The SPS is also an ideal example to illustrate the importance of including the contribution of the quadrupolar impedance in the interpretation of the measurements of coherent tune shift with intensity for a certain machine. Figure 2 shows the expected tune shift with intensity in both the horizontal and vertical planes when the quadrupolar impedance of the SPS (as known from the global impedance model of the machine) is included in the calculation or not.

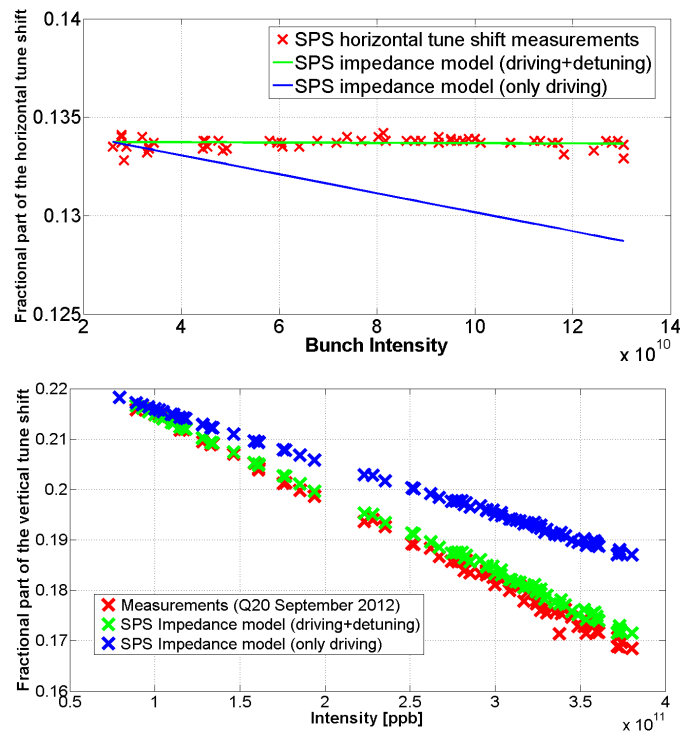


Figure 2: Fractional part of the horizontal (top) and vertical (down) tune as a function of the bunch intensity in the CERN SPS. The blue lines show the expected tune shift with intensity if only the dipolar component of the impedance is included in the calculation.

It is clear that, without the quadrupolar impedance, we would expect roughly similar tune shifts with intensity in both planes (i.e. $\Delta Q_{x,y}/10^{11} \approx 0.05$). However, this value acquires an additional 30% in the vertical plane, while it is basically compensated in the horizontal plane, only due to the contribution of the quadrupolar impedance. The negative quadrupolar impedance in the horizontal plane comes from both the flat vacuum chambers, which occupy more than 60% of the full SPS circumference, and the magnetic kickers (for which the negative quadrupolar impedance is even larger in absolute value than the dipolar one).

Another set of measurements conducted at the CERN SPS is that of the growth rates of the $l=0$ mode instability for negative chromaticity. Here single bunches with very low intensity (2×10^{10} p) were injected into the SPS with a kinetic energy of 25 GeV ($\gamma=27.7$), which is above the transition energy of the ring in both optics configurations for which these measurements were carried out (Q20 with $\gamma_t=18$ and Q26 with $\gamma_t=23$). By setting the

vertical chromaticity to different negative values prior to injection, the beam would become immediately unstable after injection and its rise time could be inferred from the turn-by-turn signal of a position pick up. To interpret these measurements, two different methods were considered: the first one based on the simple application of Eq. (1) with the real part of the impedance as from the global SPS impedance model and the second one based on the reproduction of the observed bunch dynamics by means of the HEADTAIL macroparticle code [4] fed with the wake function associated to the SPS impedance model. The advantage of the second method with respect to the first one was that it would include the possible effects of the nonlinear chromaticity model of the machine as well as the nonlinear longitudinal dynamics of the long bunch in its RF bucket. Figure 3 shows the measured and predicted growth rates in the Q20 (left) and Q26 (right) optics as a function of the chromatic frequency. Due to closer proximity to transition at injection in the Q26 optics, and therefore the lower value of the slippage factor η , obviously the explored frequency range is in this case could be over 3 times larger than in Q20 case.

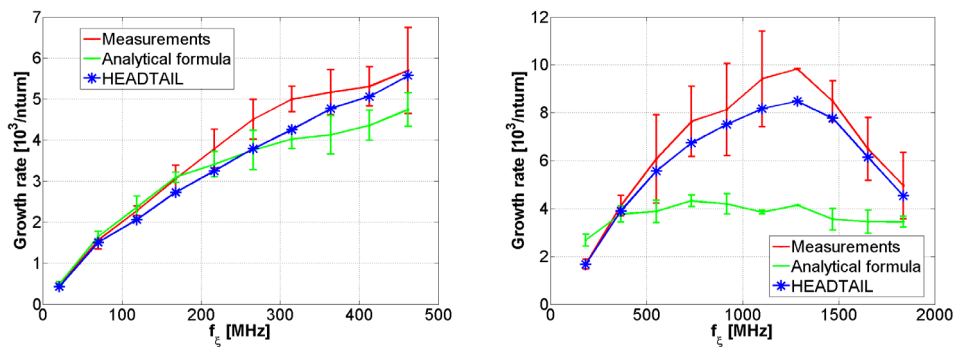


Figure 3: Growth rate of the unstable $l=0$ mode as a function of the chromatic frequency in the CERN SPS as measured (red), predicted analytically (green) and predicted with macroparticle simulations (blue) in both Q20 (left) and Q26 optics (right).

The agreement between the measurements and the HEADTAIL simulations was found to be excellent for both sets of measurements. The analytical estimation seemed to reproduce closely enough the measured growth rates in the low frequency part, while a discrepancy by up to a factor two was found for higher chromatic frequency shifts. This could be ascribed either to the important influence of nonlinearities in this frequency range, or to the fact that the knowledge of the beam coupling impedance at higher frequencies is not accurate enough to be used in the analytical formula. This is because the impedance model of the SPS was mainly built by means of time domain electromagnetic simulations of the accelerator components and the impedance was then calculated in post-processing by Fourier transforming the wake functions.

2.18.2.2 *Transverse Impedance Measurements with Beam: Transverse Mode Coupling Instability (TMCI) Thresholds*

For higher bunch intensities, the validity of Eq. (1) breaks down. In this regime, radial modes should be also considered in addition to the azimuthal modes, and the shift of the different modes becomes highly nonlinear with the bunch intensity. Above a certain intensity, adjacent modes merge together, or couple, leading to violent headtail instabilities, known as Transverse Mode Coupling Instabilities (TMCI). The threshold intensity at which

this instability sets in has a direct relation with the global transverse impedance of the machine (dipolar plus quadrupolar). Short bunches (i.e. with a $l=0$ spectrum extending well beyond the impedance spectrum of the accelerator) usually become unstable when modes 0 and -1 couple. This could be intuitively explained mainly for two reasons. First, Eq. (1) shows that the modes shift about like $2^{-|l|}$ (the Gamma function at the numerator and the factorial at the denominator roughly cancel), therefore the modes shifting faster are 0 and ± 1 . Secondly, we know that the mode 0 shifts downwards, therefore it will couple with -1, which can shift upwards or downwards according to the shape of the imaginary part of the impedance. For long bunches, the situation is more complicated and usually it is higher order modes that lead to a strong coupling and instability. Reference [5] provides analytical formulae that can be applied to predict the onset of TMCI for a bunch under the effect of a broad-band resonator impedance (defined by the parameters: shunt impedance R_T in Ω/m , resonance frequency ω_r , and quality factor Q), in the limiting cases of short and long bunch (with respect to the inverse of the resonance frequency of the resonator):

$$\begin{cases} N < \frac{2\pi \cdot 3.75cQQ_s\gamma}{\omega_r^2\sigma_z\bar{\beta}_{x,y}R_T r_{p,e}} & \text{if } \omega_r\sigma_z/c \leq 1 \\ N < \frac{2\pi \cdot 5.3Q^2Q_s\gamma\omega_r\sigma_z^2}{\bar{\beta}_{x,y}R_T r_{p,e}c^2} & \text{if } \omega_r\sigma_z/c \gg 1 \end{cases} \quad (6)$$

In the above equations, $r_{p,e}$ represent the classical radius of the proton or of the electron, according to whether we are considering a proton or a lepton machine. Written in a different form, the equations above confirm in essence the empirical criterion that the frequency shift of the lowest headtail mode should remain lower than the synchrotron frequency, but it also adds that this criterion becomes unnecessarily pessimistic for long bunches. The frequency shift only needs to be larger than the synchrotron frequency multiplied by a certain ‘mode coupling coefficient’, which lies between one and two for short bunches but increases linearly with bunch length for longer ones. If one measures the TMCI threshold in a running machine, a quick estimation of the parameters of the broad-band resonator modeling the global machine impedance can be inferred from the above formulae. Different sets of measurements with different bunch lengths or longitudinal emittances can be used to make the estimation more robust.

Alternatively to this approach, the mode shifting and coupling can be simulated with a full analytical Vlasov solver, e.g. MOSES [6] or DELPHI [7], or extracted from the results of macroparticle codes like HEADTAIL [4], and both the tune shift and the TMCI threshold can be then fitted at the same time. If the impedance model of the machine is complete, then the simulations will closely reproduce the observed behaviour. However, in most practical cases, a discrepancy will be found between the two and an additional broad-band resonator will have to be added to the impedance model to fit the measured data, providing an indication of the missing impedance.

An example of application of this technique to investigate the impedance of a relatively new machine is the measurement of the vertical TMCI threshold at the ALBA synchrotron (Barcelona, Spain) [8]. Figure 4 shows the measured vertical coherent tune shift with single bunch intensity (red points in both plots), up to the point in which the TMCI sets in and beam losses occur, at an intensity value of 9.8 mA. The blue points represent the shift predicted with HEADTAIL simulations by assuming the ALBA impedance model as known (left plot) and after adding to it a broad-band resonator with $R_T=1.6$ M Ω/m and $\omega_r = 1$ GHz.

The much better agreement of both the coherent tune slope and the TMCI threshold found with the additional broad-band resonator indicates that this resonator is a very reasonable estimation of the missing impedance in the model of the ALBA ring.

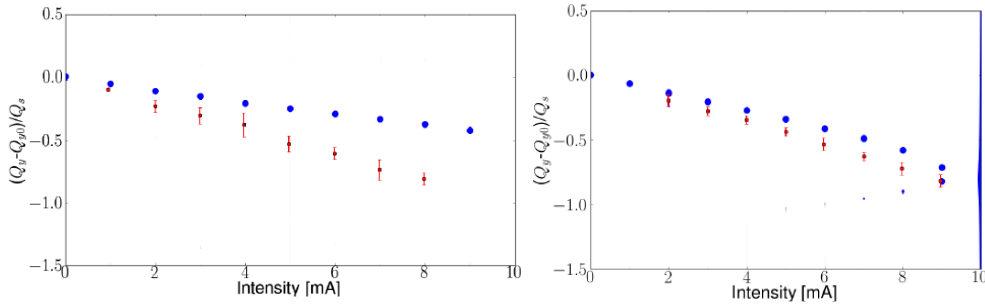


Figure 4: Mode shift as a function of bunch intensity in ALBA as measured (red points) and predicted with macroparticle simulations (blue points) up to the measured TMCI threshold (9.8 mA) with both the bare impedance model of the machine (left) and by adding to it an additional broad-band resonator (right).

TMCI thresholds in a wide range of longitudinal emittances and for the two different optics configurations Q20 and Q26 were also measured for the CERN-SPS and reproduced with HEADTAIL simulations [9]. Figure 5 shows the measured boundary between stable and unstable region for a single bunch in Q26 optics in the plane of longitudinal emittance versus bunch intensity (left) and that simulated with the HEADTAIL macroparticle code using the beam parameters as in the measurement and the SPS impedance model (right). The level of accuracy to which the measurements are reproduced by simulations is yet another confirmation of the advanced knowledge of the transverse impedance of the machine, as was discussed in the previous subsection.

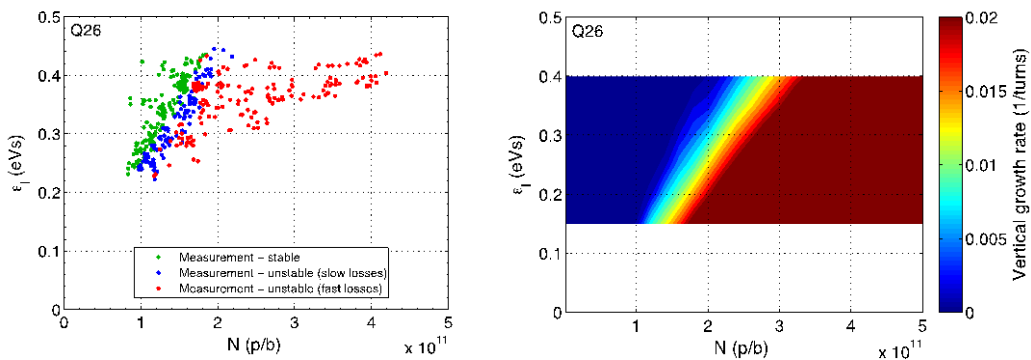


Figure 5: Growth rate of the vertical instability for different bunch intensity/longitudinal emittance pairs as measured in the SPS (left plot, color code in label) and as simulated with the HEADTAIL code (right plot, color code in palette) in Q26 optics

In the case of the Q20 optics, the detailed agreement between measurements and simulations is even more striking. In Fig. 6 the same type of plots as in Fig. 5 are displayed, but for the Q20 optics. In particular, in this case, the simulations are able to reproduce not only the onset of the strong TMCI at very high bunch intensity (red points in the left plot and light blue to red stripe in the right plot, e.g. $> 4 \times 10^{11}$ p/b for 0.35 eVs, which is the nominal value of longitudinal emittance for LHC-type beams), but also the island of weak

coupling specially pronounced for low longitudinal emittance values (blue points in the left plot, and region in lighter shades of blue in the plot of the simulations).

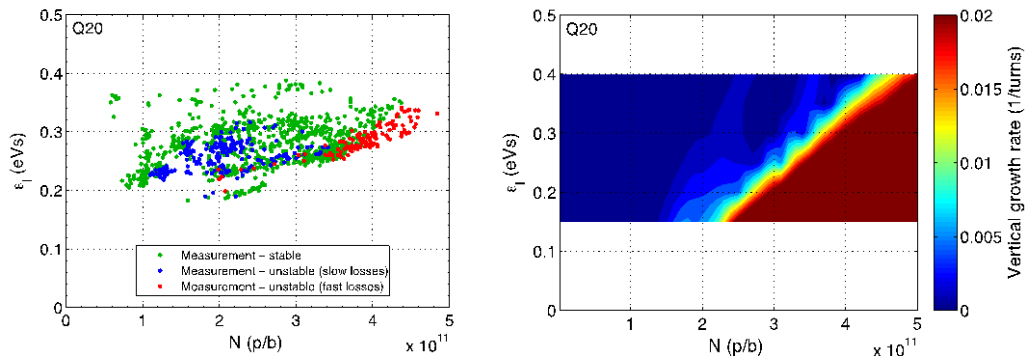


Figure 6: Growth rate of the vertical instability for different bunch intensity/longitudinal emittance pairs as measured in the SPS (left plot, color code in label) and as simulated with the HEADTAIL code (right plot, color code in palette) in Q20 optics.

Another impressive observation about the TMCI with Q20 is that the intra-bunch motion measured with a wide-band pick up is reproduced exactly in simulations for both types of instabilities, which are expected to come from the coupling of different modes. Figure 7 shows measured and simulated intra-bunch traces for the weak instability (top row, showing a quasi mode -1 mode) and for the strong TMCI (bottom row).

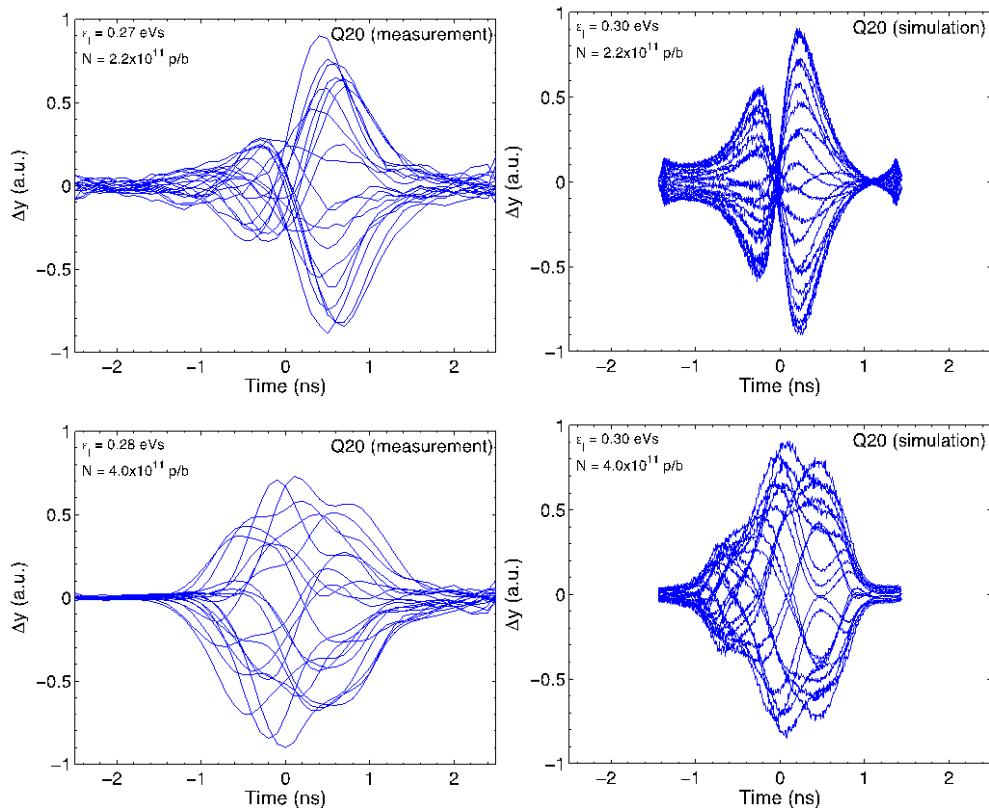


Figure 7: Intra-bunch vertical position signal measured by a wide band pick up on subsequent turns during the instability rise (left plots) for the weak (top) and strong instability (bottom). The corresponding simulated signals are plotted on the right side.

2.18.3 Longitudinal Impedance Measurements with Beam

In equilibrium, the distribution of a particle bunch in the longitudinal plane is a function of the Hamiltonian H alone, assuming a potential well defined by the total voltage seen by each particle, i.e. the sum of the external and the induced voltage. Including the effect of the induced voltage, which is the convolution of the bunch line density by the longitudinal wake function, or the product of their spectra in frequency domain, leads to what is known as the effect of ‘potential well distortion’. By adding the induced voltage to the RF voltage in the linearized longitudinal equation of motion, one can find analytical expressions for both the single particle (incoherent) synchronous phase shift and the synchrotron frequency shift due to the impedance [10, 11]:

$$\begin{aligned}\Delta\phi_s &\approx \frac{Ne\omega_0}{V_{rf} \cos \phi_s} \sum_n \Lambda_n \text{Re}[Z(n\omega_0)] \\ \Delta\omega_s &\approx \frac{Ne\omega_0\omega_{s0}}{2V_{rf}h \cos \phi_s} \sum_n n\Lambda_n \text{Im}[Z(n\omega_0)].\end{aligned}\tag{7}$$

In the equations above, V_{rf} is the applied RF voltage, ω_{s0} is the unperturbed synchrotron frequency, ϕ_s is the synchronous phase, h is the harmonic number of the RF system, Λ_n are the harmonics of the expansion in Fourier series of the line density $\lambda(z)$, $Z(\omega)$ represents the longitudinal impedance of the machine.

For a reactive impedance $\text{Im}[Z(n\omega_0)]/n$ which is constant over the stable bunch spectrum, the single particle synchrotron frequency shift can be rewritten as a function of the second derivative of the bunch line density at the bunch center in the form

$$\Delta\omega_s \approx \frac{eN\omega_0 C^2 \text{Im}[Z(n\omega_0)]/n}{2V_{rf}h \cos \phi_s} \left. \frac{d^2\lambda}{dz^2} \right|_{z=0}\tag{8}$$

In this section we will discuss only the beam-based methods for the measurement of longitudinal impedances, which make use of observables related to synchronous phase shift and synchrotron frequency shift. Other methods exist, e.g. based on the measurement of bunch lengthening with intensity, instability thresholds, loss of Landau damping or spectrum of a debunching bunch, but they will not be addressed in this newsletter.

2.18.3.1 Incoherent Synchrotron Frequency Shift

The incoherent synchrotron frequency shift can be found for a bunch in equilibrium by measuring the distance $2m\Delta f_s$ between positive and negative m^{th} synchrotron sidebands of the longitudinal Schottky spectrum [12]. This method was used in both RHIC rings [13], where the dependence on intensity was obtained from the natural intensity decay during luminosity production. The parabolas were fitted to the top 30% of the averaged bunch profiles to find the second derivative of the line density. The results obtained by this method for the two RHIC rings, blue and yellow, which are very similar, differed by more than a factor three and the source of this difference is not clear. The quadrupole ($m=2$) line of the peak detected Schottky spectrum contains information about the particle distribution in synchrotron frequency [14] and can be used to observe the synchrotron frequency shift. The measurements of $m = 2$ line performed at bottom energy of the CERN LHC for two bunches

of similar bunch length and different intensity are shown in Fig. 8. As one can see the available frequency resolution of 0.2 Hz is not sufficient and only an upper limit on $\text{Im}[Z(n\omega_0)]/n$ could be obtained ($< 0.2 \Omega$) [15]. This limit agrees with the current LHC impedance budget of 0.1Ω .

Another method, which can be used for estimation of the synchrotron frequency shift, when applied in the LHC, gave similar results. Eight bunches with intensities in the range $(0.6 - 2.0) \times 10^{11}$ and bunch length in the range $(1.2 - 1.4)$ ns were excited via cavity set point by phase modulation $\phi(t) = \phi_0 \sin(2\pi f_{\text{mod}} t)$ with modulation frequency f_{mod} changing in steps of 0.1 Hz from the value above zero-intensity synchrotron frequency $f_{s0} = 55.1$ Hz. Dipole oscillations of different bunches were observed at excitation frequencies reaching the synchrotron frequency spread inside these bunches. The results are again in agreement with an expected maximum frequency shift of 0.11 Hz. Due to the finite length of this excitation (and therefore frequency bandwidth) a constant offset in synchrotron frequencies was also observed. To improve accuracy longer excitations were applied for shorter bunches (available at the LHC flat top). Finally, the LHC impedance ($\text{Im}[Z(n\omega_0)]/n = 0.09 \Omega$) could be estimated most accurately from the measurements of thresholds of the loss of Landau damping (for bunches with various lengths and intensities) due to the incoherent synchrotron frequency shift [15], but these results are not discussed in this paper.

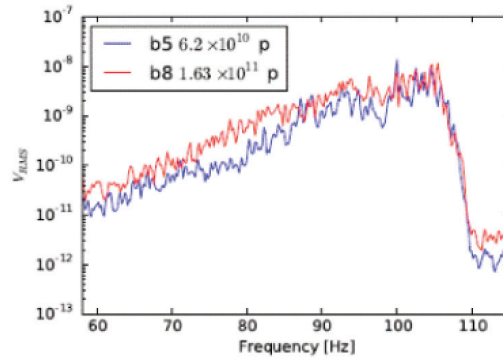


Figure 8: Quadrupole line of the peak detected Schottky signal, proportional to the particle distribution in synchrotron frequency, for two LHC bunches of Beam 1 with similar length of 1.4 ns (4σ Gaussian fit) but different intensities between 0.1 and 1.1×10^{11} at 450 GeV/c ($f_{s0} = 55.1$ Hz). The difference $2\delta f_s$ is below 1.0 Hz and $\delta f_s = 0.35$ Hz is expected from the LHC impedance model.

2.18.3.2 Coherent Synchrotron Frequency Shift

The synchrotron frequency shift can also be measured from excited oscillations of bunches with different intensities N . In this case we are dealing with the coherent synchrotron frequency shift as well as with the incoherent spectrum since now the bunch spectrum consists of both stationary and oscillating components. The frequency of bunch oscillations can be presented in the form

$$\omega_m = m(\omega_{s0} + \Delta\omega_{inc}) + \Delta\omega_{coh} \quad (9)$$

where $\Delta\omega_{inc}$ and $\Delta\omega_{coh}$ are correspondingly the incoherent and coherent synchrotron frequency shifts. The two last terms in the equation above are defined by the two different effective impedances. In fact, while the incoherent frequency shift $\Delta\omega_{inc}$ is proportional to $\text{Im}(Z_0)$, the coherent frequency shift $\Delta\omega_{coh}$ is proportional to $[\text{Im}(Z)/\omega]_m^{eff}$, where

$$[\text{Im}(Z)/\omega]_m^{\text{eff}} = \frac{\sum_{p=-\infty}^{\infty} h_m(\omega_{pm}) Z(\omega_{pm}) / \omega_{pm}}{\sum_{p=-\infty}^{\infty} h_m(\omega_{pm})} \quad (10)$$

with $\omega_{pm} = p\omega_0 + m\omega_s$. The spectral functions $h_m(\omega)$ were defined in the previous subsection. For dipole oscillations ($m = 1$) the last two terms in the equation for the longitudinal modes of the single bunch oscillation frequency practically cancel each other (exactly for a parabolic bunch in a linear RF voltage). So for beam measurements we are left with quadrupole ($m = 2$) oscillations, which, for example, can be excited at injection into a mismatched RF voltage or by nonadiabatic increase of voltage. The frequency of bunch length (or bunch peak amplitude) oscillations can be found from fitting the measured oscillations with a sine-wave. The variation of bunch intensity allows the dependence of oscillation frequency on impedance to be estimated using the expression

$$\omega_{2s} = \omega_{2s0} + bN \quad (11)$$

where for $\text{Im}(Z)/n = \text{const}$ the slope b is proportional to $\text{Im}(Z)/n$. Note that the slope b also strongly depends on bunch length (like $1/\sigma_z^3$ for $\text{Im}(Z)/n = \text{const}$) and special care should be taken when performing the reference impedance measurements, as in the CERN SPS [16], by using bunches with similar bunch lengths and longitudinal emittances. Indeed single bunches injected into mismatched voltage at 26 GeV/c (above transition) have been used in the CERN SPS to evaluate changes in longitudinal inductive impedance since 1999, see Fig. 9 (left). The first significant reduction in the inductive impedance (the slope b) could be seen after shielding the ~ 900 pumping ports in 2000 (compare measurements from 1999 and 2001) followed by impedance increase due to installation in 2003 and 2006 of kickers for beam extraction to the two LHC rings. Later the impedance of a few kickers was significantly reduced, but the effect was not measurable with beam anymore [16], mainly due to bunch length variation in measurements. Recently measurements of synchrotron frequency shift as a function of bunch length allow the frequency dependence of effective impedances to be studied as well, see Fig. 9 (right). Comparison of these measurements with particle simulations can serve as a good test of the impedance model of the ring. In the case of the CERN SPS this comparison reveals some missing inductive impedance $\text{Im}(Z)/n \sim 0.3 \Omega$ [17]. The analysis also shows that for the SPS impedance measured using the quadrupole oscillations, the frequency shift is dominated by the contribution from the incoherent frequency shift.

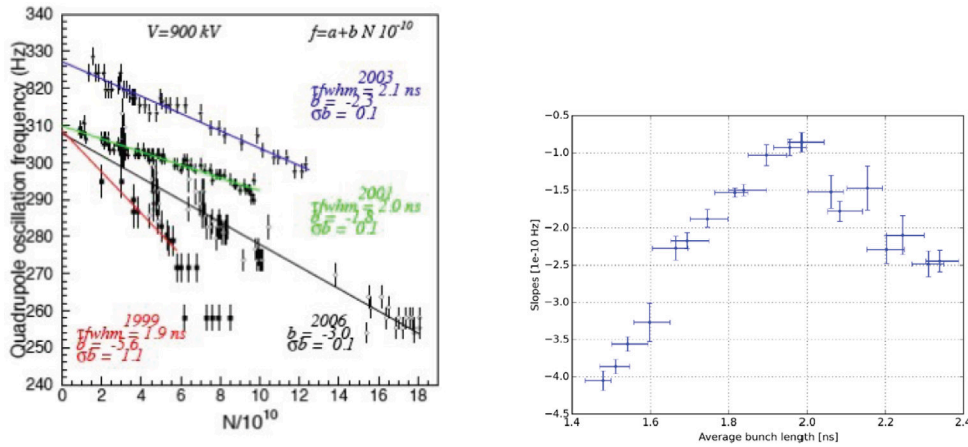


Figure 9: Left: measurements of quadrupole frequency shift as a function of intensity (slope b) over few years in the CERN SPS following the impedance evolution of the ring. Right: recent measurements of the slope b in $[\text{Hz}/10^{10}]$ as a function of average bunch length.

2.18.3.3 Synchronous Phase Shift

Measurements of the synchronous phase shift as a function of intensity are often used for the evaluation of the resistive impedance of a ring [18]. The shift of the synchronous phase ϕ_s is defined by the expression

$$\Delta\phi_s = -\frac{U}{eV_{\text{rf}} \cos \phi_s} \quad (12)$$

where U is energy loss per turn and per particle. The first equation in Section 2.17.3 describes the phase shift of a single particle with a small synchrotron oscillation amplitude. In the same way as the energy loss of a given particle, this phase shift depends on the particle oscillation amplitude. Experimentally only the total energy loss of the whole bunch can be measured. The total energy loss normalised to the number of particles can be found by measuring the synchronous phase shift $\Delta\phi_s$ at different bunch intensities. The measured dependence of energy loss on bunch length can be compared with that calculated from the known resistive impedances and the given bunch distribution. The energy loss of the whole bunch per turn and per particle can be found from the following expression

$$\Delta\phi_s = \frac{Ne\omega_0}{\pi V_{\text{rf}} \cos \phi_s} \sum_{p=0}^{\infty} \text{Re}[Z(p\omega_0)] |\Lambda(p\omega_0)|^2 \quad (13)$$

The shift of the synchronous phase $\Delta\phi_s$ can be measured from the distance between the two bunches in the ring or from the phase of beam signal relative either to the reference RF signal or to the signal from a probe in the RF cavity. When using the reference RF signal (sent from the power amplifier to the cavity) the energy loss due to the cavity fundamental impedance is included. The signal from the probe in the cavity contains information about the sum of applied RF voltage and beam induced voltage, so that in this case the beam-loading effect will be excluded from the measured phase shift. Measuring the distance between a time reference, low intensity bunch, and a witness bunch with varied intensity

(see e.g., [19]) is similar to the use of the reference RF signal since the measured loss factor can be dominated by the contribution from the RF cavities.

The measurements of synchronous phase shift done in the CERN SPS after the first impedance reduction using the RF reference signal [20] are shown in Fig. 10. Single bunches with variable intensity were injected in 4 different RF voltages to obtain the dependence of energy loss on bunch length. In the measurements $\sigma_t = \sigma_z / (\beta c)$, with β being the relativistic factor, varied in the range (0.6-0.9) ns so that impedances up to 1 GHz should be taken into account. Contributions to the normalised energy loss $|U|/(N/10^{10})$ from different SPS impedances below 1 GHz (at the time of measurements) calculated for a Gaussian bunch are shown in Fig. 10 (left). As can be seen, in these measurements the energy loss was dominated by the loss in the fundamental impedance of the 200 MHz RF system (shunt impedance $R_{sh} \sim 4.5 \text{ M}\Omega$, quality factor $Q = 140$) and the MKE kickers. Contributions due to the main impedance of the 800 MHz cavities, total $R_{sh} = 1.94 \text{ M}\Omega$ and $Q = 300$, as well as the HOM of the 200 MHz RF system, with $f_r = 629 \text{ MHz}$, $Q = 500$ and $R_{sh} = 604 \text{ k}\Omega$ are much smaller. The contribution to the energy loss from the resistive wall impedance is about 0.8 keV for a bunch with $\sigma_t = 0.6 \text{ ns}$ and decreases like $\sigma_t^{-3/2}$ for longer bunches. The measured and estimated total energy losses are presented in Fig. 10 (right) as a function of bunch length.

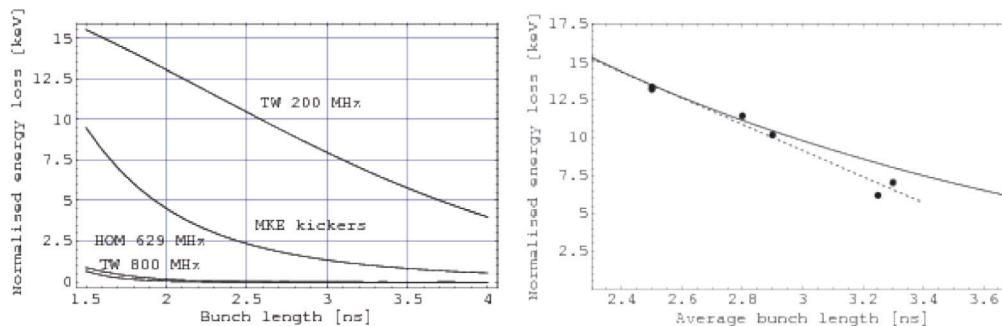


Figure 10: Left: contribution to energy loss (keV) from different SPS impedances as a function of $4\sigma_z$ bunch length. Right: Normalised energy loss (keV) calculated from the known SPS impedances (solid line) and measured from the phase shift (circles – measurement points, dashed line – their linear fit) for different bunch lengths.

The bunch-by-bunch measurements of the beam phase relative to the measured RF phase (probe) were used in the CERN LHC to estimate the energy loss of the proton bunches due to the electron cloud. Very high accuracy, below one degree, is required to accurately measure the small shifts. To obtain reliable results the first 12 bunches were used as a reference to exclude other energy losses, from (short range) impedances. The required accuracy was achieved after corrections for systematic errors and data post-processing [15]. Comparison with simulations gives a good estimate of the e-cloud density, as is discussed in deeper detail in the section of this newsletter devoted to electron cloud. From 2015 this diagnostic tool is available in the CERN Control Center and used for evaluation of results of beam scrubbing of the vacuum chamber (see Fig. 12).

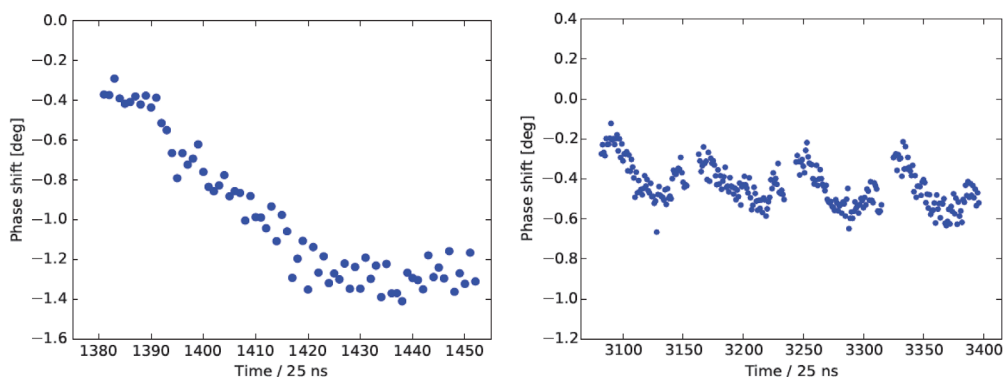


Figure 11: Bunch-by-bunch synchronous phase shift for similar bunches spaced at 25 ns before (left) and after (right) scrubbing of the CERN LHC. Measurements at 450 GeV/c flat bottom.

2.18.4 Acknowledgements

The authors would like to thank T. Argyropoulos, H. Bartosik, T. Bohl, H. Damerau, J. Esteban-Müller, E. Koukovini-Platia, G. Iadarola, A. Lasheen, K. Li, T. Linnecar, N. Mounet, H. Timkó and C. Zannini for their invaluable contributions.

2.18.5 References

1. A. W. Chao, “Physics of Collective Beam Instabilities in High Energy Accelerators”, Editor John Wiley & Sons, Inc. 1993
2. G. Rumolo, “[Beam Instabilities](#)” in Proc. of CAS, Advanced Accelerator Physics Course, 18 – 29 August 2013, Trondheim, Norway, p. 199
3. C. Zannini, “Electromagnetic Simulation of CERN accelerator Components and Experimental Applications”, [CERN-THESIS-2013-076](#) (2013)
4. G. Rumolo and F. Zimmermann, “Practical User Guide for HEADTAIL”, [CERN-SL-Note-2002-036-AP](#) (2002)
5. B. Zotter, “Transverse Mode Coupling and Headtail Turbulence”, [CERN/ISR-TH/82-10](#) (1982)
6. Y. H. Chin, “Transverse Mode Coupling Instabilities in the SPS”, [CERN-SPS-85-2-DI-MST](#) (1985)
7. N. Mounet, “DELPHI: an analytical solver for impedance driven modes”, [CERN-ACC-SLIDES-2014-0066](#) (2014)
8. E. Koukovini-Platia, “High Frequency Effects of Impedances and Coatings in the CLIC Damping Rings”, [CERN-THESIS-2015-152](#) (2015)
9. H. Bartosik, “Beam dynamics and optics studies for the LHC injectors upgrade”, [CERN-THESIS-2013-257](#) (2013)
10. J. L. Laclare, “Bunched beam coherent instabilities”, Proc. of CERN Accelerator School (CAS) 1985, CERN 87-03, p. 264 (1987)
11. J. Haissinski, Nuovo Cimento 18 B 72 (1973)
12. D. Boussard, “Schottky noise and beam transfer function diagnostics”, Proc. of CERN Accelerator School (CAS) 1985, CERN 87-03, p. 416 (1987)

13. M. Blaskiewicz, J. M. Brennan and K. Mernick, “Longitudinal impedance of RHIC”, Proc. IPAC2015, Richmond, VA, USA, p. 746 (2015)
14. E. Shaposhnikova, T. Bohl and T. Linnecar, “Longitudinal peak detected Schottky spectrum”, Proc. HB2010, Morschach, Switzerland, p. 363, TUO1C04 (2010)
15. J. Esteban Muller, Ph.D. Thesis, EPFL, Lausanne, Switzerland (2016)
16. E. Shaposhnikova *et al.*, “Reference measurements of the longitudinal impedance in the CERN SPS”, Proc. PAC09, Vancouver, Canada, (2009)
17. A. Lasheen *et al.*, “Single bunch longitudinal instability in the CERN SPS”, Proc. IPAC2016, p.1670, TUPOR009, Busan, Korea (2016)
18. M. A. Allen, J. M. Paterson, J. R. Rees, P. B. Wilson, IEEE, NS-22, No.3, p. 1838 (1975)
19. N. S. Sereno *et al.*, “A potpourri of impedance measurements at the Advanced Photon Source Storage Ring”, Proc. PAC97, p. 1700 (1997)
20. E. Shaposhnikova, T. Bohl, A. Hofmann, T. Linnecar, J. Tuckmantel, “Energy loss of a single bunch in the CERN SPS”, Proc. EPAC04, Lucerne, Switzerland and CERN AB-Note-2004-017-RF (2004)

2.19 Schottky Noise and Beam Transfer Functions

Michael Blaskiewicz
 Brookhaven National Laboratory, NY, USA
 Mail to: Blaskiewicz@bnl.gov

2.19.1 Introduction

Beam transfer functions (BTF)s encapsulate the stability properties of charged particle beams [1,2]. In general one excites the beam with a sinusoidal signal and measures the amplitude and phase of the beam response. Most systems are very nearly linear and one can use various Fourier techniques to reduce the number of measurements and/or simulations needed to fully characterize the response. Schottky noise is associated with the finite number of particles in the beam. This signal is always present. Since the Schottky current drives wakefields, the measured Schottky signal is influenced by parasitic impedances.

2.19.2 Beam Transfer Functions

BTFs can be for longitudinal or transverse motion, for a single bunch or multiple bunches. In principle they are always the same with a sinusoidal drive yielding the phase and amplitude of the response. When there are no collective effects the BTF is relatively straightforward to calculate. One simply needs to get the response of a single particle and do appropriate averaging of the initial synchrotron and betatron coordinates. When space charge and or wakefields are present things get more interesting. There is a profound difference between coasting and bunched beams. Longitudinal coasting beam BTFs are effectively a homework problem. Transverse BTFs of coasting beams can be solved within the approximation of transverse forces that vary linearly [3]. This covers the important case of arbitrary wall wakes and space charge with a transverse KV distribution. The inclusion of wall induced frequency spread from octupolar fields is straightforward to include but the effects of nonlinear space charge forces have only been addressed in crude approximation. Of course one can always do simulations but the difficulties associated with numerical convergence can be significant.

Transfer functions of bunched beams with collective effects are difficult to calculate. The author knows of no closed form solutions. Various ways to numerically solve for appropriate moments of the Vlasov equation have been developed but generally it seems that numerical simulations give the quickest, most reliable results, at least for bunches that are short compared to the circumference of the synchrotron [4]. In this case it is possible to use a relatively straightforward Fourier technique to obtain the BTF spanning an entire revolution line with only 2 independent simulations. The idea is quite simple. Suppose you have a bunch that is short compared to the radius of the accelerator so that the a signal at the revolution frequency, f_{rev} , has a small phase advance along the bunch. Then along the bunch an excitation at frequency f looks much like an excitation at frequency $f+f_{\text{rev}}$ except for a slip in phase from turn to turn. So, one just calculates the impulse response function of the bunch from single turn kicks of $\sin(2\pi ft)$ and $\cos(2\pi ft)$ and employs linearity. Figure 1 shows a simulation of the transverse beam transfer function [4].

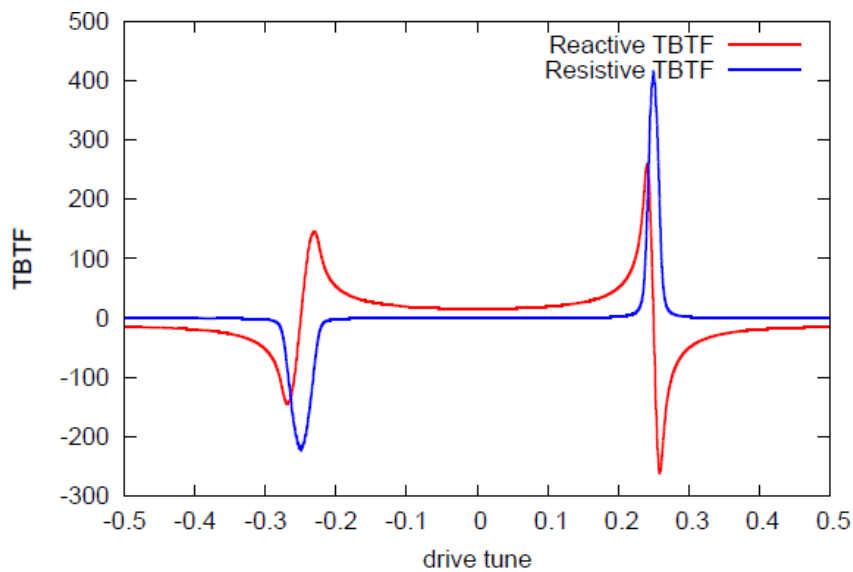


Figure 1: Transverse beam transfer function obtained from two simulations. While calculated for a bunched beam the resolution is intentionally low to suppress the synchrotron structure.

This transfer function was obtained for a bunched beam below transition with a fractional betatron tune of 0.25 and a negative chromaticity. This broadens the sideband near -0.25 and leads to enhanced Landau damping of the unstable modes with $n-Q_\beta > 0$. While this figure was made for a bunched beam the individual synchrotron lines have been smoothed over. When individual synchrotron lines are resolved the data become quite rich. Figure 2 shows the resistive part of the BTF measured at low frequency in the presence of a step wake potential (like long stripline beam position monitors) for various chromaticity values [4].

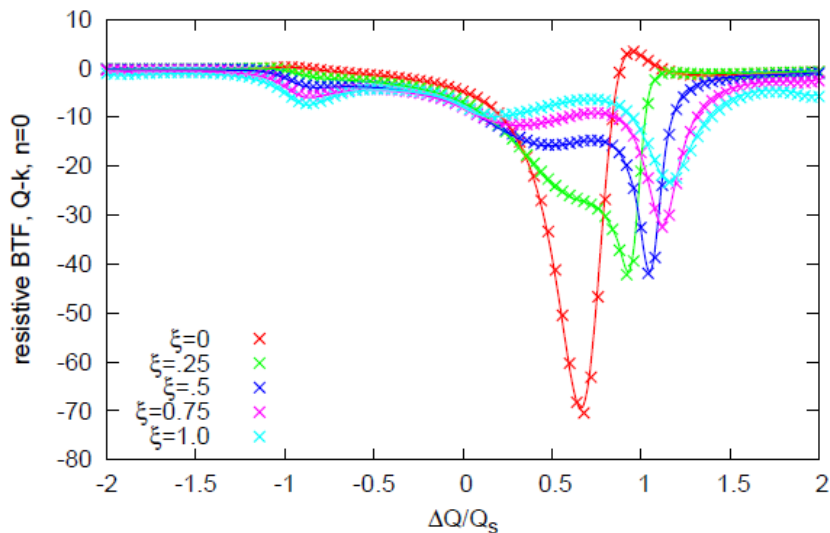


Figure 2: Low frequency transverse beam transfer function obtained from two simulations. This is a high resolution image showing the detailed synchrotron structure.

The solid lines in the figure are from simulations while the crosses are from a solution of the Vlasov equation. The near perfect agreement suggests both techniques are accurate. It is

clear there is a rich behavior waiting to be measured and in fact many measurements have been done. See [5] for a good example. It is hoped that the new methods of calculation will allow for more and better understanding of parasitic impedances.

2.19.3 Schottky Signals

Schottky signals have been used to measure the broad band longitudinal impedance in RHIC. The technique is straightforward. In a stable beam the broad band impedance creates a potential well distortion that modifies the synchrotron frequency. By measuring the synchrotron frequency as a function of intensity one gets the broad band impedance. There is one subtlety in this technique. Any measurement one makes is, by necessity, a measurement of a collective mode of the beam. This includes the self excited Schottky modes. If the center frequency of the Schottky signal is too low the coherent tune shift can be quite different from the estimated incoherent response. A toy model will illustrate the idea. Suppose we have N particles in the bunch and approximate the equation of motion for particle j as

$$\ddot{z}_j + \omega^2 z_j = \frac{2\omega\Delta}{N} \sum_{k=1}^N z_j - z_k \quad (1)$$

where ω is the unperturbed synchrotron frequency, z_j is the longitudinal position of particle j , and Δ is the small, coherent frequency shift. For an actual wake field the sum on the right would be over $W(z_j - z_k)$ with the highly nonlinear wake W . Such a wake is easily used in simulations, but not analytically tractable. Solving Eq. (1) yields

$$z_j = \bar{z} \cos(\omega t + \varphi) + (a_j - \bar{a}) \cos[(\omega - \Delta)t] + (b_j - \bar{b}) \sin[(\omega - \Delta)t] \quad (2)$$

where the overbars denote arithmetic means. Measurements that are dominated by the a_j s and b_j s are sensitive to the impedance. The current from the bunch is

$$I(t) = \frac{q}{T} \sum_{k=1}^N \sum_m \exp[im(z_k - ct)/R] \quad (3)$$

where $2\pi R = cT$ for our relativistic beam. Inserting Eq. (2) in Eq. (3) and defining $\phi = z/R$, the current for a single value of m is

$$I_m(t) = \exp(im\bar{\phi} \cos(\omega t)) \sum_{k=1}^N \sum_{p=-\infty}^{\infty} J_p(m\hat{\phi}_k) \exp(ip[(\omega - \Delta)t + \psi_k]) \quad (4)$$

With the caveat, corresponding to subtracting the arithmetic means in Eq. (2),

$$\sum_k \hat{\phi}_k \exp(i\psi_k) = 0 \quad (5)$$

The $p=0$ term in the sum of Eq. (4) has frequency ω and is the coherent mode in the toy model. Hence we need p and m to be large enough so that Eq. (5) has little effect. We also need the arguments of the Bessel functions to be significant. The data shown in Fig. 3 are the center frequencies of synchrotron lines measured in the yellow RHIC ring as a function of the central curvature of the current pulse [6]. The linear correlation, corresponding to the variation in synchrotron tune with beam current, is clear. Figure 4 shows the broad band impedance obtained from the slopes of the lines in Fig. 3. For $p > 2$ there is a nearly constant value. The larger values at $p=1$ and 2 are ascribed to low lying collective modes, similar to

the $p=0$ mode in the toy model. The blue results in Fig. 6 assume the accelerator was stable during data acquisition. The green lines allow for a linear drift of the synchrotron tune with time. The differences are comparable to the error bars.

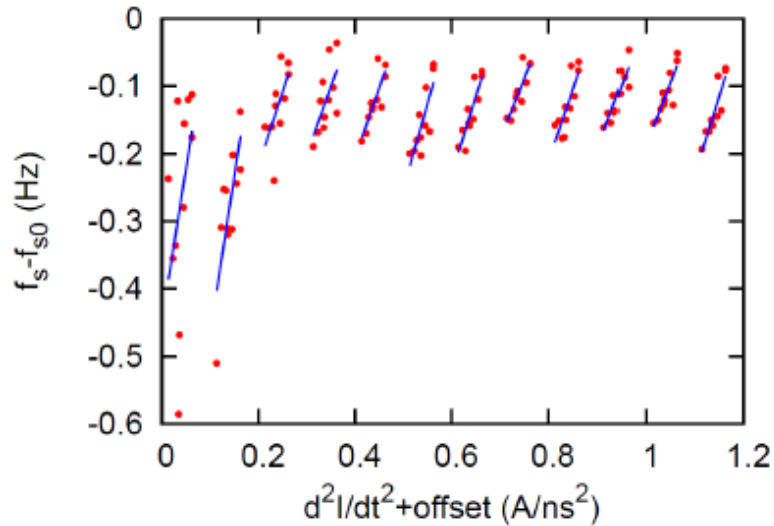


Figure 3: Measured synchrotron frequency shifts as a function of intensity for 12 synchrotron sidebands.

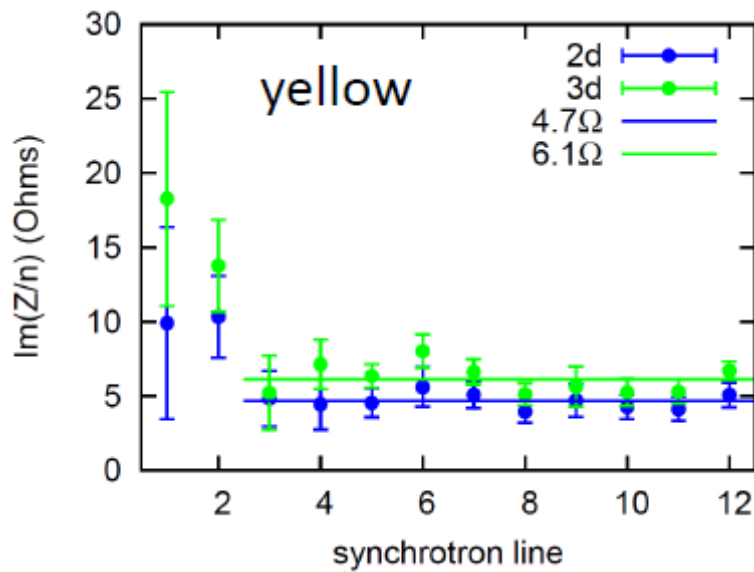


Figure 4: Broad band impedance needed to produce the slopes observed in Fig. 3.

2.19.4 Conclusions

Beam Transfer Functions and Schottky signals are useful to constrain both machine impedance and beam dynamics. BTFs can be simulated quite well allowing for a detailed comparison between model and measurement. Conversely, Schottky signals can be used to study the fields present when there are no large collective oscillations, greatly simplifying the analysis. Additionally, these measurements are made with stable beams allowing for adequate set up time and minimal beam loss.

2.19.5 References

1. D. Boussard, Schottky noise and beam transfer function diagnostics, p 416 in CERN 87-03 (1987).
2. S. Chattopadhyay, Some Fundamental Aspects of Fluctuations and Coherence in Charged-Particle Beams in Storage Rings, CERN 84-11 (1984).
3. D.V. Pestrikov, Dipole coherent oscillations and fluctuations of a coasting ion beam with strong space charge, NIMA, 562 (2006) 65-75.
4. M. Blaskiewicz and V. Ranjbar, Transverse beam transfer functions via the Vlasov equation, NAPAC13, FROAA2, p1427 (2013).
5. M.G. Minty and F. Zimmermann, Longitudinal Beam-Transfer-Function Measurements at the SLC Damping Rings, PAC97, p1741, (1997).
6. M. Blaskiewicz, J.M. Brennan, K. Mernick, Longitudinal Impedance of RHIC, IPAC2015, MOPMN020, p746, (2015).

2.20 Electron Cloud Effects

Giovanni Iadarola and Giovanni Rumolo
CERN, 1211 Geneva 23, Switzerland
Mail to: giovanni.iadarola@cern.ch

2.20.1 Introduction

Secondary electron emission in resonance with an alternating electric field can lead to avalanche electron multiplication. The underlying mechanism is called multipactor effect. Although desirable for some applications [1], it is usually associated with deleterious effects, such as voltage breakdown in radio frequency (RF) devices, outgassing, surface heating [2, 3, 4].

In the case of a particle accelerator operated with closely spaced bunches multipactor effects can occur in the beam chambers leading to the formation of so called Electron Clouds (ECs) with several negative effect on the machine performances [5, 6, 7, 8, 9]. EC effects have been observed in several accelerators all over the world, much more commonly in those operated with positively charged particles (e. g. positrons, protons, heavy ions), and are presently among the major performance limitations for high energy colliders, like the Relativistic Heavy Ion Collider (RHIC) in the USA [10], the KEKB electron positron collider in Japan [11], the DAΦNE electron positron collider in Italy [12] and, more recently, the CERN Large Hadron Collider (LHC) [13, 14, 15, 16].

A qualitative picture of the EC buildup at a section of an accelerator operated with bunches of positively charged particles is sketched in Fig. 1. The circulating beam can produce electrons due to different mechanisms, e.g. ionization of the residual gas in the beam chamber or photoemission from the chamber's wall due to the synchrotron radiation emitted by the beam. These are called "primary or seed electrons". Seeds are attracted by the passing particle bunch and can be accelerated to energies up to several hundreds of electronvolts. When an electron with this energy impacts the wall, "secondary electrons" are likely to be emitted. The secondaries have energies up to few tens of electronvolts and, if they impact the wall with these energies, they are either absorbed or elastically reflected but cannot produce any secondary. On the other hand, if they survive until the passage of the following bunch they can in turn be accelerated, projected onto the wall and produce secondaries. This can trigger an avalanche multiplication effect, which builds up the EC during the passage of an entire bunch train.

2.20.2 Secondary Electron Emission

The Secondary Electron Emission process can be described through the Secondary Electron Yield (SEY) of the surface, which is defined as the ratio between the electron current impinging the wall and the corresponding emitted current, and is a function of the energy of the impacting electrons

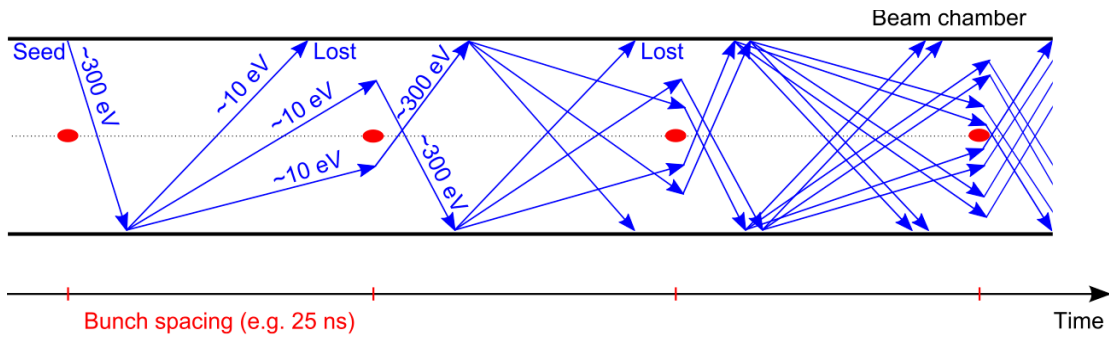


Figure 1: Schematic of the formation of an electron cloud in a particle accelerator (a similar sketch can be found in [17]).

$$\delta(E) = \frac{I_{\text{emit}}}{I_{\text{imp}}(E)} \quad (1)$$

A typical SEY curve is presented in Fig. 2. Following the approach presented in [18, 19, 20, 21, 22], this quantity can in turn be decomposed in two main components

$$\delta(E) = \delta_{\text{elas}}(E) + \delta_{\text{true}}(E) \quad (1)$$

where $\delta_{\text{elas}}(E)$ and $\delta_{\text{true}}(E)$ correspond respectively to electrons which are elastically reflected by the surface and to the so called “true secondaries”. The dependence of the two components on the energy the impacting electrons is shown by the green and red curve in Fig. 2.

We will call δ_{max} the maximum of the SEY curve. This parameter is strongly dependent on the surface material, roughness and history and plays a key role in the EC buildup, as we will describe in Sec. 2.19.3. In the following it will be often referred to simply as the “SEY parameter”. A typical energy distribution of the true secondary electrons is shown in Fig. 3.

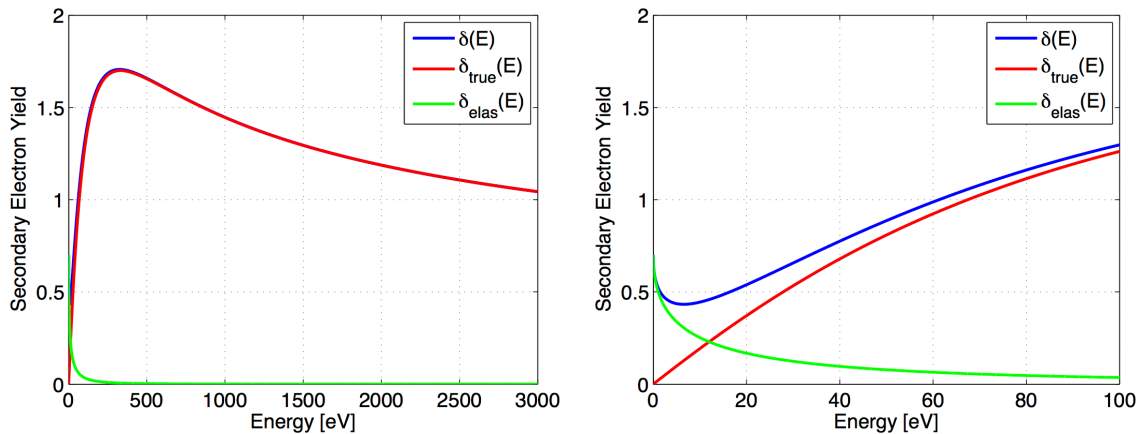


Figure 2: Left: SEY curve for $\delta_{\text{max}}=1.7$ - elastic component $\delta_{\text{elas}}(E)$, “true secondary” component $\delta_{\text{true}}(E)$, and total $\delta(E)$. Right: zoom on the low energy region.

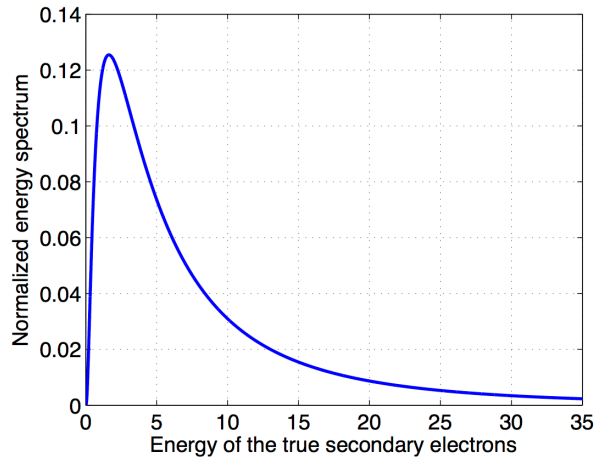


Figure 3: Energy distribution of the true secondary electrons.

2.20.3 The EC Buildup Mechanism

Let us consider a train of uniformly spaced bunches passing at a certain section of an accelerator, which does not contain any electron before the passage of the first bunch. Let n_0 be the number of primary electrons generated by a single bunch passage and n_i the number of electrons in the chamber at the instant t_i right before the passage of the i -th bunch. We can define $\delta_{\text{eff}, i}$ such that

$$n_{i+1} = \delta_{\text{eff}, i} n_i + n_0 \quad (3)$$

where $\delta_{\text{eff}, i} n_i$ is the number of electrons generated by the interaction of the EC with the chamber's wall (such a quantity can also be negative, when the wall acts like a net electron absorber). The quantity $\delta_{\text{eff}, i}$ can be directly related to the SEY of the chamber's surface $\delta(E)$ and to the energy spectrum of the impacting electrons, since we can write

$$n_{i+1} = n_i + \int_0^\infty \int_{t_i}^{t_{i+1}} \Phi(E, t) (\delta(E) - 1) dt dE + n_0 \quad (4)$$

where

$$\Phi(E, t) = \frac{dn}{dE} \quad (5)$$

is the instantaneous energy spectrum of the electrons impinging the wall. If we define the normalized energy spectrum for the i -th bunch passage as

$$\phi_i(E) = \frac{1}{n_i} \int_{t_i}^{t_{i+1}} \Phi(E, t) dt \quad (6)$$

we can rewrite the Eq. (4) as

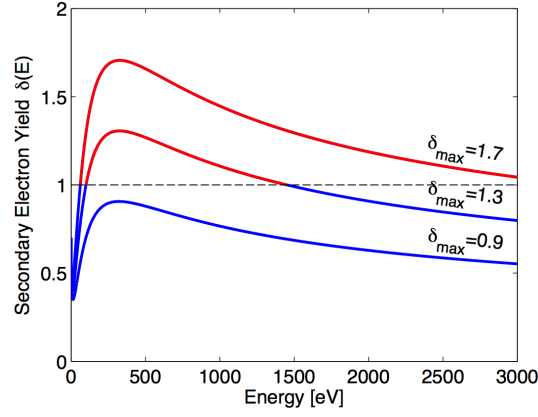


Figure 4: SEY curve for different values of the δ_{\max} parameter. The values for which the material behaves as electron absorber or emitter are plotted in blue and red respectively.

$$n_{i+1} = n_i \left(1 + \int_0^{\infty} \phi_i(E) (\delta(E) - 1) dE \right) + n_0 \quad (7)$$

and, comparing against Eq. (3), we obtain

$$\delta_{\text{eff}, i} = 1 + \int_0^{\infty} \phi_i(E) (\delta(E) - 1) dE \quad (8)$$

The meaning of this equation is quite intuitive: the SEY curve can be divided in two regions, one in which $\delta(E) < 1$ and the wall acts as an electron absorber, and the other in which $\delta(E) > 1$ and the wall acts as an electron emitter. The two regions are shown in blue and red respectively in Fig. 4, for different values of δ_{\max} . Looking at Eq. (8) we observe that, if the electron flux $\phi_i(E)$ lies mainly in the $\delta(E) < 1$ region, then the integral is negative, $\delta_{\text{eff}, i} < 1$, and the chamber's wall behaves like a net absorber. On the other hand, if $\phi_i(E)$ lies mainly in the $\delta(E) > 1$ region than the integral is positive, $\delta_{\text{eff}, i} > 1$, and the chamber's wall behaves like a net emitter.

If the electrons do not influence each other's trajectory, which means that the Coulomb forces between them are negligible, then we can assume that $\phi_i(E)$ does not depend on the bunch index

$$\phi_i(E) = \phi(E) \quad (9)$$

and hence the same holds for $\delta_{\text{eff}, i}$

$$\delta_{\text{eff}, i} = \delta_{\text{eff}} \quad (10)$$

In these conditions by recursively applying Eq. (3) we find

$$n_i = n_0 \sum_{k=1}^i \delta_{\text{eff}}^k = n_0 \frac{1 - \delta_{\text{eff}}^i}{1 - \delta_{\text{eff}}} \quad (11)$$

From this expression we can recognize two different regimes. When $\delta_{\text{eff}} < 1$ we observe that, for sufficiently large i , n_i tends to the constant value

$$n_i \simeq \frac{n_0}{1 - \delta_{\text{eff}}} \quad (12)$$

which is essentially an equilibrium condition between primary electron production and electron absorption at the chamber's wall. We will therefore call this condition "seed accumulation regime".

When $\delta_{\text{eff}} > 1$ we observe an exponential growth of the number of electrons in the chamber, i.e. for sufficiently large i :

$$n_i \simeq n_0 \frac{\delta_{\text{eff}}^i}{\delta_{\text{eff}} - 1} \quad (13)$$

which is indeed an avalanche multiplication of the electrons driven by the secondary emission. We will therefore call this condition "multipacting regime". In the seed accumulation regime, a significant amount of electrons can be accumulated only if primary electron production mechanisms are very strong, as it can be the case of synchrotron radiation in high-energy lepton machines, while typically for hadron accelerators sizable EC effects are observed only in the multipacting regime.

Equation 13 seems to suggest that the number of electrons can grow indefinitely. In fact, other mechanisms intervene to limit the number of electrons. To illustrate these effects, we use the PyECLOUD code to simulate the EC buildup in the very simple case of a cylindrical chamber (radius 22 mm, i.e. the horizontal size of the LHC arc beams screen) without any externally applied magnetic field, with nominal LHC bunch parameters, and a uniform train of 25 ns spaced bunches. For the case of $\delta_{\text{max}} = 1.75$, the results are presented in Figs. 5 and 6. In these plots we can recognize two different stages, one going from the first passage up to around the 45-th, and the second from that point onward. In the first stage the condition (9) is verified and $\delta_{\text{eff},i}$ is larger than one, which means we are in the multipacting regime. Indeed the energy spectrum $\phi_i(E)$ lies mainly in the energy region where the wall behaves like a net electron emitter, as confirmed by Figs. 5 (bottom) and 6. In this case Eq. (11) predicts an exponential growth of the number of electrons, which is exactly what is observed Fig. 5 (top).

Later on we observe that the evolution of n_i deviates from the expected exponential growth and finally "saturates" to a constant value, which is larger than the equilibrium value reached in the seed accumulation regime by several orders of magnitude. By looking at Fig. 6 we observe that during this transition the condition (9) is not fulfilled anymore since one can notice a strong increase in the number of electrons hitting the wall with extremely low energy (<10 eV). We also observe that the electron flux becomes dominated by the fraction lying in the net absorber region (see Fig. 5 - bottom) and that the effect of this change in the electron spectrum is that the parameter $\delta_{\text{eff},i}$ drops to one (see Fig. 5 - middle).

The reason of this change can be understood considering the fact that most of true secondary electrons are emitted with energies of the order of few eV (see Fig. 3), and therefore, if they impact on the wall before being accelerated by a bunch passage, they have

a high chance to be absorbed (the wall acts as net absorber for these energies, see Fig. 6 - top).

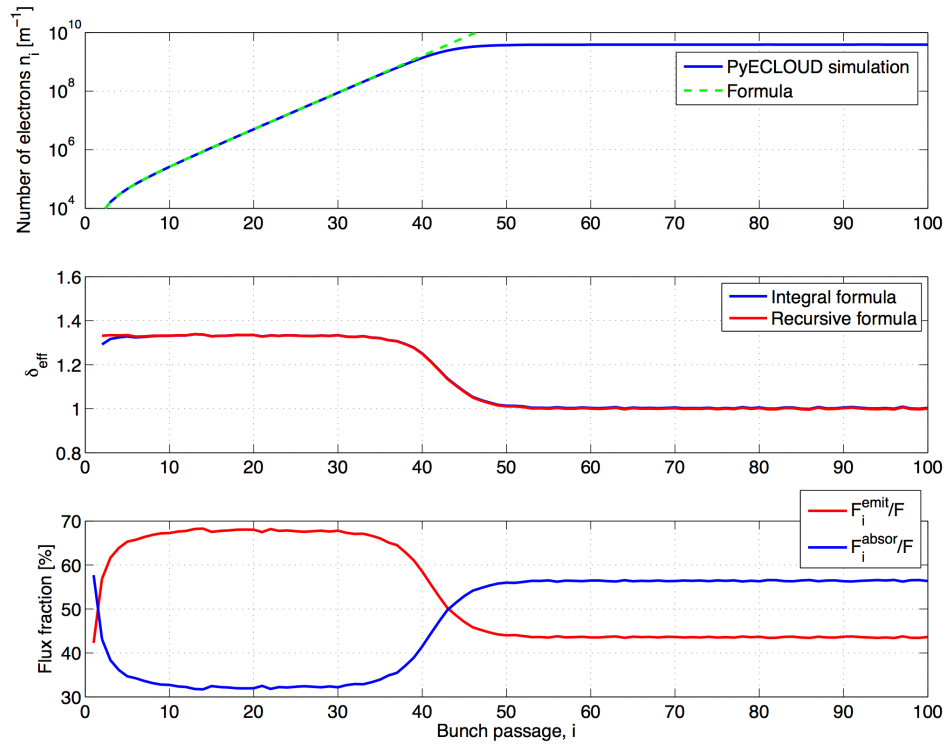


Figure 5: Simulated EC buildup for $\delta_{\text{max}} = 1.75$. Top: number of electrons before each bunch passage (directly from simulation - blue - and estimated from Eq. (11) - dashed green). Center: δ_{eff} (both from the integral formula 8 and the recursive formula 3). Bottom: fractions of the electron energy spectrum falling in the absorber/emitter regions of the SEY curve.

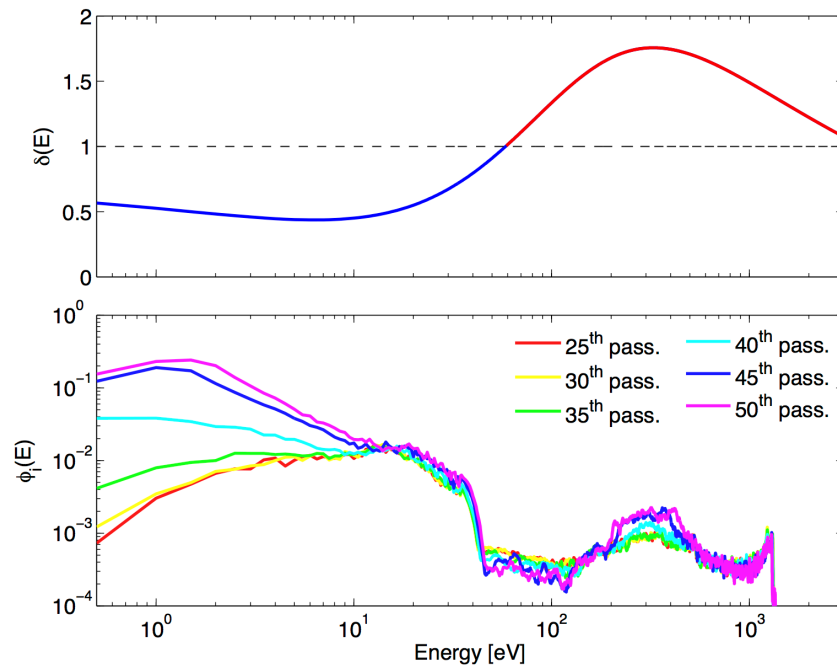


Figure 6: Top: SEY curve. Bottom: energy spectrum $\phi_i(E)$ for different bunch passages.

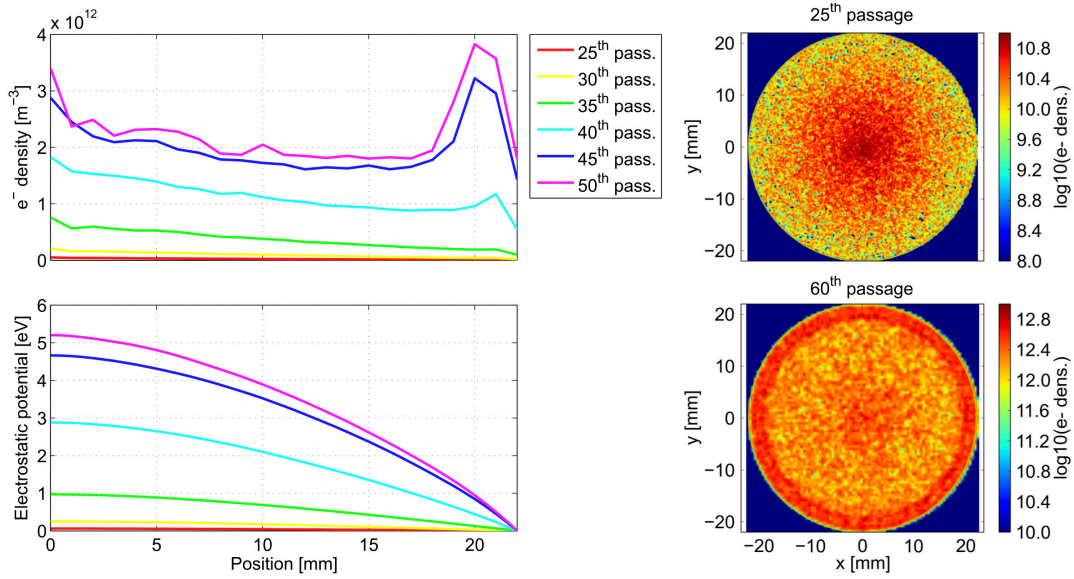


Figure 7: Simulated EC buildup for $\delta_{\max} = 1.75$. Left: electron density and electrostatic potential as a function of the distance from the center and of the bunch passage. Right: two snapshots of the electron density in the chamber, one taken right before a bunch passage during the exponential rise (top) and one taken right before a bunch passage during the saturation phase (bottom).

Figure 7 shows how the electron density and the electrostatic potential evolve during the buildup (all plots correspond to snapshots taken right before the passage of the corresponding bunch). During the first stages the electron density is quite modest, and, as a result, the electrostatic potential in the chamber (with respect to the wall) is smaller than 1 eV. In these conditions most of the true secondaries are practically free to move in the chamber. Due to their initial velocity they drift towards the center and have a high chance of avoiding to impact on the wall before the next bunch passage.

As the electron density in the chamber increases, so does also the electrostatic potential, which means that the forces due to “space charge” effects within the EC itself become increasingly stronger. Around the 45-th bunch passage the true secondaries emitted by the wall see a potential barrier comparable to their kinetic energy and therefore tend to be confined in a region close to the chamber’s wall. As a consequence the electron density assumes a ring like shape (see Fig. 7) and the probability that low energy electrons reach the wall before the next passage strongly increases. This causes the change in the energy spectrum observed in Fig. 6 towards an equilibrium condition such that:

$$\int_0^{\infty} \phi_i(E) (\delta(E) - 1) dE = 0 \quad (14)$$

Here electron emission and absorption at the wall perfectly balance one another and therefore $\delta_{\text{eff},i} = 1$ (see Eq. (8)).

Figure 8 shows how the maximum number of electrons in the chamber and the δ_{eff} coefficient in the first stage of the buildup simulation (before space charge effects become significant) depend on the SEY parameter δ_{\max} . The value of δ_{\max} for which $\delta_{\text{eff}} = 1$ is called “multipacting threshold” and separates the seed accumulation and the multipacting regimes.

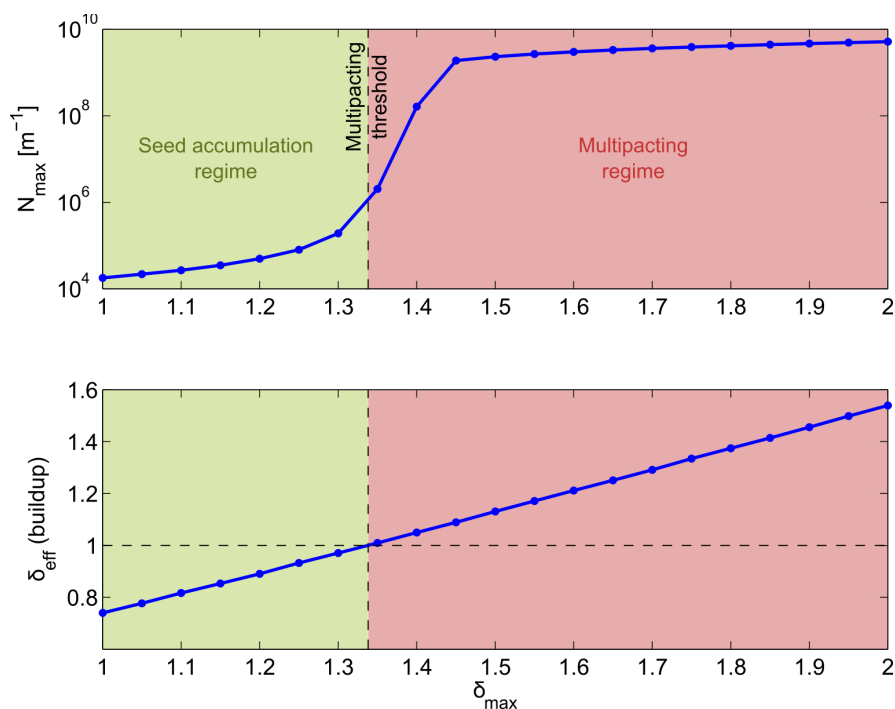


Figure 8: Maximum number of electrons in the chamber and δ_{eff} coefficient as a function of the SEY parameter.

The multipacting threshold can be easily recognized also on the number of electrons in the beam chamber (see Fig. 8 - top) since around this point an increase of several orders of magnitude is observed with respect to the seed accumulation regime. This kind of dependence is observed also on many other quantities related to the EC in the chamber, e.g. the electron flux on the wall, the electron density at the beam position, the energy deposition onto the wall. Typically, if δ_{\max} is below the multipacting threshold and therefore no avalanche multiplication is occurring, the EC is practically harmless for the machine performance, unless very strong seeding mechanisms are present.

2.20.4 Effects of Externally Applied Magnetic Fields

The features of the EC buildup are strongly influenced by externally applied magnetic fields, like those present in bending and focusing magnets of a particle accelerator. It is simple to prove [23] that a non-relativistic electron moving in a uniform magnetic field (as for example in the case of a bending magnet) follows an helicoidal trajectory around the field lines.

In a typical EC buildup, the total kinetic energy of an electron is typically not larger than 2 keV (see for example the energy spectra in Fig. 6), which implies that the cyclotron radius never exceeds a few millimeters. This means that the electrons are practically constrained to move around the field lines. Electrons trapped by different field lines will receive different kicks from the passing bunches, corresponding to different efficiencies for the multipacting process. This generates characteristic patterns of the electron density, as for example, the one shown in Fig. 9 (left).

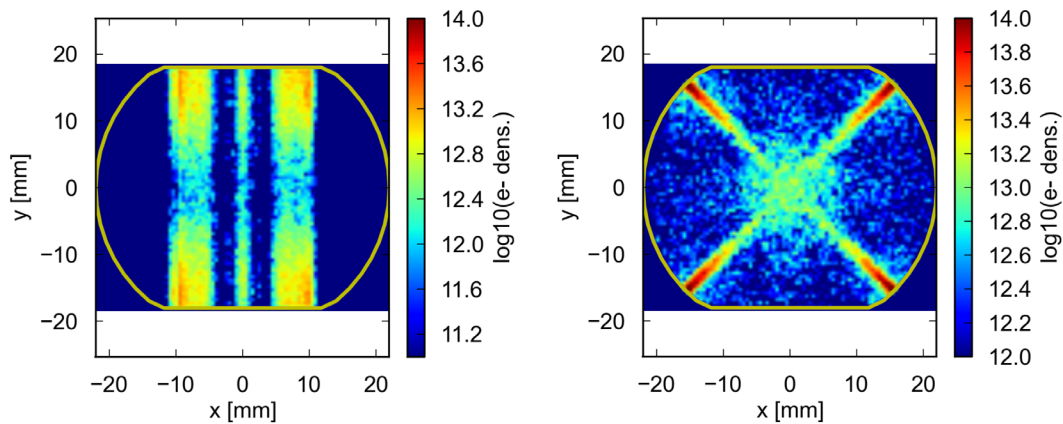


Figure 9: Snapshots of the electron cloud density in a dipole (left) and a quadrupole (right) magnet of the LHC.

Similar effects are observed also in quadrupole magnets. For example, with the chamber and beam parameters of LHC, the electron density shows an x-like shape as shown in Fig. 9 (b). In the case of quadrupoles, the presence of a magnetic field gradient can also trigger electron trapping mechanisms, which can make the EC buildup even more severe [24].

2.20.5 Impact of EC Effects on the Accelerator's Performances

The presence of EC in the beam chambers of a particle accelerator can limit its achievable performance through different effects, which will be briefly reviewed in the following. In general, the effects of the EC in a particle accelerator can be classified as

- global: the EC is present in a large fraction of the machine and can significantly influence the beam dynamics;
- local: the EC is only generated in certain machine elements (due to their geometry or wall properties), its impact on the beam dynamics is usually negligible, but it can nevertheless be responsible for local (detrimental) phenomena.

2.20.5.1 Impact on Beam Dynamics: Coherent and Incoherent Effects

When the EC covers a significant fraction of a machine, the integrated effect of its electric forces on the particle beam affects the collective beam motion leading to a coherent tune shift and well as to the onset of different types of transverse coherent instabilities above a certain electron density threshold.

EC effects can obviously only appear in a machine operating with long trains of bunches, because, as was explained in the previous sections, the EC only builds up and reaches saturation after several bunch passages. Despite that, both coupled-bunch and single-bunch phenomena (affecting typically only the last bunches in a long train) have been observed in running machines and they were studied in the past, showing that the EC can be indeed the source of unconventional wake fields which affect the beam dynamics in a similar fashion as an impedance source. A multi-bunch dipole-mode instability was observed at the KEK Photon Factory on positron beam operation, and it was subsequently explained as an effect

of the variation in the EC centroid position induced by an offset bunch, which can feed into the motion of subsequent bunches in an unstable loop [25]. More studies on this subject were carried out by an IHEP-KEK collaboration at the Beijing Electron Positron Collider [26], and at the PEP-II B factory [27].

Coupled bunch instabilities in the horizontal plane were then observed also at CERN, first at the Super Proton Synchrotron with LHC-type beams [28] and then at the Proton Synchrotron in the last phase of production of the LHC-type beams [29]. They were also recorded at the LHC during the first injections of trains of 48 bunches of 25 ns spaced beam [30]. Fortunately, due to their coupled-bunch nature, these instabilities can be usually damped by a transverse feedback system without posing too stringent requirements on its bandwidth.

With a similar mechanism, however, an EC inside the beam pipe can also be the origin of a short-range wake field for a bunch that goes through it, giving rise to head-tail coupling and single-bunch instabilities. Since this mechanism relies on the preexistence of an electron cloud when the bunch arrives, it can obviously only affect the bunches at the tail of a long train, such that the electron cloud has formed with the passage of the preceding bunches.

Assuming that the bunch goes into the EC with its head slightly offset, a global net force will be acting on the electrons around the head centroid position and consequently an accumulation of electrons will take place in that region. The newly reconfigured electron distribution will thus kick the following bunch particles toward the higher density region. The motion of the head will be therefore transmitted and potentially amplified at the tail of the bunch. The tail deflection will then increase over successive turns and it will eventually transfer back to the head thanks to the longitudinal mixing given by the synchrotron motion (after a few synchrotron periods). This head-tail coupling mechanism naturally follows the oscillation of the electrons in the bunch potential and therefore the oscillation frequency of the associated wake can be roughly expressed as:

$$\omega_{ey(x)} = \sqrt{\frac{Nr_e c^2}{2\sigma_{y(x)}\sigma_z(\sigma_x + \sigma_y)}} \quad (15)$$

In the above equation, N is the number of positively charged particles in the bunch, $\sigma_{x,y,z}$ its rms sizes in the three directions, r_e represents the classical electron radius. The frequency given by the equation above can quickly hit into the gigahertz range and above, especially for high intensity/brightness, high energy beams made of trains of short bunches. Due to the important high frequency content, the conventional transverse feedback systems are usually incapable of controlling this type of EC induced instabilities. One has to rely instead on altering the head-tail phasing through high chromaticity settings or on Landau damping [31] using octupole magnets. This type of solutions, however, can have a negative impact on transverse emittance preservation and beam lifetime [32, 33].

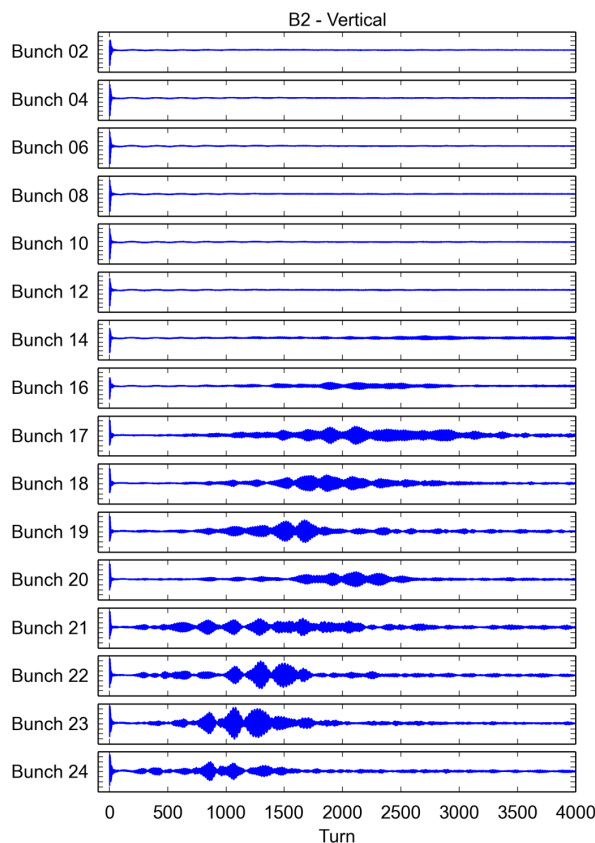


Figure 10: Vertical position of selected bunches along a train over the first 4000 turns after injection. A transverse instability developing on the trailing bunches is clearly visible.

The single-bunch instability due to the EC, observed in the SPS and in the LHC, happens mainly in the vertical plane if a large fraction of the driving EC is concentrated in the dipoles, but it can equally affect the horizontal plane if the driving EC comes from drift sections or quadrupoles. In a machine like LHC, which has 66% of the circumference covered by dipoles, the single bunch instability will mainly affect the vertical plane at least as long as the beam screen of the dipoles is not sufficiently scrubbed. The bunch-by-bunch position signal from the first 4000 turns after injection, as acquired from a beam position monitor for a train of 24 bunches, is displayed in Fig. 10 (every second bunch). It is clearly visible that, while the first 12 bunches are stable, an unstable signal begins to appear after bunch 14 and the rise-time of the instability tends to become shorter while moving to the tail of the train.

It must be noted here that the simple picture of the EC single bunch instability offered above only applies for zero chromaticity. With non-zero chromaticity the situation becomes more complex and the presence of an electron cloud can also favour the onset of 'classical' headtail instabilities in either plane, which can be damped with a classical transverse feedback system if the mode number is low enough to be handled by the system.

Even when the beam remains transversely stable, either because the integrated EC density is low enough or thanks to stabilising mechanisms (chromaticity, Landau damping, transverse feedback), its interaction with the EC can drive incoherent effects, which slowly degrade the beam quality.

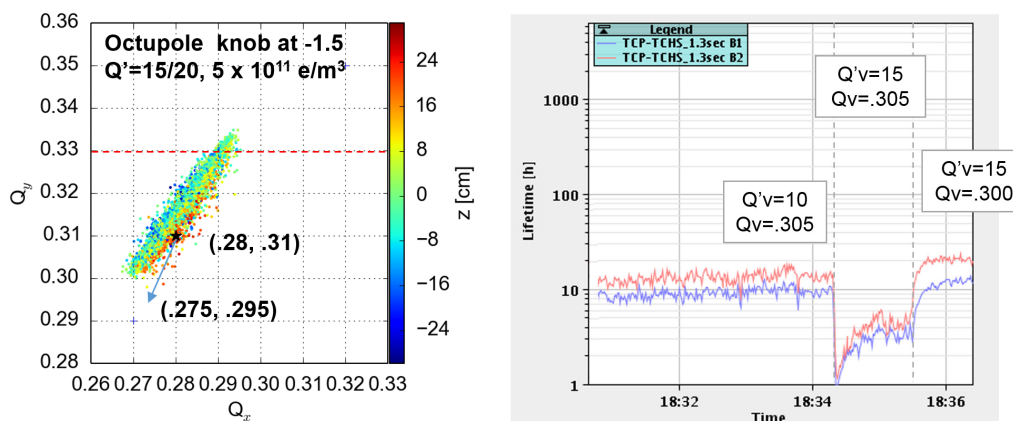


Figure 11: Left: tune footprint at 450 GeV as obtained from PyECLOUD- PyHEADTAIL simulations. Right: beam lifetime measured with 25 ns beams in the LHC for different settings of vertical tune and chromaticity.

These effects are usually caused by the fact that, even if the beam as a whole does not respond coherently to the EC excitation, the single particles are still detuned by the additional transverse force coming from the EC (usually focusing and strongly nonlinear, but in general dependent on the detailed electron distribution) and their tunes can be individually pushed onto resonance lines with consequent growth of the particles' amplitudes. Therefore, the resulting tune spread from the EC can be the origin of phenomena like slow emittance blow up or slow particle losses, which are particularly worrying in storage rings and colliders, where the aim is to store the beam in the ring for a very long time (several hours) while preserving as much as possible the beam quality and limiting all types of unwanted beam losses.

An example of incoherent effect in the LHC is illustrated in Fig. 11. The left plot shows the calculated tune spread of a single bunch in LHC at injection energy (450 GeV) assuming the operational settings for chromaticity (15 units in the horizontal plane and 20 units in the vertical plane) and octupole currents of 20 A, and in addition an electron cloud density of $5 \times 10^{11} \text{ m}^{-3}$ all around the machine dipoles. The nominal working point is (0.28, 0.31). The effect of the octupoles on the tune footprint is quite negligible compared with the one imprinted by chromaticity, while the electron cloud makes the tune spread asymmetric around the nominal tunes by pushing the footprint towards higher tune values in the vertical plane. The visible consequence of the electron cloud contribution to the footprint is that some particles come to cross the third order resonance. In this configuration, important losses are expected in LHC, affecting mainly the bunches at the tails of the long injected trains. The right plot shows an experiment in the machine, in which a strong degradation of the beam lifetime was observed when increasing the vertical chromaticity from 10 to 15 units, which could be recovered (and even slightly improved) by moving the vertical tune down by 0.005. This lifetime changes were observed only on the bunches at the tails of the trains.

2.20.5.2 Other effects

The presence of an EC in a particle accelerator can be also revealed by the observables listed here in the following:

- **Vacuum degradation:** The electron flux on the chamber's wall stimulates the desorption of gas molecules from the surface (dependent on the desorption yield of the wall for electron impingement), which results in an increased residual gas density in the beam chamber, and therefore in a pressure increase. This is obviously a local effect that can take place only in specific parts of the machine, prone to EC formation due to their geometry or surface properties, or in extended machine sectors if the beam chamber geometry and SEY are such to support widespread EC build up. The pressure rise is associated to several deleterious effects like larger equipment irradiation, worse background in the experimental areas, increased probability of breakdown in high voltage devices like kickers or electrostatic septa, and impact on the beam lifetime [34].
- **Beam energy loss and heat load:** The electrons accelerated in the beam field subtract energy from the beam and also deposit a large fraction of this energy on the chamber's wall when they hit it and produce secondary electrons (usually it takes one electron with few hundreds of eV to produce one or more electrons with few eV). Therefore two different observables can be associated to this process. First, if the amount of integrated EC on the beam path is sufficiently large in the accelerator, then the total energy loss of a bunch due to the EC over one turn can become significant and result into a measurable contribution to the stable phase shift of the bunch in the RF bucket (beside the contributions coming from beam loading and the longitudinal impedance). This is a global measurement and provides information on the total amount of EC present in the machine. Usually, this is assumed to be detectable if it is at least few tenths of a degree. Second, the energy deposited by the electrons on the chamber's wall heats it up and the additional heat load could be measured (either as increase of the chamber wall's temperature or as an increased power required from the cooling system to keep the chamber at a desired temperature). While this effect is typically negligible in room temperature accelerator components, it can become a serious issue in devices operating at cryogenic temperature like the superconducting magnets of the LHC. Here the EC induced heat load can even reach the cooling capacity limit of the cryogenic system [35].
- **Impact on beam diagnostics:** The presence of an undesired electron flux at the frequency of the bunch spacing can be the source of spurious signals, and therefore malfunctions, on beam diagnostics devices like pickups (beam position monitors) and beam gas ionization chambers [36].

All these effects have been observed at the LHC and in its injector chain.

2.20.6 Mitigation Strategies

In some cases, the accumulation of primary electrons alone inside the beam chamber of an accelerator can be the source of detrimental effects even in absence of beam induced multipacting. Since this mainly happens for photoelectron production in bending/wiggler chambers of very high energy beams, an obvious mitigation technique would be to reduce the photoelectron production rate by either using surfaces with naturally low photoelectron yield or by guiding the photons into a region where the produced photoelectrons can then do no harm. When the EC formation is mainly caused by secondary emission, it is necessary to find methods to reduce the effective SEY of the inner chamber walls in order to suppress or

at least reduce the EC build up, and thereby limit its adverse effects. In either case, other viable options for mitigation could be:

- to alter the electron dynamics to avoid large fluxes of high energy electrons towards the chamber walls. This can be achieved with electric fields (e.g. clearing electrodes) or magnetic fields (e.g. solenoids).
- not to suppress the EC, but just alleviate its effects on the beam or on the devices that could be affected.

For machines like the KEKB photon factory, LHC and even more the Future Circular Colliders (FCC) [37][38], the primary production of photoelectrons would be so high that the EC could reach saturation within a few bunch passages even without any multipacting, if no countermeasures were taken. The solutions implemented in the running machines are an antechamber (KEKB) or, for dipole fields, a sawtooth pattern impressed on the chamber wall (LHC). Weak solenoids of the order of 50 G are another possibility, which was also successfully implemented at KEKB. The solenoids do not really reduce the photoemission, but they quickly loop the emitted photoelectrons back to the wall, thus mitigating the subsequent beam-electron interaction. For the FCC machines, different schemes are under study, based on photon absorbers to intercept the photons at controlled locations and limit the associated photoelectron production, or to a novel design of the vacuum chamber with lateral slits shaped to trap the photons and subsequently shield the photoelectrons from the beam field. Electrons generated by beam loss at a collimator can be controlled by solenoids or clearing electrodes. For example, the SNS project has installed solenoids along the collimator straight sections [39].

When the EC build up is dominated by the process of secondary emission, the surface of the inner wall of the vacuum chamber needs to be treated such that its effective SEY is minimised, and ideally reduced to a value below one. This can be achieved by either coating (i.e. changing the chemical properties of the exposed surface) or machining (i.e. changing the geometrical properties of the exposed surface). A well-established method to reduce multipacting in RF couplers is coating with TiN, a material that has proven to condition to very low values of SEY. The thickness of the coating is of the order of a micron, which does not alter the resistive impedance seen by the beam.

A more favourable getter material made from TiZrV (Non-Evaporable Getter) was developed at CERN and it has the advantage of pumping while having low SEY [40]. This NEG is characterized by greater structural stability than TiN as well as low activation temperature. The warm sections of the LHC, especially those around the experimental areas (about 20% of the circumference), have been coated with this material [41]. The coating has been already widely used at several synchrotron light sources around the world (both in insertion devices and for general coating of the vacuum chambers) to guarantee Ultra High Vacuum and improve the beam lifetime while reducing the probability to excite fast beam ion instabilities.

In the last 10 years an impressive work has been done at CERN to develop a new type of coating with amorphous carbon (a-C), which does not require activation, has intrinsically a very low SEY and does not degrade with time [42]. This coating has been widely tested at the CERN SPS, where the suppression of the EC was successfully proven in dedicated strip monitors as well as in a few main bending units. In particular, an a-C coated liner has remained installed in a strip monitor since 2007 and no EC signal was ever measured in it, even after long technical stops and extensive machine venting. This confirms that the a-C coating can preserve its low SEY even after being long exposed to air.

More recently, another type of procedure based on laser engineering of the surface (applicable for example to copper, stainless steel and aluminium) has been proposed to reduce the effective SEY. The laser treatment, which imprints a surface topography made of organised microstructures, has the advantage of relatively easy application and possible retrofitting in existing machines [43].

In parallel to the research on coating and laser treating, several authors have also proposed to suppress multipacting by machining the wall surface to produce macroscopic grooves on it. These grooves essentially act as electron traps, as the electron emitted by the surface are very likely to be re-absorbed quickly before they can be accelerated in the beam field. A lot of optimisation work has been done to define the shape and the size of the grooves such as to obtain the best EC suppression [44].

Multipacting may also be suppressed by solenoids, though one should pay attention to the possibility of cyclotron resonances (i.e. conditions for which the cyclotron period of the electrons in the solenoid field is a multiple of the bunch spacing).

Electric clearing fields are also shown to be an efficient cure in simulations. They were already used to cure electron-proton instabilities for the coasting proton beams in the CERN ISR during the early 70s. At the SNS operating with long proton bunches, all beam position monitors can be biased with a clearing voltage of 1 kV. To be effective for the multipacting experienced by short bunches with close spacing, the clearing electrodes must be mounted all around the ring at close distances. The impedance introduced by many such devices could be an obvious showstopper. However, a continuous long wire on an insulating support would not necessarily exhibit a prohibitively large impedance. Other options for a practical implementation of electric clearing fields may be splitting the beam pipe into a top and bottom half, isolated from each other and held at different potential. Biasing the two jaws of a collimator against each other is a similar idea.

Finally, another way to reduce the SEY of the inner surface of an accelerator vacuum chamber is to rely on its conditioning with time thanks to the electron bombardment during beam operation with EC. This technique is called "scrubbing" and is based on the experimental observation that the SEY of a surface exposed to a continuous flux of electrons with sufficiently high energy exhibits a decreasing behaviour with the deposited electron dose. While this decrease is usually very fast at the beginning for large values of the SEY, when scrubbing means physically removing the external layers of molecules and oxides present on the surface of the bare metal, it then tends to slow down exponentially and eventually requires enormous doses to make tiny steps in the region of SEY's below 1.3-1.4.

Scrubbing has been widely used at CERN for the SPS and LHC, both of which have reached successful operation with 25 ns beams thanks to extended scrubbing runs. In the case of the LHC, an important part of the scrubbing process has been carried out not only through the dedicated scrubbing periods, necessary nevertheless to prepare the machine to operate with 25 ns beams, but also through the physics stores with 25 ns beams. Assuming the heat load in the cold arcs to be a measure of the amount of EC present in the machine, Fig. 12 displays the evolution of this quantity over to months during the 2015 run, when increasing numbers of bunches were injected into LHC and brought to collision at 6.5 TeV. The scrubbing of the surface of the beam screen in the arcs is visible as the decrease of the heat load normalised to the total beam current, which has taken place with a time constant of weeks and has led to about half the value over the full two-months period. It must be highlighted here that the decrease of the normalised heat load is not fully ascribable to the surface scrubbing, but it was also aided by relaxing the filling pattern into the LHC (moving from trains of 72 bunches to trains of 36 bunches) and increasing the bunch length at top

energy (as shown in the plot looking at the 'Filling pattern' and 'Target b. length' strips). These additional electron cloud mitigating measures were necessary to increase the number of bunches injected into LHC, while keeping the produced heat load in the arcs within the cooling capacity of the cryogenic system.

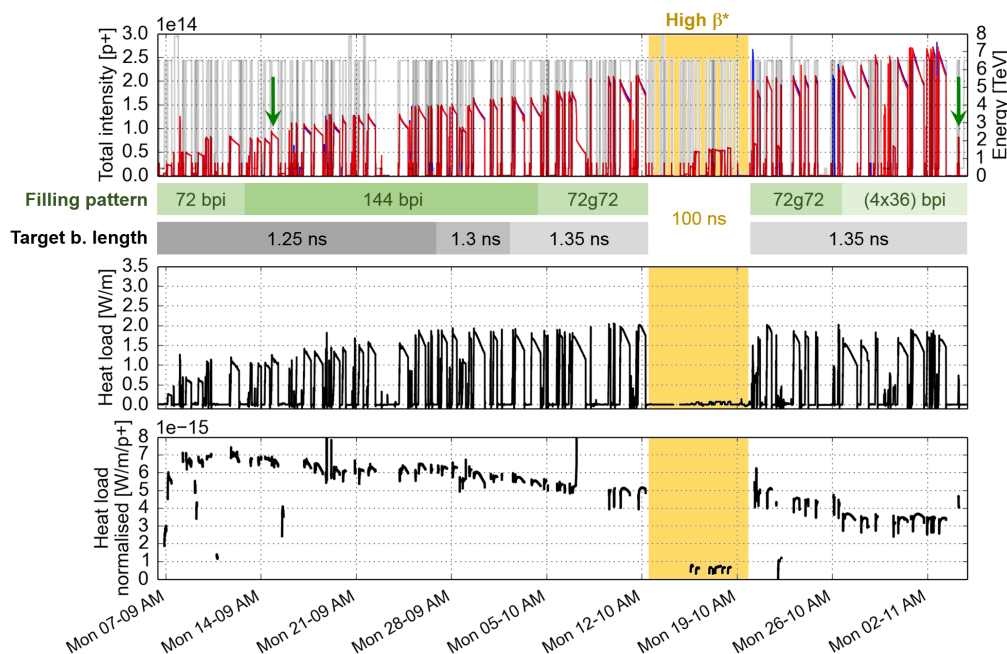


Figure 12: Evolution of the beam intensity (top), average heat load in the arc magnets (middle) and heat load normalized to the beam intensity (bottom) during the intensity ramp-up with 25 ns beams.

Proper tailoring of the bunch filling patterns (bunch spacing, bunch trains and bunch charges) is yet another way of achieving an acceptable electron density. The application of this technique can be two-fold. On one side, the arrangement of the bunches in a train can be such as to minimise the electron cloud build up and allow an EC-free operation of the accelerator. In particular, a larger bunch spacing can help, or gaps within trains can lower the EC density and reset the cloud at least to some extent. However, this usually comes at the expense of the total amount of beam intensity that can be stored in the machine, with consequent impact on the performance. Examples here include mini-trains in PEP-II, the actual bunch spacings chosen for PEP-II and KEKB operation, which are twice or three times the design spacing, and the 50 ns (until 2012) or so-called 8b+4e configuration proposed and successfully tested for the LHC, in which long trains of 25 ns spaced bunches are replaced with trains exhibiting a gap of 4 empty buckets every 8 full buckets [45]. On the other side, special beam configurations can be put in place with the goal of increasing as much as possible the EC formation and accelerate the scrubbing process. The typical example of this type of approach is the possible use of doublet beams in the SPS and LHC, i.e. beams made of 5 ns spaced bunch pairs separated by 25 ns from each other. These beams were expected and proved to produce a large EC in both the SPS and LHC, offering the potential of possibly scrubbing the wall surfaces to SEY values below the EC build up thresholds for the nominal 25 ns beams [45].

2.20.7 References

1. F. M. Mako and P. Weilhammer, "A High-Current Micro-Pulse Electron Gun," Proceedings of the 15th IEEE Particle Accelerator Conference, Washington, DC, USA, , 1993.
2. J. Vaughan, "Multipactor," *Electron Devices*, IEEE Transactions on, vol. 35, pp. 1172–1180, Jul 1988.
3. R. A. Kishek, Y. Y. Lau, L. K. Ang, A. Valfells, and R. M. Gilgenbach, "Multipactor discharge on metals and dielectrics: Historical review and recent theories," *Physics of Plasmas* (1994-present), vol. 5, no. 5, pp. 2120–2126, 1998.
4. A. Woode and J. Petit, "Investigations into multipactor breakdown in satellite microwave payloads," *ESA Journal*, vol. 14, pp. 467–478, 1990.
5. "Proceedings of E-CLOUD'02: Mini Workshop on Electron Cloud Simulations for Proton and Positron Beams, Geneva, Switzerland, edited by G. Rumolo and F. Zimmermann," CERN-2002-001, 2002.
6. "Proceedings of E-CLOUD'04: 31st Advanced ICFA Beam Dynamics Workshop on Electron-Cloud Effects, Napa, CA, USA , edited by M. Furman, S. Henderson and F. Zimmermann," CERN-2005-001, 2005.
7. "Proceedings of E-CLOUD'07: International Workshop on Electron Cloud Effects, Ithaca, New York, edited by H. Fukuma, E. S. Kim and K. Ohmi," 2007.
8. "Proceedings of E-CLOUD'10: ICFA Advanced Beam Dynamics Workshop on electron cloud physics, Ithaca, New York, edited by K. Smolenski," 2010.
9. "Proceedings of E-CLOUD'12: Joint INFN-CERN-EuCARD-AccNet Workshop on Electron-Cloud Effects, La Biodola, Isola d'Elba, Italy, edited by R. Cimino, G. Rumolo and F. Zimmermann," CERN-2013-02, 2013.
10. W. Fischer, M. Blaskiewicz, J. Brennan, H. Huang, H.-C. Hseuh, V. Ptitsyn, T. Roser, P. Thieberger, D. Trbojevic, J. Wei, S. Y. Zhang, and U. Iriso, "Electron cloud observations and cures in the relativistic heavy ion collider," *Physical Review Special Topics-Accelerators and Beams*, vol. 11, no. 4, p. 041002, 2008.
11. H. Fukuma, "Electron Cloud Observations and Predictions at KEKB, PEP-II and SuperB Factories," Proceedings of E-CLOUD12: Joint INFN-CERN-EuCARD-AccNet Workshop on Electron-Cloud Effects, La Biodola, Isola d'Elba, Italy, 2012.
12. M. Zobov, D. Alesini, A. Drago, A. Gallo, S. Guiducci, C. Milardi, A. Stella, S. De Santis, T. Demma, and P. Raimondi, "Operating experience with electron cloud clearing electrodes at DAFNE," Proceedings of E-CLOUD12: Joint INFN-CERN-EuCARD-AccNet Workshop on Electron-Cloud Effects, La Biodola, Isola d'Elba, Italy, 2012.
13. O. Domínguez, K. Li, G. Arduini, E. Métral, G. Rumolo, F. Zimmermann, and H. M. Cuna, "First electron-cloud studies at the large hadron collider," *Phys. Rev. ST Accel. Beams*, vol. 16, p. 011003, Jan 2013.
14. G. Iadarola, G. Arduini, V. Baglin, H. Bartosik, J. Esteban Müller, G. Rumolo, E. Shaposhnikova, L. Taviani, F. Zimmermann, O. Domínguez, and G. Maury Cuna, "Electron Cloud and Scrubbing Studies for the LHC," Proceedings of the IPAC13 International Particle Accelerator Conference, Shanghai, China, 2013.
15. G. Iadarola et al., "Analysis of the Electron Cloud Observations with 25 ns Bunch Spacing at the LHC," in Proceedings, 5th International Particle Accelerator Conference (IPAC 2014): Dresden, Germany, June 15-20, 2014, p. TUPME027, 2014.
16. K. Li, H. Bartosik, G. Iadarola, L. Mether, A. Romano, G. Rumolo, and M. Schenk, "Electron Cloud Observations during LHC Operation with 25 ns Beams," in

- Proceedings, 7th International Particle Accelerator Conference (IPAC 2016): Busan, Korea, May 8-13, 2016, p. TUPMW017, 2016.
17. G. Rumolo, F. Ruggiero, and F. Zimmermann, "Simulation of the electron-cloud build up and its consequences on heat load, beam stability, and diagnostics," *Phys. Rev. ST Accel. Beams*, vol. 4, p. 012801, Jan 2001.
 18. B. Henrist, N. Hilleret, M. Jiménez, C. Scheuerlein, M. Taborelli, and G. Vorlaufer, "Secondary electron emission data for the simulation of electron cloud," Mini Workshop on Electron Cloud Simulations for Proton and Positron Beams, CERN, Geneva, Switzerland, 2002.
 19. V. Baglin, I. Collins, B. Henrist, N. Hilleret, and G. Vorlaufer, "A Summary of Main Experimental Results Concerning the Secondary Electron Emission of Copper," LHC Project Report 472, 2002.
 20. R. Cimino, I. R. Collins, M. A. Furman, M. Pivi, F. Ruggiero, G. Rumolo, and F. Zimmermann, "Can Low-Energy Electrons Affect High-Energy Physics Accelerators?," *Phys. Rev. Lett.*, vol. 93, p. 014801, Jun 2004.
 21. R. Cimino and I. Collins, "Vacuum chamber surface electronic properties influencing electron cloud phenomena," *Applied Surface Science*, 2004.
 22. A. Kuzucan, H. Neupert, M. Taborelli, and H. Störi, "Secondary Electron Yield on Cryogenic Surfaces as a Function of Physisorbed Gases," Proceedings of the IPAC11 International Particle Accelerator Conference, San Sebastian, Spain, 2011.
 23. D. Halliday, R. Resnick, and J. Walker, *Fundamentals of Physics*. John Wiley & Sons, 2010.
 24. R. J. Macek, A. A. Browman, J. E. Ledford, M. J. Borden, J. F. O'Hara, R. C. McCrady, L. J. Rybarczyk, T. Spickermann, T. J. Zaugg, and M. T. F. Pivi, "Electron cloud generation and trapping in a quadrupole magnet at the Los Alamos proton storage ring," *Phys. Rev. ST Accel. Beams*, vol. 11, p. 010101, Jan 2008.
 25. F. Zimmermann, *CERN-SL-Note-2000-004*, 2000.
 26. J. Wang, Z. Guo, Y. Liu, Q. Qin, J. Xing, and Z. Zhao, "Electron cloud instability studies in the Beijing electron positron collider," *Physical Review Special Topics Accelerators and Beams*, vol. 7, no. 9, p. 094401, 2004.
 27. A. Kulikov, A. Novokhatski, and J. Seeman, "Suppression of the beam instability related to electron cloud at PEP-II B-factory," in *Electron-cloud effects. Proceedings, 31st ICFA Advanced Beam Dynamics Workshop, E-CLOUD'04, Napa, USA, April 19-23, 2004*, 2004.
 28. G. Arduini, T. Bohl, K. Cornelis, W. Hofle, E. Métral, and F. Zimmermann, "Beam observations with electron cloud in the CERN PS and SPS complex," in *Electron-cloud effects. Proceedings, 31st ICFA Advanced Beam Dynamics Workshop, E-CLOUD'04, Napa, USA, April 19-23, 2004*, 2004.
 29. R. Cappi, M. Giovannozzi, E. Métral, G. Métral, G. Rumolo, and F. Zimmermann, "Electron cloud buildup and related instability in the CERN proton synchrotron," *Phys. Rev. ST Accel. Beams*, vol. 5, p. 094401, Sep 2002.
 30. H. Bartosik, W. Höfle, G. Iadarola, Y. Papaphilippou, and G. Rumolo, "Benchmarking HEADTAIL with electron cloud instabilities observed in the LHC," *Proceedings of E-CLOUD12: Joint INFN-CERN-EuCARD-AccNet Workshop on Electron Cloud Effects, La Biodola, Isola d'Elba, Italy*, 2012.
 31. A. Chao, *Physics of Collective Beam Instabilities in High Energy Accelerators*. Wiley Series in Beam Physics and Accelerator Technology, Wiley, 1993.

32. K. Li and G. Rumolo, "Review of Beam Instabilities in the Presence of Electron Clouds in the LHC," *Proceedings of the IPAC11 International Particle Accelerator Conference, San Sebastian, Spain*, 2011.
33. K. Li, H. Bartosik, X. Buffat, W. Höfle, G. Iadarola, M. Kuhn, N. Mounet, and G. Rumolo, "LHC injection instabilities," *Presentation at 2-day internal review of LHC performance limitations during run I, 25-26. September 2013, CERN*.
34. G. Bregliozzi, G. Lanza, V. Baglin, and J.M. Jimenez, "Vacuum Pressure Observations during 2011 Proton Run," *Proceedings of the Evian 2011 LHC Beam Operation Workshop, Evian, France*, 2011.
35. L. Tavian, "Performance Limitations of the LHC Cryogenics: 2012 Review and 2015 Outlook," *Proceedings of the Evian 2012 LHC Beam Operation Workshop, Evian, France*, 2012.
36. W. Höfle, "Observations of the electron cloud effect on pick-up signals in the SPS," *10th Workshop on LEP-SPS Performance, Chamonix, France*, 2000.
37. B. Dalena, R. Alemany-Fernandez, A. Chancé, B. Holzer, J. Payet, and D. Schulte, "First Considerations on Beam Optics and Lattice Design for the Future Hadron-Hadron Collider FCC-hh," in *Proceedings, 6th International Particle Accelerator Conference (IPAC 2015): Richmond, Virginia, USA, May 3-8, 2015*, p. WEBB2, 2015.
38. F. Zimmermann et al., "FCC-ee Overview," in *Proceedings, 55th ICFA Advanced Beam Dynamics Workshop on High Luminosity Circular e+e- Colliders* Higgs Factory (HF2014): Beijing, China, October 9-12, 2014, p. THP3H1, 2015.
39. J. Wei and et al., "Electron Cloud Mitigation in the Spallation Neutron Source Ring," *Conf. Proc.*, vol. C030512, p. 2598, 2003.
40. C. Scheuerlein, B. Henrist, N. Hilleret, and M. Taborelli, "The Secondary electron yield of TiZr and TiZrV nonevaporable getter thin film coatings," *Appl. Surf. Sci.*, vol. 172, pp. 95–102, 2001.
41. O. S. Bruning, P. Collier, P. Lebrun, S. Myers, R. Ostojic, J. Poole, and P. Proudlock, *LHC Design Report*. Geneva: CERN, 2004.
42. C. Yin Vallgren, G. Arduini, J. Bauche, S. Calatroni, P. Chiggiato, K. Cornelis, P. Costa Pinto, B. Henrist, E. Metral, H. Neupert, G. Rumolo, E. Shaposhnikova, and M. Taborelli, "Amorphous carbon coatings for the mitigation of electron cloud in the CERN Super Proton Synchrotron," *Phys. Rev. Spec. Top. Accel. Beams*, vol. 14, p. 071001. 11 p, Jul 2011.
43. R. Valizadeh, O. B. Malyshev, S. Wang, S. A. Zolotovskaya, W. A. Gillespie, and A. Abdolvand, "Low secondary electron yield engineered surface for electron cloud mitigation," *Appl. Phys. Lett.*, vol. 105, p. 231605, 2014.
44. G. Stupakov and M. Pivi, 31st Advanced ICFA Beam Dynamics Workshop on Electron-Cloud Effects, Napa, CA, USA, 2004.
45. G. Iadarola, H. Bartosik, K. Li, L. Mether, A. Romano, G. Rumolo, and M. Schenk, "Performance limitations from electron cloud in 2015," *Proceedings of the 2015 Evian Workshop, 15-17 December 2015, Evian, France*.

2.21 Fast Beam-Ion Instability

Ryutaro Nagaoka
 Synchrotron SOLEIL, Saint-Aubin, Gif-sur-Yvette, France
 Mail to: nagaoka@synchrotron-soleil.fr

2.21.1 Introduction

Ions that are created via collisions of a stored beam with residual gases existing in a beam duct have historically caused performance degradations for both negatively and positively charged beams through their electrostatic interactions. In particular, a beam of ions trapped in the electrostatic potential of negatively charged particles, like electrons, may act collectively on the stored beam such as shifting their betatron tunes or inducing coherent oscillations. Many studies were made both experimentally and theoretically to understand these perturbations on the stored beam and find cures, particularly in light source storage rings where the stability of a circulating beam is of crucial importance [1-12]. The serious impact of ions had even led some of them to switch the stored beam from electrons to positrons such as DCI, ACO, APS and KEK-PF. Different means to mitigate ion trapping issues were studied and developed, such as introducing ion clearing electrodes, beam gaps and introducing octupoles that Landau damp coherent motions.

With a lower beam emittance achieved as a general trend in modern storage rings to further raise the ring performance in terms of luminosity and brilliance, the trapping of ions that suffered many rings in the past seems to have become much less of an issue as the critical mass, which represents the lightest ion that can be trapped, becomes significantly higher than known trapped species. On the other hand, however, a new direct type of interactions between a stored beam and a beam of ions occurring in a single passage of the former may become a risk for these machines due to a stronger electric field generated by the stored beam. Historically, such mechanism of two-beam instability, named as Fast Beam-Ion Instability (FBII), was first predicted theoretically by Raubenheimer and Zimmermann [13], which shall be the subject of this chapter.

The present chapter is organised as follows: In the next section, we shall follow the early study of Raubenheimer and Zimmermann, as well as some complementary theoretical works made on FBII. The experimental evidence, observations and analyses of FBII are addressed in Sec. 2.20.3. Some mitigation methods of FBII are reviewed in Sec. 2.20.4. A conclusion is given in Sec. 2.20.5.

2.21.2 Theoretical and Numerical Studies

2.21.2.1 *Early Studies Made by Raubenheimer and Zimmermann*

To understand the mechanism and characteristics of FBII, let us synthetically follow the model developed by Raubenheimer and Zimmermann [13]. The transverse coupled linear equations describing a single pass interaction of the two beams are given by

$$\frac{d^2 y_b(s, z)}{ds^2} + \omega_\beta^2 \cdot y_b(s, z) = K \cdot [y_i(s, t) - y_b(s, z)] \cdot \int_{-\infty}^z \rho(z') dz', \quad (1)$$

$$\frac{d^2 \tilde{y}_i(s, t)}{dt^2} + \omega_i^2 \cdot \tilde{y}_i(s, t) = \omega_i^2 \cdot y_b(s, z). \quad (2)$$

Three variables s , z and t are used to describe the beam motions. A longitudinal position in the ring is specified by s , at which an electron beam interacts with ions. The relative position within the electron beam is specified by z , with $z=0$ at the centre of the bunch train and extending in between $-z_0$ and $+z_0$, i.e. $-z_0 \leq z \leq +z_0$. The head of the train is defined as $z = -z_0$. Since the electron beam is assumed travel at the speed of light c , the time variable t is related to s via $t = (s+z)/c$. It must be noted that in their original paper, the assumed accelerator is not restricted to a ring and could well be a transfer line. Also, the perturbing beam is not limited to ions and could be electrons against positively charged beams. Reflecting the large difference in the mass between an ion and an electron, an ion frequency ω_i generally corresponds to an oscillation period much longer than the time spacing between bunches. The interaction between the two beams therefore becomes of coupled-bunch nature, while in the case of electron clouds, the two-beam instability is usually of single bunch nature.

In the first equation, $y_b(s, z)$ and $y_i(s, t)$ represent respectively electron and ion beam centroids. The non-perturbed motion of an electron beam centroid is a betatron oscillation represented by $\omega_\beta (= Q_{\beta y} \cdot \omega_0)$. Its motion is perturbed by an electrostatic potential of ions, as represented by the constant K , the attractive force depending proportionally on the difference of two amplitudes. What distinguishes this model from the previous ones on trapped ions is that reflecting the single pass ionization, the amplitude of ion perturbation depends explicitly on the number of electrons upstream the beam centroid $y_b(s, z)$ at the relative position z , as indicated by the last factor on the r.h.s. of Eq. (1). The longitudinal distribution of the electron bunch train is denoted by $\rho(z)$, normalized to unity. The second equation (Eq. 2) describes the vertical centroid of a transverse slice of ions $\tilde{y}_i(s, t)$ created at a position s at a certain moment t' ($< t$) due to collision of electrons with the residual gases. Reflecting the way they are generated, the initial conditions $\tilde{y}_i(s, t' | t') = y_b(s, z')$ and $d\tilde{y}_i(s, t' | t') / dt = 0$ are adopted for a transverse slice. The ion beam centroid $y_i(s, t)$ that influences the motion of an electron beam centroid $y_b(s, z)$ consists of all possible ion slices $\tilde{y}_i(s, t | t')$ with $t' = (s + z') / c$ created at the position s up till the time t . This is modelled as a $\rho(z)$ -weighted average over z' ,

$$y_i(s, t) = \int_{-\infty}^z dz' \rho(z') \cdot \tilde{y}_i(s, t | s + z') \Big/ \int_{-\infty}^z \rho(z') dz'. \quad (3)$$

The coupled equations are then solved via perturbation expansion in K/ω_β . A great simplification is introduced by assuming a rectangular distribution for $\rho(z)$, which signifies assuming no variation of the ion frequency ω_i along the bunch train. An asymptotic solution is derived in the form $y_b(s, z) \approx e^{2\sqrt{\eta}} / \eta^{1/4} \cdot \sin(\omega_i z - \omega_\beta s + \theta - \phi)$, where a variable η , given by $\eta \equiv K \cdot \omega_i \cdot (z + z_0)^2 s / (16 \omega_\beta z_0)$, is assumed to be large ($\eta \gg 1$), θ and ϕ are constants appearing from the initial phases of oscillations. From the obtained solution above, the asymptotic growth rate evaluated at the tail of a bunch train $z = z_0$ (i.e. where the instability is strongest) is given by

$$\tau_{aymp}^{-1} (s^{-1}) \approx \frac{N_e^{3/2} n_b^2}{\gamma} \times \left[5 p_{gas} (\text{Torr}) \frac{r_e r_p^{1/2} L_{sep}^{1/2} c}{\sigma_y^{3/2} (\sigma_x + \sigma_y)^{3/2} A^{1/2} \omega_\beta} \right] \quad (4)$$

where N_e is the number of electrons per bunch, n_b is the number of bunches, γ is the relativistic energy factor for the electrons, r_e and r_p are the classical electron and proton radii, σ_x and σ_y are the rms electron transverse beam sizes, L_{sep} is the longitudinal spacing between bunches, A is the mass number of the ions and p_{gas} is the residual gas pressure in Torr. The formula is obtained for a horizontally flat electron beam.

The asymptotic growth rate τ_{aymp}^{-1} is obtained in the form $y_b(s, z_0) \sim e^{\sqrt{t/\tau_{aymp}}}$ and is therefore not an e -folding time. From Eq. (4), we see that it depends strongly on the number of bunches ($\propto n_b^2$), the number of particles per bunch ($\propto N_e^{3/2}$) and the transverse beam sizes ($\propto \sigma_y^{-3/2} \cdot (\sigma_x + \sigma_y)^{-3/2}$). The assumed linear model is supposed to break down when the amplitude of the oscillation $y_b(s, z)$ exceeds the vertical beam size σ_y , where the coupling force between the two beams falls off. The growth rate above was evaluated for several existing rings in Ref. [13]. In particular, significantly short growth times result for the light source rings. However, no clear evidence of FBII was observed for these machines. The possible explanations are: 1) The developed model assumes constant ω_i , whereas these light sources have strongly varying β functions due to adoption of DBA and TBA lattices. Namely the ion frequency ω_i could effectively vary significantly around the ring. 2) Presence of Landau damping sources such as strong sextupoles and non-zero chromaticity that these rings generally possess. 3) Other important nonlinear effects not considered in the linear model.

In addition to the linear model above, Raubenheimer and Zimmermann developed a simulation code to study numerically the growth of instability as a complementary and more rigorous method. The numerical simulation using macro particles to represent the two beams has a large advantage of being able to integrate nonlinear effects such as due to finite beam sizes and follow self-consistently the evolution of bunch distributions of the two beams. In the developed scheme, the ionisation process via the beam - residual gas collisions was simulated by using the ionisation cross section and partial pressure of a specific gas species to generate ions. Then the space-charge forces of each of the two beams were calculated and applied to macroparticles of the opponent beam. The cascading process of ions growing in number due to successive arrival of electron bunches at the interaction point was correctly simulated. All ions at the end of each beam passage are discarded assuming an ion clearing beam gap from turn to turn. More details are described in Ref. [13]. Though the obtained simulation results showed certain sensitivity of the growth rate on the initial conditions of the beam, apart from this uncertainty the calculated growth rates agreed well with the predicted asymptotic growth rates.

Macro-particle simulations of FBII can generally be quite time consuming especially as the physical process of the collisional ionisation is intrinsically sequential and cannot be parallelised. If the bunch distribution of the electron beam can be assumed not to change through its interactions with ions, the beam bunch can be treated as a single rigid object. Such a model, conventionally called the weak-strong model, can bring about a great simplification and reduction in CPU time. It allows integrating other physically important ingredients into the simulation such as transverse bunch-by-bunch feedback and/or the effect of coupling impedance of a ring. There are a number of codes available today that

perform simulation of FBII with options developed for different investigation purposes [14-19].

2.21.2.2 *Nonlinear Tune Spreads*

Some further theoretical efforts were made by several groups to better describe the fast beam-ion instability. One is the influence of ion frequency spread which was ignored in the linear model above. As known, a spread in the frequency generally helps reducing the instability growth rate via Landau damping. There are at least the three following sources of ion frequency spread: 1) Due to electron beam density variations that may arise from relative transverse displacement of the two beams. 2) Amplitude dependent frequency shift due to the nonlinearity of the static potential of the electron beam. 3) Electron beam size variations along the ring arising from beta function changes. To elucidate the effect of ion decoherence analytically, Stupakov, Raubenheimer and Zimmermann [20] introduced a distribution function $f(\omega_i)$ on the ion frequency in the previous linear model, and used it in averaging over all possible transverse ion slices to get the ion beam centroid $y_i(s,t)$ in Eq. (3). Proceeding in an analogous way to solve the coupled linear equations as in the earlier model, we arrive at the following equation for the electron beam centroid $y_b(s, z)$

$$\frac{\partial^2 y_b(s, z)}{\partial s^2} + \frac{\omega_\beta^2}{c^2} \cdot y_b(s, z) = -\frac{K}{2z_0} \int_0^z z' \frac{\partial y_b(s, z')}{\partial z'} D(z - z') dz', \quad (5)$$

where $D(z - z')$ is named as a decoherence function given by the integral of $f(\omega_i)$ multiplied by $\cos[\omega_i / c \cdot (z - z')]$ over ω_i . The physical picture taken here is that the beam-ion instability develops on a time scale that is much larger than both the betatron and ion oscillation periods ($K \ll \omega_\beta^2, \omega_i^2$), which is true in most cases. The above justifies looking for a solution in the form $y_b(s, z) = A(s, z) \cdot e^{-i\omega_\beta s/c + i\omega_{i0} z/c}$ where ω_{i0} is the central ion frequency. In the absence of frequency spread $f(\omega_i) = \delta(\omega_i - \omega_{i0})$, the decoherence function becomes unity and the solution $A(s, z)$ is confirmed to consistently reduce to the asymptotic solution found in the previous subsection. In Ref. [20], the decoherence functions were explored in the exponential form to be able to derive analytically the solutions $A(s, z)$ for the first two sources of the frequency spread listed above. Analytical results were found to be in good agreement with macro particle simulations, where the treated ion tune spreads caused a reduction of the instability growth rate by roughly a factor of 2.

2.21.2.3 *Effective Wake Induced by Ions*

A first such attempt was made in describing a positron coasting beam driven unstable by an electron cloud [21]. Analogous treatment to ion clouds interacting with bunched electron beam was then made by two groups [22, 16]. Here we introduce below the work of Wang et al. [16]. The physical picture set up is that there is initially an ion cloud formed by collisions of electrons with residual gases, consisting on N_i ions. Now if there comes an electron bunch composed of N_e electrons with its centre of mass deviated by Δy_{e0} from the centre of the ion distribution, assumed to be described with a Gaussian, the ion distribution gets a kick from the electron bunch and starts oscillating coherently. The oscillating ion

distribution can in turn give a kick $\Delta\bar{y}_e'(s)$ to another electron bunch following the first bunch at a distance s behind. If the initial displacement Δy_{e0} is small enough and corresponds to the linear part of the ion distribution, all this process can be followed analytically using the relations derived in previous sections. In addition, we find that $\Delta\bar{y}_e'(s)$ is proportional to Δy_{e0} so that the transverse dipolar wake excited by a bunch of electrons defined by $W_y(s) \equiv \gamma/(N_e \varepsilon_0 r_e) \cdot \Delta\bar{y}_e'(s)/\Delta y_e$ does not depend on Δy_{e0} , namely it satisfies the linear response condition. The linearity of the wake function $W_y(s)$ as defined above was numerically confirmed. Also noticed in the numerical studies of $W_y(s)$ is the damping of the oscillation, which is due to the nonlinearity of the beam-ion space charge force, inducing an ion frequency spread. Wang et al. managed to parametrise the wake function in the usual broadband resonator function as follows,

$$W_y(s) = \hat{W}_y \cdot \exp\{-\omega_i s / (2Qc)\} \cdot \sin\left(\frac{\omega_i s}{c}\right), \quad (6)$$

with

$$\hat{W}_y = \frac{N_i}{\varepsilon_0} \left(\frac{r_p L_{sep}}{AN_e} \right)^{1/2} \cdot \left[\frac{4}{3} \cdot \frac{1}{\sigma_y (\sigma_x + \sigma_y)} \right]^{3/2} [\text{VC}^{-1} \text{m}^{-1}] \quad (7)$$

and the Q values of close to 9 was found to reproduce well the numerically obtained wakes of the most of concerned ions and electron beam sizes.

The advantage of describing the beam-ion dynamics of a wake or an impedance function is to be able to use the same linearised Vlasov equation formalism developed for conventional coupled-bunch instabilities. In Ref. [16], an application was made to study the stabilisation effect of beam gaps introduced in a bunch train.

2.21.3 Experimental Studies

2.21.3.1 *Demonstration of FBII in Some Rings by Artificially Injecting Gas into the Vacuum Chamber*

The FBII was experimentally demonstrated in ALS [23], PLS [24] and KEK [25] by artificially increasing the vacuum pressure in a ring. In the first such attempt made at ALS [23], *He* gas was injected into the ring to attain 80×10^{-9} Torr, and bunch-by-bunch transverse feedback was switched on to stabilise beam against conventional beam instability induced by the coupling impedance. A comparison of the vertical beam size was then made to the nominal pressure case as a function of the length of a bunch train, leaving always a large beam gap of more than 80 buckets. A steady increase of the vertical beam size was observed until the bunch train reached some 15 bunches and then saturated above. The evolution of the coherent signals exhibited by the beam was followed as a function of its intensity, where the measured peak frequencies turned out to well reproduce what expected from the theory. Another interesting observation was the beam current distribution along the bunch train after inserting a vertical scraper to scrape off a vertically blown up beam. As expected from the theory, the intensity tended to decrease from the head to the tail of a

bunch train. All these observations well confirmed the characteristics of FBII. Studies made at PLS and KEK equally gave good agreement with theory.

2.21.3.2 *Characterizations in SPEAR-III*

A systematic characterisation of FBII was made more recently at SPEAR3 (SLAC) by measuring the vertical betatron sideband signals over the multibunch frequency band under different beam and machine conditions without any artificial injection of gases [17]. These experimental results were compared with what expected from theory using the wake formalism referred to in the previous section. Three such sets of measurement may be cited here: the first concerned the dependence on the vertical beam size adjusted with skew quadrupoles. Without them, the beam size was about 2.3 times larger. As expected from theory, the two-beam interaction was significantly enhanced as the beam size was reduced. The dependence on the bunch filling pattern was then followed. Three different filling patterns were tested by keeping the total number of bunches, the length of the beam gap between the bunch trains, and the total beam current equal. The comparison clearly indicated the advantage of filling a beam in many short trains of bunches in fighting against FBII. The third measurement followed the dependence on the vertical chromaticity, which was increased from 2 to 7. Again, as expected the chromaticity helped suppressing FBII, supposedly through an increased tune spread of the electron beam, though the increase of chromaticity caused a significant reduction of lifetime.

2.21.3.3 *FBII Arising from Local Outgassing due to Impedance*

Beam losses, which are often total losses, have been encountered at SOLEIL at high beam current. A series of studies identify these losses as due to FBII that induces a complicated combined effect involving Resistive-Wall (RW) instability and transverse feedback [26, 27]. A feature to be noted here is that FBII does not arise from the ordinary vacuum pressure, but from localised outgassing of vacuum chambers heated by wake fields. The fact that the multibunch operation at SOLEIL is under the influence of both RW and FBII was known since the commissioning times through analyses of bunch-by-bunch transverse feedback data. At relatively low current, the beam is affected by RW alone, as seen from the amplitude and phase relations in a bunch train. Above a certain current, however, a transition to FBII dominated regime occurs. The bunch to bunch betatron phase variations of around 0.9 and 40 degrees measured respectively at the RW and FBII regimes are in agreement with what can be expected from theory. The measured growth rate versus current, averaged over bunches, follows well the curve expected from the RW instability, but with larger error bars at high current, suggesting the nature of mixture of the two instabilities.

Though the vacuum conditioning with beam over years helped reducing the relative contributions of FBII at a given beam current, FBII still persistently exists at SOLEIL at the nominal current of 500 mA, even after 10 years of operation. It can still provoke beam losses, which happen strangely at some ten minutes after ramping the current to its final value. During this period, the beam is diagnosed to be stable. To avoid the beam losses, a number of different beam fillings were tried assuming that beam gaps help suppress FBII. However, the experimental results indicated on the contrary that uniform filling gives the most stable beam. This, along with the fact that lower RF voltage reduces beam losses, led us to realise that the source of FBII is the beam-induced heating of vacuum components via longitudinal wake fields that in turn triggers outgassing. Thus, keeping the bunch current

low and the bunch length long to avoid heating suppresses the origin of instability. Besides, the puzzle of beam losses due to FBII was understood to be due to interlock that trips the RF upon detecting a rapid drop of beam current to protect the RF system.

It remained to clarify the sudden beam current drops triggering the interlock. Again, the bunch-by-bunch diagnostics used as a post-mortem helped getting a closer look into the beam motion just before the beam loss. Following the averaged amplitude of the beam versus time, we see that the beam blows up exponentially before it is lost. It suggests that the sudden current drop is due to the blown up beam being scraped off either by the chamber or by the dynamic acceptance. Analysing the phase relation between adjacent bunches, we identify the sequence of the following three regimes up to the explosion: 1) no phase correlation (i.e. absence of coherence), 2) ion regime, and 3) RW regime. Somehow transverse feedback fails in keeping the beam stable when it is in the ion regime. The last observation implies that during some ten minutes of “silence”, the gas density, and therefore the number of ions created at each turn steadily increases up to the point that the FBII growth rate exceeds the limit of feedback, since the underlying machine heating continues. What is not obvious, however, is the reason for which the beam continues to blow up in the RW regime when ions are expected to have gone due to large amplitude beam oscillations. Namely, we need to understand the failure of feedback in the third RW regime. A possible explanation is that feedback, with its filter and gain used, is not reacting adequately against the fast dynamical change of beam motions from FBII to RW. More details are found in Ref. [28]. A simulation study that includes the effect of RW, FBII and feedback reproduces the beam behaviour similar to the observation, supporting the above conjecture [28].

2.21.4 Mitigations of FBII

Cutting a long bunch train into small pieces and introducing small bunch gaps between each of them generally helps reducing the growth rate of FBII. A numerical study was made by Wang et al. by using the wake function formalism introduced earlier [16]. Introducing a pair of electrodes to clear the ions away is a known effective method in reducing the ion effects [6, 12, 29]. Ion clearing electrodes have however the risk of increasing the broadband impedance of a ring, lowering the single bunch instability thresholds or inducing local machine heating. Optimization of the electrode design should be done in advance to minimize the impedance [30].

With the performance available today on the market, transverse bunch-by-bunch feedback would be the best method to stabilise a beam against FBII. Experiences gained at the ESRF and SOLEIL confirm this feature [26, 31]. In both rings, the ion frequencies are typically in a few tens of MHz range, which is low compared to the feedback bandwidth of 176 MHz for these machines. The beam oscillations can therefore be corrected relatively easily. At SOLEIL, feedback turned out to be destructive under exceptional situations, as was described in the previous section.

Through studies of FBII, an interesting idea emerged that if an electron beam can only blow up vertically by roughly a factor of two and never gets lost due to the saturation of the two-beam interaction, one may reduce the vertical beam size by a factor of two in advance by anticipating the blow up [32]. More studies may nevertheless be needed to fully certify the absence of residual beam blow up in the saturation regime. The absence of FBII in many modern light sources suggests sources of stabilization in these machines, among which the strong variations of beta function is suspected as they induce ion frequency spreads. Going further along this direction, we may actively enhance vertical beta function variation to

stabilise the beam via Landau damping. Again, more studies would be necessary to certify the damping mechanism quantitatively.

2.21.5 Conclusion

Due to the general difficulties of measurement and non-reproducibility of vacuum conditions, ion instabilities are often not straightforward to understand quantitatively, as compared to other instabilities. However, the theoretical, numerical and experimental studies made so far creating a solid basis of the beam-ion physics allow fairly good explanations and predictions today qualitatively and quantitatively. There are yet a number of nonlinear beam-ion dynamics involving Landau damping and stabilization, which are not adequately understood and would require further efforts.

Owing presumably to lower beam emittances in modern storage rings, ion trapping does not seem to be a big issue anymore. However, FBII could jeopardise the performance of future low emittance and high beam intensity accelerators as its growth rate would get larger. For light sources, in particular, the effort of reaching an ultra-low emittance tends to render the vacuum chamber aperture smaller and smaller. The vacuum issues and hence ion-induced beam instabilities would likely remain important especially in a combined manner with other effects, as already encountered at SOLEIL. Continuation of beam-ion studies would therefore be of great importance in raising the performance of future accelerators.

2.21.6 References

1. D.G. Koshkarev, P.R. Zenkevich, "Resonance of coupled transverse oscillations in two circular beams", *Particle Accelerators* 3 (1972) p.1.
2. Technical Note – ISR Vacuum Group, "The behaviour of ions in presence of a bunched antiproton beam in the ISR", ISR-VA/EF-sm, 7 November 1978.
3. Y. Baconnier, G. Brianti, "The stability of ions in bunched beam machines", CERN/SPS/80-2 (DI), March 1980.
4. M.E. Biagini, S. Guiducci, M. Preger, M. Serio, S. Tazzari, "Observation of ion trapping at ADONE", *Proc. 11th Int. Conf. on High Energy Accelerators*, CERN, Geneva, Switzerland (1980), p.687.
5. Y. Yamazaki, M. Kihara, H. Kobayakawa, "Partially filled multi-bunch mode operation of the Photon Factory electron storage ring and cure of the vertical instability", KEK 83-17 (1983).
6. G. Brianti, "The stability of ions in bunched beam machines", CERN 84-15 (1984), p. 369.
7. Y. Kamiya, M. Izawa, T. Katsura, M. Kihara, H. Kobayakawa, S. Shibata, "Vertical instability caused by ion-trapping in KEK-PF storage ring", *Proc. of 5th Symp. Acc. Sci. Tech.* (1984) p.292.
8. Y. Baconnier, "Neutralization of accelerator beams by ionization of the residual gas", CERN 85-19 (1985), p. 267.
9. T. Kasuga, H. Yonehara, T. Kinoshita, M. Hasumoto, "Ion-trapping effect in UVSOR storage ring", *Jpn. J. Appl. Phys.* 24 (1985) 1212.
10. M.Q. Barton, "Ion trapping with asymmetric bunch filling of the NSLS VUV ring", NIM A243 (1986) 278.
11. S. Sakanaka, "The stability of ions in partially filled mode operation in the electron storage ring", KEK Preprint 86-17 (1986).

12. C.J. Bocchetta, A. Wrulich, “The trapping and clearing of ions in ELETTRA”, NIM A278 (1989) 807-817.
13. T.O. Raubenheimer, F. Zimmermann, “Fast beam-ion instability. I. Linear theory and simulations“, Phys. Rev. **E52**, 5487 (1995).
14. K. Ohmi, “Numerical study for the two-beam instability due to ions in electron-storage rings”, Phys. Rev. **E55**, 7550 (1997).
15. G. Xia, K. Ohmi, E. Elsen, “Simulation Study of Fast Ion Instability in the ILC Damping Ring and PETRA III”, unpublished; A revised version by G. Xia and E. Elsen is published in NIM **A593** (2008) 183.
16. L. Wang, Y. Cai, T.O. Raubenheimer, H. Fukuma, “Suppression of beam-ion instability in electron rings with multibunch train beam fillings”, PRSTAB **14**, 084401 (2011).
17. L. Wang, J. Safranek, Y. Cai, J. Corbett, R. O. Hettel, T. O. Raubenheimer, J. Schmerge, J. Sebek, “Beam ion instability: Measurement, analysis and simulation”, PRSTAB **16**, 104402 (2013).
18. G. Skripka, R. Nagaoka, M. Klein, F. Cullinan, P.F. Tavares, “Simultaneous computation of intrabunch and interbunch collective beam motions in storage rings”, NIM **A806** (2016) 221-230.
19. L. Mether, G. Rumolo, “Progress on macro-particle simulations of fast beam-ion instabilities in the framework of the PyHEADTAIL code”, presented at TWIICE-2, Abington, UK, February 2016.
20. G.V. Stupakov, T.O. Raubenheimer, F. Zimmermann, “Fast beam-ion instability II. Effect of ion decoherence”, Phys. Rev. **E52**, 5499 (1995).
21. K. Ohmi, F. Zimmermann, E. Perevedentsev, “Wake-field and fast head-tail instability caused by an electron cloud”, Phys. Rev. **E65**, 016502 (2001).
22. E.S. Kim, K. Ohmi, “Simulations on the Fast-Ion Instability in the International Linear Collider Damping Rings”, Jpn. J. Appl. Phys.48, 086501 (2009).
23. J. Byrd, A. Chao, S. Heifets, M. Minty, T.O. Raubenheimer, J. Seeman, G. Stupakov, J. Thomson, F. Zimmermann, “First observations of a Fast Beam-Ion Instability”, Phys. Rev. Lett. **79**, (1997) 79.
24. M. Kwon, J.Y. Huang, T.-Y. Lee, I.S. Ko, Y.H. Chin, H. Fukuma, M. Isawa, K. Ohmi, M. Tobiyama, “Experimental results on the fast beam-ion instability”, Phys. Rev. **E57**, 6016 (1998).
25. H. Fukuma, Y. Chin, S. Kato, E. Kikutani, S. Kurokawa, S. Matsumoto, K. Ohmi, Y. Suetsugu, M. Tobiyama, K. Yokoya, X.L. Zhang, “Experimental observations of the ion-related coupled bunch instability in a bunch train in TRISTAN AR”, PAC97, Vancouver, 1997, p. 1596.
26. R. Nagaoka, “Observation and analysis of fast beam-ion instabilities at SOLEIL”, International workshop on linear colliders 2010, accelerator working group 2, CERN, 2010.
27. R. Nagaoka, L. Cassinari, M. Diop, J.M. Filhol, M.P. Level, M. Labat, P. Marchand, R. Sreedharan, “Study of ion-induced instabilities and transverse feedback performance at SOLEIL”, IPAC2011, San Sebastián, Spain, September 2011, p. 712.
28. R. Nagaoka, R. Sreedharan, L. Cassinari, “Fast beam-ion instability arising from local outgassing”, TWIICE, Synchrotron SOLEIL, Gif-sur-Yvette, France, January 2014.
29. T. Kasuga, H. Yonehara, T. Kinoshita, M. Hasumoto, “Ion-trapping effect in UVSOR storage ring”, Jpn. J. Appl. Phys. 24 (1985) 1212.

30. M. Zobov, A. Battisti, A. Clozza, L. Lollo, C. Milardi, B. Spataro, A. Stella, C. Vaccarezza, “Impact of ion clearing electrodes on beam dynamics in DAΦNE”, *J. Instr.* **2** P08002 (2007).
31. E. Plouviez, Ph. Arnoux, F. Epaud, J.-M. Koch, G. Naylor, F. Uberto, “Bunch by bunch transverse feedback development at the ESRF”, EPAC08, Genoa, 2008, p. 3297.
32. K. Oide, cited as “private communication” in Ref. 13.

2.22 Beam-Beam Effects in Linear Colliders

Daniel Schulte, CERN
 CERN, 1211 Geneva 23, Switzerland
 Mail to: daniel.schulte@cern.ch

2.22.1 Overview

Linear colliders are promising candidates for future high-energy lepton colliders. In the past the SLC [1] has successfully operated at the Z-resonance. Two future linear collider projects are under consideration, the International Linear Collider (ILC [2-6]) and the Compact Linear Collider (CLIC [7-10]). ILC aims at a centre-of-mass energy of 500 GeV, potentially starting at 250 GeV. CLIC is foreseen to be implemented in three stages ranging from a centre-of-mass energy of 380 GeV up to 3 TeV. Both projects are studied by global collaborations. The use of advanced acceleration techniques, such as plasma-based acceleration, is also considered by smaller teams.

Beam-beam effects are an important driver of their design choices and affect the performance of physics experiments. In the following a short reminder of the beam-beam effects is given and their impact on the parameter choice is highlighted; as it has for example been used in the recent optimisation of CLIC parameters for the first energy stage with a centre-of-mass energy of 380 GeV [10]. Some recent improvement in the understanding of the choices by studying the performance of physics event analysis is given in the section on the choice of horizontal beam size.

2.22.2 Introduction

In ILC and CLIC, the beams are produced in an electron and a positron source, respectively. They are slightly accelerated and transported to a damping ring. Here their emittance is reduced to very small values, especially in the vertical plane. Then the beams are transported through the Ring-To-Main-Linac system (RTML). During the transport they are slightly more accelerated and compressed longitudinally. In the main linac they are accelerated to full energy. In the Beam Delivery System (BDS) the beams are then focused to the very small sizes at the collision point. Then they are disposed off in beam dumps.

The main challenges of a linear collider are first to achieve the beam energy in the main linac. This requires very high gradients for the acceleration. The second challenge is to achieve the high luminosity in a single pass. This requires very dense beams at the collision point, which results in strong beam-beam interaction. Both, ILC and CLIC, will deliver short pulses of bunches that collide with longer intervals between pulses.

The ILC is based on the use of superconducting cavities to accelerate the beam. These allow the use of long beam pulses. To provide the accelerating field, the cavity needs to be filled with energy. This energy is lost very slowly in the walls of the cavity, hence one can afford a long pulse. In contrast, CLIC is based on high-gradient normal-conducting accelerating structures. These require very short pulses since the energy in the accelerating structures is lost rapidly in the copper walls. To achieve sufficient efficiency it is therefore necessary to use very short pulses and to increase the beam current in the pulse as much as possible. This requires short distances between the bunches. The advantage of the normal conducting accelerating structures is that they allow to use higher accelerating fields than superconducting cavities (about a factor 3 between CLIC and ILC). To achieve multi-TeV

energies at practical machine length and cost thus requires the use of normal conducting technology. The main beam parameters for ILC and CLIC are given in Table 1.

Table 1: Key parameters of the linear colliders. For ILC and CLIC nominal parameters are given, for the SLC typical parameters towards the end of the operation. The latter differ significantly from the target values.

Parameter	Symbol [unit]	SLC	ILC	CLIC	CLIC
CMS energy	E_{cm} [GeV]	92	500	380	3000
Geometric luminosity	L [$10^{34} \text{cm}^{-2} \text{s}^{-1}$]	0.00015	0.75	0.8	4.3
Luminosity	L [$10^{34} \text{cm}^{-2} \text{s}^{-1}$]	0.0003	1.8	1.5	6
Luminosity in peak	$L_{0.01}$ [$10^{34} \text{cm}^{-2} \text{s}^{-1}$]	0.0003	1	0.9	2
Beam power	[MW]	0.065	10.5	0.9	28
Gradient	G [MV/m]	20	31.5	72	100
Particles per bunch	N [10^9]	37	20	5.2	3.72
Bunch length	σ_z [μm]	1000	300	70	44
Interaction point beam size	$\sigma_{x,y}$ [nm/nm]	1700/600	474/6	149/3	40/1
Normalised emittances	$\varepsilon_{x,y}$ [nm/nm]	3000/3000	$10^4/35$	950/30	660/20
Initial beam energy spread	σ_E [%]	-	O(0.1)	0.35	0.35
Bunches per train	n_b	1	1312	352	312
Bunch distance	Δz [ns]	-	554	0.5	0.5
Repetition rate	f_r [Hz]	120	5	50	50
Horizontal disruption	D_x	0.6	0.3	0.24	0.2
Vertical disruption	D_y	1.7	24.3	12.5	7.6
Photons per beam particle	n_γ	-	1.9	1.5	2.1
Average photon energy	$2E_\gamma/E_{\text{cm}}$ [%]	-	2.4	4.5	13
Coherent pairs	N_{coh} [10^8]	-	-	-	6.8
Their energy	E_{coh} [10^8TeV]	-	-	-	2.1
Incoherent pairs	N_{incoh} [10^3]	-	196	58	300
Their energy	E_{incoh} [TeV]	-	484	187	2.3×10^4

2.22.3 Beam-Beam Physics

In this section a short reminder of the beam-beam physics is given. More detailed information can be found for example in [11-14]. In the next section novel results for the choice of parameters will be presented.

2.22.3.1 Beam Parameters and Luminosity Drivers

The luminosity target for linear colliders is in the range of $10^{34} \text{cm}^{-2} \text{s}^{-1}$ following the requests of the experiments. In Table 1, one can note that ILC and CLIC use flat beams to achieve this ambitious goal and that the vertical beam size is only of the order of nm. In the following we will discuss the reason.

The luminosity L in a linear collider is given by the following formula:

$$L = H_D \frac{N^2 n_b f_r}{4\pi\sigma_x\sigma_y} \quad (1)$$

Here, N is the number of particles per bunch, $\sigma_{x,y}$ are the horizontal and vertical beam sizes at the collision point, n_b is the number of bunches per train, f_r is the rate of trains per second and H_D is a factor that contains the impact of beam-beam forces and other relevant effects. H_D is typically in the order of 1.5-2. It is useful to rewrite the formula in the following form:

$$L = H_D \frac{N}{\sigma_x} \frac{1}{\sigma_y} N n_b f_r \quad (2)$$

The term $N n_b f_r$ represents the beam current. Its upper limit arises from the power consumption of the collider and the efficiency to turn this power into beam power. As can be seen in Table 1, the beam power is quite high. It is therefore important to maximise the luminosity per beam current, i.e. the factors N/σ_x and $1/\sigma_y$. However a lower limit to the beam size arises from the beam-beam effects.

2.22.3.2 *Beam-Beam Dynamics and Disruption*

At collision, the beams generate strong electromagnetic fields that focus each other in an electron-positron collider. In circular colliders this deflection is quite small and can be understood as a thin-lens kick. In a linear collider the beams are so dense that the particles move strongly during the collision. This so-called pinch effect reduces the effective beam size and leads to an increase in luminosity.

The focusing is described using the so-called disruption parameters: $D_{x,y}$ for the horizontal and the vertical plane, respectively. $D_{x,y}$ is calculated as

$$D_{x,y} = \frac{2N r_e \sigma_z}{\gamma \sigma_{x,y} (\sigma_x + \sigma_y)} \quad (3)$$

Here, r_e is the classical electron radius and γ the relativistic factor. For $D_{x,y} \ll 1$ particles with small offsets x and y and no initial angle will receive final angles $x' = (D_x/\sigma_z) x = x/f_x$ and $y' = (D_y/\sigma_z) y = y/f_y$. This implies that in each plane, the core of the beam is focused to a single point at distance $f_{x,y}$ behind the collision plane and $D_{x,y}$ is the ratio of the bunch length to this distance. Hence $D \ll 1$ corresponds to a thin lens kick. In contrast $D \gg 1$ indicates that the particle motion during the collision is important. In ILC and CLIC $D_x \ll 1$ and $D_y \gg 1$.

For large disruption analytical models are difficult to develop and computer codes are used to simulate the effect. The two most widely used codes are GUINEA-PIG [14] and CAIN [15]. They represent the beam by a number of macro-particles. Their predictions have been experimentally verified in the SLC [16], where under some conditions the luminosity was more than doubled in good agreement with the simulations. The codes also include the beamstrahlung effect, which is described in more detail below, and the generation of the different electron-positron background processes. GUINEA-PIG also includes the generation of hadronic background and the generation of muons, both processes will not be discussed here.

2.22.3.3 *Beamstrahlung*

When the particle is forced on a curved trajectory by the other beam, it will emit radiation in a similar fashion as in a bending magnet. This radiation is called beamstrahlung. For typical parameters each particle emits one to a few photons each of which carries some percentage of the particle's energy. It is therefore important to be aware of the stochastic nature of the beamstrahlung. Due to beamstrahlung the particles lose energy during the

collision and can therefore collide with less than the initial energy. This leads to the formation of a luminosity spectrum. This obviously impacts the performance of the physics experiments. The importance depends on the physics analysis that is being carried out.

The beamstrahlung can be described by the so-called beamstrahlung parameter Ψ , which is related to the average critical energy of the radiation emitted by the beam particles. It can be calculated as

$$\Psi = \frac{2}{3} \frac{E_{crit}}{E_0} = \frac{\hbar \gamma^3 c}{\rho E_0} \quad (4)$$

Here ρ is the bending radius of the particle trajectory and γ the relativistic factor. The average $\langle \Psi \rangle$ is given by the beam parameters and the fine structure constant α as

$$\langle \Psi \rangle \approx \frac{5}{6} \frac{Nr_e}{\alpha \sigma_z (\sigma_x + \sigma_y)} \quad (5)$$

The beamstrahlung spectrum is described by the Sokolov-Ternov spectrum. For $\Psi \ll 1$ the spectrum corresponds to synchrotron radiation and one speaks of the classical regime. For $\Psi \gg 1$ the radiation is partially suppressed since the critical energy is above the beam energy. This is the so-called quantum regime. Only CLIC at 3TeV will operate in this regime. In the classical regime, the number n_γ and average energy E_γ of photons emitted per beam particle depends on the bunch charge and transverse dimensions

$$n_\gamma \propto \frac{N}{\sigma_x + \sigma_y} \quad E_\gamma \propto \frac{N}{(\sigma_x + \sigma_y) \sigma_z} \quad (6)$$

Typically one is only interested in collisions with energies very close to the nominal. In this case often the emission of a single photon is sufficient to place the particle outside of this energy range. Hence the number of emitted photons has to be limited. More detail will be given in the final section on horizontal beam size choice.

For a given N and σ_z , one has to use a relatively large sum of the transverse beam sizes $\sigma_x + \sigma_y$. The luminosity is proportional to $1/(\sigma_x \sigma_y)$, so one aims to minimise the product of the two beam sizes. Both goals can be simultaneously achieved by using a flat beam $\sigma_x \gg \sigma_y$; the horizontal beam size is chosen to be larger than the vertical, since the damping rings naturally deliver a horizontal emittance that is larger than the vertical. Using $\sigma_x + \sigma_y \approx \sigma_x$ one finds that N/σ_x in Eq. (2) is proportional to the number of beamstrahlung photons. As one can see in Table 1, all projects have a value of n_γ in the range of 1.5-2. The rationale for this choice will be revisited in section on the choice of the horizontal beam size. The typical angular distribution of the photons is small, similar to the one of the beam particles after collision. Hence the beamstrahlung does not generate direct background in the detector.

2.22.3.4 Vertical Beam Size and Waist Shift

The vertical beam size is limited by the beam emittance and by the ability to focus the beam. Here, the practical limitations for the focusing will be ignored and only the impact of the vertical beta function will be considered assuming perfectly linear behaviour of the beam. For weak beam-beam effects, the luminosity is limited by the hourglass effect similar to circular colliders. The left-hand side of Fig. 1 shows the luminosity ignoring hourglass effect (“geom.”) and including it (“hourg.”). The optimum is at $\beta_y = 0.25 \sigma_z$. The beam-beam forces shift the optimum to much larger beta functions around $\beta_y \approx \sigma_z$ (“ILC” and “CLIC”). The pinching of the beams is more efficient if their divergence is smaller.

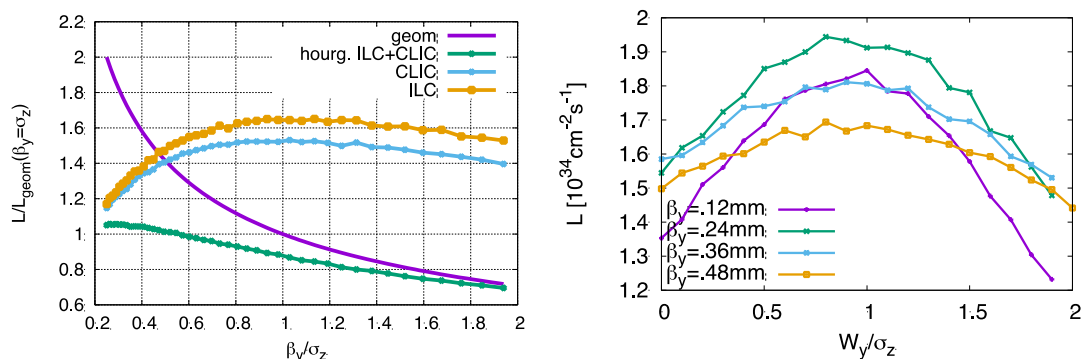


Figure 1: Left: Luminosity as a function of the vertical beta function (normalised to the bunch length). Right: The luminosity in ILC as a function of the longitudinal shift of the vertical waist for different vertical beta functions.

If the beam-beam forces are weak the maximum luminosity is obtained when the vertical waists of the two beams are placed at the collision point. A distance W_y of the waists to the collision point leads to a reduced luminosity. In presence of beam-beam forces it can be better to have the vertical waists before the collision point [16], which can increase the luminosity by up to 25%. The exact location and the luminosity gain also depend on the beta function. This is shown in Fig. 1 for ILC. A small beta function of $\beta_y=0.12\text{mm}$ gives worse performance for centred waists than $\beta_y=0.48\text{mm}$. After the optimisation of the waist it however yields more luminosity.

2.22.3.5 *Beam Offsets*

The beam-beam forces also modify the luminosity reduction resulting from vertical beam-beam offsets. For weak disruption the luminosity decreases somewhat more slowly with offset than for rigid beams because the beam attract each other. In contrast, for larger disruption, already very small offsets can lead to a large loss of luminosity. This is due to the fact that the collision becomes unstable, the so-called kink instability, which is a typical two-stream instability. Again for larger offsets, the beam-beam forces maintain more luminosity than for rigid beams. Figure 2 illustrates this for different disruption parameters.

To avoid luminosity reduction, control of the beam-beam offset is required at the level of a fraction of a nanometre. The motion of the ground and vibrations of technical components make this a challenging task. Two main methods are used to address this challenge. First, in case of CLIC, the beam guiding magnets are stabilised with active feedback systems that sense the motion of the magnet and correct it using movers. Second, in both ILC and CLIC, the beam-beam offset is measured and corrected with a beam-based feedback system. In case of ILC this feedback system can correct from one bunch to the next within the pulse, in CLIC it has a latency of a few bunch crossings and mainly acts from one pulse to the next. This feedback can easily detect an offset even of a fraction of a nm, since the resulting deflection of the beams is in the order of tens of μrad . A few metres downstream of the collision point such an angle has translated into an offset that can be easily measured with a beam position monitor.

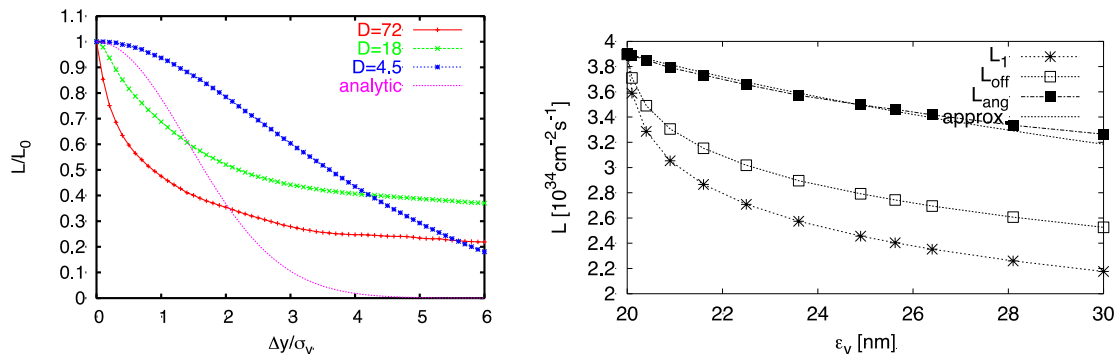


Figure 2: Left: Luminosity as a function of offset for different vertical disruption parameters. Right: The luminosity as a function of the emittance in the case of TESLA an older linear collider design.

2.22.3.6 *The Banana Effect*

For strong vertical disruption (typically $D_y \geq 15$) correct modelling of the full 6D phase space of the beam. The projected emittance is not a good measure of the luminosity any more. This is due to the so-called banana effect described in [17] for TESLA, an older linear collider design similar to the ILC. The luminosity drops much faster with increasing beam emittance than anticipated from the projected emittances [18].

The right-hand side of Fig. 2 shows an example where the main linac wakefield effects are included. Similar results are obtained for other sources of emittance growth, e.g. ground motion in the beam delivery system [19]. In the figure, the horizontal scale indicates the emittance at the interaction point, which consists of an uncorrelated part of 20 nm and an additional contribution from the main linac wakefields. The luminosity is shown on the vertical axis. The curve “approx” assumes that the luminosity scales with $1/\sqrt{\epsilon_y}$. The curve “ L_1 ” shows the luminosity if both beams are centred in position and angle. Even a small emittance increase yields a very strong luminosity loss since the collision is unstable as a result of the high disruption.

The luminosity can be recovered if a full luminosity optimisation is performed at the interaction point by varying the beam-beam offset (L_{off}) and by varying offset and angle (L_{ang}). This procedure however requires that the luminosity is measured online. Hence it takes much more time than a simple beam position monitor based feedback. In ILC it is foreseen to perform such an optimisation during each bunch train. For a smaller disruption, as in CLIC, the banana effect is negligible. Hence a luminosity optimisation scan during the train is not required.

2.22.3.7 *Beam-beam Background and its Impact on the Detector Design*

The beam-beam effects lead to the generation of background for the physics experiments. This includes the production of electrons and positrons, muons, and hadrons. These effects can significantly impact the detector design and close interaction of accelerator and detector design is required. However, this subject cannot be covered in this paper.

2.22.4 *Choice of Horizontal Beam Size*

A lower limit of horizontal beam size and beta function arises from the beamstrahlung to limit the degradation of the luminosity spectrum. It is important to note that the luminosity

spectrum is also affected by another process. If particles collide, they can emit a photon just before the collision as a part of the physics process, this is called Initial State Radiation (ISR). This emission is a radiative correction to the physics process. In contrast to beamstrahlung, it therefore happens only to colliding particles that undergo some physics process. However, it will degrade the luminosity spectrum in a similar fashion to beamstrahlung; the typical centre of mass energy spectrum of the colliding electrons and positrons is shown on the right-hand side of Fig. 3.

Usually the experiments require that the degradation of the luminosity spectrum due to beamstrahlung is similar to the degradation due to ISR. As a measure one uses the ratio of the luminosity $L_{0.01}$, i.e. the part above 99% of the nominal centre of mass energy, and the total luminosity. In case of CLIC at 380 GeV a ratio of 60% has been targeted.

The total and peak luminosity is shown in Fig. 3 for CLIC at 380 GeV and ILC at 500 GeV as a function of the horizontal beta function. One can observe that the total luminosity increases strongly for smaller beta functions. It increases even faster than the geometric luminosity. This is a result of the fact that a smaller horizontal beam size increases the disruption and therefore leads to an increase in the pinch enhancement factor H_D . However the peak luminosity only increases slightly for smaller beam sizes. Hence the ratio of peak to total luminosity decreases rapidly for small beta functions, which yields a lower limit. It should be noted that additional lower limits for the horizontal beta function exist, e.g. from the ability to design the beam delivery system. With the chosen value, CLIC indeed reaches a ratio of 60%, as one can see on the left-hand side in Fig. 3.

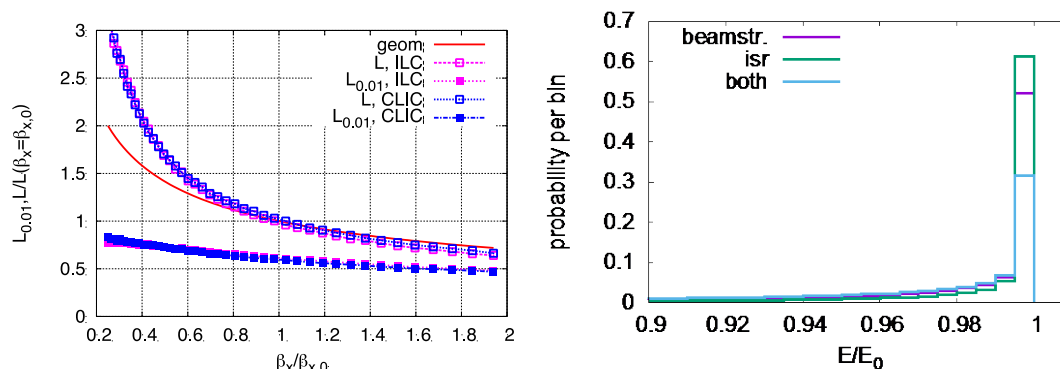


Figure 3: Left: Luminosity as a function of the horizontal beam size. Right: The luminosity spectrum from beamstrahlung and from ISR.

Recently a study has been carried to identify the optimum choice of beamstrahlung level for CLIC and ILC [20]. To this end one of the main physics processes that should be studied at 380 GeV has been selected. This is the reconstruction of the total higgs production cross section in the channel $e^+e^- \rightarrow Zh$. In this analysis only the Z is measured and from the initial beam conditions and the Z energy and momentum the missing particle is reconstructed indirectly. It is then determined whether this particle is consistent with the higgs. This measurement has the advantage that the higgs production rate can be measured independent of the higgs decay. One would even be able to see invisible higgs decays (even if they are not expected). This measurement is expected to be very sensitive to beamstrahlung since the beamstrahlung will change the initial conditions. In particular the assumed energy of the colliding particles will be wrong. This leads to a wrong reconstruction of the missing particle.

In the study the beam parameters have been optimised assuming a constant time of operation. The horizontal beam size has been varied and all other parameters were left constant. A wide beam will give less beamstrahlung but also less integrated luminosity. For each beam size the luminosity spectrum has been simulated with GUINEA-PIG and the corresponding higgs events been generated using WHIZARD [21]. In addition, also the main background events that could fake the signal have been produced; their number is larger by some orders of magnitude. The particle energies have then been randomly modified corresponding to the detector resolution. Finally the events have been analysed using TMVA [22] a boosted device tree classifier. This allowed to determine the expected accuracy of the measured higgs production cross section.

The study concluded that pushing the horizontal beam size further would improve the performance slightly. However the improvement is only a few percent compared to the nominal parameters, in spite of the fact that the luminosity would about double. Given the difficulty to obtain narrower beams this small improvement appears not too relevant. This supports that the choice that has been made for the acceptable level beamstrahlung is good.

It should be noted that in case of CLIC at 3TeV, the requirement on the spectrum quality is somewhat relaxed (30%), since also the tail of the luminosity spectrum contributes to the creation of interesting physics events. An important example is the double Higgs production, which allows to measure the Higgs self-coupling. Basically the whole luminosity spectrum contributes to this production process at high energies, increasing the importance of the total luminosity with respect to the peak luminosity.

Further studies of the optimum beam parameter choice will be useful in order to obtain the optimum exploitation strategy for future linear colliders.

2.22.5 Conclusion

Beam-beam effects drive the choices of linear collider designs; in particular the choice of flat beams. For otherwise fixed beam parameters the horizontal beam size choice is driven by the emission of beamstrahlung that leads to a degradation of the luminosity spectrum. This in turn limits the luminosity that can be achieved. Up to now, the acceptable level of beamstrahlung has been chosen by comparing to initial state radiation. An example is the recent optimisation of the CLIC parameters for the first energy stage of 380 GeV centre-of-mass. A recent study has used an important physics experiment at this energy in order to verify this choice for CLIC and ILC. It concluded that slightly higher levels of beamstrahlung would still improve the resolution of the physics analysis by a few percent. Hence a more aggressive choice of beamstrahlung level is acceptable but can yield only minor improvements of the physics in spite of a much higher luminosity.

2.22.6 References

1. The following reference can serve as a starting point: N. Phinney, "SLC final performance and lessons," eConf C **00082** (2000) MO102 [physics/0010008 [physics.acc-ph]].
2. T. Behnke *et al.*, "The International Linear Collider Technical Design Report - Volume 1: Executive Summary," arXiv:1306.6327 [physics.acc-ph]
3. H. Baer *et al.*, "The International Linear Collider Technical Design Report - Volume 2: Physics," arXiv:1306.6352 [hep-ph].
4. C. Adolphsen *et al.*, "The International Linear Collider Technical Design Report -

- Volume 3.I: Accelerator & in the Technical Design Phase,” arXiv:1306.6353 [physics.acc-ph].
5. C. Adolphsen *et al.*, “The International Linear Collider Technical Design Report - Volume 3.II: Accelerator Baseline Design,” arXiv:1306.6328 [physics.acc-ph].
 6. T. Behnke *et al.*, “The International Linear Collider Technical Design Report - Volume 4: Detectors,” arXiv:1306.6329 [physics.ins-det].
 7. M. Aicheler *et al.*, “A Multi-TeV Linear Collider Based on CLIC Technology : CLIC Conceptual Design Report,” doi:10.5170/CERN-2012-007
 8. L. Linssen, A. Miyamoto, M. Stanitzki and H. Weerts, “Physics and Detectors at CLIC: CLIC Conceptual Design Report,” doi:10.5170/CERN-2012-003 arXiv:1202.5940 [physics.ins-det].
 9. M. J. Boland *et al.* [CLIC and CLICdp Collaborations], “Updated baseline for a staged Compact Linear Collider,” CERN-2016-004; arXiv:1608.07537 [physics.acc-ph].
 10. Ph. Lebrun *et al.* “The CLIC Programme: Towards a Staged e+e- Linear Collider Exploring the Terascale : CLIC Conceptual Design Report,” CERN-2012-005, arXiv:1209.2543 [physics.ins-det]
 11. P. Chen and D. Schulte, “Beam-beam Effects in Linear Colliders”, in: A. W. Chao, K. H. Mess, M. Tigner and F. Zimmermann, “Handbook of accelerator physics and engineering,” p. 175ff
 12. K. Yokoya and P. Chen, “Beam-beam phenomena in linear colliders”, Lect. Notes Phys. **400**, 415 (1992).
 13. P. Chen *et al.* “Coherent Pair Creation in Linear Colliders”, Phys.Rev.Lett. **63** (1989) 1796 SLAC-PUB-4923
 14. D. Schulte. DESY-TESLA-97-08.
 15. P. Chen, G. Horton-Smith, T. Ohgaki, A. W. Weidemann and K. Yokoya. SLAC-PUB-6583
 16. T. Barklow *et al.* “Experimental Evidence for Beam-beam Disruption at the SLC”, SLAC-PUB-8043 (1999)
 17. R. Brinkmann, O. Napoly, D. Schulte, “Beam-Beam Instabilities Driven by Wakefield Effects in the Main Linac” PAC-2001-TPPH153
 18. D. Schulte. “Luminosity in Future Linear Collider in the Presence of Static Wakefield Effects in the Main Linac”. CLIC-Note-544 (2002).
 19. D. Schulte. “An Update on the Banana Effect”. Nanobeam 2002 and CERN-AB-2003-009
 20. F. Andrianala, R. Raboanary, Ph. Roloff, D. Schulte “Beam parameter optimization at CLIC using the process $e^+e^- \rightarrow HZ \rightarrow Hq\bar{q}$ at 380 GeV” submitte to NIM A.
 21. W. Kilian, T. Ohl, J. Reuter, “Whizard-simulating multi-particle processes at LHC and ILC”, Eur. Phys. J. C **71**:1742 (2011), hep-ph/0102195.
 22. A. Hoecker, P. Speckmayer, J. Stelzer, J. Therhaag, E. V. Toerne, H. Voss, TMVA: Toolkit for multivariate data analysis, PoS A CAT 040 (2007) [physics/0703039].

2.23 Beam-Beam Effects in Circular Hadron Colliders

Werner Herr
CERN, 1211 Geneva 23, Switzerland
Mail to: Werner.Herr@cern.ch

One of the most severe limitations in high intensity particle colliders is the beam-beam interaction, i.e. the perturbation of the beams as they cross the opposing beam. This short overview on beam-beam effects in hadron colliders concentrates on a description of the most important and relevant phenomena that are present in modern colliding hadron beams facilities

2.23.1 Introduction

For hadron beams at low energies, space charge effect play a dominant role for the beam dynamics while at higher energies they are strongly suppressed because of the cancellation of electric and magnetic fields. In the case of a collider the particles travel in opposite directions and collide at the interaction point. In such a case the cancellation does not occur and the beam-beam interaction becomes the most important non-linearity in the machine [1].

The forces are most important for high brilliance beams, i.e. high intensity and small beam sizes. After considering the forces, one can assess the most important consequences and relevant issues of the beam-beam interactions, the most important ones are

- Head-on collisions,
- Long-range collisions,
- Incoherent and coherent effects,
- Beam-beam compensation.

2.23.2 Beam-Beam Force

In the rest frame of a beam we have only electrostatic fields and to find the forces on other moving charges, we have to transform the fields into the moving frame and to calculate the Lorentz forces [2–4]. The fields are obtained by integrating over the charge distributions. The forces can be defocusing or focusing since a particle can have the same or opposite charge with respect to the counter-rotating beam producing the forces.

The distribution of particles producing the fields can follow various functions, leading to different fields and forces. Unlike lepton beams, the beams in hadron machine can be considered round which simplifies the computation of the forces considerably (see e.g. [3, 4]). In general this is a good approximation. For the Cartesian components in the two transverse planes one obtains

$$F_{(x,y)}(r) = -\frac{ne^2(1 + \beta_r^2)}{2\pi\epsilon_0} \cdot \frac{(x, y)}{r^2} \cdot \left[1 - \exp\left(-\frac{r^2}{2\sigma^2}\right) \right] \quad (r^2 = x^2 + y^2) \quad (1)$$

The forces (1) are computed when the charges of the test particle and the opposing beam have opposite signs. For equally charged beams the forces change signs. For small amplitudes the force is approximately linear and a particle crossing a beam at small

amplitudes will experience a linear field. This results in a change of the tune like in a quadrupole. At larger amplitudes (i.e. above $\approx 1 \sigma$) the force deviates strongly from this linear behaviour. Particles at larger amplitudes will also experience a tune change, however this tune change will depend on the amplitude. Already from the analytical form (1) one can see that the beam-beam force includes higher multipoles.

2.23.3 Head-On Beam-Beam Interactions

2.23.3.1 Beam-Beam Parameter

We can derive the linear tune shift of a small amplitude particle crossing a round beam of a finite length. We use the force to calculate the kick it receives from the opposing beam, i.e. the change of the slope of the particle trajectory. The radial kick $\Delta r'$ a particle with a radial distance r from the opposing beam centre receives is then

$$\Delta r' = -\frac{2Nr_0}{\gamma} \cdot \frac{1}{r} \cdot \left[1 - \exp\left(-\frac{r^2}{2\sigma^2}\right) \right] \quad (2)$$

where I have re-written the constants and use the classical particle radius

$$r_0 = e^2/4\pi\epsilon_0 mc^2 \quad (3)$$

where m is the mass of the particle. For small amplitudes r one can derive the asymptotic limit

$$\Delta r'|_{r \rightarrow 0} = -\frac{Nr_0 r}{\gamma\sigma^2} = -r \cdot f \quad (4)$$

This limit is the slope of the force at $r = 0$ and the force becomes linear with a focal length as the proportionality factor. It is well known how the focal length relates to a tune change and one can derive a quantity ξ which is known as the linear beam-beam parameter

$$\xi = \frac{Nr_0\beta^*}{4\pi\gamma\sigma^2} \quad (5)$$

r_0 is the classical particle radius, (e.g.: r_e , r_p) and β^* is the optical amplitude function (β -function) at the interaction point. For small values of ξ and a tune far enough away from linear resonances this parameter is equal to the linear tune shift ΔQ [2]. The beam-beam parameter can be generalized for the case of non-round beams and becomes

$$\xi_{x,y} = \frac{Nr_0\beta_{x,y}^*}{2\pi\gamma\sigma_{x,y}(\sigma_x + \sigma_y)} \quad (6)$$

The beam-beam parameter is often used to quantify the strength of the beam-beam interaction, however it does not reflect the non-linear nature.

2.23.3.2 *Non-Linear Effects*

First we briefly discuss the immediate effect of the non-linearity of the beam-beam force on a single particle. It manifests as an amplitude dependent tune shift and for a beam with many particles as a tune spread. The instantaneous tune shift of a particle when it crosses the other beam is related to the derivative of the force with respect to the amplitude $\partial F/\partial x$. For a particle performing an oscillation with a given amplitude the tune shift is calculated by averaging the slopes of the force over the range (i.e. the phases) of the particle's oscillation amplitudes. We get the formula for the non-linear detuning with the amplitude J [2, 5]

$$\Delta Q(J) = \xi \cdot \frac{2}{J} \cdot (1 - I_0(J/2) \cdot e^{-J/2}) \quad (7)$$

where $I_0(x)$ is the modified Bessel function and $J = A \beta / \sigma^2$. Here A is the invariant of the motion (action) and must not be confused with the beam emittance. In the 2-dimensional case, the tune shifts ($\Delta Q_x, \Delta Q_y$) of a particle with amplitudes x and y depend on both, horizontal and vertical amplitudes. The detuning must be computed and presented in a 2-dimensional form, i.e. the amplitude (x, y) is mapped into the tune space (Q_x, Q_y) or alternatively to the 2-dimensional tune change $(\Delta Q_x, \Delta Q_y)$. The maximum tune spread for a single head-on collision is equal to the tune shift of a particle with small amplitudes and for small tune shifts equal to the beam-beam parameter ξ . In the simple case of a single head-on collision the parameter ξ is therefore a measure for the tune spread in the beam.

2.23.3.3 *Dynamic β*

For small particle amplitudes the beam-beam force is approximately linear and therefore resembles a quadrupole. In addition to the tune shift a beating of the β -functions is introduced. This also changes the β at the collision point and therefore the beam size. For tunes far away from linear resonances this effect is small but otherwise it can be significant. This effect can be used deliberately to decrease the beam size and increase the luminosity [6]. Such a procedure has been used in LEP to increase the luminosity by about 40 % [6]. Whether one should work slightly above or below an integer depends on the type of particle. For particle-antiparticle collisions a tune just above the integer leads to a decrease of β^* , while working below the integer has the opposite effect.

2.23.3.4 *Landau Damping due to the Beam-Beam Interaction*

Since the beam-beam interaction results in a considerable tune spread, one expects a strong contribution to Landau damping. Comparing the detuning from octupoles, head-on and long-range beam-beam effects, one observes a very different contribution to the stability region and damping. While octupoles and long-range interactions provide the largest spread for large amplitude particles, this is not the case for the head-on interaction. Since the region with small amplitude particles is much more populated, the stability region is largely enhanced. It was shown in [7] that for an equal overall detuning the stable region is

increased by a factor ten. This strong stabilising effect is clearly observed in the operation of the LHC.

2.23.4 Long-Range Beam-Beam Interactions

In hadron colliders with a large number of bunches, unwanted collisions must be avoided. In particle-antiparticle colliders this can be achieved by separate orbits of the two beams in the same vacuum chamber. For particle-particle collisions separate vacuum chambers are required and parasitic interactions are usually avoided using a crossing angle at the interaction point.

Although the long-range interactions distort the beams much less than a head-on interaction, their large number and some particular properties require careful studies

- They break the symmetry between planes, i.e. more resonances can be excited.
- While the effect of head-on collisions is strongest for small amplitude particles, parasitic interactions mostly affect particles at large amplitudes. This leads to a reduction of the dynamic aperture and particle losses, resulting in reduced beam lifetime.
- The tune shift caused by long-range interactions has opposite sign in the plane of separation compared to the head-on tune shift.
- They cause changes of the closed orbit.
- They largely enhance the so-called PACMAN effects. The effect of the strong non-linearities of the long-range interactions was demonstrated in experiments and compared with an analytical model based on the analysis of the effective Hamiltonian obtained using a technique based on Lie transformations [8].

2.23.4.1 *Beam-Beam Induced Orbit Effects*

When two beams do not collide exactly head-on, the force has a constant contribution which can easily be seen when the kick $\Delta x'$ (for sufficiently large separation) is developed in a series

$$\Delta x' = \frac{const.}{d} \cdot \left[1 - \frac{x}{d} + O\left(\frac{x^2}{d^2}\right) + \dots \right] \quad (8)$$

A constant contribution, i.e. more precisely an amplitude independent contribution, changes the orbit of the bunch as a whole (Fig. 1). When the beam-beam effect is strong enough, i.e. for high intensity and/or small separation, the orbit effects are large enough to be observed [6]. When the orbit of a beam changes, the separation between the beams will change as well, which in turn will lead to a slightly different beam-beam effect and so on. The orbit effects must therefore be computed in a self-consistent way [9], in particular when the effects are sizable. The closed orbit of an accelerator can usually be corrected, however an additional effect which is present in some form in many colliders, sets a limit to the correction possibilities. A particularly important example is the LHC and I shall therefore use it to illustrate this feature.

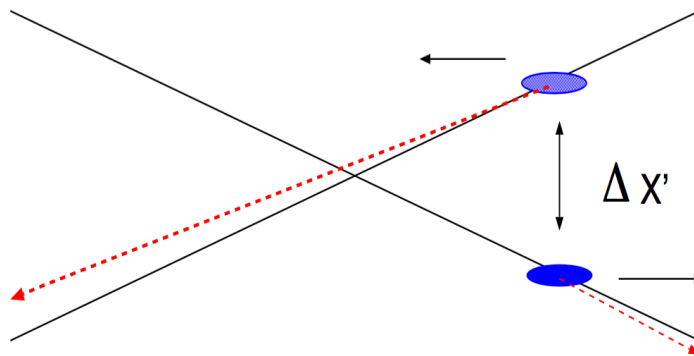


Figure 1: Beam-beam deflection leading to orbit changes.

2.23.4.2 *PACMAN Effects*

The bunches in the LHC do not form a continuous train of equidistant bunches spaced by 25 ns, but some empty space must be provided to allow for the rise time of kickers. The whole LHC bunch pattern is composed of 39 smaller batches (trains of 72 bunches) separated by gaps of various length followed by a large abort gap for the dump kicker at the end. In the LHC, only 2808 out of 3564 possible bunches are present with the above filling scheme. Due to the symmetry, bunches normally meet other bunches at the head-on collision point. For the long-range interactions this is no longer the case. This is illustrated in Fig. 2. Bunches at the beginning and at the end of a small batch will encounter a hole and as a result experience fewer long-range interactions than bunches from the middle of a batch [10]. In the limit, the first bunch of a batch near a large gap encounters no opposing bunch before the central collision and the full number of bunches after.

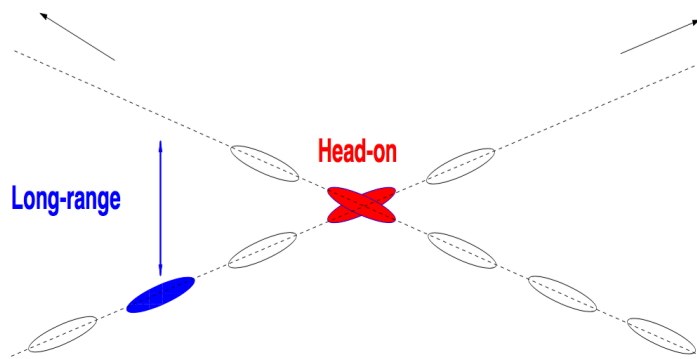


Figure 2: Long-range interactions with missing bunches.

Bunches with fewer long-range interactions have a very different integrated beam-beam effect and a different dynamics must be expected. In particular they will have a different tune and occupy a different area in the working diagram, therefore may be susceptible to resonances, which can be avoided for nominal bunches. The overall space needed in the working diagram is therefore largely increased [10]. Another consequence of reduced long-range interactions is the different effect on the closed orbit of the bunches. We have to expect a slightly different orbit from bunch to bunch. This effect is demonstrated in Fig. 3 where I show the horizontal position at one head-on collision point for 432 bunches (out of

2808). The bunches in the middle of a batch have all interactions and therefore the same orbit while the bunches at the beginning and end of a batch show a structure which exhibits the decreasing number of long-range interactions. The orbit spread is approximately 10 - 15 % of the beam size. Since the orbits of the two beams are not the same, it is impossible to make all bunches collide exactly head-on. A significant fraction will collide with an offset. Although the direct (geometrical) effect on the luminosity is small, collisions at an offset can potentially affect the dynamics and are undesirable. An example was the detrimental effect on the dynamic β in LEP [6]. The LHC design should try to minimize these offsets [10]. The variation of the orbit bunch by bunch is confirmed by reconstructing the collision vertex in the experiments.

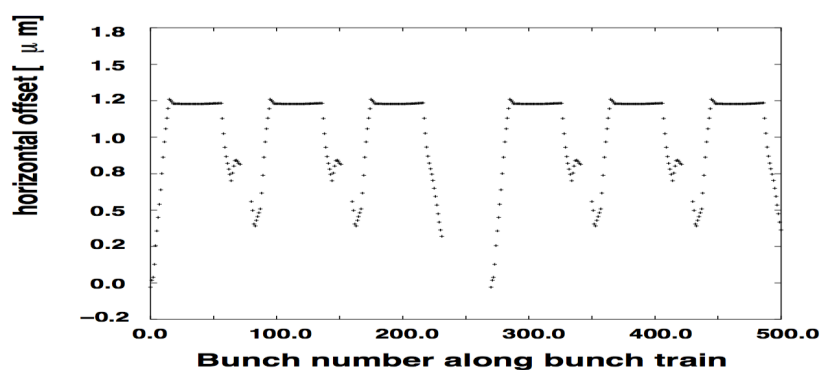


Figure 3: Horizontal orbits of the first 432 bunches at IP1.

A second effect, the different tunes of the bunches, is shown in Fig. 4. For three batches it shows a sizable spread from bunch to bunch and without compensation effects it may be too large for a safe operation. It may be noted that in other colliders such as the Tevatron or the SPS proton-antiproton collider, bunch to bunch differences may be present. Although the two beams do not have the PACMAN effects as related to a crossing angle and missing bunches, the bunches have a different collision pattern and the parasitic interactions occur at different positions around the circumference. However these effects are very small.

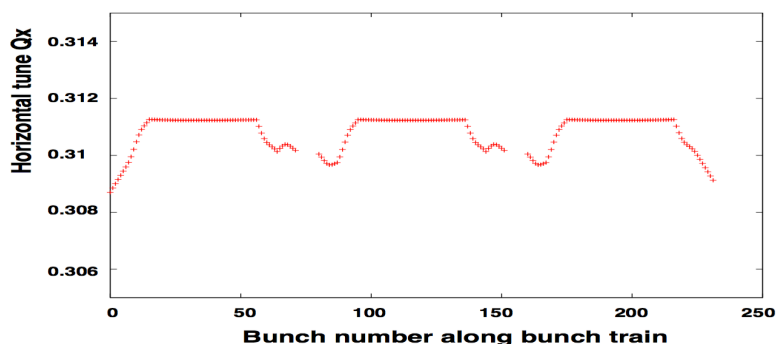


Figure 4: Tune variation along the LHC bunch pattern.

2.23.5 Coherent Beam-Beam Effects

So far we have mainly studied how the beam-beam interaction affects the single particle behaviour and treated the beam-beam interaction as a static lens. In the literature this is often called a "weak-strong" model: a "weak" beam (a single particle) is perturbed by a "strong" beam (not affected by the weak beam). When the beam-beam perturbation is important, the model of an unperturbed, strong beam is not valid anymore since its parameters change under the influence of the other beam and vice versa. When this is the case, we talk about so-called "strong-strong" conditions. The first example of such a "strong-strong" situation was the orbit effect where the beams mutually changed their closed orbits. These closed orbits had to be found in a self-consistent way. This represents a static strong-strong effect.

In the next step we investigate dynamic effects under the strong-strong condition. When we consider the coherent motion of bunches, the collective behaviour of all particles in a bunch is studied. A coherent motion requires an organized behaviour of all particles in a bunch. A typical example are oscillations of the centre of mass of the bunches, so-called dipole oscillations. At the collision effect of two counter-rotating bunches not only the individual particles receive a kick from the opposing beam, but the bunch as an entity gets a coherent kick. This coherent kick of separated beams can excite coherent dipole oscillations. Its strength depends on the distance between the bunch centres at the collision point. It can be computed by adding the individual contributions of all particles. For small distances it can be shown [2] that it is just one half of the incoherent kick a single particle would receive at the same distance. For distances large enough the incoherent and coherent kicks become the same.

2.23.6 Coherent Beam-Beam Modes

To understand the dynamics of dipole oscillations we first study the simplest case with one bunch in each beam. When the bunches meet turn after turn at the collision point, their oscillation can either be exactly in phase (0 degree phase difference) or out of phase (180 degrees phase difference). Any other oscillation can be constructed from these basic modes. The modes are sketched very schematically in Fig. 5.

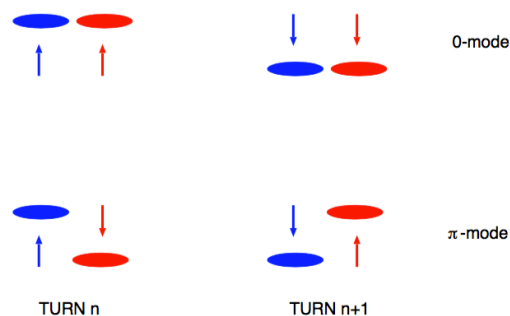


Figure 5: Basic dipole modes of two bunches. Relative position of the bunches at the interaction point at two consecutive turns.

The relative positions of the bunches as observed at the interaction point are shown for two consecutive turns n and $n + 1$. The first mode is called the 0-mode (or sometimes called

σ -mode) and the second the π -mode. In the first mode the distance between the bunches does not change turn by turn and therefore there is no net force driving an oscillation. This mode must oscillate with the unperturbed frequency (tune) Q_0 . For the second mode the net force difference between two turns is a maximum and the tune becomes $Q_0 + \Delta Q_{\text{coh}}$. The sign of ΔQ_{coh} depends whether the two beams have equal charge (defocusing case) or opposite charge (focusing case). The calculation of ΔQ_{coh} is non-trivial: when the bunches are considered as rigid objects, the tune shift can be computed easily using the coherent kick but is underestimated. The correct calculation must allow for changes of the density distribution during the collision and moreover, must allow a deviation from a Gaussian function. The computation requires to solve the Vlasov-equation for two coupled beams [11].

The 0-mode is found at the unperturbed tune as expected. The π -mode is shifted by 1.2-1.3 ξ . The precise value depends on the ratio of the horizontal and vertical beam sizes [11]. We have seen before the incoherent tune spread (footprint) the individual particles occupy and we know that it spans the interval $[0.0, 1.0] \xi$, starting at the 0-mode.

Here one can make an important observation: under the strong-strong condition the π -mode is a discrete mode outside the incoherent spectrum. This has dramatic consequences for the stability of the beams. A coherent mode that is outside an incoherent frequency spectrum cannot be stabilized by Landau damping. Under these conditions the coherent beam-beam effect could drive the dipole oscillation to large amplitudes and may result in the loss of the beam. Observations of the coherent beam-beam effects have been made at PETRA.

Coherent beam-beam modes can be driven by head-on collisions with a small offset or by long-range interactions. In the first case and for small oscillations, the problem can be linearized and the theoretical treatment is simplified. The forces from long-range interactions are very non-linear but the numerical evaluation is feasible. Since the coherent shift must have the opposite sign for long-range interactions, the situation is very different. In particular the π -mode from long-range interactions alone would appear on the opposite side of the 0-mode in the frequency spectrum.

2.23.7 Compensation of Beam-Beam Effects

For the case the beam-beam effects limit the performance of a collider, several schemes have been proposed to compensate all or part of the detrimental effects. The basic principle is to design correction devices which act as non-linear 'lenses' to counteract the distortions from the non-linear beam-beam 'lens'. For both, head-on and long-range effects schemes have been proposed

- Head on effects
 - Electron lenses,
 - Linear lens to shift tunes,
 - Non-linear lens to decrease tune spread.
- Long-range effects
 - At large distance, the beam-beam force changes like $1/r$. A wire can compensate for this behaviour at large distances.

- Passive compensation with alternating crossing schemes.

2.23.7.1 *Electron Lenses*

The basic principle of a compensation of proton-proton (or antiproton) collisions with an "electron lens" implies that the proton (antiproton) beam travels through a counter-rotating high current electron beam ("electron lens") [13, 14]. The negative electron space charge can reduce the effect from the collision with the other proton beam.

An electron beam with a size much larger than the proton beam can be used to shift the tune of the proton beam ("linear lens"). When the current in the electron bunches can be varied fast enough, the tune shift can be different for the different proton bunches, thus correcting PACMAN tune shifts. When the electron charge distribution is chosen to be the same as the counter-rotating proton beam, the non-linear focusing of this proton beam can be compensated ("non-linear lens"). When it is correctly applied, the tune spread in the beam can be strongly reduced.

Such lenses have been constructed at the Tevatron at Fermilab [14] and experiments are in progress.

2.23.7.2 *Electrostatic Wire*

To compensate the tune spread from long-range interactions, one needs a non-linear lens that resembles a separated beam. At large enough separation, the long-range force changes approximately with $1/r$ and this can be simulated by a wire parallel to the beam [15]. In order to compensate PACMAN effects, the wires have to be pulsed according to the bunch filling scheme. It is planned to install a wire in the LHC to study the feasibility of a partial compensation and it is foreseen to use this compensation effect for the high luminosity LHC (HL-LHC).

2.23.7.3 *Passive Compensation with Alternating Crossing Schemes*

In the crossing plane the long range interactions produce a detuning with a sign opposite to the other plane. This can be used to partially compensate beam-beam effects. In the case of the LHC the main experiments are exactly opposite in azimuth, the same bunches cross in the two collision points, i.e. the same is true for PACMAN bunches and the missing interactions. Alternating crossing schemes, i.e. vertical in one collision point and horizontal in the opposite, can substantially reduce the PACMAN effects. In particular the tune spread from bunch to bunch can be reduced to almost zero [16].

2.23.8 **References**

1. W. Herr and G. Papotti eds., ICFA Mini-Workshop on Beam-Beam Effects in Hadron Colliders, CERN, Geneva, Switzerland, 18-22 March 2013, CERN-2014-004 (2014).
2. W. Herr, Beam-beam effects, Proceedings of CERN Accelerator School, Zeuthen 2003, CERN- 2006-002 (2006).
3. S. Kheifets, PETRA-Kurzmitteilung 119 (DESY 1976).
4. M. Basetti and G.A. Erskine, Closed expression for the electrical field of a 2-dimensional Gaussian charge, CERN-ISR-TH/80-06 (1980).
5. W. Herr and D. Kaltchev, Effect of phase advance between interaction points in the

- LHC on the beam-beam interaction, CERN LHC Project 1082 (2008).
6. D. Brandt et al., Is LEP beam-beam limited at its highest energy?, In Proceedings of the Particle Accelerator Conference 1999, New York, (1999) p. 3005.
 7. W. Herr and L. Vos, Tune distributions and effective tune spread from beam-beam interactions and the consequences for Landau damping in the LHC, LHC Project Note 316 (2003).
 8. D. Kaltchev and W. Herr, Analysis of long-range studies in the LHC – comparison with the model, in ICFA Mini-Workshop on Beam-Beam Effects in Hadron Colliders, CERN, Geneva, Switzerland, 18-22 March 2013, CERN-2014-004 (2014).
 9. H. Grote and W. Herr; Self-consistent orbits with beam-beam effects in the LHC, In Proceedings of the 2001 workshop on beam-beam effects, FNAL, 25.6.-27.6.2001, (2001).
 10. W. Herr, Effects of PACMAN bunches in the LHC, CERN LHC Project Report 39 (1996).
 11. K. Yokoya et al., Tune shift of coherent beam-beam oscillations, Part. Acc. 27, 181 (1990).
 12. A. Chao, Coherent beam-beam effects, SSC Laboratory, SSCL-346 (1991).
 13. V.D. Shiltsev et al., Compensation of beam-beam effects in the Tevatron Collider with electron beams, In Proceedings of the Particle Accelerator Conference 1999, New York, (1999) p. 3728.
 14. V.D. Shiltsev et al., Considerations on compensation of beam-beam effects in the Tevatron with electron beams, Phys. Rev. ST Accel. Beams 2, 071001 (1999).
 15. J.P. Koutchouk et al., Correction of the Long-Range Beam-Beam Effect in LHC using Electro- Magnetic Lenses, In Proceedings of the Particle Accelerator Conference 1999, New York, (1999) p. 1681.
 16. W. Herr, Features and implications of different LHC crossing schemes, LHC Project Report 628 (2003).

2.24 Collision Schemes of Circular Electron-Positron Factories

Mikhail Zobov
INFN, Laboratori Nazionali di Frascati, Italy
Mail to: Mikhail.Zobov@lnf.infn.it

2.24.1 Present Generation Electron-Positron Factories

Present generation lepton factories have been very successful. Both B-factories, KEKB in Japan and PEP-II in USA, have largely exceeded their design goals. A collection of articles summarizing their performances can be found in [1]. The Italian Φ -factory DAΦNE has exceeded the phase-I design luminosity in 2004 [2] and obtained a luminosity increase by a factor 3 after implementation of the novel crab waist collision scheme [3]. In the beginning of this year also the Tau-Charm factory in Beijing, BEPCII, has reached its design luminosity [4].

All the present generation factories relied, at least at the beginning of their operation, on the standard strategy in choosing beam parameters in order to achieve high luminosity. The strategy can be understood by considering the well-known expressions for the luminosity L and beam-beam tune shifts. For simplicity we start with the case of head-on collisions of short bunches having equal beam parameters at the Interaction Point (IP)

$$L = N_b f_0 \frac{N^2}{4\pi\sigma_x^* \sigma_y^*} = N_b f_0 \frac{\pi\gamma^2 \xi_x \xi_y \varepsilon_x}{r_e^2 \beta_y^*} \left(1 + \frac{\sigma_y^*}{\sigma_x^*}\right)^2 \quad (1)$$

$$\xi_{x,y} = \frac{Nr_e}{2\pi\gamma} \frac{\beta_{x,y}^*}{\sigma_{x,y}^* (\sigma_x^* + \sigma_y^*)}$$

where $\xi_{x,y}$ are the space charge parameters whose maximum values are limited by the beam-beam effects, ε_x is the horizontal emittance of the beams, $\sigma_{x,y}^*$ are their rms sizes at the IP, β_y^* is the vertical beta function at the IP, N the number of particles per bunch, N_b is the number of bunches and f_0 the revolution frequency. Neglecting beam dynamics aspects, the luminosity increase in a collider at a given energy requires (according to Eq. (1))

- higher number of particles per bunch,
- more colliding bunches,
- larger beam emittance,
- smaller beta functions at the IP,
- round beams,
- higher tune shift parameters.

The present factories have obtained their good luminosity performances trying to fulfill almost all the above conditions as much as possible except that

- it was chosen to collide flat bunches $\sigma_y^* \ll \sigma_x^*$ since it is rather difficult to provide a good dynamic aperture for the round beam case with both vertical and horizontal beta functions low at the IP;

- besides, in order to eliminate parasitic collisions in multibunch operation a small horizontal crossing angle θ was necessary. In the factories a relatively small Piwinski angle $\Phi = \frac{\sigma_z}{\sigma_x} \text{tg}\left(\frac{\theta}{2}\right) \leq 1$ was mandatory to avoid excessive geometric

luminosity reduction and to diminish the strength of synchrotron resonances arising from beam-beam interaction with the crossing angle.

However, a further substantial luminosity increase based on the standard collision scheme is hardly possible due to several limitations imposed by beam dynamics requirements:

- in order to minimize the luminosity reduction due to the hour-glass effect (the dependence of the vertical beam size on the longitudinal position along the crossing region) the vertical beta function at the IP can not be much smaller than the bunch length $\beta_y^* \leq \sigma_z$;
- a drastic bunch length reduction is impossible without incurring into single bunch instabilities: bunch lengthening and microwave instabilities due to the beam interaction with the surrounding vacuum chamber. Besides, too short bunches tend to produce Coherent Synchrotron Radiation (CSR) affecting beam quality and leading to a dramatic increase of the power losses;
- a further multibunch current increase would result in different kinds of coupled bunch beam instabilities, excessive power loss due to interactions with parasitic Higher Order Modes (HOM) and increase of the required wall plug power;
- higher emittances conflict with stay-clear and dynamic aperture limitations, require again higher currents to exploit the emittance increase for the luminosity enhancement;
- tune shifts saturate and beam lifetime drops due to a strong nonlinear beam-beam interaction.

2.24.2 Novel Concepts

In order to overcome these limitations several novel collisions concepts and new collision schemes were proposed. The most known are the following

- round beam collision preserving an additional integral of motion;
- crab crossing;
- collision with large Piwinski angle (“superbunch” in hadron colliders);
- crab waist collision;
- collision with travelling waist;
- longitudinal strong RF focusing.

Recently some of these ideas, such as round beam collisions, crab crossing and crab waist have been experimentally tested.

The idea of round beams collisions preserving one of the integrals of motion was proposed by A.Ruggiero in 1982 [5] and then developed by the Novosibirsk Team for the Φ -factory design [6]. It requires equal emittances, equal small and positive fractional tunes, equal beta functions at the IP, no betatron coupling in the arcs. A 90° rotation at each passage of the transverse oscillation plane by means of solenoids in the interaction regions (IR) provides conservation of the longitudinal component of the angular moment

$M_z = yp_x - xp_y$ [7]. Thus the transverse motion becomes one-dimensional. In addition to the obvious advantages coming from Eq. (1), the round beam scheme helps to eliminate all betatron coupling resonances that are of crucial importance for tune shift saturation and lifetime degradation. The synchrobetatron resonances are also weakened since the transverse tune shift is almost independent of particle's longitudinal position. The round beam concept was successfully tested at the electron-positron collider VEPP2000 in 2007 at the energy of 510 MeV [8]. Despite the low energy a high single bunch luminosity of $1.2 \times 10^{31} \text{ cm}^{-2} \text{ s}^{-1}$ was achieved together with the maximum tune shift as high as 0.125 [9]. Another round beam collisions scheme, "Mobius accelerator", was proposed in [10] and tested at CESR providing a tune shift of 0.09 in agreement with simulations [11].

The crab crossing collision scheme was proposed by R. Palmer in 1988 [12] and further developed in [13]. This idea makes it possible to collide bunches at a large crossing angle without luminosity loss and excitation of synchrobetatron resonances. In the crab crossing scheme both bunches are tilted before collision by half the crossing angle $\theta/2$, providing head-on collision at the IP. The tilt is created by a transverse RF deflector (crab cavity) giving opposite transverse kicks to the bunch head and tail. The RF deflector is placed at a point where the betatron phase in the crossing plane is $-\pi/2$ from the IP. In the classic crab crossing scheme another RF deflector after the collision point is used to restore the tilt. The crab crossing collisions with a single crab cavity per ring were successfully performed at the KEK B-factory [14]. A world record luminosity of $2.1 \times 10^{34} \text{ cm}^{-2} \text{ s}^{-1}$ has been obtained in this configuration. However, the achieved luminosity is still lower than that predicted by numerical simulation and work is in progress to find out the reasons of the disagreement.

The idea of colliding with a large Piwinski angle is not a new one as well. In 1995, discussing beam-beam interactions with a large crossing angle, K.Hirata suggested that a large angle might have several merits for future high-luminosity colliders [15]. It has been also proposed for hadron colliders to increase the bunch length and the crossing angle [16, 17] for luminosity optimization. The advantages of a large Φ can be understood by writing down the formulae for the luminosity and tune shifts with a horizontal crossing angle. Neglecting the hour-glass effect, the expressions can be obtained from Eq. (1) simply by substituting the horizontal beam size by the effective transverse size $\sigma_x^* \rightarrow \sigma_x^* \sqrt{1 + \Phi^2}$. Then, for large Piwinski angle, $\Phi \gg 1$, the luminosity and the tune shifts scale as [18]

$$L \propto \frac{N\xi_y}{\beta_y^*}; \quad \xi_y \propto \frac{N\sqrt{\beta_y/\varepsilon_y}}{\sigma_z\theta}; \quad \xi_x \propto \frac{N}{(\sigma_z\theta)^2} \quad (2)$$

Clearly, in such a case, if it were possible to increase N proportionally to $\sigma_z\theta$, the vertical tune shift ξ_y would remain constant, while the luminosity would grow proportionally to $\sigma_z\theta$. Moreover, the horizontal tune shift would drop $\propto 1/(\sigma_z\theta)$.

The idea of using a "travelling" waist (focus) to compensate the luminosity reduction due to the hour-glass effect in circular colliders came from linear colliders [19]. In the travelling waist collision scheme, the optical focal point depends on the longitudinal position of a particle within the bunch. In other words, particles with different longitudinal coordinates in collision "see" the same and minimal beta functions. In circular colliders the travelling waist can be realized by a combination of accelerator components that provides a transformation

described by a Hamiltonian $H = H_0 - \frac{1}{2}zp_y^2$ relating the longitudinal position z and the vertical momentum p_y . For example, as proposed in [20], the travelling waist with the crab crossing can be obtained by using together crab cavities and sextupole magnets.

The longitudinal strong RF focusing is an alternative way to obtain short bunches at the IP [21]. It consists in realizing a large momentum compaction of the lattice together with a strong RF gradient. In this regime the bunch length is no longer constant, but it is modulated along the ring and can be minimized at the IP. In turn, if the main impedance generating elements of the ring are located where the bunch remains long, it is possible to minimize the strength of wake fields. This helps to avoid microwave instabilities and excessive bunch lengthening due to the potential well distortion [22]. This concept was proposed as one of the possible options for the DAΦNE upgrade [23].

2.24.3 Crab Waist Collision Scheme

Contrary to the conventional strategy, the crab waist collision scheme requires small emittance and large crossing angle; there is no need to decrease the bunch length and push beam currents beyond the values already achieved in the present factories. This scheme can greatly enhance the luminosity of a collider since it combines several potentially advantageous ideas [24]

- the first step is to provide a large Piwinski angle by decreasing the horizontal beam size σ_x and increasing the crossing angle θ . In this way, in addition to the advantages of the large Piwinski angle scheme, the length of the collision region, proportional to σ_x/θ can be substantially decreased for low emittance beams. Besides, the problem of Parasitic Crossings (PC) is automatically solved due to the larger crossing angle and a beam separation in terms of σ_x at the PC positions.
- the vertical beta at the IP can be made very low, comparable to the small length of the collision region, without significant luminosity loss due the hour-glass effect. In addition to the obvious geometric luminosity increase, the micro-beta scheme provides several advantages in beams dynamics:
 - a) possibility of bunch current increase (if it is limited by ξ_y), thus resulting in further luminosity gain;
 - b) suppression of vertical synchrotron resonances [25];
 - c) reduction of the vertical tune shift with longitudinal oscillation amplitude [25].
- a further luminosity boost is given by the “crab waist transformation” described by the Hamiltonian $H = H_0 + \frac{1}{\theta}xp_y^2$ that provides a vertical beta function rotation in such a way that the beta function waist of one beam is oriented along the central trajectory of the other one. In practice the waist rotation (that is why it is called “crab waist”) is provided by sextupole magnets placed on both sides of the IP in phase with the IP in the horizontal plane and at $\pi/2$ in the vertical one. The integrated crab sextupole strength should satisfy the following condition depending on the crossing angle and the beta function at the IP and the sextupole locations

$$K = \frac{1}{\theta} \frac{1}{\beta_y \beta_y^*} \sqrt{\frac{\beta_x^*}{\beta_x}} \quad (3)$$

The crab waist transformation yields a small geometric luminosity gain due to the vertical beta function redistribution along the collision region, while the dominating effect comes from the suppression of betatron (and synchrobetatron) resonances arising in the conventional collision scheme due to the vertical motion modulation by the horizontal betatron oscillations [26]. The effect of the resonance suppression is clearly demonstrated by using frequency map analysis technique [27] (see Fig.1).

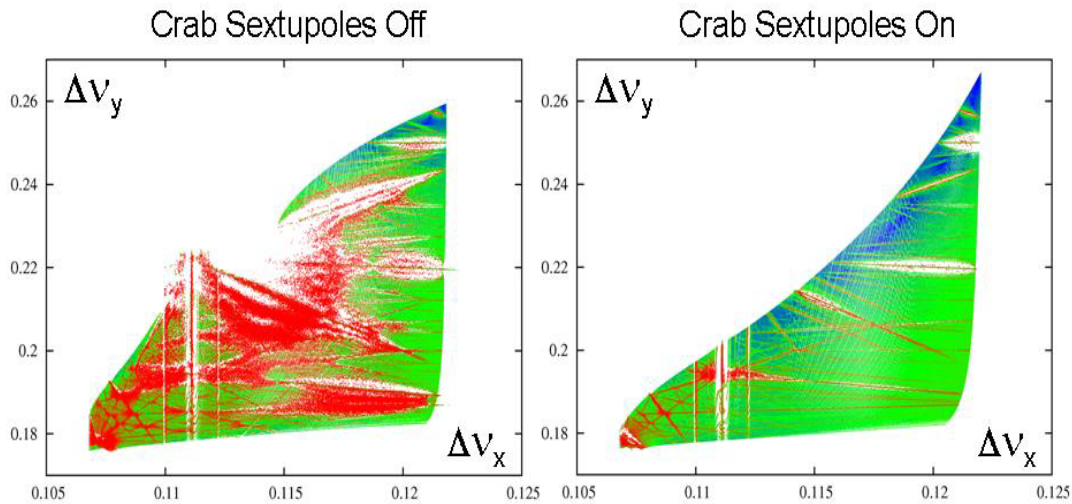


Figure 1: DAΦNE beam-beam footprint with crab sextupoles off (left) and on (right) obtained by frequency map analysis techniques [27].

The crab waist collision scheme has been successfully tested at the electron-positron collider Φ -factory DAΦNE providing luminosity increase by a factor 3 [3]. The achieved peak luminosity of $4.5 \times 10^{32} \text{ cm}^{-2} \text{ s}^{-1}$ is close (within 10%) to the design value, in a good agreement with numerical simulations [28]. The successful test provided the opportunity to continue the DAΦNE physics program with the upgraded detector of the KLOE-2 experiment [29, 30].

The advantages of the crab waist collision scheme have triggered several collider projects exploiting its potential. At present this scheme is considered to be most attractive for the next generation lepton factories since it holds the promise of increasing the luminosity of the storage-ring colliders by 1-2 orders of magnitude beyond the current state-of-art, without any significant increase in beam current and without reducing the bunch length. Several new collider projects seek to exploit the potential of the crab waist collision scheme. In particular, physics and accelerator communities are discussing and developing new projects which make use of the CW collision scheme: SuperB-factory in Japan (SuperKEKB [31]), SuperC-Tau factory in Novosibirsk [32], two Higgs-factories FCC-ee at CERN [33] and CEPC in China [34].

The SuperKEKB is a natural upgrade of the very successful KEKB, Japanese B-factory at KEK (Tsukuba). The design luminosity goal of the project is $0.8 \times 10^{36} \text{ cm}^{-2} \text{ s}^{-1}$, i.e. by a factor of 40 higher than the world record luminosity of $2.1 \times 10^{34} \text{ cm}^{-2} \text{ s}^{-1}$ achieved at KEKB.

The commissioning of SuperKEKB has successfully started in the very beginning of 2016 [35].

The Budker Institute of Nuclear Physics (Novosibirsk, Russia) is promoting the project of a new generation SuperC-Tau factory. The crab waist concept should allow reaching the project luminosity of $(1-2) \times 10^{35} \text{ cm}^{-2} \text{ s}^{-1}$ that by more than 2 orders of magnitude higher than the luminosity of $1.0 \times 10^{33} \text{ cm}^{-2} \text{ s}^{-1}$ presently achieved at the operating τ -charm factory BEPCII in Beijing [4]. SuperC-Tau has entered in the list of 6 most important Russian mega-science projects. In December 2015 the injection complex of the new collider has been successfully commissioned.

In 2014 CERN launched the Future Circular Collider (FCC) study aimed at the design of a 100-km proton-proton collider with the collision energy of 100 TeV. As an intermediate step, the electron-positron collider (FCC-ee) hosted in the same tunnel and covering the energy range between 90 GeV and 350 GeV is also under consideration and its intensive design study is ongoing. The CW scheme has been proposed [36] and recently chosen as the baseline option for the FCC-ee design. This scheme provides a substantially higher luminosity with respect to the traditional head-on collisions at low energies and approximately the same luminosity at higher energies (> 240 GeV) at much relaxed beam optics parameters. A CW lattice solution with twice higher vertical beta function at the interaction point, good dynamic aperture and energy acceptance and manageable photon energies has been found.

Presently China is considering building a 54-km long Higgs factory CEPC (Circular Electron Positron Collider). Along with the head-on collision option the collider design team has started seriously evaluating a possibility to build a local double ring option with the Crab Waist interaction region [37].

In order to complete the picture, we should mention other collider projects that were considering an application of the CW scheme such as SuperB [38] and SuperTau-Charm [39] factories in Italy, a 500 GeV e^+e^- collider in a 233-km tunnel [40] in USA, and an upgrade option of the LHC based on collisions of very flat bunches [41, 42].

2.24.4 References

1. ICFA Beam Dynamics Newsletter48, April 2009.
2. M.Zobov et al., “DAΦNE Operations and Plans for DAΦNE2”, *Proc. of PAC2005*, pp. 112-116, 2005 (SLAB-PUB-11655).
3. M. Zobov et al., “Test of Crab Waist Collisions at DAΦNE Φ-Factory”, *Phys. Rev. Lett.* **104** 174801, 2010.
4. C.H.Yu et al., “BEPCII Performance and Beam Dynamics Studies on Luminosity”, *Proc. of IPAC2016*, pp. 1014-1018, 2016.
5. A.G.Ruggiero, “Integrability of the Two-Dimensional Beam-Beam Interaction in a Special Case”, *Particle Accelerators* **12**, pp. 45-47, 1982.
6. L.M.Barkov et al., “Phi Factory Project in Novosibirsk”, *Proc. of the KEK Topical Conference on e^+e^- Collision Physics*, p. 44-54, 1989.
7. V.V. Danilov et al., “The Concept of Round Colliding Beams”, *Proc. of EPAC96*, p.1149.
8. D. Berkaev et al., “Status and Progress VEPP-2000”, *Proc. of RuPAC 2008*, p. 70.
9. A.Romanov et al., “Status the of Electron-Positron Collider VEPP-2000”, *Proc. PAC2013*, pp. 14-18, 2013.
10. R. Talman, “A Proposed Mobius Accelerator”, *Phys.Rev.Lett.* **74**, pp.1590-1593,

- 1995.
11. E. Young et al., “Collisions of resonantly coupled Beams at the Cornell Electron-Positron Ring (CESR)”, *Proc. of PAC97*, p.1542.
 12. R.B. Palmer, “Energy Scaling, Crab Crossing and the Pair Problem”, *SLAC-PUB-4707*, December 1988.
 13. K. Oide and K. Yokoya, “Beam-Beam Collision Scheme for Storage-Ring Colliders”, *Phys.Rev.* **A40**, pp. 315-316, 1989.
 14. Y. Funakoshi et al., “Recent Progress of KEKB”, *Proc .of PAC09*, pp. 2588-2590.
 15. K. Hirata, “Analysis of Beam-Beam Interactions with a Large Crossing Angle”, *Phys.Rev.Lett.* **74**, pp. 2228-2231, 1995.
 16. K. Takayama et al., “Superbunch Hadron Colliders”, *Phys.Rev.Lett.* **88** 144801, 2002.
 17. F. Ruggiero and F. Zimmermann, “Luminosity Optimization Near the Beam-Beam Limit by Increasing Bunch Length or Crossing Angle”, *Phys.Rev.ST Accel.Beams* **5** 061001, 2002.
 18. For example, D. Shatilov and M. Zobov, “Beam-Beam Collisions with an Arbitrary Crossing Angle: Analytical Tune Shifts, Tracking Algorithm without Lorentz Boost, Crab-Crossing”, *ICFA Beam Dyn.Newslett.* **37**, pp.99-109, 2005.
 19. V. Balakin, in Proc. of the Int. Workshop on Final Focus and Interaction Regions of next Generation Linear Colliders, Stanford, CA, May 2-6, 1992. SLAC-405.
 20. Y. Ohnishi, “Recent Report on Design of SuperKEKB”, *ICFA Beam Dynamics Newsletter* **48**, pp.252-259, 2009.
 21. A. Gallo, P. Raimondi and M. Zobov, “Strong RF Focusing for Luminosity Increase: Short bunches at the IP”, *Proceedings of Workshop on e+ e- in the 1-GeV to 2-GeV Range: Physics and Accelerator Prospects*, Alghero, Sardinia, Italy, 10-13 Sep 2003, *e-Print: physics/0404020*.
 22. L. Falbo, D. Alesini and M. Migliorati, “Longitudinal Beam Dynamics Simulation in Electron Rings in Strong RF Focusing Regime”, *Phys.Rev.ST Accel.Beams* **9** 094402, 2006.
 23. A. Gallo et al., “Proposal of a Strong RF Focusing Experiment at DAΦNE”, *Proc. of EPAC2004*, p.683, 2004.
 24. P. Raimondi, D. Shatilov and M. Zobov, “Beam-Beam Issues for Colliding Schemes with Large Piwinski Angle and Crabbed Waist”, *LNF-07-003-IR*, Feb 2007. 12p. *e-Print: physics/0702033*.
 25. D.V. Pestrikov, “Vertical Synchrotron Resonances Due to Beam-Beam Interaction with Horizontal Crossing”, *Nucl.Instrum.Meth.* **A336**, pp.427-437, 1993.
 26. P. Raimondi, D. Shatilov and M. Zobov, “Suppression of Beam-Beam Resonances in Crab Waist Collisions”, *Proc. of EPAC08*, p.2620, 2008.
 27. D. Shatilov, E. Levichev, E.Simonov and M. Zobov, “Application of Frequency Map Analysis to Beam-Beam Effects Study in Crab Waist Collision Scheme”, *Phys. Rev. ST Accel. Beams* **14** 014001
 28. M. Zobov et al., “Beam Dynamics in Crab Waist Collisions at DAΦNE”, *ICFA Beam Dyn.Newslett.* **48**, pp. 34-44, 2009.
 29. C. Milardi C et al., “DAΦNE Consolidation Program and Operation with KLOE-2 Detector”, *ICFA Beam Dyn. Newslett.* **67** pp. 9-27, 2015
 30. M. Zobov et al., “Simulations of Crab Waist Collisions in DAΦNE with KLOE-2 Interaction Region”, *IEEE Trans.Nucl.Sci.* **63**, no.2, pp. 818-822, 2016.
 31. Y.Ohnishi et al., “Accelerator design at SuperKEKB”, *Prog. Theor. Exp. Phys.* **2013**

03A011.

32. A. Bondar et al., “Project of Super Charm-Tau Factory at the Budker Institute of Nuclear Physics”, *Phys. Atom. Nucl.* **76**, pp.1072-1085, 2013.
33. M. Benedikt and F. Zimmermann et al., “Outline and Status of the FCC-ee Design Study”, *ICFA Beam Dyn. Newslett.* **67** pp. 86-93, 2015.
34. CEPC web page 2016, <http://cepc.ihep.ac.ch>.
35. Y. Ohnishi et al., “Commissioning of the Phase-I SuperKEKB B-Factory and Update on the Overall Status”, *Proc. of NAPAC2016*, MOB3IO01, 2016.
36. A. Bogomyagkov et al., “Beam-beam Effects Investigation and Parameters Optimization for a Circular e+e- Collider TLEP”, *Phys. Rev. ST Accel. Beams* **17** 041004.
37. D. Wang et al., “CEPC Partial Double Ring Scheme and Crab-Waist Parameters”, in *IAS Program on High Energy Physics* 18-21 January 2016, Hong Kong.
38. M. Bona M et al., “SuperB: a High-Luminosity Asymmetric e+e- Super Flavour Factory. Conceptual Design Report”, *Preprint INFN-AE-07-02* (arXiv: 0709.0451).
39. M. Biagini et al., “Tau/Charm Factory Accelerator Report”, *Preprint* arXiv:1310.6944
40. D.J. Summers et al., “A 233 km Tunnel for Lepton and Hadron Colliders”, *AIP Conf. Proc.* **1507** pp. 860-865
41. J.L. Abelleira, S. Russenschuck, F. Zimmermann, C. Milardi and M. Zobov M, “Local Chromatic Correction Scheme and Crab-Waist Collisions for an Ultra-Low Beta”, *Conf Proc.* **C1205201** 118.
42. J.L. Abelleira, S. Russenschuck, R. Tomas, F. Zimmermann. K. Ohmi, C. Milardi, M. Zobov and D. Shatilov, “LHC Optics with Crab-Waist Collisions and Local Chromatic Correction”, *Preprint* CERN-ACC-2013-0147.

2.25 Three-Beam Instability in the LHC

A. Burov

FNAL, Batavia, IL 60510, U.S.A

Mail to: burov@fnal.gov

2.25.1 Introduction

In the LHC, a transverse instability has been regularly observed at 4 TeV right after the beta-squeeze, when the beams are separated by ten transverse rms sizes, and only one of the two beams is seen as oscillating. According to the author, only a single hypothesis appeared to be consistent with all the observations and basic concepts, one about a third beam - an electron cloud, generated by the two proton beams in the high-beta areas of the interaction regions. The instability results from a combined action of the cloud nonlinear focusing and impedance.

2.25.2 Facts and Hypotheses

To prevent transverse instabilities, LHC is normally operated with Landau octupoles and with a damper on [1]. For a single beam in the machine, the octupole instability threshold never exceeded 200A for high chromaticity values, $Q'_{\geq 10}$ and e-fold damping rate 50-200 revolutions [2]. During the 4 TeV proton-proton run, LHC normally worked with maximally available 530A of the octupoles and with full damper gain, but still had regular instabilities at the end of the squeeze [3-5]. To avoid cancellation of stabilizing beam-beam and octupole anharmonicities [4, 6], octupole polarity was switched to positive since summer 2012. As a result, at the end of the squeeze beam-beam nonlinearity effectively provided additional $\sim 220A$ for the edge (“pacman”) bunches and $\sim 450A$ for regular bunches. At this stage of the process, the edge bunches had ~ 4 times more effective octupole nonlinearity than the single beam threshold, still being unstable. Typically, the instability was observed as intensity loss of the trailing bunches, accompanied with coherent activity at few synchrotron lines seen at the BBQ spectrometers.

That high sensitivity of the instability to the beams interaction inclines to suspect coupled-beam oscillations. Indeed, every pacman bunch has 8 long-range beam-beam collisions per interaction region (IR), resulting in $\sim 1.3 \cdot 10^{-3}$ of the incoherent tune shift per every one of the two main interaction regions (IR1 and IR5). This linear tune shift is more than a half of the synchrotron tune, exceeding the rms tune spread on the Landau octupoles at their maximal current. Although the linear (quadrupolar) parts of incoherent tune shifts at IR1 and IR5 are compensating each other thanks to the crossing horizontal-vertical collision scheme [7], the coherent beam-beam tune shifts are not cancelled, since the two beams have significantly different phase advances between the two interaction points (IP) [8]. Thus, reasons to suspect coupled-beam oscillations as a cause of the end-of-the-squeeze instability seem to be very serious. However, an attentive consideration of these reasons leads to a definite refutation of that suspicion.

First of all, it has to be noted that although the instability is highly sensitive to the presence of both beams in the IR, normally only one of the two beams is seen as unstable (more precisely, only one from the four transverse degrees of freedom is normally seen as unstable [3-5]). However, this observation does not refute the significant coupled-beam contribution to the instability: a role of the apparently stable beam could be hidden by a

possible asymmetry of the two-beam oscillations [9,10]. Thus, the apparent stability of one of the beams does not yet contradict to the coupled-beam hypothesis. This hypothesis is still refuted though, but by another argument, based on the damper consideration.

The LHC transverse damper normally works at rather high gain providing a damping rate of 0.02 inverse revolutions, which is 40% higher than the angular synchrotron frequency ω_s . Originally the damper worked in a narrow-band regime with FWHM of its time-domain response ~ 140 ns, so high frequency coupled-bunch modes of 50 ns beams were not effectively damped. Last several months of the Run I the damper worked in a broadband, really bunch-by-bunch regime [11], but that did not show any improvement for the instability. That new bunch-by-bunch damper is broadband enough to resolve coherent motion of every bunch, but it cannot resolve intra-bunch motion; it sees only a centroid of every individual bunch, thus reacting to every head-tail mode proportionally to a weight of the centroid in its oscillations. At a sufficiently high damper gain, this means that only those modes are unstable which have practically zero centre of mass amplitude. These modes are invisible for the damper and thus can be unstable due to the machine impedance. It is important that beam-beam coupling for that sort of potentially unstable modes is suppressed by the same reason as their visibility for the damper. Indeed, for the long-range collisions, the bunch length is much smaller than the beta-functions, so kicks of the oncoming bunches are equivalent to kicks of their centres. Since the bunch centres are blocked by the damper, the beam-beam coupling is strongly suppressed, so beam-coupling cannot play a significant role. This qualitative refutation of the coupled-beam contribution in case of a strong damper can be expressed by means of a simple model treating coupling of two head-tail modes of the two beams.

Let $A_{1,2}$ be the amplitudes of the eigenmodes in beam 1 and beam 2. Due to the beam-beam interaction, they become coupled. Assuming for simplicity a single IP, the mode dynamic equations follow

$$\begin{aligned}\dot{A}_1 &= -i\omega_c A_1 - d\alpha A_1 - iq\alpha A_2; \\ \dot{A}_2 &= -i\omega_c A_2 - d\alpha A_2 - iq\alpha A_1.\end{aligned}\quad (1)$$

Here ω_c is the impedance-related coherent tune shift of the separated beams; the parameter α reflects a weight of the centre of mass in the amplitudes A so that at zero chromaticity $\alpha = 1$ for the 0th head-tail mode; d and q are the damping rate and beam-beam tune shift. A straightforward solution shows that this system has two coupled modes (so called π and Σ modes) with frequencies

$$\Omega_{\pm} = \omega_c - id\alpha \pm q\alpha.\quad (2)$$

To be unstable and thus require some Landau damping to stabilize it, the mode centre of mass parameter has to be small enough: $\alpha < \text{Im}(\omega_c) / d$. From here, the coupled-beam tune shift is limited as

$$q\alpha < \text{Im}(\omega_c)q / d.\quad (3)$$

When the gain d is high enough, the beam-coupling correction just slightly shifts the coherent tunes, so that their positions in the stability diagram remain almost the same. In case when the beam-beam octupolar term adds up to the Landau octupoles, the stability

diagram increases, so that the two beams are more stable than one. For LHC at the end of the beta-squeeze, the beam-beam tune shift per IR and the damping rate are close to each other, $q/d \sim 1$, so the coupled-beam tune shift is limited as $q\alpha < \text{Im}(\omega_c)$. Thus, in this case, the beam-beam coupling moves coherent tune shifts along their real axis by a value not exceeding their imaginary part. However, the stability diagram width (say, FWHM) is 3-10 times higher than its height; moreover, with the damper, imaginary parts of the coherent tunes are much smaller than their real parts [12], so a shift of the real parts of the coherent tunes at the value limited by its imaginary part results only in a small increase of the required octupolar current, in any case smaller than $\sim 30\%$, and much smaller than that for the LHC impedance model. Taking into account that beam-beam octupolar term increases the stability diagram at least by 40 %, it can be concluded that the two beams have to be more stable than one – in contradiction to the observations. Thus, the effect of coupling oscillations of the two beams cannot explain the observed instability at the end of the squeeze.

For those who may be not quite convinced by the qualitative explanation and the model above, suspecting them to be over-simplified, the author provided a detailed solution of Vlasov equation, where the azimuthal, radial, coupled-bunch, and coupled-beam mode dimensions were taken into account in a framework of the Nested Head-Tail (NHT) Vlasov solver [12]. The result of that detailed computation confirmed the conclusions above: two-beam stability requires almost the same stabilizing octupolarity as a single beam does; with the beam-beam octupolar term taken into account it means the two beams have to be stable at less than 100 A of the Landau octupoles, while in reality they are not stable even at the maximally available 550 A. Almost at the same time similar result was obtained by S. White for single-bunch beam-beam tracking simulation with Beam-Beam3D program [13]. According to his results, stability conditions for weak-strong and strong-strong collisions are almost the same when the damper is fully on.

To verify these considerations, a special LHC beam experiment was run, where two beams with 78 bunches each were able to see or not see each other in the interaction regions by means of RF cogging (“cogging MD”). On top of that, tune separations of the two beams were varied up to several times the beam-beam tune shift per IR [14]. Despite a relatively small number of bunches (78×78), the end-of-squeeze instability was still observed. No sensitivity of the instability to that large tune separation was distinctly detected, while its sensitivity to simultaneous presence of the two beams in the IR1 and IR5 [15] was very clear. Thus, the three-level theoretical refutation of the coupled-beam oscillations as a cause of the instability was supported by its experimental refutation. Then, what is the cause of the instability?

Well, the fact is that when a reference beam sees another beam in the IR1 and IR5, it is much more unstable. The other beam, being rock-stable, dramatically changes life conditions of the reference beam. The Coulomb field of the other beam makes the reference beam even more stable than it would be alone. Hence, the other beam brings with itself something else, a third element, which interacting with the reference beam makes the beam much more unstable. What can that third element, created by the two beams in the IR, be?

This third element cannot be a high order mode (HOM) electromagnetic field excited by joint efforts of the two beams inside a parasitic cavity located somewhere in IR. Indeed, that sort of coherent tune shift for two beams cannot be higher than a doubled tune shift of a single beam. Moreover, the two-beam HOM-driven tune shift is coming closer to the doubled single beam tune shift only if the dominant part of the entire single beam tune shift is driven by that HOM, which cannot be the case since the observed instability for 78×78

bunches does not show any difference from $1378 \otimes 1378$ bunches. At the same time, while the single beam is stabilized by 200 A, the two beams are unstable with 750 A of the effective octupole current. That is why the sought-for third element cannot be a HOM of one or another parasitic cavity in the IR; it cannot be a free EM field. If this third element is not an EM field, it can be only matter, attracted by the two beams in the IR and disappearing when one of the beams is not there. It appears to be very clear that this matter can be nothing but an electron cloud in the IR.

2.25.3 E-Cloud as Nonlinear Lens

Electron cloud influences proton oscillations in two aspects. First, it works as a static lens, shifting up all coherent and incoherent tunes. This lens is nonlinear; the tune shifts of the transverse tails should be smaller than those of the core. Nonlinearity of this lens changes the proton stability diagram. The second aspect is that e-cloud is a reactive medium, whose response to proton perturbations is similar to a low-Q impedance [16-18]. Impedance of the electron cloud moves coherent tune shifts of the proton beam.

Electron cloud is not homogeneous along the bunch length; its line density changes and it may have multiple transverse pinches, so accurate computation of its effect on the proton coherent motion is very complicated. So far approaches in this direction are based either on simplified analytical models [16-18] or heavy multi-particle tracking [19,20]. Below, both focusing (static) and reactive (dynamic) aspects of the electron cloud are taken into account within a framework of a simplified model, where the cloud is represented as a longitudinally homogeneous electron density distribution, or a beam with zero longitudinal velocity, whose transverse profile is identical to one of the Gaussian proton beam. It can be rephrased that only electrons within the transverse radius of the proton beam are taken into account, while all the outside parts of the cloud are neglected both for the focusing and impedance aspects.

With N_e electrons along the entire LHC circumference seen by the proton beam of the normalized rms emittance $\varepsilon_n = \gamma\varepsilon$, the incoherent proton tune shift from the electrons $\Delta_e Q_x$ can be expanded over the proton actions J_x, J_y . For that, the space charge tune shift for a Gaussian bunch can be used (see Eq. (7) of Ref. [21]), leading to

$$\begin{aligned}\Delta_e Q_x &= \Delta_e Q_x^{(0)} + \Delta_e Q_x^{(1)} + \dots \\ \Delta_e Q_x^{(0)} &= \frac{N_e r_p}{4\pi\varepsilon_n}; \\ \Delta_e Q_x^{(1)} &= -\frac{3\Delta_e Q_x^{(0)}}{8} \frac{J_x + 2J_y/3}{\varepsilon}; \quad \langle J_{x,y} \rangle = \varepsilon.\end{aligned}\tag{4}$$

In the weak head-tail approximation, the eigenvalues Q are to be found as solutions of the dispersion equation [22]

$$1 = -Q_c \int \frac{J_x \partial F / \partial J_x}{Q - iQ_s - \Delta Q_x + i0} d\Gamma, \tag{5}$$

where F is a normalized phase space density defined on the phase space Γ , Q_c is the coherent tune shift, which gives the mode tune in case of no tune spread ΔQ_x , Q_s is the

synchrotron tune, l – azimuthal mode number and ϵ – infinitesimally small positive value. The stability diagram is a map of the real axis in a complex plane Q onto a complex plane

$$D = \left(- \int \frac{J_x \partial F / \partial J_x}{Q - lQ_s - \Delta Q_x + i\epsilon} d\Gamma \right)^{-1}, \quad (6)$$

so the mode is stable if and only if its tune shift Q_c is located inside the stability diagram. For Gaussian transverse distribution, and with negligible spread of the synchrotron frequencies, the 2D dispersion integral was found by R. Gluckstern [22]

$$\begin{aligned} \int_0^\infty \int_0^\infty \frac{x \exp(-x-y) dx dy}{q - ax - by + i\epsilon} = \\ - \frac{a - b + (b - q(1 - b/a)) \exp(-q/a) \text{Ei}(q/a)}{(a-b)^2} + \\ \frac{b \exp(-q/b) \text{Ei}(q/b)}{(a-b)^2} - \\ \pi i \frac{|-(b - q(1 - b/a)) \exp(-q/a) \theta(q/a) + b \exp(-q/b) \theta(q/b)|}{(a-b)^2}; \\ \text{Ei}(z) \equiv -P.V. \int_{-z}^\infty (e^{-t}/t) dt. \end{aligned} \quad (7)$$

Here $P.V.$ stands for the principle value and $\theta(z)$ is the Heaviside theta-function. Stability diagrams for distribution functions $F(J_x, J_y) \propto (1 - (J_x + J_y)/a)^n$ are discussed in Ref. [23].

The incoherent tune shift ΔQ_x in the denominator of the dispersion integral takes into account all the nonlinearities: Landau octupoles, beam-beam, e-cloud, and the remaining machine nonlinearities if they cannot be neglected: $\Delta Q_x = \Delta_o Q_x + \Delta_{bb} Q_x + \Delta_e Q_x + \dots$. The octupoles incoherent tune shift contribution is described by a symmetric matrix [24]

$$\begin{pmatrix} \Delta_o Q_x \\ \Delta_o Q_y \end{pmatrix} = \begin{pmatrix} a_o & b_o \\ b_o & a_o \end{pmatrix} \begin{pmatrix} J_x / \epsilon \\ J_y / \epsilon \end{pmatrix}, \quad (8)$$

for the normalized rms emittance $\epsilon_n = 2 \mu\text{m}$ and octupole current $I_o = +100\text{A}$, the LHC octupole matrix elements were computed at 4 TeV as [24]

$$a_o = 4.2 \cdot 10^{-5}; \quad b_o = -2.9 \cdot 10^{-5}. \quad (9)$$

Approximating the interaction region as a drift space, the long-range beam-beam octupole contribution per IR is computed as (see the Appendix)

$$\Delta_{bb} Q_x^{(1)} = \frac{3 |\Delta_{bb} Q_x^{(0)}| J_x - 2J_y}{2r^2 \epsilon} \quad (10)$$

with $\Delta_{bb}Q_x^{(0)}$ as the quadrupole beam-beam tune shift per IR, and r as the normalized beam-beam separation, or the separation in the units of rms beam sizes, which is almost the same for all the long-range collisions. At the end of the squeeze, $|\Delta_{bb}Q_x^{(0)}| = 2.5 \cdot 10^{-3}$, $r = 9.5$.

One of the main issues associated with multiple contributions to the incoherent tune shift ΔQ_x is a possibility of significant reduction of the stability diagram. When it was realized that the Landau octupoles and beam-beam contributions may almost cancel each other for negative octupole polarity [4, 6], their polarity was inverted. For positive octupole polarity, these two contributions add together. According to the LHC impedance model [7, 25], the coherent tune shifts of unstable modes are all negative [12]. At the left (defocusing) side of the stability diagram, the beam-beam contribution at the end of the squeeze is approximately equivalent to 200 A for pacman bunches.

Electron cloud may significantly change the stability diagram: defocusing anharmonicity of the cloud may almost cancel common focusing anharmonicity of the octupoles and beam-beam, resulting in a collapse of the focusing side of the diagram. The tune shifts formulas above show that at the end of the squeeze with 500 A of the Landau octupoles this requires $N_e \approx 1 \cdot 10^{10}$ seen by the proton beam within its size along the entire orbit. This collapse of the focusing part of the stability diagram would not yet lead to instability, were the coherent tune shifts of unstable modes all negative, as they are computed [12] for the LHC impedance model [25]. However, the electron cloud not only changes the stability diagram, it also introduces its own impedance. Tune shifts of unstable modes driven by this impedance are mostly positive.

2.25.4 Impedance and E-Cloud

Electron cloud is a dynamic object: it responds to collective perturbations of the proton bunches. Being excited by these perturbations, a dipole moment of the cloud oscillates, then, in the proton Coulomb field. Due to significant nonlinearity of this field, the excited electron perturbation has a high frequency spread and decoheres quickly. This consideration leads to an idea to represent the cloud coherent response by means of a resonator wake function with rather small Q -factor, $Q \sim 2-5$. [16-18]. To estimate this wake function, the proton bunch can be substituted by a piece of a coasting beam with constant 3D density, equal to an average density of a Gaussian bunch

$$\bar{n}_p = N_b^{-1} \int n_p^2(\mathbf{r}) d\mathbf{r} = \frac{N_b}{8\pi^{3/2} \sigma_x^2 \sigma_z} \quad (11)$$

In the Coulomb field of this homogeneous bunch, electrons oscillate with an angular frequency

$$\bar{\omega}_e = c \sqrt{2\pi \bar{n}_p r_e} = c \sqrt{\frac{N_b r_e}{4\sqrt{\pi} \sigma_x^2 \sigma_z}} \quad (12)$$

Let a small longitudinal sample of this bunch have a charge q and a rigid offset x_p . Due to its dipole moment qx_p , this proton sample excites an electron velocity

$$v_e = \frac{qex_p}{2\sigma_x^2 mc}, \quad (13)$$

leading to an amplitude of the electron offset $x_e = v_e / \bar{\omega}_e$. Modelling the electron beam by the transversely homogeneous one, same as the proton one, the kick to the protons is calculated. This kick can be expressed in terms of the cloud wake function; using the same convention as in Ref.[26], this yields

$$W_e(\tau) = c \frac{R_S}{Q} = \frac{N_e r_e c}{4\sigma_x^4 \bar{\omega}_e} \sin(\bar{\omega}_e \tau) \exp(\bar{\omega}_e \tau / 2Q), \quad (14)$$

where N_e is the total number of electrons seen by the proton bunch at the given part of the orbit. Note that sign of this wake is the same as for the conventional cavity modes: its derivative is positive at $\tau = -0$. This wake differs only by a factor of $\pi^{1/4} \approx 1.3$ from one suggested in Ref. [17], which appears to be well within error bars of both derivations.

Coherent tune shifts caused by the electron cloud wake field can be estimated within the air-bag approximation. Neglecting bunch coupling and assuming the weak head-tail approximation, the coherent tune shift can be presented as in Eq. (6.188) of Ref. [26]

$$Q_c = -i \frac{N_b r_p \beta_x}{8\pi^2} \int_{-\infty}^{\infty} Z_x(\omega) J_l^2(\omega \tau_b - \chi) d\omega;$$

$$Z_x(\omega) = \frac{c}{\omega} \frac{R_S}{1 - iQ \left(\frac{\omega}{\bar{\omega}_e} - \frac{\bar{\omega}_e}{\omega} \right)}. \quad (15)$$

Here β_x is the beta-function assumed to be weighed with the impedance Z_x along the orbit, $\tau_b = \sqrt{2}\sigma_z / c$ stands for the air-bag equivalent bunch length, and $\chi = Q'_x \omega_0 \tau_b / \eta$ is the conventional head-tail phase with $Q'_x \equiv pdQ_x / dp$ as a chromaticity, ω_0 as the angular revolution frequency and η as the slippage factor. Substitution of the cloud impedance into the air-bag formulas for $\chi = 1$ yields

$$\text{Im} Q_c = \chi \Delta_e Q_x^{(0)} F_R;$$

$$\text{Re} Q_c = \Delta_e Q_x^{(0)} F_I;$$

$$F_R = \sqrt{\frac{2}{\pi}} Q \phi_e \int_0^{\infty} \frac{J_l(x\phi_e) J'_l(x\phi_e)}{1 + Q^2 (x - 1/x)^2} \frac{dx}{x};$$

$$F_I = \frac{Q^2 \phi_e}{\sqrt{2\pi}} \int_0^{\infty} \frac{J_l^2(x\phi_e) (x - 1/x)}{1 + Q^2 (x - 1/x)^2} \frac{dx}{x}. \quad (16)$$

Here $\phi_e = \bar{\omega}_e \tau_b = \sqrt{2}\bar{\omega}_e \sigma_z / c$ is a phase advance of the electron oscillations on the air-bag bunch length $\sqrt{2}\sigma_z$. According to Ref. [17], for round beams $Q \approx 5$. For this Q-factor, the resonator impedance form-factors F_R, F_I as functions of the phase advance ϕ_e are presented in Figs. 1 and 2.

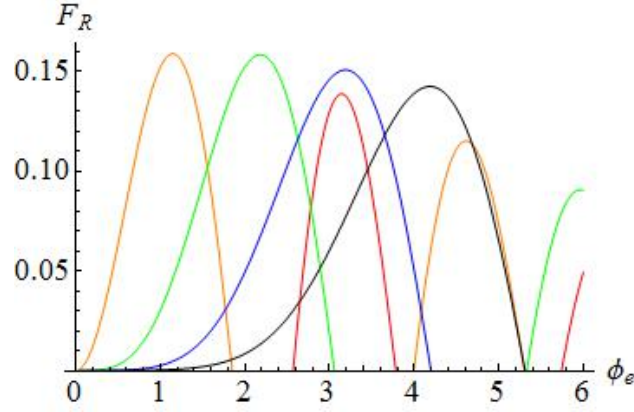


Figure 1: Growth rate form factor F_R for head-tail modes 0-4 (consequently red, orange, green, blue and black curves).

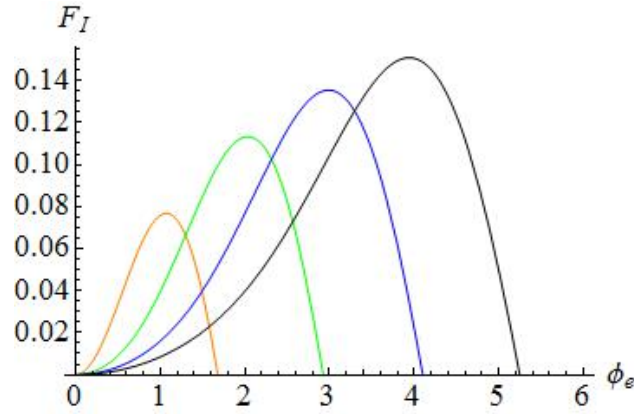


Figure 2: Same as Fig. 1 but for the tune shift form factor F_I .

As it is seen from the results above, the growth rate of the most unstable head-tail mode $\max_l(\text{Im}Q_c)$ is almost independent of the beta-function, at least directly, since the incoherent tune shift $\Delta_e Q_x^{(0)}$ does not contain any explicit dependence on that, and the form factor F_R of the most unstable mode is almost constant. Certain dependence on the beta-function is implicitly contained in the tune shift $\Delta_e Q_x^{(0)}$ due to some sensitivity of the e-cloud build-up to the beam size, but this issue is beyond the scope of this paper. It is already clearly seen that the head-tail number of the most unstable mode l_* is about equal to the integer part of the phase $l_* \approx \phi_e \propto 1/\sqrt{\beta_x}$. For the LHC, the orbit-average $\beta_x = R_0/Q_x \approx 70\text{m}$ yields the phase advance $\phi_e = 20\text{rad}$ and thus the same number of the most unstable mode, $l_* \approx 20$. In reality those high-order head-tail modes should be suppressed by a spread of the synchrotron tunes. That is why a possible e-cloud accumulation inside the regular part of the machine contributes to the Landau damping, while its contribution to the effective impedance can be neglected. The situation dramatically changes at the end of the squeeze, when beta-functions reach a level of few km

for significant part of the interaction regions. For instance, at $\beta_x = 4\text{km}$, the phase advance $\phi_e \simeq 2\text{rad}$, and so the head-tail number is not that high: $l_* = 2$.

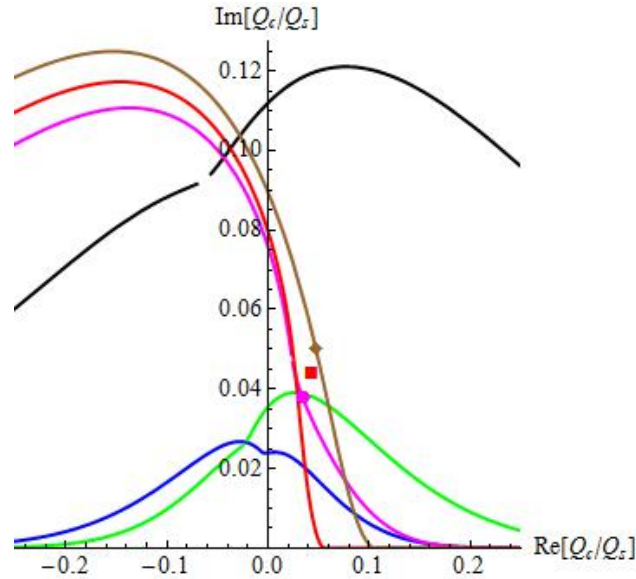


Figure 3: LHC stability diagrams: a separated stable beam with + 200A of the Landau octupoles (green); pacman beam-beam only (no octupoles) at the end of the squeeze (blue); this pacman beam-beam and + 500A of the octupoles in addition (black); same as the black line plus e-cloud with total $N_e = (1.3, 1.5, 1.7) \cdot 10^{10}$ (magenta, red, brown). Markers of the corresponding colour show the most unstable modes.

In the Fig. 3, several LHC stability diagrams are shown together with the coherent tune shifts of the most unstable modes. Several important aspects of this figure deserve to be discussed.

1. According to Fig. 3, the instability happens if and only if the total number of electrons belongs to a certain interval: $1.3 \cdot 10^{10} \leq N_e \leq 1.7 \cdot 10^{10}$. This may raise a suspicion that this instability can hardly happen since it requires a rather narrow interval of the cloud intensities. However, this suspicion can be counter-argued that the upper limit of the instability may not be so important. Indeed, as soon as the electron population reaches the lower instability threshold, the instability itself may prevent further accumulation of the electrons, and thus the cloud intensity will never reach the upper instability threshold. Still, the instability may stop due to emittance growth and intensity loss of the proton beam, caused by the instability itself. That sort of scenario appears to be consistent with observations.
2. While the collapse of the right (focusing) side of the stability diagram is driven by the total number of electrons seen by the beam along the orbit, the coherent tune shifts of the unstable modes are driven to the right by the electrons seen at high-beta ($\sim \text{km}$ -range) areas only. Figure 3 does not make any difference between these two groups of electrons; in other words, it assumes that all the electrons are mainly accumulated in the high-beta areas. If the opposite is true, the right-side collapse of the stability diagram would not lead to the instability: the electron impedance does

not play a role in that case, while all the coherent tune shifts of the unstable modes are negative [12] according to the currently accepted impedance model [25].

3. However, the LHC impedance model is not so certain. Measured single-beam thresholds and single-bunch tune shifts are consistent with 2-3 times higher impedance at the single-bunch (\sim GHz) frequency range than it is calculated in Refs. [7, 25]. An origin of this discrepancy is so far unknown. In case this lost impedance is mostly associated with a broadband resonator, underestimated in the computations, the impedance-related unstable coherent tune shifts will appear at the focusing part of the stability diagram, and a smaller value of the e-cloud impedance would be sufficient to explain the instability. In that case the fraction of the e-cloud in the interaction region may be smaller or even much smaller than the contribution of the regular part of the orbit. One more reason for reduction of the threshold electron population in the high-beta parts of the IRs can be found in Refs. [27,28] suggesting significant enhancement factor for the cloud wake function.
4. It has been mentioned above that the head-tail number of the most unstable mode depends on the beta-function of the cloud localization. For the average beta-function in the LHC, about 70 m, this number is very high, $l_* \simeq 20$, so these modes should be stabilized by the spread of the synchrotron tunes, entering as $l_* \Delta Q_s$. However, during the ramp and then at the flat top the bunch length is reduced, and so is the synchrotron tune spread. On top of that, some e-clouds could be accumulated at the areas of maximal beta-functions of the regular cells, where $\beta_{x,y} \simeq 200\text{m}$, and thus $l_* \simeq 10$. Maybe, due to the ramp these modes are not suppressed any more by the longitudinal Landau damping, and thus become unstable. Their instability cannot be seen by BBQ spectrometers since the bunch oscillations are too microwaving, at the ~ 10 GHz frequency range. Instability of these microwave modes could be an explanation for the emittance growth at the LHC ramp and losses during and after that [29, 30].
5. Computations of this paper neglect the damper. Excitation of the microwave modes $l_* > 2$ should not be sensitive to the damper seeing the bunch centre only.

One more question appearing in this context relates to the fact that normally only one beam is seen oscillating, while another appears to be rock-stable. Can this observation be consistent with the three-beam instability picture? The answer appears to be strictly positive. Indeed, the four degrees of freedom (two beams, horizontal and vertical directions) can never be identical: one of them is always closer to the instability threshold than the other three. Due to the damper, these degrees of freedom are uncoupled. Thus, when the most unstable of them, crosses its threshold, the others are not influenced. After that, the instability itself should prevent other modes to cross the threshold.

2.25.5 Summary

Accumulation of an electron cloud in the high-beta areas of the ATLAS and CMS interaction regions so far is the only hypothesis having a potential to explain the transverse instability at the end of the beta-squeeze in the LHC. According to that hypothesis the instability develops due to two different effects of the e-cloud: collapse of the focusing side of the stability diagram and introduction of the broadband impedance at GHz frequency

range at the end of the squeeze. The purpose of this paper was to show that this hypothesis is compatible with all known observations and main conventional ideas.

Finally, I would like to stress that all computations of this paper are extremely approximate, with unknown error bars. An electron cloud model applied above is very simplified; many other factors are neglected - the bunch-by-bunch damper, radial head-tail modes, couple-bunch interaction. Certainly all these factors require more detailed and thorough future analysis. The main purpose of this paper is to attract attention to the three-beam instability hypothesis as a potential explanation of the end-of-the-squeeze instability, so that the future elaborative studies will either confirm this explanation or refute it and find a real one.

2.25.6 Acknowledgment

This paper would not be possible without numerous discussions with many of my CERN colleagues that happened during my visit to CERN as a FNAL-LARP long-term visitor. I am thankful to G. Arduini, X. Buffat, S. Fartoukh, N. Mounet, T. Pieloni, E. Shaposhnikova and S. White for sharing of observations, ideas and results about instabilities in the LHC. My very special thanks are to my wonderful CERN host and favourite interlocutor E. Metral.

2.25.7 Appendix: Long-Range Beam-Beam Tune Shift

Octupole components of the long-range beam-beam tune shift can be found from an expansion of Coulomb potential of a charged cylinder $\Phi(x, y)$ at a distance r_0 from its axis, with $x^2 + y^2 \ll r_0^2$. Keeping only even terms up to 4th order, it yields

$$\begin{aligned} \Phi &= \Phi_0 \ln \left(1 / \sqrt{(r_0 + x)^2 + y^2} \right) = \text{const} + \\ &\frac{\Phi_0}{2} \left(\frac{x^2 - y^2}{r_0^2} + \frac{x^4 - 6x^2y^2 + y^4}{2r_0^4} \right). \end{aligned} \quad (\text{A1})$$

Substitution $x = \sqrt{2J_x \beta_x} \cos \psi_x$ and similar to y , after betatron phase averaging and derivation, leads to the tune shift of a round beam, with $\beta_x = \beta_y$ and $\varepsilon_x = \varepsilon_y = \varepsilon$

$$\begin{aligned} \Delta_{bb} Q_x &= \frac{\partial \Phi}{\partial J_x} = \Delta_{bb} Q_x^{(0)} \left(1 + \frac{3}{2r^2} \frac{J_x - 2J_y}{\varepsilon} \right); \\ \Delta_{bb} Q_x^{(0)} &= \frac{\Phi_0}{2\varepsilon r^2}; \quad r \equiv \frac{r_0}{\sqrt{\beta_x \varepsilon}}. \end{aligned} \quad (\text{A2})$$

2.25.8 References

1. W. Hofle, "Transverse damper", Proc. LHC Performance Workshop, Chamonix, 2012.
2. N. Mounet, "[Beam stability with separated beams](#)", talk at the LHC Beam Operation Workshop, Evian, 2012.
3. E. Metral, "[Review of the instabilities](#)", talk at the LHC Beam Operation Workshop, Evian, 2012.

4. X. Buffat, [“Instability observations”](#), talk at CERN LBOC meeting, Aug. 14, 2012.
5. G. Arduini, [“Summary on observations on the instabilities”](#), talk at CERN LMC meeting Aug 15, 2012.
6. S. Fartoukh, [“On the sign of the LHC octupoles”](#), CERN LMC talk, July 11, 2012.
7. [LHC Design Report](#), Volume 1, CERN-2004-003-V-1, 2004.
8. S. Fartoukh, private communication, 2012.
9. V. Lebedev, private communication, 2012.
10. A. Burov, “Two-beam instability in electron cooling”, Phys. Rev. ST Accel. Beams **9**, 120101.
11. D. Valuch, [“Transverse damper system”](#), talk at the LHC Beam Operation Workshop, Evian, 2012.
12. A. Burov, [“ADT suppression of coherent beam-beam”](#), ICE meeting, CERN, Oct. 30, 2012; [“Nested Head-Tail Vlasov Solver”](#), CERN AP Forum talk, Dec 4, 2012.
13. S. White, [“Update on long-range instabilities”](#), ICE section meeting, CERN, Nov. 7, 2012.
14. S. Fartoukh, “Two-beam impedance MD request”, [CERN LSWG meeting, Sep. 24, 2012](#).
15. S. Fartoukh, E. Metral, A. Burov, conclusions of the cogging MD, Dec. 2012.
16. A. Burov, N. Dikansky, [“Electron Cloud Instabilities”](#), Proc. of Int. Workshop on Multibunch Instabilities in Future Electron and Positron Accelerators, Tsukuba, KEK, 1997.
17. K. Ohmi and F. Zimmermann, “Head-Tail Instability Caused by Electron Clouds in Positron Storage Rings”, Phys. Rev. Lett. **85**, 3821–3824, 2000.
18. K. Ohmi, F. Zimmermann, E. Perevedentsev, “Wake-field and fast head-tail instability caused by an electron cloud”, Phys. Rev. E **65**, 016502, 2001.
19. K. Li, “Instabilities Simulations with Wideband Feedback Systems”, Proc. ECLOUD’12 workshop, La Biodola, Italy, 2012.
20. H. Bartosik, “Benchmarking of Instability Simulations at LHC”, *ibid*.
21. A. Burov, V. Lebedev, “Transverse instabilities of coasting beams with space charge”, Phys. Rev. ST Accel. Beams **12**, 034201 (2009).
22. J. S. Berg, F. Ruggiero, “Landau damping with two-dimensional tune spread”, CERN-SL-AP-96-071-AP, 1996.
23. E. Metral, A. Verdier, “Stability diagram for Landau damping with a beam collimated at an arbitrary number of sigmas”, CERN-AB-2004-019-ABP, 2004.
24. E. Metral, N. Mounet, private communications, 2012.
25. N. Mounet, “The LHC Transverse Coupled-Bunch Instability” PhD Thesis, EPFL, Lausanne, 2012.
26. A. Chao, “Physics of Collective Beam Instabilities in High Energy Accelerators”, 1993.
27. F. Zimmermann, “Review of single bunch instabilities driven by an electron cloud”, Phys. Rev. ST Accel. Beams **7**, 124801, 2004.
28. E. Benedetto, D. Schulte, F. Zimmermann, and G. Rumolo, “Simulation study of electron cloud induced instabilities and emittance growth for the CERN Large Hadron Collider proton beam”, Phys. Rev. ST Accel. Beams **8**, 124402, 2005.
29. F. Roncarolo, [“Beam size measurements”](#), LHC Beam Operation Workshop, Evian, 2012.
30. G. Papotti, [“Beam losses through the cycle”](#), *ibid*.

2.26 Mitigation of Collective Effects by Optics Optimization

F. Antoniou, H. Bartosik, Y. Papaphilippou
CERN, 1211 Geneva 23, Switzerland
Mail to: Yannis.Papaphilippou@cern.ch

2.26.1 Introduction

The quantities characterizing the performance of a large variety of hadron and lepton rings, as the power of synchrotron based proton drivers, the luminosity of colliders, the brightness of their associated injectors or the brilliance of X-ray storage rings, are proportional to the beam intensity or to the ratio of the intensity with the beam dimensions. The modern tendency is to push the performance frontiers towards extreme conditions, i.e. the highest beam intensity contained within the smallest beam volume, where the collective behavior of the beam becomes predominant. It is thus of paramount importance to take measures in order to alleviate collective effects, including instabilities, space-charge and intrabeam scattering (IBS), in the early phase of the design, which usually begins with the linear optics.

In the case of rings in operation, dealing with collective effects usually implicates mitigation techniques based on the use of multipole magnets [1] or higher harmonic RF cavities [2] for providing Landau damping, dedicated feedback systems [3] or the reduction of the beam interaction with its environment through careful vacuum and low-impedance component design [4]. Changing the linear optics, without major upgrade involving radical modifications of the machine configuration, is an unconventional approach, since it is subject to the constraints of the existing magnet and powering systems. It can be even more challenging because of its interplay with the already optimized operation of critical systems, such as beam transfer elements or RF. On the other hand, if a viable solution is found, it can be a very cost effective way to break existing intensity or brightness limits.

2.26.2 Impact of Optics Parameters on Collective Effects

In this section, three fundamental quantities that affect collective effects are described, following the logical route of an optics study: starting from the most basic one, the beam energy, passing to the most fundamental, the transverse beam sizes and ending with the phase slip factor, the most intimately connected to collective effects.

The beam energy is one among the basic parameters that have to be settled even before starting the optics design of a ring. Although, strictly speaking, it cannot be considered as an optics constraint, it is indirectly related through the integrated magnet strengths and the size of the lattice cells. At the same time, in the absence of synchrotron radiation damping, the transverse emittance is inversely proportional to the energy, thus reducing the physical beam size. Almost all collective effects become less pronounced with the beam energy, with the notable exception of the electron cloud instability thresholds [5]. Hence, for hadron rings, it is natural to target always the highest possible energy although this heavily depends on the users' physics needs, the reach of the pre-injectors and finally on cost. In the case of beams dominated by synchrotron radiation damping, the quadratic dependence of the horizontal equilibrium emittance to the energy puts an additional restriction to this increase, and a careful optimization has to be performed, in order to meet the specific design targets.

Transverse beam sizes are also playing an important role to the collective beam behavior, especially in the case of self-induced fields. For example, the space-charge tune-shift [6] and IBS growth rates [7] are inversely proportional to their product raised to a certain power. For high-intensity/power rings, there is usually no specific preference on the size of transverse emittances and the trend is to produce them large enough, for limiting the aforementioned effects. When the performance target is high brightness, which corresponds to small transverse emittances, the optics is one handle to increase beam sizes. For hadron rings, the FODO cells are well suited for this, due to the alternating behavior of the optics functions. In particular, weaker focusing can maximize beam sizes, within the limits set by the machine aperture. In the case of e^+e^- rings targeting low emittances, doublet-like cells are usually employed for minimizing horizontal beam sizes. On the other hand, the vertical beta functions can be increased, especially along the bending magnets, where the horizontal ones are small. Although this strategy is valid for space-charge or IBS, beam current thresholds of instabilities such as transverse mode coupling or coupled bunch, present an opposite dependence and call for a reduction of the average (vertical) beta functions.

The slippage (or phase slip) factor η is defined as the rate of change of the revolution frequency with the momentum deviation. At leading order, it is a function of the relativistic γ factor (i.e. the energy) and the momentum compaction factor α_p :

$$\eta = \alpha_p - \frac{1}{\gamma^2}. \quad (1)$$

The momentum compaction factor is the rate of change of the circumference C with the momentum spread and, again at leading order, it is given by

$$\alpha_p = \frac{1}{C} \oint \frac{D_x(s)}{\rho(s)} ds. \quad (2)$$

It depends on the variation of the horizontal dispersion function along the bending magnets. The phase slip factor unites transverse and longitudinal particle motion. In fact, the synchrotron frequency or the bunch length are proportional to $\eta^{1/2}$, which means that increasing the slippage factor makes synchrotron motion faster.

The phase slip factor vanishes when $\gamma = \alpha_p^{-1/2} = \gamma_t$ and the corresponding energy is named transition energy. It is widely known, since the commissioning of the first synchrotrons, that crossing transition can cause various harmful effects with respect to the collective behavior of the beam [8], as the longitudinal motion basically freezes at this point. Although several transition crossing schemes have been proposed and operated reliably in synchrotrons like the CERN PS for more than 40 years (see [9] and references therein), the call for beams with higher intensity (or power) resulted in the consideration of ring designs which avoid transition, either by injecting above ($\eta > 0$), or always remaining below transition ($\eta < 0$). The former case is almost always true for electron/positron rings above a few hundred MeV (unless $\alpha_p < 0$). For hadron rings, it requires the combination of high energy (i.e. large circumference) and a large momentum compaction, which is translated to larger dispersion excursions and, generally speaking, weaker focusing, thereby larger beam sizes [10]. For remaining below transition, the operating energy range has to be kept narrow and a positive momentum compaction factor should be low, which points towards stronger focusing and smaller beam sizes. The special case of negative momentum compaction

(NMC) [11] is very interesting because the beam remains below transition independent of energy. As for the rings remaining above transition, the need to excite dispersion oscillations for getting an overall negative dispersion integral on the bends results in larger beam sizes.

2.26.3 High-Power Synchrotrons

Recent optics design of high-intensity and/or high-power rings such as the J-Parc main ring [12], the PS2 [13], or the High-Power PS [14] are based on NMC arc cells, for avoiding transition and reducing losses. These are sequences of modified FODO cells with an increased number of quadrupole families (up to four) for inducing negative dispersion, leading to an overall “imaginary” γ_t [11]. In that case, the absolute value of the slippage factor could be increased for raising instability thresholds but also because a fast synchrotron frequency would be beneficial for longitudinal beam manipulation [15]. A complete picture of the achievable tuning range of a ring such as the PS2 can be obtained by the Global Analysis of all Stable Solutions (GLASS), a numerical method pioneered in low emittance rings [17], where all possible quadrupole configurations providing stable solutions are obtained. In Fig. 1 (left), the imaginary transition γ_t is presented for all stable solutions in the tune diagram, along with resonance lines up to 3rd order. The blue zones corresponding to low imaginary values of γ_t (i.e. large absolute values of the momentum compaction) are obtained for higher horizontal tunes. There is large flexibility for the vertical tunes. In Fig. 1 (right), the geometrical acceptance is computed for the most demanding beam parameters with respect to emittance. The red color corresponds to small acceptance (above a limit of 3.5σ), which means larger beam sizes. This type of global analysis including non-linear dynamics constraints was used during the conceptual design of the PS2 ring [16].

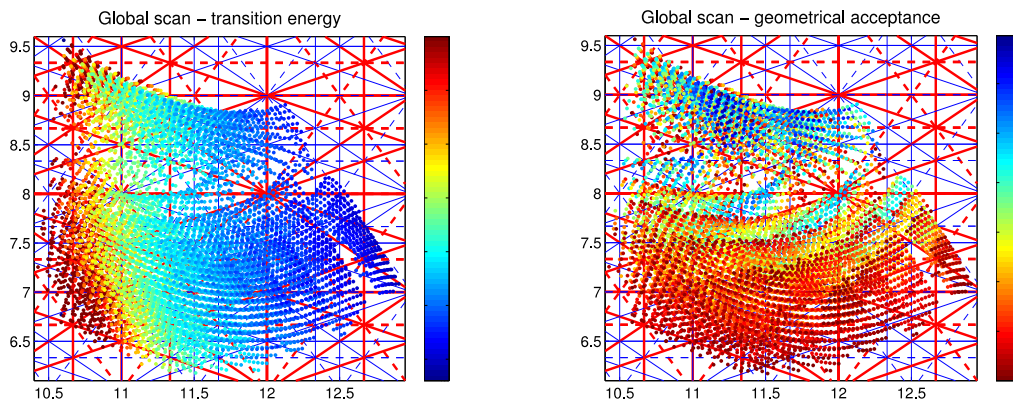


Figure 1: Transition energy γ_t (left) and geometrical acceptance in units of beam sizes $N\sigma$ (right) for a global scan of optics solutions in the tune diagram [17].

2.26.4 Low Emittance Rings

The present trend of ultra-low emittance rings is to target the highest beam intensities within the smallest dimensions, at least in the transverse plane. The additional complication in the case of damping rings (DRs) for linear colliders is that they aim to produce low longitudinal emittances, as well. The output beam dimensions are largely dominated by IBS.

Even space-charge effects become important, especially in the vertical plane. A careful optimization of the optics parameters is crucial for reducing these effects and obtaining a solid conceptual design [19].

Due to the fact that the IBS growth rates but also the equilibrium emittances vary with energy, it is important to find their interdependence, when the IBS effect is included [20]. Evaluated through a modified version of the Piwinski method [21], and for constant longitudinal emittance, the dependence of the steady state transverse emittances of the CLIC DRs on the energy is plotted in Fig. 2 (left). A broad minimum is observed around 2.6 GeV for both horizontal (blue) and vertical planes (green). The IBS effect becomes weaker with the increase of energy, as shown in Fig. 2 (right), where the emittance blow-up for all beam dimensions is presented. Although higher energies may be desirable for reducing further collective effects, the output emittance is increased above the target value, due to the domination of quantum excitation. In this respect, it was decided to increase the CLIC DR energy to 2.86 GeV, already reducing the IBS impact by a factor of two, as compared to earlier designs at 2.42 GeV [20].

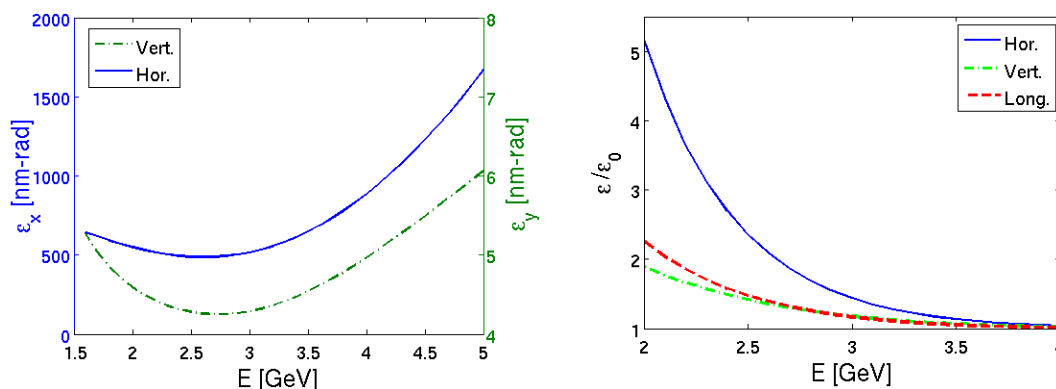


Figure 2: Steady-state emittances (left) and their blow-up (right) due to IBS, as a function of the energy [19].

In modern low emittance rings, Theoretical Minimum Emittance (TME) arc cells or multi bend achromats are employed. In order to reach minimum emittance, the horizontal beam optics is quite constrained, whereas the vertical one is free, but also completely determined by the two quadrupole families of the cell. It turns out that the vertical beta function reaches a minimum at the same location as the horizontal, which is the worst case for IBS. A way to reverse this tendency is to use a combined function dipole with a low defocusing gradient. Although this gradient does not provide a significant effect to the emittance reduction, it reverses the behavior of the vertical beta function at the middle of the dipole, maximizing the vertical beam size at that location, and thus reducing IBS growth rates [22].

A crucial step in the optimization of the TME cell with respect to its impact on collective effects is the analytical derivation of the two quadrupole focal lengths, in thin lens approximation, depending only on the horizontal optics functions at the center of the dipole and the drift space lengths [19, 23]. Using this representation, the dependence of various parameters on the cell phase advances in the case of the CLIC DRs are presented in Fig. 3, including the average IBS growth rates, the detuning from the minimum emittance, the momentum compaction factor, the vertical space-charge tune-shift and the horizontal

chromaticity. This parameterization permitted to find the best compromise for the phase advances (between 0.4 and 0.5) where the IBS growth rates, the horizontal and vertical chromaticities and the Laslett tune shift are minimized, while the momentum compaction factor is maximized. These low phase advances correspond to emittances that deviate from the absolute minimum by a factor of around 15. A similar study was performed in order to find the optimal wiggler field and wavelength, while minimizing the IBS effect [19, 24]. Based on these studies, the highest field within the limit of technology would be desirable, but a moderate wavelength is necessary for reducing IBS. These specifications were used for the super-conducting wiggler prototype under development for the CLIC DRs [24].

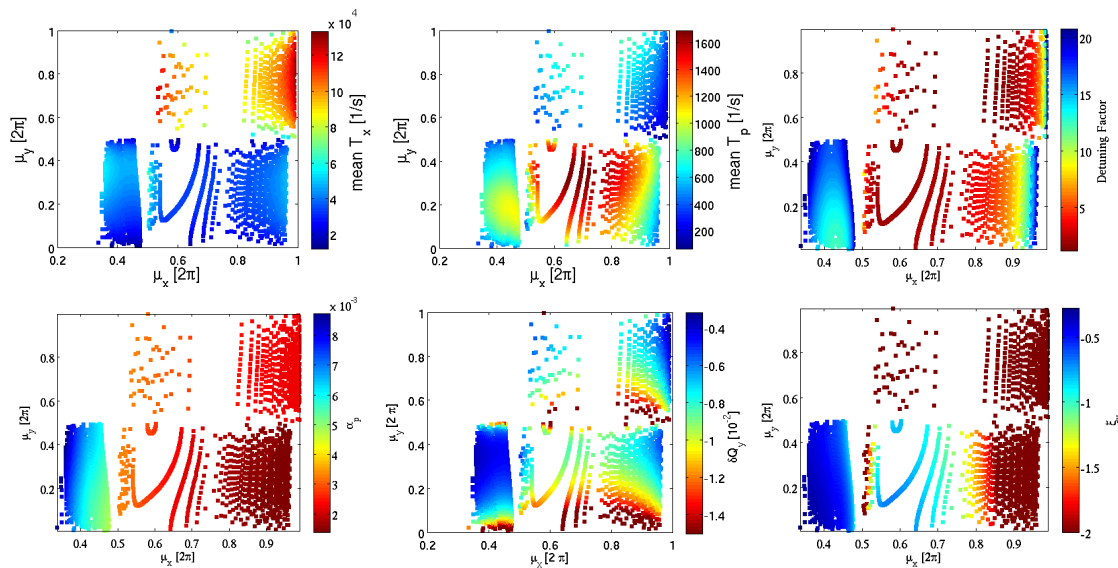


Figure 3: Analytical parameterization of the TME cell phase advances with the IBS horizontal (top, left) and longitudinal (top, middle) growth rates, the detuning factor (top, right), the momentum compaction factor (bottom, left), the Laslett tune shift (bottom, middle) and the horizontal chromaticity (bottom, right) [19].

2.26.5 High-Brightness Synchrotrons

Hadron collider injectors need to achieve the highest brightness with the smallest possible losses. A typical example is the CERN SPS whose performance limitations and their mitigations for LHC beams are the subject of a study group [25], in view of reaching the required beam parameters for the high luminosity LHC (HL-LHC). The upgrade of the main 200 MHz RF system will solve beam loading issues for reaching higher intensities, but a variety of single and multi-bunch instabilities remain to be confronted. The Transverse Mode Coupling Instability (TMCI) in the vertical plane and E-Cloud Instability (ECI) for 25 ns beams are the most prominent transverse problems, especially for HL-LHC intensities. Longitudinal instabilities necessitate the use of a higher harmonic 800 MHz RF system for providing Landau damping and the application of controlled longitudinal emittance blow-up throughout the ramp. For constant longitudinal bunch parameters and matched RF-voltage, higher intensity thresholds for the above instabilities are expected when increasing the phase slip factor.

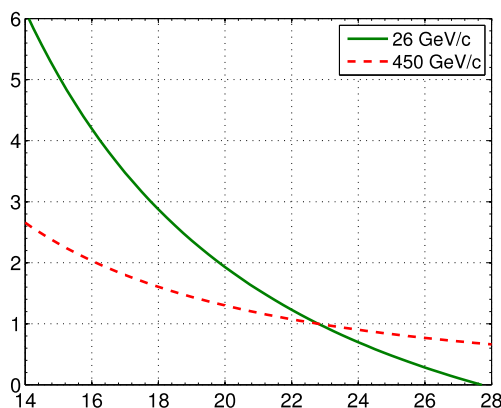


Figure 4: Slippage factor η relative to the value of the nominal SPS optics (nominal $\gamma_t = 22.8$) as a function of γ_t [26].

In the nominal SPS optics (called Q26), the phase advance per FODO cell is close to $\pi/2$, resulting in betatron tunes between 26 and 27. Low dispersion in the long straight sections is achieved setting the arc phase advance to $4 \times 2\pi$. In the case of the nominal SPS optics, the LHC-type proton beams are injected at 26 GeV/c ($\gamma = 27.7$), i.e. above transition ($\gamma_t = 22.8$). By reducing γ_t , the slippage factor is increased throughout the acceleration cycle with the largest relative gain at injection energy, as shown in Fig. 4, where η normalized to the value in the nominal SPS optics (η_{nom}) is plotted as a function of γ_t , for injection and extraction energy. Significant gain of beam stability can be expected for a relatively small reduction of γ_t , especially in the low energy part of the acceleration cycle. In 2010, alternative optics solutions for modifying γ_t of the SPS were investigated [26]. Based on the fact that in a regular FODO lattice the transition energy is approximately equal to the horizontal tune, γ_t can be lowered in the SPS by reducing the horizontal phase advance around the ring. One of the possible solutions, with low dispersion in the long straight sections, is obtained by reducing the arc phase advance by 2π , i.e. $\mu_x, \mu_y \approx 3 \times 2\pi$ so that the machine tunes are close to 20 (“Q20 optics”). In this case, the transition energy is lowered from $\gamma_t = 22.8$ in the nominal optics to $\gamma_t = 18$ and η is increased by a factor 2.85 at injection and 1.6 at extraction energy (Fig. 4). Note that the maximum β -function values are about the same in both optics, whereas the minima are increased by about 50%. The optics modification is mostly affecting peak dispersion, which is almost doubled. The fractional tunes have been chosen identical to the nominal optics in order to allow for direct comparison in experimental studies. A series of measurements with high-intensity single bunches were conducted during the last years [27, 28], in order to quantify the benefit of the Q20 optics with respect to TMCI. In the nominal optics, the threshold with nominal longitudinal emittance and close to zero chromaticity is found at 1.6×10^{11} p/b, as shown in Fig. 5 (left). In order to

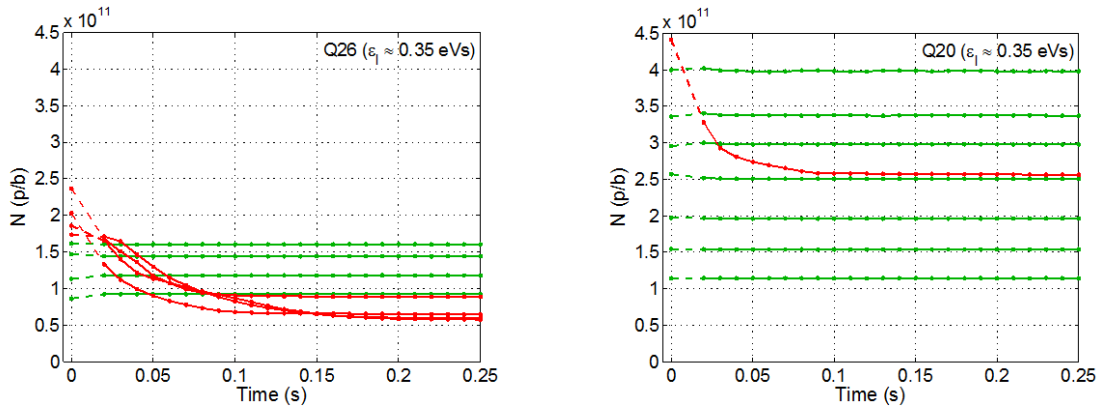


Figure 5: Examples of the intensity evolution as a function of time after injection in the Q26 optics (left) and the Q20 optics (right). Green curves correspond to stable beam conditions, red traces indicate cases above the TMCI threshold [28].

pass this threshold with the Q26 optics, the vertical chromaticity has to be increased so much that the losses are excessive due to single-particle effects. In the Q20 optics, it was demonstrated that up to 4×10^{11} p/b could be injected with no sign of the TMCI and low chromaticity, as shown in Fig. 5 (right) [28]. Such high intensity single bunches were already sent to the LHC for beam studies [29].

The ECI threshold scales with the synchrotron tune [30]. Therefore a clear benefit from the larger η in the Q20 optics is expected. Numerical simulations were performed, assuming that the electrons are confined in bending magnets [31]. The expected threshold electron density ρ_c for the ECI instability in the nominal (red) and the Q20 optics (blue), as a function of the bunch intensity N_b at injection energy, for matched RF voltages, is presented in Fig. 6. Clearly, higher thresholds are predicted for Q20.

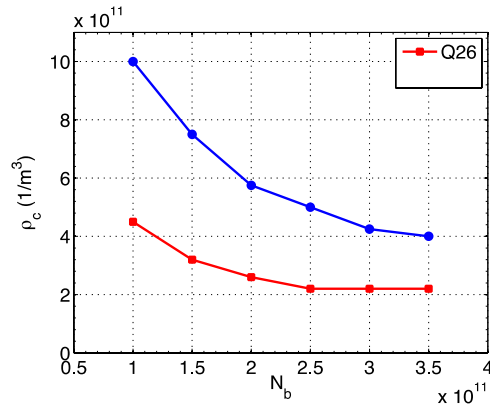


Figure 6: ECI thresholds for various intensities comparing the nominal (red) with the low γ_l SPS optics (blue) [28].

To stabilize the LHC beam at flattop in the Q26 optics from longitudinal instabilities, controlled longitudinal emittance blow-up is performed during the ramp. The maximum voltage of the 200 MHz RF system is needed in order to shorten the bunches for beam transfer to the LHC 400 MHz bucket. Due to the limited RF voltage, bunches with the same longitudinal emittance at extraction will be longer in the Q20 optics. In fact, for the same longitudinal bunch parameters of a stationary bucket, the required voltage would need to be scaled with η . However, the longitudinal instability threshold at 450 GeV/c is about 50%

higher in the Q20 optics and therefore less or no controlled longitudinal emittance blow-up is required compared to the nominal optics, for achieving the same beam stability. Figure 7 shows a comparison of the beam stability (bunch length and bunch position) in the two optics, for a single 50 ns LHC batch with 1.6×10^{11} p/b. The Q20 optics is stable even in the absence of emittance blow-up, with a mean bunch length of around $\tau = 1.45$ ns at flattop, which is compatible with injection into the LHC.

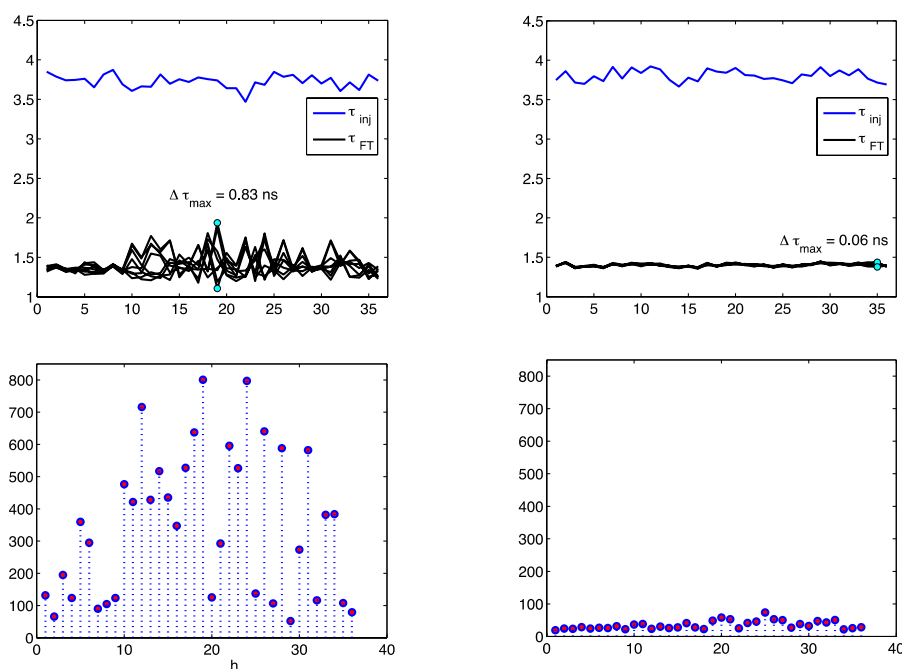


Figure 7: Bunch length (top) and bunch position oscillations (bottom), at flattop, for a single batch 50 ns LHC beam, for Q26 (left) and for Q20 (right) [27].

The low transition energy optics in the SPS became operational on September 2012. The switch to this new optics was very smooth, allowing very high brightness beams to be delivered to the LHC providing record luminosities [29]. This optics opens the way for ultra-high brightness beams to be delivered in the HL-LHC era for protons and eventually for ions [32].

2.26.6 Summary

Using analytical and numerical methods, linear optics parameters, which have a direct impact on collective effects, were optimized for specific examples of high-intensity, high brightness, hadron and lepton rings. These approaches allowed a solid conceptual design of ultra-low emittance damping rings and permitted to break intensity limitations in an existing LHC injector, without any cost impact or hardware change. It is certain that there is a growing need for the optics designer to transcend the single-particle dynamics mentality and apply such optimization procedures for reaching the optimal performance of rings, in design or operation.

2.26.7 References

1. A. W. Chao, *Physics of Collective Beam Instabilities in High Energy Accelerators*, New York, Wiley (1993).
2. T. Argyropoulos et al., TUPWA040, IPAC13 (2013).
3. W. Höfle, FRXCA01, IPAC13 (2013).
4. P. Collier et al., EPAC02, WEPRI082, p.1458 (2002).
5. G. Rumolo, et al., PRL100, 144801 (2008).
6. L. J. Laslett, BNL-7534 (1963).
7. A. Piwinski, in *Handbook of Accelerator Physics* ed. A. W. Chao, M. Tigner, World Scientific, p. 127, 2002; J. Bjorken, S. K. Mtingwa, *Part. Accel.* 13, 115 (1983).
8. J. Wei, in *Handbook of Accelerator Physics*, op. cit., p.285.
9. T. Risselada, 4th CAS, CERN-91-04, p.161 (1991).
10. K. Y. Ng, in *Handbook of Accelerator Physics*, op. cit., p. 94.
11. S. Y. Lee, K. Y. Ng, D. Trbojevic, *PRE*, 48(4), p. 3040 (1993).
12. Y. Yamazaki, KEK-2002-13 (2002).
13. Y. Papaphilippou et al., TH6PFP044, PAC09, p.3805 (2009).
14. Y. Papaphilippou et al., THPWO081, IPAC13 (2013).
15. S. Hancock, CERN-AB-Note-2006-39 (2006).
16. D. S. Robin et al., PRST-AB11, 024002 (2008).
17. H. Bartosik et al., THPE022, IPAC10 (2010).
18. Y. Papaphilippou et al., TUPPC086, IPAC12, p. 1368 (2012).
19. F. Antoniou, PhD Thesis, NTUA (2013).
20. F. Antoniou et al., WEPE085, IPAC10, p.3542 (2010).
21. K. Kubo et al., PRST-AB8, 081001 (2005).
22. H. H. Braun et al., CLIC Note 849 (2010).
23. F. Antoniou and Y. Papaphilippou, preprint (2013).
24. D. Schoerling et al., PRST-AB15, 042401 (2012).
25. LIU-SPS Beam Dynamics Working Group, chaired by E. Shaposhnikova, <http://paf-spsu.web.cern.ch/paf-spsu/>
26. H. Bartosik et al., MOPS012, IPAC11, p.619 (2011).
27. H. Bartosik et al., MOPS010, IPAC11, p. 613 (2011); WEPPI072, IPAC12, p. 3096 (2012).
28. H. Bartosik, PhD Thesis, TU Wien, (2013).
29. Y. Papaphilippou et al., THPWO080, IPAC13 (2013).
30. K. Ohmi and F. Zimmermann, *PRL*85, 3831 (2000).
31. H. Bartosik et al., MOPS011, IPAC11, p.616 (2011).
32. F. Antoniou et al., TUPME046, IPAC13 (2013).

3 Workshop and Conference Reports

3.1 The 7th International Particle Accelerator Conference, IPAC'16

Won Namkung,
Pohang Accelerator Laboratory (PAL)
Mail to: Namkung@postech.ac.kr

The 7th International Particle Accelerator Conference, IPAC'16, was held at the BEXCO Convention Center, Busan, Korea, from May 8 to 13, 2016. There were more than 1,200 attendees from 36 countries, 540 from Asia, 490 from Europe and 190 from Americas. It was hosted by the Pohang Accelerator Laboratory (PAL), the Korea Multi-purpose Accelerator Complex (KOMAC), the Korea Heavy Ion Medical Accelerator (KHIMA), and the Rare Isotope Science Project (RISP). It was organized under the auspices of the Asian Committee for Future Accelerator (ACFA), the European Physical Society Accelerator Group (EPS-AG), and the American Society of Physics Division of Physics of Beams (APS-DPB).

The traditional student poster session was held on Sunday. Seventy-six students from all over the world were able to attend the conference through the sponsorship of societies, institutes and laboratories worldwide. The organizers of IPAC'16 are grateful to all sponsors for their valuable support.

Won Namkung (PAL), Chair of the Organizing Committee (OC), In Soo Ko (PAL), Chair of the Scientific Program Committee and Kyung-Ryul Kim (PAL), Chair of the Local Organizing Committee (LOC), opened the conference. Mr. Byung Soo Suh, Busan City Mayor, and Mr. Tae-min Bae, an official from Ministry of Science, ICT & Future Planning, both addressed the conference attendees.

Sachio Komamiya (ICEPPE) opened the scientific program with a presentation on *The International Linear Collider, the Latest Status towards Realization*. An inspiring closing presentation was delivered by Wen-Long Zhan (CAS, Beijing) on *Accelerator Driven Sustainable Fission Energy*.

Ninety-eight invited and contributed oral presentations of very high quality were made during the week, including an unusual "Entertainment" presentation by Zev Handel (University of Washington, Seattle) entitled *Learn to Read Korean: An Introduction to the Hangul Alphabet*.

The conference program spanned four and a half days, with plenary sessions on Monday and Friday mornings, and Thursday afternoon. All other sessions were composed of two oral sessions in parallel, with the poster sessions scheduled alone at the end of each afternoon. There were 47 invited talks and 51 contributed oral presentations; 1300 posters were scheduled during the lively afternoon poster sessions.

An industrial exhibition took place during the first three days of the conference. Industrial exhibitors from 86 companies occupied 92 booths with additional 16 booths from non-profit organizations. They presented their high technology products and services to the delegates in an excellent atmosphere conducive to discussions.

During the Accelerator Awards Session, the ACFA/IPAC'16 best student poster prizes were awarded to Mattia Checchin (Fermilab) and Claudio Torregrosa (CERN). The Mark Oliphant Prize, awarded to a student or a trainee accelerator physicist or engineer for the quality of work and promise for the future, was awarded to Spencer Jake Gessner (SLAC).

The Hogil Kim Prize for a recent, significant, original contribution to the accelerator field, awarded to an individual in the early part of his or her career was awarded to *Sam Posen, Fermilab, USA*.

The Nishikawa Tetsuji Prize for a recent, significant, original contribution to the accelerator field, with no age limit was awarded to *Gwo-Huei Luo, NSRRC, Taiwan*.

The Xie Jialin Prize for outstanding work in the accelerator field, with no age limit was awarded to Derek Lowenstein, *BNL, USA*. Wolfram Fischer, BNL, received the prize on behalf of the Derek Lowenstein who was unable to attend due to the recent extensive flooding in Texas.

The proceedings of IPAC'16 were published on the JACoW site (www.jacow.org). The processing of the electronic files of contributions prior to, during, and immediately after the conference was achieved by the JACoW "seasoned experts". Thanks to the work of this dynamic team and the careful preparations and guidance of Christine Petit-Jean-Genaz (retired, CERN), Kyung-Sook Kim (PAL) and Dong-Eon Kim (PAL).

The high levels of participation and enthusiasm shown at IPAC'16, the third IPAC taking place in Asia, clearly indicate the strong mandate for the International Particle Accelerator Conference series from the worldwide accelerator community. May future events be even more successful than this one. The eighth IPAC will return to Europe and take place in Copenhagen, Denmark. We are convinced that the collaboration among the three regions, steadily enhanced in recent years, will continue to grow to the benefit of IPAC and the accelerator community worldwide.

3.2 The 57th ICFA ABDW on High-Intensity and High-Brightness Hadron beams, HB2016

Mamad Eshraqi, ESS
European Spallation Source, Lund, Sweden
Mail to: mamad.eshraqi@esss.se

The 57th Advanced Beam Dynamics Workshop on High-Intensity and High-Brightness Hadron Beams, HB2016, hosted by ESS, was held at the Scandic Hotel Triangeln in Malmö, Sweden from 2016 July 3 to July 8. The venue is 20 km south of the construction site of the European Spallation Source. The workshop was co-sponsored by EuCARD and ISA. More than 200 experts participated in this event, making it the largest gathering of the high intensity hadron beam experts so far.

The workshop started with a day of plenary talks, providing an overview of the high intensity accelerators under construction, improvement or operation. The first day ended with a two-hour poster session where lively discussions could continue without any time constraints.

The delicate tasks of setting the scientific program, selection of the plenary talks and selection of the conveners were performed by the International Organizing Committee (chaired by Mamad Eshraqi). Conveners of working groups carefully selected the speakers of their sessions, set the program of the parallel sessions, chaired them and mediated the discussion sessions.

There were five working groups each with special focus on a certain aspect of high intensity beams, their simulation, analysis, production or measurement. These working groups were:

- a) Beam Dynamics in Rings (Conveners: Giuliano Franchetti, Yong Ho Chin, and Wolfram Fischer)
- b) Beam Dynamics in Linacs (Conveners: Alessandra Lombardi, Yuan He and Ikegami Masanori)
- c) Accelerator systems(Conveners: Sarah Cousineau, Jean-Luc Biarotte, Shinian Fu, Luc Perrot and Sheng Wang)
- d) Commissioning and Operations (Conveners: Fernanda Garcia, Hideaki Hotchi and Angelina Perfenova)
- e) Instrumentation and Beam Interactions (Conveners: Michiko Minty, Hee Seock Lee and Tom Shea)

The last day of the workshop started with the summary talks of the five sessions and continued with an out of the box talk on ion acceleration by plasma wake field and the day and the workshop ended by a bus tour to the ESS construction site in the afternoon.

More information about the workshop and future HB workshops could be found on the webpage of HB2016 (www.hb2016.esss.se). The proceedings of the workshop are already published on the JACoW servers.



Figure 1: Participants of the HB2016.

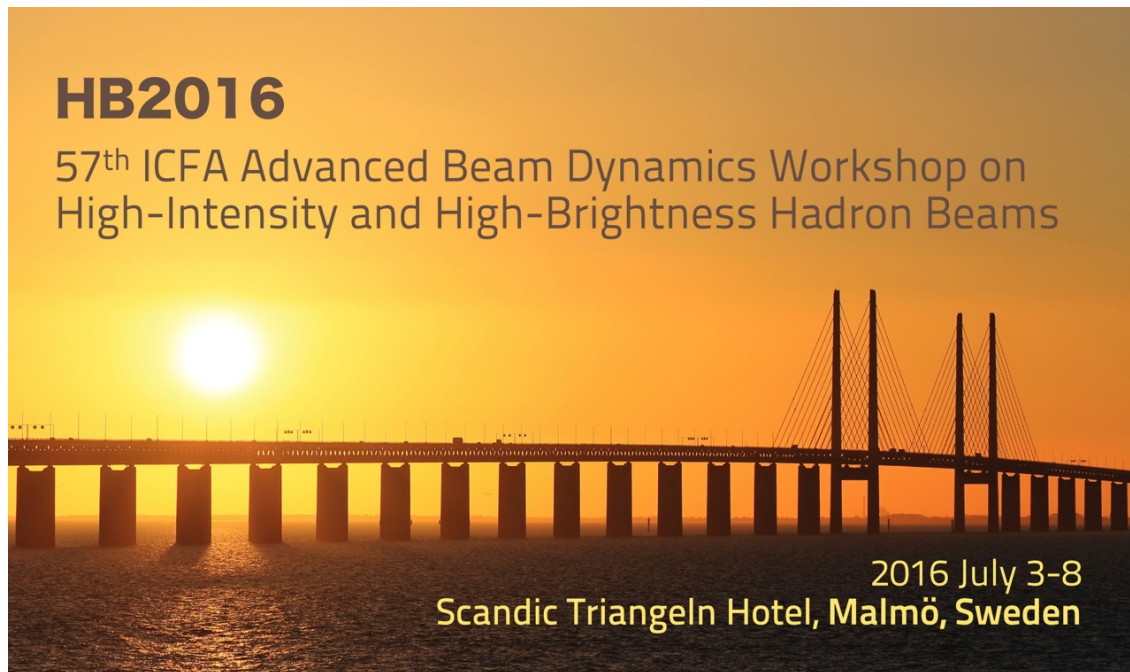


Figure 2: HB2016 workshop postcard.

3.3 The 28th International Linear Accelerator Conference, Linac 2016

Yoshishige Yamazaki

Facility for Rare Isotope Beams Laboratory, Michigan State University

Mail to: yamazaki@frib.msu.edu

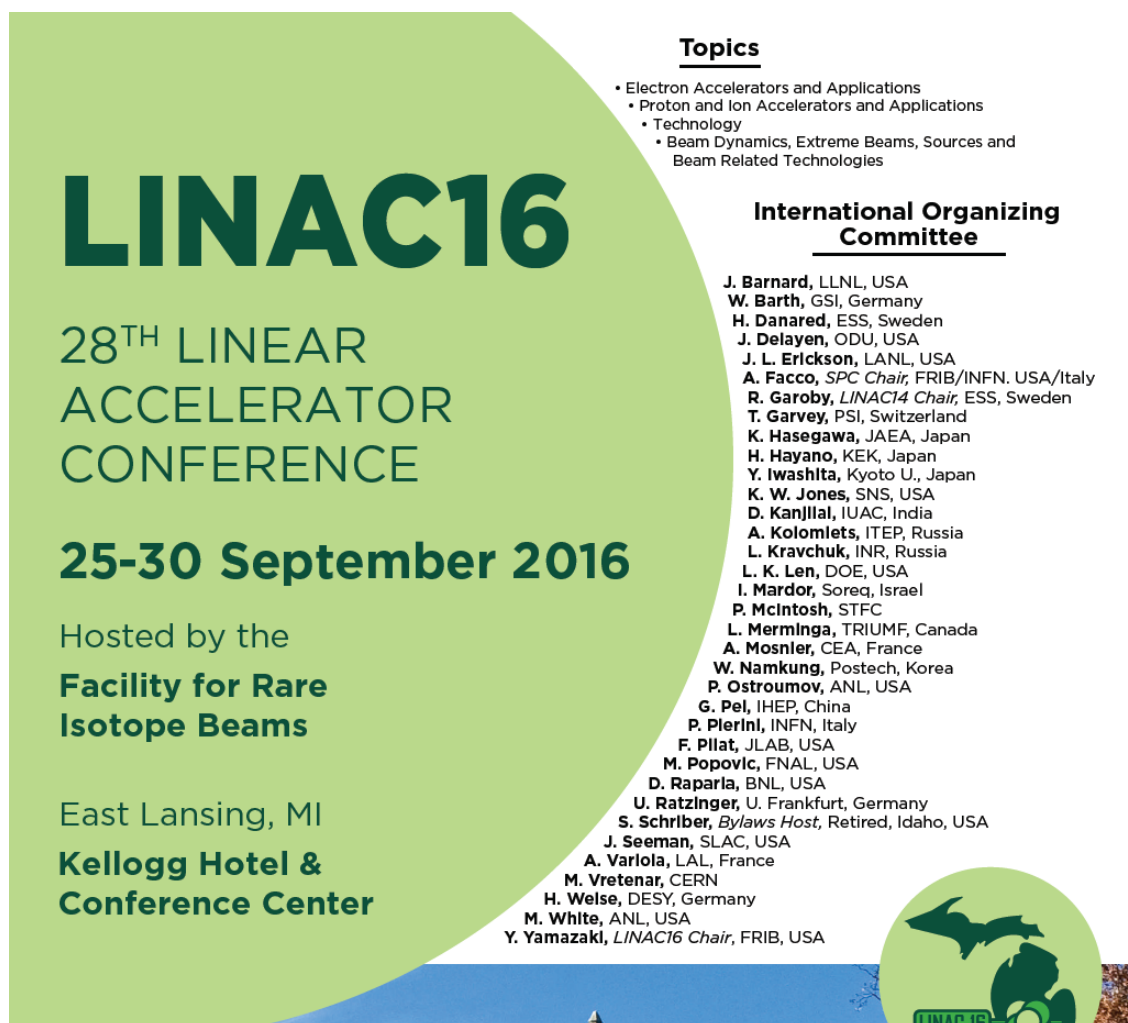
The 28th Linear Accelerator Conference (LINAC 16) hosted by Facility for Rare Isotope Beams (FRIB) took place from 25-30 September at Michigan State University (MSU) located in East Lansing, Michigan, USA. The conference is held biennially and is the largest international conference dedicated to linear accelerators. The last conference (LINAC 14) was hosted by the European Organization for Nuclear Research (CERN) and took place in Geneva, Switzerland, and LINAC 12 was held in Tel-Aviv, Israel. The conference is organized by the International Organizing Committee, chaired by Yoshishige Yamazaki (FRIB, MSU), the scientific program was set up by the Scientific Program Committee, chaired by Alberto Facco (FRIB and INFN), and the Local Organizing Committee was chaired by Yan Zhang (FRIB).

The conference is unique because all of the oral presentations are plenary and the participants are encouraged to stay in the same hotel in order to further continue technical discussions. Four-hundred and twenty delegates attended the conference from seventeen countries. In particular, LINAC 16 supported a significant number of students, who will be soon major players in the LINAC community. The student poster session was scheduled one day before the conference, and more than forty students presented their posters. Among three awarded posters, two are regarding Superconducting RF (SRF) cavities.

The conference started with two invited talks in the opening session, reporting FRIB and European XFEL statuses, followed by four invited talks in the electron linac session. Among these six talks, five were reporting SRF linacs.

FRIB hosted this year's conference partly because FRIB is under construction at the cutting edge of the linac technology. Accordingly, a tour of FRIB was one of the main conference events.

The next conference (LINAC 18) will be hosted by the Institute of High Energy Physics (IHEP) in Beijing, China, and LINAC 20 will take place at Liverpool, UK, to be hosted by Cockcroft Institute.



LINAC16

28TH LINEAR
ACCELERATOR
CONFERENCE

25-30 September 2016

Hosted by the
**Facility for Rare
Isotope Beams**

East Lansing, MI
**Kellogg Hotel &
Conference Center**

Topics

- Electron Accelerators and Applications
- Proton and Ion Accelerators and Applications
- Technology
- Beam Dynamics, Extreme Beams, Sources and Beam Related Technologies

International Organizing Committee

J. Barnard, LLNL, USA
W. Barth, GSI, Germany
H. Danared, ESS, Sweden
J. Delayen, ODU, USA
J. L. Erickson, LANL, USA
A. Facco, *SPC Chair*, FRIB/INFN, USA/Italy
R. Garoby, *LINAC14 Chair*, ESS, Sweden
T. Garvey, PSI, Switzerland
K. Hasegawa, JAEA, Japan
H. Hayano, KEK, Japan
Y. Iwashita, Kyoto U., Japan
K. W. Jones, SNS, USA
D. Kanjilal, IUAC, India
A. Kolomolets, ITEP, Russia
L. Kravchuk, INR, Russia
L. K. Len, DOE, USA
I. Mardor, Soreq, Israel
P. McIntosh, STFC
L. Merminga, TRIUMF, Canada
A. Mosnier, CEA, France
W. Namkung, Postech, Korea
P. Ostroumov, ANL, USA
G. Pei, IHEP, China
P. Pierini, INFN, Italy
F. Pilat, JLAB, USA
M. Popovic, FNAL, USA
D. Rapaia, BNL, USA
U. Ratzinger, U. Frankfurt, Germany
S. Schriber, *Bylaws Host*, Retired, Idaho, USA
J. Seeman, SLAC, USA
A. Variola, LAL, France
M. Vretenar, CERN
H. Welse, DESY, Germany
M. White, ANL, USA
Y. Yamazaki, *LINAC16 Chair*, FRIB, USA

Figure 1: LINAC 16 poster.



Figure 2: Participants of LINAC 16.

3.4 3rd ICFA Mini Workshop on High Order Modes in Superconducting Cavities 2016, HOMSC16

Thomas Flisgen and Ursula van Rienen
 Institute of General Electrical Engineering,
 University of Rostock,
 Albert-Einstein-Str. 2, 18059 Rostock, Germany
 Mail to: Ursula.van-Rienen@uni-rostock.de

High order modes (HOM) excited by the beam in superconducting cavities can create excessive heat load on the cryogenic system and dilute beam quality giving rise to a beam break up instability in the worst case. The objective of HOMSC16 was to bring together researchers studying high order mode suppression in superconducting cavities in the fields ranging from energy recovery linacs, light sources and linear collider applications. The workshop was hosted by the University of Rostock and took place from August 22 to 24, 2016 in Warnemünde at the Baltic Sea. In total, 36 participants representing Asia, Europe and America attended the workshop. HOMSC16 followed HOMSC12 at the Cockcroft Institute, Daresbury, UK and HOMSC14 at Fermilab, Batavia, USA. In order to support young academics, the conference fees of six PhD students were waived. The CST AG / Darmstadt sponsored the workshop and equipped the participants with pens, badges and paper blocks. Additionally, CST AG provided funding for the coffee breaks.

The scientific program of the workshop was generated by the Scientific Program Committee and the Local Organizing Committee (LOC). Both committees were chaired by Ursula van Rienen. She was supported by Thomas Flisgen and Dirk Hecht of the LOC.

During the two and a half days, 24 oral presentations were given. The talks covered a wide range of topics such as HOM-based diagnostics, Numerical Simulation for Superconducting Radio Frequency Cavities, Measurements of HOMs and HOM Damping schemes. Two student sessions were organized in order to give young scientists the opportunity to present their work. Based on the six student talks, the Scientific Organizing Committee awarded the HOMSC16 student prize to Franziska Reimann (University of Rostock) for her contributions to passive wakefield dechirper structures. Moreover, HOMSC16 Scientific Organizing Committee invited two speakers: Johann Heller (University of Rostock) presented his work related to the numerical investigation of external losses in superconducting radio frequency structures. Payagalage Subashini Uddika de Silva (Old Dominion University) gave a talk about HOMs in deflecting and crab cavities. The invitation of both speakers was supported by EuCARD II. Apart from the oral presentations, the delegates had the opportunity to gather in subgroups and to discuss about pending issues. The participants extensively made use of this possibility.

A special highlight of the entire event was the workshop dinner. In order to support the informal character of the workshop, a barbecue party was organized on a terrace with a fantastic view to Warnemünde beach. The delegates used the party to socialize in a pleasant atmosphere.

A detailed program and the talks are available via the workshop website <http://indico.cern.ch/event/465683>, where also some more photos are to be found. All HOMSC16 presenters were invited to submit articles to a Special Edition of the online journal Physical Reviewed Accelerators and Beams.

The poster is titled "International ICFA Mini-Workshop on High Order Modes in SC Cavities" and is held at Rostock-Warnemünde (Germany) at the Baltic Sea coast from August 22-24, 2016. It features logos for Universität Rostock, ICFA, and EuCARD². The poster includes a "General Information and Objectives" section, a "Scientific Programme Committee (SPC)" list with members from various institutions, and a "Local Organising Committee (LOC)" list. It also provides contact information for Thomas Flagen and a URL for further information.

Universität Rostock Traditio et Innovatio

ICFA

EuCARD²

International ICFA Mini-Workshop on
High Order Modes in SC Cavities
Rostock-Warnemünde (Germany) at the Baltic Sea coast | August 22 - 24, 2016

General Information and Objectives
The workshop High Order Modes in Superconducting Cavities 2016 (HOMSC16) will be held on August 22 - 24, 2016 in Rostock-Warnemünde at the Baltic Sea coast. The conference venue will be "Technologiekolonnium Warnemünde". The object of the workshop is to bring together researchers studying high order mode suppression in superconducting cavities. The workshop will discuss the current status of both experimental and theoretical work. HOMSC16 follows HOMSC12 at the Cockcroft Institute, Daresbury, UK, and HOMSC14 at Fermilab, Batavia, USA.

Scientific Programme Committee (SPC)
Gerson Weichert / Cockcroft Institute
Erik Jensen / CERN
Georg Hoffstaetter / Cornell University
Jakob Sekutowicz / SLAC
Jean Delaunay / Old Dominion University
Jeroen Koochich / Helmholtz Zentrum Berlin
John Corlett / Lawrence Berkeley National Laboratory
Matthias Lüse / Cornell University
Nicoleta Baboi / DESY
Nikolay Solovik / Fermilab
Oliver Neppel / CEAS Saclay
Roger Jones / University of Manchester
Ursula van Remen (Chair) / Universität of Rostock
Vyacheslav Yakovlev / Fermilab

Local Organising Committee (LOC)
Ursula van Remen (Chair) / Universität of Rostock
Thomas Flagen / Universität of Rostock
Dirk Hecht / Universität of Rostock

Further Information and Registration
Early Bird Deadline: 25/06/2016
<http://indico.cern.ch/event/465683>
For further information contact:
Thomas Flagen
Universität Rostock, Institut für Allgemeine Elektrotechnik
Albert-Einstein-Str. 2, 18059 Rostock, Germany
Phone: +49 - 381 - 498 - 7044
Email: Thomas.Flagen@uni-rostock.de

Institut für Allgemeine Elektrotechnik | Fakultät für Informatik und Elektrotechnik
Universität Rostock, Albert-Einstein-Str. 2 | 18059 Rostock, Germany

Figure 1: HOMSC16 Workshop poster.

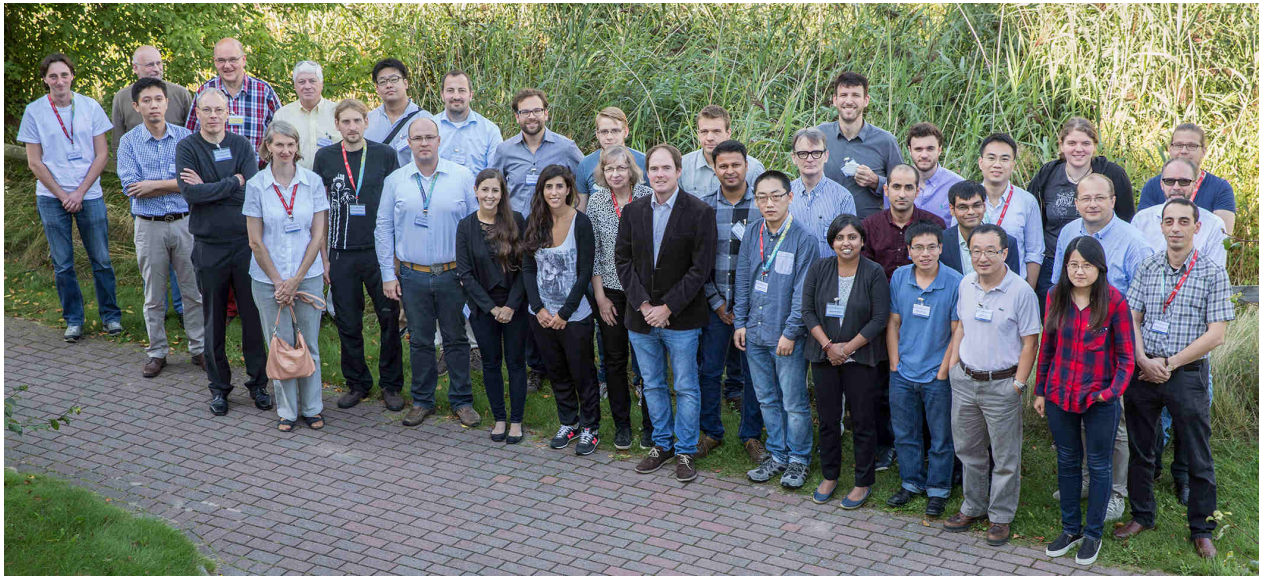


Figure 2: Participants of the HOMSC16 Workshop.

3.5 Workshop on the Frontiers of Intense Beam Physics Modeling

Stephen Webb

RadiaSoft, LLC, Boulder, Colorado, USA

Mail to: swebb@radiasoft.net

On October 3-5, a small workshop was held in Boulder, Colorado to discuss the current code capabilities, future machines, and algorithms. The workshop was sponsored by RadiaSoft, LLC with support from the ICFA Beam Dynamics Panel, and organized by Stephen Webb (RadiaSoft), Oliver Boine-Frankenheim (TU-Darmstadt), Chris Prior (Oxford Univ.), and Jean-Luc Vay (LBNL). The attendees came from across the beam and plasma modeling spectrum, with talks discussing electron and hadron linacs, high space charge rings, algorithms for plasma accelerators, low energy rf modeling, and on. Discussion was lively, with a diversity of perspectives on the topic of self-consistent modeling of beams and plasmas.

Three main questions emerged from our discussions: (1) to what extent can we rely on simulations to predict exact behavior? (2) is it possible to quantify in a meaningful way the non-symplecticity of a simulation? and (3) what does the particle-in-cell picture converge to?

An early discussion in the first day of the workshop was centered on the extent to which we can rely on simulations to predict the exact behavior of a machine. This is an important question for high current hadron machines, where beam halo at even a small fraction of a percent of the beam can cause machine protection issues. The dominant perspective that emerged is that simulations cannot be relied on at the level of precision required to say with certainty what the loss rates will be for two reasons: (1) the simulations themselves only model an approximate machine, and (2) we do not have adequate control over our machines to build the exact machine we set out to build. Instead, we should use simulations to decide whether or not a particular design of a machine is stable, so that when the actual machine deviates from the design machine, the actual machine is at least stable enough for tuning later.

Several of the talks discussed the growing field of symplectic self-consistent algorithms. Talks discussed this in the context of both space charge in conventional linacs and rings and for modeling plasma accelerators. Existing space charge algorithms in existing codes are not all symplectic. Is it possible to quantify the level of non-symplecticity in a meaningful way? Several ideas were discussed, from computing the change in the symplectic two-form due to the algorithm to computing the Jacobian matrix of the algorithm numerically and determining if it satisfies the symplectic condition. The attendees seemed to all agree that quantifying non-symplecticity would be an interesting and important research project. This would be interesting as both a theoretical exercise, and as a practical way of determining cutoffs for when we can no longer rely on the data of a simulation.

During the workshop, there was a talk concerning Vlasov algorithms and quantifying various sources of noise and other numerical artifacts. This talk drew a distinction between three sources of what is colloquially referred to as "PIC noise". There are time discretization errors, field discretization errors, and Monte Carlo or particle statistical noise. The first two are intrinsic to the algorithms, while the third can be adjusted by changing the number of particles used in a PIC simulation. This led to some discussion about what, exactly, the particle-in-cell approach converges to. It was pointed out that it converges neither to Vlasov nor Klimontovich pictures. This is not an issue with direct Vlasov algorithms, which converge to the coupled Maxwell-Vlasov equations. Because PIC does not necessarily converge to either the N-body problem or the fluid limit, we must be careful how we use the approach and how we draw conclusions from the data it produces.

There is a tentative plan to host this workshop again in Europe in two years, with a commitment to bringing together an interdisciplinary group to share new ideas and build collaborations that might not arrive in workshops more focused on a single field. A more detailed summary of the individual talks will be posted on arXiv.

4 Recent Doctorial Theses

4.1 Space Charge Effects and Advanced Modelling for CERN Low Energy Machines

Adrian Oeftiger
CERN, 1211 Geneva 23, Switzerland
Mail to: adrian.oeftiger@cern.ch

Graduation date: 07.12.2016
University: École polytechnique fédérale de Lausanne (Switzerland)
Supervisors: Prof. Rivkin Leonid, Dr. Rumolo Giovanni

Abstract:

The strong space charge regime of future operation of CERN's circular particle accelerators is investigated and mitigation strategies are developed in the framework of the present thesis. The intensity upgrade of the injector chain of Large Hadron Collider (LHC) prepares the particle accelerators to meet the requirements of the High-Luminosity LHC project. Producing the specified characteristics of the future LHC beams imperatively relies on injecting brighter bunches into the Proton Synchrotron Booster (PSB), the downstream Proton Synchrotron (PS) and eventually the Super Proton Synchrotron (SPS). The increased brightness, i.e. bunch intensity per transverse emittance, entails stronger beam self-fields which can lead to harmful interaction with betatron resonances. Possible beam emittance growth and losses as a consequence thereof threaten to degrade the beam brightness. These space charge effects are partly mitigated by the upgrade of the PSB and PS injection energies. Nevertheless, the space charge tune spreads of the future injector beams are found to exceed the values reached by present LHC or other intense fixed target physics beams.

This thesis project comprises three key tasks: detailed modelling of space charge effects, measurement at the CERN machines and mitigation of space charge impact. Throughout the course of this thesis, the simulation tool PyHEADTAIL has been developed and extended to model 3D space charge effects in circular accelerators across the wide energy range from PSB to SPS. The implementation for hardware-accelerating GPU architectures enables extensive studies, especially when employing the self-consistent particle-in-cell algorithm. The implemented models have been benchmarked with analytical results for space charge beam dynamics. In particular, the spectra of quadrupolar pick-ups – which provide a direct measurement method for the space charge tune shift – have been simulated and compared with the derived theory. The space charge situation at the SPS injection plateau has been extensively investigated in the course of comprehensive measurement studies, resulting in the identification of an optimal working point region for the SPS. The interplay of space charge and the horizontal quarter-integer resonance has been scrutinised in measurement, theory and simulation. Last but not least, a new LHC beam type with a hollow longitudinal phase space distribution has been developed for the PSB and proved to substantially mitigate space charge impact on the PS injection plateau.

4.2 Development of a High-Precision Low-Latency Position Feedback System for Single-Pass Beamlines Using Stripline and Cavity Beam Position Monitors

Neven Blaskovic Kraljevic

Mail to: neven.blaskovickraljevic@physics.ox.ac.uk

Graduation date: 16 July 2016
University: University of Oxford, United Kingdom
Supervisors: Prof. Philip Burrows (University of Oxford, United Kingdom)

Abstract:

The FONT beam-based, intra-train feedback system has been designed to provide beam stability at single-pass accelerators, such as at the interaction point (IP) of the International Linear Collider. Two FONT feedback systems have been commissioned at the Accelerator Test Facility (ATF) at KEK, Japan, and the operation, optimisation and performance of these systems is the subject of this thesis. For each system, the accelerator is operated with two-bunch trains with a bunch separation of around 200 ns, allowing the first bunch to be measured and the second bunch to be subsequently corrected.

The first system consists of a coupled-loop system in which two stripline beam position monitors (BPMs) are used to characterise the incoming beam position and angle, and two kickers are used to stabilise the beam. A BPM resolution of about 300 nm has been measured. On operating the feedback system, a factor ~ 3 reduction in position jitter has been demonstrated at the feedback BPMs and the successful propagation of this correction to a witness BPM located 30 m downstream has been confirmed.

The second system makes use of a beam position measurement at the ATF IP that is used to drive a kicker to provide a local correction. The measurement is performed using a high-resolution cavity BPM with a fast decay time of around 20 ns designed to allow multiple bunches to be resolved. The linearity of the cavity BPM system and the noise floor of the electronics are discussed in detail. The performance of the BPM system under standard ATF operation and with the beam waist at the BPM is described. A BPM resolution of about 50 nm has been measured. This IP feedback system has been used to stabilise the beam position to the 75 nm level.

4.3 Beam Measurements of the Longitudinal Impedance of the CERN Super Proton Synchrotron

Alexandre Lasheen

CERN, 1211 Geneva 23, Switzerland

Mail to: alexandre.lasheen@cern.ch

Expected graduation date: 13/01/2017
University: Université Paris-Saclay (France)
Supervisors: Prof. Petrache Costel, Dr. Chapochnikova Elena

Abstract:

One of the main challenges of the future projects in physics based on particle accelerators is the need of high intensity beams. However, collective effects are a major limitation which can deteriorate the beam quality or limit the maximum intensity due to losses. The SPS at CERN, which is the injector for the LHC, is presently not able to deliver the specifications for future projects due to longitudinal instabilities.

The numerous devices in the machine (accelerating RF cavities, injection and extraction magnets, vacuum flanges...) lead to a variation of the geometry of the chamber in which the beam is travelling. The electromagnetic interaction of the beam with its environment, described as a coupling impedance, alters the motion of the particles and eventually leads to instabilities for high intensities. Consequently, the critical impedance sources need to be identified and solutions assessed. To do so, a survey of all the devices was done and their contribution was evaluated from electromagnetic simulations and measurements.

In this thesis, the beam itself is used to probe the machine impedance by measuring its altered motion as a function of intensity. It includes the measurement of the synchrotron frequency shift with intensity and longitudinal emittance, as well as the measurement of the modulation of long bunches in absence of RF voltage. These were compared with particle simulations and demonstrated to be in good agreement. The remaining discrepancies were used to further refine the impedance model.

The next step consisted in testing the ability of the simulation model to reproduce measured instabilities for a single bunch during acceleration, in single and double RF system operation. As measurements and particles simulations were in good agreement, it eventually permitted to better understand which mechanisms were at stake, from microwave instabilities to loss of Landau damping, for proton and ion beams.

Finally, as the simulation model was shown to be trustworthy, it was used to estimate what beam characteristics could be expected in the future with realistic machine upgrades considerations. The outcome of this thesis was the adjustment of the baseline of various projects at CERN, including HL-LHC and AWAKE.

4.4 Studies of Longitudinal Coupled-Bunch Instabilities in the LHC Injectors Chain

Letizia Ventura
CERN, 1211 Geneva 23, Switzerland
Mail to: letizia.ventura@cern.ch

Expected graduation date: February 2017
University: La Sapienza, Università di Roma
Supervisors: Prof. Migliorati Mauro, Dr. Sterbini Guido

Abstract:

Among several challenging objectives of the LHC Injectors Upgrade project, one aim is to double the beam intensity of the CERN Proton Synchrotron (PS) in order to achieve the integrated luminosity target of the High-Luminosity LHC project. A known limitation to reach the required high intensity is caused by the longitudinal coupled-bunch (CB) oscillations developing above the PS transition energy. The unwanted oscillations induce large bunch-to-bunch intensity variations not compatible with the specifications of the future LHC-type beams. In 2014 a new longitudinal kicker cavity has been installed, the Finemet cavity, as a part of the new digital coupled-bunch feedback (FB) system. The

Finemet cavity allows with its large frequency bandwidth, to damp all the expected oscillation modes simultaneously.

In the framework of this PhD study the impedance contribution of this equipment has been analyzed starting from the present knowledge of the machine impedance. A model of both the 10 MHz and the Finemet has been developed as a sum of resonant modes. From simulations it has been possible to show that the 10 MHz system is the main source of instabilities and to confirm that the contribution of the Finemet cavity to the couple-bunch instability is negligible compared to the stronger effect of the 10 MHz cavities.

The complete prototype feedback chain of pick-up, digital processing and Finemet kicker has been installed and commissioned in 2014 and 2015. A dedicated measurement campaign was performed to qualify both the wide-band damper cavity as well as the new digital coupled-bunch low-level RF feedback system. Excitation measurements with FB in open loop showed that the Finemet cavity interacts with the different beam trains as expected and that the coupled-bunch oscillation modes can be individually excited.

An original algorithm has been developed and proposed to analyze the bunch train and to perform the mode analysis of the system in order to study its stability. This approach allows sub-nanosecond detection of the bunch oscillation. Due to the symmetry of the system, for equidistant bunches covering the full azimuthal length of the PS, the eigenmodes of the CB oscillations do not depend upon the machine impedance. In practice this conditions is not verified. In this work we show a numerical approach to define the eigenmodes of the system for a generic impedance and bunch pattern.

Tests during 2016 showed that coupled-bunch oscillations can be damped by the new feedback system up to an intensity of $2 \cdot 10^{11}$ protons per bunch at extraction.

4.5 Fast Luminosity Monitoring Using Diamond Sensors for SuperKEKB

Dima El Khechen

LAL Orsay, France

Mail to: elkheche@lal.in2p3.fr

Expected graduation date: 16 December 2016

Institutions: Laboratoire de l'Accelérateur Lineaire, Orsay (France)

Supervisors: Dr. P. Bambade, Dr. C. Rimbault (LAL)

Abstract:

SuperKEKB is a very high luminosity collider dedicated to the Belle II experiment, it consists of a Low Energy Ring (LER) of 4 GeV positrons and a High Energy Ring (HER) of 7 GeV electrons. The commissioning of this machine is split into three phases: Phase 1 (single-beam phase) is dedicated to vacuum scrubbing, where beams circulate without focusing at the collision point. Phase 2, for which the major part of the Belle II detector will be installed, will enable the tuning of the final focus system to achieve a luminosity of $10^{34} \text{ cm}^{-2}\text{s}^{-1}$. During Phase 3, Belle II physics runs will start with an aimed luminosity up to $8 \times 10^{35} \text{ cm}^{-2}\text{s}^{-1}$. In this context, the aim of the thesis is to develop and install a fast luminosity monitoring system, which is required for on-line correction of beam instabilities and maintenance of optimal luminosity. To reach the aimed relative precision of 10^{-3} in 1 ms, the measurement will be based on the radiative Bhabha process at zero photon scattering angle, whose cross-section is large and well-known. These particles will be detected using

diamond sensors, resistant to radiation and enabling very fast signal acquisition, to be placed outside of the beam-pipe and downstream of the interaction point.

The first part of this work is dedicated to the investigation of the best locations for the diamond sensor positioning in both rings. Using detailed simulations, we studied the dynamics of Bhabha particles during their tracking in the rings and their interaction with the beam pipe material. This led to the identification of two positions, at 11.9 m in LER and at 30 m in HER, and to considering a new geometry for the vacuum pipe in the LER.

The second part is related to the Phase 1 of the SuperKEKB commissioning and concerns the measurements performed with the diamond sensors that were installed. Single beam loss processes (Bremsstrahlung, Touschek, beam-gas Coulomb scattering) were studied in detail with respect to the LER beam and ring parameters (current, pressure, transverse beam sizes). The results of this study were then compared to the data collected from February to June 2016. We found good qualitative and quantitative agreement between our simulations and measurements. From this we could estimate that the level of background to be expected during luminosity monitoring will be two orders of magnitude smaller than the rate of the radiative Bhabha scattering signal.

4.6 Development of Diamond Sensors for Beam Halo and Compton Spectrum Diagnostics after the Interaction Point of ATF2

Shan Liu

Mail to: shan.liu@desy.de

Graduation date: 02 July 2015
Institution: Laboratoire de l'Accélérateur Linéaire (LAL), Orsay, France
Supervisor: Dr. Philip Bambade

Abstract:

The investigation of beam halo transverse distributions is an important issue for beam loss and background control in ATF2 and in Future Linear Colliders (FLC). A novel *in vacuum* diamond sensor (DSv) scanner with four strips has been designed and developed for the investigation of beam halo transverse distributions and also for the diagnostics of Compton recoil electrons after the interaction point (IP) of ATF2, a low energy (1.3 GeV) prototype of the final focus system for ILC and CLIC linear collider projects.

This thesis presents the beam halo and Compton recoil electrons studies as well as the characterization, performance studies and tests of the diamond sensors (DS) both at PHIL, a low energy (<10 MeV) photo-injector at LAL, and at ATF2. First beam halo measurement results using wire scanners (WS) and DSv at ATF2 are also presented and compared in this thesis.

Simulations using Mad-X and CAIN were done to estimate the rate of the beam halo and Compton recoil electrons. Simulation results have indicated that a large dynamic range of more than 10^6 is needed for a simultaneous measurement of the beam core, beam halo and Compton recoil electrons. A single crystalline Chemical Vapor-Deposition (sCVD) based DSv was developed for this purpose.

Prior to the diamond detector installation, first attempt of beam halo measurements have been performed in 2013 using the currently installed WS. With a limited dynamic range of $\sim 10^3$, the beam halo distribution was measured only up to $\sim \pm 6\sigma$ in the extraction (EXT) line. Parameterizations of the measured beam halo distribution showed a consistent distribution

with previous measurements done in 2005 at the old ATF beam line. Meanwhile, an asymmetric vertical beam halo distribution was observed for the first time using the post-IP WS, the origin of which is currently under investigation using the DSv.

Studies to characterize *in air* DS pads with dimensions of $4.5 \times 4.5 \times 0.5$ mm³ were carried out using the α and β sources. Charge carrier transport parameters (lifetime, saturation velocity etc.) were obtained using the transient-current technique (TCT). Furthermore, the linearity of the DS response was tested at PHIL with different beam intensities in air: a maximum signal of 10^8 electrons was measured with a linear response up to 10^7 electrons. Similar linearity studies were done for the DSv at ATF2, where we have successfully demonstrated and confirmed for the first time a dynamic range of $\sim 10^6$ by a simultaneous beam core ($\sim 10^9$) and beam halo ($\sim 10^3$) measurement using the DSv. Present limitations due to signal pick-up and saturation effects, which prevent the DSv from reaching a dynamic range higher than 10^6 , were also studied.

First measurements of the horizontal beam halo distribution using the DSv were performed up to $\pm 20\sigma_x$, where the beam halo was proved to be collimated by the apertures. A consistent horizontal beam halo distribution with the 2005 and 2013 parameterizations was confirmed. The possibility of probing the Compton recoil electrons has been investigated and different ways to increase their visibility have been proposed.

5 Forthcoming Beam Dynamics Events

5.1 59th ICFA Advanced Beam Dynamics workshop on Energy Recovery Linacs (ERL17)

Erk Jensen
CERN, 1211 Geneva 23, Switzerland
Mail to: erl17@cern.ch

We are pleased to announce that the 59th ICFA Advanced Beam Dynamics Workshop on Energy Recovery Linacs (ERL17) will be held at CERN, Geneva, Switzerland from June 18th to 23rd, 2017. This will be the 7th in the series of international workshops covering accelerator physics, technology and applications of Energy Recovery Linacs. The workshop will serve as a forum for scientists and engineers from around the world to review the latest developments in ERL physics, technologies and applications, to exchange ideas and to discuss “hot topics” of this field of research. Among the issues to be addressed are: beam stability in multi-pass ERLs, design of photoemission electron injectors, superconducting RF systems, beam optics, instrumentation, alignment, emittance requirements and test facilities. The talks will cover commissioning and operations experience, ERL applications and status presentations from different projects. Proceedings will be published on JACoW.

Workshop organizers:

Erk Jensen (erk.jensen@cern.ch), IOC Chair
Oliver Brüning (oliver.bruning@cern.ch), SPC Chair
Laurie Hemery (laurie.hemery@cern.ch), LOC Chair

Registration and abstract submission will open on 9 January 2017.

Details of the workshop are available at: www.cern.ch/ERL17.

5.2 International Conference on RF Superconductivity (SRF2017)

Jens Knobloch
Institute of SRF Science and Technology Helmholtz-Zentrum, Berlin, Germany
Mail to: jens.knobloch@helmholtz-berlin.de

The 18th conference in this series will take place from July 17 – 21, 2017 in Lanzhou, China. Every two years, the SRF conference provides a platform for scientists, engineers, students, and industrial partners to present and discuss the latest developments in the science and technology of superconducting RF systems for particle accelerator applications.

The International Conference on RF Superconductivity was first established as a workshop in 1980, when it was hosted by Kernforschungszentrum Karlsruhe, Germany. As RF superconductivity in accelerators has matured, the conference attendance has also grown dramatically. At the most recent events in Whistler, Canada (2015) and Paris, France (2013) about 350 delegates were registered.

The 2017 Conference will be hosted by the Institute of Modern Physics at the International Conference Center of Lanzhou University. The program covers a combination of fundamental research and technical aspects. It includes new SRF accelerator projects and

their challenges, novel cavity designs for a wide variety of accelerator applications, cavity fabrication and processing techniques, as well as fundamental developments and new materials for SRF to push beyond the state of the art. The format consists of plenary invited talks, poster sessions and several “hot topic” discussion sessions. Importantly, the conference includes three days of tutorials prior to the main program for newcomers to the field (July 14–16) to provide a solid foundation on subjects as varied as superconductivity, cavity design techniques, RF loss mechanisms and cryogenic systems.

Lanzhou, located in the heart of China, is a charming city on the Yellow River featuring a long history and fascinating culture. For 2,000 years it was an important landmark on the Silk Road which played a crucial role in connecting the East and the West. The Institute of Modern Physics is located in the immediate vicinity of the conference site. It operates the largest heavy ion accelerator facility and high-power superconducting proton Linac in China and delegates will be given a chance to tour the facility. Several cultural events round off the program of what is guaranteed to be an exciting week.

The conference web site can be found at <http://srf2017.csp.escience.cn>.

5.3 Advanced and Novel Accelerators for High Energy Physics Roadmap Workshop 2017 (ANARW2017)

Brigitte Cros

Laboratoire de Physique des Gaz et Plasmas, Université Paris-Sud, France

Mail to: brigitte.cros@u-psud.fr

The ANARW2017 will take place from April 25 to 28, 2017 at CERN.

Organized at the initiative of the ICFA panel for Advanced and Novel Accelerators (<http://www.lpgp.u-psud.fr/icfaana>), the ANARW2017 aims at discussing issues to be addressed in the near future to be in a position to identify promising technologies for future advanced accelerators, and to establish an international scientific and strategic roadmap. The general goal is to define an international roadmap toward colliders based on advanced accelerator concepts, including intermediate milestones, and to discuss the needs for international coordination.

The workshop is open to the scientific community at large. It is organized around working groups that will examine the various schemes that are currently under active investigation as well as those that need to be addressed in the near- mid- and long-term to reach parameters relevant to a high-energy collider.

The last part of the workshop will be dedicated to discussion of the working group results and to the strategy to push forward the development of advanced accelerators in the context of the next international project at the TeV scale.

The program and useful information can be found at the workshop website:

<https://indico.cern.ch/event/569406/>.

5.4 International Conference on Accelerators and Large Experimental Physics Control Systems (ICALEPCS2017)

David Fernández
ALBA, Barcelona, Spain
Mail to: icalepcs17-chair@cells.es

The 16th International Conference on Accelerator and Large Experimental Control Systems (ICALEPCS 2017) will take place at the Palau de Congressos de Catalunya in Barcelona, Spain, from the 8th to the 13th of October 2017 and will be hosted by the ALBA Synchrotron.

The conference takes place every two years with the most recent events being held in Melbourne / Australia (2015) and San Francisco / United States (2013).

The ICALEPCS series of conferences is intended to:

- Provide a forum for the interchange of ideas and information between control system specialists working on large experimental physics facilities around the world (accelerators, particle detectors, fusion reactors, telescopes, etc.);
- Create an archival literature of developments and progress in this rapidly changing discipline;
- Promote, where practical, standardization in both hardware and software;
- Promote collaboration between laboratories, institutes and industry.

The program covers the hardware and software technologies of the complex control and data acquisition systems, including a wide number of aspects from the user experience, machine protection, data management, timing and synchronization to the project and service management of the operational installations. The list of topics can be consulted at the conference website: <http://icalepcs2017.org>, which will be regularly updated to include the latest information as it becomes available.

Barcelona, the capital of Catalonia, is one of the major Mediterranean cities and the second largest city in Spain. There are many reasons which explain why it has attracted visitors from all over the world for many years. There are many places, architecture, districts and artworks to be explored: the old town with Roman walls, the gothic district with palaces and churches from the 16th, 17th and 18th centuries, the well-structured Eixample district, the heart of Modernism, and the new Olympic Barcelona. The synchrotron ALBA is located about 25 km from the venue and the participants will have the opportunity to visit the facilities.

5.5 Workshop on the “Status of Accelerator Driven Systems Research and Technology Development”

Giulia Bellodi
CERN, 1211 Geneva 23, Switzerland
Mail to: Giulia.Bellodi@cern.ch

It is our pleasure to announce a workshop on the “Status of Accelerator Driven Systems Research and Technology Development”, organized in the framework of the EuCARD2 WP4 (Accelerator Applications) activities.

The workshop will take place at CERN (Geneva) on February 7-9, 2017 with the aim to give a critical overview of the current state of the art of ADS programmes, addressing in particular subjects like:

- Critical aspects for operation in accelerators
- Accelerator-target interface challenges
- Status of ADS programmes around the world
- ADS coupling experiments
- Social and economic perspective of ADS
- Lessons learned and future R&D

[AccApplic](#) is a networking activity with the funded EUCARD2 European project on particle accelerators, addressing the applied areas of industry, healthcare, energy production and security. Amongst its objectives is to "determine the requirements for high power accelerator applications, in particular for Accelerator Driven Systems (ADS)".

The website of the workshop is now available in [Indico](#), along with registration details and important practical information.

We are presently in the process of defining the programme, and more details of the invited talks will be communicated soon. Please check the website for regular updates.

We invite you to attend and contribute actively to the workshop, and we would be very grateful if you could forward this announcement to all potentially interested colleagues.

5.6 ICFA Mini-Workshop on Impedances and Beam Instabilities in Particle Accelerators

Stefania Petracca (University of Sannio, Benevento, Italy)
and Giovanni Rumolo (CERN, 1211 Geneva 23, Switzerland)
Mail to: Petracca@unisannio.it

On behalf of the Organizing Committee, we are pleased to announce the *ICFA Mini-Workshop on Impedances and Beam Instabilities in Particle Accelerators*, to be held in Benevento (Italy) from September 19 to 22, 2017.

The workshop continues the tradition of dedicated conferences on beam coupling impedances, initiated with the 2014 ICFA Mini-Workshop on "Electromagnetic Wake Fields and Impedances in Particle Accelerators" held in Erice, organized by Vittorio Vaccaro, Iaia Masullo (INFN Naples) and Elias Métral (CERN). The aim of the new 2017 edition is to present an up-to-date review of the subject, and widen its scope to include recent advances on beam instabilities.

The workshop will be hosted by the University of Sannio at Benevento, under the auspices of INFN, SIF and CERN. Benevento is a world heritage city in Southern Italy, where you will find remarkable monuments and fine pieces of arts, in a unique cultural and natural environment. Benevento is easily reached (two hours from Rome by train, one hour from Naples airport, by bus). The conference venue is in the heart of the city center, in a short walking distance from all attractions, Hotels and Restaurants.

For more information, visit the workshop webpage <http://workshopwakefields.weebly.com>, which will be regularly updated to include the latest information, as it becomes available.

For any questions please contact: imped2017@unisannio.it

We look very much forward to welcoming you in Benevento, to contribute to a stimulating and memorable workshop!

5.7 International Beam Instrumentation Conference (IBIC 17)

Steve Lidia
 Facility for Rare Isotope Beams, East Lansing, MI, USA
 Mail to: lidia@frib.msu.edu

The 6th conference in this series will take place from 20-24 August, 2017 in Grand Rapids, Michigan. IBIC is a fruitful and successful gathering of the world's beam instrumentation community and it reflects the maturity of international collaboration in the field of beam instrumentation for accelerators. IBIC merged in 2012 from the Beam Instrumentation Workshop (BIW) and Diagnostics and Instrumentation for Particle Accelerators Conference (DIPAC) series.

IBIC is dedicated to exploring the physics and engineering challenges of beam diagnostic and measurement techniques for particle accelerators worldwide. The conference program will include tutorials, invited and selected talks, as well as poster sessions. An industrial exhibition and a tour to the Facility for Rare Isotope Beams (FRIB) will also be included.

IBIC 17 is hosted by the Facility for Rare Isotope Beams (FRIB) which is scheduled for completion in 2022. FRIB will be a scientific user facility for the Office of Nuclear Physics in the U.S. Department of Energy Office of Science (DOE-SC) and is funded by the DOE-SC, Michigan State University (MSU) and the State of Michigan. Supporting the mission of the Office of Nuclear Physics in the DOE-SC, FRIB will enable scientists to make discoveries about the properties of rare isotopes, nuclear astrophysics, fundamental interactions, and applications for society, including in medicine, homeland security, and industry.

Grand Rapids, the second largest city in Michigan, is located on the Grand River about 30 miles east of Lake Michigan. An international airport, regional train service from Chicago, and local bus routes serve the conference venue and local attractions. The conference website <http://indico.fnal.gov/event/ibic2017> will be updated regularly to include the latest information as it becomes available.

5.8 ICFA Mini-Workshop on “Beam Dynamics meets Vacuum, Collimations, and Surfaces”

Cristina Bellachioma (GSI, Darmstadt, Germany), Sara Casalbuoni (KIT IBPT, Karlsruhe, Germany) and Giuliano Franchetti (GSI, Darmstadt, Germany)
 Mail to: G.Franchetti@gsi.de

The ICFA Mini-Workshop on "Beam Dynamics meets Vacuum, Collimations, and Surfaces" is scheduled on 8-10th March 2017 at Karlsruhe, Germany.

This workshop is an XRING event. EuCARD-2 is an Integrating Activity Project for coordinated Research and Development on Particle Accelerators, co-funded by the European Commission under the FP7 Capacities Programme; see <http://cern.ch/eucard-2>. “Extreme Rings” (XRING) is a networking task of EuCARD-2 Work Package 5” Extreme Beams” (XBEAM; <http://cern.ch/xbeam>), targeted at creating synergies between different accelerator communities in order to enhance accelerator R&D at the forefront of global research.

The 2017 workshop "Beam Dynamics meets Vacuum, Collimations, and Surfaces" follows earlier successful XRING events. The purpose of the workshop is to bring together

in the same place experts of beam dynamics, vacuum, collimation, and surfaces. All these disciplines are together forming the foundation of present accelerators, although each of them is a science of its own. The interplay of these areas of R&D as well as the interaction of particles with surfaces is complex. Sometimes the lack of proper communications due to unavoidable jargons and conceptual distances makes the working together more difficult. The workshop is constructed to overcome barriers, prejudices, and it is a good occasion to highlight open issues and unsolved controversies. The Karlsruhe Institute of Technology (KIT) hosts the XRING and jointly with the University provides the venue for the workshop.

All details of the workshop are available on the web page, which will be regularly updated: <https://indico.gsi.de/conferenceDisplay.py?confId=5393>.

5.9 8th International Particle Accelerator Conference, IPAC'17, Copenhagen, Denmark, 14-19 May 2017

Gianluigi Arduini
CERN, 1211 Geneva 23, Switzerland
Mail to: Gianluigi.Arduini@cern.ch

The 8th International Particle Accelerator Conference, IPAC'17, will take place at the Bella Center Copenhagen, Denmark, from May 14 – 19, 2017. IPAC is the main annual event for the worldwide accelerator community and industry, with presentations of the latest results from accelerator R&D and on the progress in existing, planned and future accelerator facilities.

Copenhagen has long been an attractive destination, largely due to the city's location as a Scandinavian hub, unique combination of architecture, exquisite gastronomic experiences and characteristic Scandinavian design. The world has also discovered Copenhagen's potential as a meeting place, placing it among the top 10 congress and convention cities in Europe. With streamlined infrastructure, excellent service and a wealth of modern venues, Copenhagen offers everything it takes for a successful conference. On top of all that, Denmark was ranked (again) number 1 in the list of the world's happiest countries, according to the UN World Happiness Report 2016.

IPAC'17 is hosted by the European Spallation Source ERIC (Lund, Sweden) and supported by both MAX IV (Lund, Sweden) and Aarhus University (Denmark).

The ESS construction site and MAX IV are within a one-hour ride of the conference venue. Tours to visit both facilities will be offered. Aarhus University offers a tour to the ISA high brilliance synchrotron storage ring, ASTRID2.

<https://ipac17.org/>.

5.10 Future Circular Collider Week 2017

Michael Benedikt and Frank Zimmermann
CERN, 1211 Geneva 23, Switzerland
Mail to: Michael.Benedikt@cern.ch

Initiated by the 2013 Update of the European Strategy for Particle Physics, the Future Circular Collider (FCC) study – <http://cern.ch/fcc> – is developing various options for a

post-LHC research infrastructure. The primary focus of the FCC study is the design of a 100 TeV proton-proton collider housed in a new 100 km tunnel. The FCC study also includes a high-luminosity electron-positron collider (FCC-ee), with a range of c.m. energies between 90 and 360 GeV – serving as Z, W, Higgs and top factory – as a potential intermediate step. In addition, a lepton-hadron collider option (FCC-he) is being explored, whose 60 GeV electrons would come from an Energy Recovery Linac. The FCC study finally comprises an energy upgrade of the LHC, the so-called High-Energy LHC (HE-LHC), which would be realized by installing the FCC-hh's 16 Tesla magnets in the existing LHC tunnel

Over the past two years the FCC Collaboration has grown to a worldwide community with about 100 institutes from 30 countries. To share the latest results, to advance the vision of a circular post-LHC particle-collider research infrastructure and to strengthen our links and communication, we are preparing the next collaboration week.

The Future Circular Collider Week 2017 will take place in Berlin, Germany from 29 May to 2 June 2017. The meeting is jointly organized by CERN and DESY, with co-sponsorships from the HORIZON2020 programme of the European Commission (EuroCirCol Project), the German Physical Society, and IEEE.

The scientific program will be complemented by public engagement activities and by opportunities for leading high-tech companies to put their visionary R&D on show.

The FCC Week 2017 will conduct a major review of the study, discuss the possible impact of latest LHC Run 2 results, and allow for scientific exchanges between new and older members of the FCC collaboration. The associated FCC research efforts will culminate in a Conceptual Design Report (CDR) by 2019.

Further continually updated information is available on the conference web site

<http://fccw2017.web.cern.ch>

Registration and abstract submission are open. Hotels may be booked at preferred rates. Participants can apply for the *FCC Innovation Award* via a poster submission. We are also excited to offer, together with the IEEE, limited travel support to attend the conference for traditionally underrepresented groups in STEM, through the *FCC Accelerating Diversity Prize*. Please kindly note the deadlines 12 December 2016 for early abstract submission, and 2 February 2017 for late abstract submission.

We are looking forward to seeing you in Berlin!

5.11 CLIC Workshop 2017

The CLIC Workshop 2017 will be held from Monday 6th to Friday 10th March 2017 at CERN, in Geneva, Switzerland. This is the 11th event in a series started in 2007 and taking place every year at CERN. It is dedicated to design and physics of the Compact Linear Collider (CLIC) study of an electron/positron collider with multi-TeV energy reach.

The CLIC Workshop covers Accelerator as well as the Detector and Physics studies, with its present status and programme for the coming years. For the Accelerator studies, the workshop spans over 5 days: 6th - 10th of March. For CLIC Detector and Physics, the workshop is scheduled from Tuesday afternoon 7th to lunchtime on Friday 10th. The Scientific Programme includes an open plenary session giving an overview of the CLIC project (accelerator, physics/detector), placed in the context of LHC results and addressing

the use of CLIC-related developments in other applications, as well as a session covering High-Efficiency RF Power sources developments for CLIC and for other accelerator applications, e.g., ESS, FCC and high-power electron and proton linacs.

We are looking for the widest possible participation and encourage in particular the involvement of young colleagues. The workshop website

<https://indico.cern.ch/event/577810/>

will be regularly updated to include the latest information as it becomes available.

Roberto Corsini – CERN, on behalf of Philip Burrows, Lucie Linssen and Steinar Stapnes, CLIC Workshop Chairpersons.

6 Announcements of the Beam Dynamics Panel

6.1 ICFA Beam Dynamics Newsletter

6.1.1 Aim of the Newsletter

The ICFA Beam Dynamics Newsletter is intended as a channel for describing unsolved problems and highlighting important ongoing works, and not as a substitute for journal articles and conference proceedings that usually describe completed work. It is published by the ICFA Beam Dynamics Panel, one of whose missions is to encourage international collaboration in beam dynamics.

Normally it is published every April, August and December. The deadlines are 15 March, 15 July and 15 November, respectively.

6.1.2 Categories of Articles

The categories of articles in the newsletter are the following:

1. Announcements from the panel.
2. Reports of beam dynamics activity of a group.
3. Reports on workshops, meetings and other events related to beam dynamics.
4. Announcements of future beam dynamics-related international workshops and meetings.
5. Those who want to use newsletter to announce their workshops are welcome to do so. Articles should typically fit within half a page and include descriptions of the subject, date, place, Web site and other contact information.
6. Review of beam dynamics problems: This is a place to bring attention to unsolved problems and should not be used to report completed work. Clear and short highlights on the problem are encouraged.
7. Letters to the editor: a forum open to everyone. Anybody can express his/her opinion on the beam dynamics and related activities, by sending it to one of the editors. The editors reserve the right to reject contributions they judge to be inappropriate, although they have rarely had cause to do so.

The editors may request an article following a recommendation by panel members. However anyone who wishes to submit an article is strongly encouraged to contact any Beam Dynamics Panel member before starting to write.

6.1.3 How to Prepare a Manuscript

Before starting to write, authors should download the template in Microsoft Word format from the Beam Dynamics Panel web site:

<http://icfa-bd.kek.jp/icfabd/news.html>

It will be much easier to guarantee acceptance of the article if the template is used and

the instructions included in it are respected. The template and instructions are expected to evolve with time so please make sure always to use the latest versions.

The final Microsoft Word file should be sent to one of the editors, preferably the issue editor, by email.

The editors regret that LaTeX files can no longer be accepted: a majority of contributors now prefer Word and we simply do not have the resources to make the conversions that would be needed. Contributions received in LaTeX will now be returned to the authors for re-formatting.

In cases where an article is composed entirely of straightforward prose (no equations, figures, tables, special symbols, etc.) contributions received in the form of plain text files may be accepted at the discretion of the issue editor.

Each article should include the title, authors' names, affiliations and e-mail addresses.

6.1.4 Distribution

A complete archive of issues of this newsletter from 1995 to the latest issue is available at

<http://icfa-usa.jlab.org/archive/newsletter.shtml>.

This is now intended as the primary method of distribution of the newsletter.

Readers are encouraged to sign-up for electronic mailing list to ensure that they will hear immediately when a new issue is published.

The Panel's Web site provides access to the Newsletters, information about future and past workshops, and other information useful to accelerator physicists. There are links to pages of information of local interest for each of the three ICFA areas.

Printed copies of the ICFA Beam Dynamics Newsletters are also distributed (generally some time after the Web edition appears) through the following distributors:

John Byrd	jmbyrd@lbl.gov	North and South Americas
Rainer Wanzenberg	rainer.wanzenberg@desy.de	Europe++ and Africa
Toshiyuki Okugi	toshiyuki.okugi@kek.jp	Asia**and Pacific

++ Including former Soviet Union.

** For Mainland China, Jiu-Qing Wang (wangjq@mail.ihep.ac.cn) takes care of the distribution with Ms. Su Ping, Secretariat of PASC, P.O. Box 918, Beijing 100039, China.

To keep costs down (remember that the Panel has no budget of its own) readers are encouraged to use the Web as much as possible. In particular, if you receive a paper copy that you no longer require, please inform the appropriate distributor.

6.1.5 Regular Correspondents

The Beam Dynamics Newsletter particularly encourages contributions from smaller institutions and countries where the accelerator physics community is small. Since it is impossible for the editors and panel members to survey all beam dynamics activity worldwide, we have some Regular Correspondents. They are expected to find interesting activities and appropriate persons to report them and/or report them by themselves. We hope that we will have a "compact and complete" list covering all over the world eventually. The present Regular Correspondents are as follows:

Liu Lin
Sameen Ahmed Khan

Liu@ns.inls.br
Rohelakan@yahoo.com

LNLS Brazil
SCOT, Middle East and Africa

We are calling for more volunteers as Regular Correspondents.

6.2 ICFA Beam Dynamics Panel Members

Name	eMail	Institution
Rick Baartman	baartman@lin12.triumf.ca	TRIUMF, 4004 Wesbrook Mall, Vancouver, BC, V6T 2A3, Canada
Marica Biagini	marica.biagini@lnf.infn.it	INFN-LNF, Via E. Fermi 40, C.P. 13, Frascati, Italy
John Byrd	jmbyrd@lbl.gov	Center for Beam Physics, LBL, 1 Cyclotron Road, Berkeley, CA 94720-8211, U.S.A.
Yunhai Cai	yunhai@slac.stanford.edu	SLAC, 2575 Sand Hill Road, MS 54 Menlo Park, CA 94025, U.S.A.
Swapan Chattopadhyay	swapan@fnal.gov	Northern Illinois University, Dept. of Physics, DeKalb, Illinois, 60115, U.S.A.
Yong Ho Chin	yongho.chin@kek.jp	KEK, 1-1 Oho, Tsukuba-shi, Ibaraki-ken, 305-0801, Japan
Yoshihiro Funakoshi	yoshihiro.funakoshi@kek.jp	KEK, 1-1 Oho, Tsukuba-shi, Ibaraki-ken, 305-0801, Japan
Jie Gao	gaoj@ihep.ac.cn	Institute for High Energy Physics, Yuquan Road 19, Beijing 100049, China
Ajay Ghodke	ghodke@cat.ernet.in	RRCAT, ADL Bldg. Indore, Madhya Pradesh, 452 013, India
Ingo Hofmann	i.hofmann@gsi.de	High Current Beam Physics, GSI Darmstadt, Planckstr. 1, 64291 Darmstadt, Germany
Sergei Ivanov	sergey.ivanov@ihep.ru	Institute for High Energy Physics of National Research Centre "Kurchatov Institute", Protvino, Moscow Region, 142281 Russia
In Soo Ko	isko@postech.ac.kr	Pohang Accelerator Lab, San 31, Hyoja-Dong, Pohang 790-784, South Korea
Elias Metral	elias.metral@cern.ch	CERN, CH-1211, Geneva 23, Switzerland
Yoshiharu Mori	mori@rri.kyoto-u.ac.jp	Research Reactor Inst., Kyoto Univ. Kumatori, Osaka, 590-0494, Japan
George Neil	neil@jlab.org	TJNAF, 12000 Jefferson Ave., Suite 21, Newport News, VA 23606, U.S.A.
Toshiyuki Okugi	toshiyuki.okugi@kek.jp	KEK, 1-1 Oho, Tsukuba-shi, Ibaraki-ken, 305-0801, Japan
Mark Palmer	mpalmer@bnl.gov	Brookhaven National Lab, Upton, NY 11973, U.S.A.
Chris Prior	chris.prior@stfc.ac.uk	ISIS Accelerator Division, STFC Rutherford Appleton Laboratory, Harwell Campus, Chilton, Didcot, Oxon OX11 0QX, U.K.
Yuri Shatunov	Yu.M.Shatunov@inp.nsk.su	Acad. Lavrentiev, Prospect 11, 630090 Novosibirsk, Russia
Jiu-Qing Wang	wangjq@ihep.ac.cn	Institute for High Energy Physics, 19B YuquanLu, Shijingshan District, Beijing 100049, China
Rainer Wanzenberg	rainer.wanzenberg@desy.de	DESY, Notkestrasse 85, 22603 Hamburg, Germany

*The views expressed in this newsletter do not necessarily coincide with those of the editors.
The individual authors are responsible for their text.*